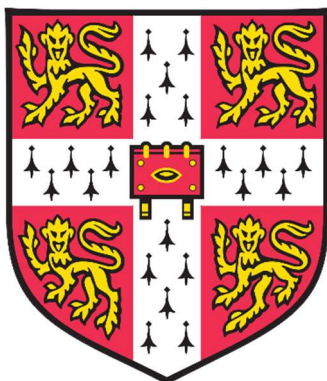


The Development of Hybrid Liquids and Glasses

Louis Michael David Longley



University of Cambridge

Department of Materials Science and Metallurgy

Fitzwilliam College

THE DISSERTATION IS SUBMITTED FOR THE DEGREE OF DOCTOR OF PHILOSOPHY

MAY 2021

Declaration

This dissertation is submitted for the degree of Doctor of Philosophy at the University of Cambridge. The experimental work described within it was carried out at the Department of Materials Science and Metallurgy at the University of Cambridge, the Diamond Light Source Synchrotron Facility and the ISIS Neutron and Muon Source between October 2017 and April 2021. The supervisor for this work was Dr Thomas D. Bennett. This thesis is the result of my own work and contains nothing which is the work of other researchers outside of that declared in this preface and in the body of the text. It is not substantially the same as any work that I have submitted or is being currently submitted for a degree, diploma or other qualification at the University of Cambridge or any other academic institution except where stated in the text. I further state that it is not substantially the same as any work that has already been submitted for a degree of other qualification at the University of Cambridge or at any other university.

It does not exceed the word limit stated by the Degree Committee for the Faculty of Physics and Chemistry.

Parts of this dissertation have already been published:

J. Zhang et al., "Structural evolution in a melt-quenched zeolitic imidazolate framework glass during heat-treatment," *Chem. Commun.*, vol. 55, no. 17, pp. 2521–2524, 2019. (Chapter 4)

C. Zhou et al., "Thermodynamic features and enthalpy relaxation in a metal–organic framework glass," *Phys. Chem. Chem. Phys.*, vol. 20, no. 27, pp. 18291–18296, 2018. (Chapter 4)

L. Longley et al., "Liquid phase blending of metal-organic frameworks," *Nat. Commun.*, vol. 9, no. 1, p. 2135, 2018. (Chapter 5)

L. Longley et al., "Flux melting of metal–organic frameworks," *Chem. Sci.*, vol. 10, no. 12, pp. 3592–3601, 2019. (Chapter 5)

C. Zhou et al., "Metal-organic framework glasses with permanent accessible porosity," *Nat. Commun.*, vol. 9, no. 1, p. 5042, 2018. (Chapter 5)

L. Longley et al., "Metal-organic framework and inorganic glass composites," *Nat. Commun.*, vol. 11, no. 1, p. 5800, 2020. (Chapter 6)

L. Longley et al., "The reactivity of an inorganic glass melt with ZIF-8," *Dalt. Trans.*, vol. 50, no. 10, pp. 3529–3535, 2021. (Chapter 7)

Abstract: The Development of Hybrid Liquids and Glasses

Louis Michael David Longley

Metal-organic framework (MOF) glasses are amorphous materials formed by heating a crystalline MOF into the liquid phase and then cooling to form an amorphous solid material. The hybrid nature, defined here as materials containing both inorganic and organic bonding, of MOF glasses makes them distinct from previous glass families which have inorganic, organic, or metallic bonding. Most of the work on MOF glasses reported in the literature has focused on a sub-set of MOFs known as Zeolitic Imidazolate Frameworks (ZIFs).

This work begins with a discussion of the structure of MOF glasses, particularly focusing on structure occurring beyond the first metal-metal correlation, also termed mid-range order. The observed mid-range order in MOF glasses, measured by X-ray total-scattering, is interpreted using existing theory for inorganic glasses.

The number of MOFs which form liquids on heating is small relative to the total number of known crystalline MOF structures due to decomposition of the framework occurring before melting in most cases. This work therefore takes an alternative approach to expanding the MOF glass domain through exploitation of the reactivity of the liquid phase as a route to the synthesis of new glass structures. 'Complex' glasses formed from two parent MOF crystals heated into the liquid phase were synthesised, and their structures investigated by a variety of techniques, including x-ray total-scattering, differential scanning calorimetry, and electron microscopy.

Following this work the scope of MOF glasses was further expanded through the production of composite materials of MOF and inorganic phosphate glasses. The structures and properties of these materials were also investigated thoroughly with attention being given to the interaction occurring at the interface between the two highly dissimilar components. Finally, as an extension of this, the interaction between a phosphate glass and a crystalline ZIF was investigated to probe the potential for inorganic glass crystalline MOF composite formation.

Acknowledgments

The sciences have always been a collaborative. The success of any scientific endeavour depends not only on the brilliance of the idea, or the work ethic of the individual, but also crucially on the material conditions of the society that undertakes it. Scientific research, especially modern research, can only occur in a society that is sufficiently advanced that it is able to and willing to support the work of large teams of people for long periods of time. Equally, the speed of scientific research would be vastly slower if not for the ease with which we can communicate with and collaborate with our fellow researchers around the world. In this way although papers, patents and theses represent proximally the principal work of one person or a small number of people, distally they represent the common treasury of the society from which they sprung.

For this reason, it is difficult to be fully complete in any list of acknowledgments. That said I would like to start with thanking the Engineering and Physical Sciences Research Council for their studentship. I would also like to thank Diamond Light Source and the Rutherford Appleton Laboratory for access to their facilities.

Naturally I would also like to thank my supervisor Dr Thomas D. Bennett for his support, experience, and advice. I will never forget the lessons that he has taught me over the course of my studentship with him. Extending out from this I would also like to thank all members of the hybrid materials group, past and present, for their support. It is impossible to quantify the amount one has learnt from casual conversations over coffee or gleaned from a work review during a group meeting. Specifically, I would like to single out Christopher W. Ashling, my fellow PhD student, for his support during our shared tribulations.

During my PhD I have had the fortune to work with many collaborators in different fields. I would like to extend a special thanks to Prof. David A. Keen (ISIS Neutron Source) for lending me his expertise in X-ray total-scattering, a technique which has proved invaluable to my research. Equally I am deeply grateful for my collaboration with the electron microscopy group at the department of materials science, without which my research and specifically my knowledge of the microstructure of my composite samples would be immeasurably worse. In this regard I would like to thank Dr Sean M. Collins for his detailed and skilful TEM and EDS work.

My collaboration with the Otto Schott institute of materials research was one of the most academically fruitful relationships of my PhD. It exposed me to a world of glass science research that I had been previously only dimly aware of and vastly improved the 'glass' half of my work on MOF glasses. Therefore, I would like to thank Prof. Lothar Wondraczek for his gracious hosting of me during my stay

in Jena. I would also like to extend special thanks to Dr Courtney Calahoo, who worked very closely with me over the course of my PhD. I cannot express the degree to which my science has been improved due to her input.

Finally, I would like to extend a set of personal thanks. To my parents Sean and Michaela for all their love and support and to Kiera, my sister, without whom life would be much duller. I would also like to thank Katherine Armstrong without whom I would have failed countless times.

Contents

Chapter 1: Introduction	1
1.1 <i>Metal-organic frameworks</i>	1
1.1.1 Metal-Organic Framework Structure	1
1.1.2 The Development of Metal-Organic Framework Synthesis and Design	2
1.1.3 Applications of Metal-organic Frameworks	7
1.2 <i>Glasses</i>	10
1.2.1 Glass Terminology.....	10
1.2.2 Glass Structures	10
1.2.3 The Glass Transition	12
1.2.4 Applications of Glass Science	15
1.3 <i>Aims</i>	16
Chapter 2: A Review of the Literature on Metal-organic Framework Glasses.....	17
2.1 <i>Introduction</i>	17
2.2 <i>Zeolitic Imidazolate Frameworks</i>	19
2.2.1 Structure of Zeolitic Imidazolate Frameworks	19
2.2.2 Physical Properties of Zeolitic Imidazolate Frameworks	21
2.3 <i>Metal-organic Framework Glass Formation in Zn(Im)₂</i>	22
2.3.1 Formation of an Amorphous Zn(Im) ₂ Phase.....	22
2.3.2 Structure of the Amorphous Phase.....	24
2.3.3 Thermal Measurements of the Amorphous-Crystalline Phase Transition.....	27
2.3.4 Summary of Liquid State Formation in Zn(Im) ₂	30
2.4 <i>Investigation into the Mechanism of Metal-organic Framework Melting</i>	32
2.4.1 The Mechanism of Melting in ZIF-4	32
2.4.2 Comparison with Other Zeolitic Imidazolate Frameworks	35
2.5 <i>Further Examples of Melting Metal-Organic Frameworks</i>	37
2.5.1 An Overview of Multivariate Melting Metal-organic Frameworks	37
2.5.2 Detailed Examination of a _g ZIF-62.....	41
2.5 <i>Potential Applications of Metal-Organic Framework Glasses</i>	46
2.5.1 Processing of Metal-Organic Framework Glasses.....	46
2.5.2 Intrinsic Porosity in Metal-Organic Framework Glasses	47
2.5.3 Composite Formation with Metal-Organic Framework Glasses	48
Chapter 3: Experimental Methods	51
3.1 <i>Theoretical Background</i>	51
3.1.1 Powder X-ray Diffraction.....	51
3.1.2 X-ray Total-Scattering and the Pair-distribution Function	54
3.1.3 Differential Scanning Calorimetry	60
3.2 <i>Experimental Methods</i>	68
3.2.1 Chapter 4: Structural Investigation of Zeolitic Imidazolate Framework Glasses via X-ray Total-Scattering	68
3.2.2 Chapter 5: Creating New ‘Complex’ Metal-Organic Framework Glasses from Two Component Frameworks	69
3.2.3 Chapter 6: Metal-Organic Framework and Inorganic Glass Composites	72
3.2.4 Chapter 7: The Reactivity of an Inorganic Glass Melt with ZIF-8	78

Chapter 4: Structural Investigation of Zeolitic Imidazolate Framework Glasses via X-ray Total-Scattering..... 80

4.1 Introduction.....	80
4.2 Existing Descriptions and Theory on Mid-range Order in Glasses.....	82
4.2.1 Hierarchical Descriptions of Order in Glasses.....	82
4.2.2 Mid-range Order and the First Sharp Diffraction Peak.....	82
4.2.3 Rationalising Changes in First Sharp Diffraction Peak Intensity and Position with Density and Temperature.....	87
4.3 Structural Changes in a_g ZIF-4 during Heat Treatment.....	88
4.3.1 Differential Scanning Calorimetry of a_g ZIF-4 during Annealing above T_g	88
4.3.2 Ambient Temperature X-ray Total-scattering on fq- a_g ZIF-4 and ht-fq- a_g ZIF-4.....	90
4.3.3 Re-analysing Variable Temperature X-ray Total-Scattering on a_g ZIF-4.....	91
4.3.4 Comparison with Ambient Temperature X-ray Total-Scattering on a_g ZIF-62.....	97
4.4 Conclusions.....	100

Chapter 5: Creating New ‘Complex’ Metal-organic Framework Glasses from Two Component Frameworks103

5.1 Introduction.....	103
5.2 Liquid Phase Blending of Metal-organic Frameworks.....	106
5.2.1 Differential Scanning Calorimetry Analysis on Blends Samples.....	108
5.2.2 Examining the Microstructure of Zeolitic Imidazolate Framework Blends through Energy-Dispersive Spectroscopy.....	110
5.2.3 Ambient and Variable Temperature X-ray Total-Scattering Measurements.....	113
5.2.4 Discussion.....	115
5.3 The Discovery of Flux-Melting in Metal-organic Frameworks Mixtures.....	116
5.3.1 Differential Scanning Calorimetry Analysis on Flux Samples.....	117
5.3.2 Examining the Microstructure of Zeolitic Imidazolate Framework Fluxes through Energy-Dispersive X-ray Spectroscopy.....	122
5.3.3 X-ray Total-Scattering Measurements.....	124
5.3.4 Discussion.....	125
5.4 Further Examples of Flux-Melting.....	127
5.4.1 Thermal and Powder X-ray Diffraction Characterisation.....	129
5.4.2 Ambient and Variable Temperature X-ray Total-Scattering Measurements.....	132
5.4.3 Discussion.....	134
5.5 Conclusions.....	136

Chapter 6: Metal-organic Framework and Inorganic Glass Composites..... 138

6.1 Introduction.....	138
6.2 Zeolitic Imidazolate Framework Component Selection.....	139
6.3 Inorganic Glass Screening.....	141
6.3.1 The Structures of Phosphate Glasses.....	141
6.3.2 Experimental Screening Results.....	144
6.4 Composition and structure of the Inorganic Glass IV.....	153
6.5 Thermal Characterisation.....	155
6.6 Powder X-ray Diffraction of the $(a_g$ ZIF-62) $_{0.5}$ (Inorganic Glass) $_{0.5}$ Samples.....	161
6.7 Spectroscopic Examination of $(a_g$ ZIF-62) $_{0.5}$ (Inorganic Glass) $_{0.5}$ Samples.....	162

6.7.1 Probing Sample Stability through Fourier Transform Infra-red and ¹ H Nuclear Magnetic Resonance Spectroscopy	162
6.7.2 Investigating the Composite Samples through ³¹ P Nuclear Magnetic Resonance Spectroscopy	166
6.7.3 Investigating the Composite Samples through Raman Scattering	168
6.8 X-ray Total-Scattering Measurements on (a_gZIF-62)_{0.5}(Inorganic Glass)_{0.5} Composites	171
6.8.1 Conventional X-ray Total-Scattering Measurements on the Composite Samples	171
6.8.2 Differential Pair-distribution Function Studies on the Composite Samples	176
6.9 Microstructural Investigations of (a_gZIF-62)_{0.5}(Inorganic Glass)_{0.5} Samples through Microscopy	182
6.9.1 Examination of the Composite Bulk Structure via Light Microscopy	182
6.9.2 Microstructural Examination of the Composites through Electron Microscopy	184
6.10 Characterisation of the Properties of (a_gZIF-62)_{0.5}(Inorganic Glass)_{0.5}	191
6.10.1 Nanoindentation and Scratch Testing of the (a _g ZIF-62) _{0.5} (base) _{0.5} Samples	191
6.10.2 Na ⁺ Conductivity Measurements on the (a _g ZIF-62) _{0.5} (Na-deficient) _{0.5} Samples	193
6.11 Discussion	197
6.12 Conclusions	201
Chapter 7: The Reactivity of an Inorganic Glass Melt with ZIF-8	202
7.1 Introduction	202
7.2 Thermal Characterisation of Samples	204
7.2.1 Characterisation of the X wt% ZIF-8 Samples by Differential Scanning Calorimetry and Thermogravimetric Analysis	206
7.2.2 Probing Stability Changes through a Differential Thermogravimetric Analysis Method	208
7.3 Characterisation of Crystallinity Loss in ZIF-8 through Powder X-ray Diffraction	210
7.4 Spectroscopic Characterisation of ZIF-8 Stability	215
7.4.1 Examining relative changes in ZIF-8 through Fourier Transform Infra-Red Spectroscopy	215
7.4.2 Examining 2-methylimidazole Loss through ¹ H Nuclear Magnetic Resonance Spectroscopy	224
7.5 Discussion	226
7.6 Conclusions	228
8. Conclusions	229
8.1 Summary of Thesis Results	229
8.1.1 Investigations into the Changing Structure Zeolitic Imidazolate Framework Glasses at High Temperatures	229
8.1.2 Expanding the Metal-organic Framework Glass Domain through Complex Glass Formation	230
8.1.2 Composite Formation between Metal-organic Frameworks and Inorganic Glasses	232
8.2 Reflection on the Thesis Aims and Conclusions	234
8.3 Further Work	235
8.4 Outlook	239
Bibliography	240

List of Figures

Figure 1.1: a. A selection of secondary building units (SBU). b. Linkers used in the synthesis of metal-organic frameworks.....	2
Figure 1.2: Examples of the varying geometry of inorganic SBUs and organic linkers found in carboxylate MOFs.	3
Figure 1.3: The structure of the prototypical metal-organic framework MOF-5.	4
Figure 1.4: Isorecticular synthesis and properties of a MOF-5 series.	5
Figure 1.5: Schematic representation of routes towards post-synthetic modification of MOFs.	6
Figure 1.6: Specific surface area and H ₂ uptake in MOFs.	8
Figure 1.7: Structure of MOF-48.	9
Figure 1.8: Schematic of the continuous random network model for a A ₂ B ₃	11
Figure 1.9: Volume-Temperature diagram showing the formation of the glass and crystalline states from a liquid.	13
Figure 1.10: Potential energy landscape model of the glass transition.	14
Figure 2.1: Examples of the four families of hybrid glass formers.	18
Figure 2.2: Linker structure in zeolitic imidazolate frameworks.	19
Figure 2.3: ZIF and zeolite structure comparison.	19
Figure 2.4: Different coordination environments in ZIFs.	20
Figure 2.5: Chemical stability of ZIF-8.	21
Figure 2.6: Unit cells of Zn(Im) ₂ ZIFs.	22
Figure 2.7: Variable temperature X-ray diffraction patterns for ZIF-4-Co (blue), ZIF-3 (red), and ZIF-1 (black). .	23
Figure 2.8: PDF on crystalline and amorphous Zn(Im) ₂ and Co(Im) ₂ frameworks.	24
Figure 2.9: Atomic correlations in the short-range order of ZIFs.	25
Figure 2.10: Continuous random network model (CRN) created for amorphous ZIF-4.	26
Figure 2.11: In situ variable pressure X-ray diffraction data on solvent containing ZIF-4 with a large sized pressure transmitting fluid (Daphne Oil 7474 (DO)).....	27
Figure 2.12: Three successive DSC scans on ZIF-4.	28
Figure 2.13: Thermal response and TGA mass curves for ZIF-4 (red) and ZIF-8 (blue).	29
Figure 2.14: Optical micrographs of heat treated ZIF-4.	31
Figure 2.15: Simulated heat capacity and Lindemann ratio in ZIF-4.	33
Figure 2.16: Correlation between melting onset temperature and spectral position shift coefficient (X _R).	34
Figure 2.17: Simulated zinc coordination in ZIF-4 as a function of temperature.	34
Figure 2.18: Visualisation of the linker exchange events that occur during melting of ZIF-4.	35
Figure 2.19: X-ray PDF functions of MOF crystals and glasses.	38
Figure 2.20: Raman spectra for crystalline and glass ZIF-62.	38
Figure 2.21: Variation of T _g and T _m as a function of blm ⁻ content for ZIF-62 and ZIF-62-Co.	40
Figure 2.22: Variation of ΔH _m and ΔS _m with blm ⁻ content in ZIF-62 and ZIF-62-Co.....	42
Figure 2.23: PXRD and DSC measurements of crystalline and glass ZIF-62 Zn(Im) _{2-x} (blm) _x	43
Figure 2.24: Distribution of zinc centres, Zn(Im) _k (blm) _{4-k} in ZIF-62 as a function of blm ⁻ content.....	45
Figure 2.25: Images of bulk a _g ZIF-62.	47
Figure 2.26: Calculated pore volume fraction for ZIF-4, ZIF-zni and a _g ZIF-4.	48
Figure 2.27: Schematic of a MIL-53 a _g ZIF-62 composite.	49
Figure 2.28: Quantity adsorbed from gas adsorption isotherms for the (MIL-53) _x (a _g ZIF-62) _{1-x} series at 1 bar using CO ₂ gas at 0 °C.	50
Figure 3.1: Schematic showing diffraction of X-rays as reflection from atomic planes.	51
Figure 3.2: Schematic showing X-ray diffraction from a powder agglomerate.....	52
Figure 3.3: Bragg-Brentano scattering geometry commonly used in powder X-ray diffraction experiments.	53
Figure 3.4: Theoretical pair-distribution function (PDF) of a square lattice.....	54
Figure 3.5: Radial distribution function, g(r) (spherically averaged) for liquid Nickel.....	55
Figure 3.6: Theoretical partial pair-distribution function (PDF) of a square lattice.	56
Figure 3.7: Schematic of a heat-flux DSC.....	61

Figure 3.8: Schematic of a power-compensation DSC.	62
Figure 3.9: Schematic of heat flow in the heat-flux DSC.	63
Figure 3.10: Schematic of features in a DSC curve.	65
Figure 4.1: Structures of ZIF-4 and a_g ZIF-4.	80
Figure 4.2: Examples of mid-range order in glasses.	83
Figure 4.3: Origin of density-density and chemical-chemical correlations in the random packing arrangement of two atom (or atom-void) mixtures.	85
Figure 4.4: Structure of CRN glasses and the FSDP.	86
Figure 4.5: Thermal response (black) and mass % curves (red) of as-synthesised ZIF-4 (dashed) and f_q - a_g ZIF-4 (solid). Measured at a heating rate of 10 °C/min.	89
Figure 4.6: Thermal response curves of f_q - a_g ZIF-4 (black) and ht- f_q - a_g ZIF-4 (red).	89
Figure 4.7: X-ray total-scattering structure factor, $S(Q)$, of f_q - a_g ZIF-4 and ht- f_q - a_g ZIF-4.	90
Figure 4.8: Pair distribution functions, $D(r)$, of f_q - a_g ZIF-4 and ht- f_q - a_g ZIF-4.	91
Figure 4.9: Variable temperature X-ray total-scattering of a_g ZIF-4 (31 – 535 °C).	92
Figure 4.10: Variable temperature X-ray total-scattering of a_g ZIF-4 (541 – 655 °C).	93
Figure 4.11: Peak parameters of the a_g ZIF-4 FSDP.	96
Figure 4.12: Pressure-temperature phase diagram of ZIF-4.	97
Figure 4.13: X-ray total-scattering structure factor, $S(Q)$, of heat treated a_g ZIF-62.	98
Figure 4.14: Pair distribution functions, $D(r)$, of heat treated a_g ZIF-62.	98
Figure 4.15: Tentative mid-range order assignments in glass MOFs.	101
Figure 5.1: Schematic of samples investigated in this chapter.	105
Figure 5.2: Crystal structures of a. ZIF-4 and b. ZIF-62.	106
Figure 5.3: PXRD pattern of synthesised ZIF-4.	107
Figure 5.4: Synthesised ZIF-4-Co batches used in this project.	108
Figure 5.5: PXRD and DSC on ZIF-4 ZIF-62 blends samples.	109
Figure 5.6: PXRD and DSC on ZIF-4-Co ZIF-62 blends samples.	110
Figure 5.7: Energy dispersive X-ray spectroscopy (EDS) images of ZIF-4-Co ZIF-62 blends samples.	112
Figure 5.8: Ambient temperature total-scattering of ZIF-4-Co ZIF-62 blends samples.	113
Figure 5.9: Variable temperature total-scattering data of ZIF-4-Co ZIF-62 blends samples.	114
Figure 5.10: Crystal structure of ZIF-8.	117
Figure 5.11: SEM images of ZIF-8, ZIF-62, and ZIF-67.	118
Figure 5.12: Thermal response (blue) and mass (red) curves of (ZIF-8)(ZIF-62)(20/80).	119
Figure 5.13: DSC and SEM data on $a_g[(ZIF-8)_{0.2}(ZIF-62)_{0.8}]$	120
Figure 5.14: PXRD patterns of (ZIF-8)(ZIF-62)(20/80) and $a_g[(ZIF-8)_{0.2}(ZIF-62)_{0.8}]$	120
Figure 5.15: PXRD on heat treated ZIF-8 control.	121
Figure 5.16: Thermal response (blue) and mass (red) curves of (ZIF-67)(ZIF-62)(20/80).	121
Figure 5.17: PXRD patterns of (ZIF-67)(ZIF-62)(20/80) and $a_g[(ZIF-67)_{0.2}(ZIF-62)_{0.8}]$	122
Figure 5.18: Energy dispersive X-ray spectroscopy (EDS) images of ZIF-67 ZIF-62 flux-melted samples.	123
Figure 5.19: Ambient temperature X-ray total-scattering of ZIF-8 ZIF-62 flux-melted samples.	125
Figure 5.20: Crystal structure of ZIF-76.	128
Figure 5.21: Crystal structures of a. ZIF-UC-5 and b. TIF-4.	128
Figure 5.22: PXRD patterns of (ZIF-76-mblm)(TIF-4) and (ZIF-76)(ZIF-UC-5).	129
Figure 5.23: Thermal response (blue) and mass (red) curves of a. (ZIF-76)(ZIF-UC-5) and b. $a_g[(ZIF-76)(ZIF-UC-5)]$	130
Figure 5.24: Thermal response (blue) and mass (red) curves of a. (ZIF-76-mblm)(TIF-4) and b. $a_g[(ZIF-76-mblm)(TIF-4)]$	130
Figure 5.25: PXRD patterns of ZIF-76 ZIF-UC-5 flux-melted samples.	131
Figure 5.26: PXRD patterns of ZIF-76-mblm TIF-4 flux-melted samples.	131
Figure 5.27: Ambient temperature total-scattering of ZIF-76 ZIF-UC-5 flux-melted samples.	132
Figure 5.28: Ambient temperature total-scattering of ZIF-76-mblm TIF-4 flux-melted samples.	133
Figure 5.29: Variable temperature X-ray total-scattering data of (ZIF-76)(ZIF-UC-5).	134
Figure 6.1: PXRD and optical microscopy of ZIF-62.	140
Figure 6.2: Schematic phosphate glass structure.	143

Figure 6.3: Schematic structure of AlF_3 and SO_4^{2-} in phosphate glasses.....	144
Figure 6.4: Thermal response (red) and mass curve (blue) of the (50/50) ZIF-62 Inorganic glass I sample.....	145
Figure 6.5: Thermal response (red) and mass curve (blue) of the (50/50) ZIF-62 Inorganic glass II sample.....	146
Figure 6.6: Thermal response (red) and mass curve (blue) of the (50/50) ZIF-62 Inorganic glass III sample.....	146
Figure 6.7: Recovery SDT and PXRD on the (50/50) ZIF-62 Inorganic glass III sample.	147
Figure 6.8: Thermal response (red) and mass curve (blue) of the (50/50) ZIF-62 Inorganic glass IV sample.	148
Figure 6.9: Recovery SDT and PXRD on the (50/50) ZIF-62 Inorganic glass IV sample.	148
Figure 6.10: Thermal response (red) and mass curve (blue) of the (50/50) ZIF-62 Inorganic V glass sample. ...	149
Figure 6.11: Recovery SDT and PXRD on the (50/50) ZIF-62 Inorganic glass V sample.	149
Figure 6.12: Thermal response (red) and mass curve (blue) of the (50/50) ZIF-62 Inorganic glass VI sample. .	150
Figure 6.13: Recovery SDT and PXRD on the (50/50) ZIF-62 Inorganic glass VI sample.	150
Figure 6.14: Thermal response (red) and mass curve (blue) of the (50/50) ZIF-62 Inorganic VII glass sample. .	151
Figure 6.15: Recovery SDT and PXRD on the (50/50) ZIF-62 Inorganic glass VII sample.	151
Figure 6.16: The local structure of the $(1-x)[\text{Na}_2\text{O}]_x[\text{P}_2\text{O}_5]_x-x[\text{AlO}_{3/2}][\text{AlF}_3]_y$ glass series.	154
Figure 6.17: Powder X-ray diffraction patterns of the ball milled evacuated (ZIF-62)(Inorganic Glass)(50/50) mixtures and pure ZIF-62.	155
Figure 6.18: Thermal response of ZIF-62 control during the first (red) and second (blue) heating scans.	156
Figure 6.19: Thermal responses of the inorganic glass controls.	157
Figure 6.20: Thermal response of (ZIF-62)(Al-rich)(50/50) during the first (red) and second (blue) heating scans.	158
Figure 6.21: Thermal response of (ZIF-62)(Na-deficient)(50/50) during the first (red) and second (blue) heating scans.	159
Figure 6.22: Thermal response of (ZIF-62)(base)(50/50) during the first (red) and second (blue) heating scans.	159
Figure 6.23: Mass curves of the (ZIF-62)(Inorganic Glass)(50/50) samples.....	160
Figure 6.24: X-ray diffraction patterns of the $(a_g\text{ZIF-62})_{0.5}(\text{Inorganic Glass})_{0.5}$ samples.	161
Figure 6.25: Solution ^1H NMR spectra of crystalline and glass ZIF-62 controls.	162
Figure 6.26: Solution ^1H NMR spectra of the $(a_g\text{ZIF-62})_{0.5}(\text{Inorganic Glass})_{0.5}$ samples.	164
Figure 6.27: FTIR spectra of the $(a_g\text{ZIF-62})_{0.5}(\text{Inorganic Glass})_{0.5}$ samples.	165
Figure 6.28: FTIR spectra of the inorganic glasses.....	166
Figure 6.29: ^{31}P solid state NMR and $^{31}\text{P}\{^1\text{H}\}$ cross polarisation NMR of Al-rich and $(a_g\text{ZIF-62})_{0.5}(\text{Al-rich})_{0.5}$	167
Figure 6.30: ^{31}P solid state NMR and $^{31}\text{P}\{^1\text{H}\}$ cross polarisation NMR of Na-deficient and $(a_g\text{ZIF-62})_{0.5}(\text{Na-deficient})_{0.5}$	167
Figure 6.31: ^{31}P solid state NMR and $^{31}\text{P}\{^1\text{H}\}$ cross polarisation NMR of the base and $(a_g\text{ZIF-62})_{0.5}(\text{base})_{0.5}$	168
Figure 6.32: Raman spectra of the heat treated ZIF-62 control samples.	169
Figure 6.33: Raman spectra of the $(a_g\text{ZIF-62})_{0.5}(\text{Inorganic Glass})_{0.5}$ samples.....	169
Figure 6.34: Raman spectra of the Zn—N peak (ca. 175 cm^{-1}) peak.	170
Figure 6.35: Structure factor $S(Q)$ of $(a_g\text{ZIF-62})_{0.5}(\text{Al-rich})_{0.5}$	171
Figure 6.36: Structure factor $S(Q)$ of $(a_g\text{ZIF-62})_{0.5}(\text{Na-deficient})_{0.5}$	172
Figure 6.37: Structure factor $S(Q)$ of $(a_g\text{ZIF-62})_{0.5}(\text{base})_{0.5}$	172
Figure 6.38: Pair-distribution function $D(r)$ of $(a_g\text{ZIF-62})_{0.5}(\text{Al-rich})_{0.5}$	173
Figure 6.39: Pair-distribution function $D(r)$ of $(a_g\text{ZIF-62})_{0.5}(\text{Na-deficient})_{0.5}$	174
Figure 6.40: Pair-distribution function $D(r)$ of $(a_g\text{ZIF-62})_{0.5}(\text{base})_{0.5}$	175
Figure 6.41: Recovered total-scattering of $(a_g\text{ZIF-62})_{0.5}(\text{Al-rich})_{0.5}$	178
Figure 6.42: Recovered total-scattering of $(a_g\text{ZIF-62})_{0.5}(\text{Na-deficient})_{0.5}$	178
Figure 6.43: Recovered total-scattering of $(a_g\text{ZIF-62})_{0.5}(\text{base})_{0.5}$	179
Figure 6.44: $S(Q)^{\text{Diff}}$ for the $(a_g\text{ZIF-62})_{0.5}(\text{Inorganic Glass})_{0.5}$ samples.....	179
Figure 6.45: $D(r)^{\text{Diff}}$ of the SRO in the $(a_g\text{ZIF-62})_{0.5}(\text{Inorganic Glass})_{0.5}$ samples.	181
Figure 6.46: $D(r)^{\text{Diff}}$ of the LRO in the $(a_g\text{ZIF-62})_{0.5}(\text{Inorganic Glass})_{0.5}$ samples.	181
Figure 6.47: Reflected light microscopy of the $(a_g\text{ZIF-62})_{0.5}(\text{Inorganic Glass})_{0.5}$ samples.	182
Figure 6.48: Top-illuminated confocal microscopy images of the $(a_g\text{ZIF-62})_{0.5}(\text{Inorganic Glass})_{0.5}$ samples.....	183
Figure 6.49: Side-illuminated z-scan digital microscopy images of the $(a_g\text{ZIF-62})_{0.5}(\text{Inorganic Glass})_{0.5}$ samples.	184

Figure 6.50: SEM of $(a_g\text{ZIF-62})_{0.5}(\text{Al-rich})_{0.5}$	185
Figure 6.51: SEM of $(a_g\text{ZIF-62})_{0.5}(\text{Na-deficient})_{0.5}$	186
Figure 6.52: SEM of $(a_g\text{ZIF-62})_{0.5}(\text{base})_{0.5}$	186
Figure 6.53: SEM Images of crystallites in $(a_g\text{ZIF-62})_{0.5}(\text{base})_{0.5}$ - 1 min.	187
Figure 6.54: EDS of $(a_g\text{ZIF-62})_{0.5}(\text{Al-rich})_{0.5}$ – 1 min.....	188
Figure 6.55: EDS of $(a_g\text{ZIF-62})_{0.5}(\text{Al-rich})_{0.5}$ – 30 min.....	188
Figure 6.56: EDS of $(a_g\text{ZIF-62})_{0.5}(\text{Na-deficient})_{0.5}$ – 1 min.	189
Figure 6.57: EDS of $(a_g\text{ZIF-62})_{0.5}(\text{Na-deficient})_{0.5}$ – 30 min.	189
Figure 6.58: EDS of $(a_g\text{ZIF-62})_{0.5}(\text{base})_{0.5}$ – 1 min.....	190
Figure 6.59: EDS of $(a_g\text{ZIF-62})_{0.5}(\text{base})_{0.5}$ – 30 min.....	190
Figure 6.60: Nanoindentation experiments on the $(a_g\text{ZIF-62})_{0.5}(\text{base})_{0.5}$ samples.	192
Figure 6.61: Scratch testing on the $(a_g\text{ZIF-62})_{0.5}(\text{base})_{0.5}$ – 1 min glass sample.....	193
Figure 6.62: Conductivity measurements on $(a_g\text{ZIF-62})_{0.5}(\text{Na-deficient})_{0.5}$ samples.	194
Figure 6.63: Electronic properties of $(a_g\text{ZIF-62})_{0.5}(\text{Na-deficient})_{0.5}$ samples.....	195
Figure 6.64: Schematic of the potential structure of the interface between the inorganic glass and the MOF glass domains.	200
Figure 7.1: Schematic representation of the observed destabilising reaction between ZIF-8 and fluoroaluminophosphate glass.	204
Figure 7.2: Pawley refinement of evacuated ZIF-8.....	205
Figure 7.3: Powder X-ray diffraction patterns of the evacuated ZIF-8: inorganic glass mixtures 5 – 30 wt% ZIF-8.	205
Figure 7.4: Thermal response curves of the ZIF-8, inorganic glass, and X wt% ZIF-8.	206
Figure 7.5: Mass curves of the ZIF-8, inorganic glass, and X wt% ZIF-8 samples.....	207
Figure 7.6: $\Delta m(T)$ for the X wt% ZIF-8 samples.....	209
Figure 7.7: Powder X-ray diffraction patterns of the controls.	211
Figure 7.8: Powder X-ray diffraction patterns of the background subtracted 30 wt% ZIF-8 samples.	211
Figure 7.9: Powder X-ray diffraction patterns of the background subtracted 15 wt% ZIF-8 samples.....	212
Figure 7.10: Powder X-ray diffraction patterns of the background subtracted 10 wt% ZIF-8 samples.....	212
Figure 7.11: Powder X-ray diffraction patterns of the background subtracted 5 wt% ZIF-8 samples.	213
Figure 7.12: FTIR spectra of the ZIF-8 controls.....	215
Figure 7.13: FTIR spectra of the inorganic glass controls.....	216
Figure 7.14: FTIR spectrum of the 30 wt% ZIF-8 pressed pellet.....	218
Figure 7.15: FTIR spectrum of the 30 wt% ZIF-8 450 °C 30 min sample.....	218
Figure 7.16: FTIR spectrum of the 30 wt% ZIF-8 480 °C 1 min sample.....	219
Figure 7.17: FTIR spectrum of the 15 wt% ZIF-8 pressed pellet.....	219
Figure 7.18: FTIR spectrum of the 15 wt% ZIF-8 450 °C 30 min sample.....	220
Figure 7.19: FTIR spectrum of the 15 wt% ZIF-8 480 °C 1 min sample.....	220
Figure 7.20: FTIR spectrum of the 10 wt% ZIF-8 pressed pellet.....	221
Figure 7.21: FTIR spectrum of the 10 wt% ZIF-8 450 °C 30 min sample.....	221
Figure 7.22: FTIR spectrum of the 10 wt% ZIF-8 480 °C 1 min sample.....	222
Figure 7.23: FTIR spectrum of the 5 wt% ZIF-8 pressed pellet.....	222
Figure 7.24: FTIR spectrum of the 5 wt% ZIF-8 450 °C 30 min sample.....	223
Figure 7.25: FTIR spectrum of the 5 wt% ZIF-8 480 °C 1 min sample.....	223
Figure 7.26: ^1H NMR spectra of the ZIF-8 control and the 15 wt% ZIF-8 samples.	225
Figure 7.27: SEM images of evacuated ZIF-8.....	227
Figure 7.28: SEM images of evacuated ZIF-62.....	227
Figure 8.1: Schematic of potential complex MOF glass experiments.	236
Figure 8.2: Schematic of potential ZIF-62/ZIF-8 phosphate glass composite experiments.....	238

List of Tables

Table 2.1: Pycnometric density measurements for the crystalline ZIFs (with solvent) and amorphous ZIFs produced through heating.....	23
Table 2.2: Simulated activation energy (ΔU^\ddagger) and enthalpy (ΔS^\ddagger) associated with a bond cleavage in ZIFs.	36
Table 2.3: A list of all melting ZIFs reported in the literature.....	39
Table 5.1: Correlation lengths in the short-range order of ZIF-8 and ZIF-62 measured from crystal structures.	125
Table 6.1: Inorganic glasses used in the composite screening process.....	142
Table 6.2: Glass compositions analysed by EDS for the inorganic glass series.	153
Table 6.3: [Blm]/[Blm+Im] ratio from ^1H NMR integrals of singlet (9.5 ppm) and triplet (9.0 ppm), respectively.	163
Table 6.4: Densities (ρ), as measured by the Archimedean method, of the inorganic glass series.	195
Table 6.5: Densities (ρ), as measured by pycnometry, of the crystalline and amorphous pure ZIF-62 controls.	195
Table 6.6: Densities (ρ), as measured by pycnometry, of the $(a_g\text{ZIF-62})_{0.5}(\text{Inorganic Glass})_{0.5}$ samples.	196
Table 7.1: Thermogravimetric analysis (TGA) and differential scanning calorimetry (DSC) results for the ZIF-8: inorganic glass samples.	208
Table 7.2: Relative crystallinity results for the ZIF-8 controls and X wt% ZIF-8 samples.....	214
Table 7.3: Relative proportions of ZIF-8 and inorganic glass as determined by FTIR.....	224
Table 7.4: ^1H NMR peak integrals of the ZIF-8 control and the 15 wt% ZIF-8 samples, along with calculated values of [Imid-H]/[DMSO], [Imid-H]/[CH ₃], and [Imid-H]/[DMSO] relative to the ZIF-8 control.....	225

Glossary and Abbreviations

MOF: Metal-organic framework

ZIF: Zeolitic imidazolate framework

PXRD: Powder X-ray diffraction

PDF: Pair-distribution function

DSC: Differential scanning calorimetry

TGA: Thermogravimetric analysis

SDT: Simultaneous DSC TGA

T_m : Melting point

T_g : Glass transition temperature

T_d : Decomposition temperature

EDS: Energy-dispersive X-ray spectroscopy

SEM: Scanning electron microscopy

STEM: Scanning transmission electron microscopy

FTIR: Fourier transform infra-red spectroscopy

NMR: Nuclear magnetic resonance spectroscopy

SRO: Short-range order

MRO: Mid-range order

LRO: Long-range order

CRN: Continuous random network

FSDP: First sharp diffraction peak

Chapter 1: Introduction

Metal-organic framework (MOF) glasses are a new class of materials formed by heating crystalline MOFs into the liquid state, and then quenching to form a solid material which lacks a periodic arrangement of atoms. MOF glasses sit astride the two large and disconnected fields of MOF and glass science. This chapter provides a brief introduction to both crystalline MOFs and the glass state in general. The subsequent chapter (**Chapter 2**) will provide a review of the existing research in the MOF glass field and explain features unique to MOF glasses.

1.1 Metal-organic frameworks

1.1.1 Metal-Organic Framework Structure

Metal-organic Frameworks (MOFs) are materials formed by joining an inorganic metal node or single ion (generally termed a secondary building unit), with a rigid organic linker, in a modular fashion. The wide variety of inorganic nodes and organic linkers (**Figure 1.1**), coupled with the ease of synthesis, has led to a large number of MOFs being synthesised, with over 80,000 reported in the literature [1].

Several synthetic methods are available for the crystallisation of MOFs, though the solvothermal route remains the most used. In solvothermal synthesis, an organic ligand and metal salt, both typically in crystalline powder form, are dissolved in a suitable solvent, e.g. *N,N*-dimethylformamide, water, or ethanol. This solution is then transferred to a sealed vial and heated to 65-180 °C for 12-96 hours. Crystallisation occurs during this time, with the pore network forming around templating solvent molecules. Removal of these from the porous cavities in a secondary 'activation' step, is then necessary in order to utilize the remaining pore space [2]. Routes to scaling up the production process, are also now being investigated [3]. Screw-extrusion, where reactants are mixed together under the action of a screw has been shown to be capable of producing two commercial MOFs, HKUST-1 ($\text{Cu}_3(\text{BTC})_2$, where BTC^{3-} is benzene-1,3,5 tricarboxylate) and ZIF-8 (Znmlm_2 , where mlm^- is 2-methylimidazolate) at kg h^{-1} rates. This rate of production is orders of magnitude higher than conventional methods [4]. However, synthesis scale up on MOFs that contain more than one linker appears to be more difficult. ZIF-62 ($\text{Znlm}_{1.75}\text{blm}_{0.25}$, where lm^- is imidazolate and blm^- is benzimidazolate) produced commercially was shown to have very different thermal properties than the same framework produced by small scale methods [5], which was attributed to poor mixing of reagents in the scaled up synthesis.

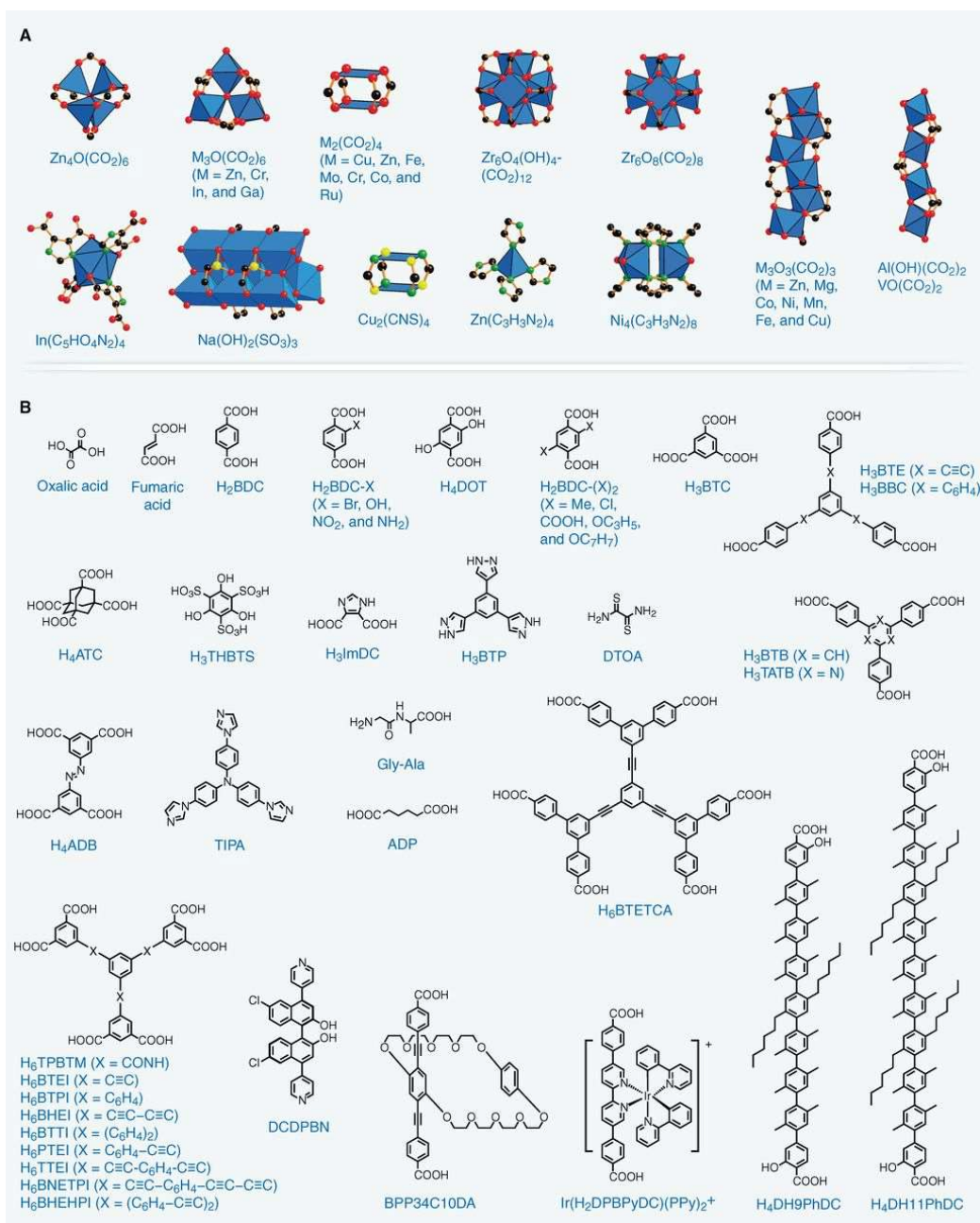


Figure 1.1: a. A selection of secondary building units (SBU). b. Linkers used in the synthesis of metal-organic frameworks. Reproduced from [6].

1.1.2 The Development of Metal-Organic Framework Synthesis and Design

The growth of MOF research as a field has led to four broad principles of MOF synthesis [6]. The first of these is the ‘geometric principle’; the SBUs that make up the framework are chosen to have a rigid shape with well-defined bonding sites for the organic linkers, as opposed to a more simple node and spacer structure (**Figure 1.2**) [7]. These nodes are formed *in situ* during the synthesis and are accommodated, with their structures intact, into the network.

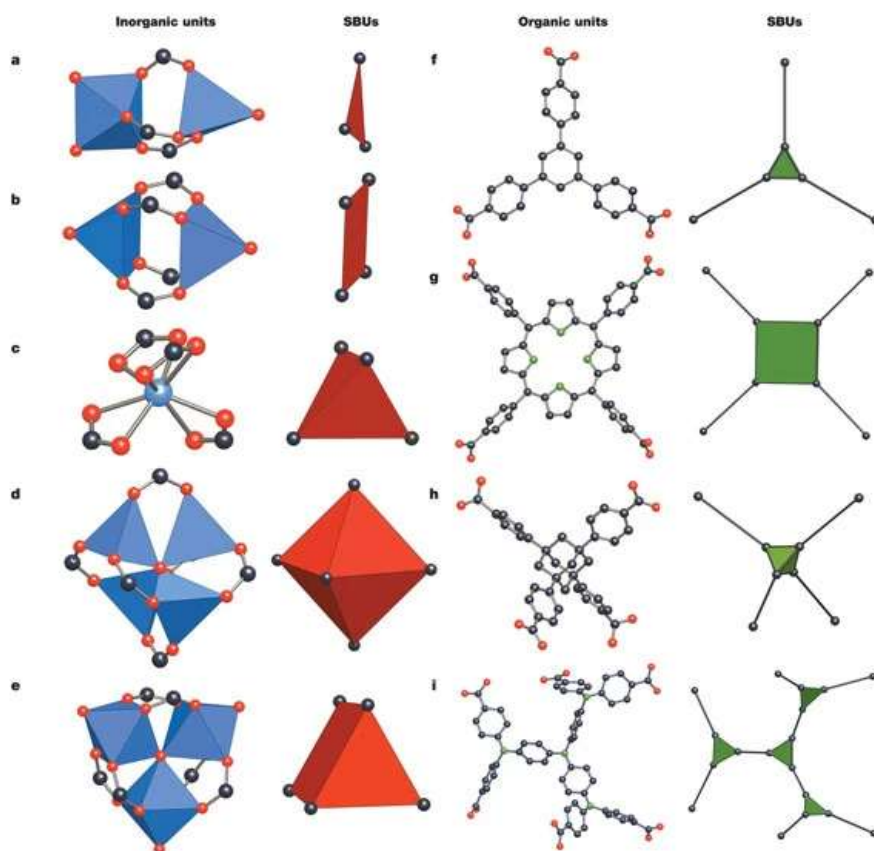


Figure 1.2: Examples of the varying geometry of inorganic SBUs and organic linkers found in carboxylate MOFs. Key: Red – Oxygen, Green – Nitrogen, Grey – Carbon, Blue – Metal atoms. The shape of the SBU polyhedra is defined by joining the points of extension in the inorganic node and organic linker. Metal-oxygen polyhedra are shown in blue, polyhedra defined by the carboxylate carbons are shown in red, and the geometry of the organic linkers are represented by the green shapes/polyhedra. Reproduced from [7].

The inter-cluster SBU-organic linker bonding within MOFs is strong, for example the Zn-O bonds in MOF-5 (**Figure 1.3**) have an energy of 360 kJ mol^{-1} per pair, each pair comprises one link between the organic linker and inorganic SBU. This is comparable with the C-C bond in diamond, 358 kJ mol^{-1} . The combination of high bond strength with the rigid shape of the organic linker creates frameworks that are permanently porous, meaning that they display reversible gas sorption isotherms at low temperatures and pressures. [6], [7]. The geometric principle also enables targeted synthesis of high symmetry ‘default’ topologies by judicious choice of the geometries of the SBU and the linker. For example the default structure for linking squares and tetrahedra is the PtS net [7]. Early MOFs synthesised using geometric principles resulted in crystalline compounds, termed ‘first generation

MOFs' [8] though these were observed to collapse upon activation. Subsequent avoidance of this collapse resulted in 'second generation MOFs' displaying permanent porosity [8], [9].

This discovery led to the second principle in MOF synthesis, the 'isorecticular principle'. Through this principle the porosity of MOFs can be increased by extending the length of the organic linker without changing the underlying topology of the framework. For example, a systematic study of MOF-5 resulted in a series of MOFs, termed IRMOF-n, with the same linker geometry, coordination bonding and framework topology, but with different linker chemistries. In some cases, the linker was functionalised through the substitution of a -Br or -NH₂ onto the benzene ring (**Figure 1.4a**). This resulted in a decrease in porosity as the groups protrude into the pores. In contrast when the BDC linker was lengthened through addition of more benzene rings, MOFs with higher surface areas were produced. It was shown that the porosity of the structure can be tuned systematically (**Figure 1.4b**) [10].

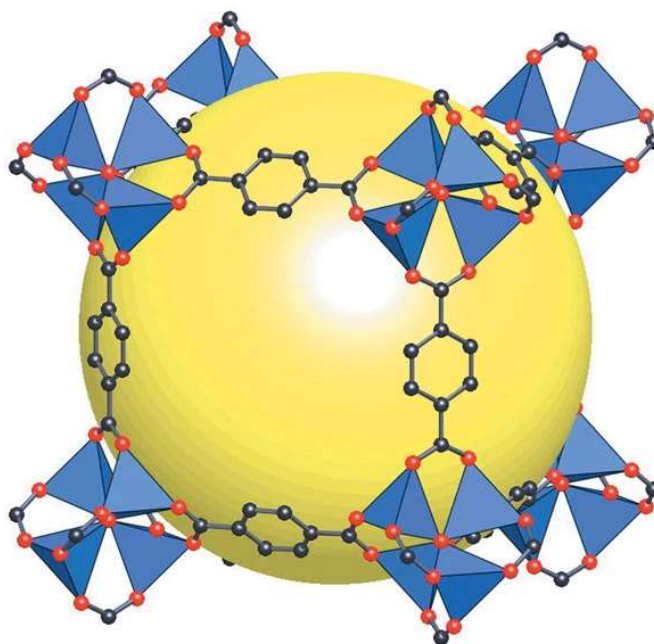


Figure 1.3: The structure of the prototypical metal-organic framework MOF-5. $Zn_4O(BDC)_3$, where BDC is benzene dicarboxylate ($C_8H_4O_4^{2-}$). Key: Blue - Inorganic zinc tetrahedra, Red - Oxygen, and Black - Carbon. The yellow sphere represents the largest sphere that can be accommodated into the pores without encountering the van der Waals radius of the atoms. Reproduced from [7].

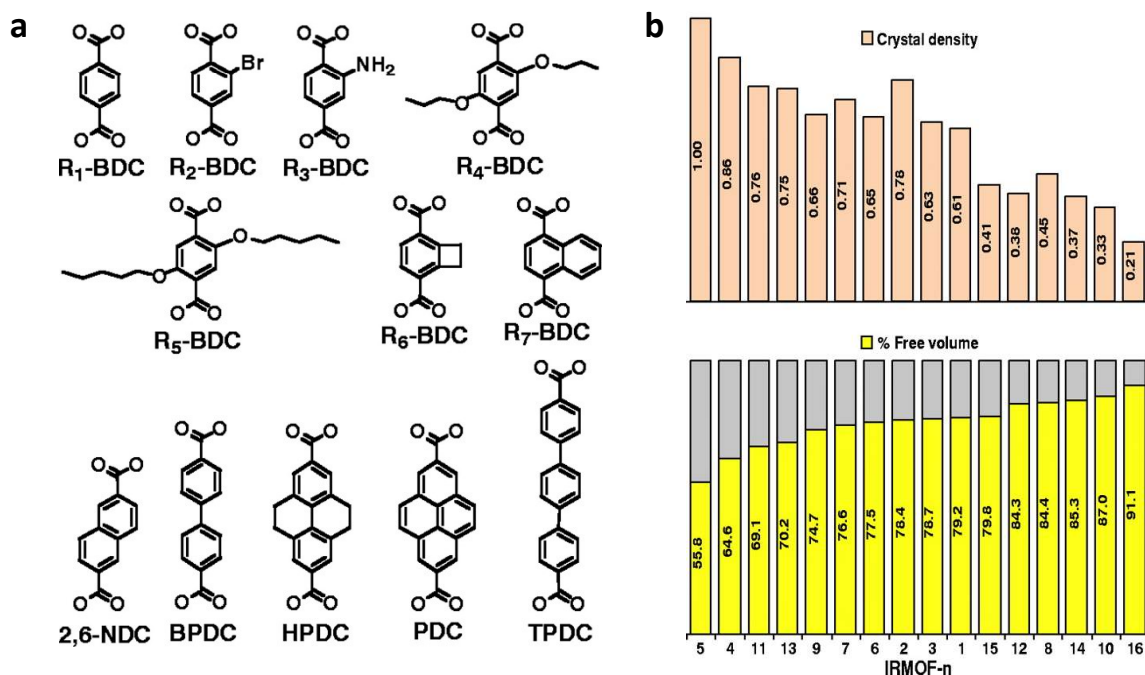


Figure 1.4: Isoreticular synthesis and properties of a MOF-5 series. **a.** Linkers used in the create the MOF-5 based IRMOF-n series using isoreticular synthesis. **b.** Calculated density and free volume (volume of the structure not occupied by framework atoms) across the IRMOF-n series. Reproduced from [10].

Application of the isoreticular principle can be limited by the phenomenon of interpenetration. Interpenetration occurs when one framework grows within the voids of another such that the two frameworks cannot be separated from each other without the breaking of bonds. It has a deleterious effect on porosity due to the filling of void space in one framework by its dual. Frameworks with a high degree of interpenetration, up to 54 fold, have been reported in the literature [11]. To avoid interpenetration, framework topologies can be chosen such that the second framework structure must have a different topology. Ideally this second topology would involve the direct joining of inorganic or organic SBUs and so cannot form [12]. Alternatively, infinite rod shaped inorganic SBUs can be chosen, which allow a close spacing of organic linkers along their length to create interactions which prevent intercalation of more rods [13]. In addition to being a function of topology, interpenetration is also a variable of synthesis conditions, with the use of more dilute synthesis conditions leading to less interpenetration [13].

The third principle of MOF design is the concept of ‘multivariate MOFs’. Multivariate MOFs contain multiple functionalities in their structure through the use of several different inorganic SBUs and organic linkers in the synthesis [6]. This principle facilitates the construction of MOFs that contain different pore environments. This increases the scope of MOF structures that can be synthesised. It

also paves the way for complex structures that could be thought of as man-made analogues of enzymes and other biological molecules [6].

The three principles outlined above are examples of directing end-material formation through the appropriate choice of starting reagents. However, the chemistry and physical properties of MOFs can also be altered post-synthesis in a process called ‘post-synthetic modification’ (PSM). PSM is defined as modification of the framework after it has been synthesised, without affecting the overall stability of the framework [14]. Post-synthetic modification is potentially less limited than pre-synthetic modification as not all functional groups are compatible or stable with MOF synthesis [14]. In PSM, both the inorganic SBU and the organic linker can be functionalised. Covalent modification involves direct modification of the organic linker (**Figure 1.5**). Whereas the SBU can also be functionalised either via i) addition of coordinating ligands into frameworks with unsaturated metal sites, termed coordinate covalent modification. ii) Through the metallisation of the linker. Metallisation is achieved by using a linker with two distinct types of metal binding sites, only one of which is used to form the framework, leaving the other free for PSM. The two processes can also be combined in covalent and coordinate covalent modification, a chelating group is bonded to the linker and then used to attach a new metal centre (**Figure 1.5**) [14].

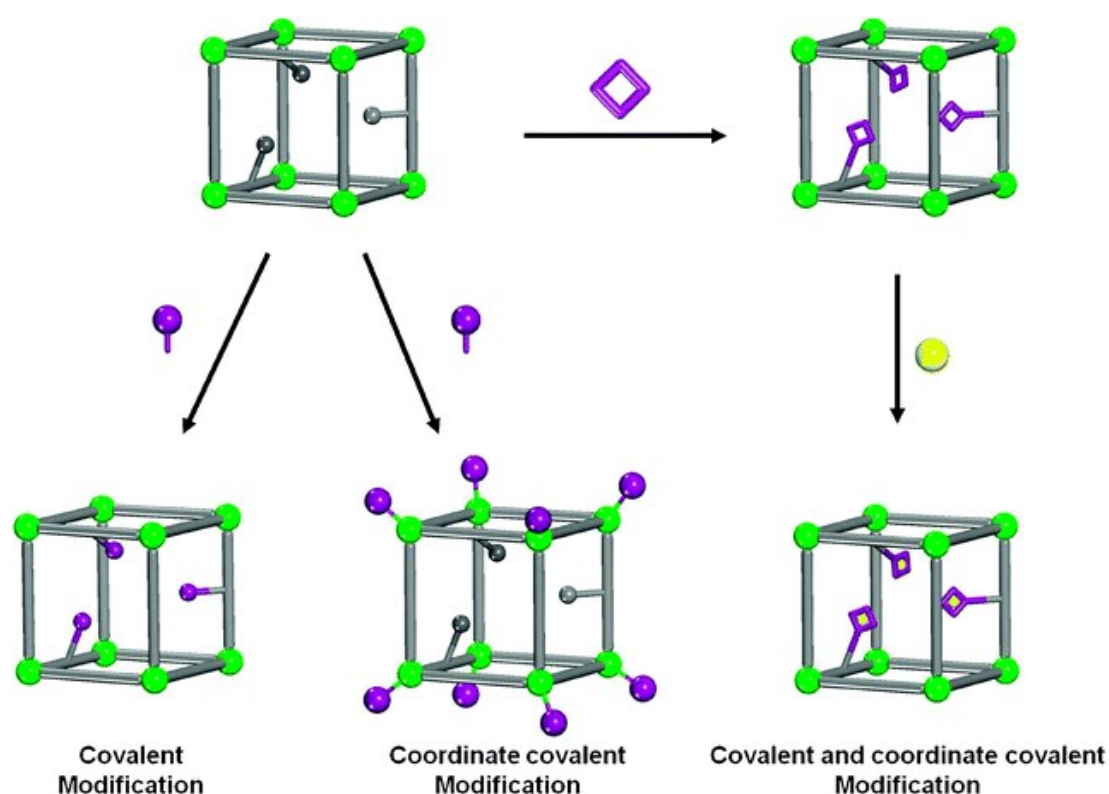


Figure 1.5: Schematic representation of routes towards post-synthetic modification of MOFs. Reproduced from [14].

1.1.3 Applications of Metal-organic Frameworks

The combination of the synthetic methodologies has facilitated the synthesis of MOFs with gravimetric surface areas that far exceed those of other porous materials such as zeolites and activated carbons; for example MOF-5 has a BET surface area of $2320 \text{ m}^2\text{g}^{-1}$ whereas those for activated carbons are typically less than $2000 \text{ m}^2\text{g}^{-1}$ [6]. It is these high surface areas that make MOFs very attractive materials for a range of gas phase applications.

There has been considerable interest in hydrogen as a carbon-free source of fuel. The United States Department of Energy has accordingly developed a series of targets for potential H_2 storage materials, aimed at achieving economical and safe on-board H_2 storage in vehicles [15]. Extensive studies have been undertaken into the potential of MOFs to fill such a role [16]–[18]. Mercedes-Benz have also developed a prototype vehicle, the F125, which uses a MOF as the H_2 storage medium [6]. At low pressure, the extent of H_2 adsorption is a strong function of the inorganic SBU, with coordinatively unsaturated metal sites enhancing H_2 uptake. Decreasing pore size, either through interpenetration or functionalisation of the linkers, was also found to increase H_2 uptake as it resulted in an increased framework- H_2 interaction energy. This is due to the attractive potential energy fields from the pore walls starting to overlap [18]. This is in contrast to observations at high pressure in which the amount of H_2 adsorbed was found to increase linearly with the surface area of the framework (**Figure 1.6**) [16].

MOFs have also been investigated as potential storage materials for methane. Studies on an isorecticular series of MOFs resulted in the discovery of frameworks with superior methane storage capacity to zeolites [10]. In a computer based study a large variety of hypothetical MOF structures were produced using purely geometric constraints and their methane adsorption isotherms evaluated using grand canonical Monte Carlo simulations [19]. This approach revealed that MOFs with ethyl and propyl functional groups had the highest predicted performance, and that there was an optimum pore size of either 4 or 8 Å. This corresponded to pores that were large enough to accommodate either one or two methane molecules respectively [19].

MOFs are also promising materials for gas separation applications. Cu_3BTC_2 , displays a strong preference for CO_2 in CO_2/CH_4 mixtures, N_2O from O_2 and N_2 mixtures, and C_2H_4 from mixtures of $\text{C}_2\text{H}_4/\text{C}_2\text{H}_6$. This was thought to be as a result of a combination of specific coulombic interactions between the gas molecules and the partial charges on the framework, and π - π interactions between the gas molecule and the benzene ring of the linker [20]. MOF crystals have also been incorporated into polymeric membranes to form hybrid membrane materials and these composites have been reported to show enhanced selectivity relative to the pure polymer phase [21].

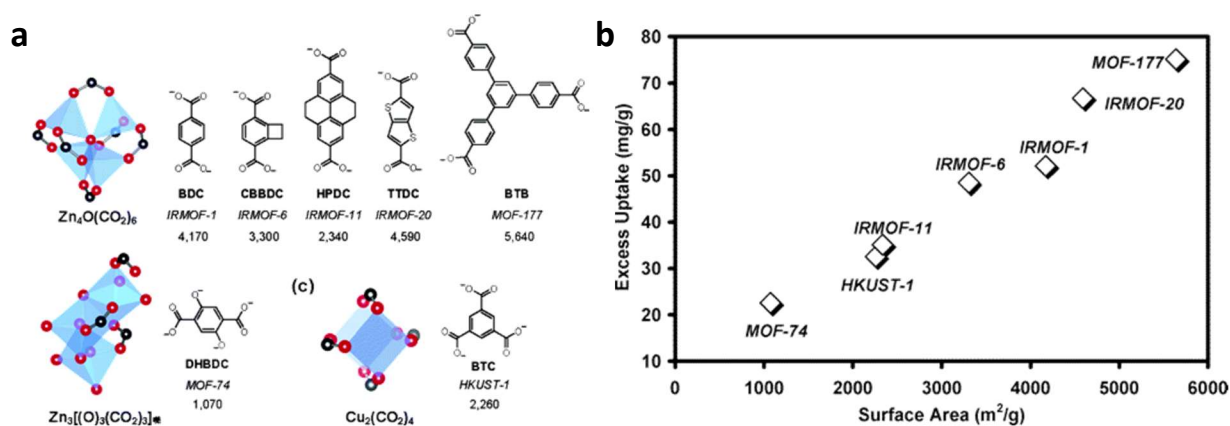


Figure 1.6: Specific surface area and H₂ uptake in MOFs. **a.** Inorganic SBUs and organic linkers and their associated specific surface areas (m²g⁻¹). **b.** Saturation H₂ uptake plotted against specific surface areas. Reproduced from [16].

The high gravimetric surface area of MOFs, combined with the variety of the chemistries accessible in the inorganic SBUs and organic linkers, have resulted in considerable research interest in the use of MOFs as catalysts. A rational materials selection process suggested that MIL-47, which is formed from vanadium oxygen clusters connected by diacetic acid linkers was found to catalyse the conversion of methane to acetic acid, which is a useful feedstock chemical. MIL-47 was chosen because its inorganic SBU is itself a molecular catalyst for the reaction [22]. MOF-48, which is isorecticular with MIL-47 but has been functionalised by the addition of a methyl group to the ortho position of the linker (**Figure 1.7**), was found to have enhance catalytic performance. This demonstrates the chemical versatility of MOFs [22].

Another feature of MOFs that can be exploited in catalysis is the existence of open metal (OM) sites at the inorganic SBUs. Such sites are difficult to stabilise inside scaffolds as they are highly reactive Lewis acids, and therefore likely to chemically bind to an electron donor, such as a solvent molecule, during synthesis. To circumvent this, activation procedures are used which remove a non-framework ligand (i.e. H₂O) from an inorganic ion or node. The result is an open metal site within a stable framework [23]. These OM sites have been found to act as Lewis acid catalysts with good selectivity [24]. They also provide sites for coordinative covalent modification, which has enabled the encapsulation of catalytic noble metals into the pores via the use of chelating amines [25].

MOFs have also been examined as proton conduction materials for use in fuel cells. Different mechanisms of hydrogen conduction in MOFs have been identified. Water mediated proton conduction is when the hydrogen bonded network of water molecules within the MOF is the proton conduction pathway. There is also anhydrous proton conduction, in which conduction is achieved by

organic molecules such as imidazole or pyrazole trapped within the framework [26]. Anhydrous conduction has the advantage that it is not a function of humidity and can occur at higher temperatures unlike current polymer conducting membranes such as Nafion [26].

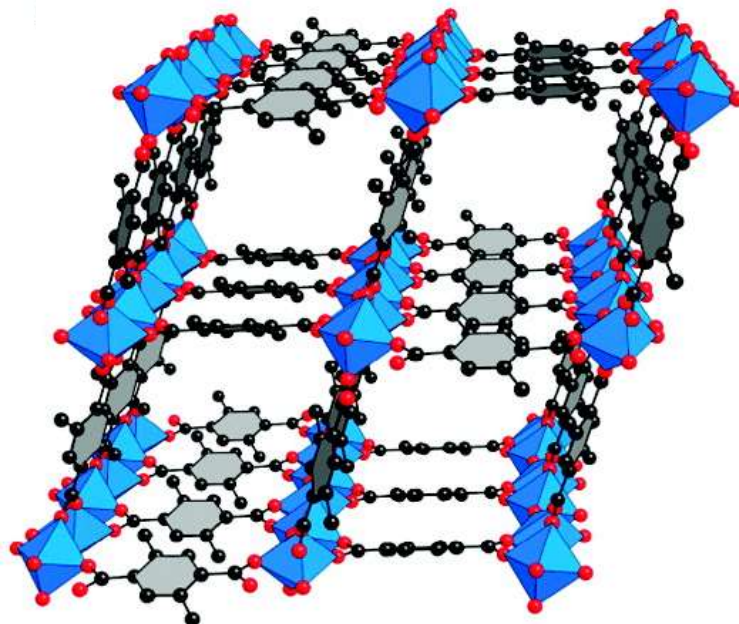


Figure 1.7: Structure of MOF-48. Key: Blue – Vanadium VO_6 polyhedra, Red - Oxygen, Black - Carbon. Hydrogen atoms omitted for clarity. Reproduced from [22].

Several MOF-based applications have been commercialized [27]; these include ION-X, used for the storage of harmful gases used in the semiconductor industry, e.g. PF_3 , and TruPick, which is used in fruit packaging to slowly release 1-methylcyclopropane, a fruit-ripening inhibitor [28]. A patent has also been filed detailing the potential of CALF-20, a zinc oxalate based MOF for use in CO_2 capture applications via adsorption of the CO_2 molecules with the porous MOF surface [29]

1.2 Glasses

1.2.1 Glass Terminology

Glass is a class of material whose applications have greatly preceded scientific understanding, the utility of glasses for architectural applications such as windows, and for items such as cookware was understood long before the scientific method was applied to them. As a result of this, definitions of the glass state itself are somewhat opaque. Traditionally glasses are defined as solid materials that have been formed by cooling from the liquid state at a sufficient rate that crystallisation has been avoided [30]. However, this definition may be too restrictive as it excludes amorphous structures formed by the sol-gel process, dissolving a crystal and then solidifying an amorphous state by gradual evaporation of that solvent. Equally amorphous structures formed by deposition of atoms from a vapour phase, and amorphous solids formed by application of stresses to crystalline phases would also be excluded by the simple definition. A broader and simpler definition of the glassy state may therefore be, 'a solid material which is amorphous, where the state of amorphousness can be measured by the absence of sharp Bragg peaks measured by X-ray diffraction' (see **Chapter 3.1**) [30], [31]. However, this definition might be too broad as it would also encompass materials such as nano-crystals, which do not display sharp Bragg peaks. but which are generally considered different from glasses [30]. The results in this thesis solely concern glasses that are formed via a liquid state and so the definition of glasses as amorphous materials formed by forming a liquid and quenching is adopted in this work.

1.2.2 Glass Structures

Another problem with the various definitions of glass stated above is that they are negative. They classify glasses as class of materials based on what they do not have i.e. crystallinity, a periodic arrangement of atoms in a lattice leading to sharp Bragg peaks. This is helpful in distinguishing glasses from the other main class of solid matter, crystals, however it is not informative as to the structure or properties of the glasses themselves.

One of the most influential pictures of the glass structure was derived by noting that some of the mechanical properties of glasses and those of crystal states with the same elemental composition are similar. It was therefore hypothesised that the bonding in both states must be at least broadly the same [32]. This led to a model known as the continuous random network model (CRN). In the CRN the local bonding of atoms in the glass state is the same as the crystal, but disorder is achieved through slight variations in bond lengths and angles (**Figure 1.8**). In this model the structure is composed of

connected polyhedra. There is order due to chemical bonding within the polyhedra but positional disorder at longer distances.

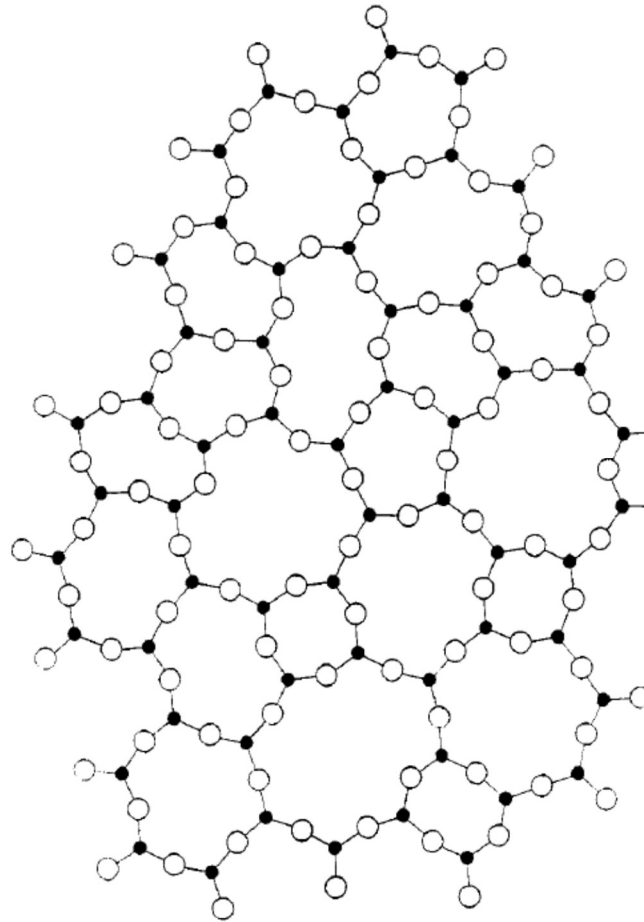


Figure 1.8: Schematic of the continuous random network model for a A_2B_3 . Key: Black – A, White - B. Reproduced from [32].

However, the CRN structure is only a theoretical model of the glass state, one which contains a large scope for variations in bond angles and ring statistics. Moreover, the CRN model is not the only model for the glassy state. At the other extreme from the CRN is the random close packed (RCP) model [33]. In this model the atoms are hard spheres with potentials that are spherically isotropic, i.e. ionic bonding, and they pack in different coordination numbers depending on the ratio of anion and cation radius sizes. These polyhedra pack together as closely as possible and crystallisation is prevented either through the geometric frustration of packing lots of different polyhedra types or via the inefficient packing resulting from the existence of distorted polyhedra.

Glasses have a wide range of chemistries, the most common being based around inorganic oxides such as SiO_2 , P_2O_5 and B_2O_3 . Other inorganic non-oxide base glasses such as the chalcogenides which are based on group IV and group V elements, i.e. $As_xSe_{(1-x)}$, halides such as $57ZrF_4-36BaF_2-4LaF_3-3AlF_3$, and

amorphous semiconductors based on Si, Ge, P and S have also been reported [30], [33]. Outside of the broad family of inorganic glasses there are also organic glasses formed from polymers, and metallic glasses. The latter require extremely fast quenching in order to avoid crystallisation. [30].

As glasses comprise such a wide variety of chemistries and bonding types it is unsurprising that they may adopt different structures. Added to this is the difficulty, in the absence of X-ray diffraction, of giving fully definitive descriptions of glass structure by knowing precise atomic positions. A structure can only be determined to be consistent with the results of X-ray total-scattering, spectroscopic measurements, properties data etc. The chance that another structure could, in principle, also give a good agreement to the measured property can never be fully discounted.

1.2.3 The Glass Transition

Under equilibrium conditions cooling of a liquid below its melting point results in a discontinuous change in volume due to crystallisation. The precise temperature this occurs at depends on the cooling rate due to the kinetics of crystallisation [30] (**Figure 1.9**). However, in glass formation the liquid is cooled at a fast enough rate that crystallisation is avoided and therefore a region of liquid metastability persists, i.e. the liquid phase is present below its equilibrium melting point. Eventually as the temperature lowers further, the sample volume (**Figure 1.9**), or equivalently enthalpy or entropy, deviates from the equilibrium liquid line. The sample then goes through the glass transition region where it departs from the liquid line. After this it follows a line parallel to the crystalline state. During the transition the viscosity of the liquid increases very rapidly [30].

The general shape of the volume – temperature (V-T) plot can be understood as being due to the atoms in the liquid spontaneously rearranging themselves to reduce their volume as the liquid is cooled. At high temperatures, i.e. just below the onset of crystallisation, there is a large amount of thermal energy. As such this rearrangement can occur quickly, and the structure of the liquid can be maintained. However, as the temperature decreases so does the thermal energy in the system. Eventually the atoms can no longer rearrange themselves over the experimental timescale. At this point the sample volume cannot follow the equilibrium line and so a glass is formed. The temperature that this departure occurs is a function of cooling rate. Slower cooling rates (bcg vs bch **Figure 1.9**) result in longer timescales for atom motion, and therefore wider regions of liquid metastability. At low temperatures the overall volume is generally higher for glasses than their corresponding crystalline phases.

On re-heating the glass, the sample volume will also transition through the glass transition region at approximately the same temperature range as the one displayed on cooling (dashed line **Figure 1.9**). Experimentally the cooling and heating V-T curves are never observed to be identical [30].

On cooling the intersection of the equilibrium liquid line and solid glass lines is termed the fictive temperature. To a reasonable approximation it is the temperature at which the liquid structure is 'frozen in' to the glass. The glass transition temperature is measured on heating and quantifies the onset of the transition between solid and liquid behaviour. Typically, this is done by an intersection of the glass curve with the steepest point of the transition region. When the same heating and cooling rates are used the fictive temperature and the glass transition temperature are generally very similar. As a result of this the distinction between the two of them is treated very loosely in the literature [30].

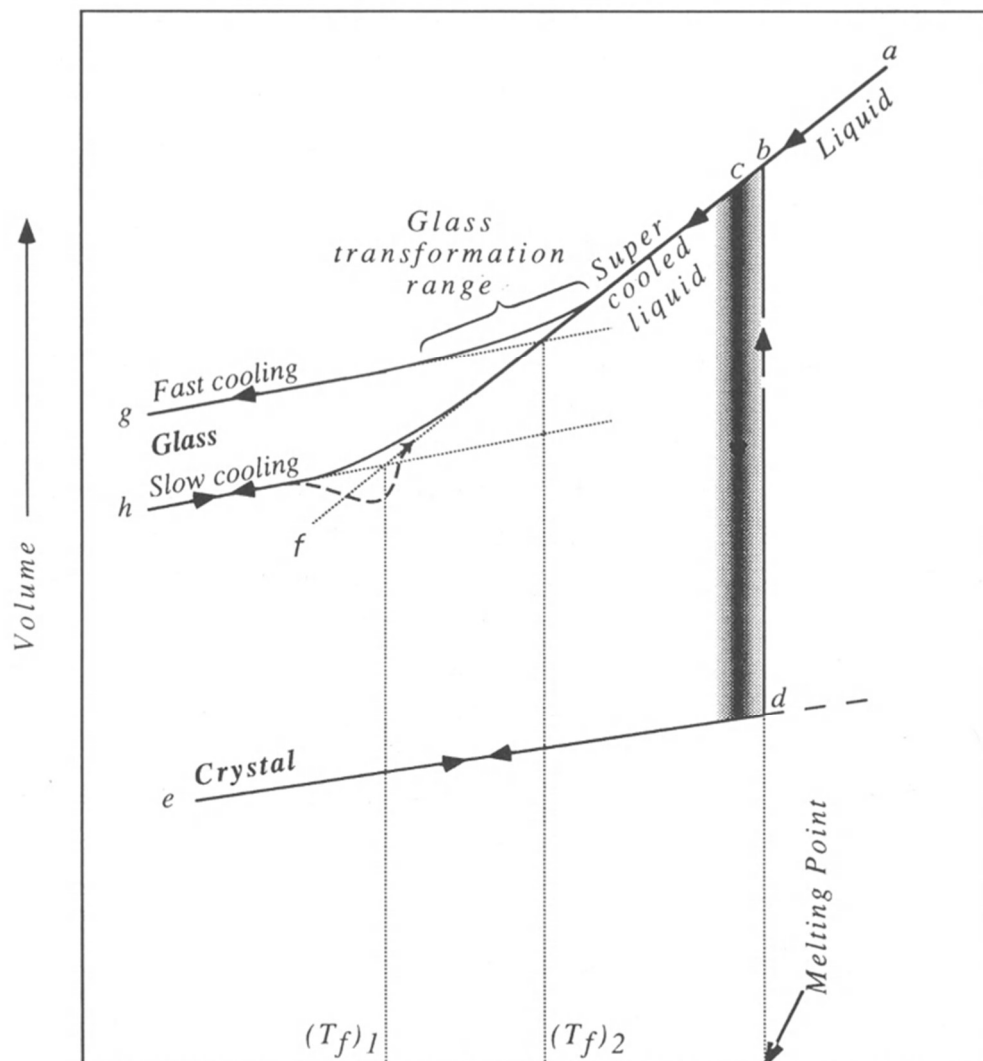


Figure 1.9: Volume-Temperature diagram showing the formation of the glass and crystalline states from a liquid. Crystallisation (abd) is shown as happening over a range of temperatures (shaded region). Reproduced from [30].

The glass transition region, and the structural changes within the sample when it transitions from a liquid to a glass state has been the subject of intense study [30], [34]. As described above, it can be thought of as a kinetic phenomenon. As the sample free volume shrinks and viscosity rises, the atoms cannot continually rearrange themselves to follow a liquid line. Therefore, the material dynamics become more and more sluggish and the sample eventually becomes frozen and solid. This may obfuscate an underlying thermodynamic transition into the glassy state however.

The idea of an energy landscape may also be a convenient framework for explaining this phenomenon [34]. For a system of N atoms the energy landscape is a $(3N + 1)$ dimensional object representing the energy of the interactions of the atoms. Minimums in the energy landscape represent ‘inherent structures’ that are meta-stable states. In contrast, the lowest energy minimum represents the stable structural configuration (**Figure 1.10a**). For a system of N atoms and constant volume this energy landscape is fixed. The relaxation of the structure as it is cooled through the glass transition region is affected by the way the atoms can rearrange to sample the energy landscape. At high temperature there is sufficient thermal energy for the glass to sample almost any inherent structure and so the energy of the average atom remains high as there are many more high energy potential minima than low energy ones (**Figure 1.10b**). As the temperature decreases to around the energy required to surmount the barrier between the states the system changes rapidly and the system can no longer

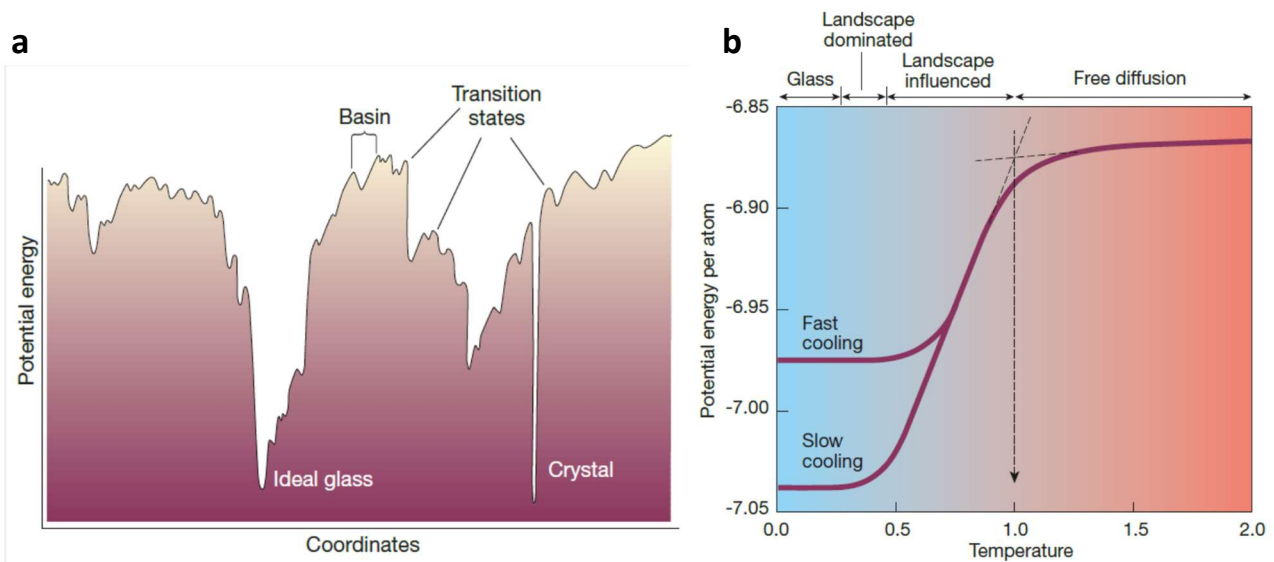


Figure 1.10: Potential energy landscape model of the glass transition. **a.** Schematic of a potential energy landscape, the x-axis represents all configurational co-ordinates. **b.** Mean inherent structural energy per particle as a function of temperature calculated by molecular dynamics simulations from a binary mixture of unequal sized atoms. Reproduced from [34].

sample the whole landscape. Instead, it is confined within the deeper basins, and the average energy per atom falls. At lower temperatures the system becomes completely confined to a single minimum, corresponding to the glass transition. The depth of this minimum is inversely correlated to the cooling rate [34].

In conclusion, it is noted here that although the energy landscape offers an attractive qualitative picture of the glass transition in terms of both thermodynamics and kinetics, it is not the only theory set forth to explain glass behaviour during this process [30]. Moreover making this description more quantitative remains a continued field of research [34].

1.2.4 Applications of Glass Science

Despite the wide range of glass families discovered by academic research, the majority of applications of glass science involve silica based glasses [35]. Pure vitreous silica is used to make high performance materials such as optical fibres and astronomical mirrors, but its high cost of production prevents its use in more mundane applications. The majority of the everyday glass objects such as windows and beverage containers, are composed of soda-lime glass, Soda-lime glass is created by combining silica with inexpensive soda ash, Na_2CO_3 , or limestone, CaCO_3 . The high thermal expansivity of soda-lime glasses, $100 \times 10^{-7} / ^\circ\text{C}$, relative to pure silica $5.5 \times 10^{-7} / ^\circ\text{C}$, means that these glasses are very prone to fracture due to thermal shock. Borosilicate glasses, which combine a relatively low thermal expansion coefficient $30\text{-}60 \times 10^{-7} / ^\circ\text{C}$ with good resistance to chemical attack are used to produce the majority of glass used in laboratories and in cookware [30].

Non-silica glasses have found some commercial uses, with chalcogenide glass powders being utilised in photocopiers due to their photoconductive properties. Metallic glasses typically display a low degree of magnetic hysteresis, meaning that little energy is required to switch the magnetic polarisation of the glass structure by an external magnetic field, and high electrical resistivity. These properties have led to their utilisation in magnetic shielding and in transformer cores to limit energy losses [30].

1.3 Aims

This thesis aims to expand the new field of glass forming MOFs using techniques and principles developed in both parent fields of crystalline MOFs and glass science. This broad aim of materials discovery can be decomposed into three specific aims:

1. To improve our understanding of the MOF glass state, especially using pre-existing theory for other similar glass forming systems.
2. To investigate the potential of using the MOF liquid state as a route by which functionality can be incorporated into the MOF glass phase.
3. To examine whether the MOF glasses can be combined with other classes of glass materials to allow the formation of composite materials.

Chapter 2: A Review of the Literature on Metal-organic Framework Glasses

2.1 Introduction

Hybrid glasses are defined here as a fourth class of glass material distinct from inorganic, polymeric and metallic glasses. This is based upon two reasons. Firstly, they contain both inorganic and organic moieties in their structures. Secondly, the dominant, structure defining bond, is co-ordinate in nature, occurring between organic linkers and metal nodes. This category of glass is still incredibly new, with the first reported examples occurring in 2014 [36]. Although there is increased interest in the field, the number of hybrid glass frameworks remains small. This is in stark contrast to the number of total crystalline MOFs which have been synthesised and characterised, which is approximately 80,000 [1].

The first class of hybrid glasses discovered were based on zeolitic imidazolate frameworks (ZIFs) which are a sub-set of MOFs (**Figure 2.1a**) [36]. However, a structurally distinct class of reversibly melting coordination polymers formed from metal phosphate and imidazoles, in a broad variety of coordination environments have also been reported (**Figure 2.1b**) [37]–[40]. More recently the discovery of a non-ZIF melting MOF with low temperature melting behaviour has also been published (**Figure 2.1c**) [41]. Finally, a recent report of melting hybrid perovskite structures has expanded the hybrid glass family to encompass another materials class (**Figure 2.1d**) [42].

The work of this thesis is based around hybrid glasses and liquids formed from melting ZIFs and therefore the literature review will focus on this class of hybrid glass formers. It begins with a general description of crystalline ZIF materials. The discovery of the molten and amorphous states, their structure, chemistry and melting mechanism is then discussed. Finally, the chemical and physical properties of MOF glasses are analysed, alongside their potential applications.

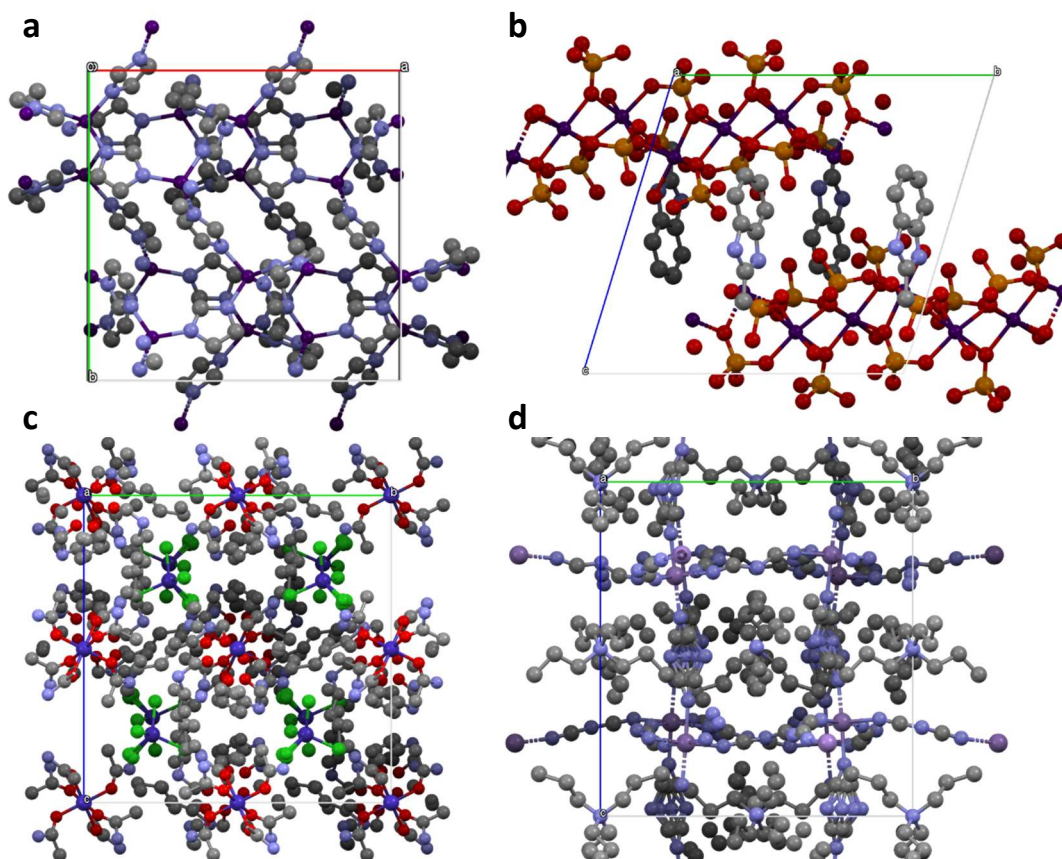


Figure 2.1: Examples of the four families of hybrid glass formers. **a.** ZIF glasses - ZIF-4 ($\text{Zn}(\text{Im})_2$), where Im^- is imidazolate ($\text{C}_3\text{H}_3\text{N}_2^-$). Reproduced from [43]. **b.** Phosphate imidazole co-ordination polymers - $[\text{Zn}_3(\text{H}_2\text{PO}_4)_6(\text{H}_2\text{O})_3]\cdot\text{H}(\text{mbIm})$, where $\text{H}(\text{mbIm})$ is 2-methylbezimidazole ($\text{C}_8\text{H}_8\text{N}_2$). Reproduced from [37]. **c.** Metal-Bis(acetamide) MOFs - $\text{Co}(\text{bba})_3[\text{CoCl}_4]$, where bba is $\text{N,N}'\text{-1,4-}$ butylenebis(acetamide) ($\text{C}_8\text{H}_{16}\text{N}_2\text{O}_2$). Reproduced from [41]. **d.** Hybrid Perovskites - $[\text{TPrA}][\text{Mn}(\text{Dca})_3]$, TPrA^+ is tetrapropylammonium ($\text{C}_{12}\text{H}_{28}\text{N}^+$) and Dca is dicyanamide (C_2N_3^-). Reproduced from [44]. Key: Grey - Carbon, Blue - Nitrogen, Green- Chlorine, Red - Oxygen, Orange - Phosphorous, Dark Blue - Cobalt, Light Purple - Manganese, Purple - Zinc. Hydrogen atoms omitted for clarity.

2.2 Zeolitic Imidazolate Frameworks

2.2.1 Structure of Zeolitic Imidazolate Frameworks

Zeolitic imidazolate frameworks (ZIFs) are a subset of MOFs with the formula $T(\text{Im})_2$ where T is a metal cation and Im^- is a linker based on the imidazolate ($\text{C}_3\text{H}_3\text{N}_2^-$) ion (**Figure 2.2**) [45]. The similarity of the T-Im-T bond angle to the Si-O-Si bond angle results in ZIFs adopting structures composed of corner sharing tetrahedra, which are also observed in inorganic zeolites (**Figure 2.3**) [45].

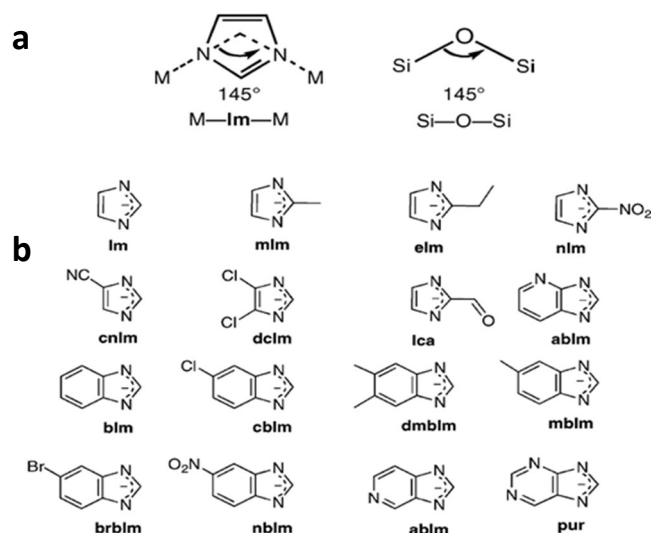


Figure 2.2: Linker structure in zeolitic imidazolate frameworks. **a.** Si-O-Si bond in Zeolites and M-Im-M bond in ZIFs. **b.** A selection of imidazolate anions found in ZIFs. Reproduced from [45].

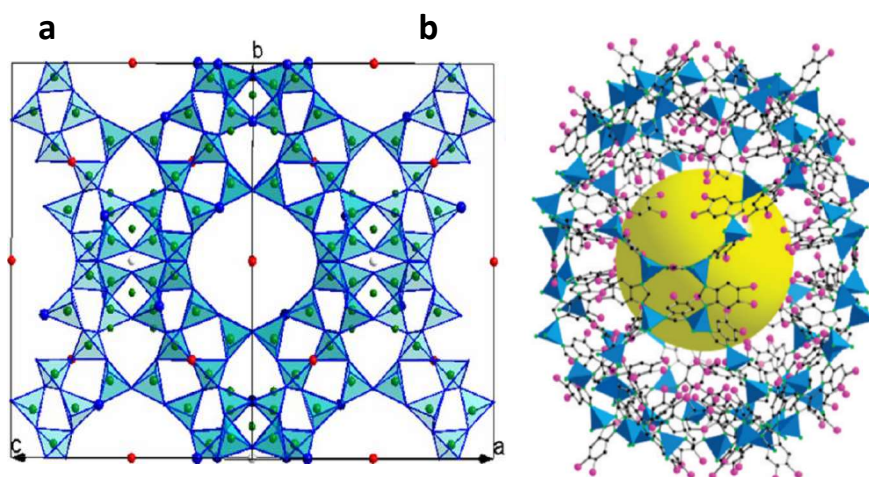


Figure 2.3: ZIF and zeolite structure comparison. **a.** Zeolite Y $\text{Na}(\text{H})_{58}[\text{Al}_{58}\text{Si}_{134}\text{O}_{384}](\text{H}_2\text{O})_{240}$. Key: Green – Silicon/Aluminium, Dark Blue – Oxygen, Red – Sodium, Light Blue – Si/ AlO_4 . Reproduced from [46]. **b.** ZIF-95 $[\text{Zn}(\text{cblm})_2]$ Key: Grey – Carbon, Green – Nitrogen, Pink – Chlorine, Blue – ZnN_4 . Hydrogen atoms omitted for clarity. The yellow ball indicates the largest cage pore, diameter 24 Å. Reproduced from [45].

The most common inorganic SBUs (**Chapter 1**) observed in ZIFs are ZnN_4 or CoN_4 , which are neutral complexes where the metal centres are tetrahedrally coordinated. However, different chemistries have also been reported in the literature. For example, Boron-Lithium Imidazolate Frameworks (BIFs) are comprised of $\text{B}(\text{Im})_2^-$ and $\text{Li}(\text{Im})_2^+$ tetrahedra, so that the framework remains neutral (**Figure 2.4a**). BIFs show a degree of flexibility in the metal centres in their structure with the B centres being connected to either four imidazolates or three imidazolates and a terminal hydrogen (**Figure 2.4b**). $\text{Cu}^+/\text{B}^{3+}$ frameworks have also been synthesised in which the Cu^+ centres can be tetrahedral and connected to either four imidazolate ions, three imidazolate ions and a terminal iodide ion or linear and connected to two imidazolate ions (**Figure 2.4c**) [47]. ZIF-5, an In(III) and Zn(II) containing ZIF with the non-zeolitic **gar** topology, has also been reported in which the indium cations are octahedrally coordinated (**Figure 2.4d**).

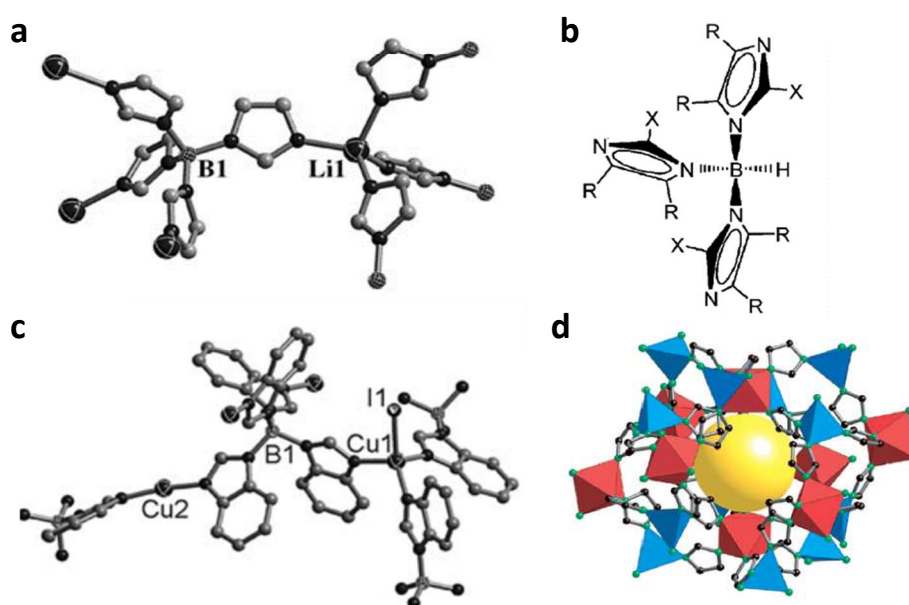


Figure 2.4: Different coordination environments in ZIFs. **a.** Tetrahedrally coordinated $\text{B}(\text{Im})_2^+$ and $\text{Li}(\text{Im})_2^-$ centres. **b.** A tetrahedrally coordinated boron centre with a terminal hydrogen. **c.** A boron copper ZIF with both tetrahedral and linear Cu^+ centres. **d.** ZIF-5, $\text{In}_2\text{Zn}_3(\text{Im})_{12}$. Key: Grey – Carbon, Green – Nitrogen, Blue – ZnN_4 , Red – InN_6 . Hydrogen atoms omitted for clarity. Reproduced from [43], [47].

The ZIF literature has a wide array of reported topologies, including nets that have not been reported in zeolites [45]. This can partially be ascribed to the ease with which ZIFs can be synthesised relative to Zeolites. A high throughput synthesis protocol involves the mixing of reactants, imidazole derivatives and metal salts (typically nitrates), in amide solvents in microplate wells. This is followed by heating in the range 85-150 °C for times between 12 and 96 hours. The products can then be rapidly

evaluated by PXRD and new structures solved using single crystal X-ray methods [48]. ZIF syntheses can then typically be scaled up to the gram scale using solvothermal synthesis methods [2].

2.2.2 Physical Properties of Zeolitic Imidazolate Frameworks

Relative to other classes of MOFs, ZIFs have almost uniquely stable structures [43]. ZIFs have chemical stabilities which rival those of mesoporous silicas. The ZIF-8 framework was unaffected by boiling in methanol, benzene, and water for seven days (**Figure 2.5**) [43]. This high chemical stability is attributed to both the hydrophobic pore surface and the strong coordinate Zn/Co-N bonding [43]. This stability renders post-synthetic modifications possible. ZIF-90, a framework in which the imidazolate contains an aldehyde functionality, can withstand strong reaction conditions to undergo both a reduction to an alcohol and reaction to form an imine, while maintaining its porosity and crystal structure [49].

ZIFs are also a highly thermally stable class of MOFs, with stabilities of up to 550 °C as measured by thermogravimetric analysis under flowing nitrogen. A sample of ZIF-8 heated to 500 °C under nitrogen and held for 1 hour, and was found to retain crystallinity. This level of thermal stability is only matched by relatively dense MOFs of other classes, for example the zinc carboxylate based MOF-5 decomposes at 450 °C [43].

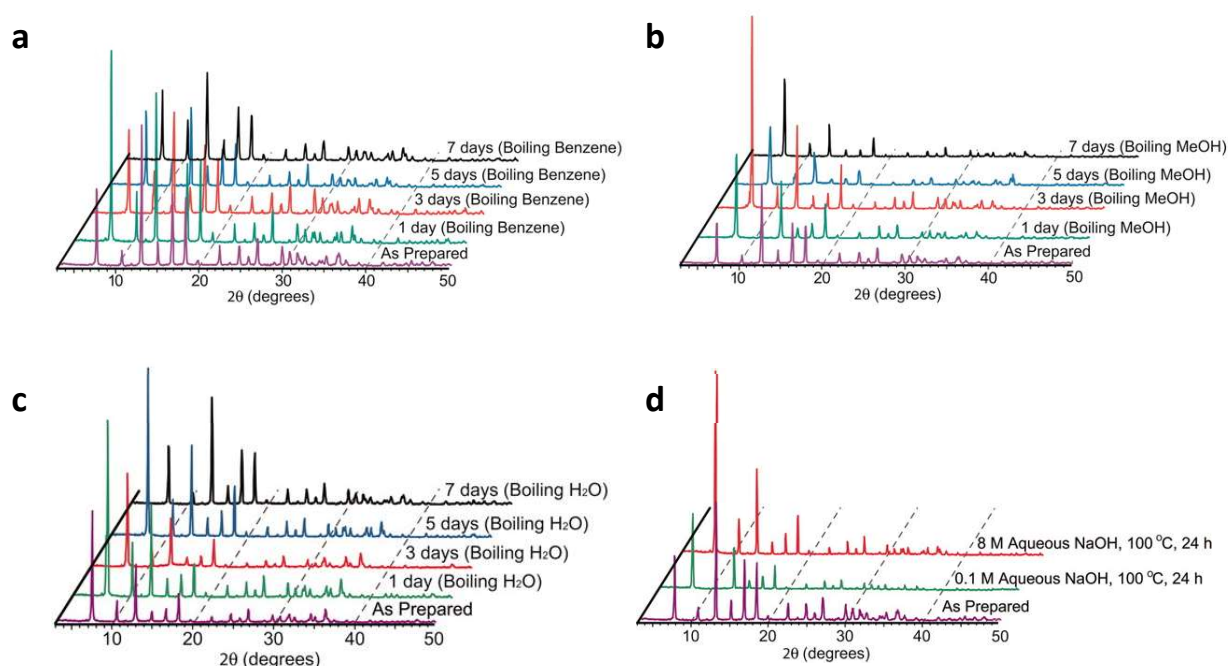


Figure 2.5: Chemical stability of ZIF-8. Framework stability is confirmed by unchanging PXRD pattern upon refluxing in **a.** Benzene **b.** Methanol **c.** Water for seven days. **d.** Aqueous NaOH for 1 day. Reproduced from [43].

2.3 Metal-organic Framework Glass Formation in Zn(Im)₂

2.3.1 Formation of an Amorphous Zn(Im)₂ Phase

A broad study was conducted on the thermal stability of Zn(Im)₂ ZIF polymorphs [50]. Four M(Im)₂ frameworks were synthesised, ZIF-1 (topology BCT, space group $P2_1/n$), ZIF-3 (topology DFT space group $P4_2/mnm$), ZIF-4 (topology **cag**, space group $Pbca$), and ZIF-4-Co (**Figure 2.6**). ZIF-4-Co is a framework isostructural with ZIF-4 but with Co replacing Zn in the SBU [51]. These different frameworks allow exploration of the effects of the metal centre, framework topology, and density on thermal stability, while controlling for the chemistry of the linker. Variable temperature PXRD measurements showed that all frameworks irreversibly amorphise at approximately 280 °C before undergoing recrystallisation to the dense ZIF-zni polymorph at 370 °C (**Figure 2.7**).

This recrystallisation is also irreversible under experimental timescales, with ZIF-zni recoverable to room temperatures without further phase changes. ZIF-zni was calculated via density functional theory calculations to be the lowest energy structure in the Zn(Im)₂ system [52].

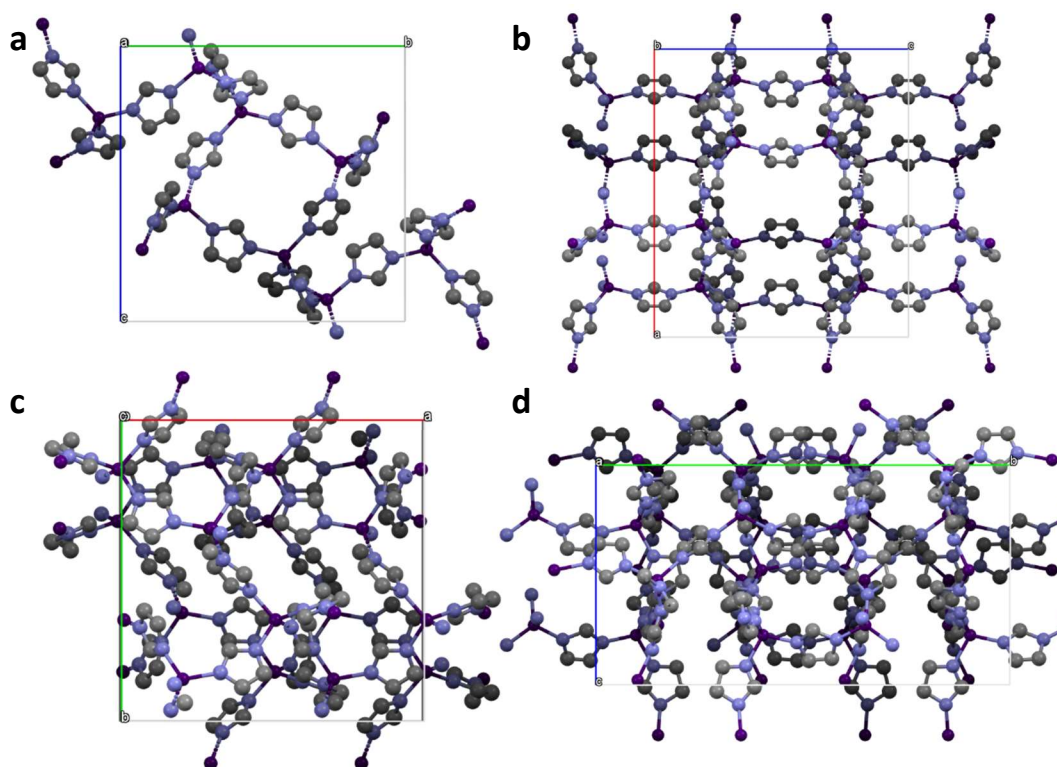


Figure 2.6: Unit cells of Zn(Im)₂ ZIFs. **a.** ZIF-1 **b.** ZIF-3 **c.** ZIF-4 and **d.** ZIF-zni. Reproduced from published structures [43], [53]. Key: Grey - Carbon, Blue – Nitrogen, Purple - Zinc. Hydrogen atoms omitted for clarity.

Nanoindentation found that the stiffness and hardness of the amorphous frameworks formed from different parent crystals were all very similar to one another and were intermediate between the values measured for the porous starting frameworks and the dense ZIF-zni phase. Equally the densities of all the amorphous zinc containing networks were, within error of each other, 1.574 g cm^{-3} . This is despite starting from a range of densities (**Table 2.1**). These densities were also intermediate between the starting frameworks and ZIF-zni. The amorphised framework formed from ZIF-4-Co had a slightly lower density, 1.562 g cm^{-3} , however this was in line with the slightly lower density of the starting framework compared to its zinc analogue. In contrast measurements on substituted linker ZIFs showed no sign of thermal amorphisation, which was attributed to the presence of bulkier linkers, which sterically inhibit framework collapse [50].

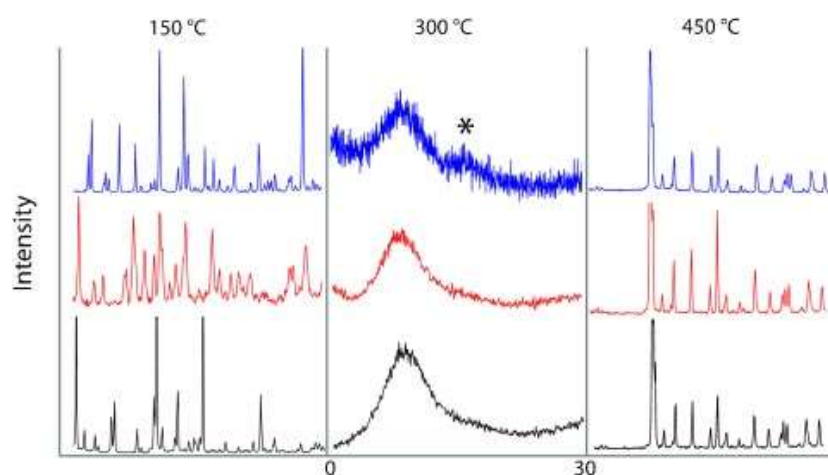


Figure 2.7: Variable temperature X-ray diffraction patterns for ZIF-4-Co (blue), ZIF-3 (red), and ZIF-1 (black). The worse data quality and secondary background feature (marked with an *) of the ZIF-4-Co sample arises due to fluorescence. Reproduced from [50].

Table 2.1: Pycnometric density measurements for the crystalline ZIFs (with solvent) and amorphous ZIFs produced through heating. Reproduced from [50].

Structure	Crystalline Density (g cm^{-3})	Amorphous Density (g cm^{-3})
ZIF-1	1.4828(6)	1.575(4)
ZIF-3	1.1763(20)	1.572(4)
ZIF-4	1.4616(5)	1.576(4)
ZIF-4-Co	1.4465(6)	1.562(6)
ZIF-zni	1.6027(3)	N/A

2.3.2 Structure of the Amorphous Phase

In order to achieve a greater understanding of the observed amorphisation phenomenon, ZIF-4 was measured using variable temperature neutron total-scattering, with the amorphised ZIF and ZIF-zni phases being formed in situ [54]. Total-scattering techniques will be described in more detail subsequently (**Chapter 3**). However, briefly, through appropriate data processing, and Fourier transformation, total-scattering measurements can be used to obtain a pair-distribution function (PDF). This PDF represents a histogram of the atom-atom correlations in the structure, with a peak in the PDF corresponding to a correlation between two atomic centres in the material that occurs at frequencies above that necessitated by the materials bulk density [55].

Neutron total-scattering confirmed the results of the variable temperature PXRD, with the amorphous ZIF lacking any sharp Bragg features. Strikingly however, both the neutron PDF and X-ray PDF of the amorphous ZIF-4 and ZIF-zni were nearly identical below approximately 6 Å (**Figure 2.8a**). Equally the X-ray PDFs of all of the amorphised structures derived from ZIF-1, ZIF-3, and Co-ZIF-4 were also identical (**Figure 2.8b**) [50].

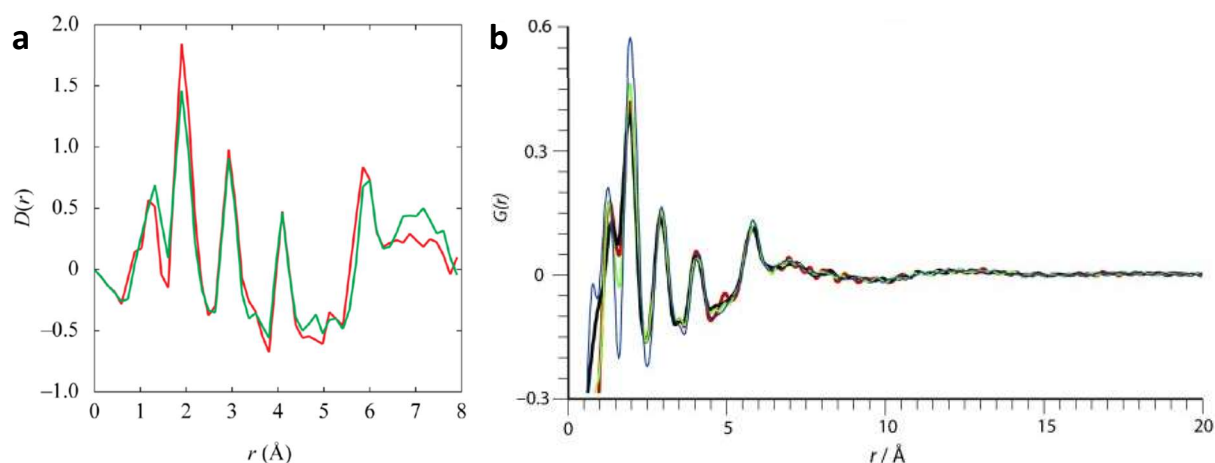


Figure 2.8: PDF on crystalline and amorphous $\text{Zn}(\text{Im})_2$ and $\text{Co}(\text{Im})_2$ frameworks. X-ray PDF functions of **a.** amorphous ZIF-4 (red) and ZIF-zni (green). **b.** amorphous ZIF-1 (black), amorphous ZIF-3 (red), amorphous ZIF-4 (green), amorphous ZIF-4-Co (blue). Reproduced from [50], [54].

This implies both that the short-range order was identical in all three ZIF-4 derived phases, and that the local order in the amorphous state is common across all $\text{Zn}(\text{Im})_2$ polymorphs. In other words the $\text{Zn}(\text{Im})_4$ tetrahedra, which is the common structural building block in the crystalline state, is preserved on formation of the amorphous ZIFs. The limit of the correspondence between the crystalline and amorphous states, approximately 6 Å, is equal to the Zn-Zn distance measured for the crystalline ZIF-4 [43]. This indicates that the structure within the first $\text{Zn}(\text{Im})_4$ tetrahedra is identical in all cases. The

identity of the peaks was assigned by measurement of distances in the ZIF-4 structure and confirmed by partial PDF simulation using PDFGUI [56], [57] (**Figure 2.9**).

Above this distance the PDFs of the crystalline and amorphous materials diverged [54]. The crystalline materials showed long range density fluctuations, which were a result of the periodicity of the unit cell. In contrast the amorphous ZIFs showed a few broad features between 6 – 20 Å before becoming featureless. These broad features indicate some structure beyond the first tetrahedra, however it is clearly of different character from the starting crystalline frameworks. The absence of long scale features in the PDF confirmed the amorphous nature of the structures.

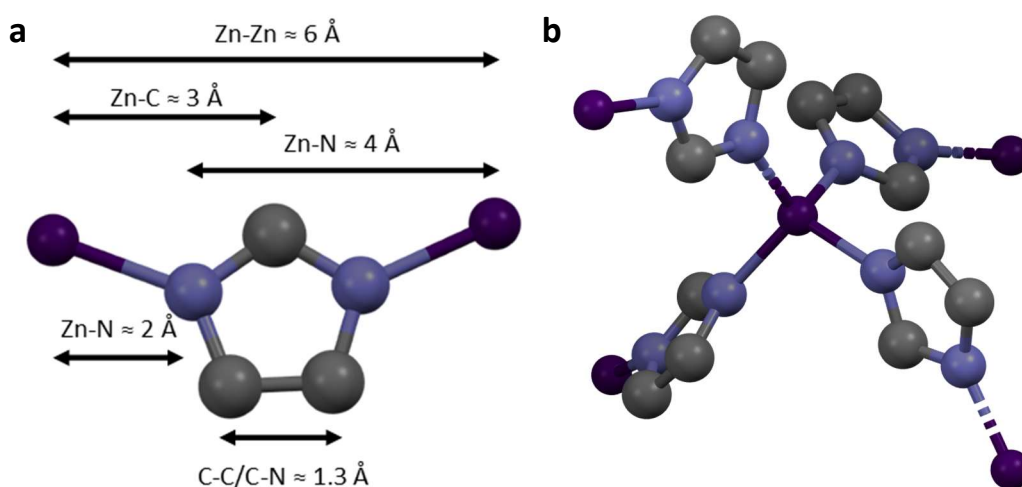


Figure 2.9: Atomic correlations in the short-range order of ZIFs. **a.** Labelled imidazolate linker (Im) showing the identity of correlations assigned in the PDF of ZIF glasses and crystals. **b.** Tetrahedral structure of the Zn(Im)₄ centre in ZIF glasses and crystals. Key: Grey - Carbon, Blue – Nitrogen, Purple - Zinc. Hydrogen atoms omitted for clarity. Reproduced from [43].

To further understand the structure of the amorphous ZIF, reverse Monte-Carlo modelling was conducted to create a structural model which fit the neutron and X-ray total scattering data. Initial refinements, which began from structures based on the crystalline topologies of either ZIF-4 or ZIF-zni, were not successful in reproducing the total-scattering. This remained the case even when significant disorder was incorporated into the model. Instead, inspired by the similarity of the O-Si-O bond and the Im-Zn-Im bond (**Figure 2.2a**) researchers constructed a model adapted from the continuous random network (CRN) (**Chapter 1**) of SiO₂ glass, which itself had been adapted from a model for amorphous Si [54]. This was achieved by lengthening the bonds and replacing Si⁴⁺ with Zn²⁺ and O²⁻ with Im⁻. The adapted CRN model had the best fit to the total-scattering data (**Figure 2.10**). Such analysis cannot definitively prove a structure, only discard structures which give large discrepancies with the available data. However, this analysis proves that the CRN model is a better fit for the structure than models starting from either of the bordering crystalline phases.

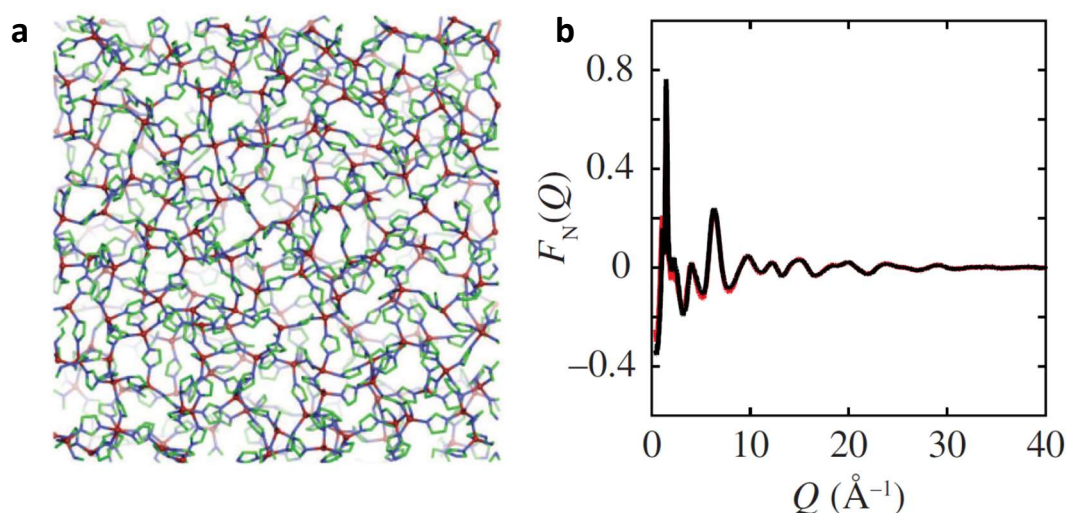


Figure 2.10: Continuous random network model (CRN) created for amorphous ZIF-4. **a.** CRN model created for the structure. Key: Blue – Nitrogen, Green – Carbon, Red – Zinc. Hydrogen/deuterium atoms omitted for clarity. **b.** Experimentally measured neutron total-scattering function (black) and reverse Monte Carlo fit obtained from the CRN model (red). Reproduced from [54].

The change in structure on formation of the amorphous phase indicates that the transition is reconstructive rather than displacive. In other words, this implies that amorphisation occurs via a series of changes in connectivity implying nucleation and growth of a new distinct structure. This contrasts with a displacive transition which occurs by distortion of the framework while maintaining underlying connectivity. An example of a potentially displacive transition in the same system is the amorphisation of ZIF-4 under moderate pressure. In contrast to thermal amorphisation this phase

change is reversible on pressure reduction (**Figure 2.11**) [58]. Here the reversibility of the transition implies that connectivity is maintained and just distorted by the applied pressure.

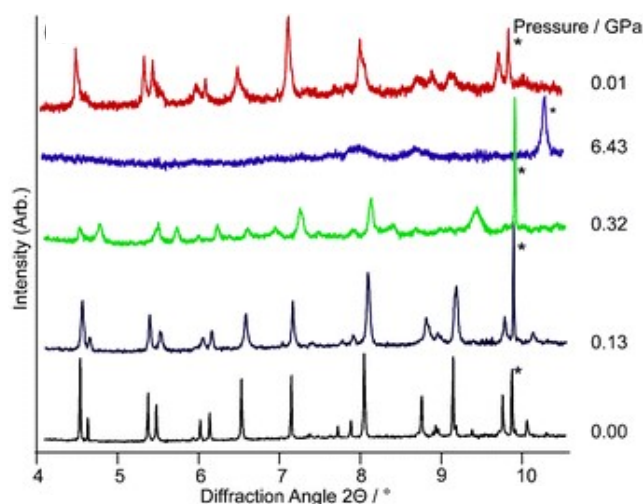


Figure 2.11: In situ variable pressure X-ray diffraction data on solvent containing ZIF-4 with a large sized pressure transmitting fluid (Daphne Oil 7474 (DO)). Black trace indicates ambient pressure, red trace indicates measurement on return to ambient pressure. The peak due to the SiO₂ standard is indicated by an *. Reproduced from [58].

Further evidence for the reconstructive nature of both the thermal amorphisation and recrystallisation to ZIF-zni is that they occur in a similar temperature range for ZIF-1, ZIF-3 and ZIF-4 [50]. In other words, the onset temperature is approximately independent of the framework structure. Moreover, the PDF of the structures are identical (**Figure 2.8b**) as are the densities of the amorphous structures (**Table 2.1**), despite their formation from parent crystals of different densities and topologies. This is most easily explained by a reconstructive transformation to a common amorphous state.

2.3.3 Thermal Measurements of the Amorphous-Crystalline Phase Transition

Differential scanning calorimetry (DSC) measurements on ZIF-4 shed further light on the amorphisation process [36]. The first heating scan on ZIF-4 (**Figure 2.12**) showed an endothermic transition due to removal of solvent from the framework's pores at approximately 230 °C, which does not cause framework collapse. This is followed by two closely spaced features, beginning at approximately 327 °C, an exothermic transition which is followed immediately by an endothermic transition. These transitions are associated with loss of crystallinity in wide-angle scattering measured

on the same samples [36] and coincide to a reasonable degree with the amorphisation measured previously via variable temperature PXRD (**Figure 2.7**) [50]. The exothermic transition is reported as being due to formation of a low density amorphous (LDA) phase, and the endotherm corresponds to its conversion to a higher density amorphous phase (HDA). Samples heated to beyond the exotherm and endotherm, cooled and then reheated, display glass transitions (T_g s) at two separate temperatures corresponding to the LDA and HDA phases at 316 °C and 292 °C respectively (**Figure 2.12**). Conversion of the LDA to the HDA is reported as being irreversible within the timeframes of the study.

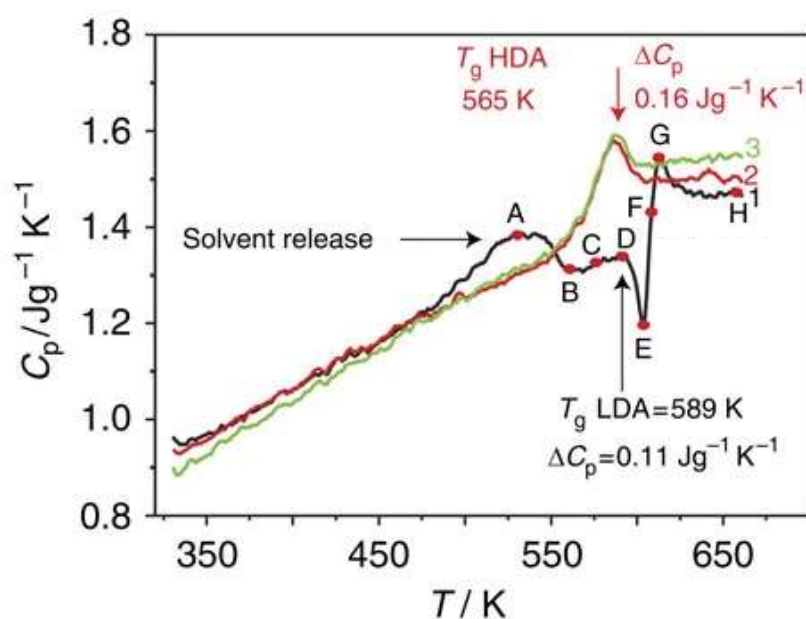


Figure 2.12: Three successive DSC scans on ZIF-4. Conducted at 10 °C/min in argon. The first scan (black) on the as-synthesised ZIF-4 shows solvent release (A), formation of LDA (D-F) followed by conversion to HDA (F-H). Subsequent scans (red and green) show the glass transition temperature of the HDA phase. Reproduced from [36].

Further heating of the HDA phase resulted in exothermic recrystallisation of ZIF-zni at around 500 °C (**Figure 2.13**) followed by a melting endotherm (T_m) with an offset at approximately 590 °C. The measured enthalpy changes on recrystallisation and melting, 49 J g⁻¹, are identical, confirming complete melting of the ZIF-zni. ZIF-zni is the densest lowest energy polymorph of the Zn(Im)₂ system [52]. This endotherm occurs shortly before decomposition, as measured by a rapid drop in mass and dramatic change in the DSC baseline. Quenching from 592 °C, i.e. above the offset of the melting endotherm, results in the formation of an amorphous structure, termed the melt-quenched glass (MQG). X-ray total-scattering measurements on the MQG and HDA structures confirmed they were

amorphous and PDF measurements were identical between HDA, MQG and ZIF-4 below the distance of 6 Å [36]. This confirmed that short-range order and linker structure are maintained on MQG formation.

In contrast DSC scans on ZIF-8 displayed no features in the DSC before decomposition at approximately the same temperature as ZIF-4. ZIF-8, $\text{Zn}(\text{mIm})_2$, where mIm^- is 2-methylimidazole, is an open substituted framework [36]. The difference in thermal behaviour of ZIF-4 and ZIF-8, as measured by DSC, confirm the earlier differences between substituted and unsubstituted frameworks measured by VT PXRD [50].

Reheating of the MQG phase in the DSC confirmed that it had a glass transition at 292 °C which is identical to the T_g recorded for the HDA phase. Moreover, the PDF of the HDA and MQG samples was identical in the 6 – 15 Å region, and distinct from that of the crystalline ZIF-4. This implies a common mid-range order which differs from that of the parent crystalline framework. The coincidence of the ZIF-zni recrystallisation and correspondence of the PDF also imply that this structure is shared with the amorphous state formed on heating other $\text{Zn}(\text{Im})_2$ polymorphs. Reverse Monte-Carlo modelling on the MQG structure via X-ray and neutron total-scattering were also able to confirm that the CRN model previously developed fits the MQG data without changes in topology [59], [60].

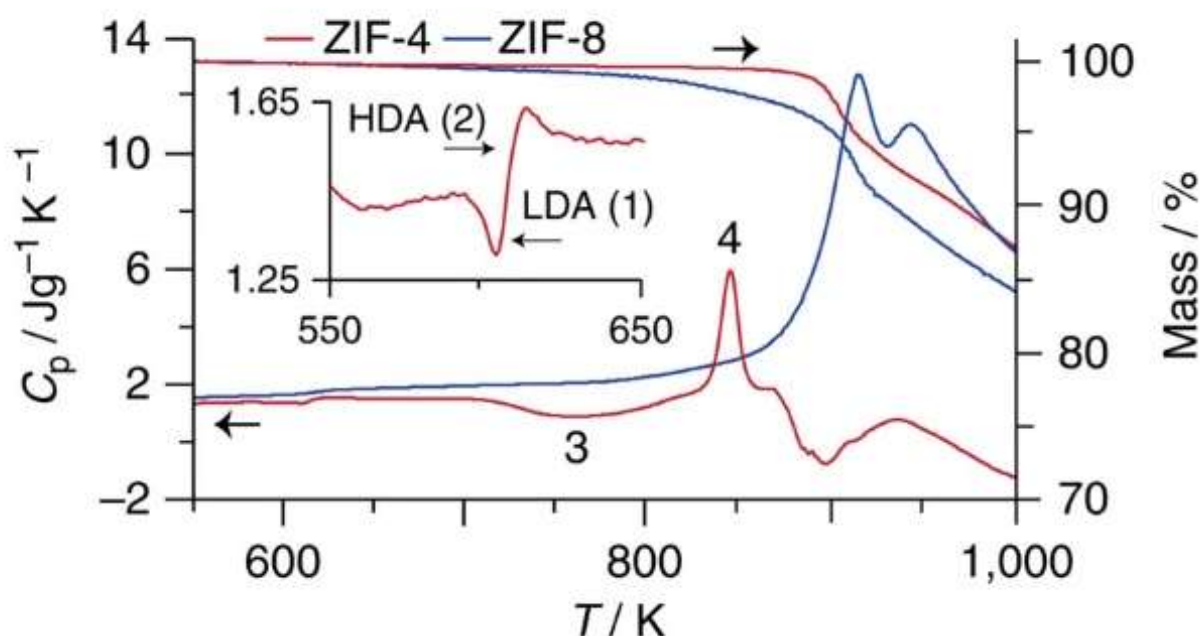


Figure 2.13: Thermal response and TGA mass curves for ZIF-4 (red) and ZIF-8 (blue). The ZIF-4 curve shows recrystallisation to ZIF-zni (3) followed by melting (4). Inset: ZIF-4 DSC curve showing LDA and HDA formation (1-2). Reproduced from [36].

2.3.4 Summary of Liquid State Formation in $\text{Zn}(\text{Im})_2$

The amorphous phase formed on heating of $\text{Zn}(\text{Im})_2$ to around 300 °C is not generally regarded as melting and liquid formation in the literature. Instead it is viewed as solid state thermal amorphisation separate from the MQG formed from heating above the melting point of ZIF-zni. However, the preponderance of the evidence taken from multiple sources seems to indicate that a liquid state is being formed:

1. Thermally amorphous frameworks formed from different parent crystals share identical densities and short and mid-range orders as measured by X-ray and neutron total-scattering.
2. The total-scattering data can be fit using a CRN model, implying that the amorphous state is topologically distinct from the crystalline ones and that it must therefore form reconstructively.
3. The MQG formed from heating ZIF-zni above its melting point and quenching and the HDA phase in ZIF-4 coincide structurally with each other. Therefore they are also the same as the amorphous states formed from heating other $\text{Zn}(\text{Im})_2$ frameworks. Moreover, they share a common glass transition temperature on re-heating, implying a similar liquid state origin.

The final evidence of ‘low-temperature’ melting of the thermally amorphous phase comes from optical microscopy on amorphous ZIF-4 produced by heating to 300 °C and cooling (**Figure 2.14**) [54]. This sample, in contrast to the crystalline phases, showed curved external and internal surfaces, which were taken as evidence of viscous flow occurring on formation of the liquid phase.

The confusion in the literature may arise from the very small degree of flow observed in the HDA/low temperature amorphous phase. However this is attributed to the high viscosity of the ZIF liquid, especially at such a low temperature where the thermal energy in the system is so low (see subsequent section) [61]. The driving force for amorphisation has been reported as due to the metastability of relatively porous starting frameworks such as ZIF-4, especially after removal of templating solvents from their pores at elevated temperatures [52], [54].

Given this metastability, the initial heating curve of porous $\text{Zn}(\text{Im})_2$ frameworks, as measured by DSC, could be thought of as follows: i) The metastable framework melts, i.e. HDA formation, resulting in a liquid state. This liquid is intermediate in stability between the porous framework and ZIF-zni. As this liquid has formed below its equilibrium T_m it is metastable with respect to ZIF-zni, in other words it is supercooled. ii) When there is enough thermal energy in the system, the supercooled liquid recrystallises to form ZIF-zni. The recrystallisation rate from supercooled liquids is generally found to

be high only at intermediate temperatures when there is a balance between driving force and growth kinetics [30].

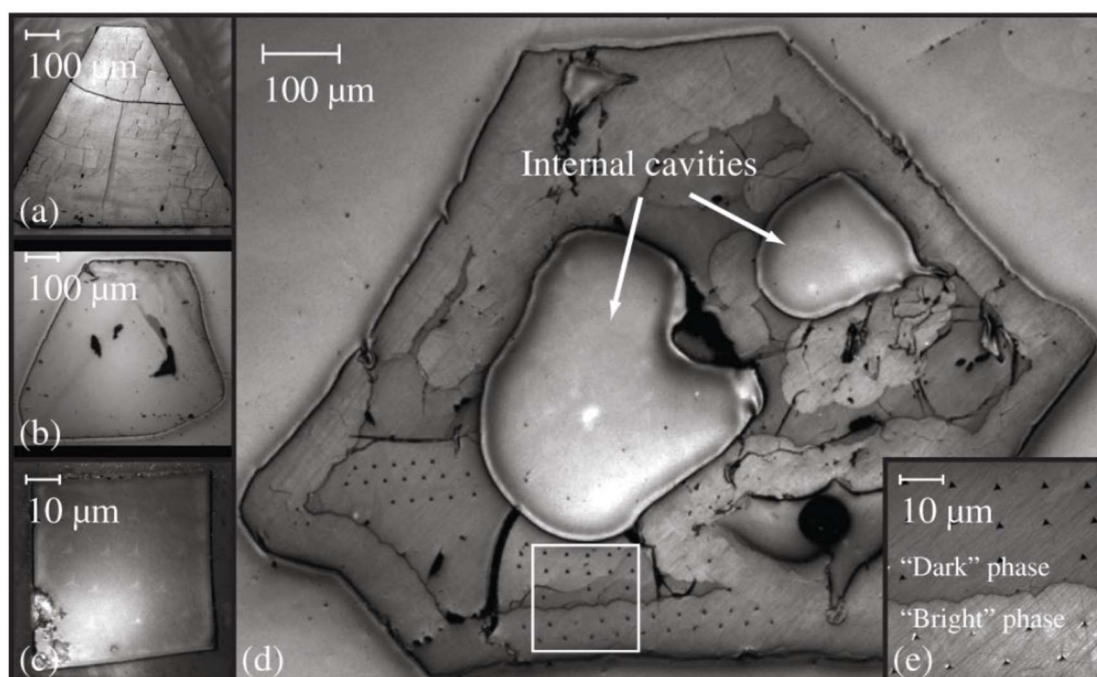


Figure 2.14: Optical micrographs of heat treated ZIF-4. **a.** A ZIF-4 crystallite. **b.** An a_g ZIF-4 monolith. **c.** A ZIF-zni crystallite **d.** A partially recrystallised amorphous ZIF-4 monolith. The “Bright” phase is ZIF-zni, whereas the “Dark” phase is a_g ZIF-4. Reproduced from [54].

iii) On further heating the ZIF-zni melts and forms the liquid as the thermodynamically stable phase. As such it can be seen that quenching from either state i) or iii) results in the formation of a MOF glass with similar structure and glass transition temperature. Thus, the heating of metastable porous ZIF frameworks is not dissimilar from reheating of glasses, in that a region of supercooled liquid formation is observed before thermodynamic recrystallisation occurs.

In the literature MOF glasses formed by heating into the high temperature liquid state and quenching are generally referred to as a_g ZIF-X where ZIF-X is the parent crystalline framework. In the body of the thesis the distinction between low temperature melting, also termed thermal amorphisation, and high temperature melting is preserved to keep consistency with the reported MOF literature and to distinguish the two separate melting events.

2.4 Investigation into the Mechanism of Metal-organic Framework Melting

2.4.1 The Mechanism of Melting in ZIF-4

Metal-organic framework glasses are a new class of glass structures, and as such the mechanism by which the liquid forms from the parent crystalline framework is of interest from a foundational scientific perspective. Equally a better understanding of MOF melting may offer practical insights into finding new crystalline frameworks that melt and into altering the melting characteristics of existing frameworks.

To understand the melting process variable temperature X-ray total scattering data was collected on a pre-formed sample of a_g ZIF-4, heated to 592 °C, past the melting endotherm for ZIF-zni observed in the DSC, [36] and cooled to room temperature. This experimental data was combined with first principal molecular dynamics (FPMD) simulations to evaluate the melting process in ZIF-4 [60]. Despite the fitting of total-scattering data for a_g ZIF-4 using an adapted CRN model, the FPMD simulations used the crystal structure of ZIF-4 as a starting point. This was done because of the computational expense of modelling the large amorphous 'unit cell'. Equally, because of the short timescale involved in FPMD simulations, temperatures up to 2000 °C were used to gather information on relatively rare events with high thermodynamic barriers. Despite these unphysical characteristics the simulated PDF functions matched all the salient features of the experimental PDF data [60].

As well as simulation of the overall PDF, partial PDFs of the Zn-N, Zn-Zn, and Zn-Im, distances were also extracted from the trajectories of the simulation. Here Zn-Im is the distance between the Zn^{2+} ion and the centroid of the imidazolate linker. These functions show broadening of peaks and loss of features at distances greater than 10 Å on increasing temperature, which is consistent with the formation of an amorphous liquid. The FWHM and peak position of the first peak in Zn-Zn and Zn-N partial PDFs was measured and used to compute the fractional spread in bond length as a function of temperature Δ :

$$\Delta = \frac{FWHM}{d_0} \quad 2.1$$

The Lindemann criterion, an empirical criterion for the onset of the melting temperature, states that melting occurs when the fractional bond length change is between 10-15 %. For both Zn-N and Zn-Zn this occurs between 730 °C and 1230 °C (**Figure 2.15a**). Simulations of the heat capacity also show a jump in this range, further confirming the onset of liquid formation (**Figure 2.15b**). The coincidence of

the jump in the heat capacity with the increased thermal vibrations in the Zn-N bond indicates the importance of Zn-N fission in melting.

The potential of mean force (PMF) between each atom was also calculated from the partial PDFs and the maxima of these potentials can be treated as the activation energy for bond breaking. The activation energy for fission decreases with increasing temperature, however the activation energy remains relatively high even at elevated temperatures. At 730 °C, the onset of the melting range identified by the Lindermann's law analysis, the barrier is 87 kJ mol⁻¹, which is 10.5 $k_B T$. Whereas at

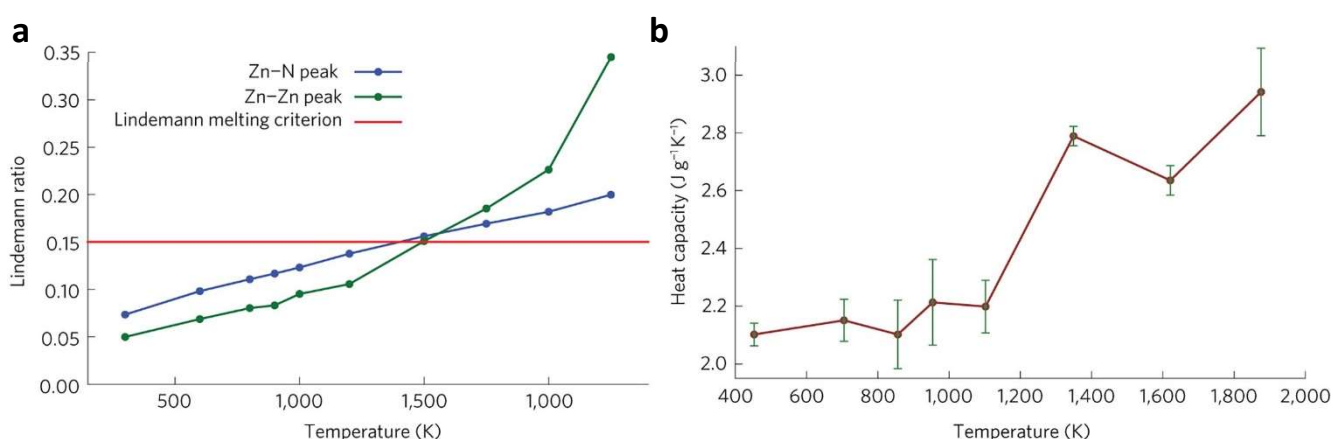


Figure 2.15: Simulated heat capacity and Lindemann ratio in ZIF-4. **a.** Simulated Lindemann's ratios for the Zn-N and Zn-Zn correlations (Equation 2.1). **b.** Simulated heat-capacity of ZIF-4. Reproduced from [60].

approximately 570 °C, i.e. close to the experimental melting temperature, it is 95 kJ mol⁻¹, which is 14 $k_B T$. In either case it can be seen from this analysis that fission of the Zn-N has a high activation energy and so it is a rare thermal event even during melting.

Further FPMD modelling on ZIF-4 examined the effect of increasing pressure on the melting process [62]. This analysis revealed that, although the melting mechanism did not appear to change, the activation energy for fission of the Zn-N bond also decreases on increasing pressure. This is in line with similar studies on ZIF-8 and Zn(Im)₂ polymorphs which show that failure occurs by shear mode softening, i.e. the shear modulus becomes 0, on increasing pressure [63], [64], which was structurally linked to softening of the Zn-Im-Zn bond angle at higher pressures.

Additional experimental evidence for the importance of Zn-N bond fission in the melting process came from in situ variable temperature THz and far Infra-red spectroscopy on a series of melting ZIF compounds with the general formula Zn(Im)_x(xblm)_{2-x}, where xblm is one of a series of halogen substituted benzimidazolate molecules [65]. This series of samples will be described further in the subsequent section (Chapter 2.5). Fitting of the vibrational frequency of the Zn-N bond at increasing

temperatures allows extraction of the spectral position shift coefficient for the Zn-N bond, X_R . This quantity is correlated with the thermal deformation of the ZnN_4 tetrahedra [65], and was found to correlate almost perfectly ($R^2 = 0.98$) with the melting temperature for the different frameworks (**Figure 2.16**). This implies that ZnN_4 tetrahedra with greater degrees of thermal fluctuation in the Zn-N bond undergo melting at lower temperatures. This data is, in essence, experimental validation of the computational Lindemann's law treatment of ZIF-4 (**Figure 2.15**).

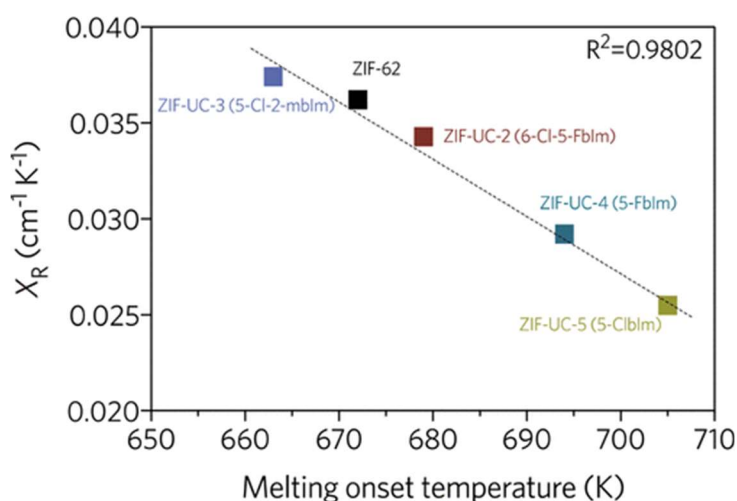


Figure 2.16: Correlation between melting onset temperature and spectral position shift coefficient (X_R). Reproduced from [65].

FPMD simulations were also utilised to compute the distribution of zinc cation coordination numbers as a function of temperature (**Figure 2.17**) [60].

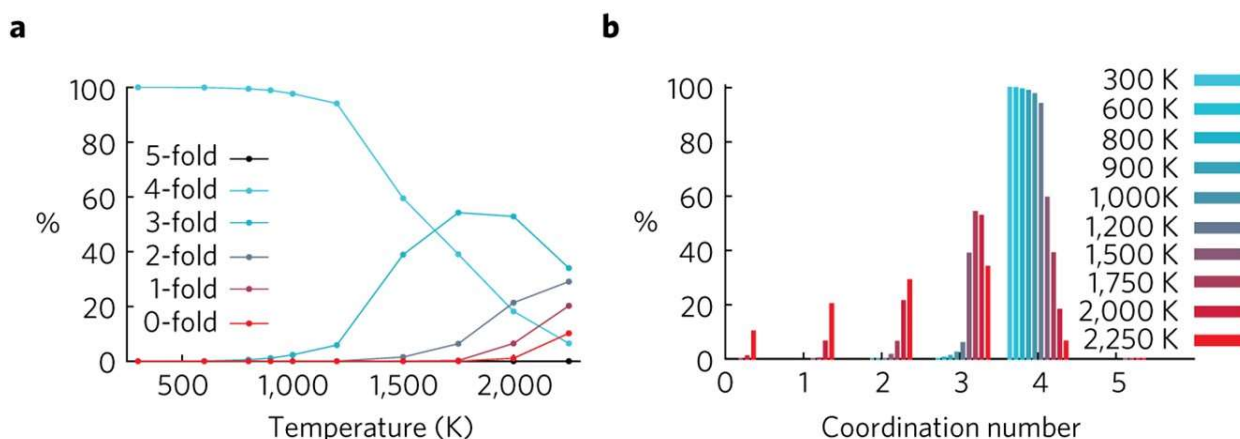


Figure 2.17: Simulated zinc coordination in ZIF-4 as a function of temperature. **a.** Distribution of zinc coordination numbers in ZIF-4 as a function of temperature obtained by FPMD simulation. **b.** Temperature evolution for different coordination numbers. Reproduced from [60].

These results show that at temperatures below 930 °C the zinc ions are, as expected from the crystal structure, 94 %, tetrahedrally coordinated with a small proportion of undercoordinated defects.

As the temperature increase there is a sharp rise in three coordinated zinc centres with them representing 39% of the structure at 1230 °C. Taken together these results indicate that there is a substantial weakening of the Zn-N bond at the melting point and substantial de-coordination of the linkers in the liquid state.

Finally, a mechanistic view of the melting process is formed by focusing on the co-ordination of linkers around a single zinc centre (**Figure 2.18**). This shows that melting is a concerted process involving rapid exchange of imidazolate linkers over the course of around 2 ps. In this context it is hypothesised that the three co-ordinate zinc ions that are present as defects at lower temperatures will act as nucleation sites for formation of the liquid at the melting point.

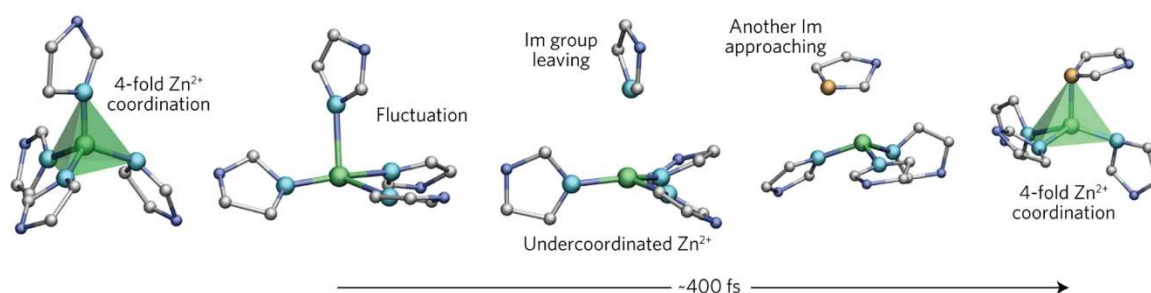


Figure 2.18: Visualisation of the linker exchange events that occur during melting of ZIF-4. Key: Green – Zinc, Light Blue - Initially coordinated Nitrogen, Orange – Nitrogen coordinated after exchange, Grey – Carbon. Hydrogens omitted for clarity. Reproduced from [60].

2.4.2 Comparison with Other Zeolitic Imidazolate Frameworks

Subsequent research used the same FPMD modelling approach to investigate the thermodynamics and dynamics of melting on ZIF-zni and ZIF-8, with the hope of illuminating the origins of the different thermal behaviour in melting and non-melting ZIFs.

A PMF analysis of the Zn-N and Zn-Im distances in the three frameworks revealed that the activation energies for bond fission in ZIF-zni and ZIF-4 are very similar, whereas the activation energy for Zn-N fission in ZIF-8 was slightly higher (**Table 2.2**). The higher activation energy may contribute somewhat to the absence of melting or other reconstructive phenomenon on heating of the ZIF-8 framework. However, in all cases the activation energies are high at the melting temperature relative to the thermal energy in the system and so small differences, of the order of a single $k_B T$, are unlikely to explain such drastic difference in behaviour.

However crucial insight into the different behaviour comes from the PMF analysis of the Zn-Im partial PDF. In this case the ZIF-4 and ZIF-zni had activation energies for fission which were, both similar to each other, and similar to the Zn-N values. ZIF-8 however, had a value that was much higher, $5 k_B T$, for Zn-Im fission than for Zn-N fission. This difference implies that the difference between melting and non-melting ZIFs may lie not in the Zn-N bond strength but in the ability of the imidazolate linker to disassociate from the zinc centre.

Table 2.2: Simulated activation energy (ΔU^\ddagger) and enthalpy (ΔS^\ddagger) associated with a bond cleavage in ZIFs. Extrapolated activation energy (ΔF^\ddagger) at the experimental melting point of ZIF-4. Reproduced from [66].

	ΔU^\ddagger (kJ mol ⁻¹)	ΔS^\ddagger (J mol ⁻¹ K ⁻¹)	ΔF^\ddagger (570 °C) (kJ mol ⁻¹)
ZIF-8 (Zn-N)	145	48	105 ($\approx 15 k_B T$)
ZIF-8 (Zn-Im)	207	77	142 ($\approx 20 k_B T$)
ZIF-4 (Zn-N)	127	37	95 ($\approx 15 k_B T$)
ZIF-4 (Zn-Im)	123	36	93 ($\approx 14 k_B T$)
ZIF-zni (Zn-N)	126	38	95 ($\approx 14 k_B T$)
ZIF-zni (Zn-Im)	128	39	96 ($\approx 14 k_B T$)

The authors hypothesised that it was the lower framework density of ZIF-8 (2.42 Zn centres nm⁻³ [67]) relative to ZIF-4 (3.68 Zn centres nm⁻³ [43]) and ZIF-zni (4.66 Zn centres nm⁻³ [53]) which increased the barrier for imidazolate motion in ZIF-8. This is due to an absence of stabilising dispersion interactions from adjacent linkers in the more open framework. However, the influence of steric hinderance, with there being a larger energy barrier for motion of a sterically larger linker, may also play a role as was hypothesised by earlier researchers [50].

These observations are in agreement with the microscopic melting mechanism that was observed in FPMD simulations [60] (**Figure 2.18**). If the imidazolate cannot dissociate from around its zinc centre then it cannot undergo exchange. This means that dissociated ligands stay localised, either recombining or creating isolated defects, preventing swapping and framework collapsed into a liquid state. Additional experimental validation for this observation also comes from infra-red spectroscopy on the Zn(Im)_x(xbIm)_{2-x} series [65]. This work showed no correlation between the melting point, measured by DSC, and the stretching frequency, and therefore bond strength of, the Zn-N bond measured at room temperature.

In summation the work in this section has used a combination of X-ray total-scattering, spectroscopy, and simulation to uncover the melting mechanism for MOF glasses. The results revealed that framework collapse involved rare Zn-N fission events and linker exchanges. This further confirms the

earlier structural experiments [50], which indicated that topology changes on formation of the glass phase. Breaking of Zn-N bonds is necessary for the connectivity of the framework to change from the crystalline state to the CRN network and therefore the confirmation that it is the melting mechanism serves to explain a wide range of observations in the field.

2.5 Further Examples of Melting Metal-Organic Frameworks

So far the discussion has focused on Zn(Im)₂ polymorphs, which have been shown to melt and form glasses. In contrast, substituted ZIFs have been reported to remain stable until decomposition at elevated temperatures. Continued work in the field revealed more melting ZIFs even though the number of melting MOFs remains a small subset of all known frameworks. All subsequent melting frameworks have been multivariate ZIFs, i.e. ZIFs which contain more than one imidazolate linker (**Table 2.3**) [36], [50], [51], [56], [61], [65], [68]–[71].

2.5.1 An Overview of Multivariate Melting Metal-organic Frameworks

All the melting multivariate MOFs contain imidazolate as a linker and crystallise in the same *Pbca* space group as ZIF-4 and share the same **cag** topology. All the glasses that were produced by heating above the measured endotherm were stable on cooling to room temperature. PXRD of the recovered and cooled samples revealed only diffuse amorphous scattering indicating that no recrystallisation occurred. However, all MOF glasses discovered can only be formed when heating under inert atmospheres, i.e. nitrogen or argon, with heating in air resulting in decomposition rather than melting in all samples [56]. Multiple X-ray total-scattering studies have demonstrated that the short-range structures of the glass ZIFs produced by melt-quenching are the same as their parent crystals (**Figure 2.19a**) [51], [56], [61]. Moreover different melt-quenched glasses are very similar to each other in both short-range and medium-range order (**Figure 2.19b**) [56]. The continued dominance of tetrahedral coordination in the room temperature glass state was also confirmed by X-ray absorption experiments which showed no major shifts in edge position or white-line intensity between crystals and glass structures of ZIF-4, ZIF-62, TIF-4 and ZIF-GIS [56]. Raman spectroscopy conducted on samples of crystalline and glass ZIF-62 demonstrate almost identical spectra, other than small shifts in both the Zn-N vibration at approximately 175 cm⁻¹ and the C-N vibration at approximately 1170 cm⁻¹ (**Figure 2.20**), which indicate slight distortions of the tetrahedra on glass formation [61].

Insight into the distribution of imidazolate and non-imidazolate linkers in the two linker multivariate MOFs was gained through detailed two dimensional spin diffusion ¹H-¹³C NMR experiments on a series of ZIF-62 samples with different fractions of incorporated benzimidazolate (bIm) linker (Zn(Im)_{2-x}(bIm)_x x = 0.25-0.36) [61]. This analysis measured the time taken for polarisation transfer between

excited ^1H - ^{13}C nuclei. This work detected direct transfer between imidazolate and benzimidazolate linkers indicating that they were spatially adjacent and therefore intimately mixed in the structure. However, the rate at which this transfer occurs slows down with increasing benzimidazolate content, implying the existence of more zinc centres with two or more benzimidazolate linkers attached. Taken together these results imply a random mixing of Im^- and blm^- linkers in the structure, naturally resulting in an increased fraction of $\text{Zn}(\text{Im})_2(\text{blm})_2$ centres at higher blm^- contents.

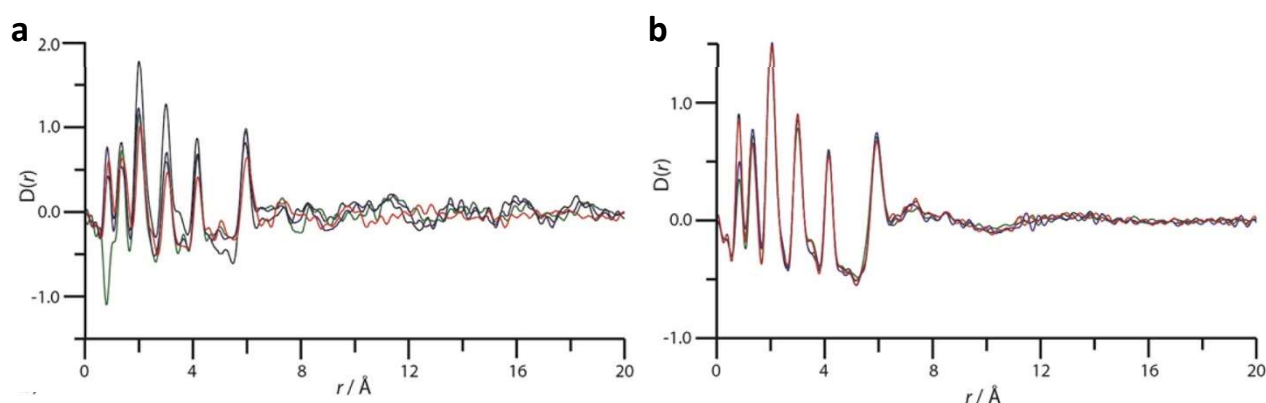


Figure 2.19: X-ray PDF functions of MOF crystals and glasses. **a.** crystalline MOF precursors, ZIF-4 (black), ZIF-GIS (red), TIF-4 (green), and ZIF-62 (blue). **b.** MOF glasses formed from heating above the melting point measured by DSC of ZIF-4 (black), ZIF-GIS (red), TIF-4 (green), and ZIF-62 (blue). Reproduced from [56].

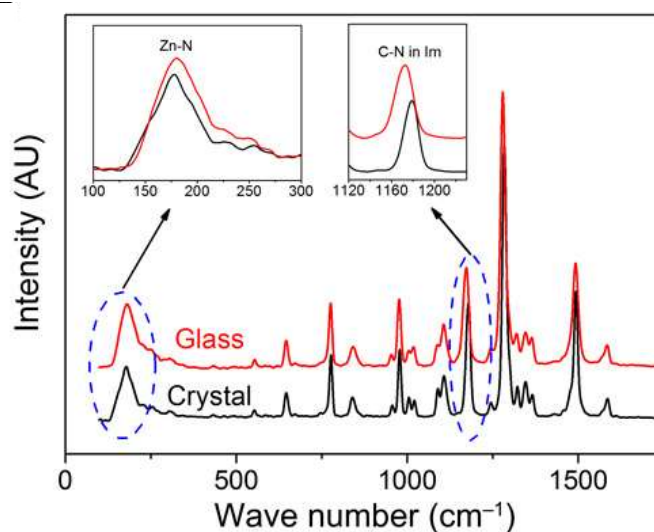


Figure 2.20: Raman spectra for crystalline and glass ZIF-62. Reproduced from [61].

However, ZIF-UC-1, the only melting framework synthesised with three different linkers, is slightly different. No direct evidence of non-random linker distribution was provided, however it was observed that despite the ratios of the different linkers added in synthesis, the two larger linkers, 5-

methylbenzimidazole and benzimidazole, are always incorporated into the structures in either a 0.5:1 or 1:1 ratio. This is attributed to a need to limit steric clashing between the two large linkers and may imply non-random incorporation in these structures [70].

Table 2.3: A list of all melting ZIFs reported in the literature. Reproduced from [36], [50], [51], [56], [61], [65], [69]–[71].

*Represents the onset of amorphisation as measured by VT PXRD not DSC [50].

†Features in brackets are reported for amorphisation that occurs coupled with solvent loss from the framework, features outside of brackets represent values related to a high temperature endotherm, but recrystallisation of ZIF-zni is not reported for this framework [56].

‡ This study used the onset to measure the melting point as opposed to the offset, which is generally used by the field.

Name	Composition	T_m (°C)	T_g (°C)	Space Group	Reference
ZIF-4	Zn(Im) ₂	327	292	<i>Pbca</i>	[36]
ZIF-zni	Zn(Im) ₂	590	292	<i>I 4₁ c d</i>	[36]
ZIF-4-Co	Co(Im) ₂	300*	N/A	<i>Pbca</i>	[50]
ZIF-zni-Co	Co(Im) ₂	550	N/A	<i>I 4₁ c d</i>	[69]
ZIF-GIS	Zn(Im) ₂	(290) 584†	(287) 292†	<i>I 4₁/ a</i>	[56]
ZIF-62	Zn(Im) _{2-x} (blm) _x $x = 0.05-0.36$	372-448	298- 329	<i>Pbca</i>	[51], [56], [61], [69]
ZIF-62-Co	Zn(Im) _{2-x} (blm) _x $x = 0.1-0.3$	386-432	260- 290	<i>Pbca</i>	[51], [69]
TIF-4	Zn(Im) _{2-x} (mbIm) _x $x = 0.2, 0.5$	440, 467	336, 343	<i>Pbca</i>	[56], [71]
ZIF-UC-1	Zn(Im) _{2-x-y} (blm) _x (mbIm) _y $x = 0.17-0.27, y = 0.09-0.21$	418-433	305- 316	<i>Pbca</i>	[70]
ZIF-UC-2	Zn(Im) _{1.9} (6-Cl-5-Fblm) _{0.1}	406‡	250	<i>Pbca</i>	[65]
ZIF-UC-3	Zn(Im) _{1.75} (5-Cl-2-mblm) _{0.25}	390‡	336	<i>Pbca</i>	[65]
ZIF-UC-4	Zn(Im) _{1.63} (5-Fblm) _{0.37}	421‡	290	<i>Pbca</i>	[65]
ZIF-UC-5	Zn(Im) _{2-x} (5-Clblm) _x $x = 0.20, 0.31$	428, 432‡	336, 320	<i>Pbca</i>	[65], [71]

The DSC work (**Table 2.3**) on melting multivariate MOFs shows that they have melting points which are higher than that of ZIF-4 (327 °C) but lower than that of ZIF-zni (590 °C). It also shows that the glass transition temperatures of these MOFs are generally greater than those of Zn(Im)₂ polymorphs with the exception of those reported for the ZIF-62-Co series [51], [69]. In this case the difference may be attributed to differing bond strengths between Co-N and Zn-N, and lack of information on the T_g of ZIF-4-Co and ZIF-zni-Co.

Extensive work by multiple authors on ZIF-62 and ZIF-62-Co shows that both the melting point and glass transition temperature increases with increasing blm⁻ content (**Figure 2.21**) [51], [61]. Separate reports on TIF-4 show an increase in melting point and glass transition with increasing mblm⁻ [56], [71]. However, the picture for ZIF-UC-5 is more complicated with T_m increasing with 5-clblm content but not T_g [65], [71]. Although, in these cases the measurements came from two separate studies, and direct comparison is complicated by differences in methodology; taking the onset or offset of the melting peak as T_m and whether the midpoint or the onset of the heat capacity rise is used to define T_g . In summation multiple reports on two linker melting MOFs show a correlative link with the amount of sterically larger substituted imidazolate linker and the melting point and glass transition temperature.

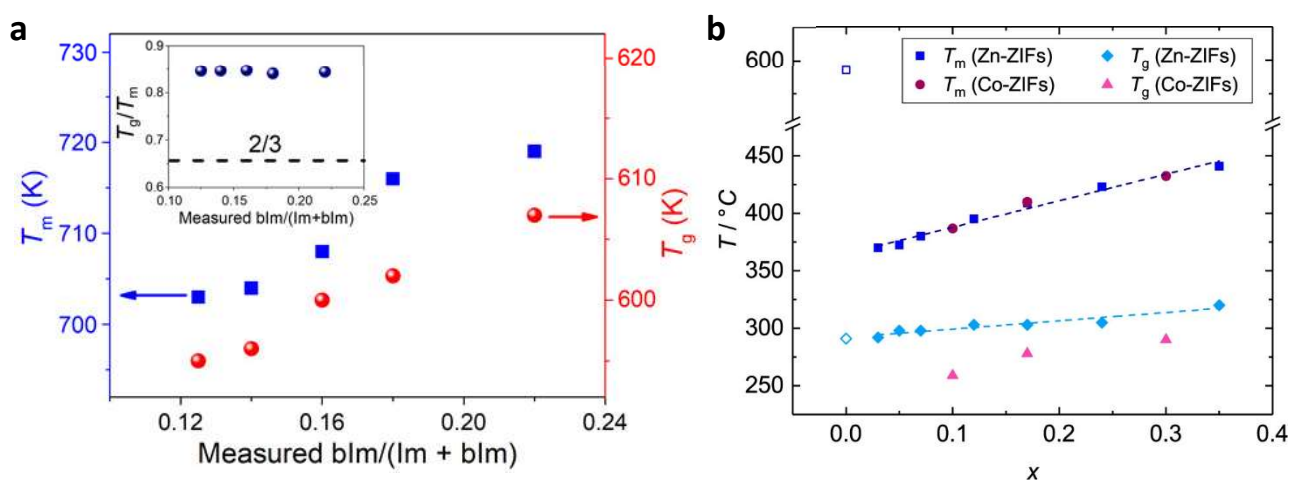


Figure 2.21: Variation of T_g and T_m as a function of blm⁻ content for ZIF-62 and ZIF-62-Co. **a.** Inset show the ratio of T_g / T_m as a function of composition. Reproduced from [61]. **b.** Note x is equal to $2[\text{blm}]/([\text{blm}] + [\text{Im}])$. Reproduced from [51]. The open shape values are the T_g and T_m for ZIF-zni reproduced from [36].

The case for three linker melting MOFs is more complicated with neither melting nor glass transition showing strong correlations with the total amount of sterically larger linker [70]. However, only a single report exists on these systems and clearly further study is needed before broader trends can be determined.

In order to examine the effect of Zn-N bond strength on the melting point of the MOF framework a series of MOFs with halogenated linkers was synthesised [65]. It was hypothesised that attaching more electron withdrawing groups to the benzimidazole linker would weaken the Zn-N bond and therefore lower T_m . However, despite bond breaking at elevated temperature being a key component to melting, as previously explained, no clear correlation between bond strength at room temperature and melting point was observed [65]. However, these results are complicated by two factors: firstly, the different frameworks have different amounts of substituted linkers, ranging from 0.1 - 0.37 [65]. This makes direct comparison of the effect of the linker chemistry between frameworks complicated by the known effect on T_g and T_m of the amount of substituted linker (**Figure 2.21**). Secondly ^{19}F NMR studies on ZIF-UC-2 and ZIF-UC-4 show that formation of the glass by melt-quenching results in formation of Zn-F bonding [65]. This means that it has a different structure from other MOF glasses discovered so far and therefore may have different behaviour.

From the following discussion on overall trends in multivariate MOFs it can be seen that they appear structurally similar to melting $\text{Zn}(\text{Im})_2$ polymorphs. Therefore, we can conclude that they will have a broadly similar CRN topology. This is further bolstered by FPMD simulations, which show that the activation energy for breaking the Zn-N bond in ZIF-62 is similar to that in ZIF-4 [62]. The effect of Zn-F formation in some halogenated melting MOFs warrants further analysis, as it is unique among melting MOFs. However CRN networks have been reported for three connected centres in inorganic systems such as P_2O_5 [72] and B_2O_3 [73], and so a structure of three connected Zn^{2+} linkers bonded to monodentate F^- can be accommodated into the same broad CRN model. Equally F^- is a bridging ligand in some fluoride glass systems [33] and so the possibility of Zn-F-Zn bonds cannot be ruled out a priori, as unlikely as it may seem given the large distance between zinc centres.

2.5.2 Detailed Examination of $a_g\text{ZIF-62}$

ZIF-62 had the widest range of temperatures, approximately 165 °C, between melting and decomposition of the initially discovered melting multivariate MOFs [56]. This has prompted a large amount of research into its structure and properties, with work particularly focusing on how both change as a function of benzimidazole content.

The effect of varying blm^- on the melting enthalpy (ΔH_m) and entropy (ΔS_m) changes have been examined by multiple researchers [51], [61]. Both reports show that melting enthalpy and entropy increase with increasing benzimidazolate content (**Figure 2.22**). Further evidence for the effect of blm^- inclusion on enthalpy comes from variable temperature single crystal X-ray diffraction studies on a succession of cobalt containing frameworks, ZIF-4-Co, ZIF-zni-Co, $\text{Co}(\text{Im})_{1.7}(\text{blm})_{0.3}$, $\text{Co}(\text{Im})_{1.9}(\text{blm})_{0.1}$ [51]. The mean equivalent isotropic displacement factors for the nitrogen atoms were measured in

each structure as a function of temperature from -173 °C – 127 °C. These factors give the spread of atoms around the mean position in the structure, and although the values of the ZIF-62-Co frameworks were higher due to disorder in their structures they showed a weaker temperature dependence than ZIF-4-Co. This is taken to indicate stiffer and therefore stronger bonding in ZIF-62-Co relative to ZIF-4-Co due to the inclusion of blm^- . ZIF-zni-Co had the weakest temperature dependence over the range, which is explained by its dense structure and high observed melting point, 550 °C (Table 2.3).

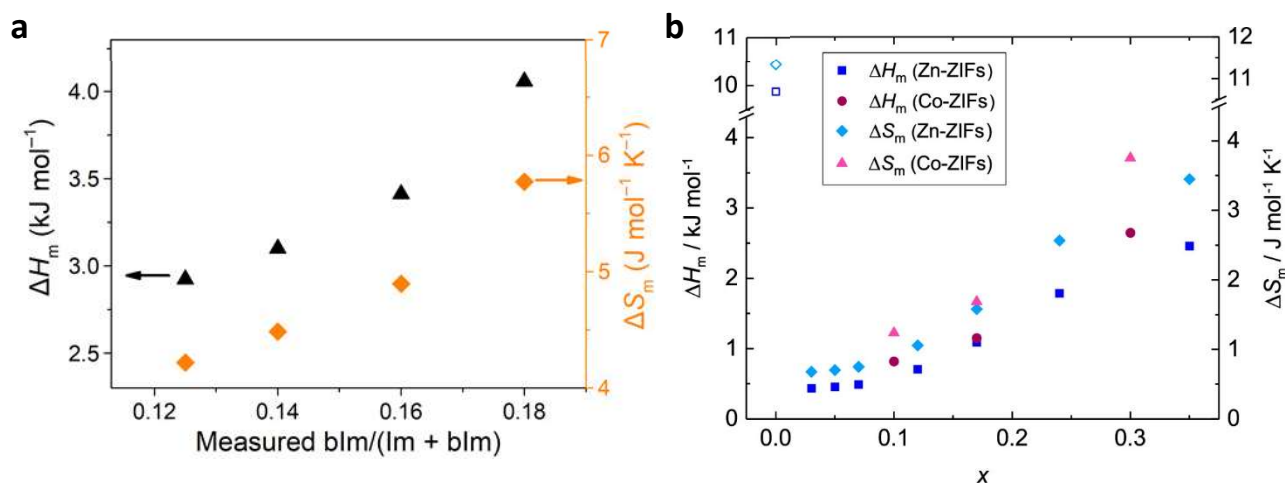


Figure 2.22: Variation of ΔH_m and ΔS_m with blm^- content in ZIF-62 and ZIF-62-Co. **a.** Reproduced from [61]. **b.** Note x is equal to $2[\text{blm}^-]/([\text{blm}^-] + [\text{lm}^-])$. Reproduced from [51]. The open shape values are the ΔH_m and ΔS_m for ZIF-zni reproduced from [36].

The rise in entropy is attributed to an increase in the available configurational states in the liquid at T_m with increasing blm^- content [61]. Interestingly for $\text{Zn}(\text{lm})_{2-x}(\text{blm})_x$ samples with $x < 0.1$ the melting entropy change is reported to almost vanish, which is taken to imply that the vibrational entropy of the crystal and the configurational entropy of the liquid are almost identical at the melting point [51].

Another key difference between multivariate MOFs and $\text{Zn}(\text{lm})_2$ polymorphs is the absence of recrystallisation to ZIF-zni on heating that is generally observed. Three key features which contribute to the resistance to recrystallisation, also termed glass forming ability (GFA), in ZIF-62 are [61]:

1. GFA is measured by the T_g/T_m ratio and ZIF-62 has the highest T_g/T_m ratio, 0.84, recorded for any glass [61].
2. The liquid ZIF-62 has a high viscosity at T_m of $10^{5.1}$ Pa S, which is comparable to that of silica at its own T_m . This implies that diffusion within the structure is very sluggish, inhibiting nucleation and growth of any crystalline phases.

- The random nature of benzimidazole incorporation into the framework prohibits recrystallisation to a dense phase due to a combination of steric hinderance and random position within the structure inhibiting nucleation of a uniform dense crystalline unit cell.

The subsequent synthesis of ZIF-62 frameworks with very low blm^- contents has shed further light on the resistance of multivariate MOFs to recrystallisation [51]. It was shown through a combination of DSC and PXRD (**Figure 2.23**) that below a limit of blm^- content, found to be approximately $x < 0.05$, recrystallisation to ZIF-zni was observed to take place at around 500 °C in agreement with results measured for ZIF-4 [36], [51]. At the critical point, $x = 0.03$, the framework appears to exhibit a shallow melting endotherm but heating of the sample to 480 °C and cooling resulted in the appearance of peaks matching ZIF-zni in the diffraction pattern. Below this amount of blm^- the ZIF-62 melting endotherm becomes even shallower, or is absent entirely, and a recrystallisation exotherm is observed in the DSC curve.

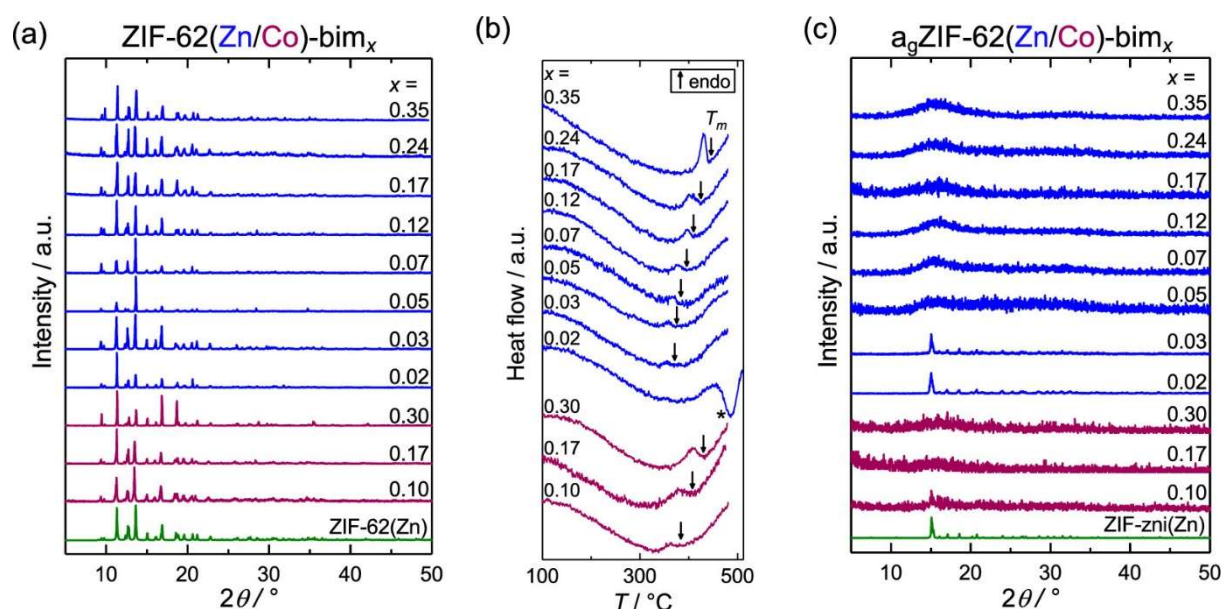


Figure 2.23: PXRD and DSC measurements of crystalline and glass ZIF-62 $\text{Zn}(\text{Im})_{2-x}(\text{blM})_x$. **a.** PXRD patterns of ZIF-62 ($\text{M}(\text{Im})_{2-x}(\text{blM})_x$). The simulated diffraction pattern for $\text{Zn}(\text{Im})_{1.65}(\text{blM})_{0.35}$ (green) reproduced from [69] is presented for comparison. **b.** DSC heating scans of the ZIF-62 ($\text{M}(\text{Im})_{2-x}(\text{blM})_x$) samples. Black arrows indicate T_m and * indicates recrystallisation exotherms. **c.** PXRD patterns of the glass ZIF-62 ($\text{M}(\text{Im})_{2-x}(\text{blM})_x$) samples obtained by heating to 480 °C and cooling to room temperature. The simulated diffraction pattern for ZIF-zni (green) reproduced from [53] is presented for comparison. Reproduced from [51].

The T_g/T_m ratio of these samples is uniformly greater than 0.8, in the same range as the values found in the earlier samples. Moreover, the ratio increases with decreasing blm^- content due to the weaker effect of blm^- on T_g vs T_m in this composition range (**Figure 2.21b**). This implies that even samples that

recrystallise do so during a small window of liquid metastability. However, this analysis is complicated by the fact that the melting point used in this analysis is the melting point of ZIF-62, which is believed to be metastable with respect to a denser polymorph.

No direct measurements of the changing viscosity at high temperatures as function of blm^- content have been made and so it is not known for certain whether substitution of lm^- for blm^- results in a large reduction in the viscosity of the sample. Due to blm^- 's larger size it could be anticipated that melts with larger blm^- contents have higher viscosities because of a higher average barrier to linker diffusion due to steric hinderance. However, simulations of the dynamics of the liquid $\text{Zn}(\text{lm})_2$ shows that diffusion coefficients of zinc and imidazolate are very similar and therefore the diffusion of both in the melt is clearly linked [60]. Therefore, due to the large size of the diffusing units and cooperative nature of diffusion in the MOF liquid, it is also plausible that viscosity remains very high across the full composition range of ZIF-62.

The random arrangement of blm^- linkers as the reason for recrystallisation resistance could be a reason why frameworks with low concentrations of blm^- recrystallise to ZIF-zni. Assuming a random distribution of linkers around each centre, the probability of different configurations of zinc centres $\text{Zn}(\text{lm})_k(\text{blm})_{4-k}$ as a function of the overall composition $\text{Zn}(\text{lm})_{2-x}(\text{blm})_x$ is given by the Binomial distribution [70]:

$$f(k) = \frac{4!}{k!(4-k)!} p^k (1-p)^{4-k} \quad 2.2$$

$$p(x) = \frac{x}{2}$$

From this analysis the probability of finding zinc configurations with one or more benzimidazolate linkers, $f(\text{blm}^- > 0)$, can be found as a function of overall sample composition (**Figure 2.24**). This analysis shows that as the overall blm^- content, x , decreases the probability of finding any zinc centres with a blm^- attached becomes incredibly small. At $x = 0.03$, the point at which recrystallisation is first observed, only approximately 6% of zinc centres have even a single benzimidazolate linker attached. This implies that most of the sample has the same composition as ZIF-4 and therefore its recrystallisation to ZIF-zni in the same temperature range is unsurprising. This analysis does not provide a justification for where the threshold composition of x would be expected to be. However, it does indicate that at low concentrations of blm^- large sections of crystallites, or perhaps even whole crystallites, will essentially be ZIF-4. This is true even if the blm^- remains homogeneously distributed throughout the sample, and indeed no phase separation at low blm^- contents was observed via PXRD analysis (**Figure 2.23**) [51].

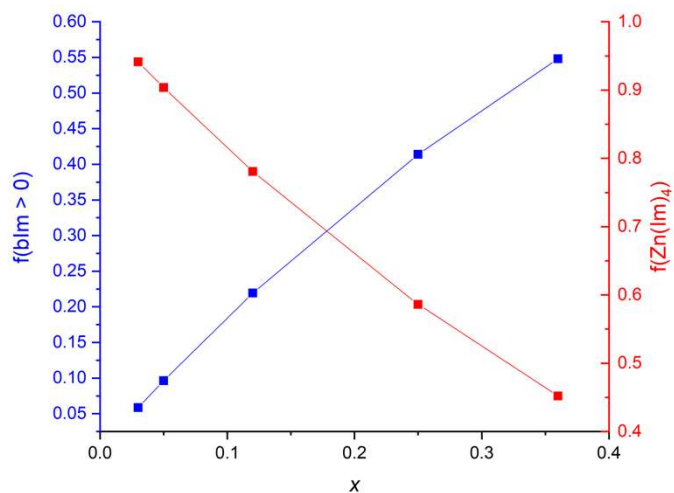


Figure 2.24: Distribution of zinc centres, $\text{Zn}(\text{Im})_k(\text{bIm})_{4-k}$ in ZIF-62 as a function of bIm^- content. Probability (Equation 2.2) of finding a zinc centre with at least one bIm^- attached, $f(\text{bIm}^- > 0)$, or no bIm^- linkers attached, $f(\text{Zn}(\text{Im})_4)$, as a function of composition in ZIF-62 ($\text{Zn}(\text{Im})_{2-x}(\text{bIm})_x$).

2.5 Potential Applications of Metal-Organic Framework Glasses

2.5.1 Processing of Metal-Organic Framework Glasses

For MOF glasses to be used in practical applications they must be able to be processed and shaped, which is one of the key advantages of glasses over crystalline materials. The high viscosity of MOF glasses means that processing needs to be done near or above T_m where the glass is sufficiently liquid for appreciable flow to occur [61]. One practical difficulty is the decomposition of the framework occurring during high temperature heat treatment. Work on ZIF-8 heated in a variety of atmospheres for extended lengths of time has shown that ZIFs display continual, though small, mass loss on holding at elevated temperatures. This occurs even if those temperatures are below the onset of decomposition measured during a continuous heating scan [74].

For this reason, it is highly desirable to lower the melting point of the MOF. The work of the previous section shows that the presence of even a small amount of benzimidazole or other second linker effectively suppress recrystallisation of the melt to ZIF-zni. This therefore widens the processing range available to the melt relative to ZIF-4. However, inclusion of a larger fraction of benzimidazole or other bulky linkers increases the melting point. Combined high temperature high pressure work with in situ PXRD has demonstrated that both ZIF-62 and ZIF-4 display a reduction in their melting temperatures on application of pressure [62], [75]. This is attributed to the densification of the framework which is reported to occur on melting in both systems. Therefore, production of low blm^{-} containing ZIF-62, combined with the application of pressure during synthesis, i.e. through hot pressing, may further expand the processing range of MOF glasses.

One attempt to produce bulk, defect free, pieces of ZIF-62 glass has been reported in the literature [76]. Initial attempts focused on using vacuum hot pressing. Crystalline ZIF-62 was compressed at a pressure of 15 MPa in a vacuum at 450 °C for 1 hour. The resulting product was fully amorphous, but SEM showed that there were inhomogeneities within the sample caused by incomplete sintering. This was attributed to inhomogeneity of the temperature profile in the hot-pressing apparatus.

A second attempt to produce a bulk piece of ZIF-62 glass involved annealing a pre-formed glass piece for an extended period of time above its T_g [76]. The glass was pre-formed by heating to 450 °C and then cooling. Then the glass was ball-milled to produce a glass powder, which was compressed to a pellet. This pellet was then reheated at 400 °C for 5 hours.

This temperature was selected because it was above the measured T_g of 318 °C but TGA showed that the mass of the ZIF-62 glass remained stable during isothermal treatment at this temperature. The resulting pellet was transparent and much more homogeneous, though some large pores could still be seen (**Figure 2.25**). Interestingly a similar approach was attempted to produce a bulk sample of a_g ZIF-4; crystalline ZIF-4 was heated to 590 °C, i.e. above the T_m of ZIF-zni, and then the glass was remelted at 400 °C for 5 hours. This sample showed substantial recrystallisation to ZIF-zni during the heat treatment. This further emphasises the processing advantage of multivariate ZIFs over $Zn(Im)_2$ in the formation of MOF glasses. Nanoindentation and scratch testing on the bulk sample produced showed no evidence of ductile fracture, which generally occurs in metallic and inorganic glasses. This could indicate the potential for MOF glasses in some mechanical applications such as screens.

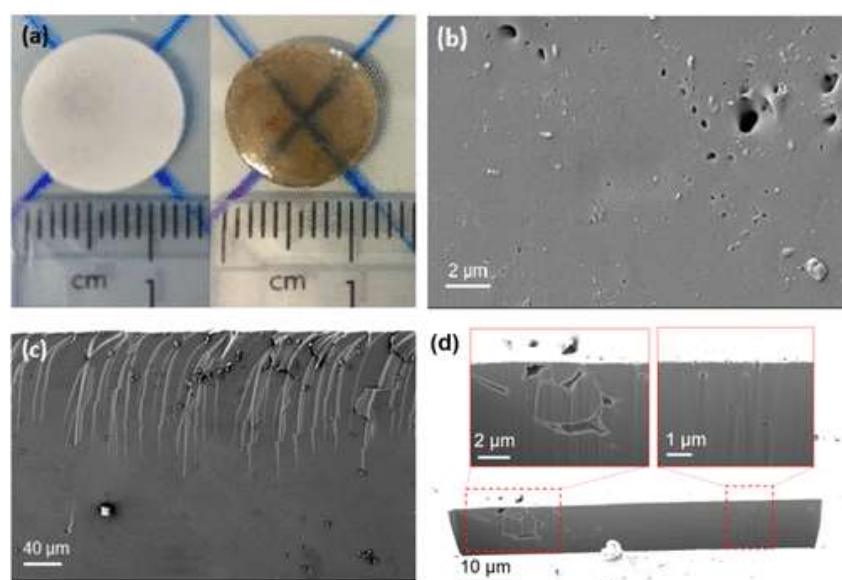


Figure 2.25: Images of bulk a_g ZIF-62. **a.** Optical photographs of a_g ZIF-62 before (left) and after (right) remelting. **b.** Scanning electron microscopy (SEM) images of the surface and **c.** cross-sectional morphology of remelted a_g ZIF-62. **d.** Optical images of a trench cut into remelted a_g ZIF-62 using a focused ion beam (FIB). Reproduced from [76].

2.5.2 Intrinsic Porosity in Metal-Organic Framework Glasses

MOF crystals typically have high porosities and as such have many potential applications in the gas phase (**Chapter 1**). Initially MOF glasses were thought to be completely non-porous, with N_2 sorption isotherm measurements showing negligible porosity in a_g ZIF-4, a_g ZIF-62, a_g TIF-4 and a_g ZIF-GIS [56]. However, positron annihilation lifetime spectroscopy (PALS), which can probe the internal pore structure of materials, was conducted on ZIF-4, ZIF-zni and a_g ZIF-4 [77]. The glass ZIF was found to have porosity intermediate between ZIF-4 and ZIF-zni. Critically the porosity in the glass was found to

be above the critical window size, the largest probe size which can transport across a material, for both Li^+ and Na^+ (**Figure 2.26**). This indicates the potential for the use of MOF glasses in small ion applications such as solid-state electrolytes for batteries or fuel-cells.

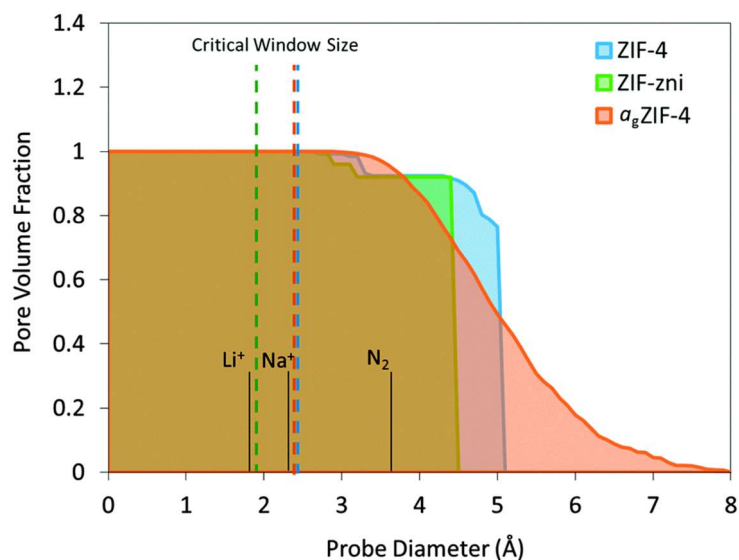


Figure 2.26: Calculated pore volume fraction for ZIF-4, ZIF-zni and a_g ZIF-4. Dashed lines represent the calculated critical window size for free transport in each framework. The diameters for various probes (Na^+ , Li^+ , and N_2) are also indicated. Reproduced from [77].

Although MOF glasses had negligible porosity when measured using N_2 (kinetic diameter 3.6 Å) research has shown that a_g ZIF-62 has considerable accessible porosity for smaller gasses such as H_2 (kinetic diameter 2.9 Å) and CO_2 (kinetic diameter 3.3 Å) [51], [62]. a_g ZIF-62 has also been demonstrated to absorb larger compounds, showing preferential adsorption of propylene over propane [51]. Interestingly this effect was found to be tuneable, with samples containing more blm^- linkers having slower adsorption profiles due to larger blm^- linkers blocking the pores. This could indicate a potential application for MOF glasses in membrane separations.

2.5.3 Composite Formation with Metal-Organic Framework Glasses

MOF glasses have also been combined with MOF crystals to produce crystal-glass composite materials (CGCs) [78]–[80]. These composite materials were formed by mixing crystalline ZIF-62 with the crystalline MOF of choice through ball-milling. The glass was then formed in situ by heating above the melting point of the ZIF-62 and then cooling [78], [79]. X-ray total-scattering measurements, combined with NMR and PXRD, confirmed the structural integrity of the crystalline and glass components of the composite during formation. A series of CGCs was formed between a_g ZIF-62 and MIL-53. MIL-53 is an

a aluminium benzenedicarboxylate MOF ($\text{Al}(\text{OH})(\text{O}_2\text{C}-\text{C}_6\text{H}_4-\text{CO}_2)$), which has several crystalline phases (**Figure 2.27**). The as-synthesised structure, MIL-53-as, is stabilised by solvent and un-reacted benzenedicarboxylate linkers in the pores. On heating these solvent and unreacted linker molecules are released from the pores resulting in an open structure with large pores, MIL-53-lp. In the pure crystalline state water uptake on cooling causes this structure to spontaneously convert to a contracted narrow pore structure, MIL-53-np.

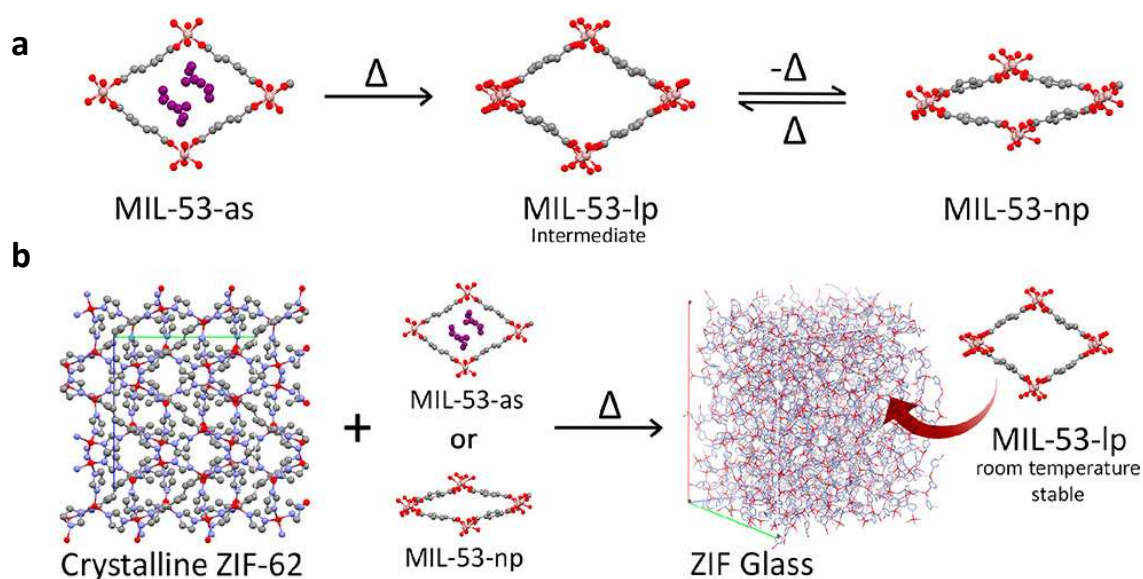


Figure 2.27: Schematic of a MIL-53 a_g ZIF-62 composite. **a.** Diagram of the activation process of MIL-53 and the transition between different phases. Key: Grey – Carbon, Red – Oxygen, Pink – Aluminium, Purple – solvent. Hydrogen omitted for clarity. Δ indicates changing volume between different crystalline phases. **b.** Schematic of the composite formation and stabilisation of the MIL-53-lp phase. Reproduced from [79].

In the CGC however the presence of the relatively rigid glass matrix prevents formation of the MIL-53-np phase on cooling and therefore stabilises the MIL53-lp phase to room temperature. This leads to a CGC with gas phase properties which are comparable to or exceeding that of the room temperature crystalline phase [78], [79] (**Figure 2.28**).

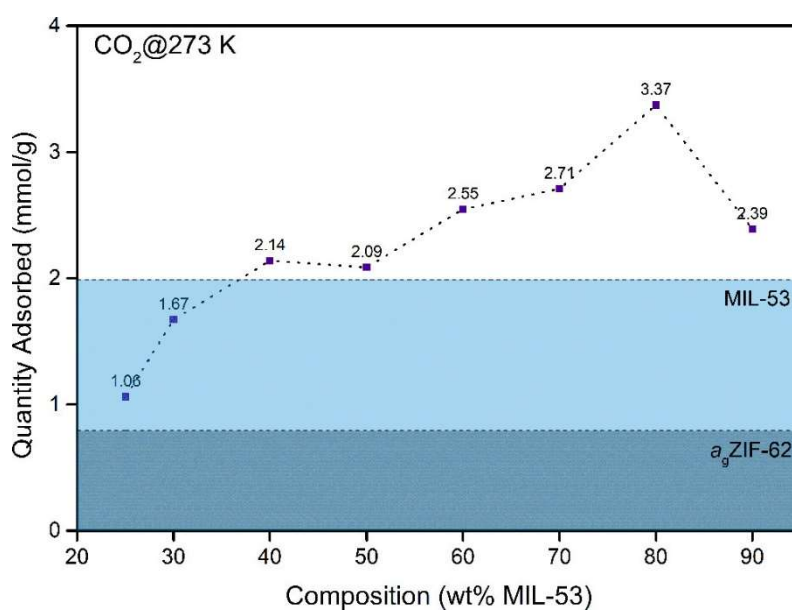


Figure 2.28: Quantity adsorbed from gas adsorption isotherms for the $(\text{MIL-53})_x(\text{agZIF-62})_{1-x}$ series at 1 bar using CO_2 gas at 0°C . The quantities adsorbed for samples of activated MIL-53 (MIL-53-np, 1.99 mmol/g) and agZIF-62 (0.79 mmol/g) are displayed by light-blue and dark-blue areas respectively. Reproduced from [78], [79].

The research so far, although still nascent, shows that there is a broad scope for different MOF glass applications. This includes both applications for MOF glasses on their own due to their unique mechanical behaviour and intrinsic porosity, and MOF glasses as a basis for composite materials, where they can provide stability and processability to the crystalline phase of non-melting MOFs.

Chapter 3: Experimental Methods

3.1 Theoretical Background

3.1.1 Powder X-ray Diffraction

X-ray photons interacting with atoms are scattered, resulting in them changing direction in a process known as diffraction [31]. In crystalline materials this diffracted intensity forms sharp spots, as scattering is occurring from every atom in the lattice simultaneously and the overall resultant beam is only measurable when the interference between all the individual scattering events is constructive. In a simplified but useful model of the diffraction process, the atomic structure of the material can be replaced by a series of periodically repeating lattice planes and diffraction can be visualised as reflection of the beam from these planes (**Figure 3.1**). Constructive interference from the reflected beams then occurs only when the difference in path length travelled by beams reflecting from each plane is an integer multiple of the wavelength of the light being scattered. This condition gives rise to Bragg's law of diffraction:

$$n\lambda = 2d\sin\theta \quad 3.1$$

Where n is an integer, d is the planar spacing, λ is the wavelength of the incident photons and 2θ is the diffraction angle, where the factor of 2 comes from the difference between the diffracted and un-diffracted beams.

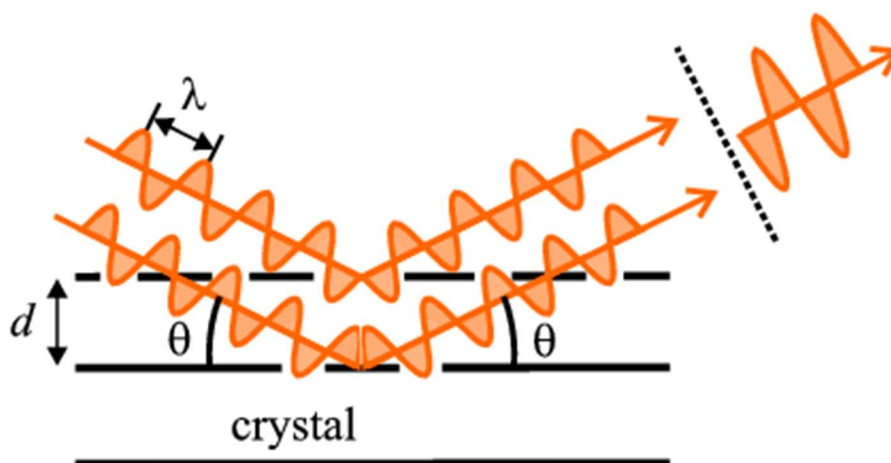


Figure 3.1: Schematic showing diffraction of X-rays as reflection from atomic planes. The planes are spaced d apart. The planes are diffracted by θ , for a total 2θ angular difference between the direct and diffracted beam. Reproduced from [31].

This equation shows that for a material with given spacings of atomic planes diffraction will only occur at angles θ_B , where the resultant path length satisfies the Bragg equation. This means that the diffraction pattern will consist of peaks located at these Bragg angles [81]. This is in contrast to measured diffraction from glasses where the absence of structural periodicity, i.e. repeating equally spaced families of lattice planes, means that instead of sharp peaks the diffraction pattern consists of very broad ‘humps’ [30].

In single crystal diffraction the crystal must be in the right orientation for the diffracted beam to be scattered into the detector. In contrast, in powder X-ray diffraction (PXRD) the sample consists of a large number of small randomly packed crystallites (**Figure 3.2**). Therefore, assuming a large enough number of crystallites is present that the sample does not display a ‘texture’, then all sample orientations are sampled simultaneously. This means that diffraction occurs as cones with opening angles of $2\theta_B$ (**Figure 3.2**) a fraction of which are sampled by the detector. In a typical powder diffraction experiment the X-ray source and the detector rotate around the same goniometer circle, and the resulting pattern is recorded as a function of diffracted angle 2θ . This is known as the Bragg-Brentano geometry (**Figure 3.3**) [81].

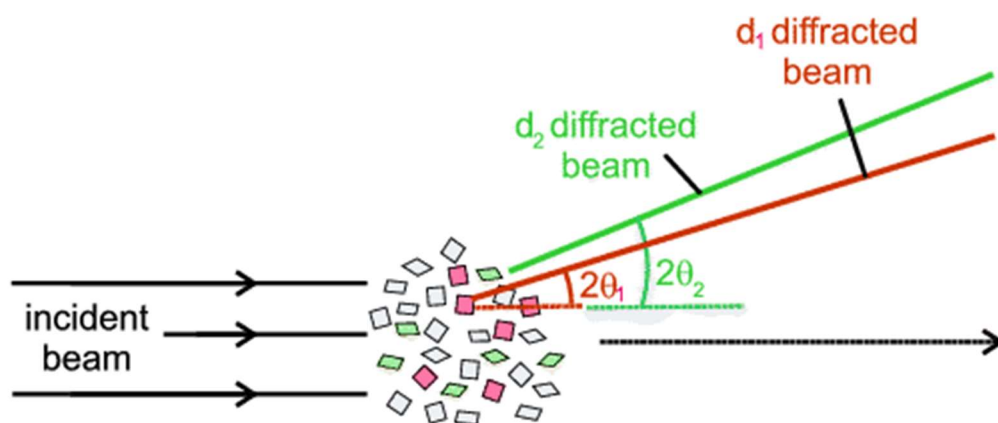


Figure 3.2: Schematic showing X-ray diffraction from a powder agglomerate. Differently orientated crystallites in the powder (red and green) result in different diffracted beams. Reproduced from [31].

Although the presence or absence of a peak can be determined through the simplifying assumptions of Bragg’s law, in order to determine the intensity of the peak the relative positions of all of the atoms in the unit cell need to be taken into account. This is done through the calculation of the structure factor:

$$F(hkl) = \sum_n f_n e^{2\pi i(hx_n + ky_n + lz_n)} \quad 3.2$$

Where the sum is over the n atoms with positions (x_n, y_n, z_n) in the unit cell and $\{hkl\}$ are families of atomic planes with equivalent spacing d_{hkl} . f_n is the atomic form factor, which determines the extent to which a given atom scatters the incoming beam, values of which are tabulated as a function of scattering angle for different elements [82].

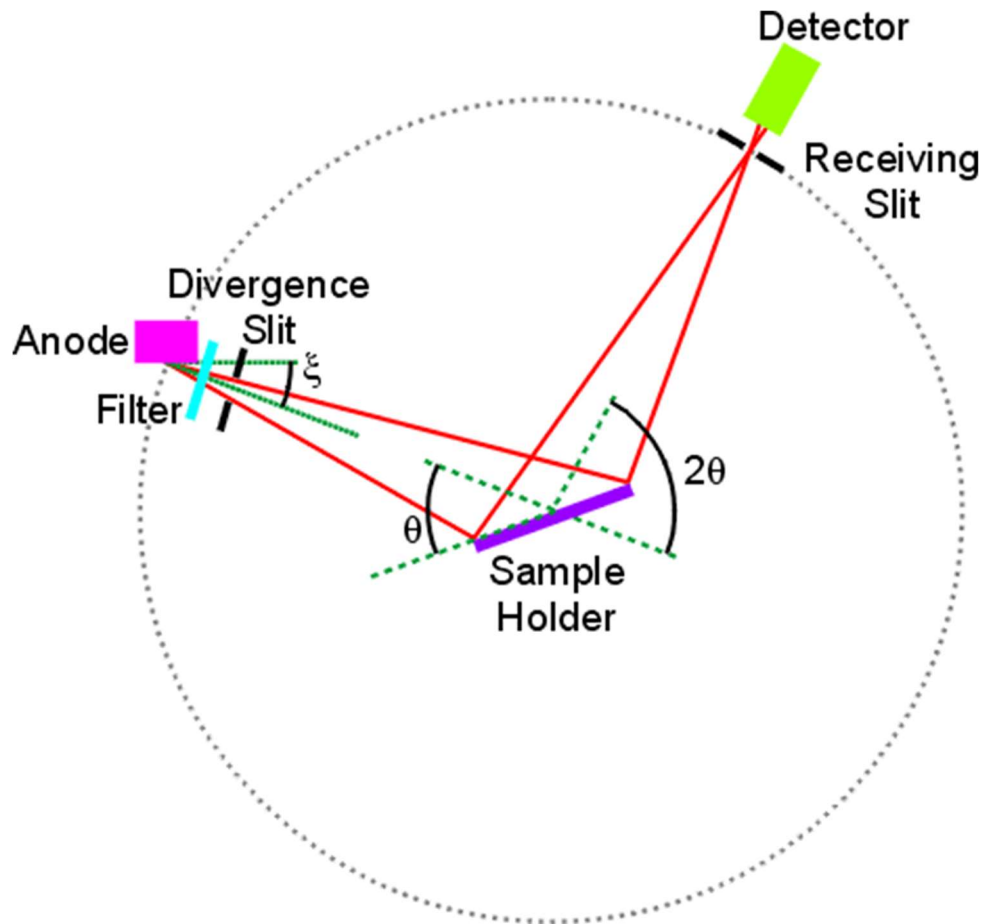


Figure 3.3: Bragg-Brentano scattering geometry commonly used in powder X-ray diffraction experiments. Reproduced from [31].

The measured intensity of the peak is then given by:

$$I(hkl) = \alpha(2\theta)m_{hkl}F(hkl)F^*(hkl) \quad 3.3$$

Where m_{hkl} is the number of symmetrically equivalent planes, and therefore on average the number of crystallites in the right orientation to diffract, and $\alpha(2\theta)$ is an angle dependent constant of proportionality which varies with experimental set-up [31].

This section has shown that for crystalline powders X-ray diffraction results in a pattern of sharp peaks, the position and intensity of which is related to the positions of atoms in the unit cell. PXRD can therefore be used as a measurement of atomic phase identity. Either through simple comparison with

measured or calculated standards or via least-squares regression fitting of the X-ray diffraction data using a model of the atomic structure of the given phase [83].

3.1.2 X-ray Total-Scattering and the Pair-distribution Function

This section outlines how the pair-distribution function (PDF) is derived from measured total-scattering data. If we consider the structure of matter unconstrained by periodic boundary conditions, space group symmetry, or molecular identity we can still describe the material in terms of the local number density, $n(\mathbf{r})$, using the following function:

$$n(\mathbf{r}) = \sum_i \delta(\mathbf{r} - \mathbf{R}_i) \quad 3.4$$

Where \mathbf{R}_i is the position of the i^{th} atom and $\delta(\mathbf{r} - \mathbf{R}_i)$ is the Dirac delta function. This function indicates that there are peaks in the local number density at atomic positions measured from an arbitrary origin (**Figure 3.4**). Though in reality atoms in coordination shells are likely to be spread over a small band of distances, broadening the delta function peaks. [84], [85].

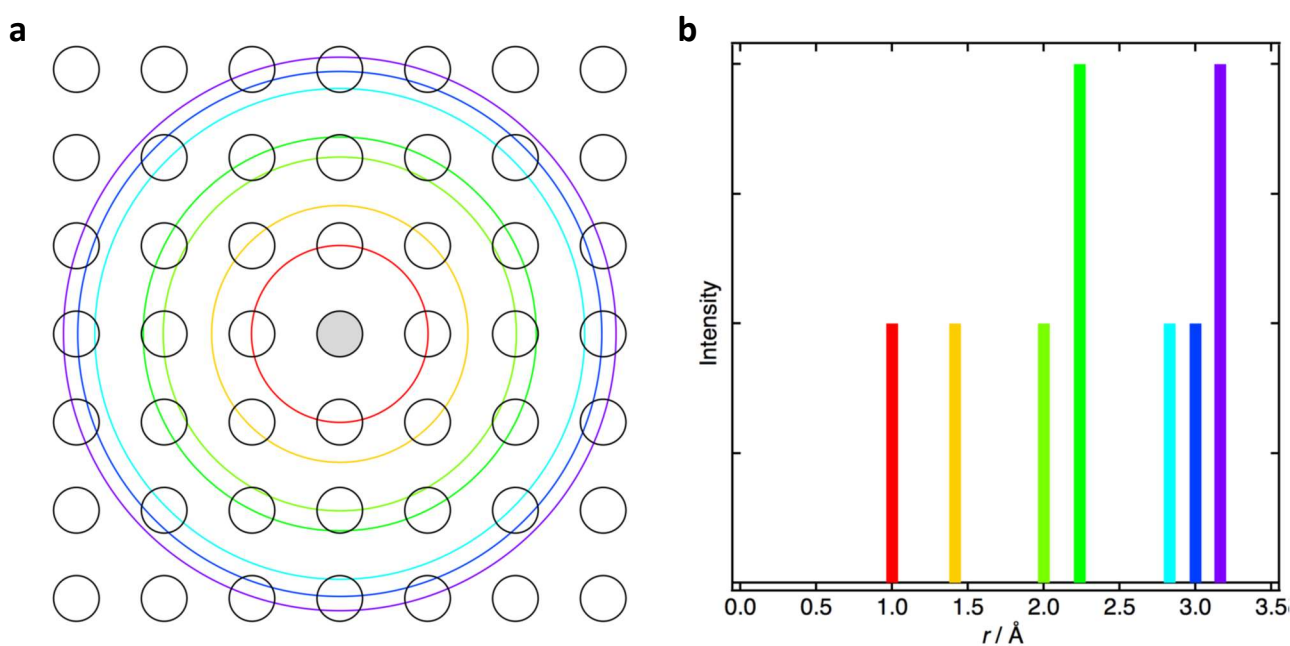


Figure 3.4: Theoretical pair-distribution function (PDF) of a square lattice. **a.** A square lattice. **b.** Schematic of the $n(r)$ for a square lattice. Coloured circles in **a.** correspond to peaks in **b.** Reproduced from [85].

This function is difficult to plot however, as the number of atoms present will always increase with increasing distance from the origin due to the widening search sphere.

Therefore a 'radial distribution function', $g(r)$, is defined:

$$g(r) = \frac{1}{4\pi r^2 p_o} n(r) \quad 3.5$$

Where p_o is the atomic number density and is present as a normalising factor. Integration of $g(r)4\pi r^2 p_o dr$ between r_1 and r_2 returns the number of atoms between these two values. An indefinite integral would return a function of the overall number of atoms in a given volume. This function becomes 0 at $r = 0$ and tends to unity at large r as no correlations are present at amounts above that which would be expected from the number density p_o (**Figure 3.5**).

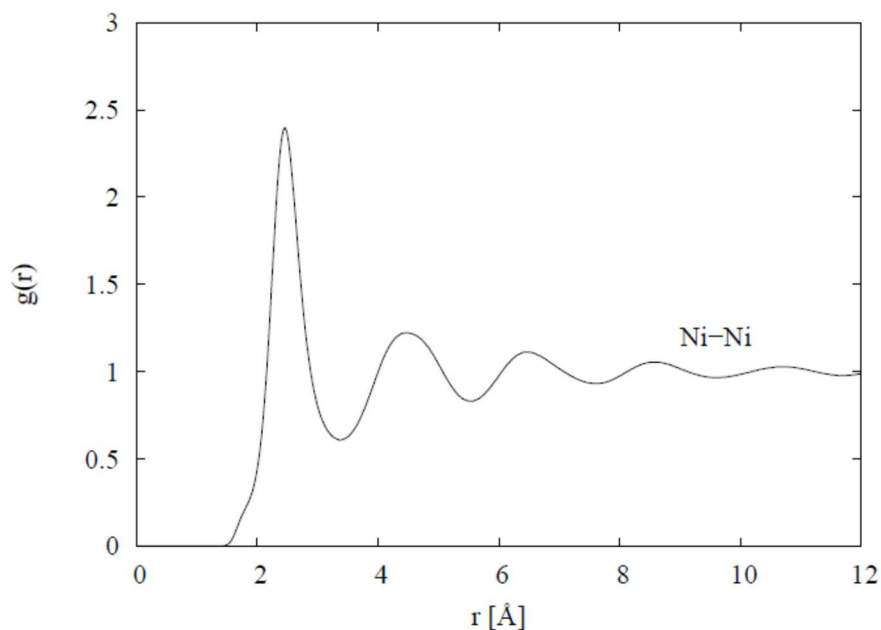


Figure 3.5: Radial distribution function, $g(r)$ (spherically averaged) for liquid Nickel. Reproduced from [86].

In systems with more than one type of atom these functions can be written in a partial form (**Figure 3.6**) as:

$$g_{\alpha\beta}(r) = \frac{1}{4\pi r^2 c_\beta p_o} n_{\alpha\beta}(r) \quad 3.6$$

Where $n_{\alpha\beta}(r)$ represents the number of β atoms around an α atom within a distance $r + dr$ and c_β is the atomic concentration of the β atoms [85].

As previously mentioned, in a diffraction experiment the extent to which the incident X-ray beam interacts with, and is therefore scattered by, an atom depends on the atom's scattering length. In X-ray scattering this interaction occurs between the photons and the electron density around the atom

and therefore this scattering length, $f(r)$, is also a function of the atom's electron density and therefore varies in space.

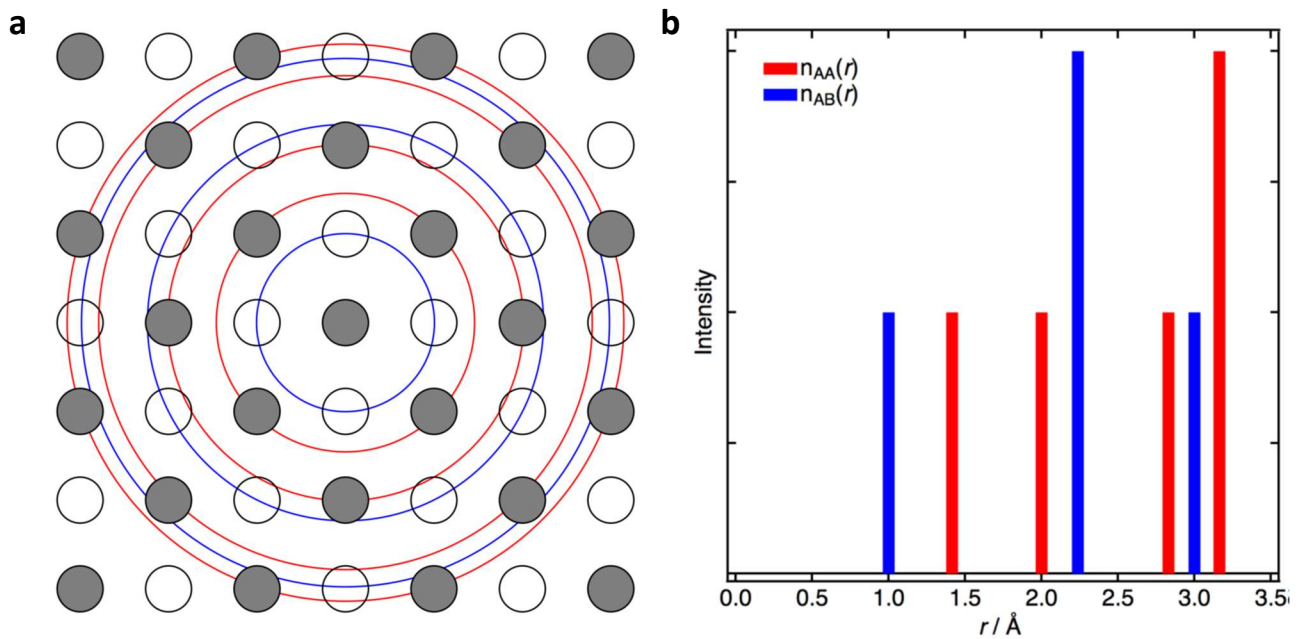


Figure 3.6: Theoretical partial pair-distribution function (PDF) of a square lattice. **a.** A square lattice with alternating A (white) and B (dark) atoms. **b.** Schematic partial $n(r)$ coloured peaks corresponding to circles marked in **a.** Reproduced from [85].

The scattering length density, $A(r)$ is therefore a convolution of this function with the atomic position (**Equation 3.4**) [84]:

$$A(\mathbf{r}) = \sum_i (f_i * n)(\mathbf{r}) = \sum_i f_i(\mathbf{r} - \mathbf{R}_i) \quad 3.7$$

In essence (**Equation 3.7**) states that due to the delocalised nature of the electron density around atoms, from the perspective of the incoming X-ray beam, the 'sharp' atomic structure (**Equation 3.4**) is replaced by a diffuse picture of electron clouds centred on each atoms position.

During the scattering experiment the X-ray is scattered simultaneously by the whole array of atoms and therefore considering this interference the measured scattering amplitude is:

$$\psi(\mathbf{Q}) = \int A(\mathbf{r}) e^{i\mathbf{Q}\mathbf{r}} d\mathbf{r} = \int \sum_j f_j(\mathbf{r} - \mathbf{R}_j) e^{i\mathbf{Q}\mathbf{r}} d\mathbf{r} = \sum_j f_j(\mathbf{Q}) e^{i\mathbf{Q}\mathbf{R}_j} \quad 3.8$$

Where, again, 2θ is the diffraction angle, and λ is the experimental wavelength and \mathbf{Q} is the scattering coordinate defined as:

$$Q = \frac{4\pi \sin(\theta)}{\lambda} \quad 3.9$$

This expression (**Equation 3.8**) is a more general form of the structure factor $F(hkl)$ previously introduced for crystalline materials (**Equation 3.2**), where now due to the absence of lattice periodicity the summation must be done over every atom in the sample. This procedure is known as a Fourier transform, and is a mathematical tool for converting from real to reciprocal space. The functions $f_j(\mathbf{Q})$ are known as the atom form factors (**Equation 3.2**), and the diffuse shape of the electron density around atoms leads to them being functions of \mathbf{Q} .

The measured intensity, normalised by the number of atoms N , is therefore proportional to the square of this scattering amplitude:

$$F(\mathbf{Q}) = \frac{1}{N} |\psi(\mathbf{Q})|^2 = \frac{1}{N} \sum_{jk} f_j(\mathbf{Q}) f_k(\mathbf{Q}) e^{i\mathbf{Q}(\mathbf{R}_j - \mathbf{R}_k)} \quad 3.10$$

This summation can be separated into two distinct components, namely the ‘self’ terms where $j = k$, and the ‘distinct’ terms where $j \neq k$:

$$F(Q) = f(Q)^2 + \frac{1}{N} \sum_{j \neq k} f_j(Q) f_k(Q) e^{i\mathbf{Q}(\mathbf{R}_j - \mathbf{R}_k)} \quad 3.11$$

These ‘self’ terms contain no information about the atomic distribution of atoms within the structure, as they do not depend on $\mathbf{R}_j - \mathbf{R}_k$, whereas the distinct terms provide the structural information in terms of the distribution of atomic distances.

Up to this point we have treated \mathbf{r} , \mathbf{R}_i , and \mathbf{Q} as vectors whose value has an angular dependence, however amorphous materials, and crystalline powders are isotropic in terms of angle and therefore an angular average can be taken such that the measured intensity then becomes:

$$F(Q) = f(Q)^2 + \frac{1}{N} \sum_{j \neq k} f_j(Q) f_k(Q) \frac{\sin(Qr_{jk})}{Qr_{jk}} \quad 3.12$$

Where $r_{jk} = |\mathbf{R}_j - \mathbf{R}_k|$. From the form of (**Equation 3.12**) it is apparent that the measured diffraction intensity depends on the distances between atoms, r_{jk} as opposed to the positions of atoms themselves. This result should be unsurprising given that diffraction occurs via interference between scattered waves, the relative path length between which, depends on the distance between scattering centres. So far, the summations have been conducted over all the atoms in the system, however the summation could also be done over the different types of atoms in the system.

If this is done then **(Equation 3.12)** can also be recast in terms of number density **(Equation 3.4)** or radial distribution function **(Equations 3.5 and 3.6)** [84]:

$$F(Q) = \sum_{\alpha} c_{\alpha} f_{\alpha}(Q)^2 + \frac{1}{N} \sum_{\alpha} N_{\alpha} f_{\alpha}(Q) \sum_{\beta \geq \alpha} (2 - \delta_{\alpha\beta}) f_{\beta}(Q) n_{\alpha\beta}(r) \frac{\sin(Qr)}{Qr} \quad 3.13.1$$

$$F(Q) = \sum_{\alpha} c_{\alpha} f_{\alpha}(Q)^2 + \sum_{\alpha} c_{\alpha} f_{\alpha}(Q) \sum_{\beta \geq \alpha} (2 - \delta_{\alpha\beta}) f_{\beta}(Q) n_{\alpha\beta}(r) \frac{\sin(Qr)}{Qr} \quad 3.13.2$$

$$F(Q) = \sum_{\alpha} c_{\alpha} f_{\alpha}(Q)^2 + \sum_{\alpha} c_{\alpha} f_{\alpha}(Q) \sum_{\beta \geq \alpha} (2 - \delta_{\alpha\beta}) f_{\beta}(Q) \int 4\pi r^2 c_{\beta} p_0 g_{\alpha\beta}(r) \frac{\sin(Qr)}{Qr} dr \quad 3.14.1$$

$$F(Q) = \sum_{\alpha} c_{\alpha} f_{\alpha}(Q)^2 + \sum_{\alpha\beta \geq \alpha} (2 - \delta_{\alpha\beta}) c_{\alpha} c_{\beta} f_{\alpha}(Q) f_{\beta}(Q) 4\pi p_0 \int r^2 g_{\alpha\beta}(r) \frac{\sin(Qr)}{Qr} dr \quad 3.14.2$$

Where $\delta_{\alpha\beta}$ is the Kronecker delta and is included to avoid double counting atom correlation functions where the atoms in the atom pairs are chemically identical. There is a subtle distinction between self-scattering and the $n_{\alpha\alpha}(r) / g_{\alpha\alpha}(r)$ correlation functions; in self-scattering the atom is scattering with itself (i.e. $r = 0$), whereas in the $n_{\alpha\alpha}(r) / g_{\alpha\alpha}(r)$ the correlations occur between atoms of the same chemistry but which are spatially separated.

Finally, it is also common to see the PDF described in terms of the ‘total-correlation function’:

$$h_{\alpha\beta}(r) = g_{\alpha\beta}(r) - 1 \quad 3.15$$

Which goes to -1 as $r \rightarrow 0$ and 0 as $r \rightarrow \infty$. This is done because the direct Fourier transform of $g_{\alpha\beta}(r)$, i.e. via **(Equation 3.14.2)** would contain a component at $Q = 0$, which cannot be measured in practice due to the direct beam. However, when the total-correlation function is used this term becomes a delta function at $Q = 0$, i.e. entirely localised to the unmeasurable region of space [84]. This is then generally discarded resulting in the final form for the scattering intensity:

$$F(Q) = \sum_{\alpha} c_{\alpha} f_{\alpha}(Q)^2 + \sum_{\alpha\beta \geq \alpha} (2 - \delta_{\alpha\beta}) c_{\alpha} c_{\beta} f_{\alpha}(Q) f_{\beta}(Q) 4\pi p_0 \int r^2 [g_{\alpha\beta}(r) - 1] \frac{\sin(Qr)}{Qr} dr \quad 3.16.1$$

$$F(Q) = \sum_{\alpha} c_{\alpha} f_{\alpha}(Q)^2 + p_0 \int 4\pi r^2 G(r) \frac{\sin(Qr)}{Qr} dr \quad 3.16.2$$

Where:

$$G(r) = \sum_{\alpha\beta \geq \alpha} (2 - \delta_{\alpha\beta}) c_{\alpha} c_{\beta} f_{\alpha}(Q) f_{\beta}(Q) [g_{\alpha\beta}(r) - 1] \quad 3.17$$

$G(r)$ is the function which is generally known as the PDF. A related function, also commonly referred to as the PDF, though with increased r scaling to emphasise longer correlations in real-space $D(r)$, is also commonly seen [85]:

$$D(r) = 4\pi p_0 r G(r) \quad 3.18$$

It can therefore be seen that the structural information in the measured X-ray total-scattering comes from the distinct scattering which oscillates around a background due to the self-scattering terms. Additionally, the PDF still contains the broadening effect due to the convolution of the atom positions with the electron density (**Equation 3.7**), and therefore the data is divided by a 'de-broadening function' $B(Q)$ which represents the broadening effect due to the electron distribution. This process is also commonly referred to as normalising the structure factor. Taken together it can be seen that the distinct, normalised, total-scattering, $S(Q)$, is then:

$$S(Q) = \frac{F(Q) - \sum_{\alpha} c_{\alpha} f_{\alpha}(Q)^2}{B(Q)} \quad 3.19$$

$B(Q)$ is commonly defined as either:

$$B(Q) = \left[\sum_{\alpha} c_{\alpha} f_{\alpha}(Q) \right]^2 \quad 3.20.1$$

Or

$$B(Q) = \sum_{\alpha} c_{\alpha} f_{\alpha}(Q)^2 \quad 3.20.2$$

At this point it should be noted that the X-ray total-scattering field is incredibly idiosyncratic in terms of terminology, with multiple closely related functions all in regular use and some functions with the same name defined differently by different researchers [87]. The nomenclature choices made here, most notably to define the distinct total-scattering as $S(Q)$, are done to be consistent with many MOF researchers.

In theory the PDF is obtained from $S(Q)$ (**Equation 3.19**) via a direct inverse Fourier transform but experimental difficulties complicate this in practice [84], [88]. Firstly, detectors have both a dark current, a current which flows through them even without photon illumination, and a deadtime, a time between measurements in which the detector needs to refresh. The dark current is directly subtracted from the measured data and the data is then corrected for deadtime, which is a count-rate dependent error [88]. Secondly the sample is present in a container, i.e. a glass capillary, and scans of this empty container and of the instrument background must be subtracted from the sample

measured container. This subtraction also considers the effects of beam attenuation and multiple scattering in the sample and container, empty container, and empty instrument. An additional background due to inelastic scattering, which is caused by the recoil of weakly bound electrons during scattering (Compton Scattering) is also subtracted from the data. Finally an iterative process is used to normalise the data, however it is almost impossible to put X-ray total-scattering data on a truly absolute scale [84].

In addition to these corrections a top-hat function is used to generate a smoothly varying Q dependent background which can be tuned by the user. This background can be used to account for any lingering background effects in the data due to imperfect corrections as described above and is subtracted from the measured intensity prior to the Fourier transform to produce the PDF. Another background function, this time designed to flatten the PDF function at low r where peaks would be unphysical, is also subtracted from the data. Finally the Soper-Lorch function is also used to reduce high-frequency noise in real space, this is achieved by taking a volume average of the real space data within a small range or r [84].

This section has detailed the process by which total-scattering data can be processed to produce the pair-distribution function, a real-space function which contains information on the atom-atom correlation distances within the material. The PDF was shown to be analogous to a histogram of atom correlations within the structure. It was also demonstrated that this process makes no assumptions as to structural symmetry and therefore is valid for both amorphous and crystalline materials. For this reason, X-ray total-scattering methods are of great utility in the study of glasses, whose structures cannot be interrogated by conventional X-ray diffraction.

3.1.3 Differential Scanning Calorimetry

Differential scanning calorimetry (DSC) is a thermal analysis technique in which a sample and an inert reference are subjected to the same heating regime. This reference is generally an empty crucible made of the same type that is used to hold the sample. The temperature of both the sample and the reference are measured during the heat treatment and this temperature difference is the measured signal of the device. In heat-flux DSC the sample and the reference are placed within the same furnace (**Figure 3.7**) and heat exchanged between the sample and reference with the environment takes place through a well-defined pathway with a known thermal resistance [89]. In contrast, in power-compensation DSC the sample and the reference are placed in different furnaces and the power to each furnace is adjusted separately to minimise the measured temperature difference (**Figure 3.8**) [89].

Despite the different measurement set-ups both heat-flux and power-compensation DSCs produce the same output after calibration, a measure of sample heat flow which is proportional to the measured temperatures difference between sample and reference:

$$\Phi_m = k\Delta T \quad 3.21$$

Where Φ_m is the measured heat flow into, or out of, the sample, ΔT is the temperature difference between the sample and the reference and k is a constant of proportionality. This measured sample heat flow is due to thermal activity of the sample in-excess of that occurring in the reference at the same point in the heat-treatment. The following discussion will focus on heat-flux DSC as this was the instrument type used to obtain the data in this thesis.

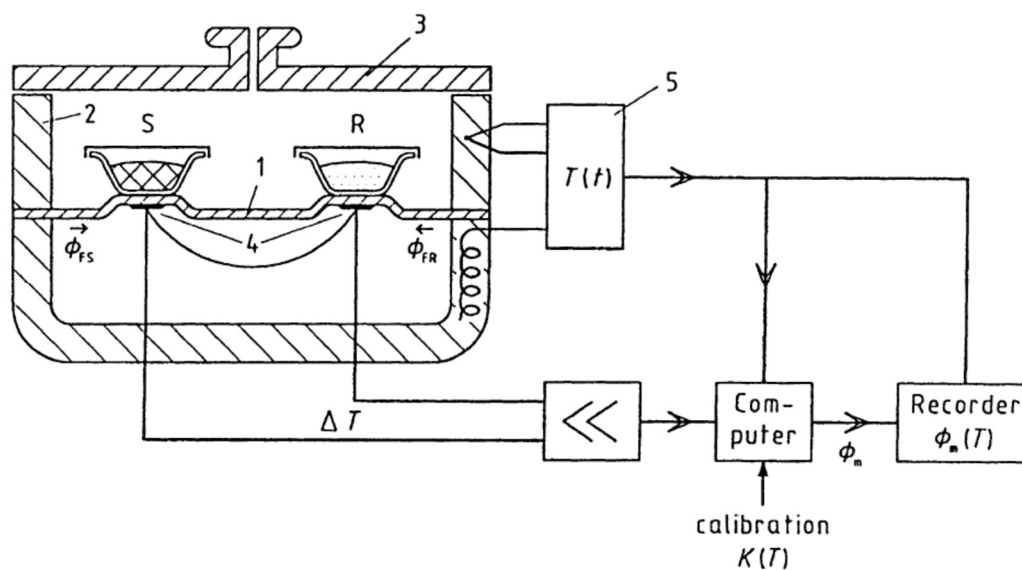


Figure 3.7: Schematic of a heat-flux DSC. Reproduced from [89]. 1. Crucible support disk. 2. Furnace. 3. Lid. 4. Differential thermocouples. 5. Programmer and controller. S sample crucible and R. reference crucible. Φ_{FS} and Φ_{FR} heat flow into the sample and reference.

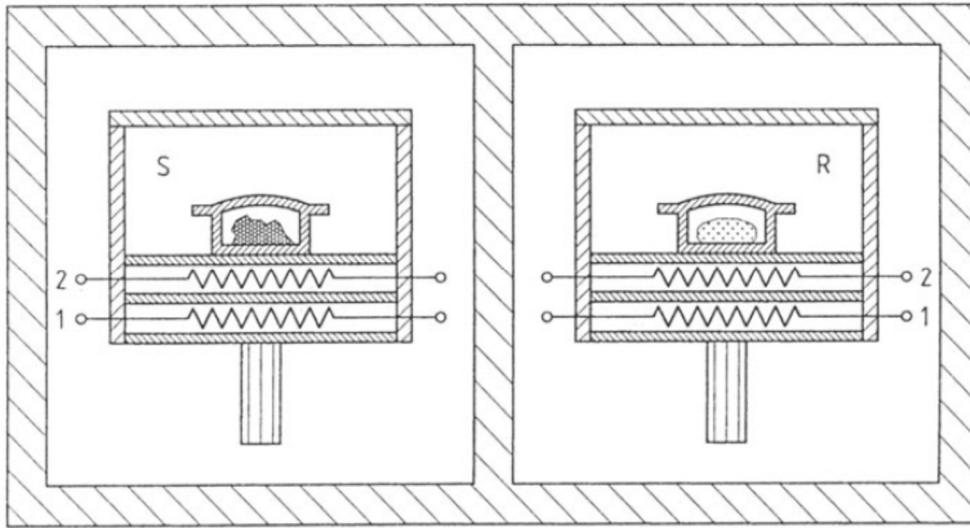


Figure 3.8: Schematic of a power-compensation DSC. Reproduced from [89]. Both systems are thermally isolated from one another and placed in a block of constant temperature. 1. Heating wires. 2 Thermocouples. S sample crucible. R reference crucible.

Starting with a simple steady-state assumption the relationship between measured temperature difference, ΔT , and the heat flow due to thermal events in the sample Φ_S is derived. This model assumes that the heat flow from the furnace to the sample and reference happens via a single well-defined pathway (**Figure 3.9**) with a single value for the thermal conductivity, λ .

The heat flow from the furnace to the sample (or reference) can then be calculated by the Biot-Fourier equation:

$$\frac{\Phi_{FS}}{A} = \frac{-\lambda(T_F - T_S)}{\Delta l} \quad 3.22.1$$

$$\frac{\Phi_{FR}}{A} = \frac{-\lambda(T_F - T_R)}{\Delta l} \quad 3.22.2$$

Where Φ_{FS} and Φ_{FR} are the heat flows from the furnace into the sample and the reference respectively due to differences in temperature between the sample T_S , reference T_R and furnace T_F . The other quantities are geometric constants related to the experimental set-up (**Figure 3.9**).

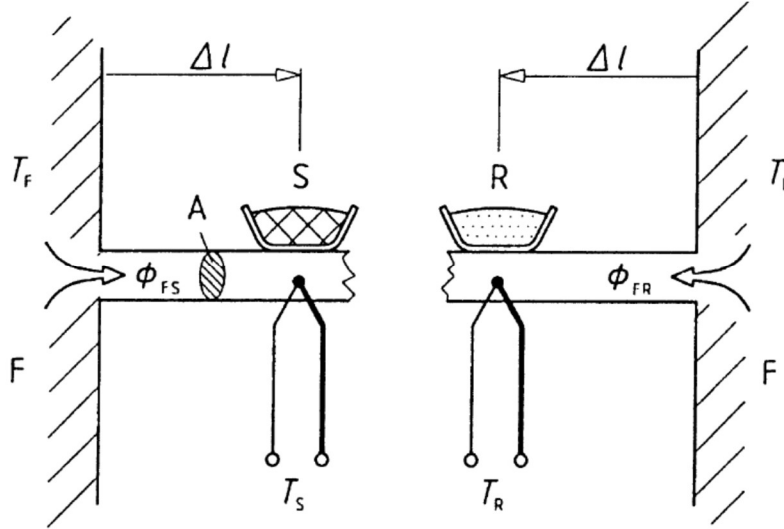


Figure 3.9: Schematic of heat flow in the heat-flux DSC. Reproduced from [89]. Cross section (A) and distance (Δl) of the conductor between the furnace (F), sample (S) and reference (R).

If the sample and reference were thermally identical, i.e. two empty crucibles of the same mass were being measured, then, assuming complete thermal symmetry, $T_S = T_R$ and $\Phi_{FS} = \Phi_{FR}$. In this case the measured signal, $\Delta T = T_S - T_R$, would be 0. Instead if a constant exothermic heat flow rate is produced in the sample, $\Phi_S < 0$, then the sample temperature will increase relative to the reference temperature. As such the difference in temperature between the sample and the furnace will decrease leading to a change in heat flow rate between them. Given that the reference temperature remains constant can be written in the following terms:

$$\frac{\Phi'_{FS}}{A} = \frac{\Phi_{FR}}{A} + \frac{\Phi_S}{A} = \frac{-\lambda(T_F - T'_S)}{\Delta l} = \frac{-\lambda(T_F - (T_R + \Delta T))}{\Delta l} \quad 3.23$$

Which, if the heat flow into the unchanging reference sample is then subtracted, can be written as:

$$\frac{\Phi'_{FS}}{A} - \frac{\Phi_{FR}}{A} = \frac{\Phi_S}{A} = \frac{-\lambda(T_F - (T_R + \Delta T))}{\Delta l} - \frac{-\lambda(T_F - T_R)}{\Delta l} = \frac{\lambda(\Delta T)}{\Delta l} \quad 3.24.1$$

$$\Phi_S = \frac{A\lambda(\Delta T)}{\Delta l} = k\Delta T \quad 3.24.2$$

Therefore the result previously stated (**Equation 3.21**) is recovered, where the measured signal Φ_m is the signal due to thermal activity in the sample Φ_S , i.e. due to the additional energy required to heat the sample at the same rate as the reference. This analysis assumes that there is only one thermal resistance, which is the same between the sample and the reference crucibles, and that there is no heat exchange between the sample and reference and between the system and the surroundings. Another major assumption made in this analysis is thermal symmetry i.e. that all the temperature

conducting pathways and measurement circuitry leading to the sample and reference are identical. This is unlikely to be true in reality but the asymmetry of the machine can be accounted for using a zero line correction, a measurement run is made with two empty crucibles. The signal in this measurement, assuming the crucibles are the same mass, is due solely to asymmetry in the machine. This measured asymmetry can then be subtracted from sample measurements.

Importantly the condition of steady state is also assumed, i.e. Φ_s/Φ_m is a constant, which is not valid during first order sample transitions in the sample, which appear as peaks in the DSC signal. When this condition is not valid the sample heat flow is not strictly proportional to the measured temperature difference because there is a thermal lag. However when peaks are integrated, providing that the sample heat capacities and instrument properties are only weakly dependent on temperature then this lag-term vanishes [89].

The measured signal of Φ_m , after subtraction of the zero line, can be decomposed into two parts:

$$\Phi_m(T) = \Phi_{cp}(T) + \Phi_r(T) \quad 3.25$$

Where $\Phi_{cp}(T)$ is the signal due to the heat capacity of the sample and $\Phi_r(T)$ is the signal due to phase changes or reactions.

Thermodynamically the heat energy can be represented as:

$$dQ = dH - VdP - \sum_i E_i \quad 3.26$$

Where H is the enthalpy, V is the system volume, P is the measured pressure and $\sum_i E_i$ represents energy changes due to changing 'energy forms' i.e. changing surface energies or particle sizes. Assuming that the system is at approximately constant pressure, which is the case in most DSCs even for closed crucibles [89], then the heating rate can be written in differential form as:

$$dQ_m = \left(\frac{\partial H}{\partial T}\right)_P dT - \sum_i dE_i \quad 3.27.1$$

$$\frac{\delta Q_m}{dt} = \Phi_m = \left(\frac{\partial H}{\partial T}\right)_P \frac{dT}{dt} - \sum_i dE_i \quad 3.27.2$$

Where the temperature gradient of enthalpy at constant pressure is equal to the heat capacity of the sample:

$$C_p(T) = \left(\frac{\partial H}{\partial T}\right)_P \quad 3.28$$

And the enthalpy change during a thermal event, also accounting for other energy changes, can be calculated from the integral form of (Equation 3.27.1) in terms of temperature:

$$\int dQ_m = \Delta H + \Delta E \quad 3.29$$

These equations lead to a clear picture of the thermal properties represented by the DSC measurement signal Φ_m (Equation 3.25) (Figure 3.10). The baseline signal, when the zero line has been subtracted, constitutes the signal due to the heat capacity of the sample (Equation 3.28). In other words the input thermal energy necessary to keep the sample heating at the same rate as the empty reference crucible. Changes in sample heat capacity, such as on heating through the glass transition temperature, are therefore detectible by step changes in the DSC baseline. In contrast $\Phi_r(T)$ is responsible for peaks in the measured signal. The integral of these peaks represents the enthalpy changes due to first order events like phase changes (Equation 3.29).

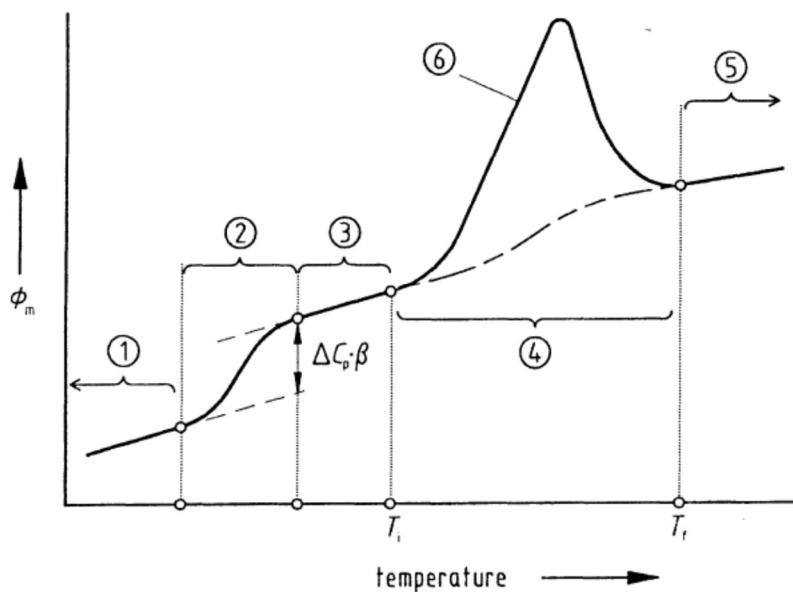


Figure 3.10: Schematic of features in a DSC curve. Curve measured by a DSC showing a step in the DSC baseline $\Delta C_p \beta$ i.e. due to a glass transition (1-3) and an endothermic melting peak (4-6) with interpolated baseline (dashed). Reproduced from [89].

In endothermic transitions heat is taken in and the flow of heat into the sample is positive so the peak points upwards, the reverse is true for exothermic events in which heat is released by the sample [89].

It can be seen from the diagrams (Figure 3.7 and Figure 3.8) that the thermocouples are not placed directly into the sample and reference. This means that the measured temperature is not the actual

sample temperature. In order to account for this difference calibration must be carried out. This can be achieved by measurement of the onset of melting in pure calibration substances whose melting temperatures are known. Substances with melting endotherms which span the temperature range of interest are chosen and then a curve is fitted to determine the temperature calibration factor [89]:

$$T_{true} = T_{meas} + \Delta T(T) \quad 3.30$$

Where T_{true} and T_{meas} are the literature reported and measured melting onsets and $\Delta T(T)$ is the temperature dependent correction extracted from the fitted curve.

Similarly, the true heat flow rate Φ_{true} must be obtained through calibration using the measured heat flow rate Φ_m . This can be carried out in two ways, either by measuring a sample of well-known heat capacity, i.e. synthetic sapphire, or via measuring samples of well-known melting enthalpies. It can be seen (**Equations 3.27 and 3.28**) that the baseline of the DSC signal is equal to the heat capacity and therefore:

$$\Phi_{true} = C_P(T) \frac{dT}{dt} \quad 3.31.1$$

$$K_\phi(T) = \frac{C_P(T) \frac{dT}{dt}}{\Phi_m} \quad 3.31.2$$

This produces a calibration constant $K_\phi(T)$ which can then be used to recover the true heat flow rate from the measured temperature difference (**Equation 3.24.2**).

Equally integration of the melting endotherm of a pure substance, whose enthalpy of fusion is known, can reasonably be assumed to occur without substantial changes in energy form (i.e. $\sum_i dE_i = 0$) and therefore integration in terms of temperature (**Equation 3.27.1**) or time (**Equation 3.27.2**) yields the calibration constant $K_Q(T)$:

$$\Delta H_{fusion} = K_Q(T) \int_{T_i}^{T_f} dQ_m dT \quad 3.32$$

Where T_i and T_f represent the limits of the observed endothermic peak. Unlike heat flow calibration this yields values of the calibration constants at discrete melting temperatures, therefore much like in temperature calibration a set of calibration standards spanning the investigated temperature range is used and a continuous function for $K_Q(T)$ is achieved by fitting a curve [89].

This section has shown that DSC represents a method by which the thermal properties of a sample can be investigated. Of particular interest to the study of glasses is the ability to measure the glass transition temperature through changes in the baseline and to investigate melting and potential

recrystallisation, which are present as endothermic and exothermic peaks respectively. In studies on melting MOFs the melting temperature is conventionally given by the offset of the melting peak rather than the onset [56]. DSC, especially when combined with a simultaneous measurement of sample mass in thermogravimetric analysis (TGA), is also a technique by which the limits of sample thermal stability can be assessed through rises in DSC baseline and loss of sample mass.

3.2 Experimental Methods

3.2.1 Chapter 4: Structural Investigation of Zeolitic Imidazolate Framework Glasses via X-ray Total-Scattering

ZIF-4 Synthesis:

The method for synthesising the crystalline ZIF-4 phase was modified from previous literature [36]. Specifically, $\text{Zn}(\text{NO}_3)_2 \cdot 6\text{H}_2\text{O}$ (0.73 g, 2.45 mmol) and imidazole (0.5 g, 7.34 mmol) were each dissolved in *N,N*-dimethylformamide (DMF) (25 ml). The resulting solutions were then mixed and stirred for approximately 10 min before the mixture was placed in a 90 ml Teflon-lined stainless-steel autoclave. The autoclave was tightly sealed and heated to 130 °C for 72 hours in an oven. After cooling to room temperature, the obtained products were separated from the mother liquor and washed with DMF (50 ml) three times. The final product was then dried in a vacuum oven at 110 °C for 12 hours.

ZIF-62 Synthesis:

ZIF-62 was synthesised by a solvothermal method previously reported [56], [90], in which $\text{Zn}(\text{NO}_3)_2 \cdot 6\text{H}_2\text{O}$ (1.515 g, 8 mmol), imidazole (7.35 g, 108 mmol), and benzimidazole (1.418 g, 12 mmol) were dissolved in DMF (75 ml) and transferred into a 100 ml glass jar. The jar was sealed tightly and heated to 130 °C for 48 hours in an oven. After cooling to room temperature, ZIF-62 crystals were collected from the mother liquid and washed DMF (30 ml) three times and dichloromethane (DCM) (30 ml). The crystalline sample was characterized before drying at 100 °C under vacuum for 10 hours.

Powder X-ray Diffraction:

Room-temperature powder X-ray diffraction data on the ZIF-4 samples were collected with a Rigaku-RU 200B diffractometer using $\text{Cu K}\alpha$ ($\lambda = 1.542 \text{ \AA}$) radiation, whereas scans of the ZIF-62 samples were conducted with a PANalytical empyrean XRD using $\text{Cu K}\alpha$ radiation ($\lambda = 1.542 \text{ \AA}$).

Thermal Characterisation:

DSC experiments on both ZIF-62 and ZIF-4 samples were carried out using a Netzsch STA 449 F1 Jupiter instrument in an argon atmosphere. The samples were placed in a platinum crucible. The C_p curve for each measurement was calculated relative to the C_p curve of a sapphire reference material of comparable mass. Heating and cooling rates for each sample are indicated in the text of the chapter.

X-ray Total-Scattering:

Ambient temperature X-ray total-scattering data on both ZIF-4 and ZIF-62 samples data were collected at the I15-1 beamline at the Diamond Light Source, UK ($\lambda = 0.161669 \text{ \AA}$, 76.7 keV). Samples were loaded into borosilicate glass capillaries of 1.17 mm (inner) diameter. Data on the sample, empty instrument and capillary were collected in the region of $0.4 < Q < 26 \text{ \AA}^{-1}$. Corrections for empty instrument and empty container scattering, multiple scattering, Compton scattering and absorption were performed using the GudrunX program [91].

The variable temperature X-ray total-scattering measurements on a_gZIF-4, which had previously been reported in the literature [60], were collected at the Advanced Photon Source, USA on the 11-ID-B beamline ($\lambda=0.143 \text{ \AA}$, 86.7 keV), in the range $0.6 < Q < 24 \text{ \AA}^{-1}$. In this work the data was reanalysed by fitting the first sharp diffraction peak (FSDP) in the measured $S(Q)$ with a Pseudo-Voigt function in Fityk [92] in order to obtain values for peak height, position, full-width at half-maximum and area as a function of temperature.

3.2.2 Chapter 5: Creating New 'Complex' Metal-Organic Framework Glasses from Two Component Frameworks

ZIF-4 Synthesis:

ZIF-4 was synthesised using a method previously reported in the literature [36]. A solid mixture of zinc nitrate hexahydrate $\text{Zn}(\text{NO}_3)_2 \cdot 6\text{H}_2\text{O}$ (1.2 g, 4.6 mmol) and imidazole (0.9 g, 13 mmol) was dissolved in DMF (90 ml) in a 100 ml vial. After vigorous stirring the vial was capped tightly and heated to 100 °C for 72 hours. The vial was removed from the oven, and after manual cooling to room temperature the mother liquor was decanted. Crystals of ZIF-4 were collected, washed three times with DCM (30 ml) and dried in air.

ZIF-62 Synthesis:

The ZIF-62 was synthesised according to a method reported in the literature [90]. Stock solutions of $\text{Zn}(\text{NO}_3)_2 \cdot 6\text{H}_2\text{O}$ (0.2 M), benzimidazole (0.2 M) and imidazole (1.5 M) in DMF were prepared. The stock solutions were then mixed in Zn:Im:blm molar ratio of 1:13.5:1.5 and topped up with DMF to reach a total volume of 75 ml. The solution was stirred for 1 hour followed by heating at 130 °C for 96 hours before being cooled to room temperature. The sample was then filtered under vacuum, washed twice with DMF (20 ml) to yield ZIF-62 as a powder.

ZIF-4-Co Synthesis:

ZIF-4-Co was synthesised according to methods previously reported [50]. A solid mixture of $\text{Co}(\text{NO}_3)_2 \cdot 6\text{H}_2\text{O}$ (0.14 g, 0.46 mmol) and imidazole (0.09 g, 1.3 mmol) was dissolved in DMF (9 ml) in a 20 ml vial. After vigorous stirring the vial was capped tightly and heated to 130 °C for 48 hours. The vial was removed from the oven, and after cooling to room temperature, the mother liquor was decanted. Crystals of ZIF-4-Co were collected, washed three times with ethanol (3 mL), and dried in air.

ZIF-67 Synthesis:

ZIF-67 was synthesised according to a previously reported method [93]. $\text{Co}(\text{OAc})_2 \cdot 2\text{H}_2\text{O}$ (0.11 g, 0.5 mmol) and 2-methylimidazole (0.41 g, 5 mmol) were placed in a small glass vial, which was supported by a Teflon holder. Each vial and holder were placed in a Teflon-lined stainless-steel autoclave. H_2O (2.0 mL) was added to the bottom of the autoclave. The sample was heated for 24 hours at 120 °C. After cooling the autoclave to room temperature, the solid products were separated by filtration and washed with distilled water.

ZIF-76 and ZIF-76-mblm Synthesis:

ZIF-76 were prepared via procedures reported in the literature [94]. Specifically, imidazole (0.12 g, 1.725 mmol) and 5-chlorobenzimidazole (0.13 g, 0.866 mmol) were mixed together in a solution of *N,N*-dimethylformamide (8.28 ml) and *N,N*-diethylformamide (5.73 ml). $\text{Zn}(\text{NO}_3)_2 \cdot 6\text{H}_2\text{O}$ (0.25 g, 0.859 mmol) was subsequently added, along with NaOH (0.52 ml, 2.5 M). The turbid solution was then heated to 90 °C for 5 days, and the microcrystalline powder collected by filtration. The frameworks were activated by heating under vacuum at 200 °C for 6 hours. To synthesise ZIF-76-mblm, 5-methylbenzimidazole (0.115 g, 1.17 mmol) was used in place of 5-chlorobenzimidazole.

Powder X-ray Diffraction:

Data were collected with a Bruker-AXS D8 diffractometer using $\text{Cu K}\alpha$ ($\lambda = 1.542 \text{ \AA}$) radiation and a LynxEye position sensitive detector in Bragg–Brentano parafocusing geometry.

Thermal Characterisation:

DSC experiments in this chapter were carried out using a Netzsch STA 449 F1 Jupiter instrument in an argon atmosphere. The samples were placed in a platinum crucible. C_p measurements were calculated relative to the C_p curve of a sapphire reference material of comparable mass. Heating and cooling rates of 10 °C/min were used.

For the (ZIF-8)(ZIF-62)(20/80), (ZIF-67)(ZIF-62)(20/80), $a_g[(ZIF-8)_{0.2}(ZIF-62)_{0.8}]$, and $a_g[(ZIF-67)_{0.2}(ZIF-62)_{0.8}]$ samples simultaneous DSC-TGA data were performed using a TA instruments Q-600 series differential scanning calorimeter in argon. An alumina crucible was used. The data were also obtained using a heating rate of 10 °C/min.

Electron Microscopy:

Scanning transmission electron microscopy data were acquired using an FEI Osiris microscope equipped with a high-brightness X-FEG electron source and operated at 80 kV. The beam convergence was set to 11.0 mrad. X-ray energy dispersive spectroscopy (EDS) was acquired using a 'Super-X' EDS detector system with four detectors mounted symmetrically about the optic axis of the microscope (200 ms per pixel). For all spectroscopic data, images were also simultaneously recorded on annular dark field (ADF) detectors. These images contain atomic number and thickness contrast, giving information in parallel with the mapping obtained in the EDS data. Data were processed using Hyperspy [95], an open-source software coded in Python.

In the EDS tilt-series tomography measurements on the (ZIF-4-Co)(ZIF-62)(50/50) and $(ZIF-4-Co)_{0.5}(ZIF-62)_{0.5}$ samples, EDS spectrum images were acquired from -70° to 70° in 10° increments. Data were then processed using Hyperspy [95] to create the three-dimensional images.

X-ray Total-Scattering:

Ambient temperature X-ray total-scattering measurements on (ZIF-4-Co)(ZIF-62)(50/50), $(ZIF-4-Co)_{0.5}(ZIF-62)_{0.5}$, (ZIF-76)(ZIF-UC-5), $a_g[(ZIF-76)(ZIF-UC-5)]$, (ZIF-76-mblm)(TIF-4) and $a_g[(ZIF-76-mblm)(TIF-4)]$ were conducted at the I15-1 beamline at the Diamond Light Source, UK ($\lambda = 0.161669 \text{ \AA}$, 76.7 keV). Samples were loaded into borosilicate glass capillaries of 1.17 mm (inner) diameter. Data on the sample, empty instrument and capillary were collected in the region of $0.4 < Q < 26 \text{ \AA}^{-1}$. Corrections for empty instrument and empty container scattering, multiple scattering, Compton scattering and absorption were performed using the GudrunX program [91].

Variable temperature measurements on $(ZIF-4-Co)_{0.5}(ZIF-62)_{0.5}$ and (ZIF-76)(ZIF-UC-5) samples were conducted using an identical measurement set-up though the capillaries were sealed with araldite and empty capillary measurements were conducted for each temperature examined.

Ambient temperature X-ray total-scattering data on the ZIF-8, (ZIF-8)(ZIF-62)(20/80), and $a_g[(ZIF-8)_{0.2}(ZIF-62)_{0.8}]$ samples were conducted using a PANalytical Ag-source Empyrean lab diffractometer ($\lambda = 0.561 \text{ \AA}$, 22.1 keV). Data collection was carried out using loaded 1.0 mm (inner) diameter quartz capillaries and collection times of approximately 6 hours. Background, multiple scattering, container

scattering, Compton scattering and absorption corrections were performed using the GudrunX program [91].

3.2.3 Chapter 6: Metal-Organic Framework and Inorganic Glass Composites

ZIF-62 Synthesis:

ZIF-62 was synthesised according to the following method adapted from the literature [61]: Zn(NO₃)₂·6H₂O (1.65 g, 5.55 mmol), imidazole (8.91 g, 131 mmol) and benzimidazole (1.55 g, 13.12 mmol) were added to *N,N*-dimethylformamide (DMF) (75 ml). The mixture was then heated at 130 °C and stirred for 48 hours. The resultant product was washed twice with DMF (20ml) under vacuum to obtain a crystalline powder. To increase the yield the filtered reaction mixture was placed back into the oven at 130 °C for a further 48 hours and then more product obtained through washing under vacuum twice with DMF (20 ml).

For the heat-treated samples (a_gZIF-62)_{0.5}(Inorganic Glass)_{0.5} samples a mixture of the two filtrations was used to obtain enough ZIF-62. The ZIF-62 used in the screening samples, controls and evacuated powder mixtures (ZIF-62)(Inorganic Glass)(50/50) were synthesised in separate batches but in each case only the powder from the first filtration was used.

Before direct experiments on the (ZIF-62)(Inorganic Glass)(50/50) mixtures and ZIF-62 controls were conducted, the powders were activated by soaking in DCM for 24 hours, followed by heating to 175 °C for 3 hours under vacuum. This was done to remove framework templating DMF from within the pores of the ZIF-62.

(1-x)([Na₂O]_z[P₂O₅])-x([AlO_{3/2}][AlF₃]_y) Synthesis:

High purity reagents (optical grade) of NaPO₃ and AlF₃ were melted in a Pt crucible in an electric muffle furnace. Due to the known volatility of fluoride, care was taken to initially melt all mixtures at 800 °C for one hour to allow NaPO₃ to melt and dissolve the AlF₃ before higher temperatures were used for complete dissolution. Generally, longer melting times were preferred over higher melting temperatures when producing a homogeneous melt.

The base glass (0.78([Na₂O]_{1.6}[P₂O₅])-0.22([AlO_{3/2}][AlF₃]_{0.7})) sample was melted at 800 °C for one hour before being taken up to 850 °C for half an hour before pouring. Higher amounts of AlF₃ required higher melting temperatures, with the Al-rich (0.66([Na₂O]_{1.7}[P₂O₅])-0.34([AlO_{3/2}][AlF₃]_{0.4})) and Na-deficient (0.67([Na₂O]_{0.9}[P₂O₅])-0.33([AlO_{3/2}][AlF₃]_{1.5})) glasses requiring 950 and 1000 °C to be completely homogeneous, respectively. Since the glasses were then to be pulverized and remelted, no attempts at annealing were conducted on the powders used for synthesis of the composites.

Instead they were pulverized in a Retsch PM 100 grinder at 350 rpm with 1 min intervals for half an hour using ZrO₂ or Si₃N₄ balls (with roughly equal sample and ball volume). A bulk piece was saved from each composition to later be annealed for elemental analysis and mechanical measurements. The annealing temperatures were 40—60 °C above the T_g of the inorganic phase; the glass specimens were then cut and polished to one micron.

To make 80 g of the base inorganic glass, 66.3 g of dry NaPO₃ powder and 13.7 g of AlF₃ powder were mixed thoroughly by hand before melting. The Na-deficient composition was made from 59.1 g of dry NaPO₃ powder and 20.9 g AlF₃, while the Al-rich used 51.6 g and 28.4 g, respectively.

Composite Samples (a_gZIF-62)_{0.5}(Inorganic)_{0.5} Production:

Approximately 300 mg of crystalline ZIF-62 and 300 mg of inorganic glass powders were mixed together through ball-milling in a stainless steel jar (15 ml) for 5 minutes at 25 Hz with one 5 mm stainless steel ball bearing in a Retsch MM400 grinder mill. 200 mg samples of the ball milled powder mixture were placed in a 13 mm die and compacted into a pellet using 10 tons of pressure applied for one minute. These pellets were placed in a tube furnace (Carbolite 12/65/550) which was left to equilibrate under argon for one hour before heating to 410 °C at 10 °C/min and holding for either 1 or 30 minutes. All heating was done under constant argon flow. The heat treated pellets were left to cool under argon at the natural rate of the tube furnace; the samples were removed from the tube furnace at temperatures equal to or below 200°C.

Thermal Characterisation:

Combined DSC TGA scans of the screening samples were carried out using a TA instruments Q-600 series differential scanning calorimeter. Approximately 10 mg powdered sample was placed in open alumina crucibles and heated under argon. Heating rates are indicated in the text of the chapter.

DSC characterisation of the (ZIF-62)(Inorganic Glass)(50/50) samples was conducted using a Netzsch 214 Polyma. Approximately 10 mg of sample was placed in aluminium crucibles with a pierced concave lid. Heating and cooling steps were conducted under argon at a rate of 10 °C/min. Features in the DSC traces were processed by smoothing and analysed using the Netzsch analysis software, with glass transition temperatures (T_g) calculated using the midpoint.

TGA curves were recorded using a TA instruments Q-600 series differential scanning calorimeter. Approximately 10 mg powdered sample was placed in open alumina crucibles and heated at 10 °C/min under argon. The TGA data was analysed using the TA Universal Analysis software.

Powder X-ray Diffraction:

Data on the screening samples was collected on a B1 (BB) Bruker D8 DAVINCI diffractometer using Cu K α ($\lambda = 1.542 \text{ \AA}$) radiation and a LynxEye position sensitive detector in Bragg–Brentano parafocussing geometry.

Data on the (ZIF-62)(Inorganic Glass)(50/50) and (a_g ZIF-62) $_{0.5}$ (Inorganic Glass) $_{0.5}$ composite samples was collected using a B3 (BB) Bruker D8 DAVINCI diffractometer using Cu K α ($\lambda = 1.542 \text{ \AA}$) radiation and a LynxEye EX position sensitive detector in Bragg–Brentano parafocussing geometry.

Density:

The densities of the inorganic glasses were measured 3 – 4 times by the Archimedes principle at room temperature in absolute ethanol.

The densities of the crystalline and a_g ZIF-62, as well as the (a_g ZIF-62) $_{0.5}$ (Inorganic) $_{0.5}$ were measured using a Quantachrome Ultrapyc 1200e He pycnometer at 20.0 °C for 5 sets of 30 cycles each.

Optical Microscopy:

Reflected light microscopy images of the samples were produced using a Leica MZ95 microscope equipped with a Moticam camera with a resolution of 2 Mpixels was used to take reflected light microscopy images of the composite materials.

A Keyence VHX-6000 digital microscope equipped with VHX-H2MK software and VHX-500 3D Viewer 1.02 was used to produce digital optical microscopy images of the samples. The camera is a CCD detector with a resolution of 54 Mpixels. Images were generated by focal scanning along the z-axis and image stacking. Photos with different lighting (top-lit vs. side-lit) and magnifications (300 X, 600 X and 1000 X) were taken.

Nuclear Magnetic Resonance (NMR) Spectroscopy:

To carry out ^1H NMR, approximately 6 mg of powder was digested in a mixture of DCl (20%)/D $_2$ O (0.1 ml) and DMSO- d_6 (0.6 ml) and the spectra recorded using a Bruker 500 MHz DCH Cryoprobe Spectrometer. Processing and analysis were conducted in TopSpin (3.6.1).

All the ^1H NMR samples contained an extra peak located at around 6 ppm, which previous studies on ZIF frameworks digested by the same solvent system have identified as being due to D $_2$ O, which is reported as being highly variable in both its position and shape [51]. Peak positions are reported ranging from 3.5 to 6 ppm and occasionally observed peak shapes that resemble solid spectra rather than the expected sharp Lorentzian of a liquid resonance are seen [96].

D₂O (and likely D₃O⁺) can easily exchange with acidic protons in the system, rendering acidic protons from the sample 'invisible' and producing visible (H,D)₃O⁺. This exchange process is employed as a technique called 'D₂O shake' for the express purpose of identifying acidic protons, and works extremely efficiently on any acidic protons [97]. Interestingly, the exchange between water and acidic protons is a continuous process happening at rates sufficiently fast to result in a single resonance peak located between the two starting proton resonances (H₂O and acidic proton in this case). As a result of this exchange, the hydronium proton peak is an averaged resonance of the electronic environments participating in acid-base reactions and possible hydrogen bonding. Therefore, these additional peaks in the ¹H NMR spectra are assigned to H₃O⁺.

³¹P Magic angle spinning NMR spectra were measured on a Bruker Avance III 400 (9.4 T magnet, 162 MHz for ³¹P) with a 4 mm MAS probe spinning at 12.5 KHz. All spectra were referenced to a non-spinning rotor filled with 85wt% H₃PO₄. Quantitative single-pulse experiments were conducted with a 60° pulse length (2–2.5 μs) and delay times between 150–400 s. In cases when insufficient sample was available, Teflon tape was used to ensure the rotor was full before spinning. Subtraction to produce residual signals was done using TopSpin (3.6.1).

Scanning Electron Microscopy and Energy Dispersive X-ray Spectroscopy:

Scanning electron microscopy and energy dispersive X-ray spectroscopy (EDS) were conducted using a FEI Nova NanoSEM detecting back-scattered electrons. Samples were mounted on steel stubs using carbon tape and sputter coated with gold using a current of 20 mA for 2 minutes using an Emtech K575 sputter coater. EDS spectra were analysed using the Esprit software created by Bruker.

For the inorganic glasses, EDS was performed using a desktop SEM Phenom ProX instrument at 10kV. The samples were fixed with an adhesive carbon tape on an aluminium sample holder.

Infra-red Spectroscopy:

Fourier transform infra-red spectra of the powdered samples, approx. 5 mg, were collected on a Thermo Scientific Nicolet iS10 model FTIR spectrometer with an attenuated total reflection mode. All scans had a resolution of 2 cm⁻¹. A background scan was collected between each sample.

Raman Spectroscopy:

The samples were embedded in epoxy and polished to 1 micron. Spectra were collected on Renishaw inVia Raman microscope at 100x magnification using an excitation wavelength of 784 nm in a 180-scattering geometry; the resolution was 2 cm⁻¹ and the wavenumber region was 100–1500 cm⁻¹. The a_gZIF controls were collected at 100% laser power, but due to fluorescence only 1 s collection time

(180 scans) could be used without detector saturation; in the case of the 30 min heat treatment 30 s of bleaching was also required to prevent saturation. Longer bleaching times and more scans did not result in a better S/N ratio. The composite samples were significantly more fluorescent, therefore, requiring lower laser powers (5–10%) and longer bleaching times (up to 300 s was found to increase the S/N ratio). In general, lower $T_g(\text{inorg})$ composites needed the lowest laser powers and longest bleaching times, indicating the highest fluorescence. The technique was also found to be extremely sensitive to the surface quality with rough surface absorbing strongly. The resulting spectra were processed in Renishaw software WiRe 4.0.

Mechanical Properties Measurements:

Nanoindentation to measure the Young's modulus (E) and hardness (H) mapping was performed on the $(a_g\text{ZIF-62})_{0.5}(\text{base})_{0.5}$ samples at room temperature using a KLA Nanoindenter G200 equipped with a three-sided Berkovich diamond indenter tip. The tip area function and instrument's frame compliance were calibrated prior to the first experiments on a fused silica reference glass specimen following the Oliver and Pharr method [98]. Indentations with a depth limit of 500 nm were performed at a strain rate of 0.05 s^{-1} . In total, 121 indents were created across an area of $100 \times 100 \mu\text{m}^2$ with a spacing of $10 \mu\text{m}$ between individual indentation marks. The values of H were calculated from the load divided by the project contact area of the indenter tip at the maximum load and the values of E were derived from the reduced modulus:

$$E_s = (1 - \nu_s^2) \left[\frac{1}{E_r} - \frac{(1 - \nu_i^2)}{E_i} \right]^{-1} \quad 3.33$$

Where E and ν are the Young's modulus and Poisson's ratio, respectively, of the indenter tip (subscript 'i') and the material tested (subscript 's'). Since the exact values of ν_s of the individual phases present in the composite materials are unknown, we defined the modulus as:

$$E = \frac{E_s}{(1 - \nu_s^2)} \quad 3.34$$

Optical micrographs of the indented surface area were recorded using a Zeiss Smartproof 5 wide-field confocal microscope.

The scratch resistance was also analysed in constant-load scratch tests with a three-sided Berkovich diamond tip in edge-forward orientation using the nanoindentation setup mentioned above. The indenter tip was moved across the sample surface along a distance of $100 \mu\text{m}$ at a fixed scratch velocity of $10 \mu\text{m/s}$ and under a prescribed normal load of 10 mN, while monitoring the lateral force (F_L) and indenter displacement (h). In total, ten such scratch tests were performed on each sample.

Impedance Spectroscopy:

The surface areas and thicknesses of the Na-deficient, $(a_g\text{ZIF-62})_{0.5}(\text{Na-deficient})_{0.5} - 1 \text{ min}$ and $(a_g\text{ZIF-62})_{0.5}(\text{Na-deficient})_{0.5} - 30 \text{ min}$ samples were measured (1 cm² and around 1 mm; roughly 2 mm² and 0.7 mm). All samples were well-polished; the Na-deficient sample was sputtered with a gold layer on both sides, however, the composites were left bare for electrical measurements.

The impedance measurements were performed on a Novocontrol Alpha-A spectrometer paired with a Novotherm Temperature Control System. The measured frequency range was from 10⁻¹ to 10⁷ Hz. The temperatures from 50 to 250 °C with intervals of 25 °C were measured for the Na-deficient sample and for the ZIF samples $(a_g\text{ZIF-62})_{0.5}(\text{Na-deficient})_{0.5} - 1 \text{ min}$ and $(a_g\text{ZIF-62})_{0.5}(\text{Na-deficient})_{0.5} - 30 \text{ min}$ from 50 to 200 °C with intervals of 30 °C.

The resistance under direct current (R_{DC}) was determined as the right intersection of the x-axis with the half circle of the Nyquist Plot (real and imaginary part of the impedance, Z' VS Z''). The conductivity (σ) is calculated as:

$$\sigma = \frac{1}{R_{DC}} \frac{l}{A} \quad 3.35$$

where l is the thickness and A is the area of the sample.

The temperature dependency of the ionic conductivity was described by the Arrhenius relation:

$$\sigma T = \sigma_0 \exp\left(-\frac{E_a}{K_B T}\right) \quad 3.36$$

where σ_0 is the pre-factor, K_B is the Boltzmann constant and E_a is the activation energy of the ionic conductivity.

X-ray Total-Scattering:

X-ray total-scattering data were collected at the I15-1 beamline at the Diamond Light Source, UK ($\lambda = 0.161669 \text{ \AA}$, 76.7 keV). Samples were loaded into borosilicate capillaries of 1.17 mm inner diameter. Data on the samples, empty instrument and capillary were collected in the region of $0.4 < Q < 22 \text{ \AA}^{-1}$. Corrections for background, multiple scattering, container scattering, Compton scattering, and absorption were performed using the GudrunX program [91].

3.2.4 Chapter 7: The Reactivity of an Inorganic Glass Melt with ZIF-8

ZIF-8 Synthesis:

ZIF-8 was synthesised using the method previously reported in the literature [99]. $\text{Zn}(\text{NO}_3)_2 \cdot 6\text{H}_2\text{O}$ (8.75 g, 29.41 mmol) was added to 2-methylimidazole (5 g, 60.9 mmol) and both powders were dissolved in DMF (375 ml). The mixture was covered and stirred for 1 hour at room temperature to ensure a homogenous solution. The solution was decanted in equal volume amounts into 5 solvothermal jars, which were then heated at 120 °C for 24 hours. The product was then collected under vacuum and washed with DMF to yield a crystalline powder.

X wt% ZIF-8 – Inorganic Glass Mixture Formation:

The as-synthesised ZIF-8 and $0.78([\text{Na}_2\text{O}]_{1.6}[\text{P}_2\text{O}_5]) - 0.22([\text{AlO}_{3/2}][\text{AlF}_3]_{0.7})$ glass were added in appropriate ratios to produce 5, 10, 15 and 30 wt% ZIF-8 samples, to a total mass of 1.6 g, into a 15 ml stainless steel jar. The powders were mixed through ball milling with one 5 mm stainless steel ball, for 5 minutes at 25 Hz in a Retsch MM400 grinder mill. These ball milled powdered mixtures were then activated by soaking in *n*-butanol for 24 hours followed by vacuum filtration and heating under vacuum at 120 – 130 °C for 24 hours. Pellets of the evacuated powders were produced by placing 200 mg samples of the ball milled powder mixture into a 13 mm die and compacted using 10 tons of weight applied for one minute. Heat treated samples were produced by heating approximately 10 mg samples of these pellets in a TA instruments Q600 SDT to either: i) 450 °C for 30 minutes or ii) 480 °C for 1 minute, under argon at 10 °C /min. Following this samples were cooled under argon to 150 °C at 10 °C /min and then in air to room temperature at approximately 40 °C /min.

Thermal Characterisation:

Thermogravimetric analysis (TGA) and differential scanning calorimetry (DSC) curves were recorded using a TA instruments Q-600 series differential scanning calorimeter. Approximately 10 mg of powdered sample was placed in open alumina crucibles. The samples were left to equilibrate for 5 minutes under argon before any heat treatment. Heating and cooling rates, under argon, of 10 °C /min were used. Data were analysed using TA Universal Analysis software, and the glass transition temperature ($T_g^{\text{Inorg.}}$) and recrystallisation temperature ($T_c^{\text{Inorg.}}$) determined using the onset of the gradient change and the exothermic peak respectively.

Powder X-ray Diffraction:

Data on the samples were collected using a B3 (BB) Bruker D8 DAVINCI diffractometer using Cu K α ($\lambda = 1.542 \text{ \AA}$) radiation and a LynxEye EX position sensitive detector in Bragg–Brentano parafocussing geometry.

Nuclear Magnetic Resonance (NMR) Spectroscopy:

To carry out ^1H NMR, approximately 6 mg of powder was digested in a mixture of DCI (35%)/D $_2$ O (0.1 ml) and DMSO-d $_6$ (0.6 ml) and the spectra recorded using a Bruker 500 MHz DCH Cryoprobe Spectrometer. Processing and analysis were conducted in TopSpin (3.6.1). All the ^1H NMR samples contained an extra peak located between 7.4 and 8.1 ppm, which was assigned to H $_3$ O $^+$ following the same reasoning used on the ZIF-62 samples examined in Chapter 6.

Fourier Transform Infra-red spectroscopy:

Fourier Transform Infra-red (FTIR) spectra of the powdered samples, approx. 2 mg, were collected on a Bruker Tensor 27 FTIR model FTIR spectrometer in attenuated total reflection mode. All scans had a resolution of 4 cm $^{-1}$. A background scan was collected between each sample. Quantification of relative changes in ZIF-8 and inorganic glass via curve fitting was achieved by fitting in Fityk and is discussed further in the text of the chapter [17].

Scanning Electron Microscopy:

To get an estimate of the particle size of the ZIF-8, evacuated samples were mounted on pin stubs using carbon tape. The powder was then coated with palladium using an Emtech K575 sputter coater with a deposition current of 40 mA under a pressure of 1×10^{-2} mbar for approximately five minutes. These samples were then imaged using a FEI Nova NanoSEM scanning electron microscope detecting backscattered electrons.

Chapter 4: Structural Investigation of Zeolitic Imidazolate Framework Glasses via X-ray Total-Scattering

4.1 Introduction

The structural changes exhibited by crystalline MOFs on heating has been investigated extensively, with different frameworks displaying a wide range of unusual behaviours, including high-temperature recrystallisation to different crystalline phases [100], gate-opening mechanisms [101] and negative thermal expansion [102]. The polymorphism of the glass forming ZIFs, notably ZIF-62 ($\text{Zn}(\text{Im})_{1.75}(\text{blm})_{0.25}$) and ZIF-4 ($\text{Zn}(\text{Im})_2$), has also been studied in detail. ZIF-62 is generally reported as melting from the as-synthesised *Pbca* crystalline phase outside of desolvation with no further phase changes [61]. In contrast, ZIF-4 undergoes amorphisation/melting and an irreversible phase transition from a low-density to a high-density amorphous phase on heating, before recrystallising to the dense ZIF-zni phase, which then undergoes melting [36].

The long-range structure of amorphous ZIF-4 has been studied by reverse Monte Carlo modelling of X-ray and Neutron total-scattering data and was found to be consistent with a continuous random network structure (CRN), which is the same topology adopted by silica glass (**Figure 4.1**) [54], [59]. A comparison of thermally amorphised ZIF-4 with a_g ZIF-4, and a sample of ZIF-4 amorphised through ball milling demonstrated only minor variations in structure, which have been explained solely by differences in macroscopic density [59].

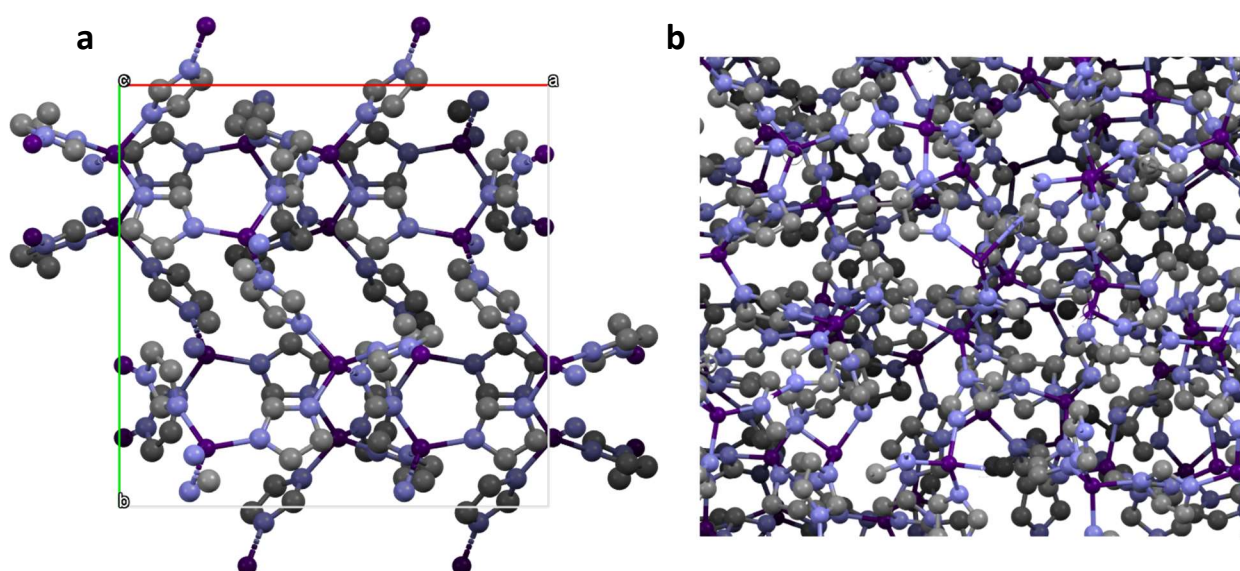


Figure 4.1: Structures of ZIF-4 and a_g ZIF-4. **a.** Unit cell structure of crystalline ZIF-4 [43]. **b.** Reverse Monte Carlo model of the CRN structure of a_g ZIF-4 [59]. Key: Grey – Carbon, Blue- Nitrogen, Purple – Zinc. Hydrogen atoms omitted for visual clarity.

Changes in the local structure of the Zn centres, i.e. Zn-N bond breaking and ligand swapping, in a_g ZIF-4 as it is heated from room temperature to 655 °C has already been reported in the literature. This report also noted a substantial shift occurred in the position of the first peak in the $S(Q)$ at elevated temperatures [60].

Motivated by this dramatic structural change, which was not expected from previous literature, pre-formed a_g ZIF-4 was annealed above its T_g for different lengths of time and ambient temperature X-ray diffraction was used to investigate the unusual shifts in scattering which had been observed during dynamic heating of the glass. In addition the variable temperature X-ray total-scattering data measured on a sample of a_g ZIF-4, which had been previously reported in the literature [60], was reanalysed to focus on explaining this dramatic change using pre-existing theory developed for other glass families. Finally, to both provide contrast with the studies on a_g ZIF-4 and to fill a gap in the existing literature left by the detailed studies on structural changes during annealing at temperatures $0.88 < T/T_m$ [61], ambient temperature X-ray total-scattering was also used to investigate changes in the structure of a related glass, a_g ZIF-62, which had been annealed below its glass transition temperature for varying lengths of time.

The work on ZIF-4 in this chapter was previously published in:

J. Zhang *et al.*, "Structural evolution in a melt-quenched zeolitic imidazolate framework glass during heat-treatment," *Chem. Commun.*, vol. 55, no. 17, pp. 2521–2524, 2019.

Whereas the results pertaining to ZIF-62 were reported in:

C. Zhou *et al.*, "Thermodynamic features and enthalpy relaxation in a metal–organic framework glass," *Phys. Chem. Chem. Phys.*, vol. 20, no. 27, pp. 18291–18296, 2018.

In both cases I was responsible for the collection, correction, and interpretation of the ex-situ X-ray total scattering data, with assistance from Dr Philip A. Chater (Diamond Light Source) and Prof. David A. Keen (ISIS). I also contributed to the analysis and re-interpretation of the in-situ variable temperature total scattering results. All sample preparation and thermal properties analysis was done by other researchers.

4.2 Existing Descriptions and Theory on Mid-range Order in Glasses

The degree to which glass displays order beyond that which is dictated by their chemical bonding is difficult to determine and subject to controversy [103]. Glasses clearly do not have the translational symmetry of the unit cell that characterises the long-range order of crystals. Instead, in the case of network glasses such as silicates, borates, and ZIFs, the long-range structure is understood to be a continuous random network of joined tetrahedra where disorder arises due to variations in bond angles and lengths. The degree to which order exists at scales between the local bonding within the tetrahedra and the overall disorder of the CRN, the so called 'mid-range' order (MRO), has been extensively discussed in the glass science literature. This section begins with a hierarchical description of structures at different length scales within the mid-range order region, before progressing to the existing theory on how the degree of order in a sample can be assessed through scattering methods.

4.2.1 Hierarchical Descriptions of Order in Glasses.

Mid-range order can be thought of as correlations occurring between clusters of neighbouring tetrahedra. These occur in regular patterns at frequencies above that which would be expected to occur due to random chance within the CRN network. The MRO can be sub-divided further into three regions of increasing length scale [104]: i) Near mid-range order, which is comprised of ordered correlations between neighbouring tetrahedra and is therefore described in terms of the dihedral angle between adjacent tetrahedra (**Figure 4.2a**). ii) Intermediate mid-range order, which consists of multiple centres being joined together into well defined 'superstructural units', which are connected together in a network. An example of this would be the existence of the regular six-membered boroxol ring structure in glassy B_2O_3 , which exists within the CRN structure (**Figure 4.2b**) [73]. Finally, far mid-range order, which is related to the local dimensionality of the network, i.e. the formation of chain like connectivity in metaphosphates (**Figure 4.2c**) [72].

4.2.2 Mid-range Order and the First Sharp Diffraction Peak

The first sharp diffraction peak (FSDP), sometimes referred to as the 'chemical-order prepeak', is the first diffraction peak in the broad scattering observed in the total-scattering patterns of both liquids and glasses [104]. Due to the nature of reciprocal space, this first feature is related to the features in real space with the longest correlation lengths. Therefore, it has been taken as a manifestation of the MRO in glasses and liquids. It should be noted that this feature is not sharp relative to Bragg peaks in crystalline materials but is typically the sharpest feature in the diffraction patterns of amorphous structures.

The origin of the structural features that give rise to the FSDP has long been unclear. The FSDP appears at a wide range of Q values in different materials systems [105]. However, it has been observed that in covalent glass systems, AX_2 where A is a cation and X an anion, the position of Q is proportional to the nearest neighbour bond length, so that by scaling by this length the FSDP all lie at approximately the same value of Q [105], [106].

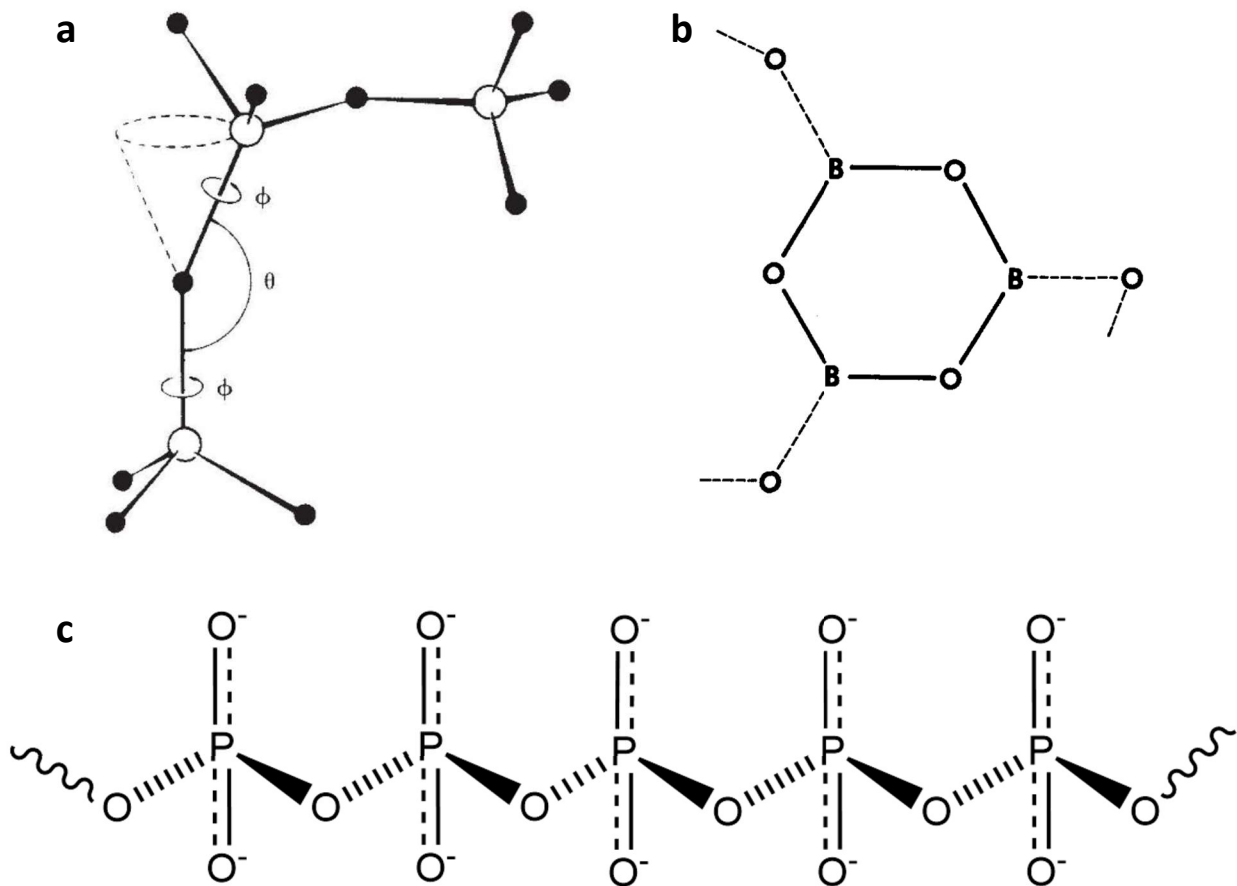


Figure 4.2: Examples of mid-range order in glasses. **a.** Dihedral angle (ϕ) and A-X-A bond angle (θ) between two AX_2 tetrahedra Key: White – A, Black – X reproduced from [104]. **b.** Planar boroxol B_2O_3 ring reproduced from [73]. **c.** Metaphosphate, MPO_3 chain structure, modifier M^+ cations omitted for clarity.

This means that, for a wide range of glasses such as GeO_2 , BeF_2 and $GeSe_2$, the position of the FSDP, Q'_1 , can be well approximated by scaling the position of the FSDP in silica, Q_{silica} by the nearest neighbour bond length in both systems [106]:

$$Q'_1 = \frac{Q_{silica} b_{silica} (Si - O)}{b_1 (A - X)} \quad 4.1$$

Where b_{silica} (Si-O) and b_1 (A-X) are the nearest neighbour bond length in SiO₂ and AX₂ respectively. The ability to plot the FSDP positions on top of one another using this relative scale may indicate a shared structural origin of this feature, which is independent of the varying local chemistries of the system. Moreover, it has been reported that for many glasses the removal of the FSDP from the Fourier transform results in negligible change in the correlations in the short-range order (SRO) [106]. This indicates that it contains information from a longer length scale [106]. It further implies that the origin of the FSDP does not lie in the specific local chemistries of any given glass system, but in some feature common to all of them.

The correspondence that has been reported for chalcogenide glasses, between the position of the FSDP in the glass phase and the interlayer spacing of structures in crystalline analogues, has led to a ‘quasi-crystalline’ picture of the FSDP [104]. This ‘quasi-crystalline’ picture of the FSDP implies that the structural origin of the FSDP can be attributed to a single feature in the glass structure, i.e. the layer spacing in a layered chalcogenide structure [106]. In this case the FSDP is a single harmonic component resulting from a ‘loosely periodic’ feature in the glass [106]. The position of the FSDP in reciprocal space is related to the mid-range order by two approximate relations [105]:

$$r_{MRO} \approx \frac{2\pi}{Q_{FSDP}} \quad 4.2$$

$$d_{MRO} \approx \frac{2\pi}{FWHM_{FSDP}} \quad 4.3$$

Where Q_{FSDP} and $FWHM_{FSDP}$ are the peak position and the full-width at half maximum of the FSDP, r_{MRO} is the period of the real space correlation associated with the FSDP, i.e. how regularly the correlation repeats, and d_{MRO} is the maximum correlation length over which the correlation associated with the FSDP persists. These relationships are only approximate however, as features in the total-scattering function are unlikely to arise solely from a single harmonic. Though these relationships are attractive due to their simplicity and ease of application, the relatively universal appearance of the FSDP in all classes of glasses, [105] and its persistence in the liquid state again implies that it is unlikely to originate from quasi-crystalline features, such as sheet like structures, as these would not necessarily be present in all classes of glass and are unlikely to persist into the liquid state [106].

An indication of what this common feature might be comes from calculations based on the random packing of spheres, which either represent two atoms, or in the case of single element systems, atoms and voids. The origin of the FSDP is then explained as arising from the longest distance correlations in the system, which arise between atoms of the same chemistry (**Figure 4.3**). These calculations have

been reported as giving a reasonable approximation to the FSDP in a variety of systems ranging from metallic glasses to tetravalent amorphous silicon and germanium [107].

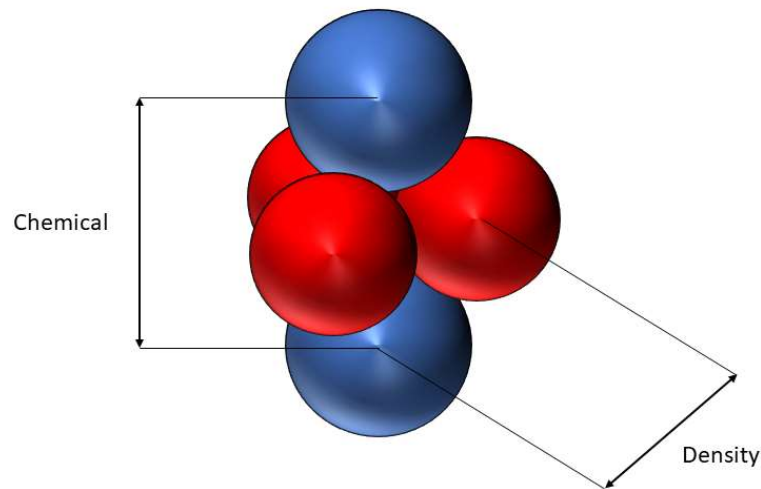


Figure 4.3: Origin of density-density and chemical-chemical correlations in the random packing arrangement of two atom (or atom-void) mixtures. Adapted from [107].

This approach was then extended to explain the scaling of the FSDP position in covalent glasses of the formula AX_2 , [106]. To do this the structure is assumed to be made up of cation-centred, soft, i.e. partially overlapping, quasi-spherical clusters that are surrounded by an equal number of quasi-spherical voids (**Figure 4.4**). The longest-range correlation in these structures, given a CRN (**Figure 4.4a**) arrangement, then comes from correlations between adjacent A centred clusters (**Figure 4.4b**). These structural units are identified as being A centred because there is more positional disorder in the X atoms due to variations in the dihedral angle of the tetrahedra [105], [106]. Although when the A-X-A bond angle is close enough to 180° the static positional disorder in the anions due to dihedral angle variations is diminished and so anion-anion correlations may also be significant in contributing to the FSDP. This description of the FSDP leads to a prediction of the FSDP position for a given covalent network glass [107]:

$$Q_1'' \approx \frac{3\pi}{2d} \quad 4.4$$

Where d is the A-A correlation length between the centres of the structural units. However, **Equation 4.4** assumes that the voids and cation spheres are equally sized. If the voids and cation centred spheres are different sizes the FSDP position is instead predicted to follow the equation [106], [107]:

$$Q_1'' = \frac{3\pi(1 - \epsilon/2)}{2d} \quad 4.5$$

$$\varepsilon = \frac{D - d}{d}$$

Where d is the A-A correlation length between the centres of the structural units and D is the A-V distance. These equations have been shown to be generally valid for a wide variety of different AX_2 covalent network glasses [106].

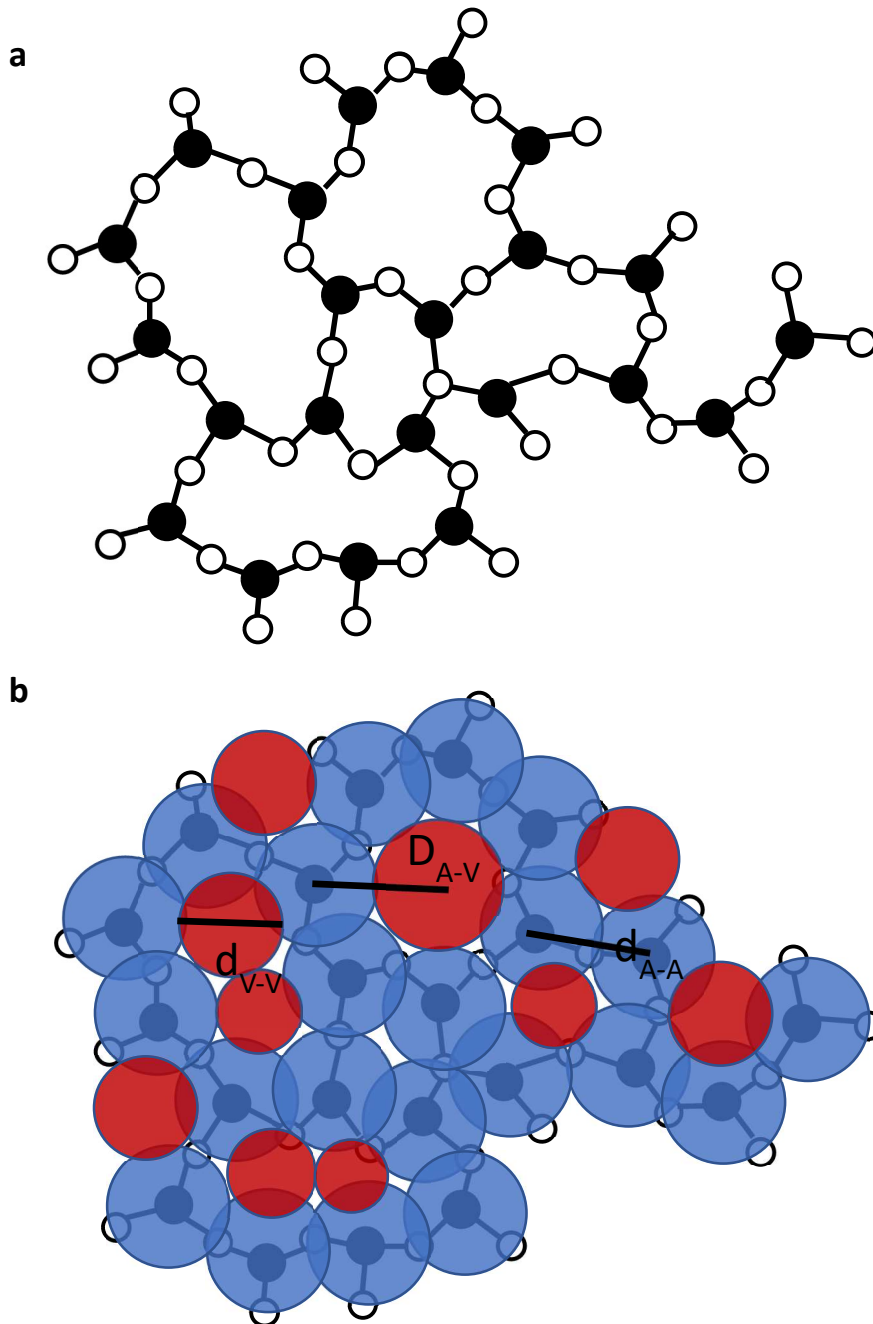


Figure 4.4: Structure of CRN glasses and the FSDP. **a.** Continuous random network (CRN) model for AX_2 glasses as described in the literature [32]. Key: A - Black, X - White. **b.** A cation centred soft quasi-sphere void model elucidated in the literature to explain the FSDP in glass network [106], [107]. Key: Blue - cation centred quasi-spheres, Red - voids.

4.2.3 Rationalising Changes in First Sharp Diffraction Peak Intensity and Position with Density and Temperature

The intensity of the FSDP has also been linked to the macroscopic density of glasses [106], with denser structures producing FSDPs with diminished intensity even when the local bonding remains the same [108]. These changes can be understood in terms of the theory outlined in the previous section, if the FSDP arises due to chemical ordering of A centred spheres and voids then this change is understood as being due to a decrease in the volume of the voids, whose presence defines the structural units whose correlations contribute to the FSDP [104].

The dependence of FSDP intensity, I , with temperature (at constant pressure P) can be expressed in the following terms [109]:

$$\left(\frac{\partial I}{\partial T}\right)_P = \left(\frac{\partial I}{\partial T}\right)_\rho + \left(\frac{\partial I}{\partial \rho}\right)_T \left(\frac{\partial \rho}{\partial T}\right)_P \quad 4.6$$

Where ρ is the density. $(\partial I/\partial T)_\rho$, which is the change in intensity with temperature at constant density, is negative due to the Debye-Waller factor [110]. $(\partial \rho/\partial T)_P$ is the constant pressure thermal expansivity, which is negative if density decreases due to thermal expansion. Finally, $(\partial I/\partial \rho)_T$ is the change in FSDP intensity with density at constant temperature, which, given the above discussion, we would expect to be negative for covalent network glasses. Therefore, the intensity of the FSDP could be predicted to either increase or decrease on changing temperature depending on the balance of the terms on the right side of the equation.

Finally the position of the FSDP has been reported as decreasing with temperature according to [109]:

$$\alpha = -\left(\frac{1}{Q_1}\right)\left(\frac{\partial Q_1}{\partial T}\right)_P \quad 4.7$$

The FSDP positions of network glasses are reported to decrease linearly with increasing temperature, and the gradient generally becomes larger as the glasses are heated through the glass transition temperature. The values range from $\alpha \approx 10^{-5} \text{ K}^{-1}$ in borates and silicas [111], [112] to $\alpha \approx 10^{-4} \text{ K}^{-1}$ in vitreous As_2Se_3 [113]. This change can be understood in terms of decreasing density on heating with the centres of the spheres moving apart and therefore d_{A-A} increasing resulting in the position of the FSDP decreasing (**Equation 4.4** and **4.5**). The difference in magnitude of the coefficient between different families of glasses can be understood as due to the differences in thermal expansivity due to different bond strengths [106].

4.3 Structural Changes in a_gZIF-4 during Heat Treatment

The shift to higher values of Q for the FSDP position, reported in the literature as occurring at elevated temperatures during variable temperature X-ray total-scattering studies on a_gZIF-4, may be understood in terms of a change in MRO [60]. The reported coincidence of this feature with a reduction in the Zn-Zn distance also broadly agrees with the theory outlined involving cation centred spheres. To further understand the nature of this structural shift, and the implications on the MRO in terms of the theory outlined above, DSC and ambient temperature PDF data was collected on annealed ZIF-4 glass samples, and the data reported in [60] was reanalysed to specifically focus on the shift in the FSDP.

4.3.1 Differential Scanning Calorimetry of a_gZIF-4 during Annealing above T_g

DSC measurements on a crystalline ZIF-4 sample showed desolvation (A) with an associated mass loss in the TGA curve. The other features in the DSC, i.e. amorphisation/melting (B), recrystallisation to ZIF-zni (C), melting of ZIF-zni (D), all occurred without a loss of mass, indicating framework stability. Finally decomposition, in a manner consistent with prior studies on the framework, occurred shortly after melting as demonstrated by the onset of mass lost in the TGA curve (**Figure 4.5**) [36].

In a second experiment, a sample of ZIF-4 was heated to 580 °C, i.e. above the melting point, followed by quenching to room temperature at 20 °C/min. This is twice as fast the standard quenching rate used to determine the T_g . A second heating scan of this sample (**Figure 4.5**), termed fast-quenched a_gZIF-4 or fq-a_gZIF-4, measured at 10 °C/min, demonstrated a transition temperature of 302 °C. This is higher than the reported literature value for T_g of 292 °C [56]. However this is expected as faster quenching rates are known to lead to higher values for the apparent glass transition due to the sample departing from the equilibrium liquid line at higher temperatures when cooled more rapidly [30]. Above the fictive temperature, a broad exotherm was observed between 452- 547 °C, with an enthalpy change of 29 J/g, approximately half that of the enthalpy of recrystallisation of ZIF-4 to ZIF-zni (50 J/g). Decomposition of the liquid ZIF was then evident from a rise in the baseline of the DSC and a drop in mass at approximately 570 °C, 30 °C lower than measured for the decomposition of the liquid ZIF formed by directly melting ZIF-zni without first quenching.

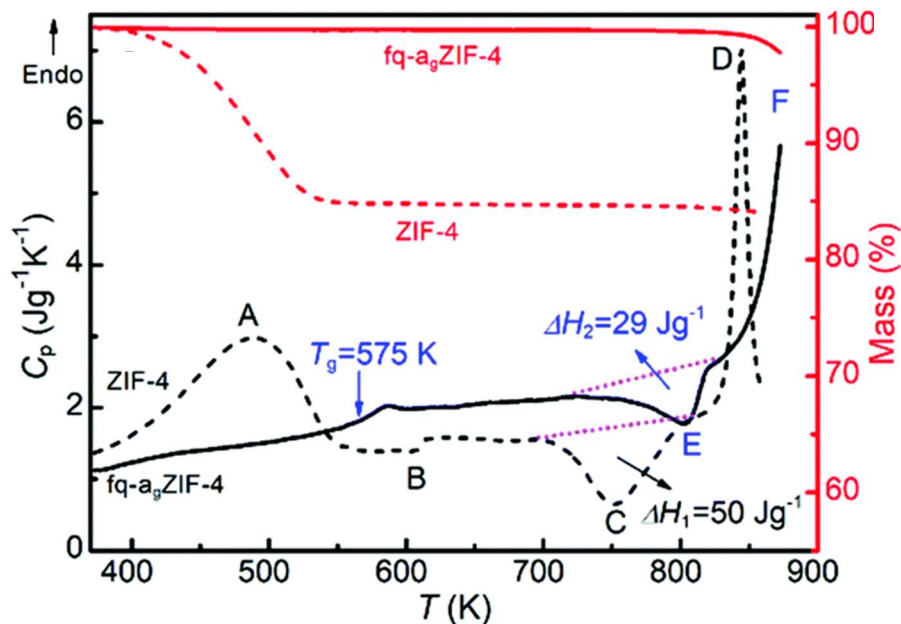


Figure 4.5: Thermal response (black) and mass % curves (red) of as-synthesised ZIF-4 (dashed) and fq-a_gZIF-4 (solid). Measured at a heating rate of 10 °C/min.

To examine the effect of annealing time at elevated temperatures a sample of fq-a_gZIF-4 was heated to 520 °C, i.e the peak of the observed exotherm, and held for 420 minutes, before quenching to room temperature at a rate of 20 °C/min. This sample was termed heat treated fast-quenched a_gZIF-4 (ht-fq-a_gZIF-4), and still displayed a glass transition and exotherm on reheating in the DSC at 10°C/min, however both were shallower (**Figure 4.6**). Pycnometric density measurements determine that annealing results in densification of the structure with the density increasing from 1.67 g cm⁻³ in fq-a_gZIF-4 to 1.76 g cm⁻³ in ht-fq-a_gZIF-4.

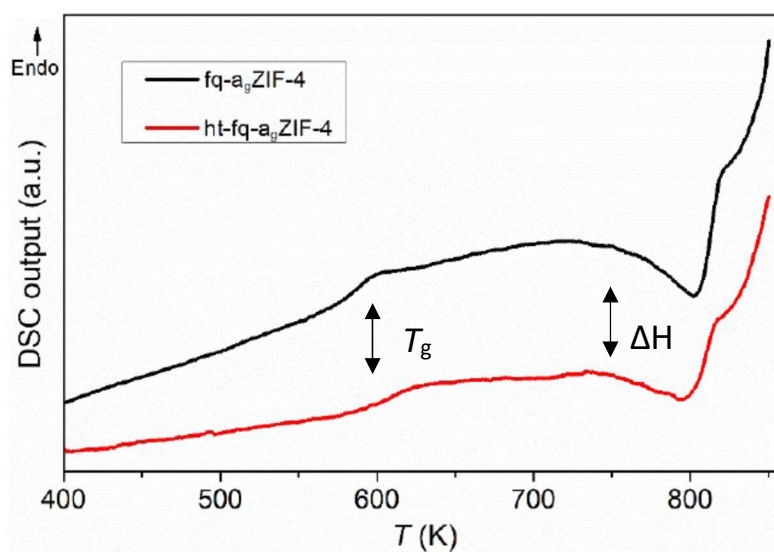


Figure 4.6: Thermal response curves of fq-a_gZIF-4 (black) and ht-fq-a_gZIF-4 (red). Measured at a heating rate of 10 °C/min.

4.3.2 Ambient Temperature X-ray Total-scattering on fq-a_gZIF-4 and ht-fq-a_gZIF-4

To probe any structural differences induced by heat-treatment, room temperature X-ray total-scattering measurements were performed on fq-a_gZIF-4 and ht-fq-a_gZIF-4 (**Figure 4.7**). The absence of Bragg diffraction in the structure factor $S(Q)$ of both samples confirm their amorphous nature. This also confirmed that the observed exotherm is not related to recrystallisation of ZIF-zni from the molten ZIF, despite it occurring in the same temperature range as observed in the first heating scan (**Figure 4.5**).

The FSDP was broader and less intense in the ht-fq-a_gZIF-4 sample relative to the fq-a_gZIF-4 sample, and had shifted from around 1.1 to 1.15 Å⁻¹ (**Figure 4.7** inset). This is broadly in agreement with what was observed in the variable temperature data on a_gZIF-4, however the extent of the peak shift, 1.15 vs 1.3 Å⁻¹, is considerably lower. Outside of the FSDP the higher Q peaks in the ht-fq-a_gZIF-4 are diminished relative to fq-a_gZIF-4, but of qualitatively similar position and FWHM.

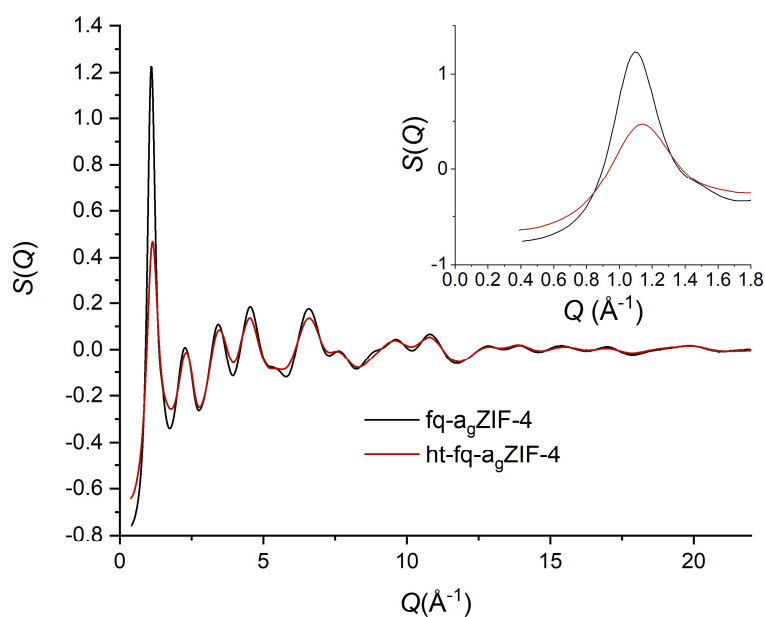


Figure 4.7: X-ray total-scattering structure factor, $S(Q)$, of fq-a_gZIF-4 and ht-fq-a_gZIF-4. The inset shows the FSDP.

The PDFs produced by a Fourier transform of these data (**Figure 4.8**) showed that the SRO of the samples was consistent with the previous literature for melt-quenched MOF glasses [56], i.e that correlations up to the length of the first Zn-Zn distance are maintained from the crystalline framework. No new peaks are evident in the SRO of the ht-fq-a_gZIF-4 relative to fq-a_gZIF-4, confirming that no decomposition occurred. Further comparison between the fq-a_gZIF-4 and ht-fq-a_gZIF-4 samples revealed that the correlations at 1.3 Å (C-C/C-N) and 2 Å (Zn-N) are relatively unaffected by annealing

time. This implies that the internal structure of the imidazolate linker and the local ZnN_4 tetrahedral environments are unchanged during annealing.

Above this distance, distance broadening and de-coordination are evident in the SRO. This is particularly pronounced at the 6 Å correlation due to the Zn-Zn distance, which also shifts to a slightly lower r value in ht-fq- a_g -ZIF-4 compared to fq- a_g -ZIF-4 (**Figure 4.8** insert).

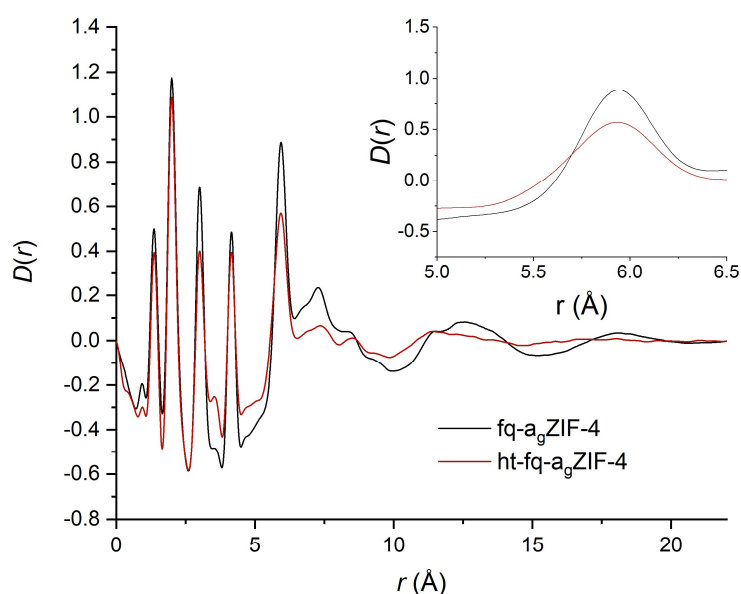


Figure 4.8: Pair distribution functions, $D(r)$, of fq- a_g -ZIF-4 and ht-fq- a_g -ZIF-4. Inset: Peak at approximately 6 Å.

At longer distances the PDFs of fq- a_g -ZIF-4 and ht-fq- a_g -ZIF-4 are much less similar, implying a greater difference beyond the first Zn-Zn distance. The features in the ht-fq- a_g -ZIF-4 are diminished relative to those in the fq- a_g -ZIF-4 sample in line with the lower FSDP seen in the $S(Q)$ for that sample.

4.3.3 Re-analysing Variable Temperature X-ray Total-Scattering on a_g -ZIF-4

The variable temperature X-ray PDF data, on the in-situ heating of a_g -ZIF-4, previously reported in the literature [60] was then re-examined. The overall measured total-scattering (**Figure 4.9a**) is relatively invariant on heating from room temperature to 403 °C, even on passing through the glass transition at approximately 292 °C [56]. The corresponding $D(r)$ (**Figure 4.9b**) show decreases in peaks in the SRO other than the peak at 1.3 Å, which as previously mentioned, is due to correlations between atoms that are directly bonded to one another within the imidazolate ligands.

This is consistent with the de-coordination of ligands from zinc centres in the liquid state, which has been previously reported [60]. At higher temperatures (**Figure 4.9c**) a sharp discontinuity in the FSDP is observed with the position shifting to higher Q , the FWHM increasing and the amplitude falling. Moreover, this shift occurs before the growth of shoulders and appearance of new peaks is seen in the SRO at approximately 535 °C (**Figure 4.9d**), which unambiguously indicates the start of linker decomposition.

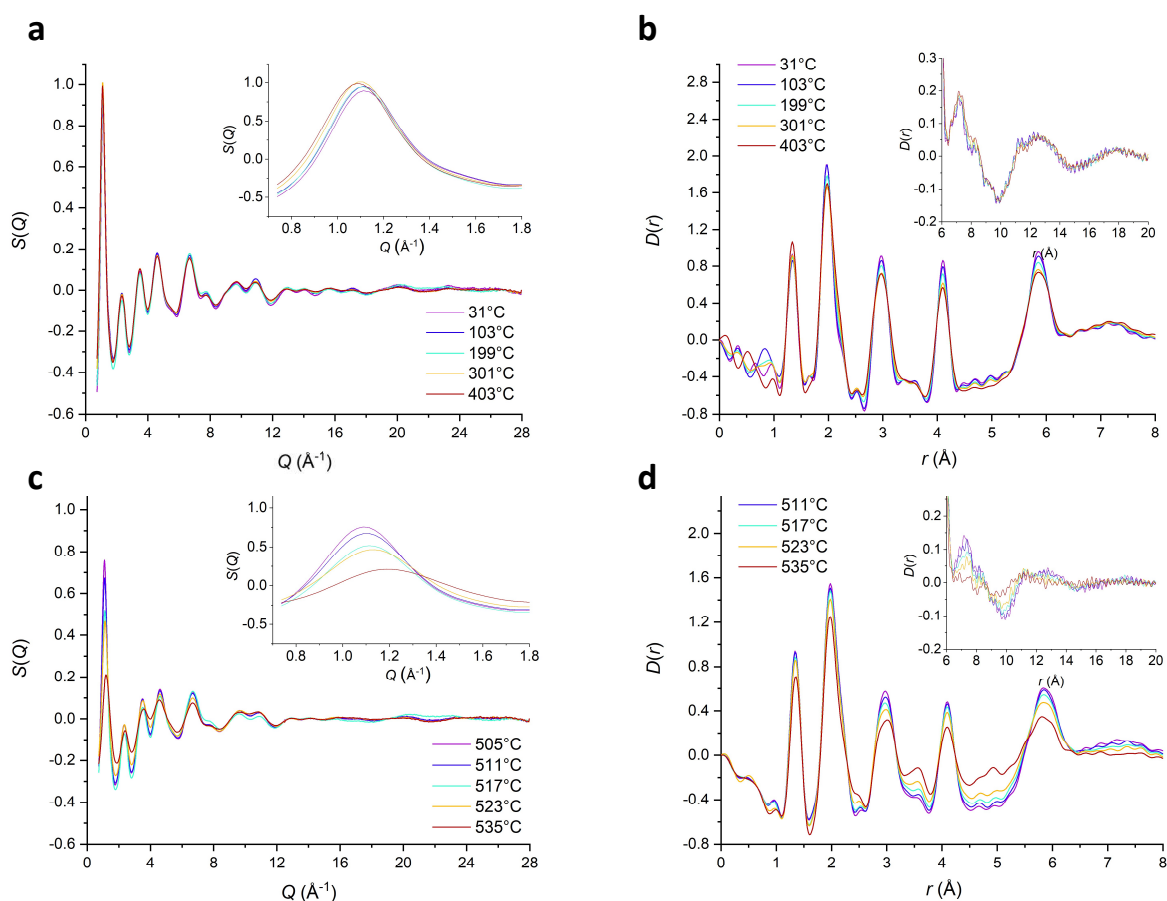


Figure 4.9: Variable temperature X-ray total-scattering of a_3 ZIF-4 (31 – 535 °C). Previously reported in [60]. **a.** $S(Q)$ with inset showing the FSDP. **b.** $D(r)$ with inset showing the mid-range order. **c.** $S(Q)$ with inset showing the FSDP. **d.** $D(r)$ with inset showing the mid-range order.

The FSDP changes very little in position, intensity and FWHM between 541-565 °C (**Figure 4.10a**). However, the intensity of zinc – imidazolate peaks in the $D(r)$ continues to decrease, moreover the Zn-Zn correlation at 6 Å strongly diminishes. Whereas the new peak at approximately 5 Å, which was first seen at 535°C, continues to increase in intensity (**Figure 4.10b**). The position of the FSDP shows another shift to a higher Q between 589 °C and 655 °C (**Figure 4.10c**), however this time with an increase in intensity. This second shift is accompanied by drastic changes in all peaks in $S(Q)$, and changes in both local structure and MRO clearly visible in the $D(r)$ (**Figure 4.10d**). Taken together,

these changes indicate that total framework decomposition has occurred, and a new amorphous framework material has formed which contains distinct chemistry and mid-range order.

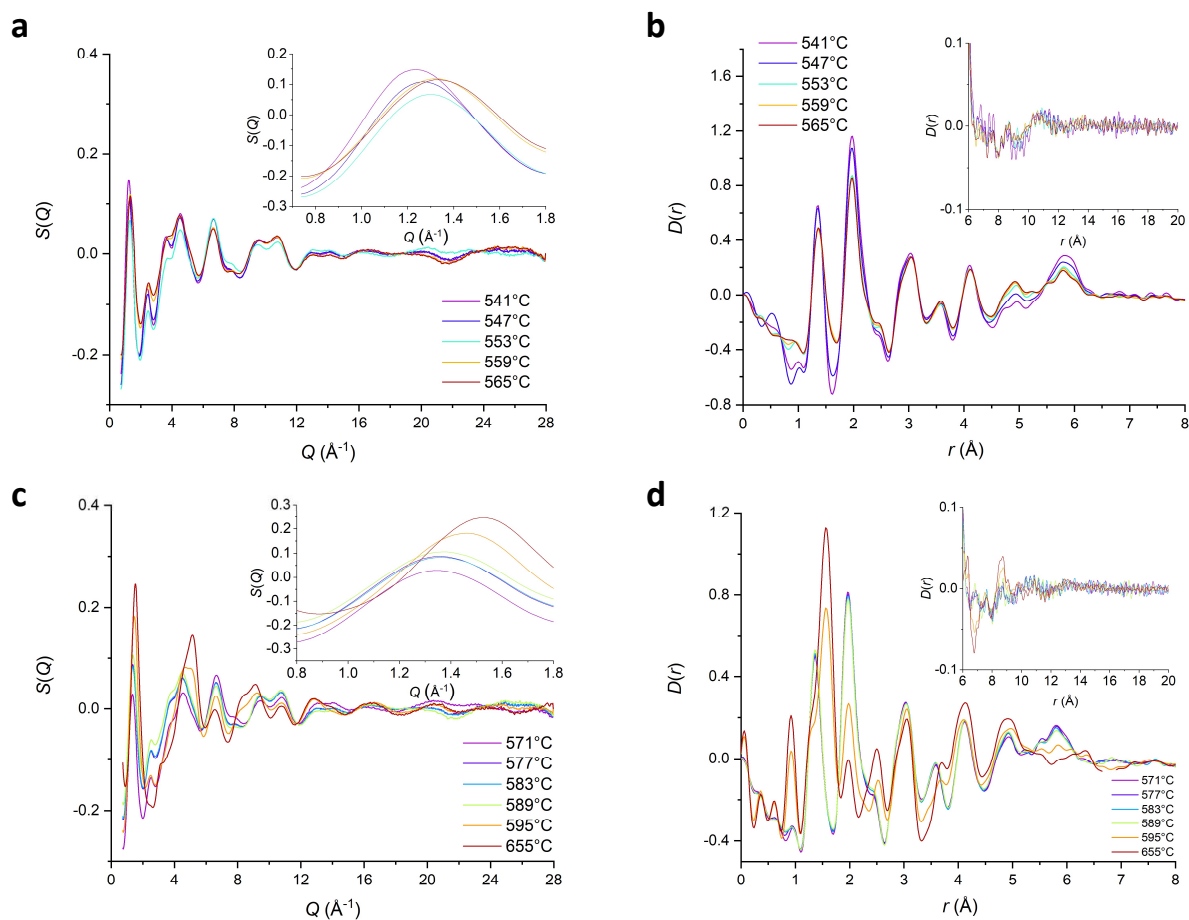


Figure 4.10: Variable temperature X-ray total-scattering of a_g ZIF-4 (541 – 655 °C). Previously reported in [60]. **a.** $S(Q)$ with inset showing the FSDP. **b.** $D(r)$ with inset showing the mid-range order. **c.** $S(Q)$ with inset showing the FSDP. **d.** $D(r)$ with inset showing the mid-range order.

In order to apply the theory outlined in the previous section to MRO in a_g ZIF-4, the peak position, amplitude, FWHM, and intensity of the FSDP in the variable temperature samples was determined by fitting the peak using a Pseudo-Voigt function in FityK [92]. The choice of function is not intended to have any physical meaning, as such it is not a ‘model’ of the FSDP feature, instead it was simply chosen to allow extraction of the parameters of the peak.

The room temperature sample had an FSDP at 1.13 \AA^{-1} , with a FWHM of 0.36 \AA^{-1} . The ‘quasi-crystalline’ picture (Equation 4.2 and 4.3), indicates the period in the ZIF to be 5.56 \AA and the correlation length is 17.5 \AA . This is in reasonable agreement with the Zn-Zn distance, measured to be approximately 5.9 \AA in the crystalline ZIF-4 framework [43] and the limit to which correlations are observed in real space, before the PDF becomes featureless (Figure 4.9b). It is worth noting that a period of 5.56 \AA , i.e. slightly

shorter than the measured Zn-Zn distance, is also consistent with the picture of partially overlapping cation centred spheres (**Figure 4.4b**). However the shorter distance may also be due to the influence of scattering due to Zn-N correlations on the FSDP as was demonstrated via reverse Monte Carlo modelling of the a_g ZIF-4 [59].

The existing theory developed for other network glasses (**Section 4.2.2**) was then applied. To do this, it is assumed that the imidazolate molecule can be represented by a single X atom in the formula AX_2 . The A cation is therefore Zn^{2+} and it occupies the centre of the ‘matter spheres’, which are $Zn(Im)_4$ tetrahedra. Using values of the FSDP and Si-O bond length for SiO_2 reported in [106], and a Zn-N bond length of 2 Å obtained from the PDF (**Figure 4.9a**), the scaled predicted value of the FSDP in a_g ZIF-4 is predicted to be 1.22 \AA^{-1} (**Equation 4.1**). This is an 8% difference with the actual measured value, which is in line with the scale of differences observed for other systems reported in the paper [106].

The sphere model, starting with an assumption of equally sized voids (**Equation 4.4**), and taking d to be approximately 6 Å, as measured from the PDF, predicts a FSDP position at 0.80 \AA^{-1} . This is a 30% difference from the actual measured value, which is an error far in excess of those measured for other glass systems [104], [106]. However, the relatively large nature of the imidazolate linker means that it is unlikely that the voids would be as equally sized as the A centred cation spheres.

The void structure of a_g ZIF-4 was previously studied using positron annihilation lifetime spectroscopy (PALS) [77], which has the ability to probe all voids present in the structure, i.e. not just those which are accessible to gases. Two separate populations of voids were found, a broad distribution centred at $2.56 \pm 0.28 \text{ \AA}$ and a narrower distribution at $6.86 \pm 0.03 \text{ \AA}$. Although the size distribution of the voids is therefore well known, the distribution of these voids in the structure is not clear, and therefore it is unclear how to extract a precise value of D_{A-V} (**Figure 4.4b**). Previous studies on silica glasses have extracted such values via theoretical examination of models generated by molecular dynamics [114]. Moreover the description of the structure outlined in [106], [107] only takes into account of a single population of voids, whereas a_g ZIF-4 clearly contains two separate void populations. To account for this, a first order approximation was made based on a simple average of the two void sizes (4.71 \AA). Moreover from the structural descriptions of the model outlined in [107] (**Figure 4.3**) it is clear that the void and matter spheres are in direct contact. Therefore, given this assumption, the A-V distance is then approximated as:

$$D(A - V) \approx \frac{d_{V-V} + d_{A-A}}{2} \quad 8$$

Where d_{v-v} is the average void diameter. This then predicted $D(A-V)$ to be 5.4 \AA , which via equation (5) predicts the FSDP position as 0.87 \AA^{-1} , i.e. closer to the actual measured position, and may be considered a reasonable prediction for the FSDP given the simplicity of the assumptions made.

As the temperature was increased, an initially very slight decrease in the FSDP position with temperature was observed (red line **Figure 4.11a**) in line with behaviour observed in other glasses [106]. The value for α was calculated from the gradient of this line (**Equation 4.7**) to be $-5 \times 10^{-5} \text{ K}^{-1}$, which is of the same order of magnitude for silicas and borates as discussed previously [111], [112]. No substantial change in the gradient could be seen on heating through T_g as has been reported for other systems [106], however this may be due to the small number of data points in this range. Below $500 \text{ }^\circ\text{C}$, the FSDP FWHM, and height were found to be approximately invariant with temperature (**Figure 4.11b** and **4.11c**). However, the area and therefore overall peak intensity decreases slightly (**Figure 4.11d**).

The sharp discontinuity in the FSDP previously observed qualitatively (**Figures 4.9c**) was found to occur in all features of the FSDP. Its onset was determined by linear interpolation to be $491 \pm 10 \text{ }^\circ\text{C}$, where the error bar represents a standard deviation of the onset value determined for peak position, peak height, FWHM and area (**Figure 4.11**). This is in the middle of the temperature range, $452\text{-}547 \text{ }^\circ\text{C}$ (**Figure 4.5**), of the broad exotherm observed in the fast-quenched sample and below the heat treatment temperature for the ht-fq-a_gZIF-4 sample ($520 \text{ }^\circ\text{C}$).

The sharp discontinuity in the features of the FSDP at high temperatures is relatively unusual and has not been reported in the structurally similar silica, where no similar changes are observed on heating the glass far above its glass transition temperature [115]. The lengthening peak position and larger FWHM as temperature increases indicate a shorter period and lower overall correlation length respectively (**Equation 4.2** and **4.3**). Whereas the falling intensity of the FSDP indicates densification of the structure, i.e. $(\partial\rho/\partial T)_P$ (**Equation 4.6**) becomes strongly positive at the transition point. Interpolation of the value of the FSDP position at $520 \text{ }^\circ\text{C}$, the heat treatment temperature, using the fitted post-edge line (red line **Figure 4.11a**) yields a projected value of 1.13 \AA^{-1} , which is in reasonable agreement of the fitted value from ht-fq-a_gZIF-4 of 1.15 \AA^{-1} . This is especially true given that the value for ht-fq-a_gZIF-4 was measured at room temperature not at $520 \text{ }^\circ\text{C}$. This agreement indicates that the structural change in MRO is not reversible on cooling of the liquid, but instead persists into the glassy state. Moreover, it implies that the different thermal histories of the glasses, i.e. the fast-quenching from the initial melt in ht-fq-a_gZIF-4 did not have a substantial effect, which is explained by the onset occurring far above the glass transition.

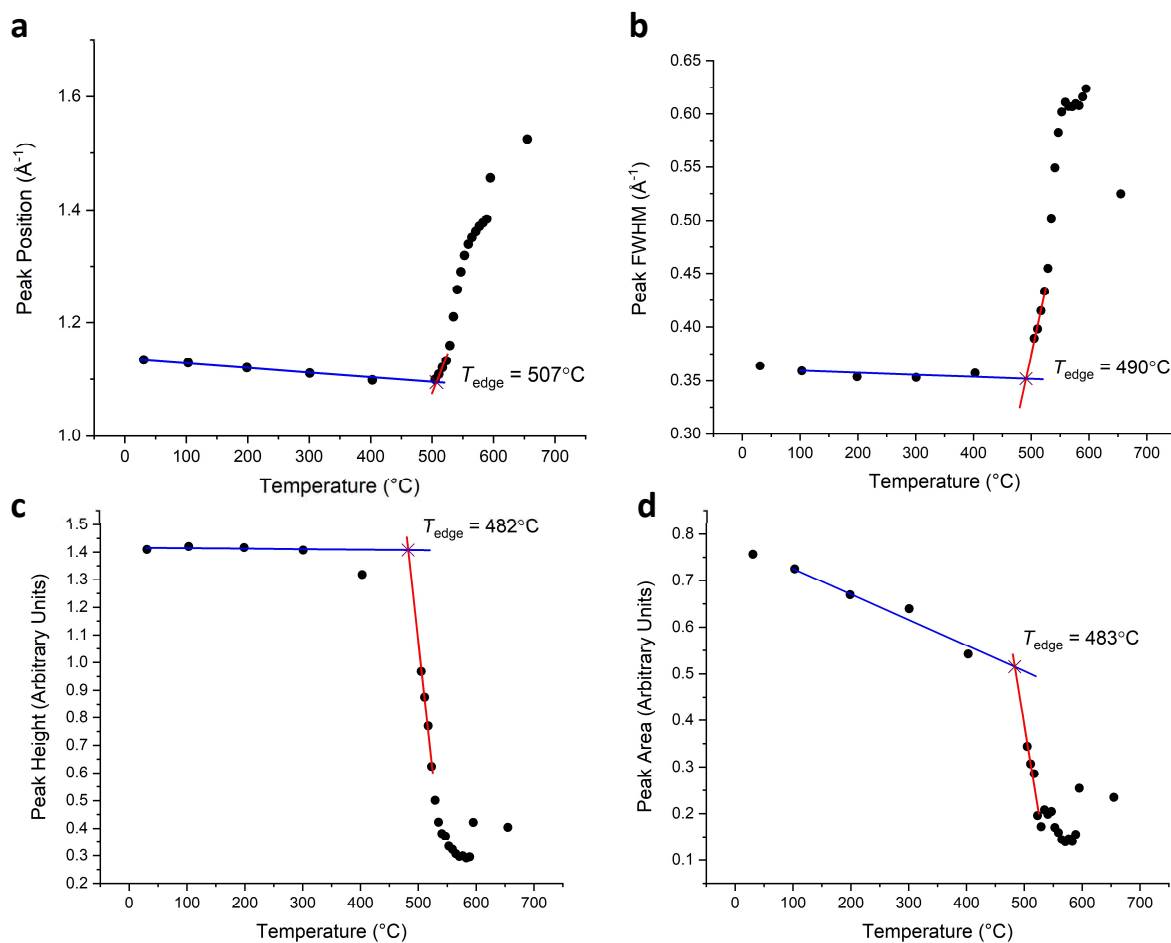


Figure 4.11: Peak parameters of the a_g ZIF-4 FSDP. **a.** Peak Position. **b.** Full width at half maximum. **c.** Peak height. **d.** Peak area. Red and blue lines indicate linear fits with temperature to calculate the onset of the discontinuity.

The unusual behaviour of a_g ZIF-4 can be understood in light of the reported pressure temperature phase diagram for the ZIF-4 system (**Figure 4.12**), which has been measured at high pressures through in-situ variable temperature and variable pressure PXRD and ex-situ morphological studies, and at ambient pressure using DSC [62]. This phase diagram demonstrates that ZIF-4 shows a decrease in its melting temperatures on increasing pressure. This indicates that the volume change on melting is negative, i.e. that the liquid ZIF is denser than the crystalline frameworks that occur before melting. This is also consistent with both the reported porosity in a_g ZIF-4 [77] and the measured increase in density of the ht-fq- a_g ZIF-4 relative to fq- a_g ZIF-4, and indicates that high temperature treatment of the glass results in densification of the structure, in line with the observed changes in the FSDP.

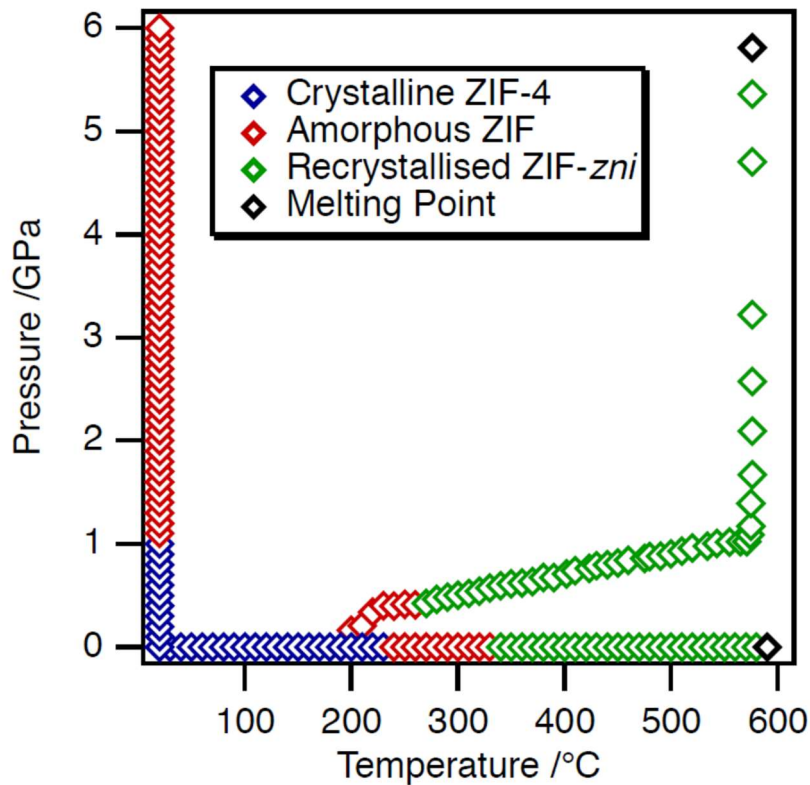


Figure 4.12: Pressure-temperature phase diagram of ZIF-4. Derived from synchrotron PXRD data, reproduced from [62].

4.3.4 Comparison with Ambient Temperature X-ray Total-Scattering on a_g ZIF-62

To provide a point of comparison for the analysis conducted on a_g ZIF-4, ambient temperature X-ray total-scattering was carried out on samples of glass ZIF-62 produced in the DSC. Three samples were investigated: i) One heated to 480°C and then cooled to room temperature (a_g ZIF-62). ii) A sample of a_g ZIF-62 formed as in i) but which had also been heated to 280 °C and then immediately cooled (a_g ZIF-62-280C). iii) A sample of a_g ZIF-62, which had been annealed at 280 °C for 72 hours (a_g ZIF-62-280C-72 hrs).

All the samples were fully amorphous and almost no changes in the FSDP were evident between the samples (**Figure 4.13** inset). The higher Q features in the structure factor were also completely unchanged by annealing for either length of time (**Figure 4.13**). The MRO is found to persist to approximately the same length in all the samples, as would be expected from the invariant position and FWHM of the FSDP. Moreover, as expected from the invariance at higher Q , the SRO was found to be unchanged by annealing time (**Figure 4.14**). This is not unexpected given that the short-range order is also found to be invariant during formation of the liquid and glass from their crystalline

precursors [36] and therefore is unlikely to change substantially on annealing at a lower temperature where there is less kinetic energy available for structural rearrangement.

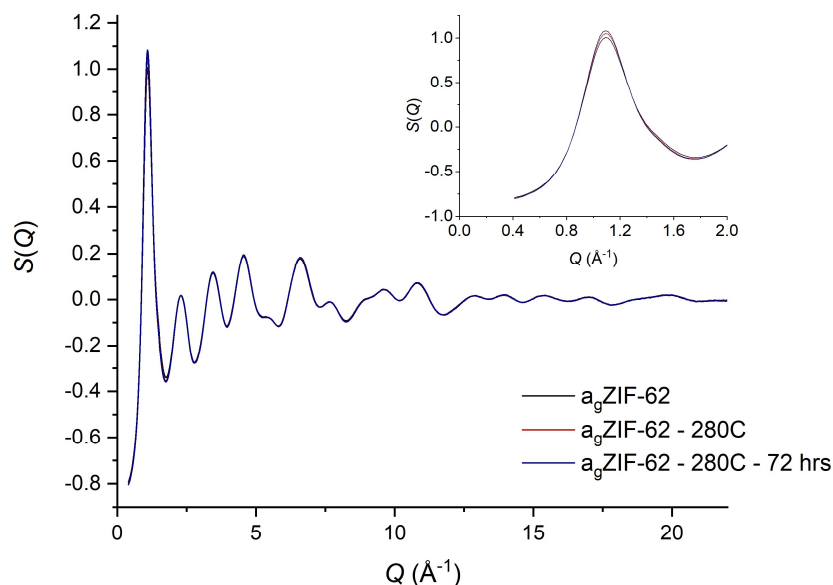


Figure 4.13: X-ray total-scattering structure factor, $S(Q)$, of heat treated a_g ZIF-62. The inset shows the FSDP. The heat treatments are melt-quenching (black), annealing at 280 °C for negligible time (red) and annealed at 280 °C for 72 hours (blue).

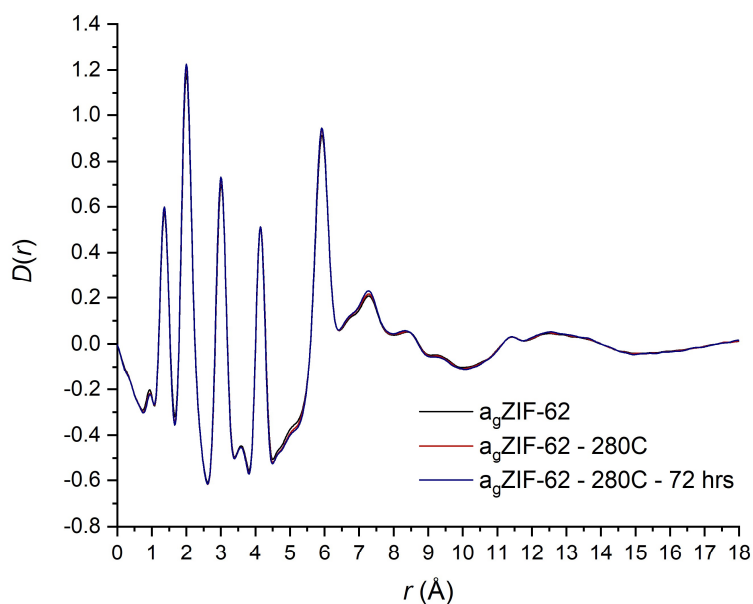


Figure 4.14: Pair distribution functions, $D(r)$, of heat treated a_g ZIF-62. The heat treatments are melt-quenching (black), annealing at 280 °C for negligible time (red) and annealed at 280 °C for 72 hours (blue).

The FSDP of the melt-quenched a_g ZIF-62 sample was also fitted using a Pseudo-Voigt function in FityK [92]. The peak position of the FSDP was found to be 1.13 \AA^{-1} and the FWHM was found to be 0.48 \AA^{-1} , which corresponds to a period and correlation length of 5.56 \AA and 13.00 \AA respectively (**Equations 4.2 and 4.3**). These are very similar to the values measured for the a_g ZIF-4 sample. This is unsurprising given that the Zn-N bond in a_g ZIF-62 is the same length as the Zn-N bond in a_g ZIF-4. The identical Zn-N bond length also means that the SiO_2 scaled position of a_g ZIF-62's FSDP is 1.22 \AA (**Equation 1**), which is well within the same errors observed in other covalent glass systems. PALS data on a_g ZIF-62 reported in the literature [61] reveals voids of $2.46 \pm 0.35 \text{ \AA}$ and $6.62 \pm 0.02 \text{ \AA}$, which are similar to those measured for a_g -ZIF-4 ($2.56 \pm 0.28 \text{ \AA}$ and $6.86 \pm 0.03 \text{ \AA}$ [77]). As a result, the predicted FSDP position is 0.98 \AA^{-1} (**Equations 4.5 and 4.8**), which is also in reasonable agreement with the observed value.

4.4 Conclusions

Broadly, this section investigated the effect of annealing on ZIF-glass structure, particularly focusing on the MRO, and used inorganic glass literature to place the ZIF-glasses into context with existing vitreous materials. During this section, the behaviour of the ZIF glasses $a_g\text{ZIF-4}$ ($\text{Zn}(\text{Im})_2$) and $a_g\text{ZIF-62}$ ($\text{Zn}(\text{Im})_{1.75}(\text{blm})_{0.25}$), during annealing above and below their T_g s respectively has been studied, and X-ray total scattering used to investigate how the structure evolves in both cases. A substantial change in the $S(Q)$, principally in the FSDP, is observed during high temperature annealing of $a_g\text{ZIF-4}$, which indicates substantial structural rearrangement within the liquid phase and the collapse of porosity. In contrast, low temperature annealing was found to have almost no discernible structural effect on $a_g\text{ZIF-62}$ samples. This is unsurprising considering the high reported viscosity of ZIF-62 at much higher temperatures and the size of the diffusing units [60], [61]. These factors mean that at temperatures below T_g the amount of thermal energy in the system, proportional to k_bT , precludes rearrangement of the structure despite any thermodynamic driving force to do so.

The FSDP in both $a_g\text{ZIF-4}$ and $a_g\text{ZIF-62}$ had very similar characteristics at room temperature, indicating that the MRO in both samples have comparable mid-range order. This is relatively unsurprising considering that NMR studies have shown that blm^- linkers are included in the ZIF-62 framework in a random manner [61], which might prevent the blm^- from having a systematic contribution to the long-range order of glass structures. Previous literature on thermally amorphised/ low temperature melting ZIF-4, had a period of 5.7 Å [50]. This similarity is also unsurprising considering the similar structures between low temperature thermally amorphised ZIF-4 and the high temperature melt-quenched glass phase (**Chapter 2**).

Both ZIF glasses show the same scaling of FSDP position with respect to the Zn-N and the position of the FSDP in glassy SiO_2 as is reported for other covalent network glasses. This observation further underscores the generally observed structural similarity between amorphous ZIFs and silicas which has already been reported in the literature [54]. Starting from simple assumptions, and previously published PALS data [61], [77] on the void structure in $a_g\text{ZIF-4}$ and $a_g\text{ZIF-62}$, a reasonable prediction for the FSDP position in both glasses could be obtained using existing theory developed for inorganic network glasses. However, although the predictions were reasonable first approximations, they still diverged more from the measure predictions than for other glasses reported [106]. One reason for this may be the simplicity of the assumptions used. In SiO_2 $D(\text{A-V})$ was calculated from theoretical modelling of the void structure in vitreous silica [114], and so similar studies on ZIFs may allow for more accurate estimation of the distance between the centres of the cation tetrahedra and the voids

and therefore more accurate FSDP peak prediction. Equally a more fundamental reason for the disagreement may be that, unlike in other AX_2 glass systems, the imidazolate linkers in ZIF glasses are molecular in nature with a distinct shape and their own internal degrees of freedom, neither of which are accounted for by the model [107].

The above discussion has focused on both comparing how ZIF glasses fit within existing theoretical descriptions for mid-range order in network glasses, and in using changes in the FSDP to examine transitions in the MRO in the ZIFs during heating. However specific structural details of what these features correspond to, outside of the generalised picture of correlations between cation centred spheres, has not been given. The exact structure of glasses and other amorphous materials beyond the local chemical bonding, which is discernible via spectroscopic techniques, and the overall topology of the continuous random network structure [32] is difficult to quantify. However as previously stated (**Section 4.2**), mid-range order in glasses comprised of joint tetrahedra could be understood in correlations between dihedral angles between tetrahedra (**Figure 4.15a**) [104].

The correlation length in the ZIF glasses studied is here is found to be between 13-18 Å, which is a reasonable match for the distances across rings identified from the crystal structure of ZIF-4 (**Figure 4.15b**). Tentatively this could indicate the retention of these rings from the crystalline phase into the melt-quenched glass, in amounts beyond what is expected to be randomly present in the CRN topology. This could explain the relatively high porosity found in the glass phase [77] and the observed densification of the network at high temperatures may be due to collapse of these structures in the liquid phase.

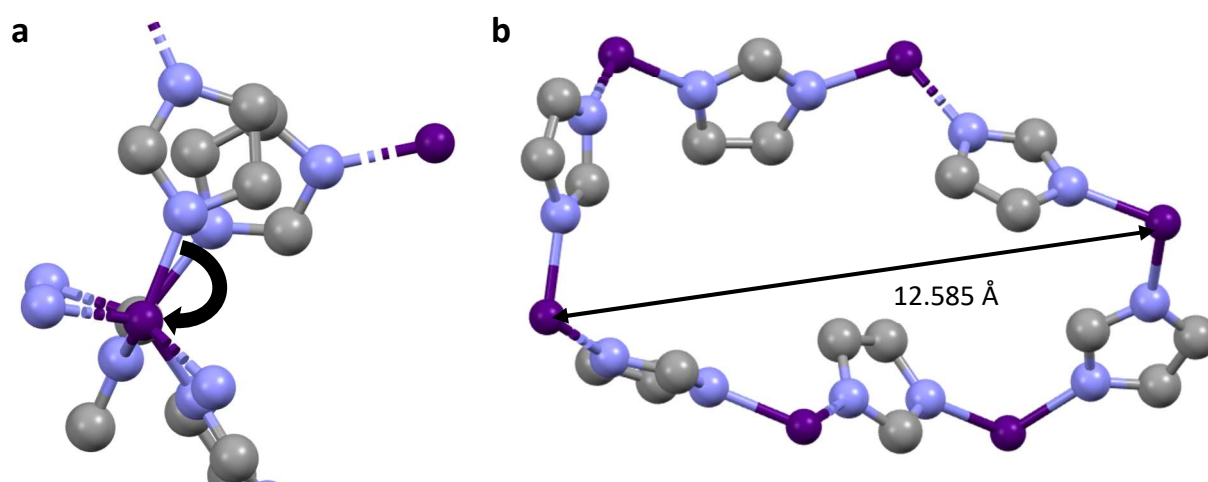


Figure 4.15: Tentative mid-range order assignments in glass MOFs. **a.** Dihedral angle between different Zn centred tetrahedra. **b.** Six membered ring present in the crystal structure of ZIF-4 [43]. Key: Grey – Carbon, Blue– Nitrogen, Purple – Zinc. Hydrogen atoms emitted for visual clarity.

The observation of densification in a_g ZIF-4 during high temperature heat treatment has implications for our understanding of the porosity of MOF glasses which may have industrial relevance if MOF glasses are ever used in contexts where their porosity in the glass or liquid state is functionally important. Further study of these glasses, especially via variable temperature total-scattering, small angle scattering, or modelling could be very fruitful in shedding further light on these initial observations. The use of neutron total-scattering, where the elemental scattering lengths do not scale directly with atomic number, may also shed more light on the role of the imidazolate linkers in the mid-range order.

This collapse could be due to rotation of linkers to allow for better packing and more Van der Waals stabilisation of the structure. This theory is supported by the relatively unvarying C-N /C-C (1.3 Å) and Zn-N (2 Å) correlations in the SRO of the ht-fq- a_g ZIF-4 and fq- a_g ZIF-4 samples compared to the rest of the SRO. This indicates that although a substantial change in the MRO is observed, the structure of the $Zn(N)_4$ tetrahedra and Im^- linkers remains relative intact, which supports a picture of increased disorder in ligand angles as opposed to change in the chemistry of the linkers themselves. This would also explain why these high temperature densifying transitions have not been reported for any other glass systems, as the enhanced degree of freedom due to the molecular nature of the X^- anion in ZIF glasses is a feature unique to MOF glasses.

Chapter 5: Creating New ‘Complex’ Metal-organic Framework Glasses from Two Component Frameworks

5.1 Introduction

The previous chapter discussed the similarities and differences between MOF glasses and covalent network glasses especially centred around discussion of mid-range order. This chapter examines the reactivity of the MOF liquid phase, and its utility in forming new MOF glass structures. Inspiration is taken from inorganic glass chemistry, where structures can be tuned via liquid phase mixing. Different inorganic glass systems have considerable miscibility and can be combined in the liquid phase to create new glass phases [30]. Moreover, many organic polymer systems are also miscible as liquids, and can form polymer blended structures which possess a single T_g [116]. The use of liquid miscibility to form such glasses allows materials with a range of properties between the parent endmembers to be produced.

As discussed in the literature review (**Chapter 2**), comparatively few melting MOFs have been discovered, with most frameworks decomposing on heating instead of forming a stable liquid state. Motivated equally by the observed structural similarities between MOF glasses and other glass systems, and the desire to form new MOF glass structures, this chapter details work on forming ‘complex’ MOF glasses. We use this term to describe glasses which are formed from more than one parent crystalline MOF framework.

The chapter begins with a description of MOF blends, which are structures formed by heating two crystalline MOFs, both of which melt in the pure state, above the melting point of the highest melting MOF (**Figure 5.1a**). The crystalline frameworks used in this case were ZIF-4 ($Zn(\text{Im})_2$) and ZIF-62 ($Zn(\text{Im})_{1.75}(\text{blm})_{0.25}$), which are reported as melting at approximately 590°C and 437°C respectively in the literature [56]. The blended structures formed were referred to as $(a_g\text{ZIF-4})_{0.5}(a_g\text{ZIF-62})_{0.5}$, where the subscript refers to the mass fraction of each framework in the blend. The results presented in this section were published previously in:

L. Longley *et al.*, “Liquid phase blending of metal-organic frameworks,” *Nat. Commun.*, vol. 9, no. 1, p. 2135, 2018.

I contributed to the preparation of the MOF samples and experimental planning. DSC and PXRD measurements were carried out by Dr Chao Zhou (University of Aalborg) in collaboration with Prof. Yue Yuanzheng (University of Aalborg). All X-ray total-scattering data presented here was collected, corrected, analysed, and interpreted primarily by me with the assistance of Prof. David A. Keen (ISIS)

and Dr Phillip A. Charter (Diamond Light Source). EDS/SEM data were collected and analysed by Dr Sean M. Collins (University of Cambridge). These results were then interpreted by me in context with the other experimental data.

A second class of complex glasses known as fluxes, in which one of the parent crystalline frameworks melts, but the other is reported as decomposing before melting when heated alone, is then discussed (**Figure 5.1b** and **Figure 5.1c**). This section begins with a discussion of fluxes formed from ZIF-8 [Zn(mIm)₂] and ZIF-62 (**Figure 5.1b**), in which the formation of the flux state is described in detail. The flux-melted structures formed here are referred to as $a_g[(\text{ZIF-8})_{0.2}(\text{ZIF-62})_{0.8}]$, with the distinct terminology from blends used to emphasise that the ZIF-8 does not form a glass state on its own. Once again subscript numbers refer to the mass fractions of the component frameworks. The results presented in this section were published previously published in:

L. Longley et al., "Flux melting of metal–organic frameworks," *Chem. Sci.*, vol. 10, no. 12, pp. 3592–3601, 2019.

I contributed to the preparation of the samples as well as the experimental planning. All X-ray total-scattering data presented here was collected, corrected, analysed, and interpreted primarily by me with assistance from Prof. David A. Keen. EDS/SEM data were collected and analysed by Dr Sean M. Collins and DSC/TGA measurements were performed by Dr Ang Qiao (Wuhan University of Technology).

In the next section fluxes formed from ZIF-76 (Zn(Im)_{1.62}(5-ClbIm)_{0.38}) with ZIF-UC-5 (Zn(Im)_{1.8}(ClbIm)_{0.2}) and ZIF-76-mbIm (Zn(Im)_{1.33}(5-mbIm)_{0.67}) with TIF-4 (Zn(Im)_{1.5}(mbIm)_{0.5}) are then discussed (**Figure 5.1c**). Initially ZIF-76 and ZIF-76-mbIm were thought to have an accessible liquid state as pure phase materials, however later work revealed that melting was due to the presence of a small amount of ZIF-UC-5 and TIF-4 in the ZIF-76 and ZIF-76-mbIm (respectively). Therefore, this constitutes another example of flux-melting. As such these glasses are referred to here as $a_g[(\text{ZIF-76})(\text{ZIF-UC-5})]$ and $a_g[(\text{ZIF-76-mbIm})(\text{TIF-4})]$ for the sake of consistency.

The results from this work are therefore re-interpreted here in that context. This section draws on work reported in:

C. Zhou et al., "Metal-organic framework glasses with permanent accessible porosity," *Nat. Commun.*, vol. 9, no. 1, p. 5042, 2018.

Dr Thomas D. Bennett (University of Cambridge) and Dr Glen J. Smales (University College London) designed the experiments and wrote the manuscript, and all sample preparation and DSC

measurements were carried out by Dr Chao Zhou. X-ray total-scattering measurements were collected and then analysed primarily by me with assistance from Dr Philip A. Charter and Prof. David A. Keen.

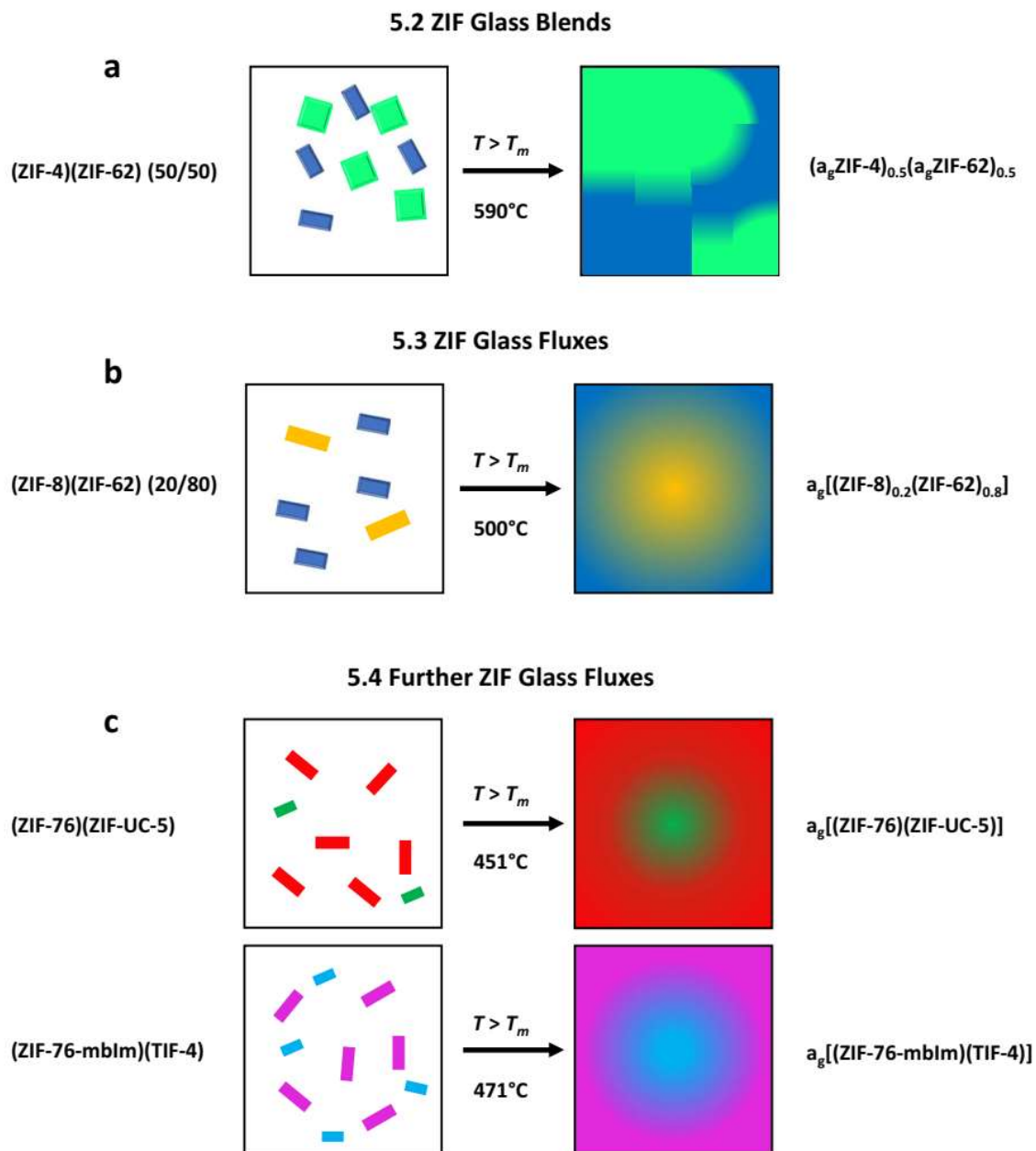


Figure 5.1: Schematic of samples investigated in this chapter.

5.2 Liquid Phase Blending of Metal-organic Frameworks

ZIF-62 [$\text{Zn}(\text{Im})_{1.75}(\text{blm})_{0.25}$] and ZIF-4 [$\text{Zn}(\text{Im})_2$] were chosen as frameworks for the formation of the blends because they both have accessible melting states and are principally composed of imidazolate linkers (**Figure 5.2**). Additionally they possess the widest separation of melting points, 437 °C and 590 °C respectively, known in melting frameworks at the time [56]. This, we hoped, would facilitate deconvolution of any thermal features observed during DSC characterisation. Given the need for inert atmospheres during melting [56], which necessitates use of either a DSC or tube furnace, ZIF-62 and ZIF-4, were mixed together in their crystalline phases before being heated. Crystalline ZIF-4 and ZIF-62 were synthesised using reported solvothermal procedures (see **Chapter 3.2.2**) [50], [90]. Equal weights of each MOF were then mixed through ball milling 0.25 g of each MOF for 5 mins with 2 x 7 mm stainless steel balls in a Retsch MM400 ball mill at 25 Hz to form a crystalline powdered mixture. Blends of a_g ZIF-4 and a_g ZIF-62 were prepared by heating a mixture of the two parent crystalline frameworks to a point at which both were liquid (590°C) in a Netzsch STA 449 F1 DSC under argon at 10 °C/min heating and cooling.

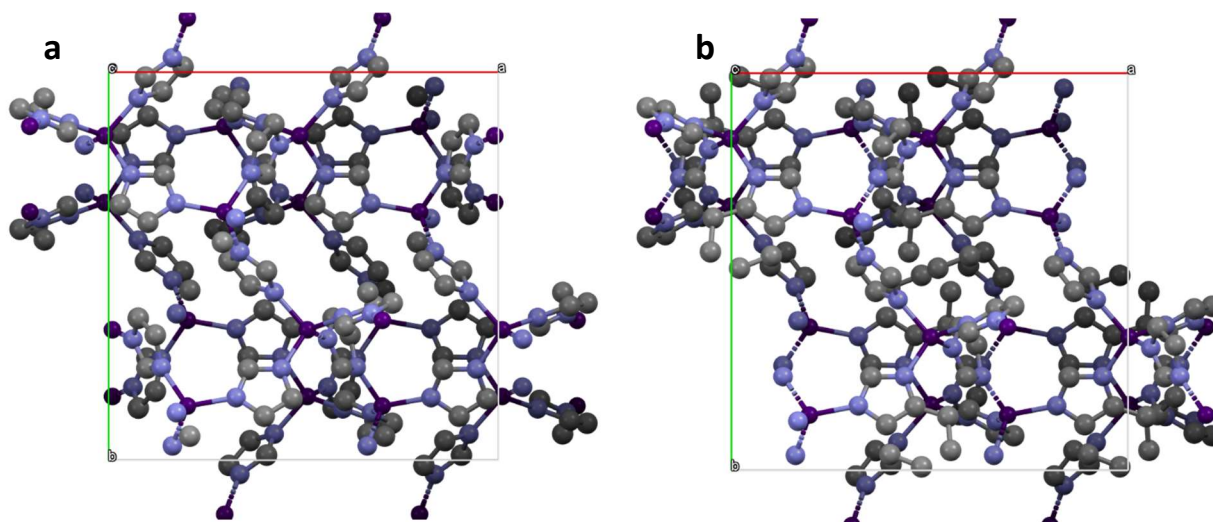


Figure 5.2: Crystal structures of a. ZIF-4 and b. ZIF-62. Viewed down the a axis. Key: Grey - Carbon, Blue – Nitrogen, Purple - Zinc. Hydrogen atoms omitted for clarity. Reproduced from [43], [48].

To study the microstructure of the resulting blends formed, a second set of samples were produced in which ZIF-4 had been replaced with a cobalt analogue possessing the same space group (*Pbca*) and topology (*cag*). This analogue, ZIF-4-Co, was synthesised by reported methods (see **Chapter 3.2.2**) [50]. The same ball milling procedure was used to produce crystalline mixtures of the ZIF-4-Co and ZIF-62 frameworks. An amorphous structure was then formed by heating this mixture to 425°C in the DSC.

These cobalt containing samples enabled the regions of the material originating from each parent framework to be identified by energy dispersive X-ray spectroscopy (EDS). To distinguish between the two frameworks used the suffix -Co is also added to indicate experiments carried out on the ZIF-4-Co analogue samples.

Ball milled mixtures of the parent crystalline phases are referred to as (ZIF-4)(ZIF-62)(50/50) and the amorphous blends formed by heating are termed $(a_g\text{ZIF-4})_{0.5}(a_g\text{ZIF-62})_{0.5}$. The (ZIF-4-Co)(ZIF-62)(50/50) and $(\text{ZIF-4-Co})_{0.5}(a_g\text{ZIF-62})_{0.5}$ samples were also characterised using EDS and X-ray total-scattering. To obtain enough sample for EDS and X-ray total-scattering methods, samples of the ball-milled crystalline mixture, (ZIF-4-Co)(ZIF-62) (50/50), were heated in a Carbolite 12/65/550 tube furnace under argon, to around 425 °C at 20°C/min and held for 5 minutes, followed by cooling back to room temperature at the natural rate of the furnace.

On re-examining the data on the as synthesised ZIF-4 used in this study (**Figure 5.3**) it was found that the PXRD pattern was not a complete match for literature published structures of ZIF-4 despite using a synthesis reported in the literature [36]. There is some degree of mismatch in relative intensities on some peaks, and small un-accounted for peaks. The $\text{Zn}(\text{Im})_2$ system has a large number of polymorphs [43] and there are also multiple different reported structures for ZIF-4 with small differences in their powder patterns [43], [51]. Equally different polymorphs of $\text{Zn}(\text{Im})_2$ have been reported as thermally amorphising [50] and melting [56] (**Chapter 2**).

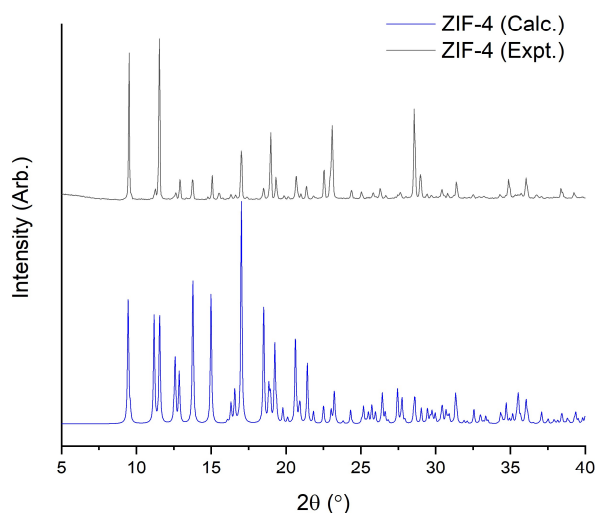


Figure 5.3: PXRD pattern of synthesised ZIF-4. A simulated pattern from the literature is plotted for comparison [43].

The ZIF-4-Co used in this section came from three separate batches, all following the same method [50]. Although all the patterns produced were a reasonable match for the ZIF-4-Co structure reported in the literature [51] there were discrepancies between batches (**Figure 5.4a**). These discrepancies are also attributed to the rich polymorphism displayed by the $\text{Co}(\text{Im})_2$ system [117]. Despite these differences melt-quenching of these samples from approximately 425 °C resulted in samples which were majority amorphous with FSDPs in the same approximate position of 15 ° 2 θ (**Figure 5.4b**). ZIF-4-Co produced by an identical method was also shown to amorphise on heating in the literature [50]. Due to the generally reported amorphisation/melting of ZIF-4-Co and ZIF-4 on heating [50] and the reported melting of other $\text{Zn}(\text{Im})_2$ polymorphs [56], the results of this section still represent the production of MOF glass blends between ZIF-4 and ZIF-62.

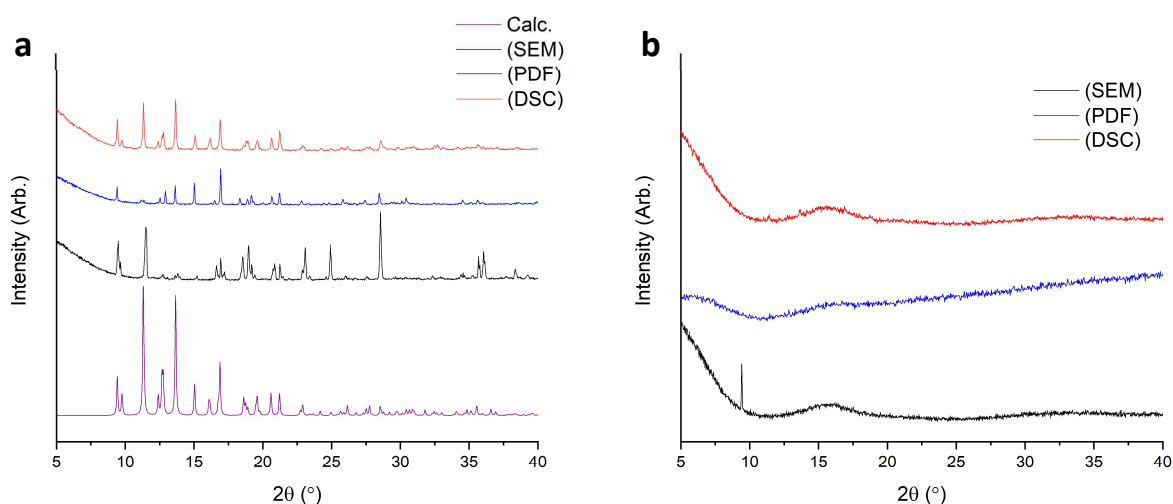


Figure 5.4: Synthesised ZIF-4-Co batches used in this project. The batches are labelled by the way the samples they contributed to were characterised. A simulated pattern from the literature is also shown [51]. Note: The PDF synthesis used partially deuterated imidazole to facilitate analysis by neutron total-scattering. **a.** Crystalline ZIF-4-Co **b.** Heat treated $(\text{ZIF-4-Co})_{0.5}(\text{a}_g\text{ZIF-62})_{0.5}$ samples.

5.2.1 Differential Scanning Calorimetry Analysis on Blends Samples

DSC experiments were performed on the $(\text{ZIF-4})(\text{ZIF-62})(50/50)$ sample up to 590 °C in an argon atmosphere (**Figure 5.5a**). The first endothermic feature at 225 °C is ascribed to desolvation. This was followed by a small endothermic feature at approximately 325 °C attributed to thermal amorphisation of ZIF-4 [36]. As expected, two endothermic features belonging to the respective melting points of ZIF-62 and ZIF-4 (445 °C and 580 °C) were then noted, agreeing well with those reported literature for

each framework [56]. A second sample was heated to 590 °C, held for 2 minutes and then cooled under argon to room temperature at 10 °C/min.

A second heating curve then revealed a T_g , at 306 °C, which fell between the T_g s for the constituent frameworks, 292 °C (ZIF-4- Zn) and 318 °C (ZIF-62), which had been previously reported in the literature [36], [56] (**Figure 5.5a**). This sample was shown by PXRD to be amorphous (**Figure 5.5b**). Taken together these results indicate the formation of a blended structure, $(a_g\text{ZIF-4})_{0.5}(a_g\text{ZIF-62})_{0.5}$, i.e. in good agreement with literature on polymeric, metallic and inorganic glasses [30], [116], [118].

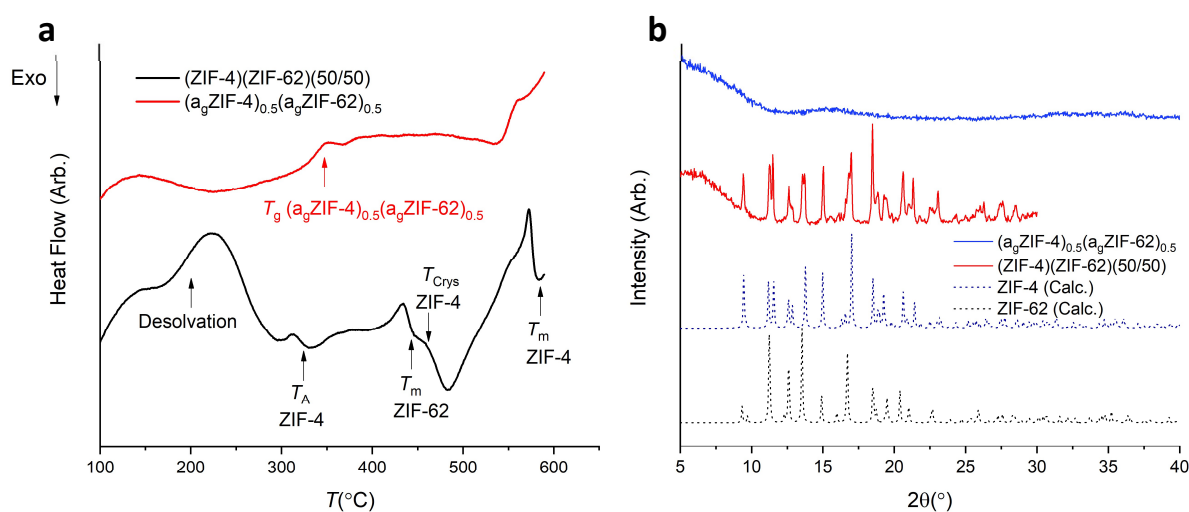


Figure 5.5: PXRD and DSC on ZIF-4 ZIF-62 blends samples. **a.** Thermal response curves of the (ZIF-4)(ZIF-62)(50/50) and $(a_g\text{ZIF-4})_{0.5}(a_g\text{ZIF-62})_{0.5}$ during heating at 10 °C/min. **b.** Powder X-ray diffraction (PXRD) data on (ZIF-4)(ZIF-62)(50/50) and $(a_g\text{ZIF-4})_{0.5}(a_g\text{ZIF-62})_{0.5}$. Simulated PXRD for ZIF-62 [48] and ZIF-4 [43] patterns indicated by broken traces.

DSC experiments were also performed on the (ZIF-4-Co)(ZIF-62) (50/50) mixture. The first heating scan (**Figure 5.6a**) showed amorphisation/melting of ZIF-4-Co at approximately 350°C, followed by the ZIF-62 melting endotherm at around 425°C. Finally, an exotherm due to recrystallisation of ZIF-4-Co to a dense ZIF-zni phase was observed at 500°C. These features are in reasonable agreement with those observed previously via variable temperature PXRD on ZIF-4-Co reported in the literature, where peaks from the starting crystalline phase disappear at 300°C and Bragg peaks matching ZIF-zni started to appear at 370°C [50]. Above this temperature the DSC baseline displays rapid changes, which is indicative of decomposition. As such no melting of ZIF-4-Co was observable in the (ZIF-4-Co)(ZIF-62) (50/50) mixture. This is in line with the thermal behaviour of ZIF-4-Co reported in the literature where lower decomposition temperatures precludes melting from ZIF-zni [69].

Despite this, quenching of the sample from 425 °C, i.e. a region containing amorphous ZIF-4-Co and liquid ZIF-62, revealed a structure with a single glass transition at 300 °C during a second heating scan (**Figure 5.6a**). Moreover, PXRD of the heat treated sample, $(\text{ZIF-4-Co})_{0.5}(\text{a}_g\text{ZIF-62})_{0.5}$, revealed that it was completely amorphous (**Figure 5.6b**). Differences between $(\text{ZIF-4-Co})_{0.5}(\text{a}_g\text{ZIF-62})_{0.5}$ and $(\text{a}_g\text{ZIF-4})_{0.5}(\text{a}_g\text{ZIF-62})_{0.5}$ are perhaps expected to be small, given the very high viscosities for both ZIF-4 and ZIF-62 reported previously [60], [61].

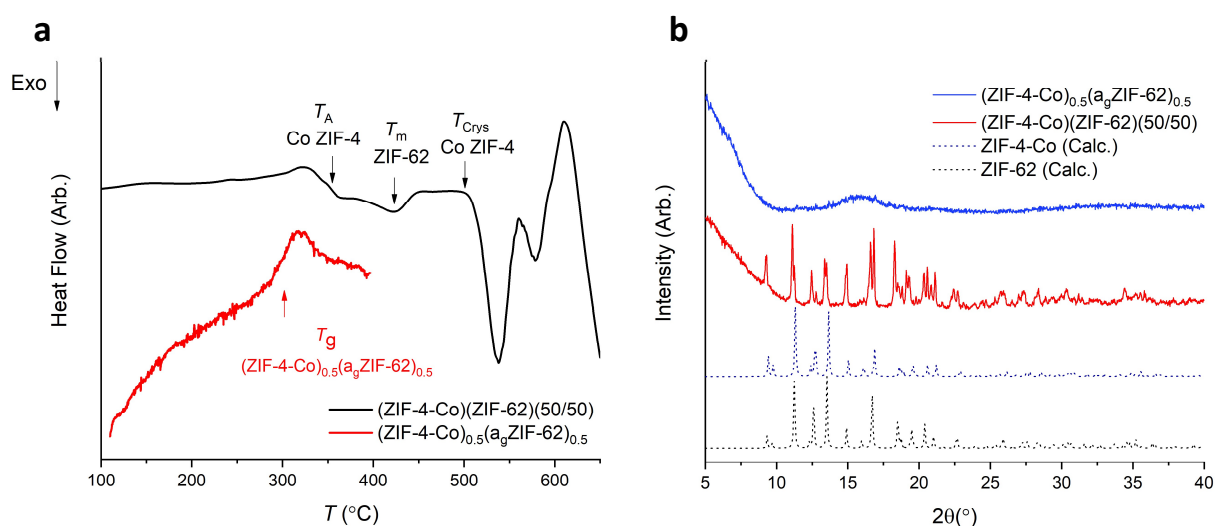


Figure 5.6: PXR and DSC on ZIF-4-Co ZIF-62 blends samples. **a.** Thermal response curves of the $(\text{ZIF-4-Co})(\text{ZIF-62})(50/50)$ and $(\text{ZIF-4-Co})_{0.5}(\text{a}_g\text{ZIF-62})_{0.5}$ during heating at 10 °C/min. **b.** Powder X-ray diffraction (PXR) data on $(\text{ZIF-4-Co})(\text{ZIF-62})(50/50)$ and $(\text{ZIF-4-Co})_{0.5}(\text{a}_g\text{ZIF-62})_{0.5}$. Simulated PXR patterns for ZIF-62 [48] and ZIF-4-Co [51] indicated by broken traces.

5.2.2 Examining the Microstructure of Zeolitic Imidazolate Framework Blends through Energy-Dispersive Spectroscopy

As previously mentioned, the different metal centres from in each parent framework allow regions of the $(\text{ZIF-4-Co})_{0.5}(\text{a}_g\text{ZIF-62})_{0.5}$ that originate from each of the parent frameworks to be identified through energy-dispersive X-ray spectroscopy (EDS). Annular dark-field scanning transmission electron microscopy images (STEM) of the $(\text{ZIF-4-Co})(\text{ZIF-62})(50/50)$ and $(\text{ZIF-4-Co})_{0.5}(\text{a}_g\text{ZIF-62})_{0.5}$ samples, were obtained alongside EDS results. These results revealed an extended network exhibiting relatively sharp interfaces between Co and Zn domains in $(\text{ZIF-4-Co})_{0.5}(\text{a}_g\text{ZIF-62})_{0.5}$. Domain sizes were observed ranging from 200 nm to >1 μm in width. This is markedly different to $(\text{ZIF-4-Co})(\text{ZIF-62})(50/50)$, where separate particles of each framework, without domain mixing and with a markedly different morphology, were observed (**Figure 5.7a** and **Figure 5.7b**).

In STEM analyses, the electron probe is transmitted through the sample, resulting in EDS signals that arise from the entire volume through the three-dimensional sample. As a result, these two-dimensional analyses alone were not sufficient to fully characterize the interfaces between the lamellar domains of Co and Zn MOFs. Two-dimensional interface regions with a mixed signal composition are not distinguishable from single-phase compositional domains overlapping along the electron beam direction. EDS tomography was performed in order to address this uncertainty and to characterize the sharpness of the interface between the Co- and Zn-containing regions (**Figure 5.7c**). A single piece of $(\text{ZIF-4-Co})_{0.5}(\text{a}_g\text{ZIF-62})_{0.5}$ was located that contained two large domains of predominantly Co and Zn, respectively. At the interface there were two regions characteristic of heterogeneous mixing between the Co and Zn phases and exhibiting a similar interlocked microstructure as those observed in the two-dimensional analysis (labelled 1 and 2 in **Figure 5.7c**). Inspection of the tomographic reconstruction volumes at these features revealed that, at feature 1, the Co protrusion is present in a region with negligible Zn content. In contrast at feature 2, both Co and Zn were found in the same three-dimensional region, suggesting some minor homogeneous mixing. While some regions of the three-dimensional interface exhibited micro-scale mixing of Co and Zn, the majority were segregated into single-metal domains within an interlocked network microstructure.

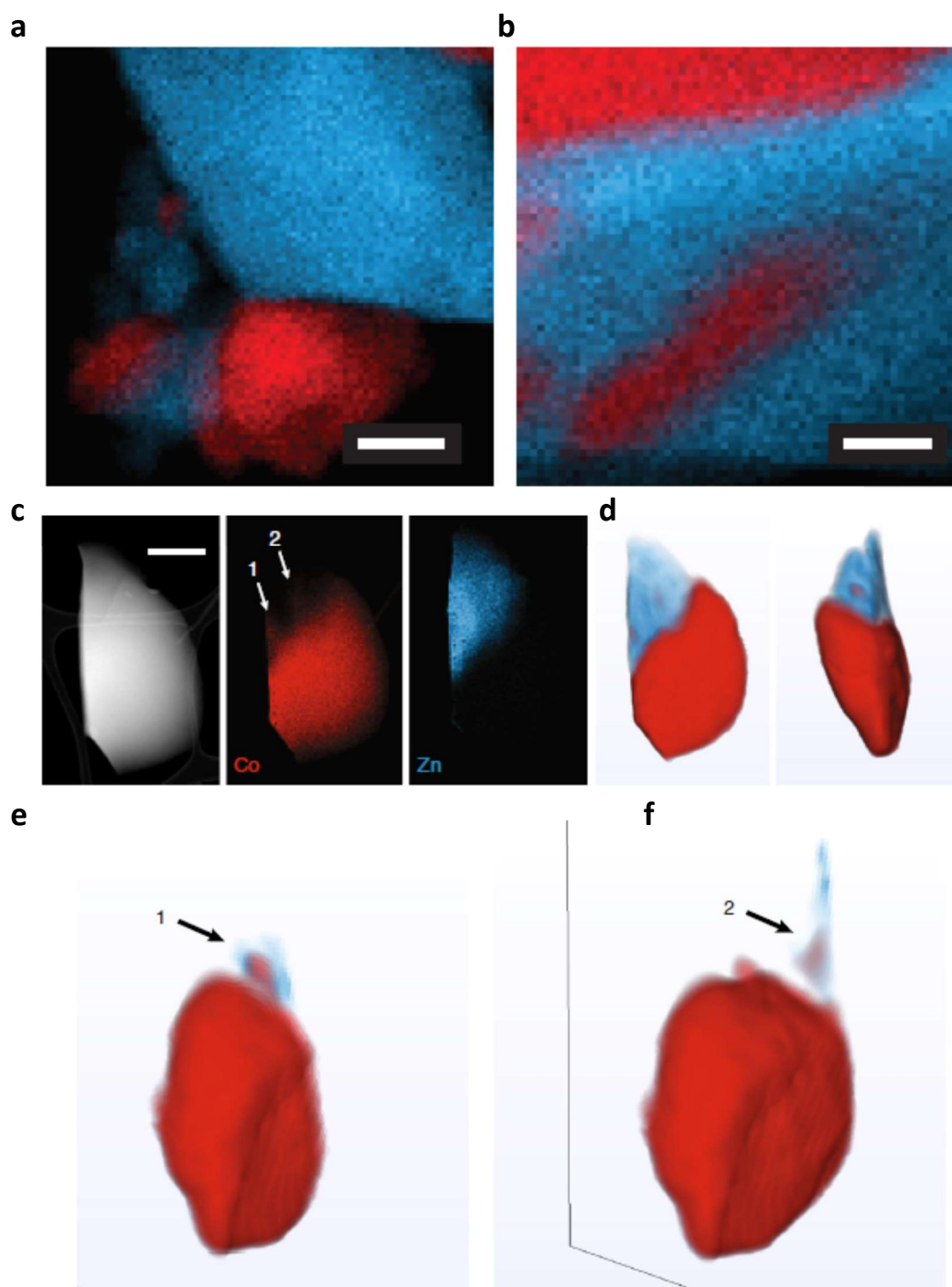


Figure 5.7: Energy dispersive X-ray spectroscopy (EDS) images of ZIF-4-Co/ZIF-62 blends samples. **a.** (ZIF-4-Co)/(ZIF-62)(50/50) and **b.** (ZIF-4-Co)_{0.5}(aZIF-62)_{0.5}. The white scale bar corresponds to 200 nm. **c.** Two-dimensional ADF-STEM and EDS chemical map measurements of a particle of (ZIF-4-Co)_{0.5}(aZIF-62)_{0.5} used for EDS tomography, the scale bar here corresponds to 500 nm. **d.** Volume rendering of the tomographic reconstructions for the Co and Zn signals (two orthogonal viewing directions). **e., f.** Discrete two-dimensional slices from the three-dimensional volume reconstruction for Zn plotted with the transected volume rendering of the Co reconstruction. Two protrusions from the principal Co domain are highlighted with the numbers 1 and 2.

5.2.3 Ambient and Variable Temperature X-ray Total-Scattering Measurements

The atomic scale structure of the blend was probed through synchrotron X-ray total-scattering. Whereas the X-ray structure factor $S(Q)$ of (ZIF-4-Co)(ZIF-62)(50/50) contained sharp peaks due to Bragg diffraction, that of $(\text{ZIF-4-Co})_{0.5}(\text{a}_g\text{ZIF-62})_{0.5}$, as expected from laboratory PXRD measurements, did not (**Figure 5.8a**). The real-space $D(r)$ (**Figure 5.8b**) showed peaks at distances of 1.3, 2, 3, 4 and 6 Å, which were common between both the crystal mixture and glass blend samples. This is consistent with previous conclusions on near-identical short-range order between crystal and glass ZIFs [60]. At distances beyond the SRO several lower intensity broader features were evident in the 6-15 Å region, which indicates that the MRO in the $(\text{ZIF-4-Co})_{0.5}(\text{ZIF-62})_{0.5}$ is similar to that of $\text{a}_g\text{ZIF-4}$ and $\text{a}_g\text{ZIF-62}$ (**Chapter 4**). Above this distance, oscillations at high r were present from the crystalline mixture (ZIF-4-Co)(ZIF-62)(50/50) though the PDF of $(\text{ZIF-4-Co})_{0.5}(\text{a}_g\text{ZIF-62})_{0.5}$ was relatively featureless. This is expected, as the high r correlations in the (ZIF-4-Co)(ZIF-62)(50/50) are due to periodic density fluctuations associated with the crystalline lattices of ZIF-4-Co and ZIF-62, whereas the $(\text{ZIF-4-Co})_{0.5}(\text{a}_g\text{ZIF-62})_{0.5}$ sample is amorphous and so has no long-range order.

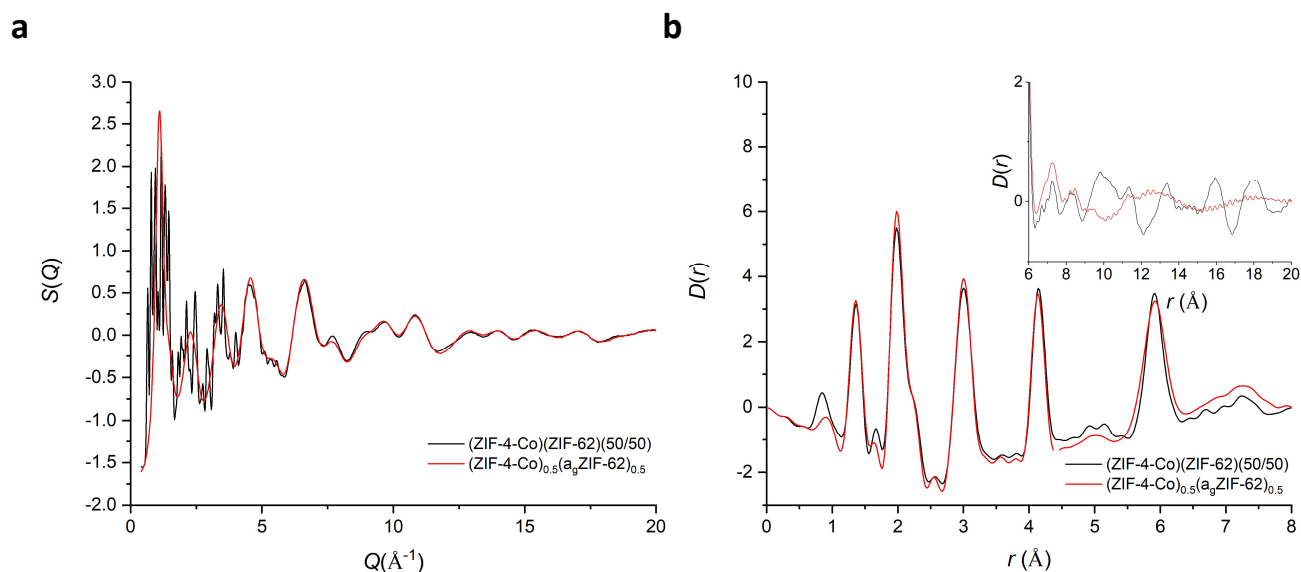


Figure 5.8: Ambient temperature total-scattering of ZIF-4-Co ZIF-62 blends samples. **a.** X-ray structure factors $S(Q)$ of (ZIF-4-Co)(ZIF-62)(50/50) and $(\text{ZIF-4-Co})_{0.5}(\text{a}_g\text{ZIF-62})_{0.5}$. **b.** Corresponding X-ray pair distribution functions, $D(r)$, in the SRO region. Inset: Expanded scale showing MRO and LRO.

To investigate structural changes on heating, synchrotron X-ray diffraction data were collected on a sample of $(\text{ZIF-4-Co})_{0.5}(\text{a}_g\text{ZIF-62})_{0.5}$ heated from room temperature to 460 °C (**Figure 5.9a**). No Bragg peaks emerged during heating indicating that the sample did not recrystallise, moreover the first sharp diffraction peak in the $S(Q)$ varied little in intensity or position, which indicates very little long or mid-

range structural rearrangement in the liquid state relative to the glass. This is unsurprising given the variable temperature data on the a_g ZIF-4 structure (**Chapter 4**) showed that the FSDP does not change substantially until around 500 °C.

The second and third peaks in the measured total-scattering also remained approximately invariant on heating. Some ‘flattening’ of features at high Q values however occurred upon heating above 300 °C (**Figure 5.9a**). This temperature corresponds to the T_g of $(\text{ZIF-4-Co})_{0.5}(\text{ZIF-62})_{0.5}$. The Fourier transform of the variable temperature X-ray total-scattering further clarifies these observations (**Figure 5.9b**). The peak in the $D(r)$ at 1.3 Å, which only contains contributions from C-C and C-N pairs i.e. direct chemical bonds, remained constant in intensity and position, indicating the stability of the imidazolate and benzimidazolate linkers on heating above T_g . However, those peaks arising mainly from M-N1 (2 Å), M-C (3 Å), M-N2 (4 Å) and M-M (6 Å) correlations, where M is either Co or Zn, were observed to undergo a reduction in intensity upon heating. This confirms that de-coordination of the imidazolate linkers is occurring on heating of the blended sample in a manner analogous to the behaviour of single phase ZIF glass samples reported previously in the literature [60]. The intensity recovered upon cooling back to ambient temperature, showing that no permanent change in short-range order had taken place.

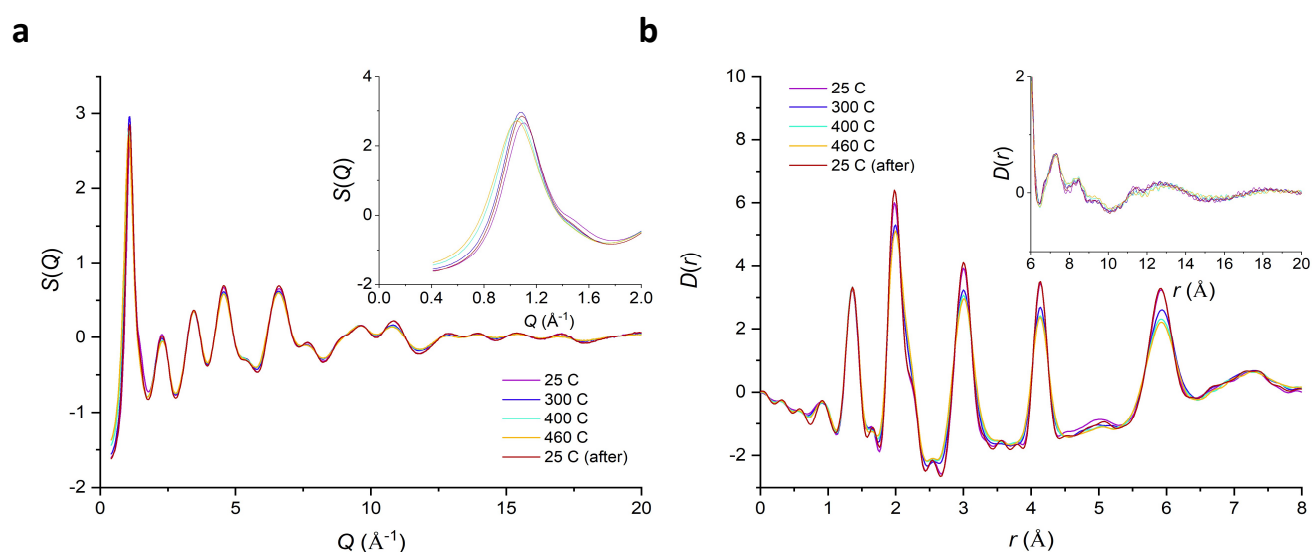


Figure 5.9: Variable temperature total-scattering data of ZIF-4-Co/ZIF-62 blends samples. **a.** Variable temperature X-ray structure factors $S(Q)$ of $(\text{ZIF-4-Co})_{0.5}(\text{ZIF-62})_{0.5}$. Inset: Expanded scale showing the FSDP. **b.** Corresponding variable temperature X-ray pair distribution functions, $D(r)$, in the SRO region. Inset: Expanded scale showing MRO and LRO.

5.2.4 Discussion

The results in this section demonstrate that two MOF liquids derived from ZIF-4 and ZIF-62 can be blended together. DSC measurements revealed that the melt-quenched glass formed possesses a single T_g , intermediate between the glass transitions reported in the literature for the constituent ZIF-4 and ZIF-62 frameworks [56]. The resultant glass microstructure was probed through electron microscopy on an analogue glass blend sample derived from ZIF-4-Co and ZIF-62, $(\text{ZIF-4-Co})_{0.5}(\text{a}_g\text{ZIF-62})_{0.5}$, finding heterogeneous domain formation. Binding between the domains was investigated using electron tomography, showing regions of homogeneous Co and Zn concentration, which is indicative of a small degree of liquid–liquid mixing. The limited degree of mixing was attributed to the high viscosities of the liquid ZIF phases reported in the literature [60], [61]. Ambient temperature PDF measurements on $(\text{ZIF-4-Co})(\text{ZIF-62})(50/50)$ and $(\text{ZIF-4-Co})_{0.5}(\text{a}_g\text{ZIF-62})_{0.5}$ demonstrated that SRO was maintained on glass blend formation, as would be expected from the behaviour of single phase networks reported in the literature. Variable temperature PDF measurements on the $(\text{ZIF-4-Co})_{0.5}(\text{a}_g\text{ZIF-62})_{0.5}$ sample as it was heated through the T_g revealed a broadening and loss of intensity in features in the SRO due to the increased de-coordination of the zinc centre in the liquid phase. These features are recovered on cooling, indicating that this is a reversible process. The FSDP remains essentially invariant during heating revealing that no longer range structural reorganisation or relaxation occurs.

Taken together these results indicate that hybrid glass blends can be formed as a way of tuning the properties of a MOF glass between its two endmembers. This discovery of MOF glass blends also expands the new material category of hybrid glasses and continues the observed structural similarity between ZIF glasses and inorganic silica glasses [30], [59].

5.3 The Discovery of Flux-Melting in Metal-organic Frameworks Mixtures

The preceding section has shown that ZIF-62 and ZIF-4, which are each capable of melting separately, can be heated together and quenched to form a single amorphous phase. However, the majority of ZIFs do not have an accessible liquid state and instead decompose during heating. Inspired by the literature on inorganic glass fluxes [30] we investigated the potential for using a liquid ZIF to promote formation in a crystalline ZIF framework which would not melt on its own. In this study ZIF-62 was chosen to use as the molten ZIF because of the approximately 150 °C difference between its melting temperature and decomposition temperature which indicates that the liquid state is stable over a wide range of temperatures. ZIF-8 (**Figure 5.10**), was chosen as the non-melting ZIF, because it has been extensively studied in the literature [119].

ZIF-62 was synthesised using a procedure reported in the literature (see **Chapter 3.2.2**) [90], whereas ZIF-8 was purchased from Sigma Aldrich and used as received. To prepare the composite, the two frameworks were mixed as crystalline powders prior to heating, so that the ZIF-62 liquid would form in-situ. To prepare the crystalline mixture, designated (ZIF-8)(ZIF-62)(20/80), 0.1 g and 0.4 g of ZIF-8 and ZIF-62 respectively were ball milled with 2 x 7mm at 25 Hz for 5 minutes. This mixture was then heated at 180 °C under vacuum for 3 hours to remove the templating solvent. The composite flux sample after heat treatment is referred to as $a_g[(ZIF-8)_{0.2}(ZIF-62)_{0.8}]$ to distinguish it from the mixture of the parent crystalline frameworks.

To probe the microstructure of the resulting glass formed after heat treatment, the same method as used in the blends samples was employed here; ZIF-8 was exchanged for ZIF-67, which is the cobalt analogue. This was done in order for the parts of the composite that originated from each parent crystalline phase to be distinguished by EDS. Apart from the change in metal centre the two structures are identical, both crystallising in the $I\bar{4}3m$ space group with the SOD topology [48], [67].

A sample of (ZIF-67)(ZIF-62)(20/80) was accordingly prepared by first synthesizing ZIF-67 by a method reported in the literature (see **Chapter 3.2.2**) [93]. 0.1 g of ZIF-67 was ball milled with 2 x 7mm at 25 Hz for 15 minutes with 0.4 g ZIF-62 to make the crystalline powder mixture (ZIF-67)(ZIF-62)(20/80). The additional 10 minutes of ball milling time was used because of the larger starting crystalline size of the ZIF-67 relative to the as-purchased ZIF-8 (**Figure 5.11**). The cobalt containing composite produced after heat treatment was termed $a_g[(ZIF-67)_{0.2}(ZIF-62)_{0.8}]$.

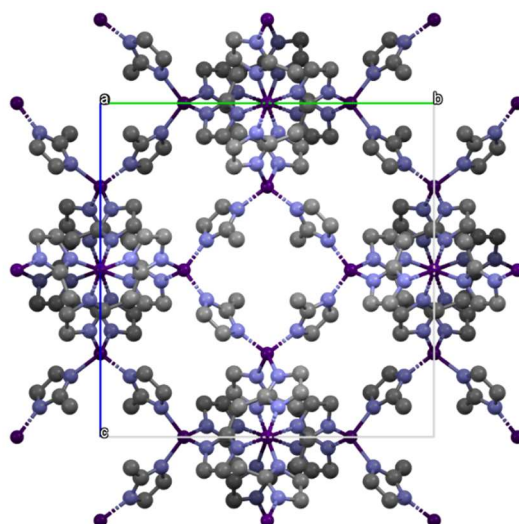


Figure 5.10: Crystal structure of ZIF-8. Reproduced from [67]. Key: Grey - Carbon, Blue – Nitrogen, Purple - Zinc. Hydrogen atoms omitted for clarity.

Bulk glass samples were produced by heating 0.25 g samples of (ZIF-8)(ZIF-62)(20/80) and (ZIF-67)(ZIF-62)(20/80) in a Carbolite 12/65/550 tube furnace under argon at 10 °C/min to approximately 500 °C followed by cooling at the natural rate of the furnace.

5.3.1 Differential Scanning Calorimetry Analysis on Flux Samples

An initial DSC/TGA experiment, to investigate the overall stability of the (ZIF-8)(ZIF-62)(20/80) was performed up to 700°C at 10 °C/min in an inert argon atmosphere. A broad endotherm, at approximately 100 °C, with an associated mass loss in the TGA, indicative of desolvation, followed by an endothermic melting peak with an offset at approximately 500 °C was observed (**Figure 5.12**). This was broadly consistent with prior observations [56], however with a melting offset that was around 50°C higher than that reported in the literature for melting of the pure ZIF-62 framework. An abrupt increase in noise coupled with a sharp rise in the DSC baseline and loss of mass measured in the TGA occurs simultaneously at approximately 525 °C, this is taken to be the onset of thermal decomposition of the sample (**Figure 5.12**). This value is 75 °C lower than the value reported in the literature for the pure ZIF-62 phase but matches that of ZIF-8 well, indicating that the thermal stability of the crystalline mixture may be dominated by the least stable framework [56], [74].

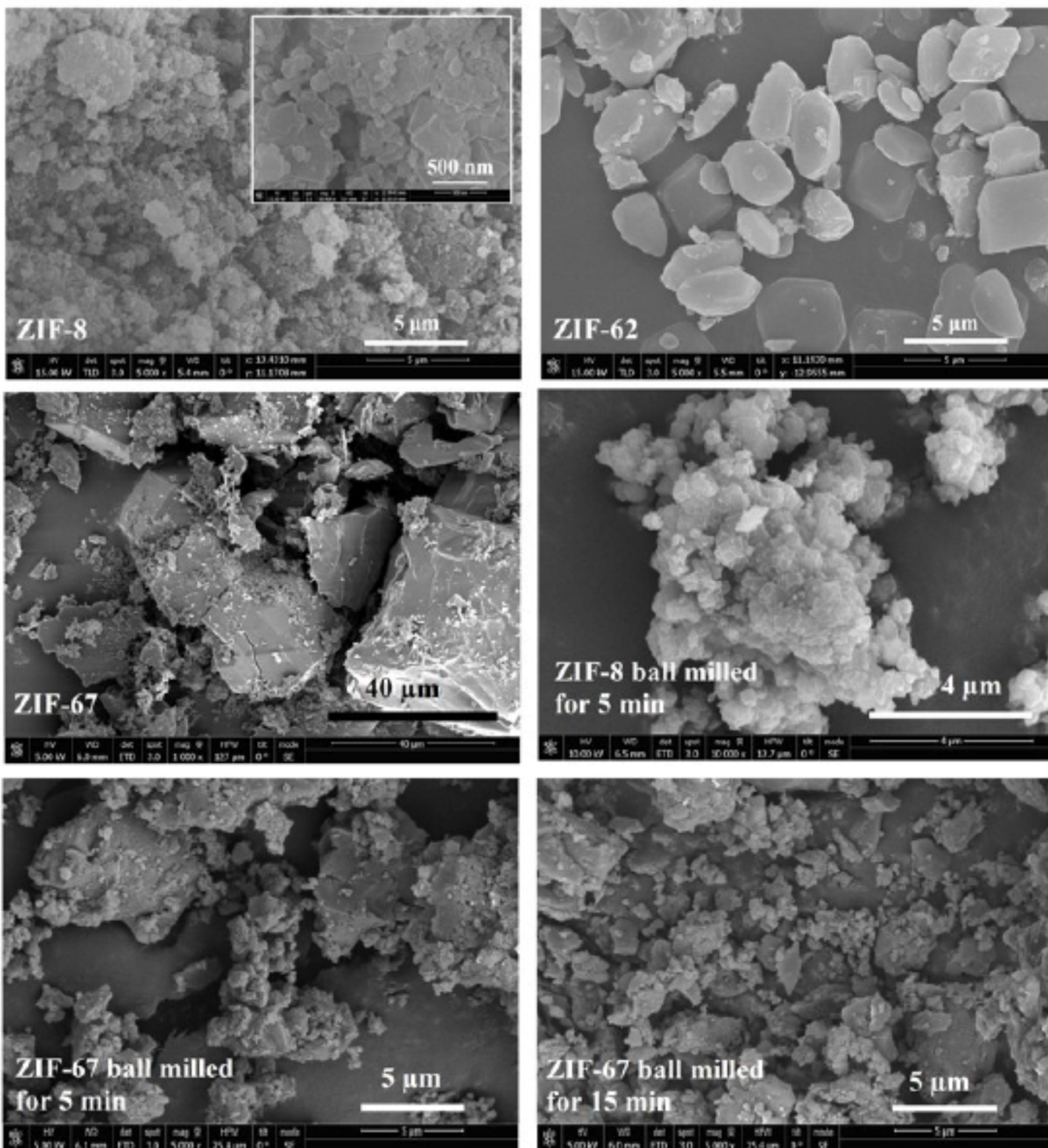


Figure 5.11: SEM images of ZIF-8, ZIF-62, and ZIF-67. ZIF-8, ZIF-62 as-synthesized, ZIF-67 as-synthesized, ZIF-8 (~500 mg) ball-milled for 5 minutes, ZIF-67 (~100 mg) ball-milled for 5 minutes, ZIF-67 (~40 mg) ball-milled for 15 minutes.

In a separate experiment the (ZIF-8)(ZIF-62)(20/80) sample was heated to 500 °C at a rate of 10 °C/min, above the offset of the endotherm measured in the previous scan, and then quenched at a rate of 10 °C/min back to room temperature (**Figure 5.13a**). The glassy nature of $a_g[(ZIF-8)_{0.2}(ZIF-62)_{0.8}]$ was confirmed by a second DSC heating curve, which demonstrated a glass transition at 334°C. The glass transition determined for $a_g[(ZIF-8)_{0.2}(ZIF-62)_{0.8}]$ is greater than that for pure ZIF-62 ($T_g = 318$ °C) [56]. This increase is consistent with the increase in the observed melting point and the linear relationship between the melting and glass transition temperatures reported in the literature for MOF and other glasses [36], [61]. The heat treatment produced a solid self-supporting monolith (**Figure 5.13b**), referred to as $a_g[(ZIF-8)_{0.2}(ZIF-62)_{0.8}]$, of strikingly different external appearance to the ball milled powders prior to heating (**Figure 5.11**). Scanning electron microscopy demonstrated that the individual particles coalesce upon their transformation into $a_g[(ZIF-8)_{0.2}(ZIF-62)_{0.8}]$, with no distinct, remnant particles from either ZIF-8 or ZIF-62 observable in this material. Moreover, rounding of edges and formation of necks is clearly visible, which is consistent with the flow of a viscous liquid (**Figure 5.13b**).

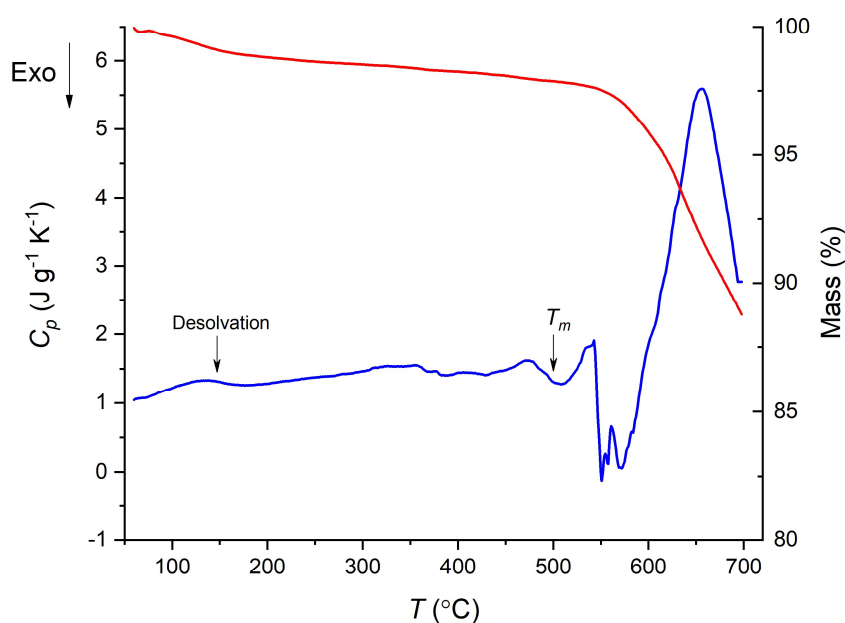


Figure 5.12: Thermal response (blue) and mass (red) curves of (ZIF-8)(ZIF-62)(20/80). Measured at 10 °C/min.

The PXRD pattern of $a_g[(ZIF-8)_{0.2}(ZIF-62)_{0.8}]$, contained no Bragg scattering (**Figure 5.14**) further confirming that the sample was glassy after heat treatment. A sample of pure ZIF-8 was also ball-milled for 5 minutes and heated under argon to 500 °C, then subsequently cooled to room

temperature. A PXRD scan on the recovered sample showed that the crystallinity was preserved (Figure 5.15).

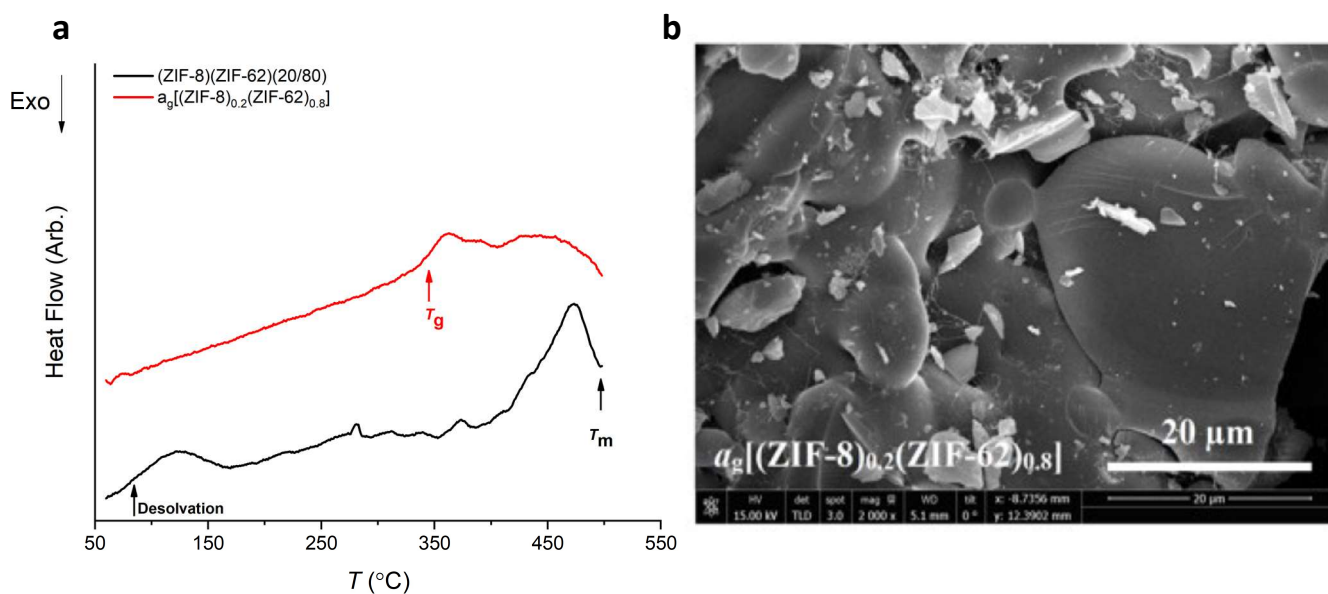


Figure 5.13: DSC and SEM data on $a_g[(ZIF-8)_{0.2}(ZIF-62)_{0.8}]$. **a.** In-situ formation of $a_g[(ZIF-8)_{0.2}(ZIF-62)_{0.8}]$, measured at 10 °C/min. **b.** SEM image of $a_g[(ZIF-8)_{0.2}(ZIF-62)_{0.8}]$.

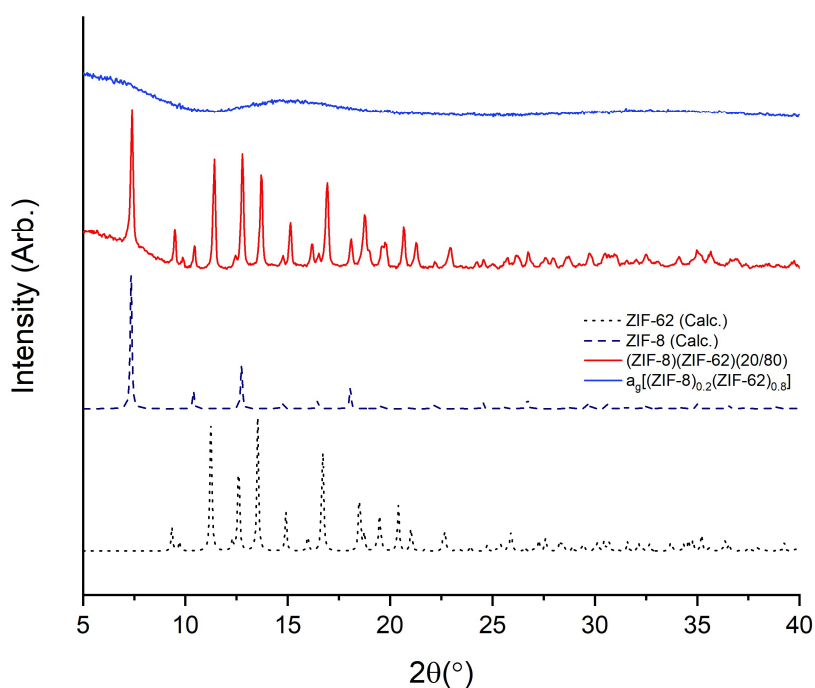


Figure 5.14: PXRD patterns of $(ZIF-8)(ZIF-62)(20/80)$ and $a_g[(ZIF-8)_{0.2}(ZIF-62)_{0.8}]$. Simulated PXRD patterns of ZIF-8 and ZIF-62 produced from published structures are also plotted [48], [67].

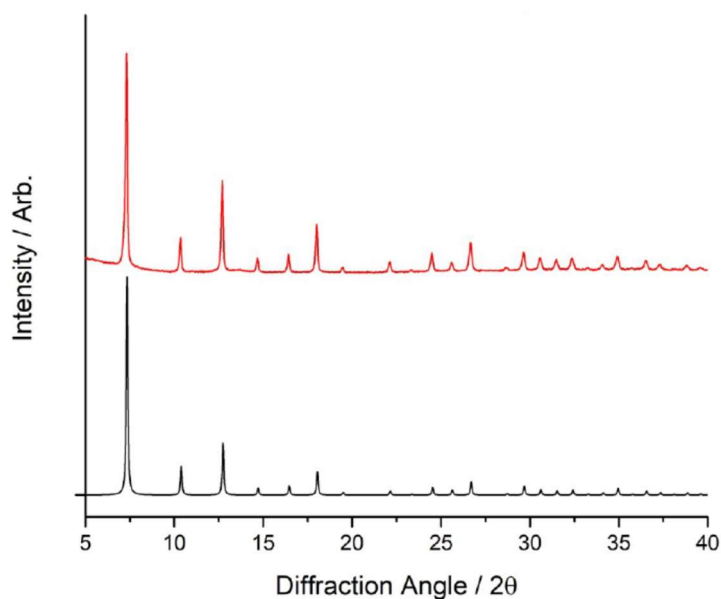


Figure 5.15: PXRD on heat treated ZIF-8 control. Experimental (red) PXRD pattern of ZIF-8, which has been ball milled for five minutes then heated to 500 °C and quenched back to room temperature at 10 °C / min. Simulated (black) PXRD pattern of ZIF-8 reproduced from [67].

An SDT scan on the (ZIF-67)(ZIF-62)(20/80) sample revealed a broad melting endotherm at approximately 460 °C with decomposition occurring just above 500 °C as demonstrated by a rise in the DSC baseline and a decrease in sample mass in the TGA curve (**Figure 5.16**). A sample of $a_g[(ZIF-67)_{0.2}(ZIF-62)_{0.8}]$ was then prepared by heating this mixture to around 500°C in the tube furnace. PXRD demonstrated that the sample was amorphous after heat treatment (**Figure 5.17**).

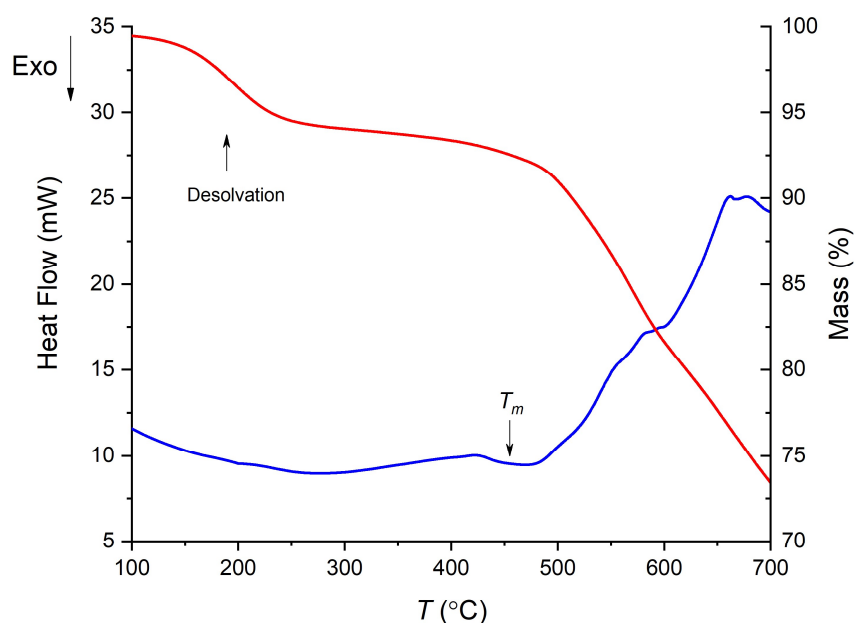


Figure 5.16: Thermal response (blue) and mass (red) curves of (ZIF-67)(ZIF-62)(20/80). Measured at 10 °C/min.

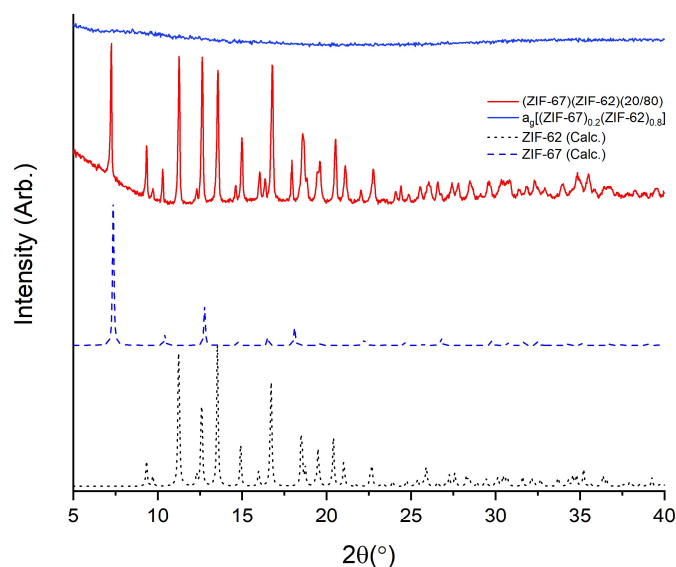


Figure 5.17: PXRD patterns of (ZIF-67)(ZIF-62)(20/80) and $a_g[(ZIF-67)_{0.2}(ZIF-62)_{0.8}]$. Simulated PXRD patterns of ZIF-67 and ZIF-62 produced from published structures are also plotted [48].

5.3.2 Examining the Microstructure of Zeolitic Imidazolate Framework Fluxes through Energy-Dispersive X-ray Spectroscopy

ADF STEM and X-ray EDS were then used to provide chemical element maps in both the crystalline mixture and flux-melted glass samples. In (ZIF-67)(ZIF-62)(20/80), Zn, C, and N were observed in one set of particles, while Co, C and N are seen in a different, segregated set of particles (**Figure 5.18a**). Investigation of a shard of the flux-melted glass, $a_g[(ZIF-67)_{0.2}(ZIF-62)_{0.8}]$, indicated a much more homogeneous distribution of Zn and Co (**Figure 5.18b**), with regions of extensive Co and Zn mixing evident.

However, as mention previously in section 5.2.3, these maps show a two-dimensional representation of a three-dimensional interface. Therefore, it is not possible to unambiguously state that the regions where both Co and Zn observed (**Figure 5.18b**) are due to homogeneous mixing rather than individual, unmixed, Co and Zn domains running through the thickness of the sample. However, particularly in the Co and Zn maps, the preponderance of smooth interfaces observed in $a_g[(ZIF-67)_{0.2}(ZIF-62)_{0.8}]$ contrasts vividly with the prevalence of abrupt interfaces observed in (ZIF-67)(ZIF-62)(20/80).

The gradual variation of Zn and Co in $a_g[(ZIF-67)_{0.2}(ZIF-62)_{0.8}]$ suggests that zinc(II) and cobalt(II) are able to diffuse across significant distances in the flux-mediated melt. These results confirm that the $a_g[(ZIF-67)_{0.2}(ZIF-62)_{0.8}]$ sample has a very distinct microstructure from the $(ZIF-4-Co)_{0.5}(ZIF-62)_{0.5}$

sample detailed in the previous section (**Figure 5.7**), in which the degree of interphase mixing was small and instead mostly separate Zn and Co domains were observed. The microstructural distinction between the flux-melted composites of ZIF-67 and ZIF-62 detailed in this section and glass blends of ZIF-4-Co and ZIF-62 described in the previous section is the reason why we use a distinct terminology to distinguish MOF fluxes from MOF blends.

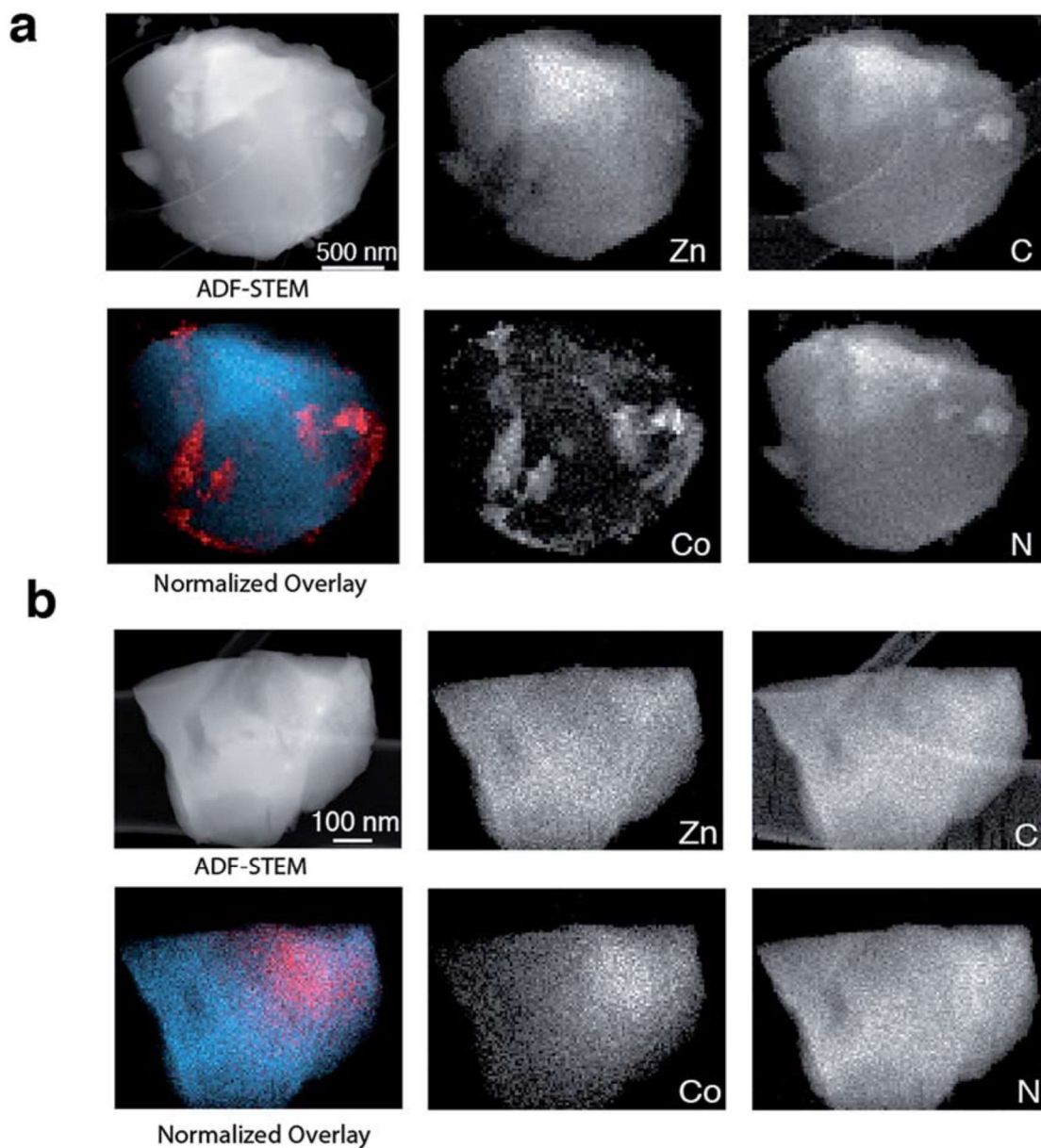


Figure 5.18: Energy dispersive X-ray spectroscopy (EDS) images of ZIF-67/ZIF-62 flux-melted samples. ADF STEM image, EDS elemental maps for C, N, Zn and Co signals, and Zn (blue) and Co (red) component map overlay of **a.** (ZIF-67)(ZIF-62)(20/80). **b.** A shard of $a_g[(ZIF-67)_{0.2}(ZIF-62)_{0.8}]$.

5.3.3 X-ray Total-Scattering Measurements

X-ray total-scattering experiments were carried out on crystalline ZIF-8, (ZIF-8)(ZIF-62)(20/80), and $a_g[(\text{ZIF-8})_{0.2}(\text{ZIF-62})_{0.8}]$. A laboratory based silver source instrument ($\lambda = 0.561 \text{ \AA}$, $Q_{\text{max}} = 22.4 \text{ \AA}^{-1}$) was used to collect total-scattering data. The structure factor $S(Q)$ for the (ZIF-8)(ZIF-62)(20/80) contained Bragg scattering, as expected for this crystalline mixture. On the other hand, consistent with its glassy nature, $a_g[(\text{ZIF-8})_{0.2}(\text{ZIF-62})_{0.8}]$ did not exhibit Bragg diffraction (**Figure 5.19a**). The total-scattering of the $a_g[(\text{ZIF-8})_{0.2}(\text{ZIF-62})_{0.8}]$ and that of the $a_g\text{ZIF-62}$ sample measured in section 4.3.4 were broadly similar, especially beyond the FSDP. This is taken to imply that the $a_g[(\text{ZIF-8})_{0.2}(\text{ZIF-62})_{0.8}]$ sample has SRO and MRO that is consistent with other glassy ZIF structures. The lower position of the FSDP in the $a_g[(\text{ZIF-8})_{0.2}(\text{ZIF-62})_{0.8}]$ sample is interesting, as it may indicate an overall longer maximum correlation length (see Chapter 4), however it is difficult to interpret the significance of the differences in position given the very different measurement set-ups used in each case.

The pair distribution functions, $D(r)$ s, of both (ZIF-8)(ZIF-62)(20/80) and $a_g[(\text{ZIF-8})_{0.2}(\text{ZIF-62})_{0.8}]$ contain peaks at distances in the range 1.3–6 Å that are characteristic of ZIFs (**Figure 5.19b**). The Zn–Zn correlation at around 6 Å in the PDFs of both (ZIF-8)(ZIF-62)(20/80) and $a_g[(\text{ZIF-8})_{0.2}(\text{ZIF-62})_{0.8}]$ is shorter than that measured for the pure ZIF-8 but corresponds well with a simple average of the Zn–Zn distances determined from the CIF files of ZIF-8 (6.012 Å) and ZIF-62 (5.913 Å), [48], [67]. Below this distance there is a much better correspondence between the positions of the peaks in the SRO between $a_g\text{ZIF-62}$, ZIF-8, (ZIF-8)(ZIF-62)(20/80) and $a_g[(\text{ZIF-8})_{0.2}(\text{ZIF-62})_{0.8}]$. This reflects the largely similar intra-ligand bonding between the ZIF-8 and ZIF-62 frameworks and so no peak shifts are observed in the $D(r)$ (**Table 5.1**). The similarity of the peaks in (ZIF-8)(ZIF-62)(20/80) and $a_g[(\text{ZIF-8})_{0.2}(\text{ZIF-62})_{0.8}]$ confirms that the short-range order is maintained on glass formation. The PDF of $a_g[(\text{ZIF-8})_{0.2}(\text{ZIF-62})_{0.8}]$ also shows MRO that is consistent with that of $a_g\text{ZIF-62}$, and flat above approximately 16 Å as would be expected from the amorphous structure. The appearance of large features below 1 Å in the $D(r)$ as well as the increased high frequency noise in the ZIF-8, (ZIF-8)(ZIF-62)(20/80), and $a_g[(\text{ZIF-8})_{0.2}(\text{ZIF-62})_{0.8}]$ samples relative to the $a_g\text{ZIF-62}$ is attributed to the PDFs being acquired on a lab source as opposed to a synchrotron source.

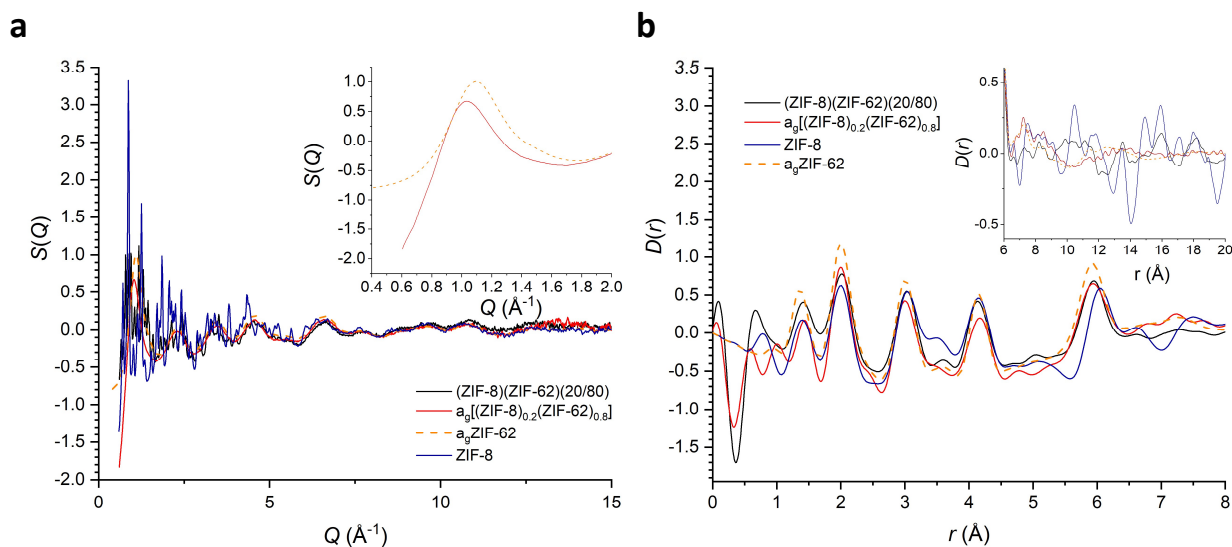


Figure 5.19: Ambient temperature X-ray total-scattering of ZIF-8/ZIF-62 flux-melted samples. **a.** Structure factors $S(Q)$ of (ZIF-8)(ZIF-62)(20/80), $a_g[(ZIF-8)_{0.2}(ZIF-62)_{0.8}]$ and ZIF-8, alongside that of $a_gZIF-62$ (Chapter 4.3.4) **b.** Corresponding X-ray pair distribution functions $D(r)$ the inset shows the MRO.

Table 5.1: Correlation lengths in the short-range order of ZIF-8 and ZIF-62 measured from crystal structures. Published structures reproduced from [48], [67]. When multiple different distances of a given correlation are present, an average is reported along with a standard deviation.

Correlation Identity	Correlation Length ZIF-8 (Å)	Correlation Length ZIF-62 (Å)
C-N/C-C	1.39 ± 0.06	1.36 ± 0.05
Zn-N	1.99	1.98 ± 0.01
Zn-C	3.01	3.00 ± 0.04
Zn-N/Zn-C	4.16 ± 0.01	4.14 ± 0.02
Zn-Zn	6.01	5.91 ± 0.02

5.3.4 Discussion

The results in this section have demonstrated that the presence of the high temperature liquid phase of ZIF-62 can result in amorphisation of crystalline ZIF-8, a framework which does not form a stable high temperature liquid or amorphous state when heated on its own. DSC showed only a single broad melting endotherm and a single glass transition. SEM results showed clear evidence of liquid flow in the heat treated samples. EDS conducted on the cobalt analogue framework samples showed a much

more homogeneous distribution of Co and Zn in $a_g[(\text{ZIF-67})_{0.2}(\text{ZIF-62})_{0.8}]$ than in $(\text{ZIF-67})(\text{ZIF-62})(20/80)$. Finally, the PDF results showed that the SRO of the flux samples was consistent with the SRO of the ZIF-8 and ZIF-62 endmembers as would be expected from the retention of SRO observed during melting of single-phase MOF glasses [56].

From a fundamental view, the successful realisation of flux-melting, which uses the liquid state of ZIF-62 to facilitate the melting of ZIF-8, presents a method by which the T_m of a non-melting framework can be accessed. The importance of parent crystalline framework density in stabilising the liquid state of MOFs has been reported in the literature as a reason for the limited number of existing MOF frameworks which have been found to have an accessible liquid phase [60], [71]. Therefore, MOF fluxes may be a general processing route to the formation of a much wider ranging array of glassy MOF materials than are capable of being formed via melting in the pure phase.

5.4 Further Examples of Flux-Melting

It was initially believed that ZIF-76 and ZIF-76-mblm (**Figure 5.20**) had accessible liquid states when heated in inert atmospheres and could be quenched to form glasses. These frameworks stand in contrast to the melting ZIFs discovered previously as they have much lower framework densities. ZIF-76 possesses a framework density of 2.07 zinc centres per nm³, which is extremely low when compared with ZIF-4 which has a density of 3.68 zinc centres per nm³ [43], [48]. Moreover ZIF-76 and ZIF-76-mblm both have the LTA topology in contrast with the other previously discovered mixed linker melting frameworks which have the **cag** topology (**Chapter 2.5**) [56]. As such this discovery was viewed as extremely surprising. Later work revealed that small amounts of other ZIF frameworks, ZIF-UC-5 for ZIF-76 and TIF-4 for ZIF-76-mblm were necessary to promote melting in these samples (**Figure 5.21**). ZIF-UC-5 has a density of 3.50 zinc centres per nm³ and TIF-4 has a density of 3.46 zinc centres per nm³, and subsequent research has shown that without the presence of these dense phases neither framework melted on its own [71]. Considering these findings, the PXRD of the as-synthesised ZIF-76-mblm used in this study was re-evaluated, which revealed clear evidence of TIF-4 impurities (**Figure 5.22a**). However, ZIF-UC-5 impurities are less obvious in the sample of as-synthesised ZIF-76 (**Figure 5.22b**). Despite this other subsequent research on the ZIF-62 system has revealed that the presence of even a small proportion of an impurity phase can have a dramatic effect on the observed thermal behaviour; with small ZIF-zni impurities and poor imidazolate mixing drastically changing the melting behaviour of industrially produced ZIF-62 [5].

Therefore, the results presented here are an unintended example of flux-melting, which shows that the flux-melting process can be generalised to other ZIF chemistries. During this section the crystalline mixed phases are written as (ZIF-76)(ZIF-UC-5) and (ZIF-76-mblm)(TIF-4) and the amorphous flux-melted glasses as a_g[(ZIF-76)(ZIF-UC-5)] and a_g[(ZIF-76-mblm)(TIF-4)] to emphasise that the pure phases do not melt on their own. However, as TIF-4 and ZIF-UC-5 are unintentional impurities their precise amounts were not known and so are not stated.

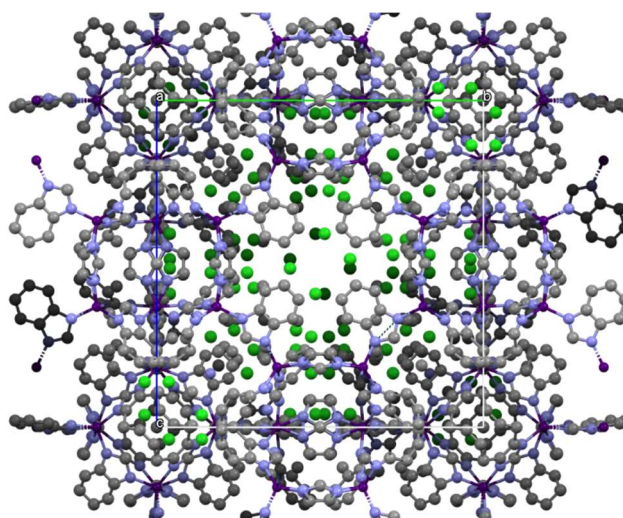


Figure 5.20: Crystal structure of ZIF-76. Reproduced from [48]. Note: this structure exhibits a large amount of positional disorder in the linkers. Key: Grey - Carbon, Blue – Nitrogen, Purple - Zinc. Hydrogen atoms omitted for clarity.

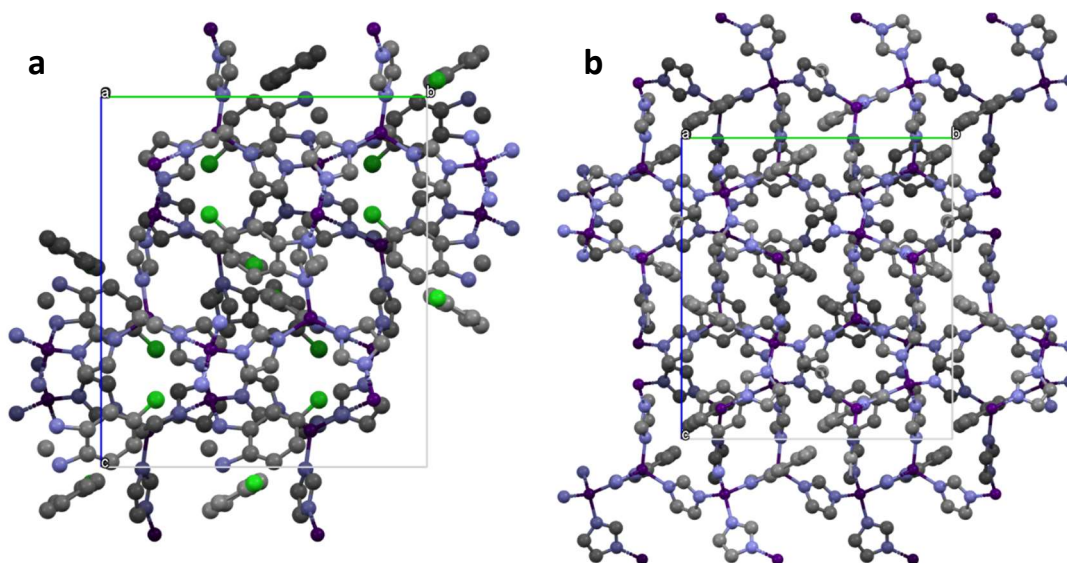


Figure 5.21: Crystal structures of **a.** ZIF-UC-5 and **b.** TIF-4. Reproduced from [65], [120]. Key: Grey - Carbon, Blue – Nitrogen, Purple - Zinc. Hydrogen atoms omitted for clarity.

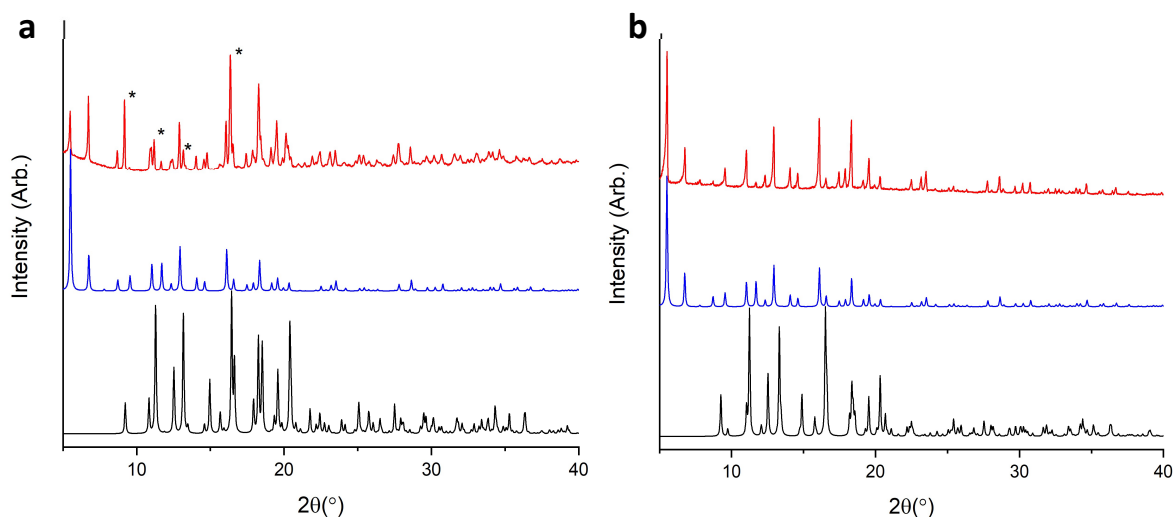


Figure 5.22: PXRD patterns of (ZIF-76-mblm)(TIF-4) and (ZIF-76)(ZIF-UC-5). **a.** (ZIF-76-mblm)(TIF-4) (red) alongside PXRD patterns of ZIF-76 (blue) and TIF-4 (black) simulated from published structures [48], [120]. TIF-4 impurities are marked with asterisks. **b.** (ZIF-76)(ZIF-UC-5) (red) alongside PXRD patterns of ZIF-76 (blue) and ZIF-5-UC (black) simulated from published structures [48], [65].

5.4.1 Thermal and Powder X-ray Diffraction Characterisation

DSC measurements showed that the (ZIF-76)(ZIF-UC-5) sample displayed a melting endotherm, with an offset at 451 °C, when heated in an argon atmosphere. This endothermic peak in the DSC is not accompanied by change in the TGA signal, and occurs before the onset of decomposition (approximately 515 °C) which is defined by the large change in both DSC baseline and rapid loss of sample mass (**Figure 5.23a**). An abrupt peak in the TGA curve, and an accompanying smaller peak in the DSC curve (asterisk **Figure 5.23a**), are clearly unphysical, however as they occur above decomposition they were not investigated further.

A bulk sample of the glass $a_g[(ZIF-76)(ZIF-UC-5)]$ was produced by heating samples of the powdered mixtures in alumina crucibles in a Carbolite 12/65/550 tube furnace under argon to 451 °C at 10 °C/min, followed by cooling, still under argon, at the natural rate of the furnace back to room temperature. A heating scan on this sample revealed a T_g at 310 °C which occurred before decomposition at 511 °C (**Figure 5.23b**).

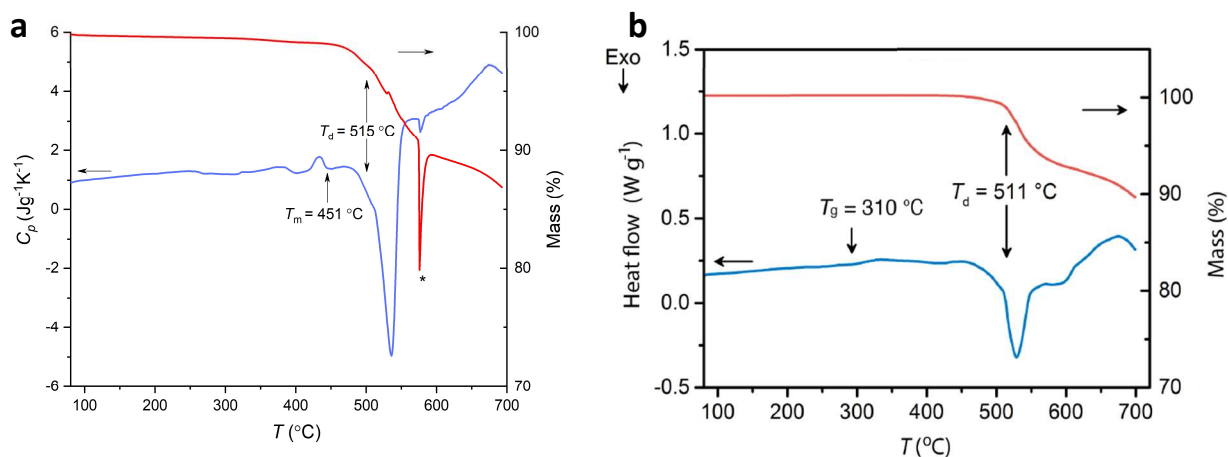


Figure 5.23: Thermal response (blue) and mass (red) curves of **a.** (ZIF-76)(ZIF-UC-5) and **b.** $a_g[(ZIF-76)(ZIF-UC-5)]$. Measured at 10 °C/min.

Similarly, the (ZIF-76-mblm)(TIF-4) sample had a melting endotherm with an offset of approximately 471 °C (**Figure 5.24a**), which occurs below the decomposition temperature of approximately 596 °C. A bulk glass sample of $a_g[(ZIF-76-mblm)(TIF-4)]$ was prepared by heating at 10 °C/min in the tube furnace under argon to 471 °C followed by cooling at the natural rate to room temperature. A scan of this sample was reported as displaying a glass transition at 317 °C (**Figure 5.24b**) [68].

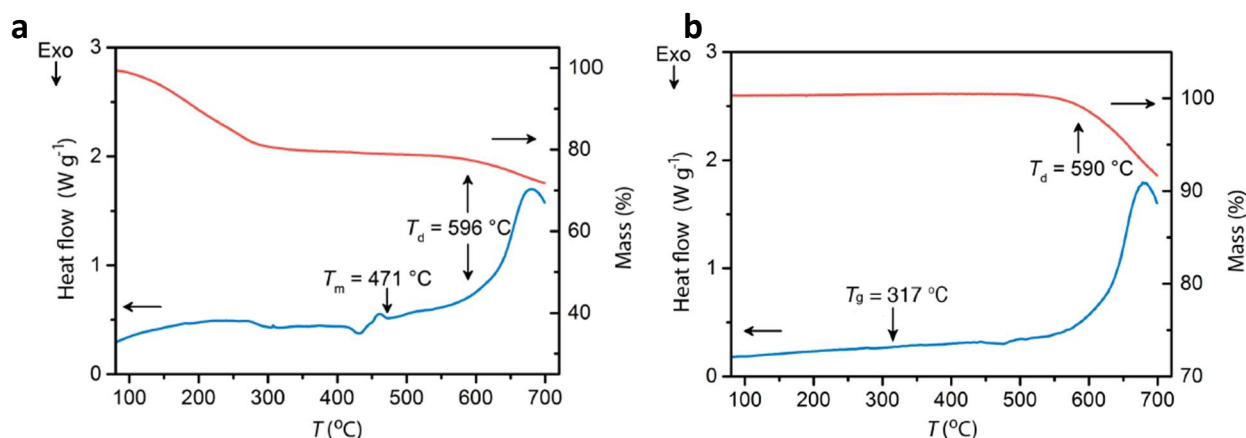


Figure 5.24: Thermal response (blue) and mass (red) curves of **a.** (ZIF-76-mblm)(TIF-4) and **b.** $a_g[(ZIF-76-mblm)(TIF-4)]$. Measured at 10 °C/min.

PXRD conducted on the $a_g[(ZIF-76)(ZIF-UC-5)]$ sample confirmed that it was fully glassy with no evidence of residual crystallisation, which is in contrast to a sample of (ZIF-76)(ZIF-UC-5) heated to just below the melting endotherm (400 °C), which retained Bragg peaks (**Figure 5.25**). Similarly PXRD on the $a_g[(ZIF-76-mblm)(TIF-4)]$ also confirmed that Bragg peaks were absent (**Figure 5.26**).

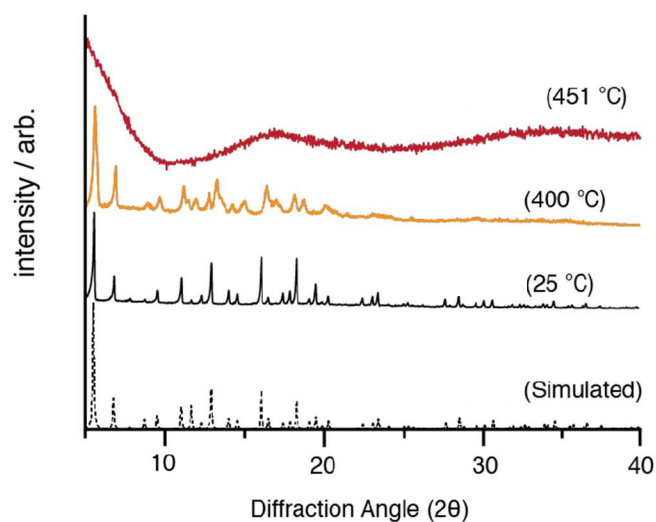


Figure 5.25: PXRD patterns of ZIF-76 ZIF-UC-5 flux-melted samples. As-synthesised (ZIF-76)(ZIF-UC-5) (black), (ZIF-76)(ZIF-UC-5) heated to 400°C (orange) and a_g [(ZIF-76)(ZIF-UC-5)] heated to 451 °C (red). A simulated ZIF-76 pattern based on a literature published structure (dashed) [48] is also shown.

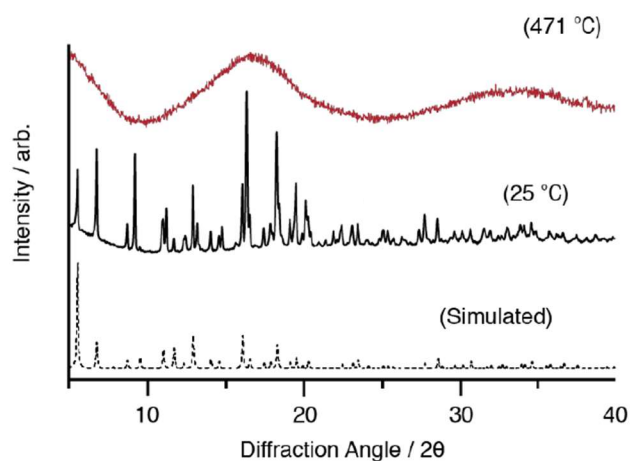


Figure 5.26: PXRD patterns of ZIF-76-mblm TIF-4 flux-melted samples. As-synthesised (ZIF-76-mblm)(TIF-4) (black), and a_g [(ZIF-76-mblm)(TIF-4)] heated to 471 °C (red). A simulated ZIF-76 pattern based on a literature published structure (dashed) [48] is also shown.

5.4.2 Ambient and Variable Temperature X-ray Total-Scattering Measurements

To further probe the structures of the ZIFs before and after vitrification, synchrotron X-ray total-scattering measurements were performed on (ZIF-76)(ZIF-UC-5), (ZIF-76-mblm)(TIF-4), $a_g[(\text{ZIF-76})(\text{ZIF-UC-5})]$ and $a_g[(\text{ZIF-76-mblm})(\text{TIF-4})]$. Room temperature total-scattering data confirmed the glassy nature of $a_g[(\text{ZIF-76})(\text{ZIF-UC-5})]$ with no evident Bragg scattering (**Figure 5.27a**). The pair-distribution function, $D(r)$, confirms that short-range order is retained into the glassy state in $a_g[(\text{ZIF-76})(\text{ZIF-UC-5})]$, as no new peaks or peak shifts are observed in the 1-6 Å range (**Figure 5.27b**). Although there is a broadening and reduction in intensity of features in $a_g[(\text{ZIF-76})(\text{ZIF-UC-5})]$ relative to (ZIF-76)(ZIF-UC-5), which is indicative of de-coordination and increased disorder on forming the glass phase. The MRO is different in (ZIF-76)(ZIF-UC-5) and $a_g[(\text{ZIF-76})(\text{ZIF-UC-5})]$, with $a_g[(\text{ZIF-76})(\text{ZIF-UC-5})]$ lacking features beyond approximately 15 Å, which is indicative of an amorphous structure.

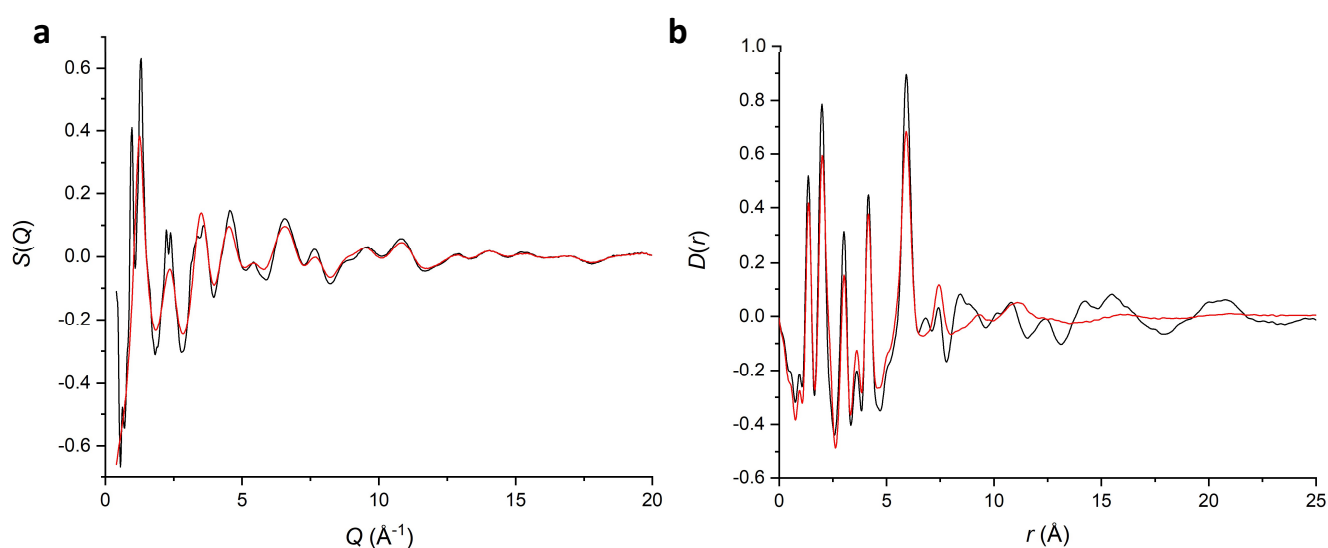


Figure 5.27: Ambient temperature total-scattering of ZIF-76 ZIF-UC-5 flux-melted samples. **a.** Structure factors, $S(Q)$, of (ZIF-76)(ZIF-UC-5) (black) and $a_g[(\text{ZIF-76})(\text{ZIF-UC-5})]$ (red). **b.** Corresponding pair-distribution functions $D(r)$.

The total-scattering of the $a_g[(\text{ZIF-76-mblm})(\text{TIF-4})]$ sample contained a few small Bragg features, although these were much reduced compared to (ZIF-76-mblm)(TIF-4) (**Figure 5.28a**). This could indicate a degree of residual crystallinity, however it may also be due to a small degree of oxidation of Zn during glass formation, resulting in a minor ZnO phase (**Figure 5.28a** inset). The discrepancy between the total-scattering and PXRD results is ascribed to the much higher intensity of the synchrotron source relative to a laboratory source, meaning small peaks are visible in the total-scattering data that are not above the background in the PXRD pattern. The PDF of the $a_g[(\text{ZIF-76-mblm})(\text{TIF-4})]$ sample also shows that SRO is maintained, and less broadening/reduction in features is

observed on glass formation than in $a_g[(ZIF-76)(ZIF-UC-5)]$ (**Figure 5.28b**). This difference is attributed to the small degree of retained crystallinity in $a_g[(ZIF-76-mblm)(TIF-4)]$ relative to in $a_g[(ZIF-76)(ZIF-UC-5)]$. At longer distances in real space, i.e. $r > 7 \text{ \AA}$, small recurring features can be seen in $a_g[(ZIF-76-mblm)(TIF-4)]$, which are also due to the residual crystallinity.

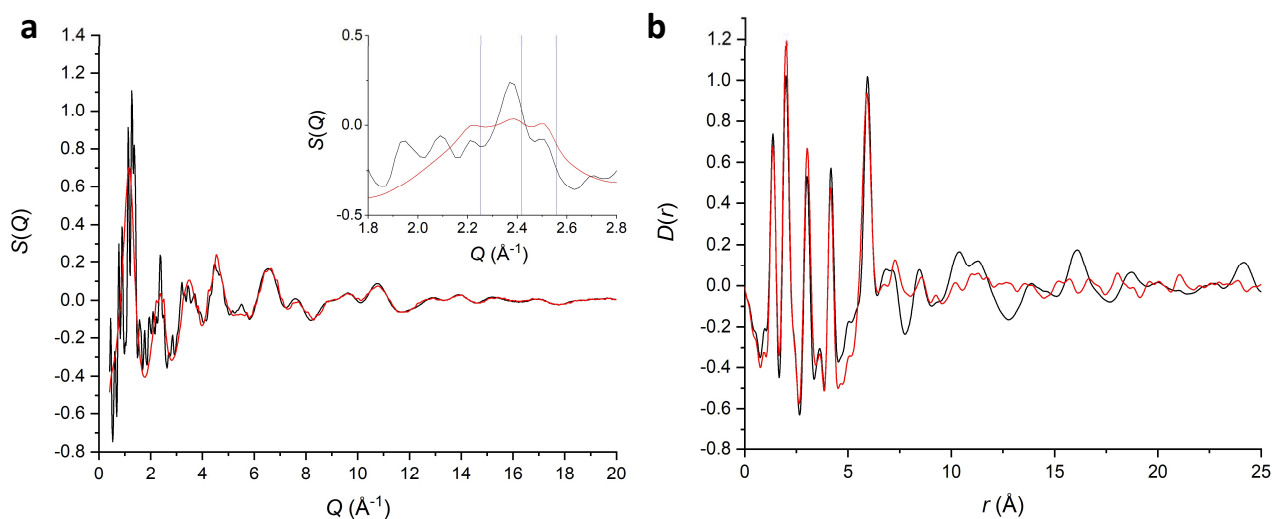


Figure 5.28: Ambient temperature total-scattering of ZIF-76-mblm TIF-4 flux-melted samples. **a.** Structure factors, $S(Q)$, of (ZIF-76-mblm)(TIF-4) (black) and $a_g[(ZIF-76-mblm)(TIF-4)]$ (red). Inset: $S(Q)$, of (ZIF-76-mblm)(TIF-4) (black) and $a_g[(ZIF-76-mblm)(TIF-4)]$ (red) with droplines indicating calculated peak positions of ZnO [121] **b.** Corresponding pair distribution functions $D(r)$.

Variable temperature synchrotron X-ray total-scattering data were collected during the melting process of (ZIF-76)(ZIF-UC-5). Below 470 °C the Bragg peaks remain at approximately the same intensity, however there is an increase in the background between the two peaks (**Figure 5.29a** inset). Bragg peaks disappear completely from the measured total-scattering between 470 – 480 °C, which is in reasonable agreement with the T_m measured in the DSC (451 °C) especially given the very different experimental setups (**Figure 5.23a**). A flattening of features at higher Q is also seen with increasing temperature, particularly at high temperatures after the sample has become amorphous and these higher Q peaks do not fully recover on cooling back to room temperature (**Figure 5.29a**). No dramatic FSDP shifts are observed in the liquid. In real space (**Figure 5.29b**) we see an accompanying increase in the width and drop in intensity of the peaks in the SRO with increasing temperature except for the correlation at approximately 1.3 \AA which varies much more slowly.

These results indicate an increase in disorder and/or de-coordination in the distribution of Zn-linker correlations due to increased amounts of thermal energy in the system. In contrast the intra-linker correlations, i.e. C-N and C-C, at 1.3 \AA [60], which all involve direct covalent bonds, remain

approximately constant. As expected from the observed high Q behaviour and the ambient temperature data (**Figure 5.27b**), the increase in peak widths and drop in amplitudes in the SRO was maintained on cooling back to room temperature. The $D(r)$ of the recovered glass sample also contained no long-range correlations confirming that it remained amorphous (**Figure 5.29b inset**).

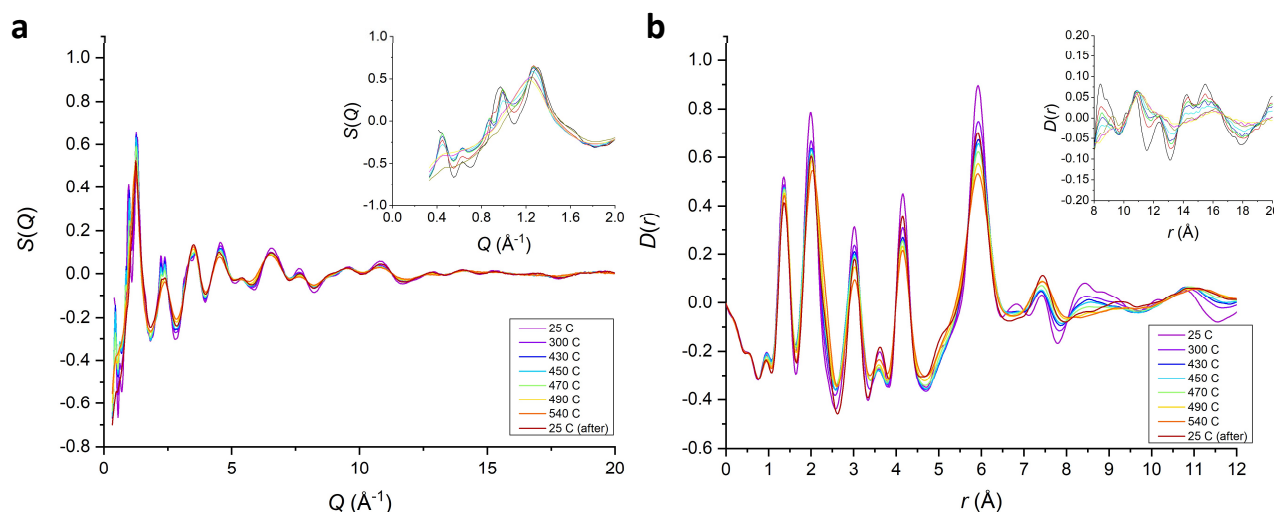


Figure 5.29: Variable temperature X-ray total-scattering data of (ZIF-76)(ZIF-UC-5). **a.** Structure factors $S(Q)$, inset: expanded scale showing the FSDP. **b.** Corresponding pair distribution functions $D(r)$ showing the short-range order, inset: expanded scale showing the long-range structure.

5.4.3 Discussion

The apparent discovery that ZIF-76 and ZIF-76-mblm display endotherms on heating and can be quenched to form a glassy phase was surprising due to the low density of the starting crystalline frameworks. Indeed, subsequent research has shown that phase pure ZIF-76 and ZIF-76-mblm do not melt, and instead decomposed on heating. It was then discovered that a small amount of dense frameworks with the same linker chemistry are required to observe melting [71]. This was found to be ZIF-UC-5 ($\text{Zn}(\text{Im})_{1.8}(\text{Clblm})_{0.2}$) for ZIF-76 and TIF-4 ($\text{Zn}(\text{Im})_{1.5}(\text{mblm})_{0.5}$) for ZIF-76-mblm. Both frameworks crystallise in the $Pbca$ space group with the **cag** topology, structural features which have been shared by all melting heterolinker ZIFs previously identified (**Chapter 2.4**). Re-evaluation of the experimental data confirmed that this was also the case in this study. The discovery that neither ZIF-76 nor ZIF-76-mblm are actually melting frameworks further underscores the importance of the parent crystalline framework density, in supporting the formation of the liquid phase [60]. This effect is believed to be mediated through dispersion interactions which support under-coordination at zinc centres during formation of the melt phase.

Despite unintentional impurities the melting behaviour displayed by the (ZIF-76-mblm)(TIF-4) and (ZIF-76)(ZIF-UC-5) samples demonstrates that the phenomenon of flux-melting described in detail in the previous section can be applied to different ZIF systems. In this case ZIF-76 and ZIF-76-mblm are the frameworks which do not melt on their own, and inclusions of ZIF-UC-5 and TIF-4, which are reported as melting in the pure phase [71], serve as the fluxes which promote melting in the crystalline mixture.

The PDF data showed that the local bonding is maintained on glass formation, as would be expected from previous studies on other glass forming ZIF frameworks. Moreover, variable temperature PDF measurements capture the loss of crystallinity and de-coordination of ligands associated with liquid and glass formation from the parent crystalline framework. Interestingly although local bonding is maintained on glass formation both ambient and in-situ measurements show that the $a_g[(ZIF-76)(ZIF-UC-5)]$ and $a_g[(ZIF-76-mblm)(TIF-4)]$ glasses have lower and broader peaks than their parent crystals, implying more disorder and/or de-coordination in the glass phase.

The higher melting point and glass transition temperature for $a_g[(ZIF-76-mblm)(TIF-4)]$ (471 °C and 317 °C) than for $a_g[(ZIF-76)(ZIF-UC-5)]$ (451 °C and 310 °C) is attributed to the chemical difference between the 5-methylbenzimidazole and 5-chlorobenzimidazole linker. Firstly the methyl group has been reported in the literature as having a larger van der Waals volume of (13.67 cm³ mol⁻¹) compared to a chlorine atom (12.00 cm³ mol⁻¹) [122] and therefore the 5-methylbenzimidazole linker is sterically larger than the 5-chlorobenzimidazole linker. Secondly the chlorine group is electron withdrawing from the conjugate system, thus the imidazolate anion is stabilised in 5-chlorobenzimidazolate. In contrast the methyl group is electron donating and therefore increases the energy of the anion. Less stable anions will have a lower driving force for Zn-N bond fission. Moreover, sterically larger linkers are likely to have a higher activation energy for diffusion away from the centre. Taken together, and given that the mechanism of ZIF melting involves de-coordination and linker exchange at the zinc centre [60], these two factors result in a higher melting temperature in (ZIF-76-mblm)(TIF-4) relative to (ZIF-76)(ZIF-UC-5). These factors also explain the higher T_g of $a_g[(ZIF-76-mblm)(TIF-4)]$ relative to $a_g[(ZIF-76)(ZIF-UC-5)]$, as more thermal energy would be required for viscous flow to occur in a more sterically hindered system.

5.5 Conclusions

Total-scattering methods, PXRD, DSC, and SEM were used to characterise complex glass samples formed from multiple parent crystalline ZIF frameworks. Initially a blended sample was formed between two glass forming frameworks ZIF-4 and ZIF-62. EDS data on the $(\text{ZIF-4-Co})_{0.5}(\text{a}_g\text{ZIF-62})_{0.5}$ sample revealed a structure of interlocking domains originating from the parent crystalline frameworks. This observation is entirely consistent with the observed mechanism of MOF melting, which proceeds via imidazolate dissociation from a M^{2+} centre, and subsequent association of a different imidazolate ligand [60]. We therefore attribute the domain structure to an interfacial ligand 'swapping' between both frameworks, resulting in a fully amorphous, interlocking but heterogenous structure. The limited degree of mixing observed is ascribed to both the high viscosity of the ZIF-62 and ZIF-4 liquid phases and the difficulty of infiltration of MOF liquid into the dense frameworks. This picture of de-coordination in the liquid phase of the blend was further confirmed by variable temperature PDF data, which showed a reversible drop intensity in SRO correlations as the sample was heated above its T_g .

The discovery of blends formation, and particularly the miscibility of the interface in the $(\text{ZIF-4-Co})_{0.5}(\text{a}_g\text{ZIF-62})_{0.5}$ sample, led to the attempt to use a liquid ZIF to drive melting in a structure which would not amorphise if heated in isolation. This resulted in the discovery of flux-melting in ZIF frameworks and the formation of amorphous $\text{a}_g[(\text{ZIF-67})_{0.2}(\text{ZIF-62})_{0.8}]$ and $\text{a}_g[(\text{ZIF-8})_{0.2}(\text{ZIF-62})_{0.8}]$ samples. EDS mapping revealed a more homogeneous structure in the flux-melted sample. This microstructural difference between $\text{a}_g[(\text{ZIF-67})_{0.2}(\text{ZIF-62})_{0.8}]$ and $(\text{ZIF-4-Co})_{0.5}(\text{a}_g\text{ZIF-62})_{0.5}$ is attributed to both the higher temperatures required to achieve melting in the flux-melted sample and to the higher porosity of ZIF-67 than ZIF-4-Co, which may allow more infiltration of the framework by the melt and therefore more homogeneous mixing to occur. Indeed, the existence of flux-melting is rationalised by the presence of the molten ZIF stabilising de-coordination in the ZIF-8/ZIF-67 centres through ligand swapping and dispersion interactions, both of which imply intimate mixing.

Flux-melting due to the presence of dense TIF-4 and ZIF-UC-5 MOF phases was also found to be necessary for glass formation in ZIF-76-mblm and ZIF-76 respectively. This finding expands the work on flux-melted frameworks by demonstrating that flux-melting occurs in systems where both the porous frameworks and the dense flux have the same chemistry. This shows that flux-melting is a general phenomenon which can be used to promote glass formation in a wide variety of parent crystalline frameworks.

Variable temperature PDF data on the $(\text{ZIF-76})(\text{ZIF-UC-5})$ phase showed that some degree of de-coordination of correlations in the SRO observed during melting is maintained into glass formation.

This finding is distinct from the observations from the variable temperature total-scattering reported for the $(\text{ZIF-4-Co})_{0.5}(\text{a}_g\text{ZIF-62})_{0.5}$ sample. In this case the broadening and loss of amplitude in peaks in the SRO region of the $D(r)$, which had been observed on heating through T_g , was seen to be reversible on cooling.

Importantly studies on $(\text{a}_g\text{ZIF-4})_{0.5}(\text{a}_g\text{ZIF-62})_{0.5}$, $\text{a}_g[(\text{ZIF-8})_{0.2}(\text{ZIF-62})_{0.8}]$, $\text{a}_g[(\text{ZIF-76-mblm})(\text{TIF-4})]$, and $\text{a}_g[(\text{ZIF-76})(\text{ZIF-UC-5})]$ have shown that the reactivity of the ZIF melt is an important route towards the production of a broad range of hybrid glasses. The work of this chapter has demonstrated two different routes, blend and flux formation, by which the range of linker chemistries which are accessible to the MOF glass phase can be expanded and by which the physical properties of MOF glasses might be tuned.

Chapter 6: Metal-organic Framework and Inorganic Glass Composites

The work in this chapter was published in:

L. Longley et al., "Metal-organic framework and inorganic glass composites," *Nat. Commun.*, vol. 11, no. 1, p. 5800, 2020.

The inorganic glasses used in the screening section were made by Dr Quyen Huyen Le (University of Jena) and used as received. Aside from this, synthesis of the samples in this section was done in collaboration with Courtney Calahoo (University of Jena). I performed PXRD, thermal characterisation, SEM, EDS and reflected light microscopy measurements. Confocal microscopy, NMR, IR and Raman results were carried out by Dr Courtney Calahoo. René Limbach (University of Jena) was responsible for nanoindentation and scratch testing and Yang Xia (University of Jena) and Courtney Calahoo carried out conductivity measurements. X-ray total-scattering measurements were carried out by Dr Dean S. Keeble (Diamond Light Source) and I, and interpretation of the data and development of the differential total-scattering technique was carried out by Prof. David Dave A. Keen (ISIS) and me.

6.1 Introduction

This thesis has previously described how new 'complex' MOF glass materials can be produced by exploiting the reactivity of high temperature MOF liquids (**Chapter 5**). The fabrication of such materials is very similar to those observed with other classes of glass materials, i.e. organic polymer blends [116] or borosilicates, mixed-alkali glasses and aluminosilicates in the inorganic domain, or metallic glass alloys [30], [118]. This ability to tune physical properties via the miscibility of the liquid phase is highly advantageous in industrial and technological applications, for example, in order to achieve specific mechanical performance [123].

The structural similarity of glass MOFs to inorganic SiO₂ has been examined in the literature [54], [59] and expanded here (**Chapter 4**). Moreover, blend formation in ZIF glass systems in a manner analogous to compatible polymer blends has been described in the previous chapter (**Chapter 5.2**). Similarly the observation of flux-melting in ZIF-8 - ZIF-62, ZIF-76-mblm – TIF-4 and ZIF-76 – ZIF-UC-5 systems (**Chapter 5.3** and **5.4**) has demonstrated that the MOF liquid is capable of acting as a solvent to incorporate other MOF components.

Therefore, motivated by the prior work and the well described miscibility of other glass systems, this section describes the formation and characterisation of an unconventional class of composite materials, containing domains of both inorganic- and MOF glasses. The aim of these composite

materials is to incorporate the mechanical, thermal, and chemical properties of inorganic glasses, and the chemical versatility of the metal-organic framework component into a single glassy phase.

The novelty of these proposed composite materials, and the wide variety of available MOF glass – inorganic glass pairs means that consideration needs to be given to the choice of both the MOF, and inorganic glass. One key factor is thermal compatibility. The processing temperature must be sufficiently above the T_g of the inorganic glass, and the T_m of the ZIF that sufficient liquid flow can occur during heat treatment; this is to enable good mixing between the two liquid phases and therefore promote formation of strong interfacial bonding between the components. However, this temperature must also be low enough that the ZIF phase remains below its decomposition temperature (T_d), i.e. $T < T_d$, during heat treatment, and that recrystallisation of the inorganic glass is avoided. The other important consideration is chemical compatibility, the chemistry of the inorganic and ZIF glasses must be such that reactions leading to decomposition during high temperature liquid phase mixing do not occur.

6.2 Zeolitic Imidazolate Framework Component Selection

At the time of the start of this work the number of ZIF melting frameworks, which had been described in detail in the literature, was limited to ZIF-4, ZIF-GIS, TIF-4 and ZIF-62 [56]. ZIF-62 was chosen, as it had the widest reported window between T_m (437 °C) and the onset of decomposition (approx. 600 °C) [56]. This enabled us to maximise the temperature region available for composite synthesis.

Crystalline ZIF-62 was synthesised by a method adapted from the literature [61] (**Chapter 3.2.3**). Three separate batches of ZIF-62 were used in this study, one for the screening experiments (**Chapter 6.3**), one for the production of the heat treated composites, and one for the evacuated powder mixtures and controls (**Chapter 6.4**). The same synthesis methodology was followed, with the exception that the synthesis used to produce the composite samples involved a mixture of two filtrations of product (**Chapter 3.2.3**). PXRD showed that the batches were equivalent (**Figure 6.1a**). Pawley refinement of data of the activated framework from the control sample confirmed that the products of the synthesis were consistent with the literature (**Figure 6.1b**).

To provide a point of comparison with the composite samples, a bulk sample of pure a_g ZIF-62 glass was produced by heating under argon in a tube furnace to 410 °C at 10 °C/min and holding for 1 minute. PXRD showed that the sample was completely amorphous with a broad FSDP centred at approximately 16 ° (**Figure 6.1c**). Visually the a_g ZIF-62 was a completely transparent series of glass shards (**Figure 6.1d**).

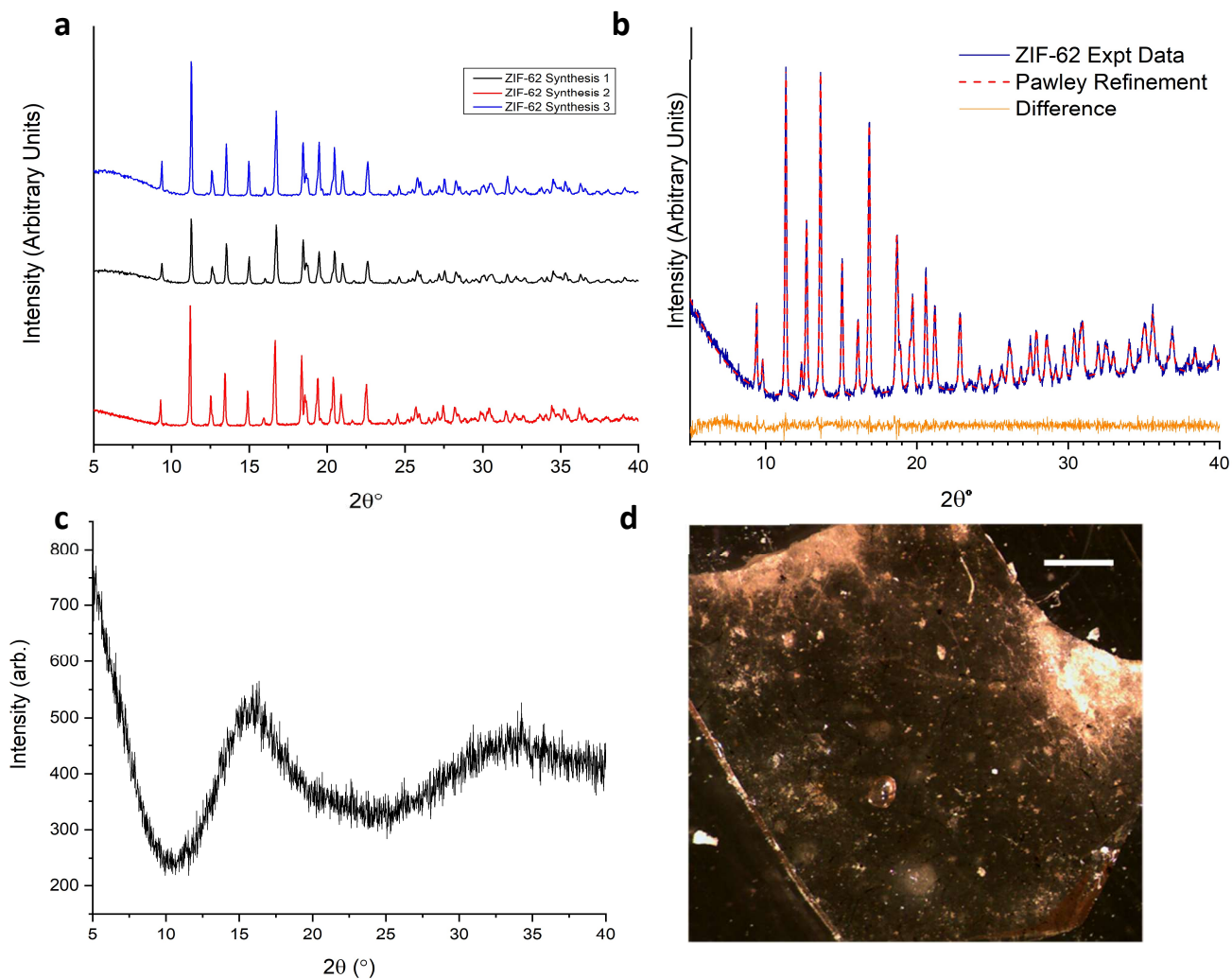


Figure 6.1: PXRD and optical microscopy of ZIF-62. **a.** PXRD Patterns of the three as-synthesised ZIF-62 batches used in this study. **b.** Pawley refinement of the evacuated ball milled ZIF-62 sample. $R_{wp} = 5.535$. Refined unit cell values: $a = 15.486 \pm 0.005 \text{ \AA}$, $b = 15.545 \pm 0.005 \text{ \AA}$, $c = 17.984 \pm 0.004 \text{ \AA}$. Initial parameters ($a = 15.6620 \text{ \AA}$, $b = 15.6621 \text{ \AA}$, $c = 18.2073 \text{ \AA}$) were obtained from [48]. **c.** PXRD pattern of the a_g ZIF-62 sample. **d.** Reflected light microscopy of the a_g ZIF-62 sample, the white bar in the image is 1 mm.

6.3 Inorganic Glass Screening

Inorganic glasses exhibit a very broad range of chemistries and thermal and physical properties [30], and therefore a screening process was undertaken to identify a composition which was both thermally and chemically compatible for composite formation. Although no prior direct investigations on the reactivity of the liquid ZIF phase with inorganic glasses has been published, there are extensive literature reports of a system of hybrid glassy materials produced from zinc phosphate chains intercalated with imidazole [37]–[39], which may indicate a broader compatibility between imidazole ligands and phosphate glasses. Additionally, researchers have reported that benzimidazole can be used as a solvent to dissolve a zinc metaphosphate glass. This formed a single amorphous phase that ^{13}C MAS-NMR revealed showed evidence of coordination of benzimidazole around the zinc centres [124].

6.3.1 The Structures of Phosphate Glasses

Taken together these results indicate potential compatibility between phosphate glasses and the zinc imidazolate chemistry of ZIFs. The screening therefore focused primarily on combinations of ZIF-62 and phosphate glasses. However phosphate glasses have a wide array of structures and properties [72] and therefore even narrowing the search to this inorganic glass family still leaves a large scope and necessitates a screening process.

A wide variety of different phosphate glass compositions were provided for this screening process by Dr Le (**Table 6.1**). The compositions involving sodium as well as Inorganic VII were described in detail in the literature [125], the compositions involving caesium are unpublished, but were produced in a similar way to the sodium-containing compositions. In all cases the compositions stated (**Table 6.1**) are nominal and based off the ratios of reagents added to the melt. As these inorganic glass samples were only intended for use as part of a broad screening process no further characterisation of them was undertaken.

Table 6.1: Inorganic glasses used in the composite screening process.

Sample Code	Composition
I	Na ₂ O-P ₂ O ₅
II	CsO-P ₂ O ₅
III	25CsO-25ZnO-50P ₂ O ₅
IV	60NaPO ₃ -40AlF ₃
V	70NaPO ₃ -20Na ₂ SO ₄ -10AlF ₃
VI	55NaPO ₃ -10Cs ₂ SO ₄ -35AlF ₃
VII	(10 MgF ₂ + 23.4 CaF ₂ + 19.4 SrF ₂ + 32.2 AlF ₃) + 15 SrSO ₄

Pure vitreous phosphate, a_gP₂O₅, has structures based around tetrahedral coordination of oxygen atoms around phosphorous. Unlike in silica the phosphorous has 5 valence electrons, one of which is promoted into a 3d orbital, which forms π bonding interactions with electrons in the 2p orbital of oxygen [72] resulting in a double bond (**Figure 6.2a**). This creates a structure in which tetrahedra are only joined to three other tetrahedra at the corners. Despite this difference a_gP₂O₅ is reported as adopting a CRN network much like a_gSiO₂ [72].

The introduction of network modifiers, ionic oxides formed with alkali metals (M'₂O) or alkaline earth metals (MO), into the structure disrupts the connectivity of the network by creating non-bonding oxygens. The connectivity of each phosphate centre is described by Q^x terminology where x is the number of bridging oxygens in each tetrahedra (**Figure 6.2b**). The effect of modifier cations can therefore be understood in terms of the pseudo reaction and example equation:



Glasses with 50 mol % modifier cation composition, MPO₃, are known as metaphosphates and are composed of long chains of Q² phosphates. At higher proportions of modifiers, pyrophosphate structures composed of Q¹ dimers form. Finally at the highest modifier contents invert glasses form, which are molecular, i.e. not CRN, in nature and are composed of Q¹ and Q⁰ units [72].

Samples I, II and III examined here are metaphosphates. These structures are structurally similar to the chain like zinc phosphate imidazolate hybrid structures previously discussed [37]–[39]. Across the I-III series, the effect of varying the modifier cation is examined; different cations have different field strengths due to their varying sizes and this affects the strength of the ionic bonds in the glass structure. In sample III the effect of including Zn^{2+} in the inorganic phase is examined, this is of interest as it was hypothesised that having Zn^{2+} present in both the inorganic and ZIF-62 phases might facilitate bonding at the interface.

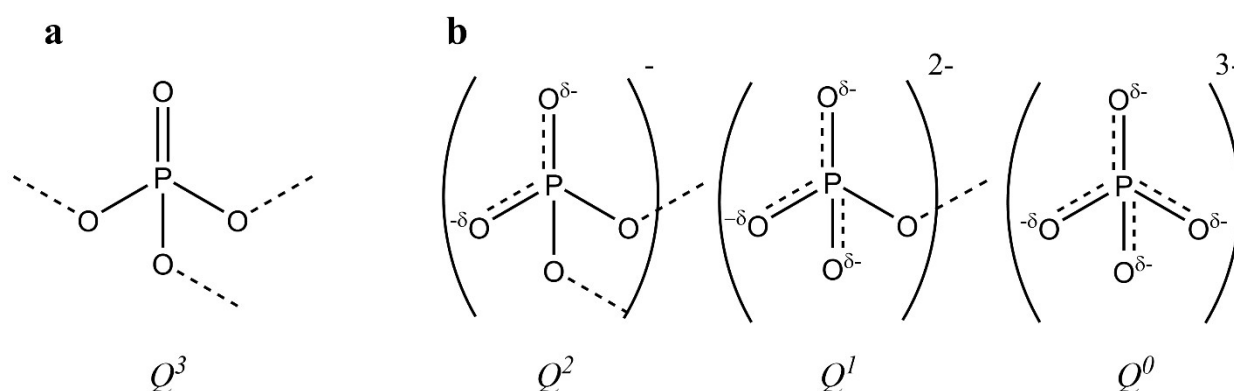


Figure 6.2: Schematic phosphate glass structure. **a.** Fully connected (Q^3) phosphate tetrahedra. **b.** Phosphate tetrahedra with increasing numbers of non-bonding oxygen as modifier is added (modifier cations omitted for clarity).

Sample IV is a metaphosphate glass to which AlF_3 has been added. Al^{3+} is octahedrally coordinated, forming $Al(OP)_4F_2$ structures (**Figure 6.3a**) which break up the Q^2 phosphate chains through the conversion of P-O-P bonds to Al-O-P bonds. However this also increases the average connectivity of the structure, due to the crosslinking effect of the six-coordinate Al, which causes more topological constraint raising the activation energy for chain motion and therefore increasing T_g [126]. This glass was included to examine the effect of varying T_g while ensuring that the structure remained broadly polymeric and metaphosphate in nature.

Samples V and VI are analogous structures in which Na_2SO_4 or Cs_2SO_4 has also been introduced. In contrast to Al^{3+} , SO_4^{2-} does not bond directly to the phosphate network, i.e. no P-O-S bonds are formed. Instead SO_4^{2-} exists as isolated tetrahedral ions (**Figure 6.3b**), [127]. As sulfate ions do not increase the cross linking of the network their inclusion lowers the T_g while having even less of an effect on the

overall polymeric bonding of the metaphosphates than AlF_3 . As such they were included to examine the effect of lowering T_g while also maintaining broadly metaphosphate connectivity.

The final glass composition, VII, is a fluorite as opposed to a phosphate glass. Fluorite glasses adopt a wide variety of structures, from CRN type structures to more ionic random close-packed network structures comprised of packed distorted polyhedra, in which the bonding is predominantly ionic in character [33]. This composition was published in [125] where it is included as the end member of a phosphate containing series, and its structure was not characterised in detail. It was included as part of the screening process as a partial control for the IV-VI samples as it would allow the effect of SO_4^{2-} and AlF_3 inclusion to be investigated in the absence of the phosphate backbone.

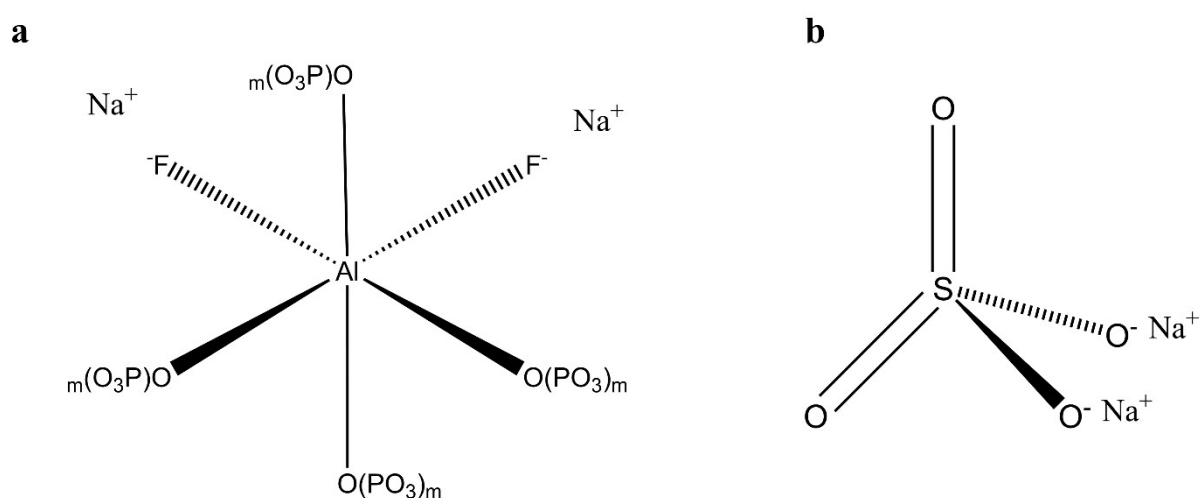


Figure 6.3: Schematic structure of AlF_3 and SO_4^{2-} in phosphate glasses. **a.** Octahedrally coordinated $\text{Al}(\text{OP})_4\text{F}_2$ structure formed when AlF_3 is added to metaphosphates, $(\text{PO}_3)_m$ chains indicate phosphate of variable length composed of Q^2 and Q^1 phosphates [126]. **b.** Tetrahedral SO_4^{2-} anion which exists as an isolated structural unit when MSO_4 is added to the metaphosphate glass [127].

6.3.2 Experimental Screening Results

50 mg of as-synthesised ZIF-62 and 50 mg of each inorganic glass were mixed through 5 minutes of grinding with a pestle and mortar. This was done instead of ball milling, owing to the small amounts of mixture required for the screening process. These mixtures are then referred to as (50/50) ZIF-62 Inorganic X, where X = I-VII (**Table 6.1**). The screening process had two stages; first the powdered mixture was heated under argon to 700 °C in a simultaneous DSC TGA (SDT), overall stability was monitored by the onset of mass loss as measured by TGA and interesting thermal features were identified in the DSC curve. Secondary scans heated new samples of the powdered mixtures past these regions of interest and then recovered them back to room temperature so that PXRD could help elucidate the identity of any features observed in the PXRD. To save time during the screening process

these samples were air-cooled rather than cooling more slowly under argon, despite this, due to the speed of the cooling (approximately 40 °C/min), no evidence for oxidation of the ZIF component was observed.

During these experiments the baseline in the DSC was found to be highly variable and features were broad and shallow. Different combinations of annealing temperatures (100°C or 200°C) and heating rates (10°C/min and 20°C/min) were used to attempt to improve this and enhance the visibility of thermal features. The specific details of the method used for each sample are described in the caption of the relevant figure.

The TGA curve of the (50/50) ZIF-62 Inorganic glass I sample demonstrated continual mass loss across the entire temperature range (**Figure 6.4**). No evidence of a ZIF-62 melting endotherm could be observed, however this may be due to the appearance of a broad exothermic feature with an onset at 404°C. The large and continuous mass loss was indicative of ZIF-62 decomposition and this composition was not investigated further. A broad endothermic feature with an onset at approximately 420°C was observed in (50/50) ZIF-62 Inorganic glass II which may be ZIF-62 melting. However, the sample still lost mass continuously and so was not investigated further (**Figure 6.5**).

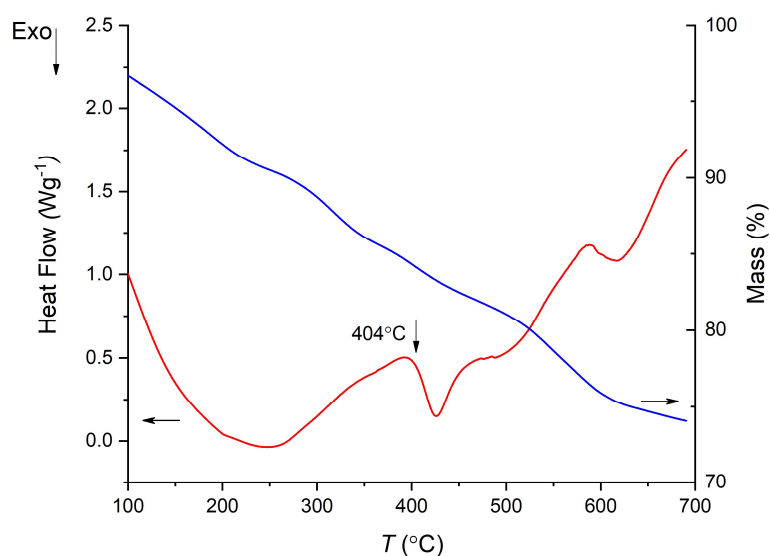


Figure 6.4: Thermal response (red) and mass curve (blue) of the (50/50) ZIF-62 Inorganic glass I sample. Heated under argon at 20°C/min.

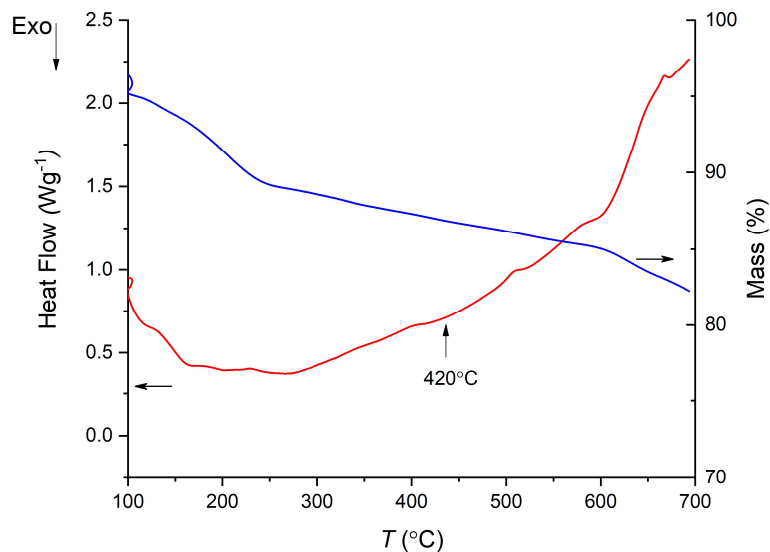


Figure 6.5: Thermal response (red) and mass curve (blue) of the (50/50) ZIF-62 Inorganic glass II sample. Heated under argon at 20°C/min to 100°C, isothermal for 5 minutes, then heated to 700°C at 10°C/min.

The mass of the (50/50) ZIF-62 Inorganic glass III sample was stable after desolvation up to approximately 350°C before it began to continually lose mass again at approximately 350 °C (**Figure 6.6**). A broad endothermic feature within this temperature range, with an offset of 310°C was investigated via PXRD.

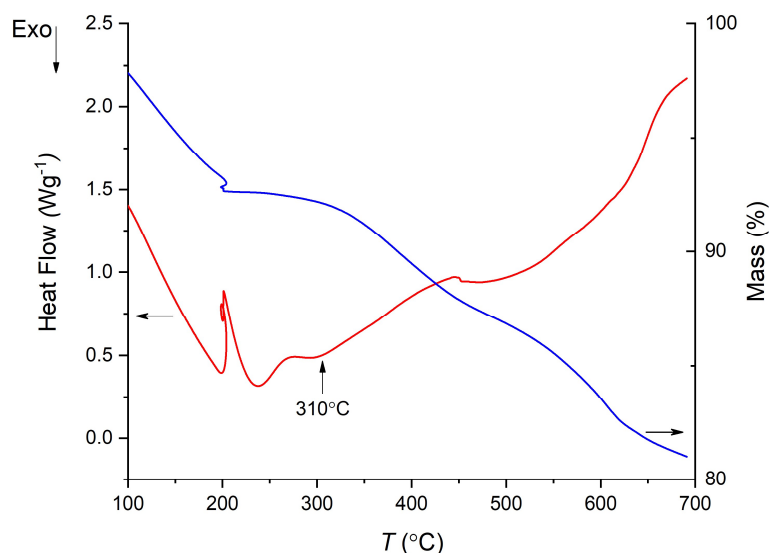


Figure 6.6: Thermal response (red) and mass curve (blue) of the (50/50) ZIF-62 Inorganic glass III sample. Heated under argon at 20°C/min to 200°C, isothermal for 15 minutes, then heated to 700°C at 20°C/min. Note the odd feature at approx. 200 °C is an artifact caused by displaying isothermal data on a temperature scale.

The recovered sample was found to have small residual ZIF-62 peaks and so had not formed a fully amorphous composite (**Figure 6.7**). This, combined with vastly reduced stability of the ZIF framework, 350 °C as opposed to 600 °C as measured in the literature [56], precluded further investigation of this inorganic glass.

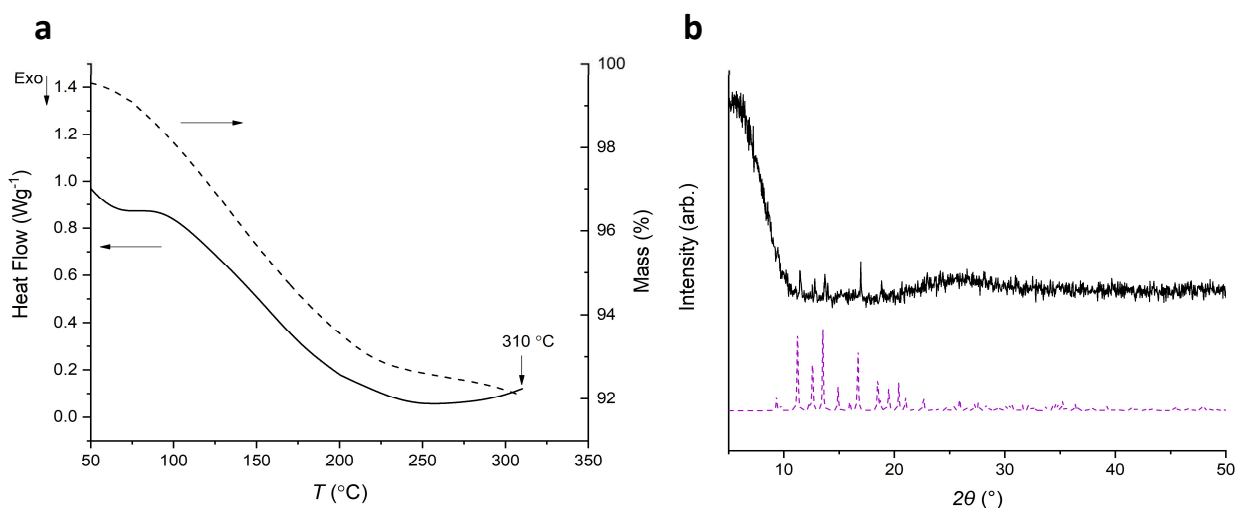


Figure 6.7: Recovery SDT and PXRD on the (50/50) ZIF-62 Inorganic glass III sample. **a.** Thermal response (black) and mass curve (dashed) of (50/50) ZIF-62 Inorganic glass III heated under argon to 310 °C at 20 °C/min. **b.** PXRD of the (50/50) ZIF-62 Inorganic glass III sample recovered alongside a reference pattern of ZIF-62 [48].

The (50/50) ZIF-62 Inorganic glass IV had a constant mass after desolvation at approximately 200 °C, before the onset of mass loss at approximately 500 °C. A broad endotherm with an offset of approximately 450 °C was also observed which is consistent with ZIF-62 melting (**Figure 6.8**). A sample recovered from past this endotherm (**Figure 6.9a**) showed diffuse scattering with broad peaks at approximately 16 and 32 °2 θ (**Figure 6.9b**), consistent with the scattering from the a_g -ZIF-62 (**Figure 6.1c**).

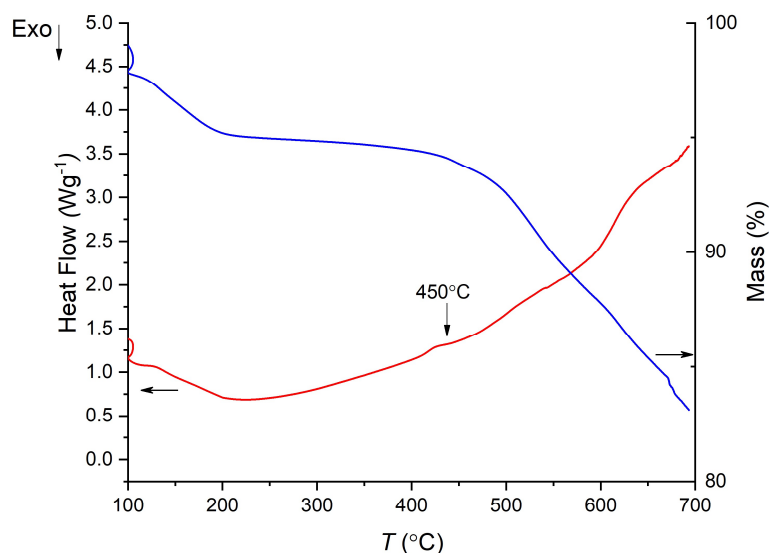


Figure 6.8: Thermal response (red) and mass curve (blue) of the (50/50) ZIF-62 Inorganic glass IV sample. Heated under argon at 20°C/min to 100°C, isothermal for 5 minutes, then heated to 700°C at 10°C/min.

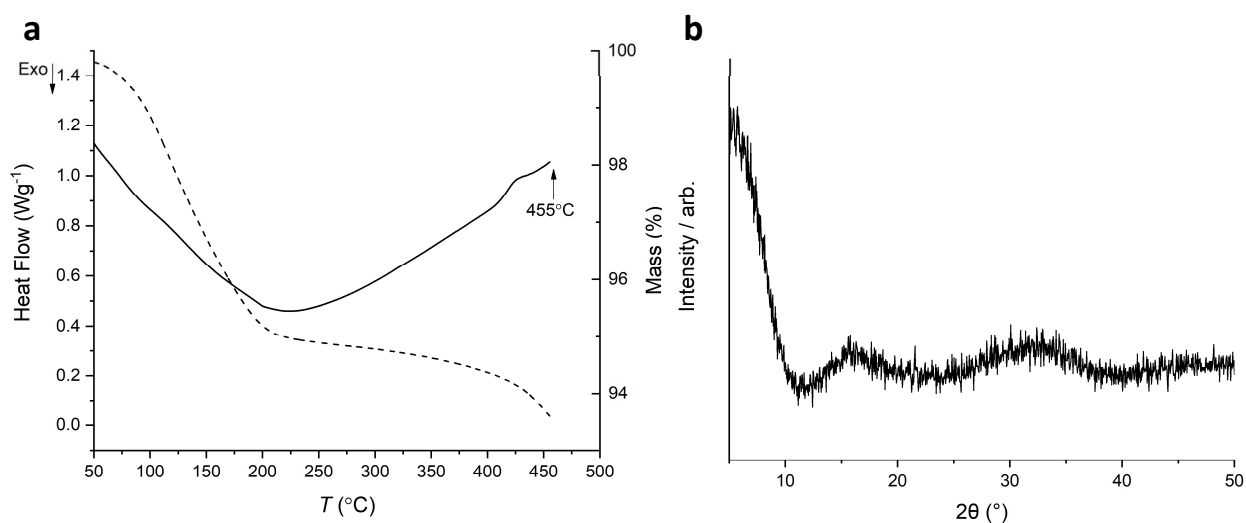


Figure 6.9: Recovery SDT and PXRD on the (50/50) ZIF-62 Inorganic glass IV sample. **a.** Thermal response (black) and mass curve (dashed) of (50/50) ZIF-62 Inorganic IV glass heated under argon to 455°C at 10°C/min. **b.** PXRD of the recovered (50/50) ZIF-62 Inorganic IV glass sample.

The (50/50) ZIF-62 Inorganic V glass sample had slightly lower thermal stability than (50/50) ZIF-62 Inorganic glass IV with a drop in mass occurring at around 450°C (**Figure 6.10**). A T_g at 298°C was observed followed by an exothermic feature between 360-430°C. The sample recovered from 361°C had residual ZIF-62 peaks, whereas the sample recovered from 431°C had a small number of broad

low intensity Bragg peaks, which were attributed to recrystallisation of an inorganic phase from its coincidence with the observed exotherm (**Figure 6.11**)

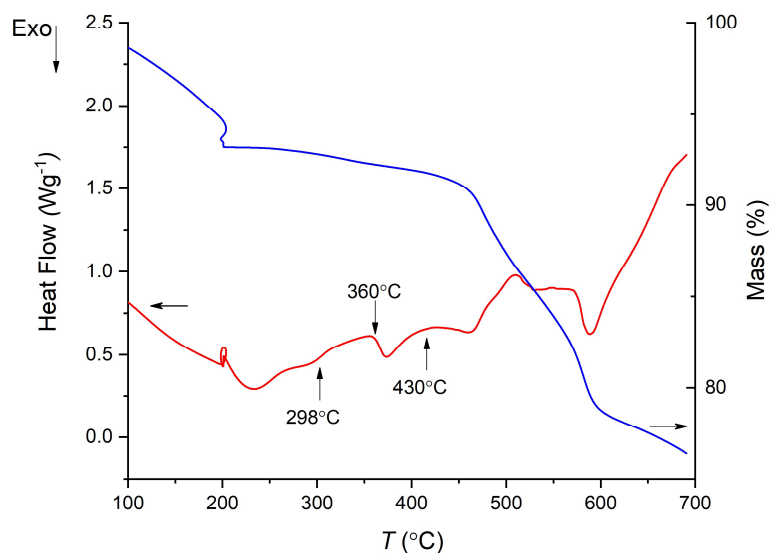


Figure 6.10: Thermal response (red) and mass curve (blue) of the (50/50) ZIF-62 Inorganic V glass sample. Heated under argon at 20°C/min to 200°C, isothermal for 15 minutes, then heated to 700°C at 20°C/min.

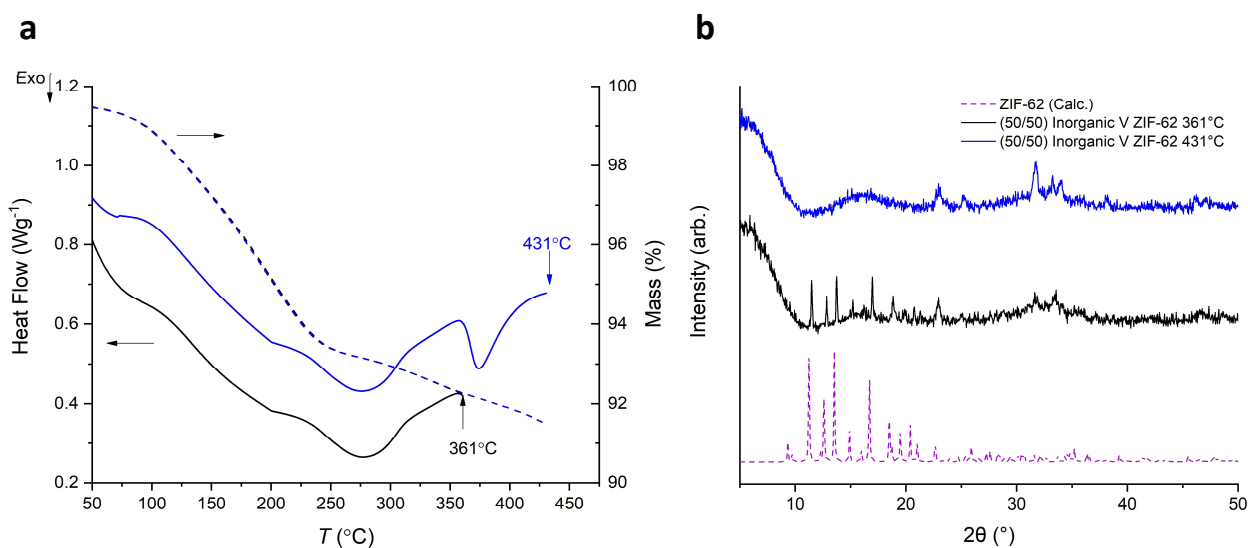


Figure 6.11: Recovery SDT and PXRD on the (50/50) ZIF-62 Inorganic glass V sample. **a.** Thermal responses (solid) and mass curves (dashed) of (50/50) ZIF-62 Inorganic glass V heated to 361 °C (black) and 431 °C (blue) at 20 °C /min under argon. **b.** PXRD of the recovered (50/50) ZIF-62 Inorganic glass V samples, alongside a reference pattern of ZIF-62 [48].

The (50/50) ZIF-62 Inorganic glass VI had a wide range of thermal stability, displaying a gradual mass loss after approximately 500 °C (**Figure 6.12**). In the DSC a broad endothermic feature at 315°C, followed by a T_g at 380 °C, before an exotherm with an onset at 425°C was observed. PXRD scans on samples recovered from 316 °C, 434 °C, and 479 °C revealed that the ZIF-62 remained crystalline at 316°C and that the exotherm was due to recrystallisation of the inorganic glass (**Figure 6.13**).

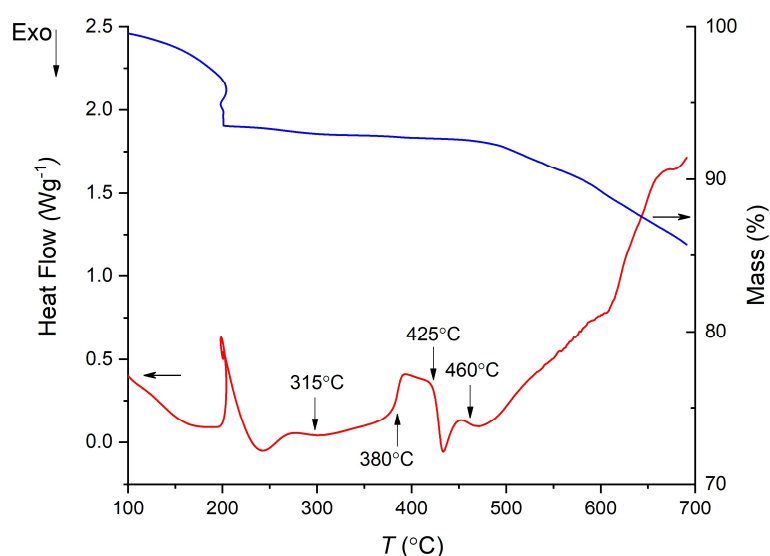


Figure 6.12: Thermal response (red) and mass curve (blue) of the (50/50) ZIF-62 Inorganic glass VI sample. Heated under argon at 20°C/min to 200°C, isothermal for 15 minutes, then heated to 700°C at 20°C/min.

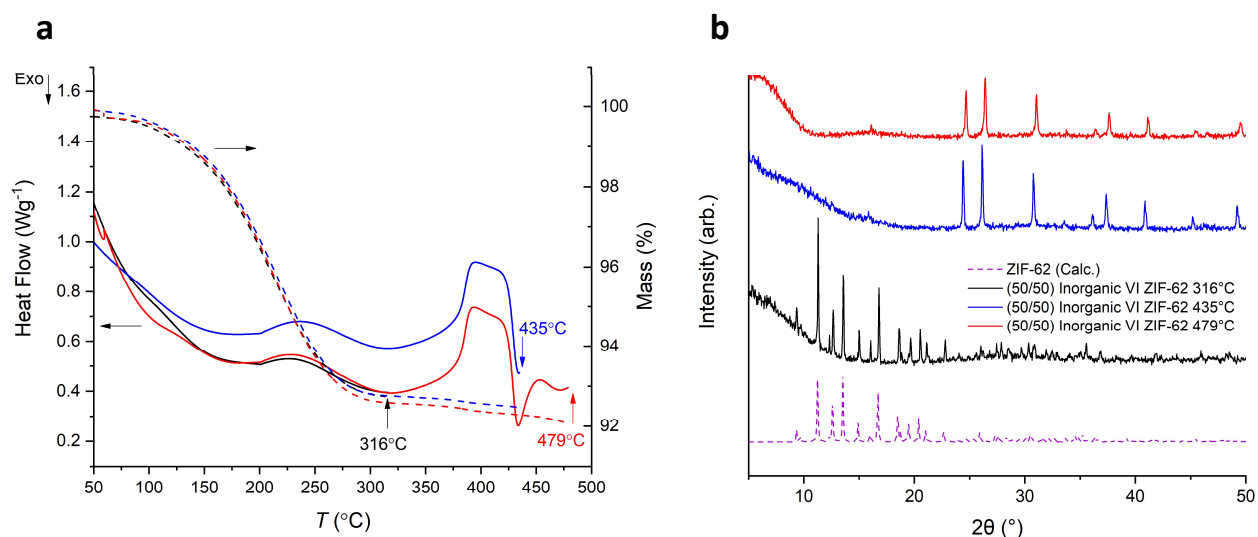


Figure 6.13: Recovery SDT and PXRD on the (50/50) ZIF-62 Inorganic glass VI sample. **a.** Thermal responses (solid) and mass curves (dashed) of (50/50) ZIF-62 Inorganic glass VI heated to 316 °C (black) and 435 °C (blue) and 479 °C (red) at 20 °C/min under argon. **b.** PXRD of the recovered (50/50) ZIF-62 Inorganic VI glass samples alongside a reference pattern of ZIF-62 [48].

Finally, and surprisingly given it is not a phosphate glass, (50/50) ZIF-62 Inorganic glass VII had the largest region of stable mass with the onset of decomposition not occurring until 600°C, at approximately the same value reported for pure phase ZIF-62 [56] (**Figure 6.14**). A rise in the baseline at 405°C followed by a sharp exotherm between 454-500 °C was observed in the DSC. PXRD on samples heated in the SDT to 431 °C, 460 °C and 505 °C revealed that a sample recovered from 431°C was fully amorphous whereas those recovered from higher temperatures contained Bragg peaks due to recrystallisation of the inorganic glass (**Figure 6.15**).

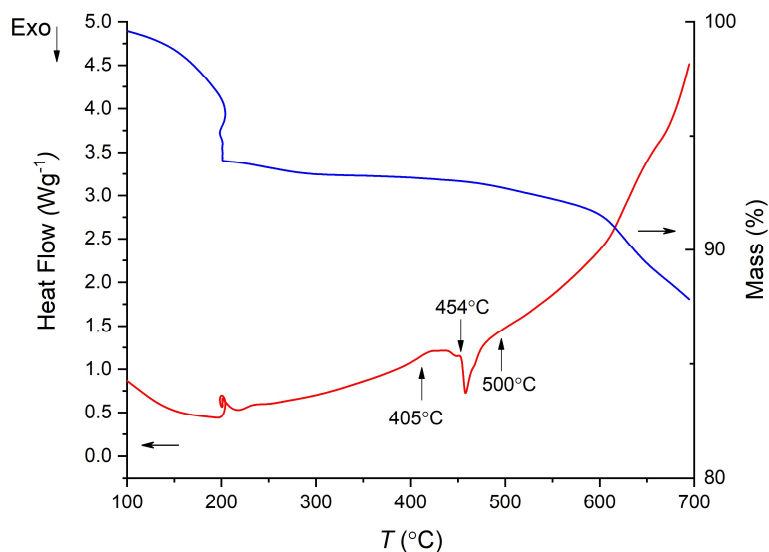


Figure 6.14: Thermal response (red) and mass curve (blue) of the (50/50) ZIF-62 Inorganic VII glass sample. Heated under argon at 20°C/min to 200°C, isothermal for 15 minutes, then heated to 700°C at 10°C/min.

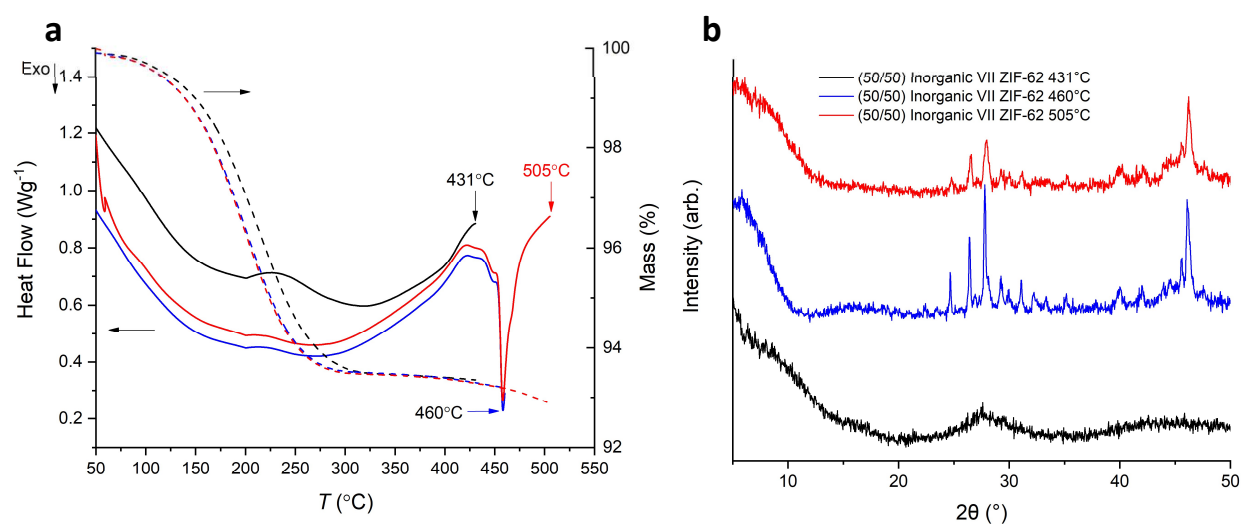


Figure 6.15: Recovery SDT and PXRD on the (50/50) ZIF-62 Inorganic glass VII sample. **a.** Thermal responses (solid) and mass curves (dashed) of (50/50) ZIF-62 Inorganic glass VII heated to 431 °C (black) at 10 °C /min under argon and 460 °C (blue) and 505 °C (red) at 20 °C /min under argon. **b.** PXRD of the recovered (50/50) ZIF-62 Inorganic glass VII samples.

This screening process reveals that full amorphous samples can be produced from the (50/50) ZIF-62 Inorganic glass IV and (50/50) ZIF-62 Inorganic glass VII samples through heating to 455°C and 431°C respectively. These temperatures are below the onset of thermal decomposition as assessed by the TGA curve. It was decided to proceed with composite formation and detailed characterisation using a series of inorganic glasses structurally similar to Inorganic glass IV as the recrystallisation of Inorganic glass VII at 454 °C limits the processing range available for composite formation. Moreover, the kinetic theory of glass formation [30], indicates that recrystallisation may be more of an issue in bulk samples produced in the tube furnace where cooling rates are much slower and time spent at elevated temperatures is therefore much longer.

6.4 Composition and structure of the Inorganic Glass IV

Following from the promising results on Inorganic glass IV, we synthesised a series of similar inorganic glasses (**Chapter 3.2.3**). Their precise composition was determined by EDS (**Table 6.2**). The formulae reported for this series are different from the nominal $x\text{NaPO}_3\text{-(100-x)AlF}_3$ formula of Inorganic glass IV due to the difficulties in synthesising fluorine-rich glasses. Fluorine can exchange with oxygen present as water in the raw materials or in the melt atmosphere and then leave the melt as HF gas leading to a reduction in the amount of AlF_3 , which is replaced with Al_2O_3 , in the final glass [128].

The glass formulae are written as a series with general composition $(1-x)([\text{Na}_2\text{O}]_z[\text{P}_2\text{O}_5])\text{-}x([\text{AlO}_{3/2}][\text{AlF}_3]_y)$ where z and y represent 1: z and 1: y ratios of P_2O_5 : Na_2O and $\text{AlO}_{3/2}$: AlF_3 respectively to emphasise the amounts of each reagent that are in the glass sample. The precise formulae of the glasses are specified according to this scheme (**Table 6.2**). Due to the lengthy names of the formula these compositions are subsequently referred to as base, Na-deficient and Al-rich. The names Na-deficient and Al-rich are chosen relative to the base composition to express the fact that these samples have a lower amount of Na and a higher $[\text{Al}]/[\text{P}]$ ration respectively.

Table 6.2: Glass compositions analysed by EDS for the inorganic glass series.

Inorganic Glass	Analysed (mol%)			
	P_2O_5	Na_2O	Al_2O_3	AlF_3
base	31.6 ± 0.2	52.0 ± 0.1	7.1 ± 0.1	9.4 ± 0.1
	$0.78([\text{Na}_2\text{O}]_{1.6}[\text{P}_2\text{O}_5])\text{-}0.22([\text{AlO}_{3/2}][\text{AlF}_3]_{0.7})$			
Na-deficient	38.7 ± 0.2	33.3 ± 0.1	7.1 ± 0.1	20.9 ± 0.2
	$0.67([\text{Na}_2\text{O}]_{0.9}[\text{P}_2\text{O}_5])\text{-}0.33([\text{AlO}_{3/2}][\text{AlF}_3]_{1.5})$			
Al-rich	28.3 ± 0.2	47.2 ± 0.1	13.6 ± 0.1	11.0 ± 0.1
	$0.66([\text{Na}_2\text{O}]_{1.7}[\text{P}_2\text{O}_5])\text{-}0.34([\text{AlO}_{3/2}][\text{AlF}_3]_{0.4})$			

The $(1-x)([\text{Na}_2\text{O}]_z[\text{P}_2\text{O}_5])\text{-}x([\text{AlO}_{3/2}][\text{AlF}_3]_y)$ glass is comprised of two major domains [126]: (i) chains of phosphate tetrahedra connected through bridging P-O-P, with some terminal non-bridging oxygens (NBOs) associated with sodium ($\text{P-O}\cdot\text{Na}^+$) marked as $Q^1\text{-}Q^2\text{-}Q^1$ linkages (**Figure 6.16**). (ii) Islands of AlO_4F_2 octahedra, which are strongly bonded to the phosphate chains through Al-O-P bridging bonds and that are connected to some isolated phosphate tetrahedra, Q^0 (**Figure 6.16**) [126]. AlO_4F_2 octahedra may also be connected to each other through Al-F-Al bonds, particularly at the higher aluminium content Al-rich and Na-deficient samples. Fluorine is also present in the form of P-F bonds in some phosphate tetrahedra (PO_3F), where it occupies a similar role to a non-bonding oxygen with

its charge counter-balanced by a Na^+ counterion. P-F-Al bonding is not reported to occur due to unfavourable energetic considerations involving the high valence of P [126].

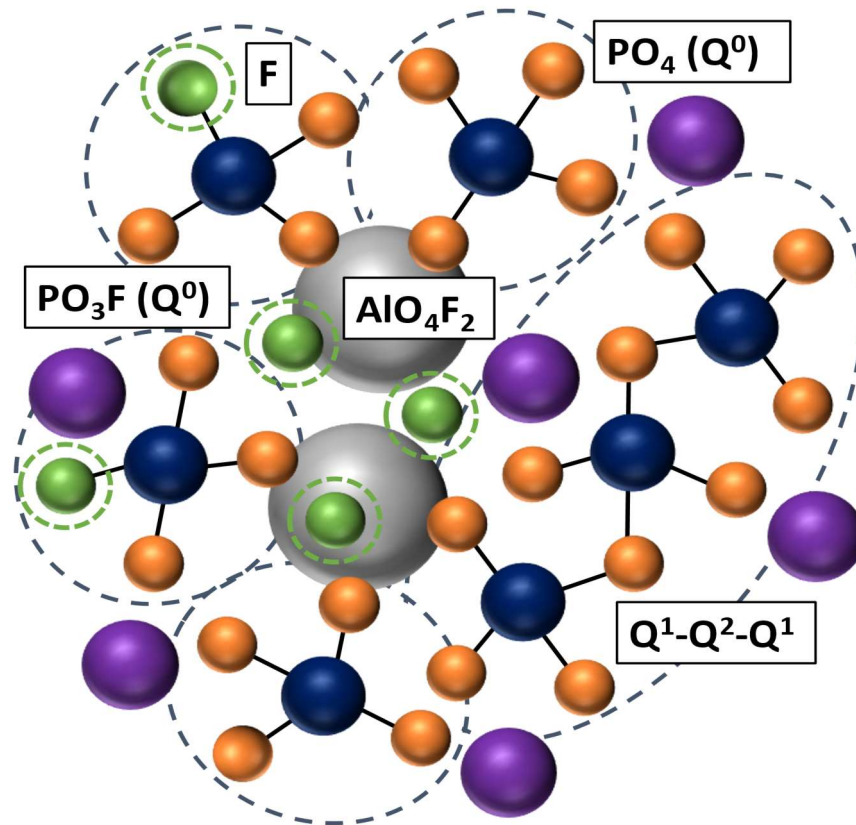


Figure 6.16: The local structure of the $(1-x)([\text{Na}_2\text{O}]_z[\text{P}_2\text{O}_5])_x([\text{AlO}_{3/2}][\text{AlF}_3]_y)$ glass series. Key: Dark blue - Phosphorus, Orange - Oxygen, Light Grey – Aluminium, Green - Fluorine, Purple - Sodium.

6.5 Thermal Characterisation

Approximately 300 mg of crystalline ZIF-62 and 300 mg of inorganic glass powders were mixed through ball milling in a stainless-steel jar (15 ml) for 5 minutes at 25 Hz with one 5 mm stainless steel ball (**Figure 6.17**). Consistent with previous literature on MOF blends and composites [129], the full name for these physical mixtures takes the form (ZIF-62)((1-x)[Na₂O]_z[P₂O₅])_z-x([AlO_{3/2}][AlF₃]_y) (50/50). We also note that this naming convention is distinct from that used for the composite samples in which the crystalline ZIF-62 and inorganic glass powders were combined via hand grinding. We use the shortened naming convention (ZIF-62)(Inorganic Glass) (50/50) here, for readability and clarity.

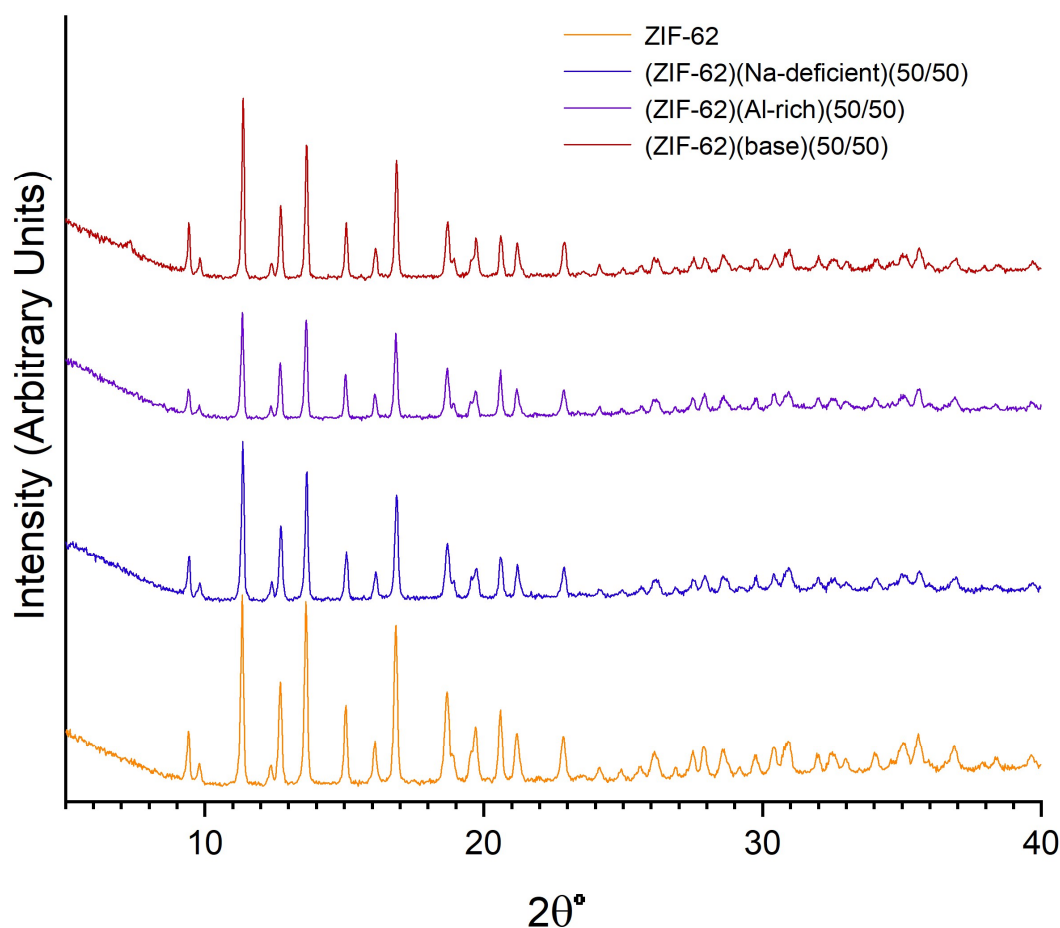


Figure 6.17: Powder X-ray diffraction patterns of the ball milled evacuated (ZIF-62)(Inorganic Glass)(50/50) mixtures and pure ZIF-62.

To provide a point of comparison for the thermal behaviour of the composite samples, a sample of crystalline ZIF-62 was heated in the DSC. The initial heating curves of ZIF-62 samples showed a melting event, with an offset at approx. 434 °C (**Figure 6.18**). The second heating curve of these samples, i.e. after they were held at 450 °C for 1 or 30 minutes and then cooled, displayed clear T_g at 322 °C (**Figure 6.18a**) and 314 °C (**Figure 6.18b**) respectively, which is consistent with literature data on ZIF-62 [56]. Additionally, to enable identification of features in the DSC scans of the (ZIF-62)(Inorganic Glass) (50/50) samples, DSC scans on each of the inorganic glasses were conducted in order to measure the position of their T_g s (**Figure 6.19**). Al-rich was found to have a T_g at 449 °C, Na-deficient at 414 °C and the base at 372 °C.

Each of the (ZIF-62)(Inorganic Glass) (50/50) samples was then heated above the melting endotherm of ZIF-62, i.e. to 450 °C, and the mixtures held for either 1 or 30 minutes at this temperature. Measurements on all samples were also made during a second heating ramp to 450 °C after cooling under argon at 10 °C/min. The two different high temperature isothermal times were used to measure the effect of liquid phase mixing between the inorganic glass and the ZIF-62 on the structure of the resulting composite.

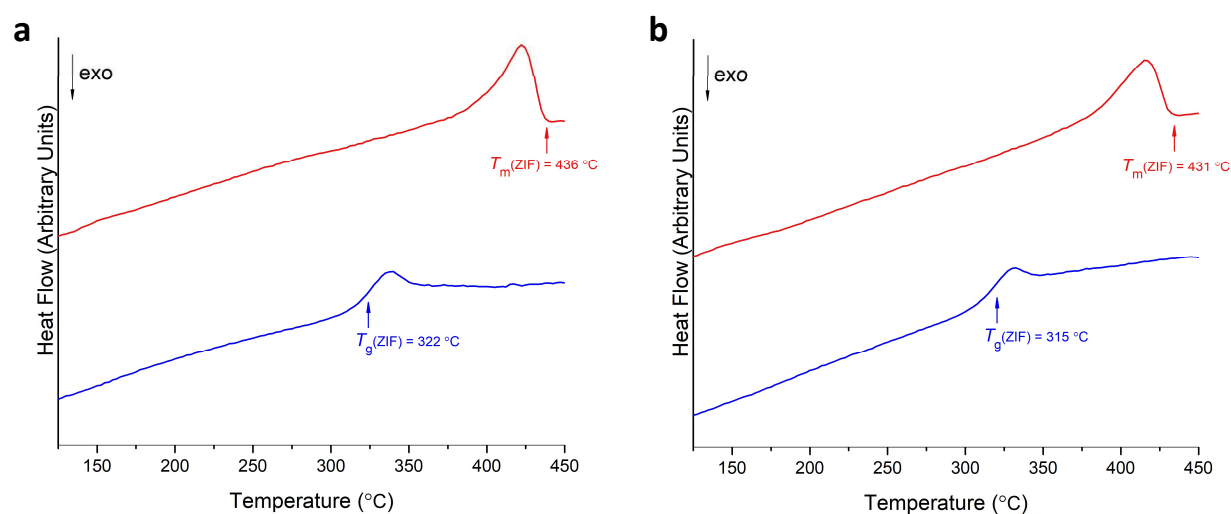


Figure 6.18: Thermal response of ZIF-62 control during the first (red) and second (blue) heating scans. **a.** Held at 450 °C for 1 minute. **b.** Held at 450 °C for 30 minutes. All heating and cooling was done at 10 °C/min under argon.

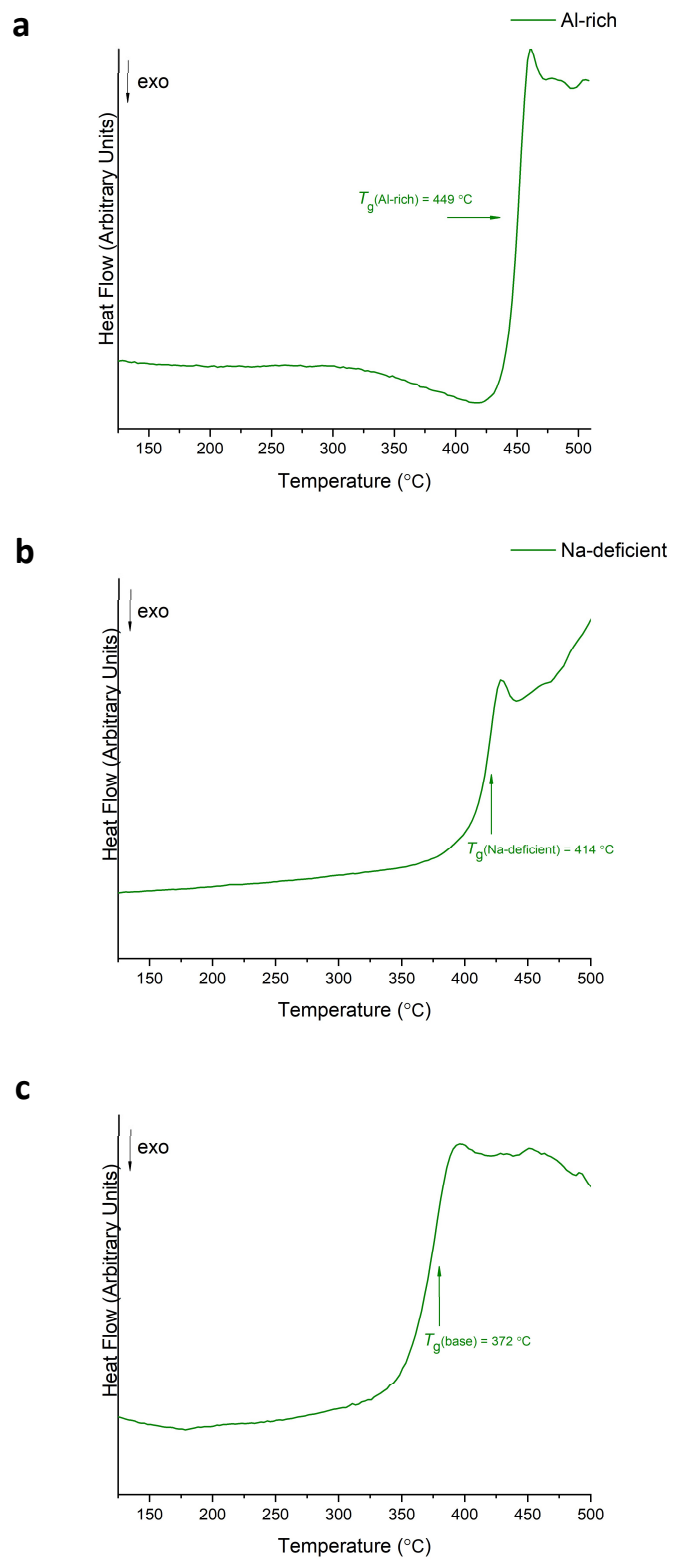


Figure 6.19: Thermal responses of the inorganic glass controls. **a.** Al-rich **b.** Na-deficient **c.** base. The samples were heated under argon at a rate of 10 °C/min.

The (ZIF-62)(Al-rich)(50/50) sample heated for 1 minute at 450 °C demonstrated the melting of ZIF-62 ($T_m(\text{ZIF})$), at 435 °C. This was followed by a rise in the baseline at approx. 440 °C (**Figure 6.20a**), which was assigned to the glass transition of the inorganic glass ($T_g(\text{Al-rich})$) by comparing with a DSC scan of the pure Al-rich glass sample (**Figure 6.19a**). The second heating scan showed two glass transitions; one assigned to Al-rich at approx. 440 °C, and the other assigned to $a_g\text{ZIF-62}$ at approx. 318 °C by comparing with that of the ZIF-62 control (**Figure 6.18**). The (ZIF-62)(Al-rich)(50/50) sample heated for 30 minutes (**Figure 6.20b**) at 450 °C showed almost identical behaviour; the first upscan showed an endotherm from ZIF-62 melting at 428 °C followed by the inorganic T_g . As with the "1 minute" sample, the second heating scan contained two glass transitions, assigned to the inorganic, again at approx. 440 °C and $a_g\text{ZIF-62}$ at approx. 319 °C.

The ZIF-62 melting endotherm was not evident in DSC experiments on the (ZIF-62)(base)(50/50) and (ZIF-62)(Na-deficient)(50/50) samples due to the overlap of the inorganic glass T_g with the melting point of ZIF-62. However, the second heating cycle of the (ZIF-62)(Na-deficient)(50/50) and (ZIF-62)(base)(50/50) samples did contain separate $a_g\text{ZIF-62}$ and inorganic glass transitions irrespective of the length of time spent at 450 °C (**Figure 6.21** and **Figure 6.22**).

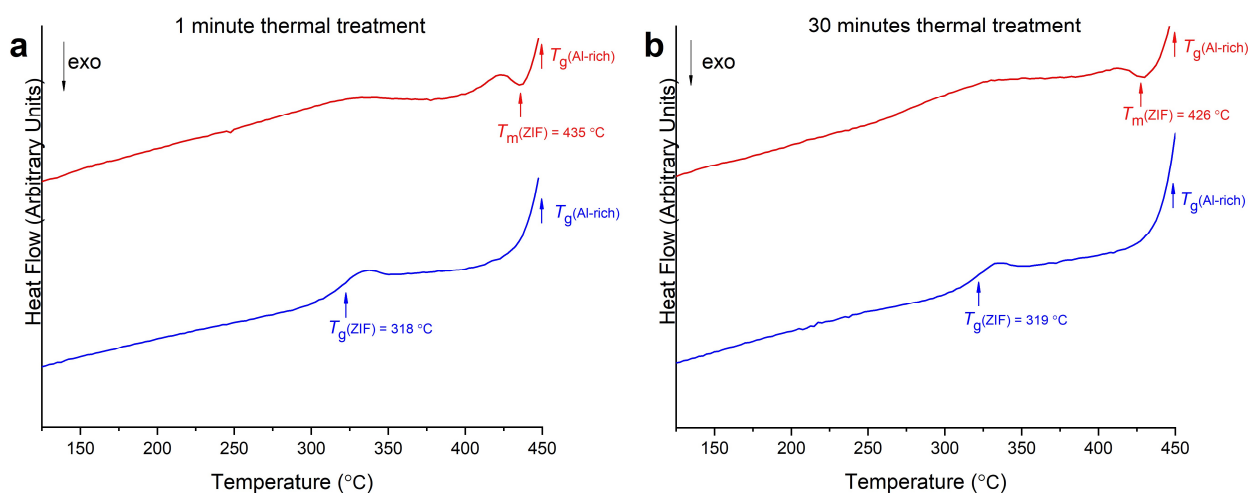


Figure 6.20: Thermal response of (ZIF-62)(Al-rich)(50/50) during the first (red) and second (blue) heating scans. **a.** Held at 450 °C for 1 minute. **b.** Held at 450 °C for 30 minutes. All heating and cooling was done at 10 °C/min under argon.

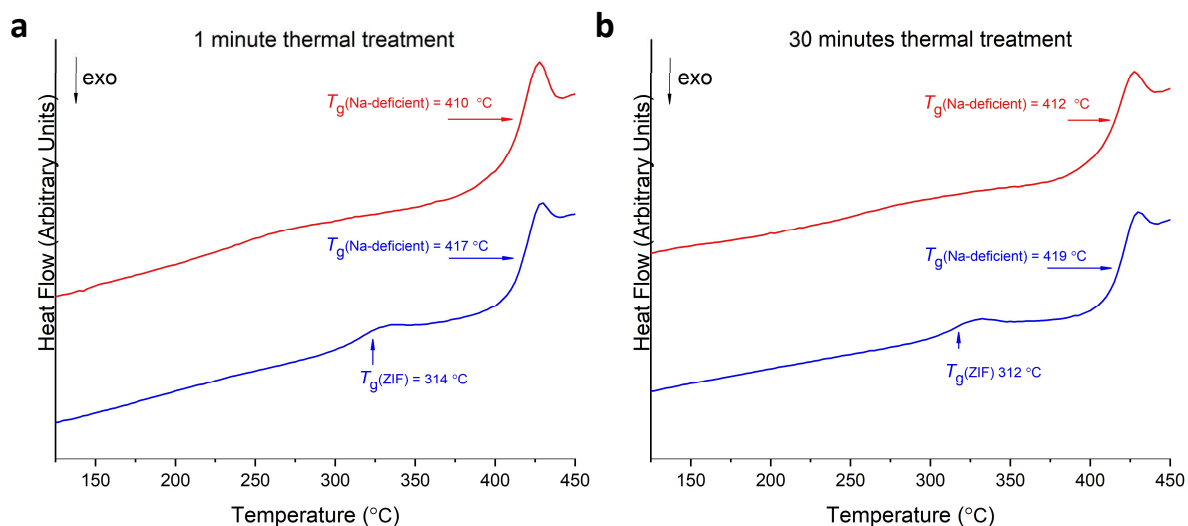


Figure 6.21: Thermal response of (ZIF-62)(Na-deficient)(50/50) during the first (red) and second (blue) heating scans. **a.** Held at 450 °C for 1 minute. **b.** Held at 450 °C for 30 minutes. All heating and cooling was done at 10 °C/min under argon.

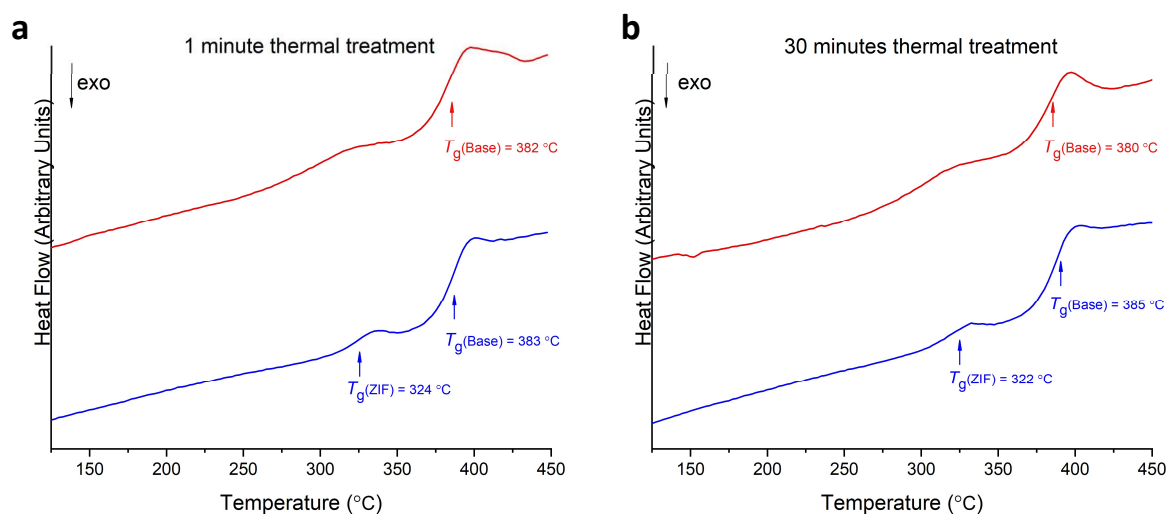


Figure 6.22: Thermal response of (ZIF-62)(base)(50/50) during the first (red) and second (blue) heating scans. **a.** Held at 450 °C for 1 minute. **b.** Held at 450 °C for 30 minutes. All heating and cooling was done at 10 °C/min under argon.

Separate TGA scans were conducted on each of the (ZIF-62)(Inorganic Glass) (50/50) samples and confirmed that none of the samples had any substantial mass loss upon heating to 450 °C (**Figure 6.23**). The decomposition temperature was measured as the onset of mass loss determined by the intersections of linear fits to the curves in the stable mass and mass loss regions. T_d was 466 °C in (ZIF-62)(Al-rich)(50/50), 489 °C in (ZIF-62)(Na-deficient)(50/50), and 488 °C in (ZIF-62)(base)(50/50). The

wide spread in onset temperatures between the (ZIF-62)(Al-rich)(50/50) sample and the others is due to the small mass loss in this region, which makes the determination of the onset approximate. Likewise, a T_d is not reported for ZIF-62 because the mass loss prior to 600 °C is too low for it to be meaningful.

To allow for the characterisation of the composite samples by PXRD, microscopy, solid state NMR, nanoindentation, and X-ray total-scattering methods, bulk samples were produced by heating the as-synthesised (ZIF-62)(Inorganic Glass) (50/50) crystalline mixtures in a Carbolite 12/65/550 tube furnace under argon.

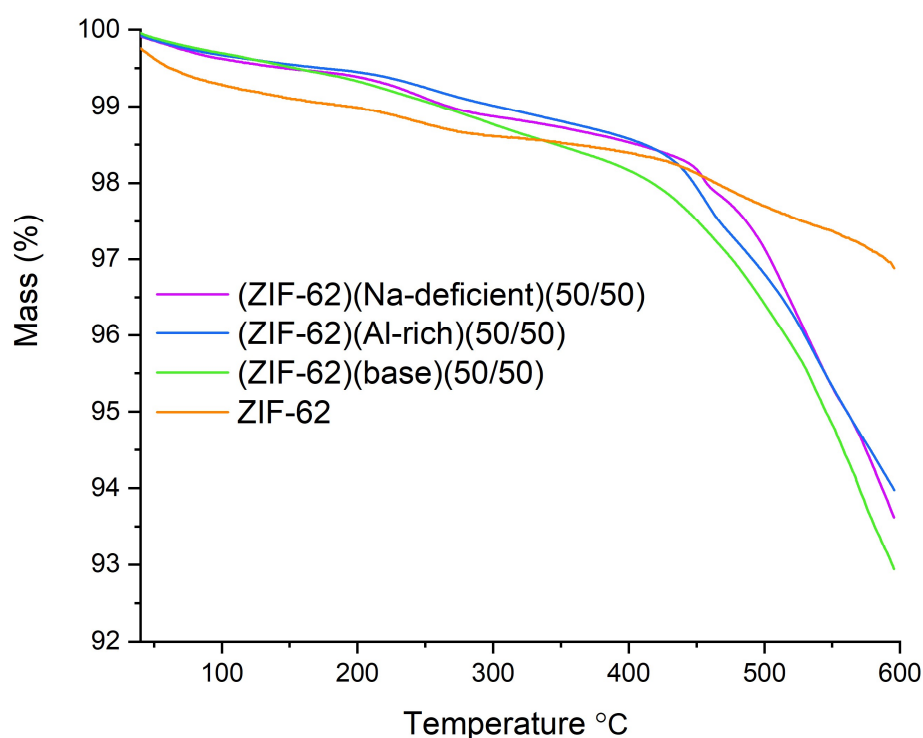


Figure 6.23: Mass curves of the (ZIF-62)(Inorganic Glass)(50/50) samples. All samples display less than 3 % mass loss below 450 °C. The scans were conducted under argon with a heating rate of 10 °C/min.

In keeping with the DSC results above, pressed pellets (**Chapter 3.2.3**) of the three (ZIF-62)(Inorganic Glass)(50/50) powders were heated to 410 °C for 1 minute, and, in a separate experiment, for 30 minutes. This lower temperature is still greater than the onset of melting for ZIF-62 and was used due to the much slower cooling rate of the tube furnace, and therefore longer time that was spent at elevated temperatures for the tube furnace samples. Using the same naming convention from complex ZIF-ZIF glass blends these heat treated samples were referred to as $(a_g\text{ZIF-62})_{0.5}(\text{Inorganic Glass})_{0.5} - 1 \text{ min}$ and $(a_g\text{ZIF-62})_{0.5}(\text{Inorganic Glass})_{0.5} - 30 \text{ min}$ where 1 or 30 minutes refers to their high temperature isothermal heat treatment time, and subscripts refer to mass fraction.

6.6 Powder X-ray Diffraction of the $(a_g\text{ZIF-62})_{0.5}(\text{Inorganic Glass})_{0.5}$ Samples.

PXRD on the $(a_g\text{ZIF-62})_{0.5}(\text{Inorganic Glass})_{0.5}$ samples (**Figure 6.24**) confirmed melting had occurred as no samples contained ZIF-62 Bragg peaks. Equally there was no indication of any inorganic glass recrystallisation, which is in good agreement with the absence of any exothermic features observed in the DSC (**Figure 6.19**).

The $(a_g\text{ZIF-62})_{0.5}(\text{Na-deficient})_{0.5} - 1 \text{ min}$ and $(a_g\text{ZIF-62})_{0.5}(\text{Al-rich})_{0.5} - 1 \text{ min}$ PXRD patterns appeared completely amorphous. The PXRD pattern of the $(a_g\text{ZIF-62})_{0.5}(\text{base})_{0.5} - 1 \text{ min}$ however contained a small number of low intensity Bragg peaks (**Figure 6.24a**). The position of these peaks, and in particular the most intense peaks at approx. $15^\circ 2\theta$, were found to match the reference pattern for ZIF-zni, a dense zinc imidazolate ($\text{Zn}(\text{Im})_2$) framework, reported in the literature [53]. The Bragg peaks at around 15° , which are ascribed to the closely spaced 400, 112, and 321 reflections from ZIF-zni [53], were also present, though at an even lower intensity, in the PXRD patterns of the $(a_g\text{ZIF-62})_{0.5}(\text{Na-deficient})_{0.5} - 30 \text{ min}$ and $(a_g\text{ZIF-62})_{0.5}(\text{Al-rich})_{0.5} - 30 \text{ min}$ samples. In contrast to the diffraction pattern of $(a_g\text{ZIF-62})_{0.5}(\text{base})_{0.5} - 30 \text{ min}$, which appeared completely amorphous (**Figure 6.24b**).

These results show that the $(a_g\text{ZIF-62})_{0.5}(\text{Inorganic Glass})_{0.5}$ composite samples are mainly amorphous. This is as expected from the DSC results, which showed two glass transition temperatures on the second heating scan for all the samples. The appearance of the minor ZIF-zni phase seems to be dependent on both inorganic glass composition and sample treatment time.

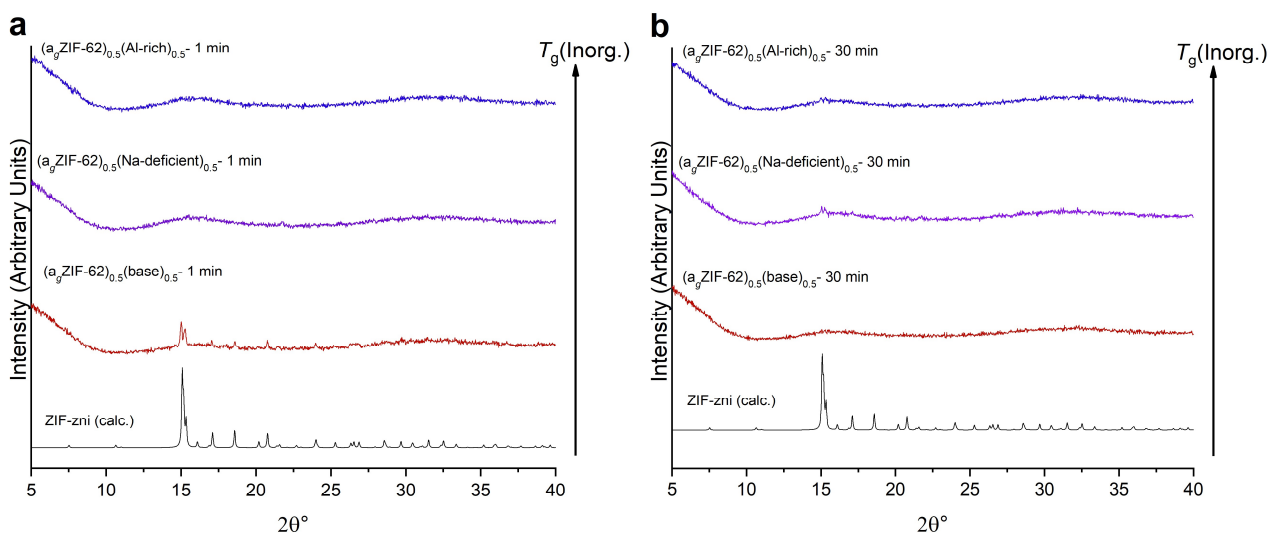


Figure 6.24: X-ray diffraction patterns of the $(a_g\text{ZIF-62})_{0.5}(\text{Inorganic Glass})_{0.5}$ samples. **a.** $(a_g\text{ZIF-62})_{0.5}(\text{Inorganic Glass})_{0.5} - 1 \text{ min}$. **b.** $(a_g\text{ZIF-62})_{0.5}(\text{Inorganic Glass})_{0.5} - 30 \text{ min}$. A reference pattern for ZIF-zni reproduced from [53] is also shown.

6.7 Spectroscopic Examination of $(a_g\text{ZIF-62})_{0.5}(\text{Inorganic Glass})_{0.5}$ Samples

6.7.1 Probing Sample Stability through Fourier Transform Infra-red and ^1H Nuclear Magnetic Resonance Spectroscopy

Although the TGA trace (**Figure 6.23**) confirmed no mass loss and the DSC traces displayed glass transitions consistent with $a_g\text{ZIF-62}$ (**Figures 6.20-22**) ^1H nuclear magnetic resonance (NMR) spectroscopy was also carried out to confirm the stability of the imidazolate and benzimidazolate linkers. ^1H NMR on the ZIF-62 controls showed the expected linker resonances in both the crystal and the glass samples and the linker ratio remained constant on glass formation (**Figure 6.25**). The ratio of imidazolate to benzimidazolate linkers remained essentially unchanged on glass formation in the pure ZIF-62 implying a precise sample composition of $\text{Zn}(\text{Im})_{1.76}(\text{blm})_{0.24}$. This is consistent with existing literature on ZIF glasses in which the linker ratio is maintained upon glass formation [56]. All samples contained a peak at around 6 ppm which we identify as resulting from H_2O contamination, which forms H_3O^+ in the acidic solvent (**Chapter 3.2.3**).

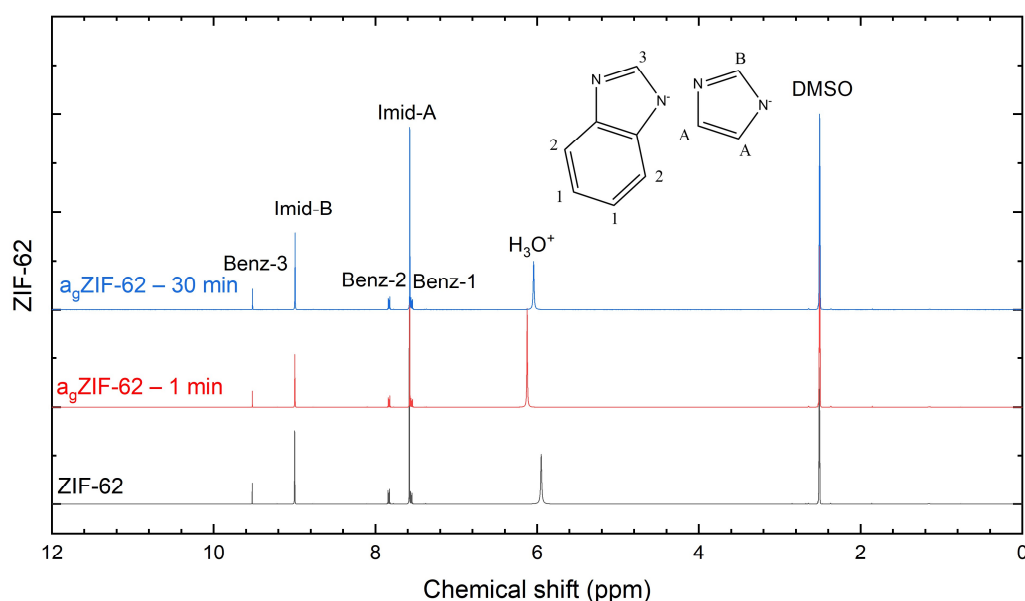


Figure 6.25: Solution ^1H NMR spectra of crystalline and glass ZIF-62 controls. The anions of the imidazolate and benzimidazolate linkers are presented without the acid H. The solvent used was a mixture of DCl (20%)/ D_2O (0.1 ml) and DMSO-d_6 (0.6 ml).

Table 6.3: [Blm]/[Blm+Im] ratio from ¹H NMR integrals of singlet (9.5 ppm) and triplet (9.0 ppm), respectively.

Pure ZIF-62 Controls		
ZIF-62	a _g ZIF-62 – 1 min	a _g ZIF-62 – 30 min
0.118	0.117	0.117
Treatment Time		
Composite	1 min	30 min
(a _g ZIF-62) _{0.5} (base) _{0.5}	0.118	0.120
(a _g ZIF-62) _{0.5} (Na-deficient) _{0.5}	0.116	0.120
(a _g ZIF-62) _{0.5} (Al-rich) _{0.5}	0.116	0.120

No new peaks emerged and there were also no appreciable changes in the organic linker ratio upon heating the (a_gZIF-62)_{0.5}(Inorganic Glass)_{0.5} samples for 1 minute (**Figure 6.26a**). However, despite no new peaks, in the (a_gZIF-62)_{0.5}(Inorganic Glass)_{0.5} – 30 min samples the [blm]/[blm+Im] ratio was 0.3% higher, implying a common equilibrium state independent of the inorganic composition (**Figure 6.26b**). This also implies that the stability of benzimidazolate may be marginally higher than that of imidazolate during composite formation.

The Fourier transform infra-red (FTIR) spectra of the a_gZIF-62 controls (**Figure 6.27**) was consistent with reported literature on other ZIFs [130]. Although the complex structure of ZIFs prohibits assignment of every stretch, the spectra can be separated into four distinct regions; the expected vibration at 1590 cm⁻¹ due to C=N stretching, peaks between 1350-1500 cm⁻¹ due to ring stretching, between 900-1350 cm⁻¹ due to in-plane bending, and stretches below 800 cm⁻¹ due to out of plane bending [130]. The (a_gZIF-62)_{0.5}(Inorganic Glass)_{0.5} - 1 min and (a_gZIF-62)_{0.5}(Inorganic Glass)_{0.5} – 30 min samples contained almost identical patterns of sharp peaks, which further confirmed the integrity of the a_gZIF-62 component within the composites (**Figure 6.27**). There were consistent small changes in the approx. 700 and 1450 cm⁻¹ peaks which have been assigned to out-of-plane bending and ring stretching indicating some added deformation due to the presence of inorganic glass (**Figure 6.27**).

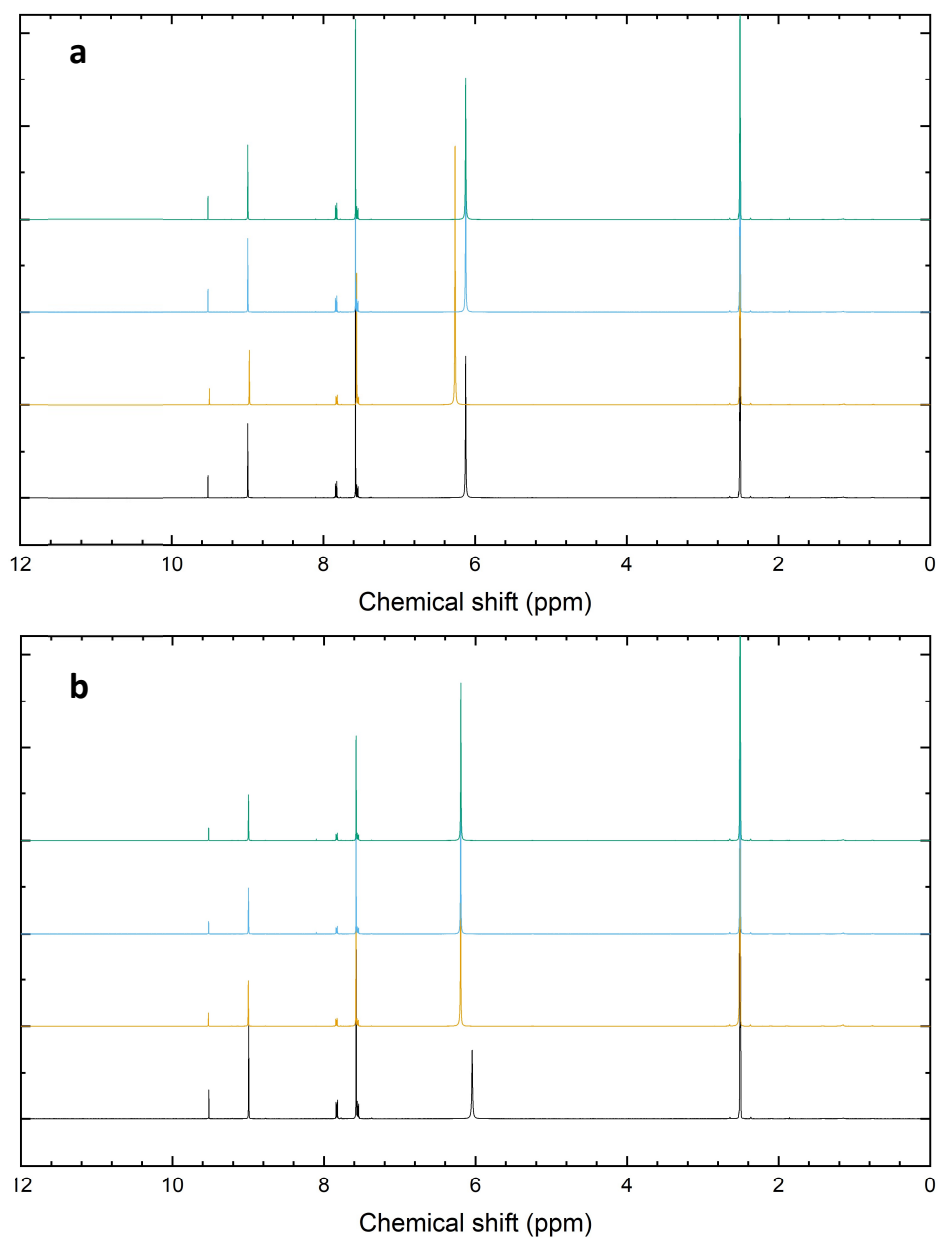


Figure 6.26: Solution ^1H NMR spectra of the $(\text{agZIF-62})_{0.5}(\text{Inorganic Glass})_{0.5}$ samples. **a.** $(\text{agZIF-62})_{0.5}(\text{Inorganic Glass})_{0.5}$ – 1 min. **b.** $(\text{agZIF-62})_{0.5}(\text{Inorganic Glass})_{0.5}$ – 30 min. Key: Teal - $(\text{agZIF-62})_{0.5}(\text{Al-rich})_{0.5}$, Blue - $(\text{agZIF-62})_{0.5}(\text{Na-deficient})_{0.5}$, Yellow - $(\text{agZIF-62})_{0.5}(\text{base})_{0.5}$, and Black- agZIF-62 . The solvent used was a mixture of DCl (20%)/ D_2O (0.1 ml) and DMSO-d_6 (0.6 ml).

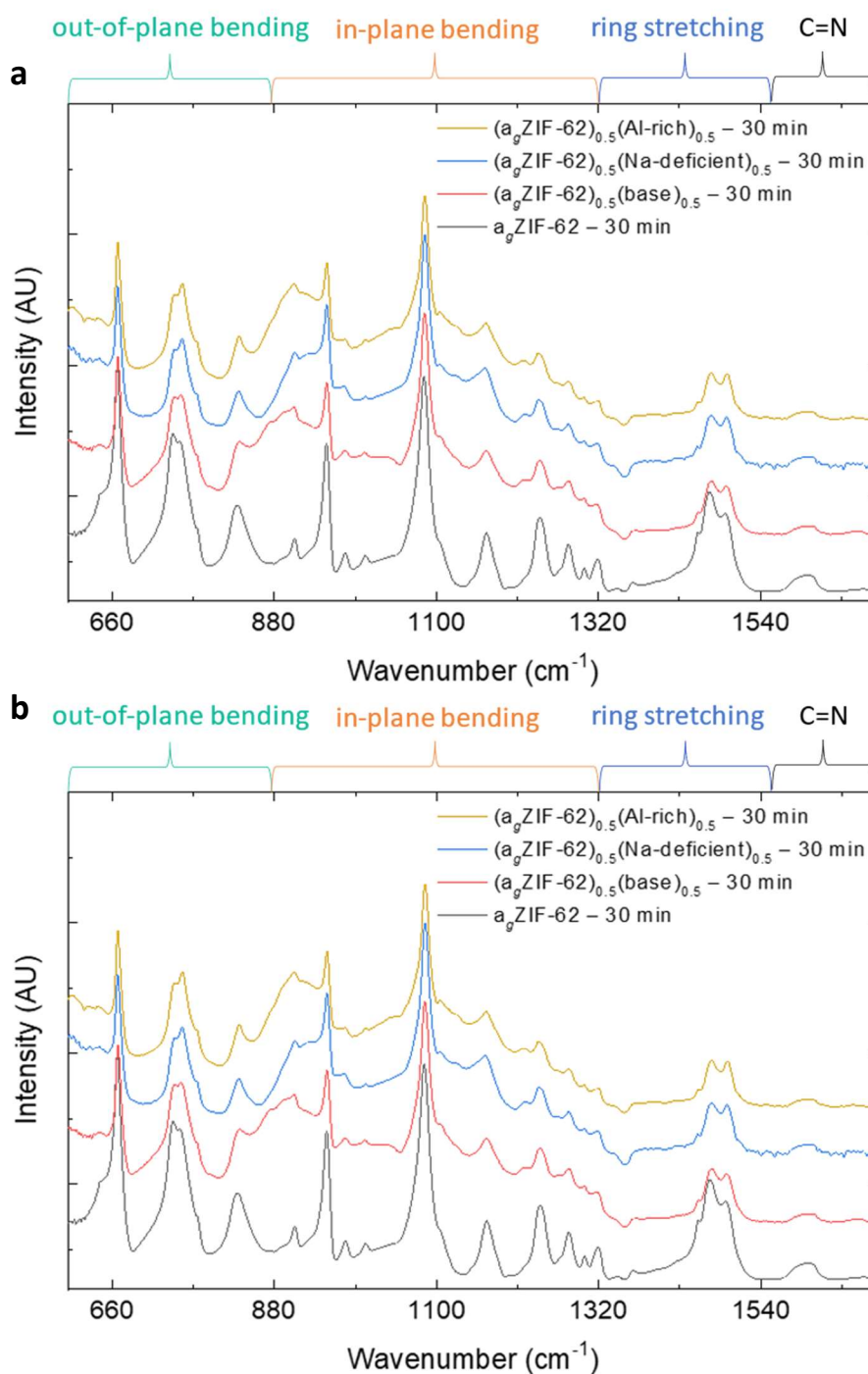


Figure 6.27: FTIR spectra of the $(a_g\text{ZIF-62})_{0.5}(\text{Inorganic Glass})_{0.5}$ samples. **a.** $(a_g\text{ZIF-62})_{0.5}(\text{Inorganic Glass})_{0.5} - 1$ min and $a_g\text{ZIF-62} - 1$ min **b.** $(a_g\text{ZIF-62})_{0.5}(\text{Inorganic Glass})_{0.5} - 30$ min and $a_g\text{ZIF-62} - 30$ min

The FTIR spectra of the $(a_g\text{ZIF-62})_{0.5}(\text{Inorganic Glass})_{0.5}$ samples also contained broader absorbances. These broad features of the spectra are due to the broad spectra of the different inorganic glasses (Figure 6.28). These spectra are broad due to the structural disorder, which leads to a wide variety of

vibrational modes [131]. The broad peaks are in the same regions previously observed in the literature of fluoro-aluminophosphates [125].

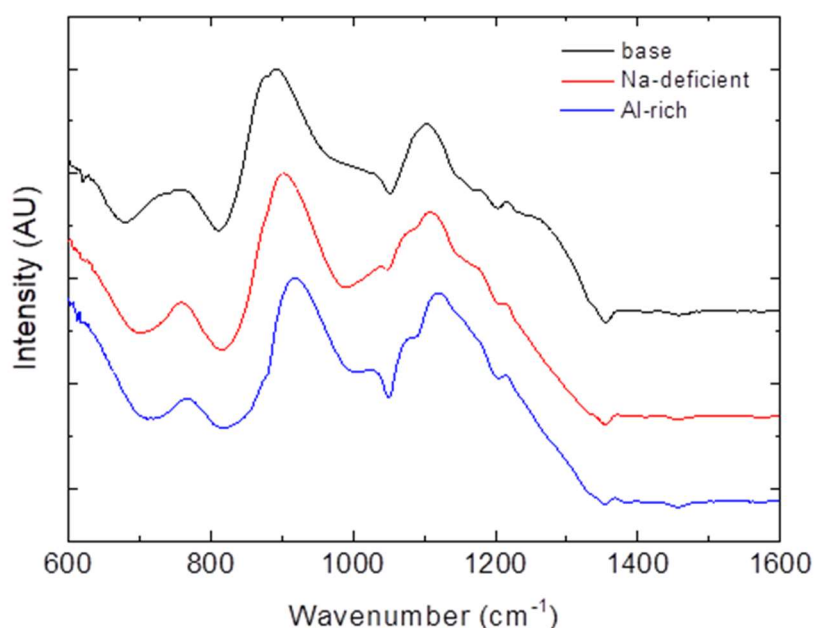


Figure 6.28: FTIR spectra of the inorganic glasses.

6.7.2 Investigating the Composite Samples through ^{31}P Nuclear Magnetic Resonance Spectroscopy

^{31}P MAS (magic-angle spinning) NMR spectroscopy was also carried out to investigate changes in the phosphate component of the inorganic glass. Except for the $(a_g\text{ZIF-62})_{0.5}(\text{Na-deficient})_{0.5}$ -1 min sample all the samples were found at a higher chemical shift than their respective pure inorganic glasses. Additionally, new intensity in the ^{31}P spectra appeared in the region 5 to -15 ppm, which increased proportionally with heat treatment time. This relatively subtle effect is most evident in the residual curves created by subtracting the $(a_g\text{ZIF-62})_{0.5}(\text{Inorganic Glass})_{0.5}$ spectra from the relevant inorganic glass (**Figures 6.29-31**). This is consistent with literature values for the shifts of ^{31}P in PO_3N and PO_2N_2 species at -10 and 0 ppm, respectively [132], indicating the possibility of P—N bond formation between the phosphate tetrahedra and the Im^- ring.

$^{31}\text{P}\{^1\text{H}\}$ cross polarisation (CP) NMR measurements were performed on the same samples to further interpret this additional intensity. CP NMR experiments measure the proximity of nuclei in space; the efficiency of the transfer of magnetization is mediated by the dipolar coupling of heteronuclear spins (which has an r^{-3} dependence) [133]. Thus, $^{31}\text{P}\{^1\text{H}\}$ CP NMR experiments (**Figure 6.29-31**) shed light on

these new peaks found in the 1d ^{31}P spectra, specifically they reveal that the new intensity in the 1d ^{31}P spectra can be assigned to phosphorus atoms with protons nearby.

In addition to this the $^{31}\text{P}\{^1\text{H}\}$ CP NMR experiments also contain a peak at approx. 12 ppm, despite no discernible intensity in the corresponding 1d ^{31}P spectra. This is in the ppm range of a phosphate tetrahedra without any bridging P–O–P bonds [134]. The efficiency of magnetization transfer from ^1H to ^{31}P (as evidenced by increased intensity in the CP spectra) is commensurate with the proximity and number of nearby protons, thus, this new peak at approx. 12 ppm may reflect that an isolated phosphate tetrahedron is more mobile within the composite, and therefore, is found close to the protons of the imidazolate or benzimidazolate rings. All the samples exhibit an increase in the intensity of the peaks in the $^{31}\text{P}\{^1\text{H}\}$ CP NMR spectra as a function of heat treatment time, including the peak located at 12 ppm.

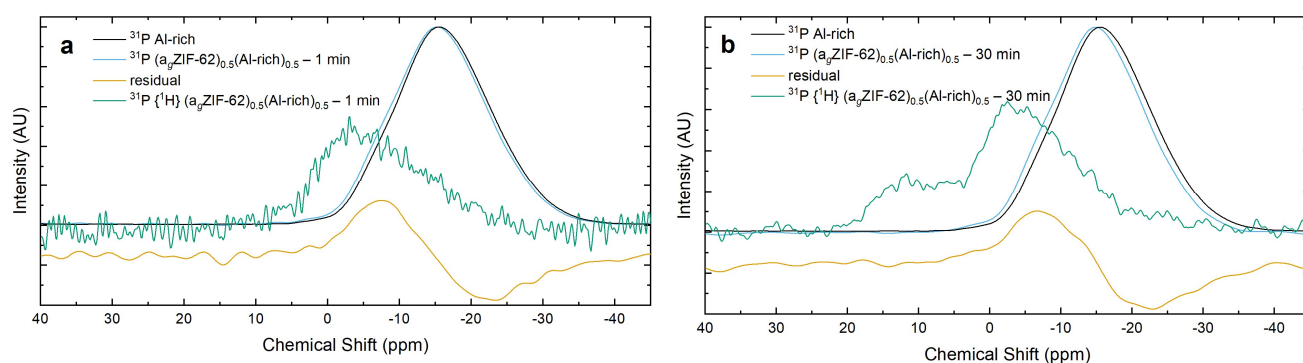


Figure 6.29: ^{31}P solid state NMR and $^{31}\text{P}\{^1\text{H}\}$ cross polarisation NMR of Al-rich and $(a_g\text{ZIF-62})_{0.5}(\text{Al-rich})_{0.5}$. Heat-treated for **a.** 1 min. **b.** 30 min.

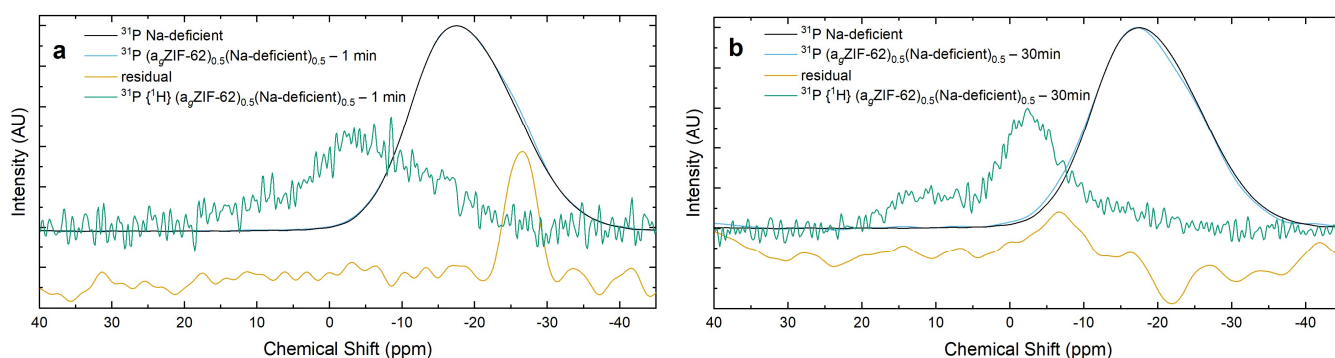


Figure 6.30: ^{31}P solid state NMR and $^{31}\text{P}\{^1\text{H}\}$ cross polarisation NMR of Na-deficient and $(a_g\text{ZIF-62})_{0.5}(\text{Na-deficient})_{0.5}$. Heat-treated for **a.** 1 min. **b.** 30 min.

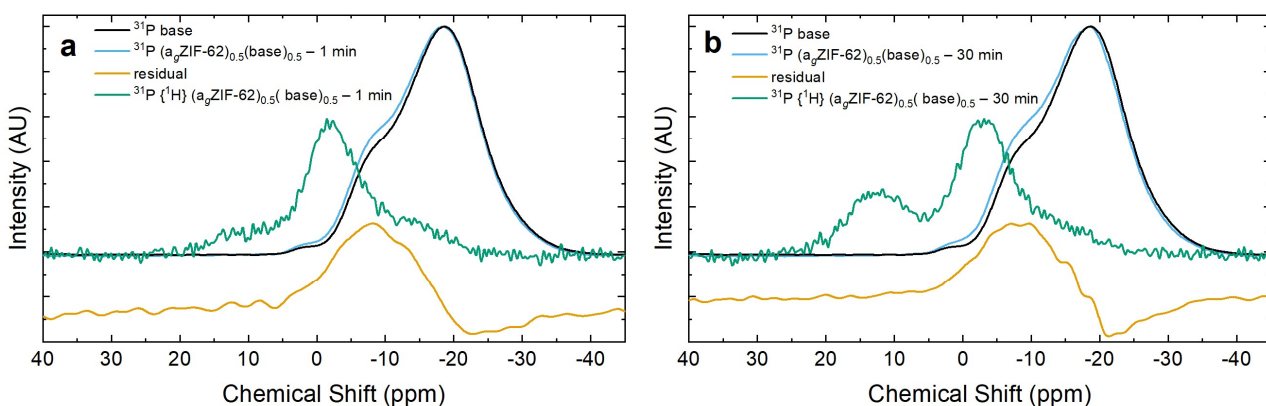


Figure 6.31: ^{31}P solid state NMR and $^{31}\text{P}\{^1\text{H}\}$ cross polarisation NMR of the base and $(a_g\text{ZIF-62})_{0.5}(\text{base})_{0.5}$. Heat-treated for **a.** 1 min. **b.** 30 min.

6.7.3 Investigating the Composite Samples through Raman Scattering

Finally, the composites were characterised by Raman scattering, a complementary technique to FTIR which is sensitive to different bonds. The Raman spectra for $a_g\text{ZIF-62} - 1$ min and $- 30$ min samples were very similar to each other and were also in excellent agreement with the Raman spectra previously reported for glassy and crystalline ZIF-62 [61] (**Figure 6.32**). A small degree of red-shifting at approx. 175 cm^{-1} in the 30 min sample relative to the 1 min sample was apparent, this peak is identified as Zn-N by comparison with the reported Raman characterisation of ZIF-8 [135] (**Figure 6.32** inset). Raman spectra for the $(a_g\text{ZIF-62})_{0.5}(\text{Inorganic Glass})_{0.5} - 1$ min and $- 30$ min samples contained similar features, ascribed to the $a_g\text{ZIF-62}$ component (**Figure 6.33**). The most significant change was in the low frequency Zn—N region (approx. 175 cm^{-1}) where a second, peak emerges at approx. 145 cm^{-1} (**Figure 6.34**). We link the reaction to the formation of new Na—N bonds, given similar peaks in sodium imidazolate-containing compounds at 161 and 136 cm^{-1} [136]. No discernible features arising from the inorganic glass were able to be unambiguously determined. This was due to the high surface roughness (see **Section 6.9**) in the composite samples, which meant that low laser powers and short collection times had to be used, leading to the broad absorbances from the inorganic glasses being lost in the noise.

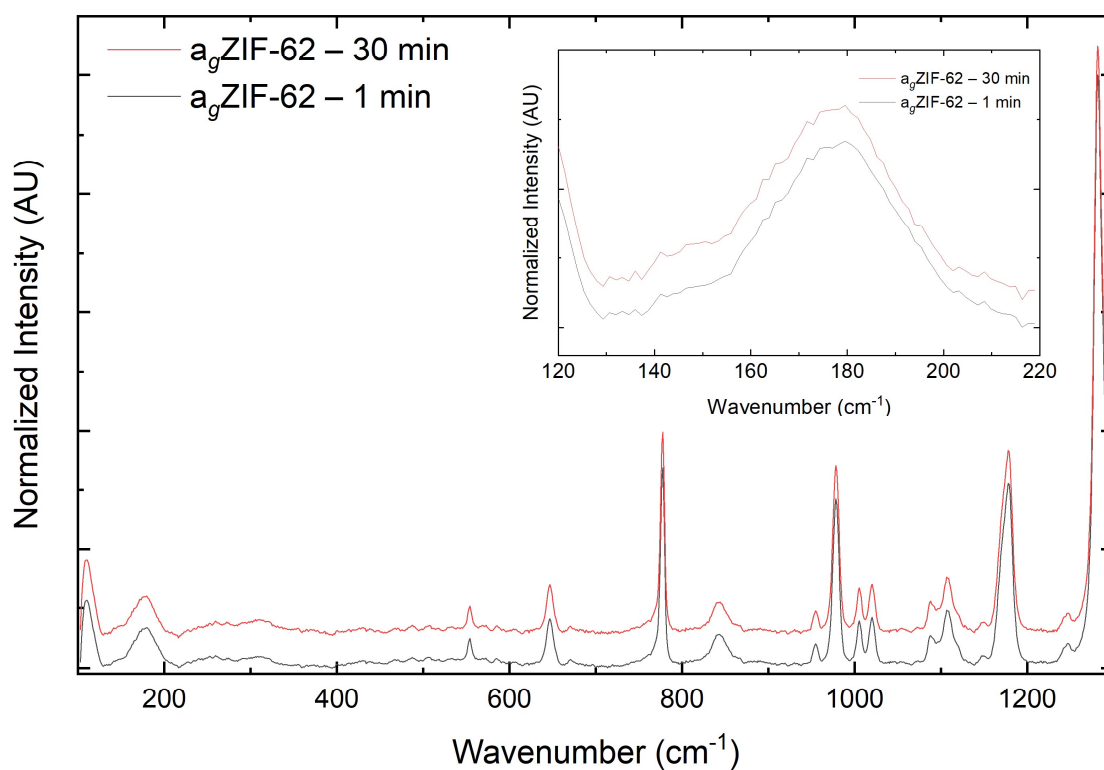


Figure 6.32: Raman spectra of the heat treated ZIF-62 control samples. Inset: Magnified 120 – 220 cm^{-1} region.

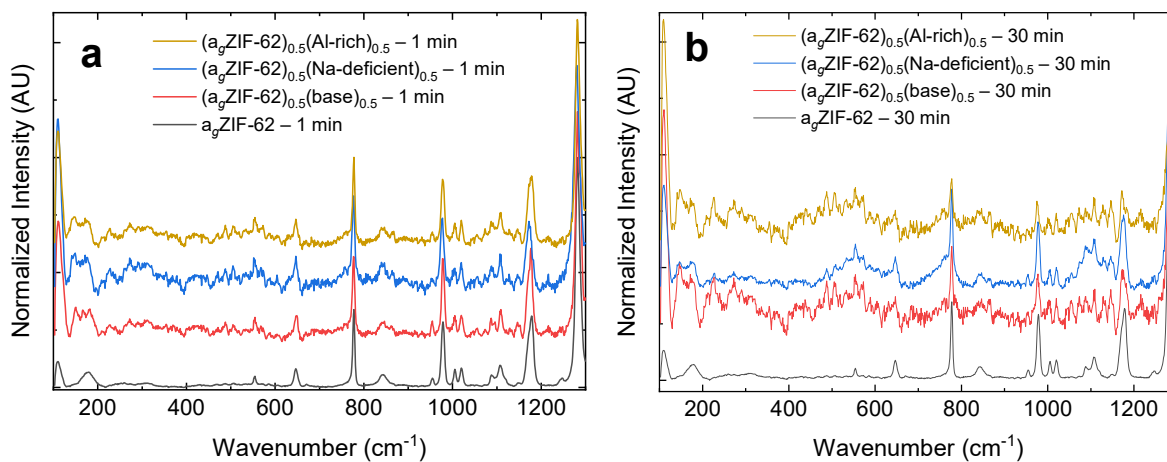


Figure 6.33: Raman spectra of the $(a_g\text{ZIF-62})_{0.5}(\text{Inorganic Glass})_{0.5}$ samples. **a.** $(a_g\text{ZIF-62})_{0.5}(\text{Inorganic Glass})_{0.5}$ – 1 min and **b.** $(a_g\text{ZIF-62})_{0.5}(\text{Inorganic Glass})_{0.5}$ – 30 min samples.

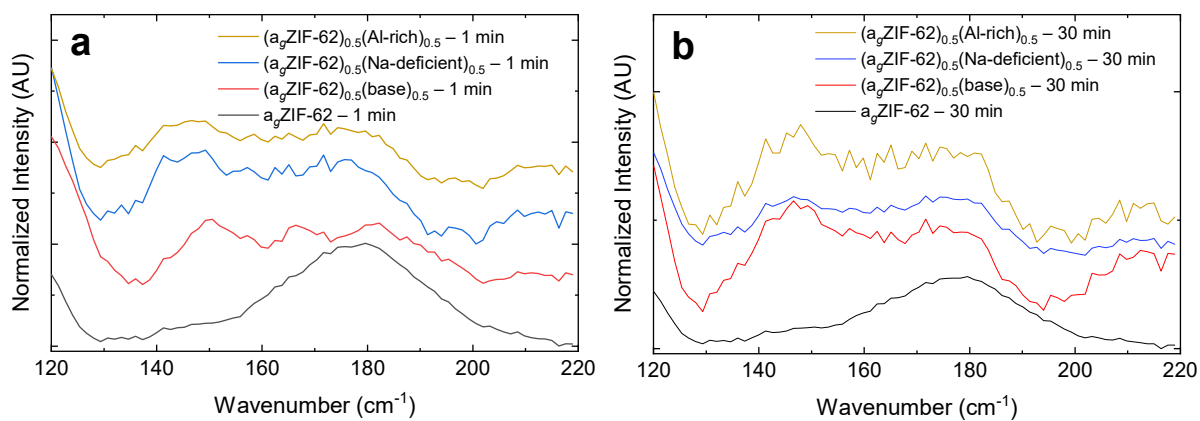


Figure 6.34: Raman spectra of the Zn—N peak (ca. 175 cm^{-1}) peak. **a.** $(a_9\text{ZIF-62})_{0.5}(\text{Inorganic Glass})_{0.5} - 1\text{ min}$ and **b.** $(a_9\text{ZIF-62})_{0.5}(\text{Inorganic Glass})_{0.5} - 30\text{ min}$ samples

6.8 X-ray Total-Scattering Measurements on $(a_g\text{ZIF-62})_{0.5}(\text{Inorganic Glass})_{0.5}$ Composites

6.8.1 Conventional X-ray Total-Scattering Measurements on the Composite Samples

To further investigate the structure of the composites, total-scattering experiments were conducted on the $(a_g\text{ZIF-62})_{0.5}(\text{Inorganic Glass})_{0.5} - 1 \text{ min}$ and $(a_g\text{ZIF-62})_{0.5}(\text{Inorganic Glass})_{0.5} - 30 \text{ min}$ samples, as well as the pure inorganic glasses and $a_g\text{ZIF-62}$ controls. The X-ray total-scattering data, $S(Q)$ was broadly consistent with the results of the PXRD (**Figure 6.24**), in that the $(a_g\text{ZIF-62})_{0.5}(\text{Inorganic Glass})_{0.5}$ samples appeared to be generally amorphous with inclusions of a small fraction of a crystalline phase. The crystalline features were less apparent in the $S(Q)$ than in the PXRD due to the coincidence of the most intense Bragg peak with the FSDP from the $a_g\text{ZIF-62}$. However a sharpening of the peak, consistent with a Bragg feature overlapping with more diffuse amorphous scattering, in $(a_g\text{ZIF-62})_{0.5}(\text{Al-rich})_{0.5} - 30 \text{ min}$ relative to $(a_g\text{ZIF-62})_{0.5}(\text{Al-rich})_{0.5} - 1 \text{ min}$ was observed (**Figure 6.35**). A similar effect was also observed in the $(a_g\text{ZIF-62})_{0.5}(\text{Na-deficient})_{0.5}$ samples (**Figure 6.36**), with the additional appearance of some Bragg features at approximately 3.5 \AA^{-1} in the $(a_g\text{ZIF-62})_{0.5}(\text{Na-deficient})_{0.5} - 30 \text{ min}$ sample. Additionally, a small Bragg peak, absent from PXRD patterns, is also seen in the $S(Q)$ of the Na-deficient glass and of the $(a_g\text{ZIF-62})_{0.5}(\text{Na-deficient})_{0.5}$ composites at approximately 2 \AA^{-1} . This is due to a small amount of recrystallisation on the formation of the inorganic glass itself. The $(a_g\text{ZIF-62})_{0.5}(\text{base})_{0.5} - 1 \text{ min}$ sample had clear Bragg features whereas the $(a_g\text{ZIF-62})_{0.5}(\text{base})_{0.5} - 30 \text{ min}$ sample seemed amorphous (**Figure 6.37**).

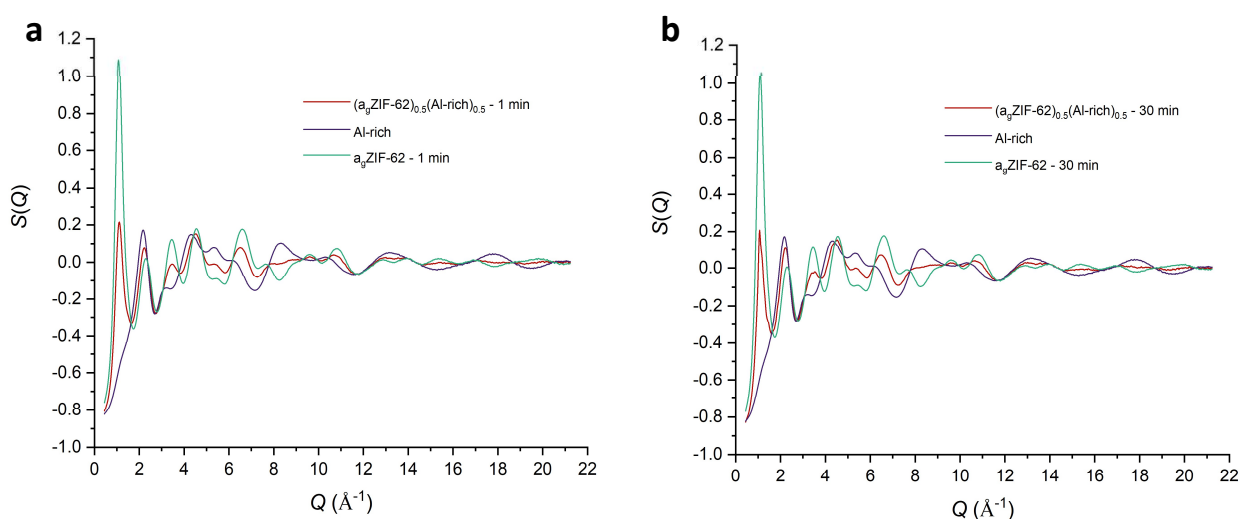


Figure 6.35: Structure factor $S(Q)$ of $(a_g\text{ZIF-62})_{0.5}(\text{Al-rich})_{0.5}$. **a.** $(a_g\text{ZIF-62})_{0.5}(\text{Al-rich})_{0.5} - 1 \text{ min}$, $a_g\text{ZIF-62} - 1 \text{ min}$ and Al-rich. **b.** $(a_g\text{ZIF-62})_{0.5}(\text{Al-rich})_{0.5} - 30 \text{ min}$, $a_g\text{ZIF-62} - 30 \text{ min}$ and Al-rich.

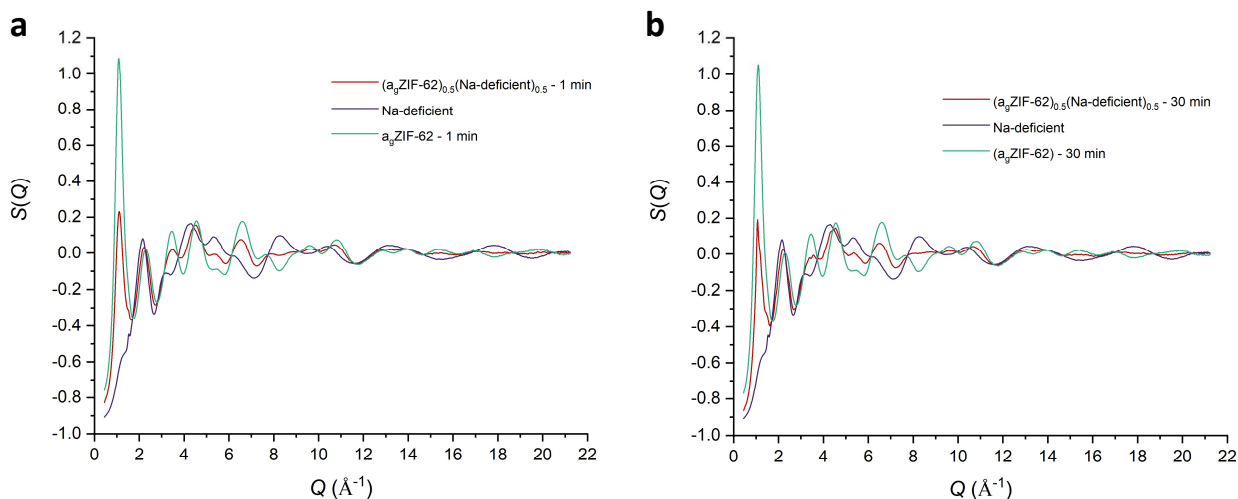


Figure 6.36: Structure factor $S(Q)$ of $(a_g\text{ZIF-62})_{0.5}(\text{Na-deficient})_{0.5}$. **a.** $(a_g\text{ZIF-62})_{0.5}(\text{Na-deficient})_{0.5}$ – 1 min, $a_g\text{ZIF-62}$ – 1 min and Na-deficient. **b.** $(a_g\text{ZIF-62})_{0.5}(\text{Na-deficient})_{0.5}$ – 30 min, $a_g\text{ZIF-62}$ – 30 min and Na-deficient.

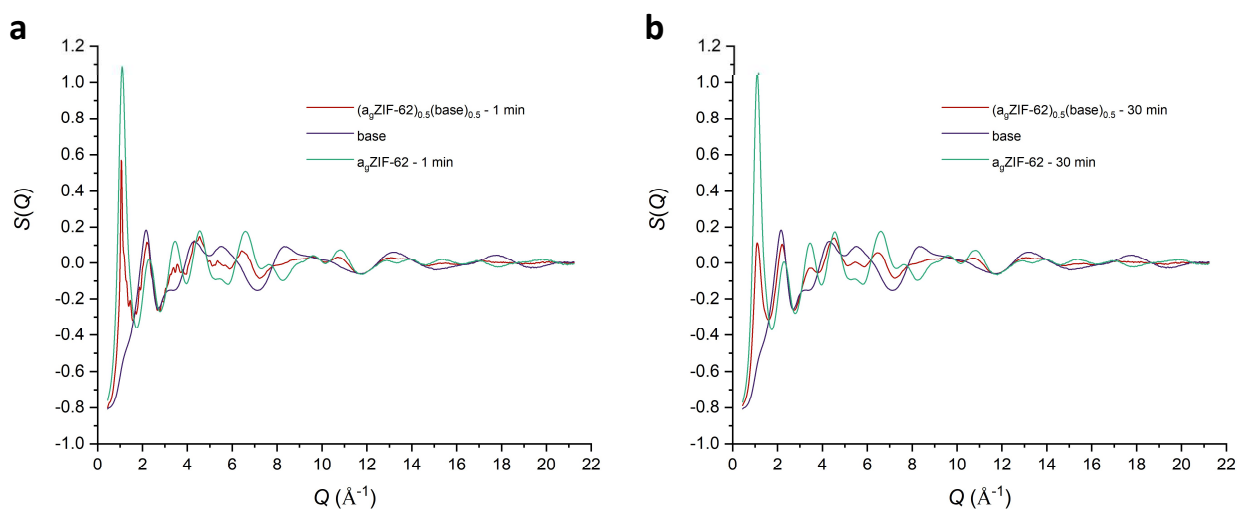


Figure 6.37: Structure factor $S(Q)$ of $(a_g\text{ZIF-62})_{0.5}(\text{base})_{0.5}$. **a.** $(a_g\text{ZIF-62})_{0.5}(\text{base})_{0.5}$ – 1 min, $a_g\text{ZIF-62}$ – 1 min and base. **b.** $(a_g\text{ZIF-62})_{0.5}(\text{base})_{0.5}$ – 30 min, $a_g\text{ZIF-62}$ – 30 min and base.

The corresponding pair distribution functions for the composites, $D(r)$, showed that the short-range order of the composite samples corresponded to peaks found in the $a_g\text{ZIF-62}$ and relevant inorganic glass samples (**Figure 6.38-40**). In other words, if a peak from an end member was the only correlation within a given range, such as the peak at 2 Å in $a_g\text{ZIF-62}$ or the peak at 4.9 Å in the inorganic glasses, then a nearly identical peak was found in the composite samples. Whereas, if a correlation from the $a_g\text{ZIF-62}$ and the inorganic glass overlap, i.e. at 3-3.2 Å, then the correlation in the composite sample

lies between them. Very little difference in the SRO is evident between the $(a_g\text{ZIF-62})_{0.5}(\text{Inorganic Glass})_{0.5} - 1 \text{ min}$ and the $(a_g\text{ZIF-62})_{0.5}(\text{Inorganic Glass})_{0.5} - 30 \text{ min}$ samples. However, the LRO order shows, as expected from the $S(Q)$, long-range density correlations in samples which contain sharp Bragg features and is flat in amorphous samples (**Figure 6.38-40** insets).

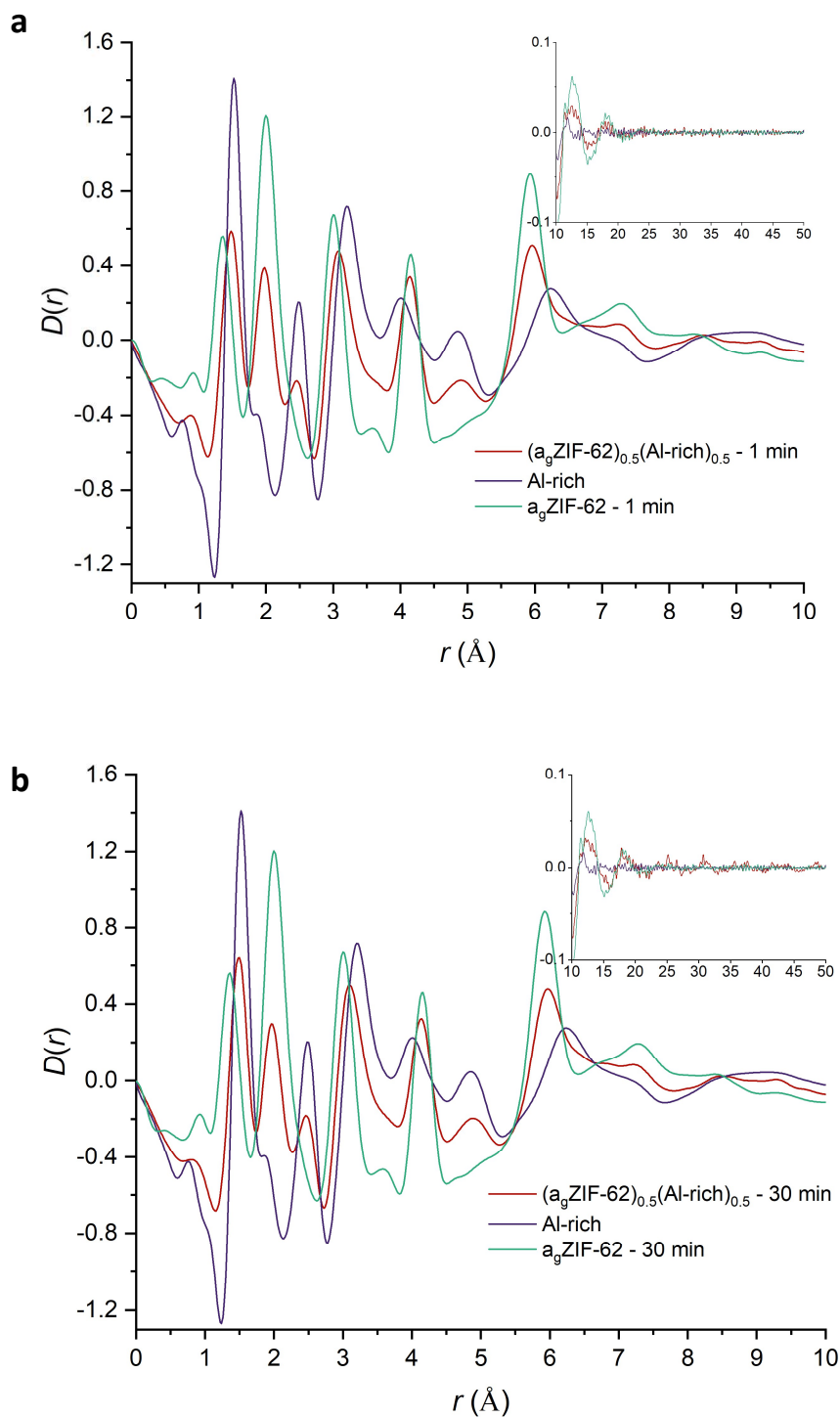


Figure 6.38: Pair-distribution function $D(r)$ of $(a_g\text{ZIF-62})_{0.5}(\text{Al-rich})_{0.5}$. **a.** $(a_g\text{ZIF-62})_{0.5}(\text{Al-rich})_{0.5} - 1 \text{ min}$, $a_g\text{ZIF-62} - 1 \text{ min}$ and Al-rich. **b.** $(a_g\text{ZIF-62})_{0.5}(\text{Al-rich})_{0.5} - 30 \text{ min}$, $a_g\text{ZIF-62} - 30 \text{ min}$ and Al-rich.

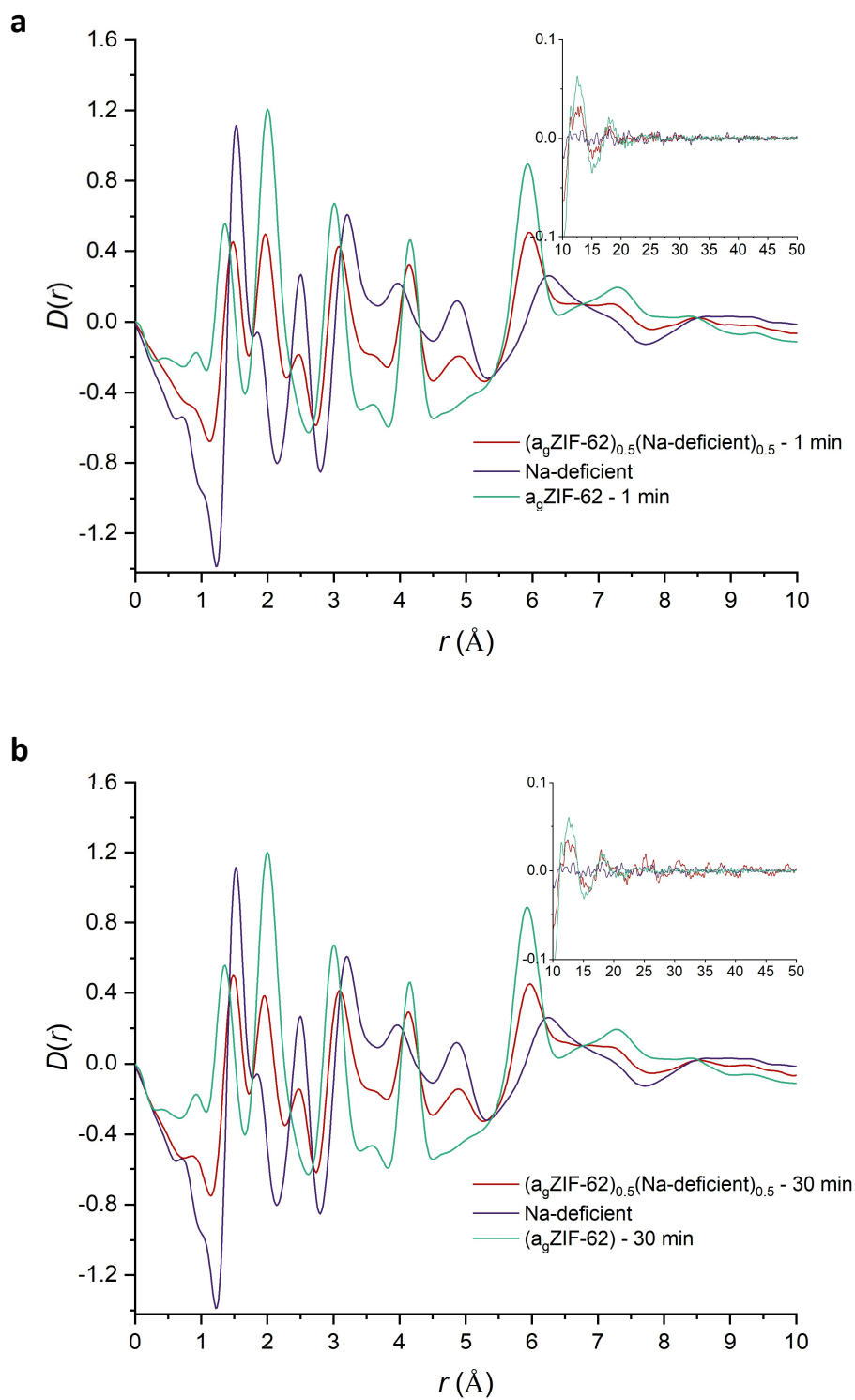


Figure 6.39: Pair-distribution function $D(r)$ of $(a_g\text{ZIF-62})_{0.5}(\text{Na-deficient})_{0.5}$. **a.** $(a_g\text{ZIF-62})_{0.5}(\text{Na-deficient})_{0.5}$ – 1 min, $a_g\text{ZIF-62}$ – 1 min and Na-deficient. **b.** $(a_g\text{ZIF-62})_{0.5}(\text{Na-deficient})_{0.5}$ – 30 min, $a_g\text{ZIF-62}$ – 30 min and Na-deficient.

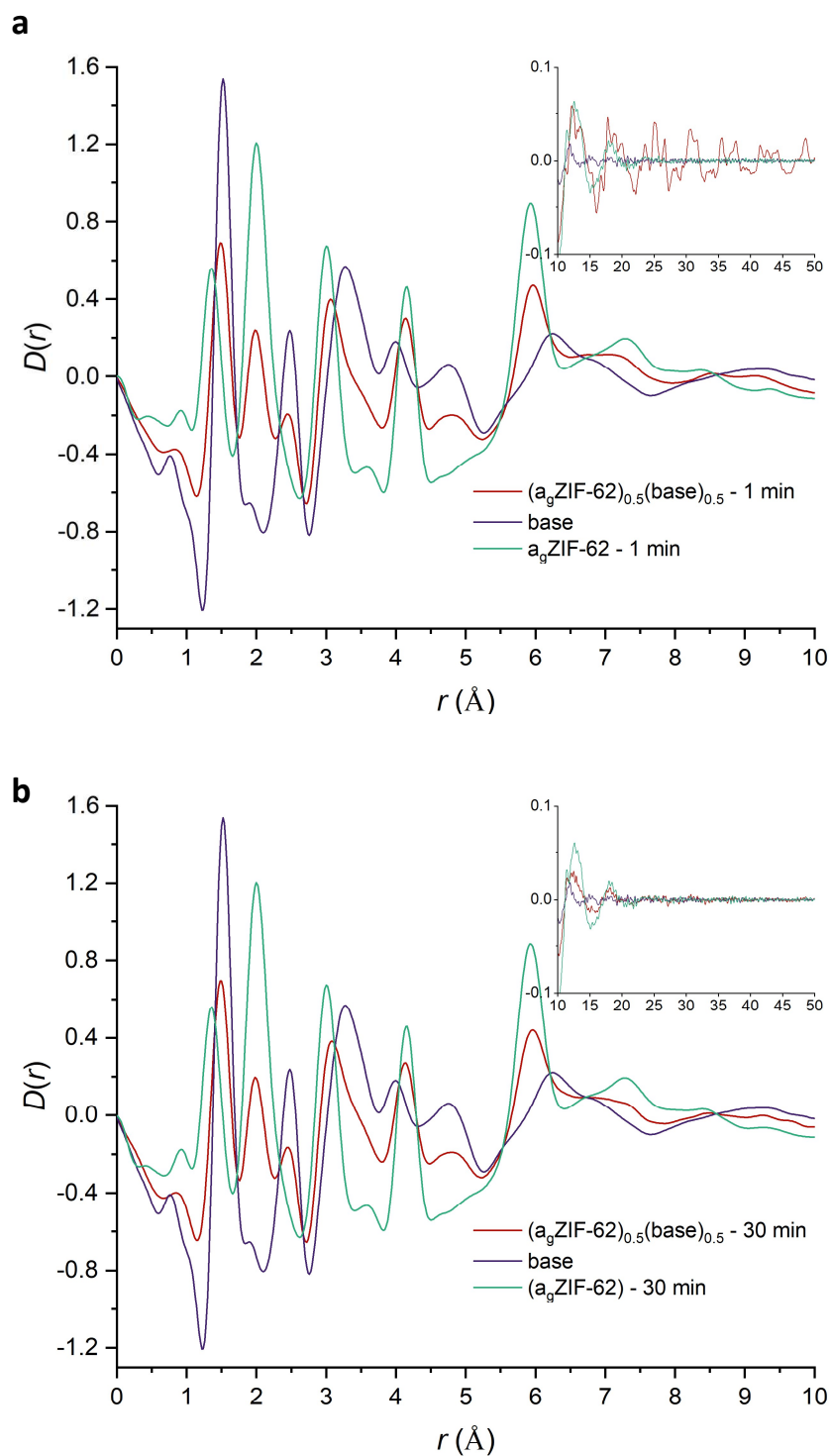


Figure 6.40: Pair-distribution function $D(r)$ of $(a_g\text{ZIF-62})_{0.5}(\text{base})_{0.5}$. **a.** $(a_g\text{ZIF-62})_{0.5}(\text{base})_{0.5} - 1 \text{ min}$, $a_g\text{ZIF-62} - 1 \text{ min}$ and base. **b.** $(a_g\text{ZIF-62})_{0.5}(\text{base})_{0.5} - 30 \text{ min}$, $a_g\text{ZIF-62} - 30 \text{ min}$ and base.

6.8.2 Differential Pair-distribution Function Studies on the Composite Samples

The Raman spectra (**Figure 6.32-34**) indicate the formation of a Na-N bond in the composite samples. Equally the $^{31}\text{P}\{^1\text{H}\}$ CP NMR provide evidence for close contact between H and P and therefore indicate potential P-N bond formation (**Figure 6.29-31**). However, the nature of PDF means that all these correlations fall within the same approximate 1-8 Å range. Therefore, in the absence of dramatic changes in bonding, an effect not seen spectroscopically here, then small peaks due to new correlations are likely to overlap with existing peaks. To attempt to address this problem a differential method was used [87], [137].

The raw X-ray diffraction data for each sample were corrected for the effects of background, multiple scattering, container scattering, Compton scattering, and absorption using the GudrunX programme [84], [91]. The resulting total scattered intensity per atom, $\frac{1}{N} d\sigma/d\Omega$, is converted [87] to the distinct total-scattering structure factor, $S(Q)$, which is the scattering due to atom-atom correlations, which will oscillate about a baseline determined by the coherent self-scattering (**Chapter 3.1.2**). A ‘sharpening’ term is also introduced to enhance scattering at high Q [87]:

$$S(Q) = \frac{\left[\frac{1}{N} \frac{d\sigma}{d\Omega} - \sum_{i=1}^n c_i f_i(Q)^2 \right]}{\sum_{i=1}^n c_i f_i(Q)^2} \quad 6.2$$

Where there are N atoms in the sample, c_i is the proportion of element i and $f_i(Q)$ is the X-ray atomic form factor of element i [82]. Q is the scattering vector determined by the X-ray wavelength, λ , and the scattering angle 2θ :

$$Q = \frac{4\pi \sin \theta}{\lambda} \quad 6.3$$

For a non-interacting mixture of M phases the total intensity is assumed to be the weighted sum of intensities of each phase (not accounting for attenuation and the presence of interfaces) [137]:

$$\frac{d\sigma}{d\Omega} = \sum_{k=1}^M \frac{d\sigma^k}{d\Omega} \quad 6.4$$

Where $\frac{d\sigma^k}{d\Omega}$ is the total scattered intensity of the k^{th} phase in the multiphase sample, which is obtained from a measurement of $\frac{1}{N} d\sigma/d\Omega$ from a sample of phase k on its own, i.e. $\frac{d\sigma^k}{d\Omega} = N_k \left(\frac{1}{N} d\sigma/d\Omega \right)_k$ where N_k is the atomic proportion of k within the multiphase sample. However due to the difficulty of placing X-ray scattering data on an absolute scale [91] a set of additional scaling factors are introduced:

$$a_k I_k^{\text{Norm}} = \frac{d\sigma^k}{d\Omega} \quad 6.5$$

Where I_k^{Norm} is the approximately normalised intensity and a_k is a constant close to unity. Equation 6.4 now becomes:

$$a_{\text{Expt.}} I_{\text{Expt.}}^{\text{Norm}} = \sum_{k=1}^M a_k I_k^{\text{Norm}} \quad 6.6$$

In this study the values of a_k were determined such that the difference between the calculated mixture and the experimentally measured scattering, was minimised for each different inorganic glass composition.

In order to produce the expected total-scattering intensity of a non-interacting mixture the experimental total-scattering intensities per atom of the pure $a_g\text{ZIF-62}$ and inorganic glasses are recovered from their respective $S(Q)$ (**Figure 6.35-37**) (**Equation 6.2**) and added together weighted by their atomic proportions and normalisation constants a_k (**Equation 6.6**). The directly measured total-scattering intensity for the composite samples, $(a_g\text{ZIF-62})_{0.5}(\text{Inorganic Glass})_{0.5} - 1 \text{ min}$ and $(a_g\text{ZIF-62})_{0.5}(\text{Inorganic Glass})_{0.5} - 30 \text{ min}$, the experimental total-scattering, are also recovered from their respective $S(Q)$ s (**Equation 6.2**).

The difference between measured intensity from a sample and the calculated intensity from a non-interacting mixture of the same chemistry therefore represents changes in the diffracted intensity resulting from interaction of the $a_g\text{ZIF-62}$ and inorganic glass phases in the composite. This difference is then re-sharpened by dividing through by $\sum_{i=1}^n c_i f_i(Q)^2$:

$$S(Q)^{\text{Diff}} = \frac{a_{\text{Expt.}} I_{\text{Expt.}}^{\text{Norm}} - (a_{\text{Inorg.}} I_{\text{Inorg.}}^{\text{Norm}} + a_{\text{ZIF}} I_{\text{ZIF}}^{\text{Norm}})}{\sum_{i=1}^n c_i f_i(Q)^2} \quad 6.7$$

The difference curves of the $(a_g\text{ZIF-62})_{0.5}(\text{Al-rich})_{0.5} - 1 \text{ min}$ and $(a_g\text{ZIF-62})_{0.5}(\text{Na-deficient})_{0.5} - 1 \text{ min}$ samples are relatively featureless except for small features associated with each of the FSDP. In contrast the $(a_g\text{ZIF-62})_{0.5}(\text{Al-rich})_{0.5} - 30 \text{ min}$ and $(a_g\text{ZIF-62})_{0.5}(\text{Na-deficient})_{0.5} - 30 \text{ min}$ samples contain sharp Bragg features in the difference matching the PXRD results (**Figure 6.24** and **Figure 6.41-42**). The same pattern of peaks is also seen in the $(a_g\text{ZIF-62})_{0.5}(\text{base})_{0.5} - 1 \text{ min}$ sample (**Figure 6.43a**). Interestingly the $(a_g\text{ZIF-62})_{0.5}(\text{base})_{0.5} - 30 \text{ min}$ sample also contains Bragg peaks, even though they were not observable in the PXRD data or in the $S(Q)$, though they are much weaker (**Figure 6.43b**). In general, the Bragg features are more obvious in all samples in the $S(Q)^{\text{Diff}}$ than in the $S(Q)$ due to the subtraction of the FSDP from the $a_g\text{ZIF-62}$. Comparison of the $S(Q)^{\text{Diff}}$ allows us to confirm that the pattern of Bragg scattering is the same in all samples (**Figure 6.44**).

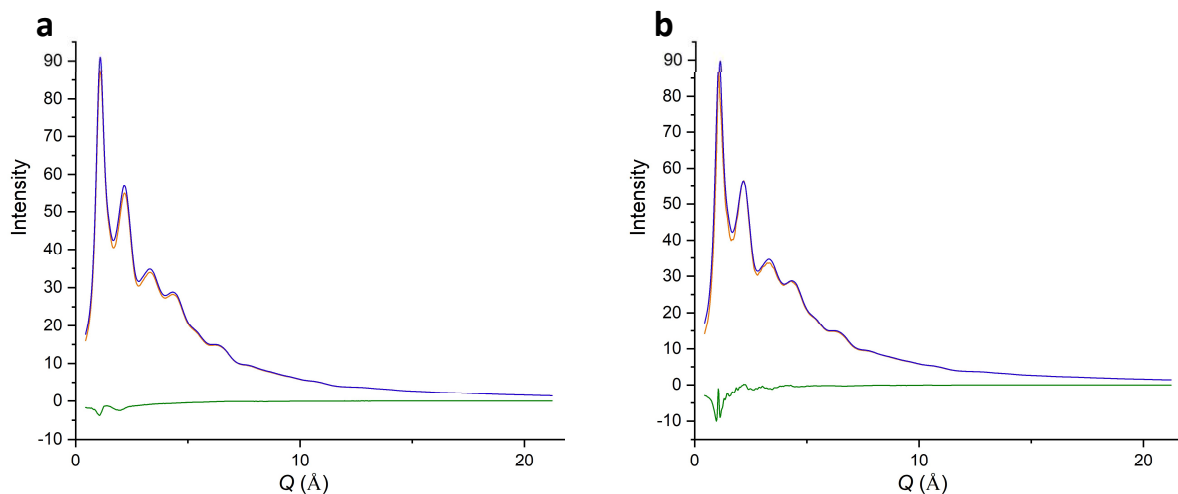


Figure 6.41: Recovered total-scattering of $(a_g\text{ZIF-62})_{0.5}(\text{Al-rich})_{0.5}$. Experimental (orange) vs calculated (blue) total-scattering and difference (green) of **a.** $(a_g\text{ZIF-62})_{0.5}(\text{Al-rich})_{0.5} - 1$ min. **b.** $(a_g\text{ZIF-62})_{0.5}(\text{Al-rich})_{0.5} - 30$ min.

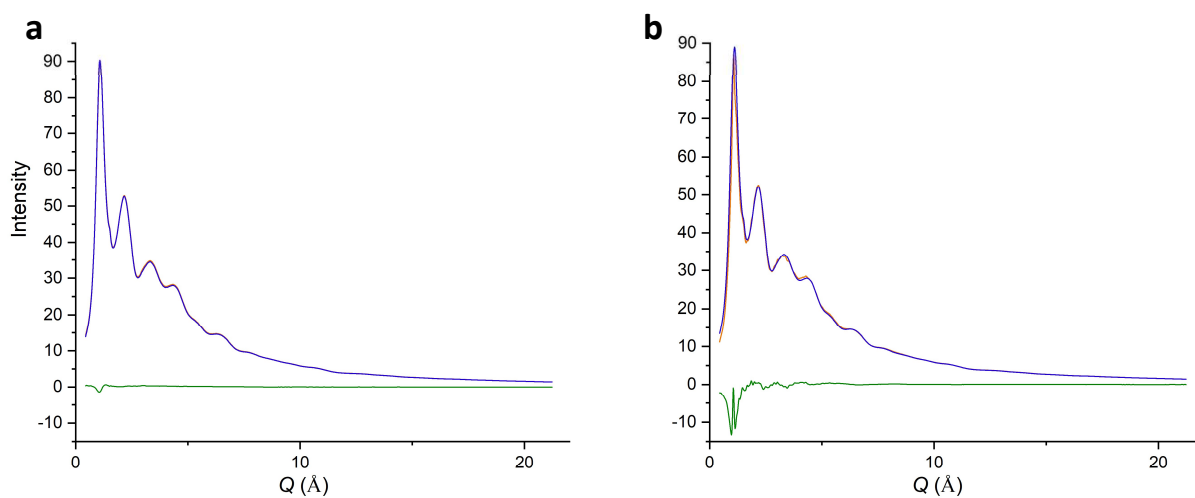


Figure 6.42: Recovered total-scattering of $(a_g\text{ZIF-62})_{0.5}(\text{Na-deficient})_{0.5}$. Experimental (orange) vs calculated (blue) total-scattering and difference (green) of **a.** $(a_g\text{ZIF-62})_{0.5}(\text{Na-deficient})_{0.5} - 1$ min. **b.** $(a_g\text{ZIF-62})_{0.5}(\text{Na-deficient})_{0.5} - 30$ min.

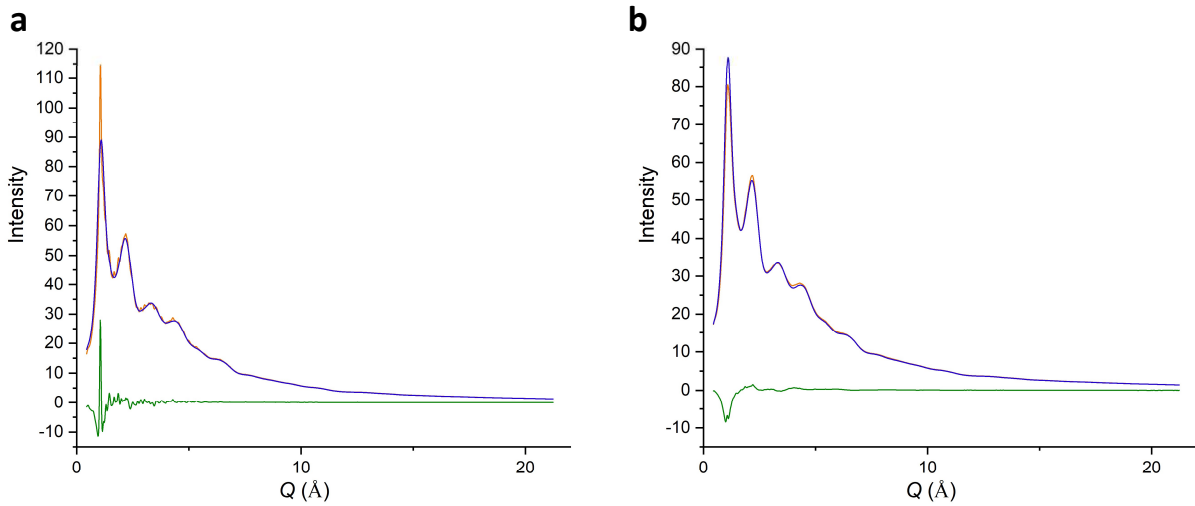


Figure 6.43: Recovered total-scattering of $(a_g\text{ZIF-62})_{0.5}(\text{base})_{0.5}$. Experimental (orange) vs calculated (blue) total-scattering and difference (green) of **a.** $(a_g\text{ZIF-62})_{0.5}(\text{base})_{0.5} - 1$ min and **b.** $(a_g\text{ZIF-62})_{0.5}(\text{base})_{0.5} - 30$ min.

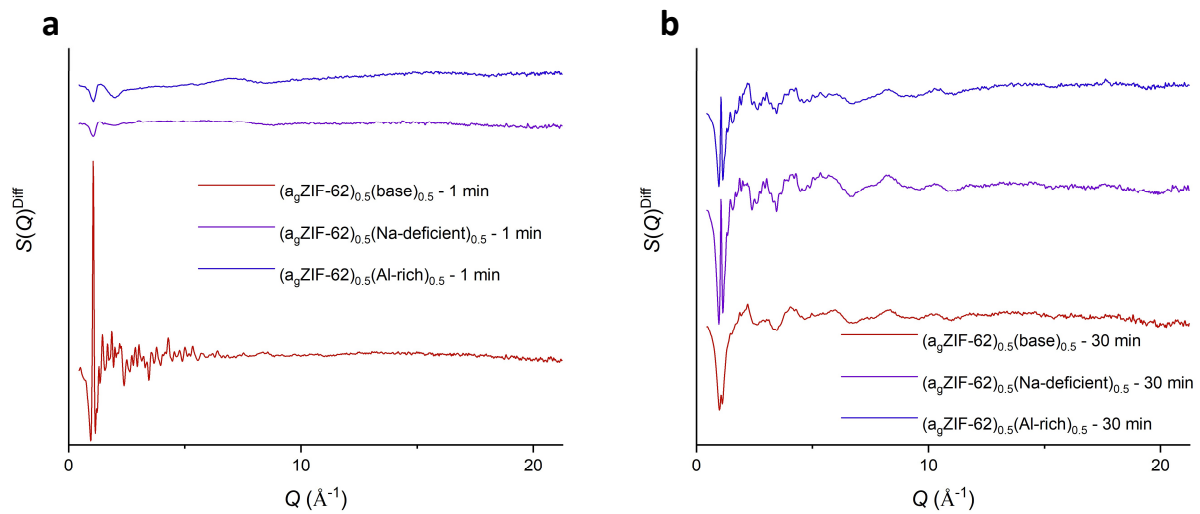


Figure 6.44: $S(Q)^{\text{Diff}}$ for the $(a_g\text{ZIF-62})_{0.5}(\text{Inorganic Glass})_{0.5}$ samples. **a.** $(a_g\text{ZIF-62})_{0.5}(\text{Inorganic Glass})_{0.5} - 1$ min. **b.** $(a_g\text{ZIF-62})_{0.5}(\text{Inorganic Glass})_{0.5} - 30$ min.

The $S(Q)^{\text{Diff}}$ can then be Fourier transformed, *via* the StoG script [91], to produce $G(r)^{\text{Diff}}$ [84]. Where the $G(r)^{\text{Diff}}$ now represents a weighted histogram of the distribution of atom-atom distances in the composite sample which are due to interactions between the inorganic glass and $a_g\text{ZIF-62}$. In other words, peaks represent new correlations formed because of the interaction between the two phases; either new bonds formed at the interface or changes in the structure of either phase due to the presence of the other. Finally, to aid visualisation of new correlations across the full range of real space

an alternative form of the usual $D(r)$ function is plotted:

$$D(r)^{\text{Diff}} = (G(r)^{\text{Diff}} - 1)r \quad 6.8$$

The normal weighting constants for conversion of $D(r)$ to $G(r)$, i.e. $4\pi\rho_0$ [87], are omitted in the conversion of $G(r)^{\text{Diff}}$ to $D(r)^{\text{Diff}}$ as the density of the atoms contributing to the difference cannot be known. Any quantitative examination of either $G(r)^{\text{Diff}}$ or $D(r)^{\text{Diff}}$ would be difficult due to scaling problems.

The $D(r)^{\text{Diff}}$ of all the $(a_g\text{ZIF-62})_{0.5}(\text{Inorganic Glass})_{0.5} - 1 \text{ min}$ and $(a_g\text{ZIF-62})_{0.5}(\text{Inorganic Glass})_{0.5} - 30 \text{ min}$ samples (**Equation 6.8**) contain residual features due to the inorganic glass, and ZIF-62 (**Figure 6.45**). The size and shape of this 'erroneous' difference is dependent on the scale factors (a_k) used. The presence of these additional features in the $S(Q)^{\text{Diff}}$ complicates interpretation of the $G(r)^{\text{Diff}}$ and $D(r)^{\text{Diff}}$; underweighting of the total-scattering from a constituent phase will lead to positive peaks from that phase in the $G(r)^{\text{Diff}}$ and $D(r)^{\text{Diff}}$ as residual scattering from that phase remains in the $S(Q)^{\text{Diff}}$. Conversely, overweighting will lead to negative peaks in the $G(r)^{\text{Diff}}$ and $D(r)^{\text{Diff}}$ as the total-scattering from a phase is over-removed from the $S(Q)^{\text{Diff}}$. As a result of this interpretation of the real space data should always be done in the context of the correlations expected from the phases in the calculated mixture.

No correlations that could be definitively ascribed to the new bonds observed through Raman scattering or ^{31}P NMR data could be observed. However, the $D(r)^{\text{Diff}}$ of the $(a_g\text{ZIF-62})_{0.5}(\text{Inorganic Glass})_{0.5} - 30 \text{ min}$ and the $(a_g\text{ZIF-62})_{0.5}(\text{base})_{0.5} - 1 \text{ min}$ are all qualitatively similar as expected from the similar Bragg scattering observed in the $S(Q)^{\text{Diff}}$ (**Figure 6.45**). The long-range order (LRO) was also evident in the $D(r)^{\text{Diff}}$ from $(a_g\text{ZIF-62})_{0.5}(\text{base})_{0.5} - 1 \text{ min}$, $(a_g\text{ZIF-62})_{0.5}(\text{Na-deficient})_{0.5} - 30 \text{ min}$ and $(a_g\text{ZIF-62})_{0.5}(\text{Al-rich})_{0.5} - 30 \text{ min}$ samples. However the $D(r)^{\text{Diff}}$ $(a_g\text{ZIF-62})_{0.5}(\text{base})_{0.5} - 30 \text{ min}$ sample appeared flat at extended distances, which is due to the very small proportion of crystalline component as seen in the very small Bragg features in the $S(Q)^{\text{Diff}}$ (**Figure 6.46**).

The insensitivity of X-ray total-scattering to the new correlations observed in $^{31}\text{P}\{^1\text{H}\}$ CP NMR (**Figure 6.29-31**) and Raman (**Figure 6.32-34**) is believed to be due principally to two things: firstly, the crystallisation of a small amount of ZIF-zni. As ZIF-zni has very similar local bonding to $a_g\text{ZIF-62}$ its correlations appear in the same place and make unambiguous interpretation of the SRO in the $D(r)^{\text{Diff}}$ difficult. Secondly the changes measured spectroscopically are relatively small with most of the spectra in Raman and IR remaining unchanged and the changes observed in the ^{31}P NMR spectra being relatively subtle. This means that these changes may be below the detection limit of a technique such

as PDF which is sensitive to the whole volume of the sample. Added to this is also, as previously mentioned, the difficulty of putting X-ray total-scattering data on an absolute scale [91].

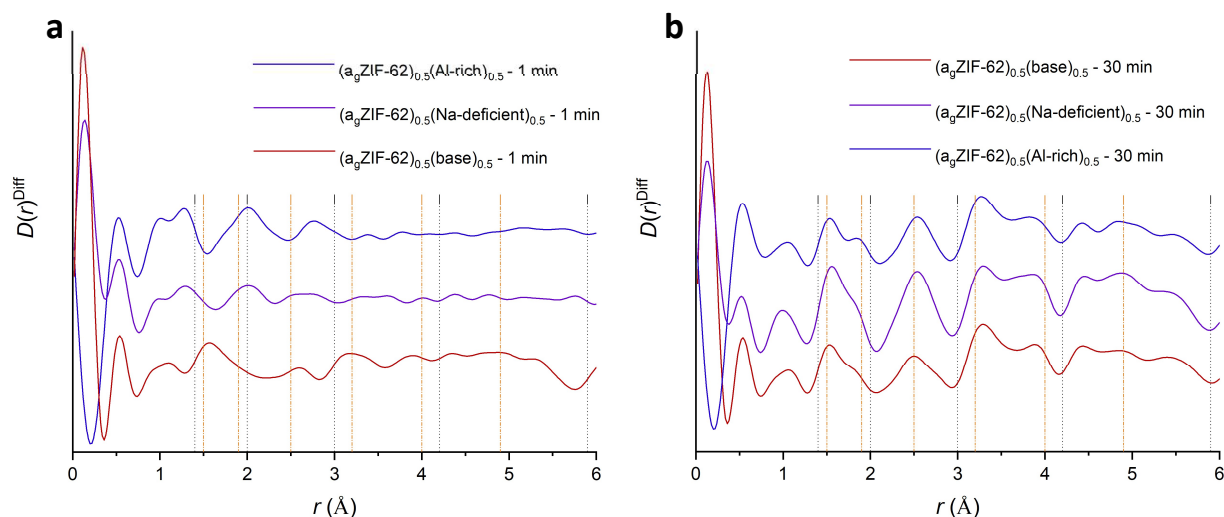


Figure 6.45: $D(r)^{\text{Diff}}$ of the SRO in the $(a_g\text{ZIF-62})_{0.5}(\text{Inorganic Glass})_{0.5}$ samples. **a.** $(a_g\text{ZIF-62})_{0.5}(\text{Inorganic Glass})_{0.5}$ – 1 min and **b.** $(a_g\text{ZIF-62})_{0.5}(\text{Inorganic Glass})_{0.5}$ – 30 min samples. Droplines indicate correlations from $a_g\text{ZIF-62}$ (black) and the inorganic glass (orange).

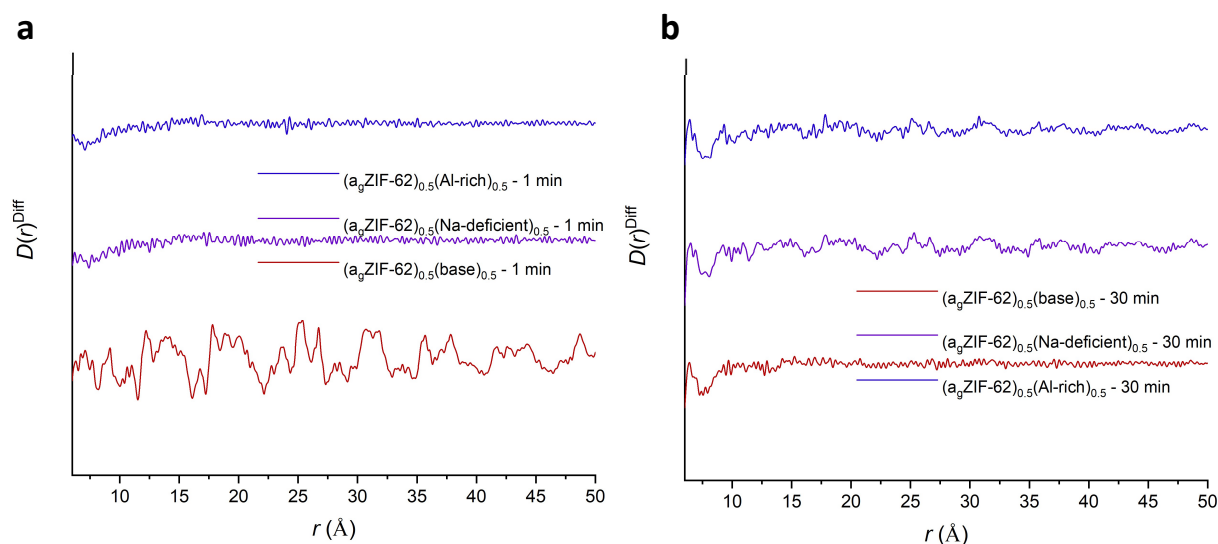


Figure 6.46: $D(r)^{\text{Diff}}$ of the LRO in the $(a_g\text{ZIF-62})_{0.5}(\text{Inorganic Glass})_{0.5}$ samples. **a.** $(a_g\text{ZIF-62})_{0.5}(\text{Inorganic Glass})_{0.5}$ – 1 min and **b.** $(a_g\text{ZIF-62})_{0.5}(\text{Inorganic Glass})_{0.5}$ – 30 min samples.

6.9 Microstructural Investigations of $(a_g\text{ZIF-62})_{0.5}(\text{Inorganic Glass})_{0.5}$ Samples through Microscopy

6.9.1 Examination of the Composite Bulk Structure via Light Microscopy.

The macroscopic appearance of the bulk composites was recorded using reflected light microscopy (**Figure 6.47**). The $(a_g\text{ZIF-62})_{0.5}(\text{Na-deficient})_{0.5} - 1 \text{ min}$ and $(a_g\text{ZIF-62})_{0.5}(\text{Al-rich})_{0.5} - 1 \text{ min}$ were white, and appeared to be sintered powder bodies, though $(a_g\text{ZIF-62})_{0.5}(\text{Na-deficient})_{0.5} - 1 \text{ min}$ was darker and more resembled a single glass piece. In contrast to this $(a_g\text{ZIF-62})_{0.5}(\text{base})_{0.5} - 1 \text{ min}$ was inhomogeneous in appearance, with both white 'sintered powder' regions, darker 'macroscopically glassy' regions, and distinct 'orange' regions (**Figure 6.47**). These regions correspond well with the original crystalline mixture pellet, with the region closer to edge appearing lighter and the region nearest the centre appearing 'orange'. This indicates that the inhomogeneity might arise from the edges of the pellet cooling faster than the centre. The $(a_g\text{ZIF-62})_{0.5}(\text{Na-deficient})_{0.5} - 30 \text{ min}$ and $(a_g\text{ZIF-62})_{0.5}(\text{Al-rich})_{0.5} - 30 \text{ min}$ samples looked generally darker and more macroscopically glassy. However, $(a_g\text{ZIF-62})_{0.5}(\text{base})_{0.5} - 30 \text{ min}$ appeared different in appearance from $(a_g\text{ZIF-62})_{0.5}(\text{base})_{0.5} - 1 \text{ min}$, with evidence of large pores and cracking in the pellet.

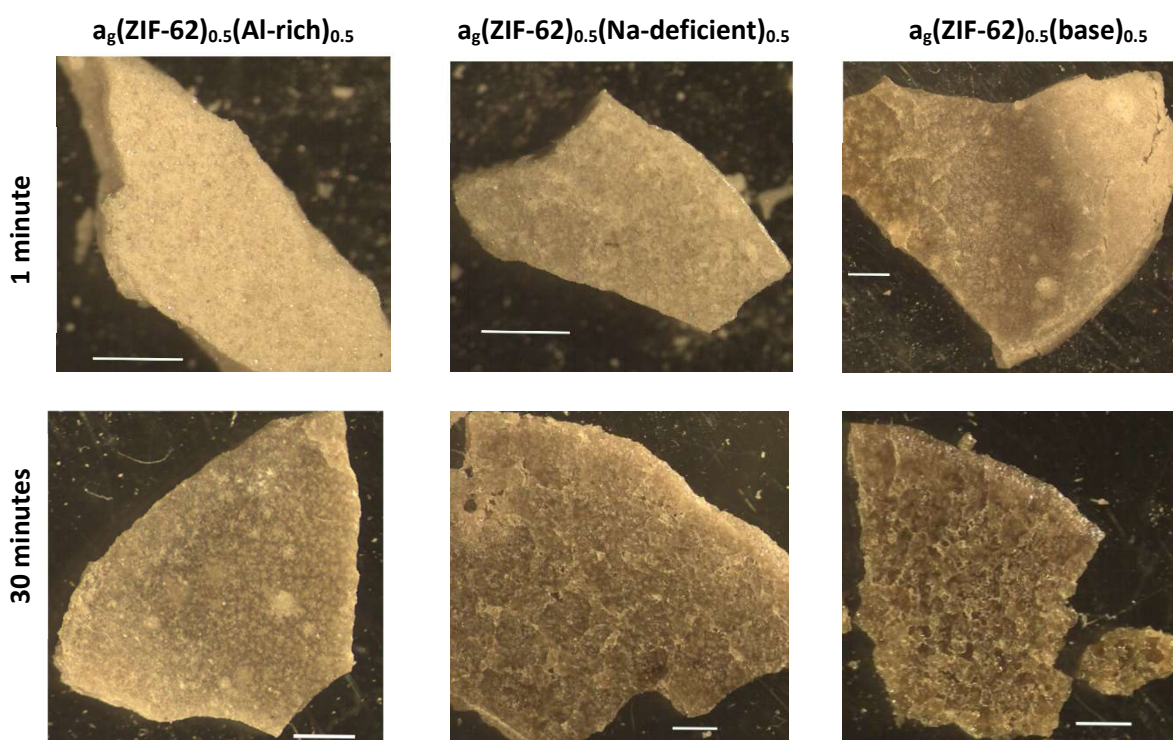


Figure 6.47: Reflected light microscopy of the $(a_g\text{ZIF-62})_{0.5}(\text{Inorganic Glass})_{0.5}$ samples. The white bar in each image is 1 mm.

Confocal microscopy was then used to characterise the microstructural appearance of the composite samples. Top-lit confocal microscopy revealed clear evidence of flow in the microstructure of the heat-treated composites (**Figure 6.48**). Evidence of remnant particles from the crystalline mixture can still be seen, particularly in the $(a_g\text{ZIF-62})_{0.5}(\text{Al-rich})_{0.5}$ – 1 min and $(a_g\text{ZIF-62})_{0.5}(\text{Na-deficient})_{0.5}$ – 1 min samples. This explains their macroscopic particulate appearance. However, the formation of necks between the particles can be seen in all $(a_g\text{ZIF-62})_{0.5}(\text{Inorganic Glass})_{0.5}$ – 1 min samples, implying the onset of particle coalescence is occurring during the liquid phase. The $(a_g\text{ZIF-62})_{0.5}(\text{Inorganic Glass})_{0.5}$ – 30 min samples showed evidence of grain growth with larger areas of smooth surfaces evident.

Side-illuminated confocal microscopy provided an indication of the through thickness microstructure of the composites (**Figure 6.49**). Clear evidence of flow in all cases was observed, with heat treatment for longer periods of time resulting in grain growth, reduction of interfaces and greater light transmittance through the samples. Additionally features indicating the action of surface tension were found, such as rounding of grains to form ‘islands’, spheroidal bubbles and surface droplets [138].

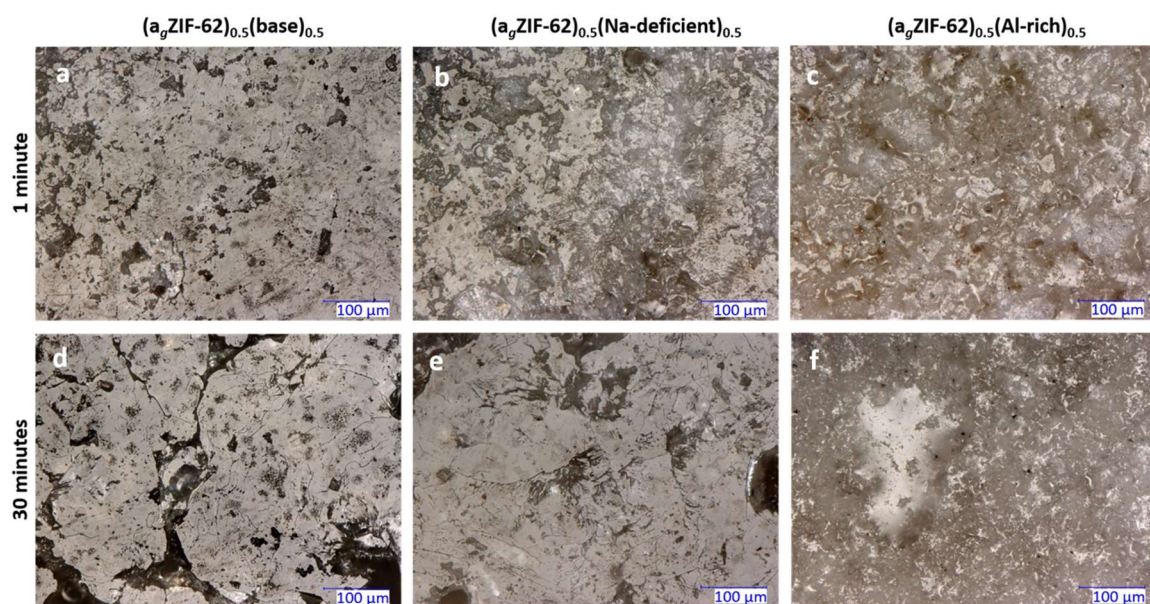


Figure 6.48: Top-illuminated confocal microscopy images of the $(a_g\text{ZIF-62})_{0.5}(\text{Inorganic Glass})_{0.5}$ samples.

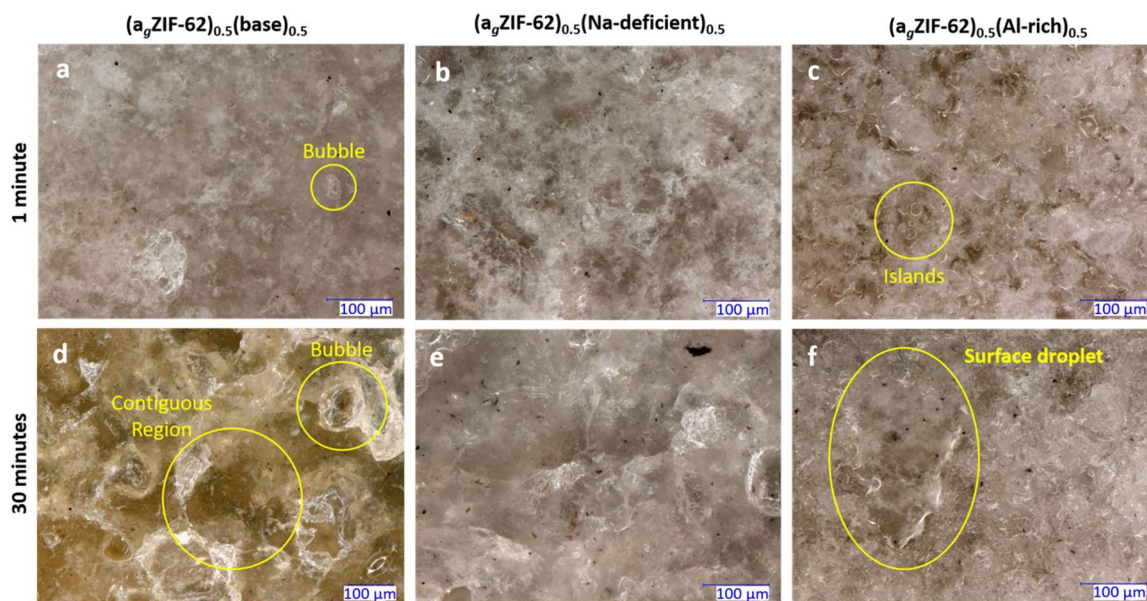


Figure 6.49: Side-illuminated z-scan digital microscopy images of the $(a_g\text{ZIF-62})_{0.5}(\text{Inorganic Glass})_{0.5}$ samples.

6.9.2 Microstructural Examination of the Composites through Electron Microscopy

Scanning electron microscopy (SEM) was used to study the fine structure of the composite samples. The $(a_g\text{ZIF-62})_{0.5}(\text{Al-rich})_{0.5}$ sample showed inhomogeneity even at this scale (**Figure 6.50**) with evidence of remnant particles ranging from around 5 - 60 μm in diameter visible in the $(a_g\text{ZIF-62})_{0.5}(\text{Al-rich})_{0.5}$ – 1 min sample (**Figure 6.50**). However, the $(a_g\text{ZIF-62})_{0.5}(\text{Al-rich})_{0.5}$ – 30 min sample showed evidence of decreased inhomogeneity with fewer remnant particles being visible (**Figure 6.50**). The $(a_g\text{ZIF-62})_{0.5}(\text{Na-deficient})_{0.5}$ – 1 min sample appeared much more homogeneous at this length scale with much fewer remnant interfaces visible (**Figure 6.51**) and the $(a_g\text{ZIF-62})_{0.5}(\text{Na-deficient})_{0.5}$ – 30 min appears to be a single piece at this magnification (**Figure 6.51**). The $(a_g\text{ZIF-62})_{0.5}(\text{base})_{0.5}$ – 1 min sample appeared to be a single piece (**Figure 6.52**) and despite the macroscopic cracking and porosity observed in the $(a_g\text{ZIF-62})_{0.5}(\text{base})_{0.5}$ – 30 min sample (**Figure 6.47** and **Figure 6.52**) the bulk of the sample remained smooth. The results of the SEM therefore confirm the PXRD and X-ray total-scattering measurements, i.e. that the bulk of the composites are glassy.

However, a few small crystallites, were observed in the $(a_g\text{ZIF-62})_{0.5}(\text{base})_{0.5}$ – 1 min sample (**Figure 6.53**). These crystallites were easily distinguishable from the remnant particles due to their faceted appearance. They also appear to be embedded within the otherwise contiguous structure, which supports the idea of their formation in-situ during heating. No similar crystallites could be observed in the other composite samples, despite Bragg peaks being discernible in all the $(a_g\text{ZIF-62})_{0.5}(\text{Inorganic Glass})_{0.5}$ – 30 min samples (**Figure 6.44b**). However, this may be due to the smaller degree of

crystallisation, which leads to crystallites being fewer in number and/or smaller in size and therefore harder to discern from the amorphous bulk.

The above results confirm that there is evidence for liquid phase mixing and flow in all the composite samples. With the degree of both liquid flow and sintering between the inorganic glass and a_g ZIF-62 increasing with increasing treatment time and decreasing T_g of the inorganic glass.

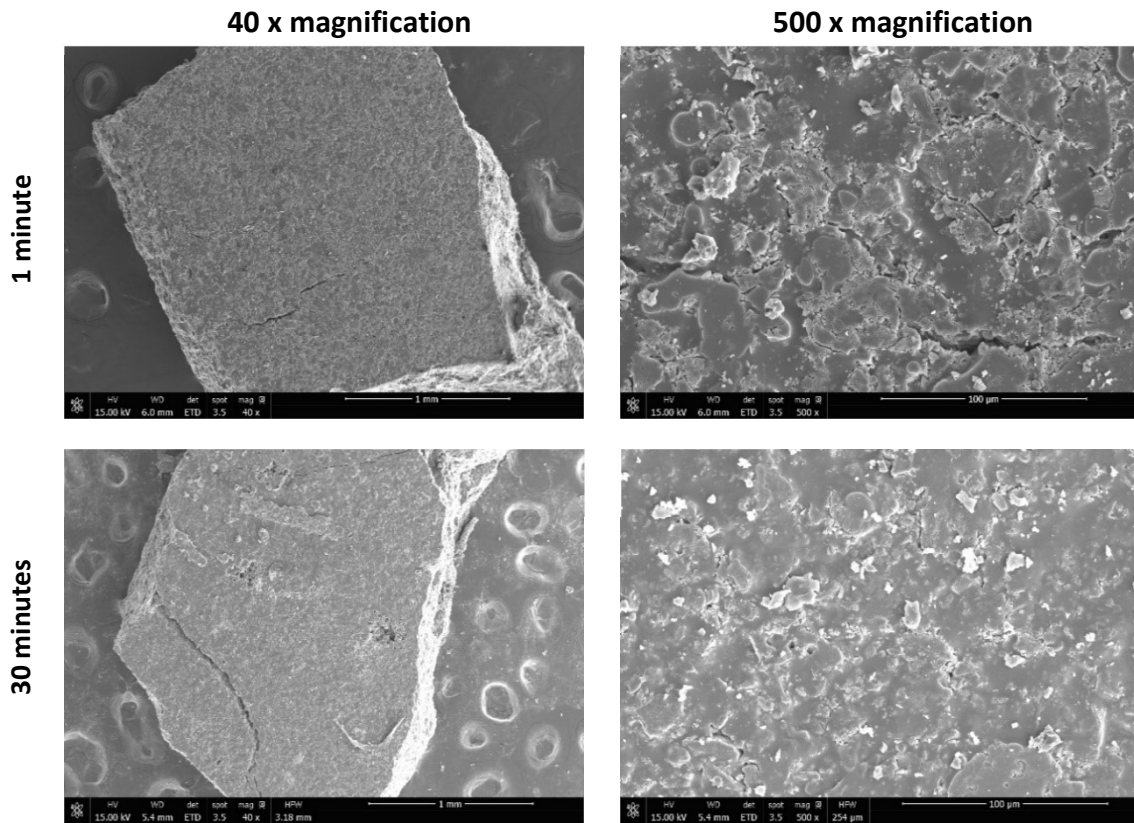


Figure 6.50: SEM of $(a_g\text{ZIF-62})_{0.5}(\text{Al-rich})_{0.5}$.

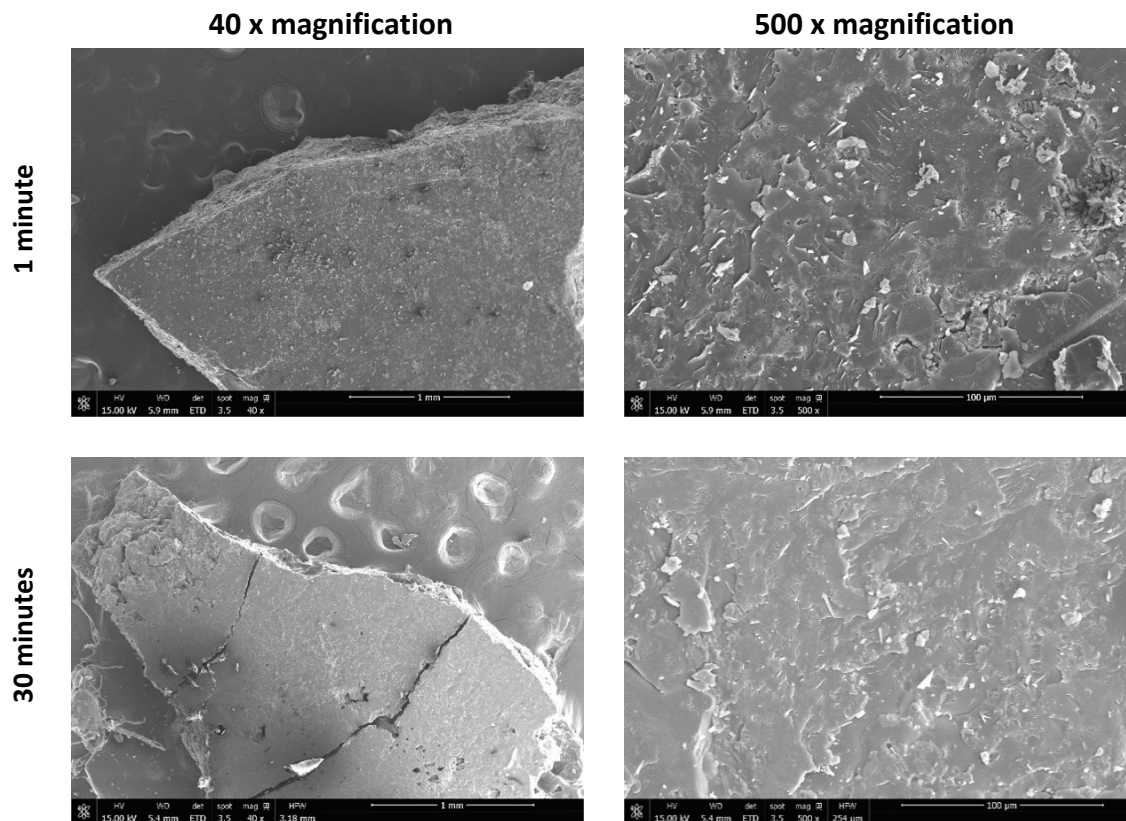


Figure 6.51: SEM of $(\text{agZIF-62})_{0.5}(\text{Na-deficient})_{0.5}$.

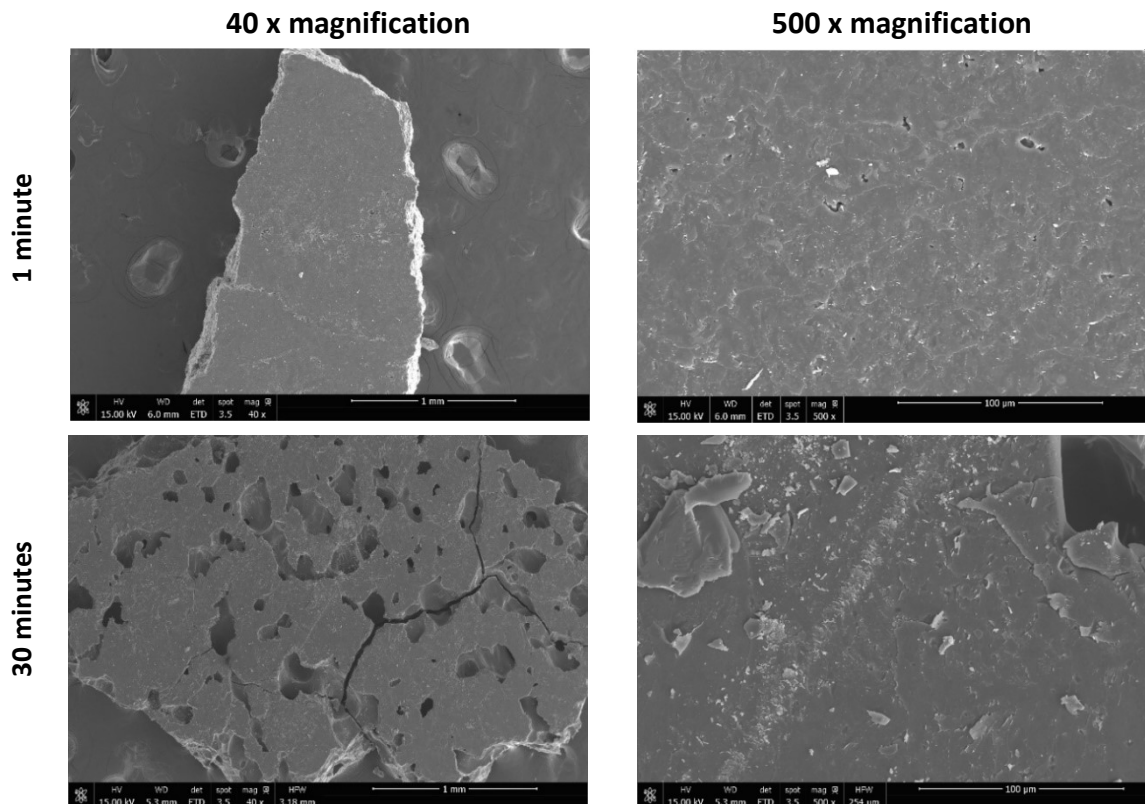


Figure 6.52: SEM of $(\text{agZIF-62})_{0.5}(\text{base})_{0.5}$.

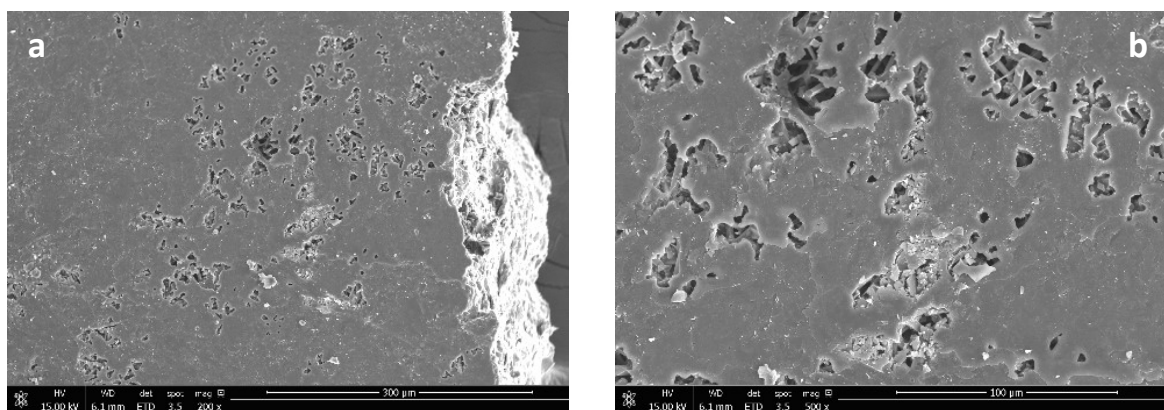


Figure 6.53: SEM Images of crystallites in $(a_g\text{ZIF-62})_{0.5}(\text{base})_{0.5}$ - 1 min. **a.** 200 times magnification. **b.** 500 times magnification.

To investigate the distribution of $a_g\text{ZIF-62}$ and inorganic glass in the composite samples energy-dispersive X-ray spectroscopy (EDS) was also used to investigate the microstructure. The locations of the $a_g\text{ZIF-62}$ glass domains were identified using the zinc signal, whereas those from the inorganic glass were determined by signals from aluminium and phosphorus. In each case the heaviest elements from each component, $\text{Zn}(\text{Im})_2$, NaPO_3 and AlF_3 , were used to obtain the clearest signal. We note that unfortunately, the $\text{Na K}\alpha$ edge (1.040 keV) and $\text{Zn L}\alpha$ edges (1.012 keV) are too close in energy to observe simultaneously using EDS [139], so we are unable to validate the observed appearance of Na-N bonding in the Raman results (**Figure 6.34**) with elemental mapping.

The EDS results demonstrate that all the composite samples show distinct regions of Zn and Al/P signal (**Figure 6.54-59**). This indicates that the composite samples are composed of distinct domains of $a_g\text{ZIF-62}$ and the relevant inorganic glass. This microstructure of isolated domains is consistent with the starting crystalline mixture having distinct ZIF-62 and inorganic glass particles. However the size of both the $a_g\text{ZIF-62}$ and inorganic glass domains decreases with heat treatment time in both the $(a_g\text{ZIF-62})_{0.5}(\text{Al-rich})_{0.5}$ (**Figure 6.54-55**) and $(a_g\text{ZIF-62})_{0.5}(\text{Na-deficient})_{0.5}$ samples (**Figure 6.56-57**), implying that increased heat treatment time results in a better degree of mixing between $a_g\text{ZIF-62}$ and Al-rich/Na-deficient. As the degree to which the starting crystalline mixtures were ball milled was kept constant, this mixing must have occurred at high temperatures, facilitated by the liquid phase. The domain sizes in the $(a_g\text{ZIF-62})_{0.5}(\text{base})_{0.5}$ samples did not change substantially in size with increasing heat treatment time (**Figure 6.58-59**), however this is because the domains in the $(a_g\text{ZIF-62})_{0.5}(\text{base})_{0.5}$ - 1 min sample were already comparable in size to the $(a_g\text{ZIF-62})_{0.5}(\text{Al-rich})_{0.5}$ - 30 min and $(a_g\text{ZIF-62})_{0.5}(\text{Na-deficient})_{0.5}$ -30 min samples. The non-particulate morphology of the larger domains in the $(a_g\text{ZIF-62})_{0.5}(\text{base})_{0.5}$ samples are also indicative of a substantial degree of liquid flow in the base glass.

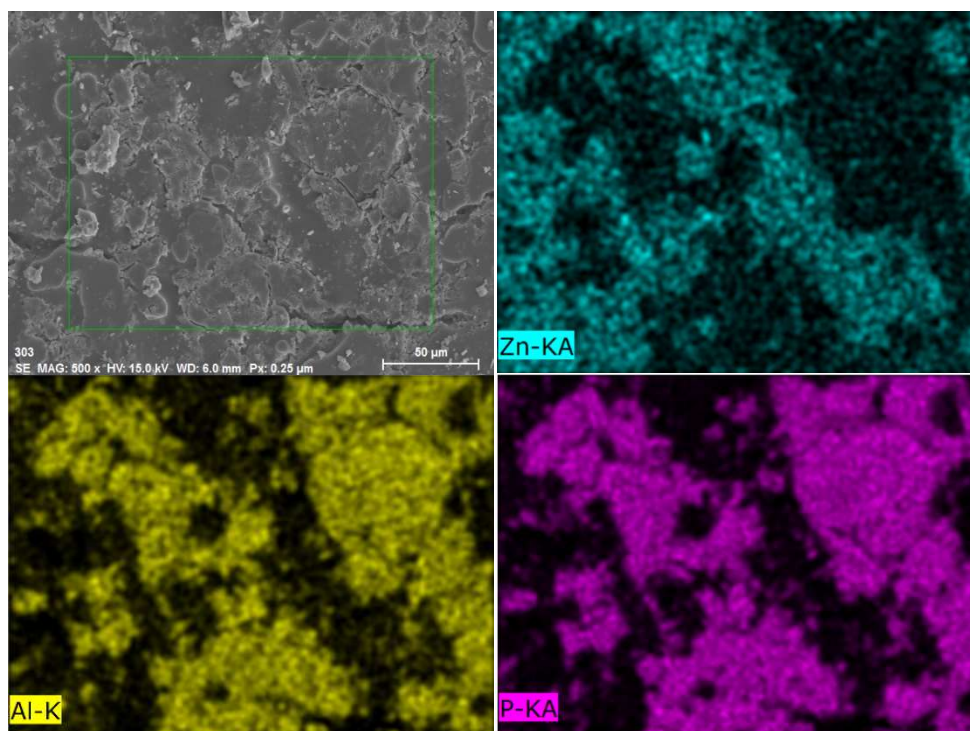


Figure 6.54: EDS of $(a_gZIF-62)_{0.5}(Al-rich)_{0.5}$ – 1 min.

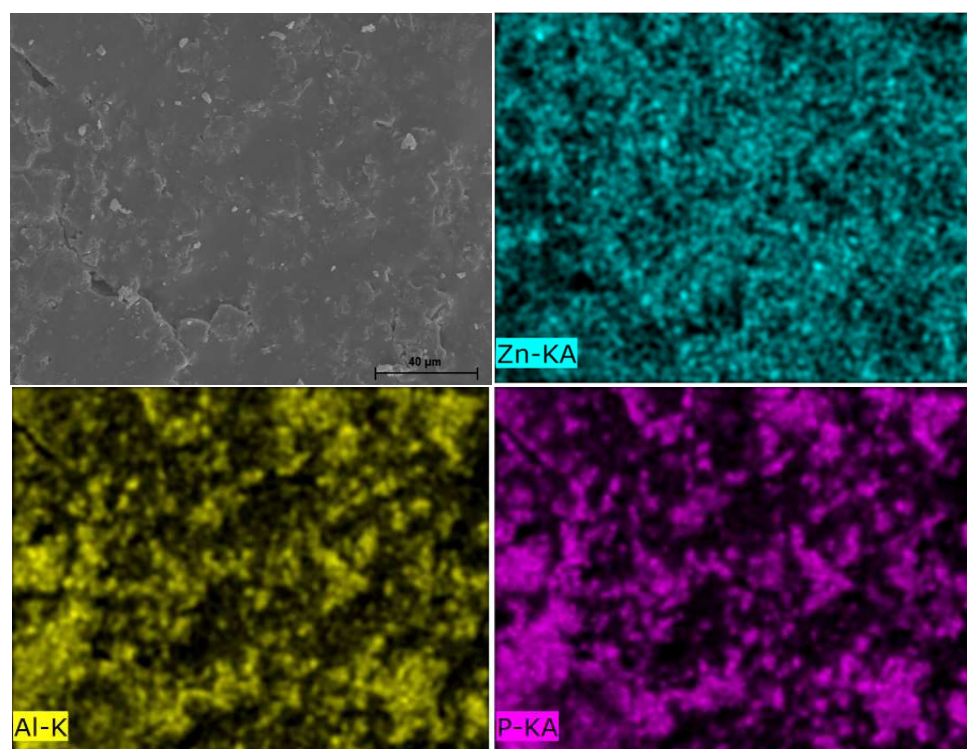


Figure 6.55: EDS of $(a_gZIF-62)_{0.5}(Al-rich)_{0.5}$ – 30 min.

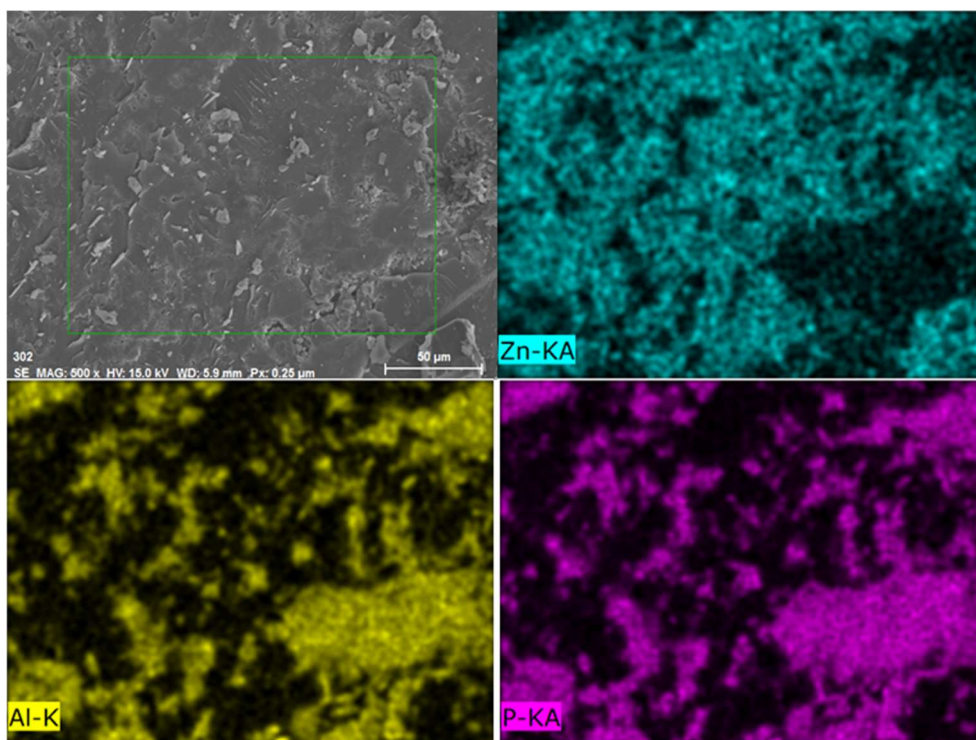


Figure 6.56: EDS of $(a_g\text{ZIF-62})_{0.5}(\text{Na-deficient})_{0.5} - 1 \text{ min.}$

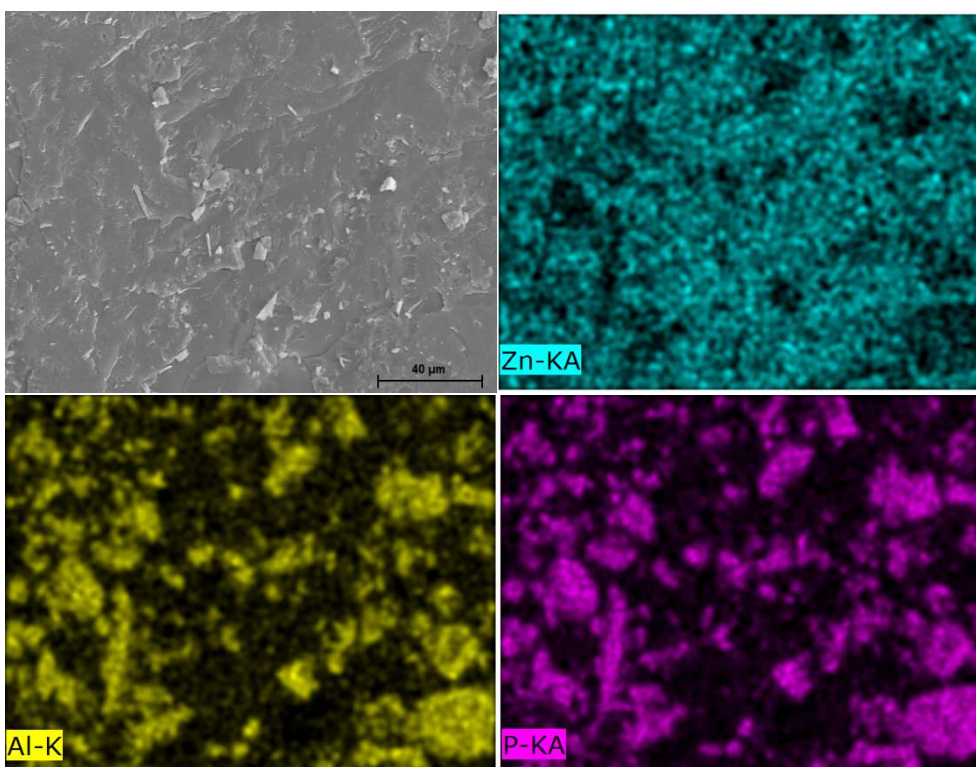


Figure 6.57: EDS of $(a_g\text{ZIF-62})_{0.5}(\text{Na-deficient})_{0.5} - 30 \text{ min.}$

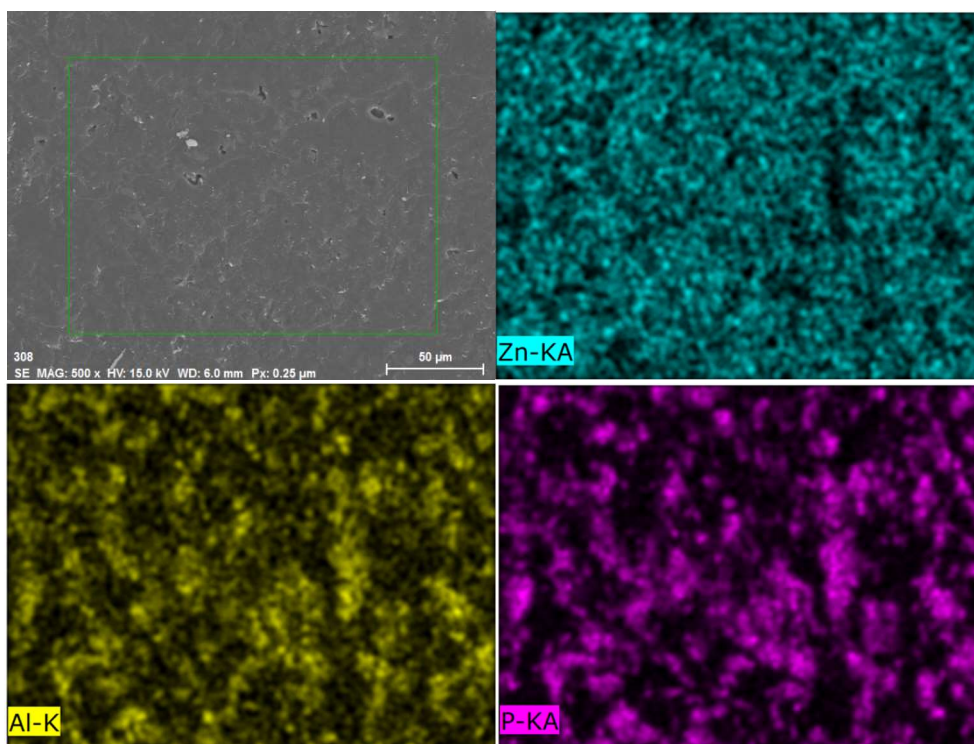


Figure 6.58: EDS of $(agZIF-62)_{0.5}(base)_{0.5} - 1 \text{ min.}$

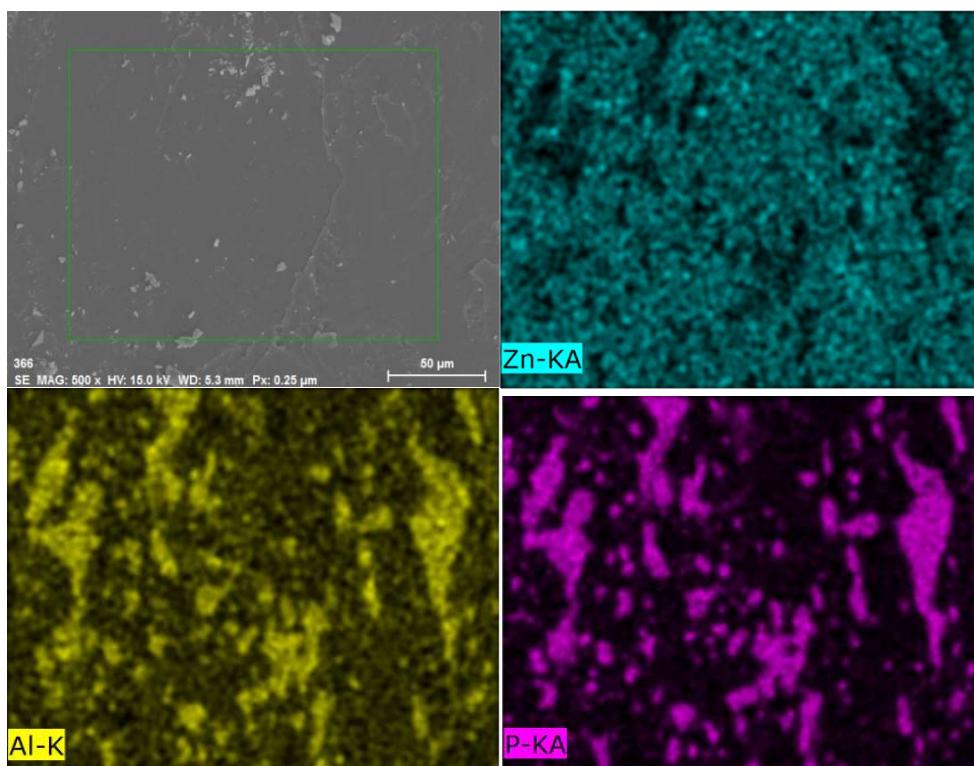


Figure 6.59: EDS of $(agZIF-62)_{0.5}(base)_{0.5} - 30 \text{ min.}$

6.10 Characterisation of the Properties of $(a_g\text{ZIF-62})_{0.5}(\text{Inorganic Glass})_{0.5}$

The local bonding, long-range order, and microstructures of the composite materials have now been characterised in detail, and to expand on these experiments the mechanical and ionic conductivity properties of the composites were then investigated.

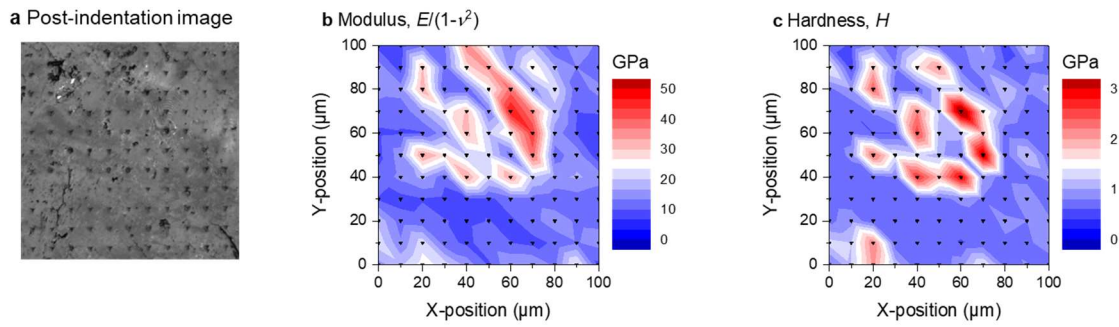
The mechanical properties of the composite samples were investigated as the microstructural characterisation of the previous section demonstrated the domain structure of the $(a_g\text{ZIF-62})_{0.5}(\text{Inorganic Glass})_{0.5}$ samples. Mechanical characterisation via nanoindentation and scratch testing was therefore conducted to explore whether this microstructure conferred any mechanical advantages in terms of stiffness, hardness, and scratch resistance to the composite materials relative to the $a_g\text{ZIF-62}$ glass phase.

The indication from Raman spectroscopy, that Na^+ ions enter the $a_g\text{ZIF-62}$ domains of the $(a_g\text{ZIF-62})_{0.5}(\text{Inorganic Glass})_{0.5}$ samples, led us to perform ionic conductivity measurements on the $(a_g\text{ZIF-62})_{0.5}(\text{Na-deficient})_{0.5}$ – 1 min and 30 min samples. These were carried out to evaluate the nature of the bonding and mobility of sodium ions in the composites, and how both were affected by heat treatment time.

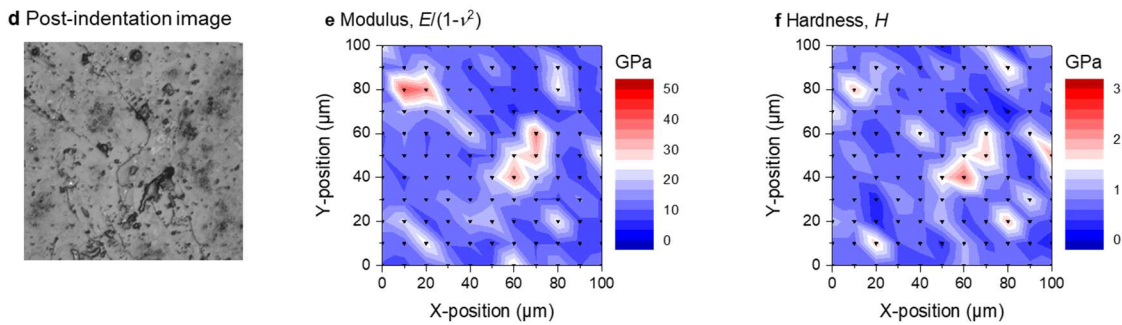
6.10.1 Nanoindentation and Scratch Testing of the $(a_g\text{ZIF-62})_{0.5}(\text{base})_{0.5}$ Samples

Given the sensitivity of nanoindentation to surface roughness, microscopy on the $(a_g\text{ZIF-62})_{0.5}(\text{Na-deficient})_{0.5}$ and $(a_g\text{ZIF-62})_{0.5}(\text{Al-rich})_{0.5}$ confirmed that they were unsuitable for the technique, however, the comparatively more homogeneous, $(a_g\text{ZIF-62})_{0.5}(\text{base})_{0.5}$ samples were suitable (**Figure 6.60**). The $(a_g\text{ZIF-62})_{0.5}(\text{base})_{0.5}$ results show clear heterogeneity in the sample, even on the 100 μm scale, with regions of high, and low hardness (H) and modulus (E). Stiffness values for pure samples of $a_g\text{ZIF-62}$ and the base inorganic glass are approx. 6.6 GPa [76] and 51 GPa respectively. The results show a significant decrease in heterogeneity in the samples heated for 30 minutes. This is accompanied by a decrease in the average E , suggesting a more compliant structure is formed upon mixing MOF and inorganic glass.

$(a_g\text{ZIF-62})_{0.5}(\text{base})_{0.5} - 1 \text{ min}$



$(a_g\text{ZIF-62})_{0.5}(\text{base})_{0.5} - 30 \text{ min}$



Control: $a_g\text{ZIF-62}$: $E/(1-\nu^2) = 7.15 \pm 0.02 \text{ GPa}$; $H = 0.712 \pm 0.006 \text{ GPa}$
Inorganic base glass: $E/(1-\nu^2) = 64.0 \pm 0.3 \text{ GPa}$; $H = 4.49 \pm 0.03 \text{ GPa}$

Figure 6.60: Nanoindentation experiments on the $(a_g\text{ZIF-62})_{0.5}(\text{base})_{0.5}$ samples. Modulus (E), and hardness (H) contour maps, together with wide-field confocal microscopy images of the area mapped across the surface of the $(a_g\text{ZIF-62})_{0.5}(\text{base})_{0.5}$ samples.

The scratch resistance of the $(a_g\text{ZIF-62})_{0.5}(\text{base})_{0.5} - 1 \text{ min}$ sample, $a_g\text{ZIF-62}$, and the inorganic base glass was also investigated (**Figure 6.61**). Due to the lower hardness of $a_g\text{ZIF-62}$ ($H(a_g\text{ZIF-62}) = 0.71 \text{ GPa}$) as compared to the inorganic glass ($H(\text{base}) = 4.49 \text{ GPa}$) a considerably larger sample volume of $a_g\text{ZIF-62}$ is deformed during scratching (**Figure 6.61a**). Despite this mismatch in the indenter displacement (h), very similar values of lateral force (F_L), monitored during a constant load test, were recorded for these two glasses (**Figure 6.61b**). This indicates a substantially lower resistance of $a_g\text{ZIF-62}$ against the lateral movement of the indenter tip, i.e. a lower scratch hardness [140] compared to the inorganic base glass.

When probing the $(a_g\text{ZIF-62})_{0.5}(\text{base})_{0.5} - 1 \text{ min}$ glass sample, pronounced fluctuations in both h and F_L are clearly visible during scratching. The length scale of these variations corresponds very well to the microstructural scale of the composite constituents, an effect also observed in the mechanical resistance, i.e hardness and modulus, of the composite material as revealed by nanoindentation (**Figure 6.60**). Mean values of h (**Figure 6.61a**) and F_L (**Figure 6.61b**) for the $(a_g\text{ZIF-62})_{0.5}(\text{base})_{0.5} - 1 \text{ min}$ glass sample are in-between the $a_g\text{ZIF-62}$ and base glasses. This confirms that the composite

materials are, on average, more compliant than the inorganic base glass but mechanically more stable than pure $a_g\text{ZIF-62}$. The work of deformation, W_s , as derived from the integral of F_L across 80 μm , neglecting the first and last 10 μm of each scratch, was also measured (**Figure 6.61c**). The values for the $(a_g\text{ZIF-62})_{0.5}(\text{base})_{0.5} - 1 \text{ min}$ samples were intermediate between the values of the end members and unsurprisingly given the variations in both h and F_L the W_s had a greater variance in the composite than in either $a_g\text{ZIF-62}$ or the base glass. The scratch hardness (H_s), defined as the slope of the linear regression curve of W_s versus V_s , represents the work, W_s , which is required to generate (deform) a scratch groove of volume V_s [140]. The value of W_s/V_s for the $(a_g\text{ZIF-62})_{0.5}(\text{base})_{0.5} - 1 \text{ min}$ glass sample is consistently above that of pure $a_g\text{ZIF-62}$ ($H_s(a_g\text{ZIF-62}) = 0.45 \text{ GPa}$), and close to that of the pure inorganic base glass ($H_s(\text{base}) = 4.84 \text{ GPa}$).

$(a_g\text{ZIF-62})_{0.5}(\text{base})_{0.5} - 1 \text{ min}$

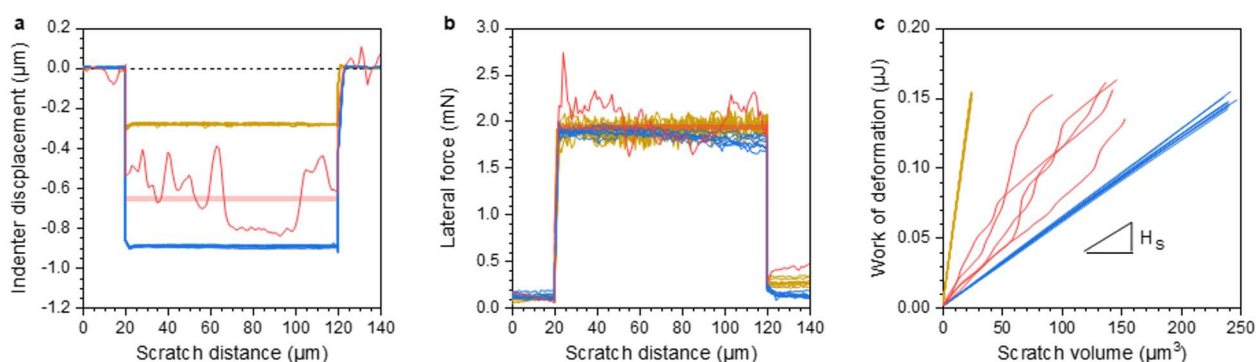


Figure 6.61: Scratch testing on the $(a_g\text{ZIF-62})_{0.5}(\text{base})_{0.5} - 1 \text{ min}$ glass sample. **a.** Spatial variation in indenter displacement (h). **b.** Spatial variation in lateral force (F_L). **c.** Work of deformation (W_s). Key: $(a_g\text{ZIF-62})_{0.5}(\text{base})_{0.5} - 1 \text{ min}$ – Red, base – Gold, and $a_g\text{ZIF-62}$ - Blue. Red shades display the confidence intervals (95 %) for **a.** h and **b.** F_L as derived from multiple such scratch tests performed on the $(a_g\text{ZIF-62})_{0.5}(\text{base})_{0.5} - 1 \text{ min}$ glass sample.

6.10.2 Na^+ Conductivity Measurements on the $(a_g\text{ZIF-62})_{0.5}(\text{Na-deficient})_{0.5}$ Samples

The ionic conductivity was measured between 110–200 $^{\circ}\text{C}$ for the $(a_g\text{ZIF-62})_{0.5}(\text{Na-deficient})_{0.5}$ samples heat treated for 1 minute and 30 minutes, and between 50–250 $^{\circ}\text{C}$ for the pure Na-deficient glass and the activation energy (E_a) for ion motion was extracted (**Figure 6.62**). The $a_g\text{ZIF-62} - 1 \text{ min}$ had measurements of less than 10^{-10} S/cm , meaning that an accurate measurement of the conductivity and activation energy could not be obtained due to the lack of mobile ions in the $a_g\text{ZIF-62}$ phase. Therefore, the $a_g\text{ZIF-62}$ conductivity is reported at the limit of 10^{-10} S/cm , representing an upper bound of conductivity (**Figure 6.63**). Although the E_a for sodium conduction in $a_g\text{ZIF-62}$ is unknown, as no Na^+

is present, the conductivity of ionic liquid impregnated amorphous ZIF-8 showed an E_a of approximately 0.3 eV for Na^+ [141], and therefore $\text{a}_g\text{ZIF-62}$ is assumed to have a similar value.

The $(\text{a}_g\text{ZIF-62})_{0.5}(\text{Na-deficient})_{0.5}$ – 1 min sample showed a reduction in conductivity at 200 °C relative to the Na-deficient glass. This is explained by the addition of the non-conductive $\text{a}_g\text{ZIF-62}$ phase which reduces the concentration of sodium ions per volume. This is corroborated by the decrease in densities in the composite (Tables 6.4-6). Furthermore, the microstructure of the $(\text{a}_g\text{ZIF-62})_{0.5}(\text{Na-deficient})_{0.5}$ – 1 min sample consists of remnant particles (Figure 6.48-49), whose interfaces will act as defects reducing conduction. The conductivity of the $(\text{a}_g\text{ZIF-62})_{0.5}(\text{Na-deficient})_{0.5}$ – 30 min sample is larger, indicating that conductivity increases with annealing time. This is explained by densification (Table 6.6) and more efficient sintering, as evident from confocal microscopy and SEM (Figure 6.48-49 and Figure 6.51), indicating an enhanced $[\text{Na}^+]/\text{cm}^3$ and resulting in a reduction in interfaces and defects.

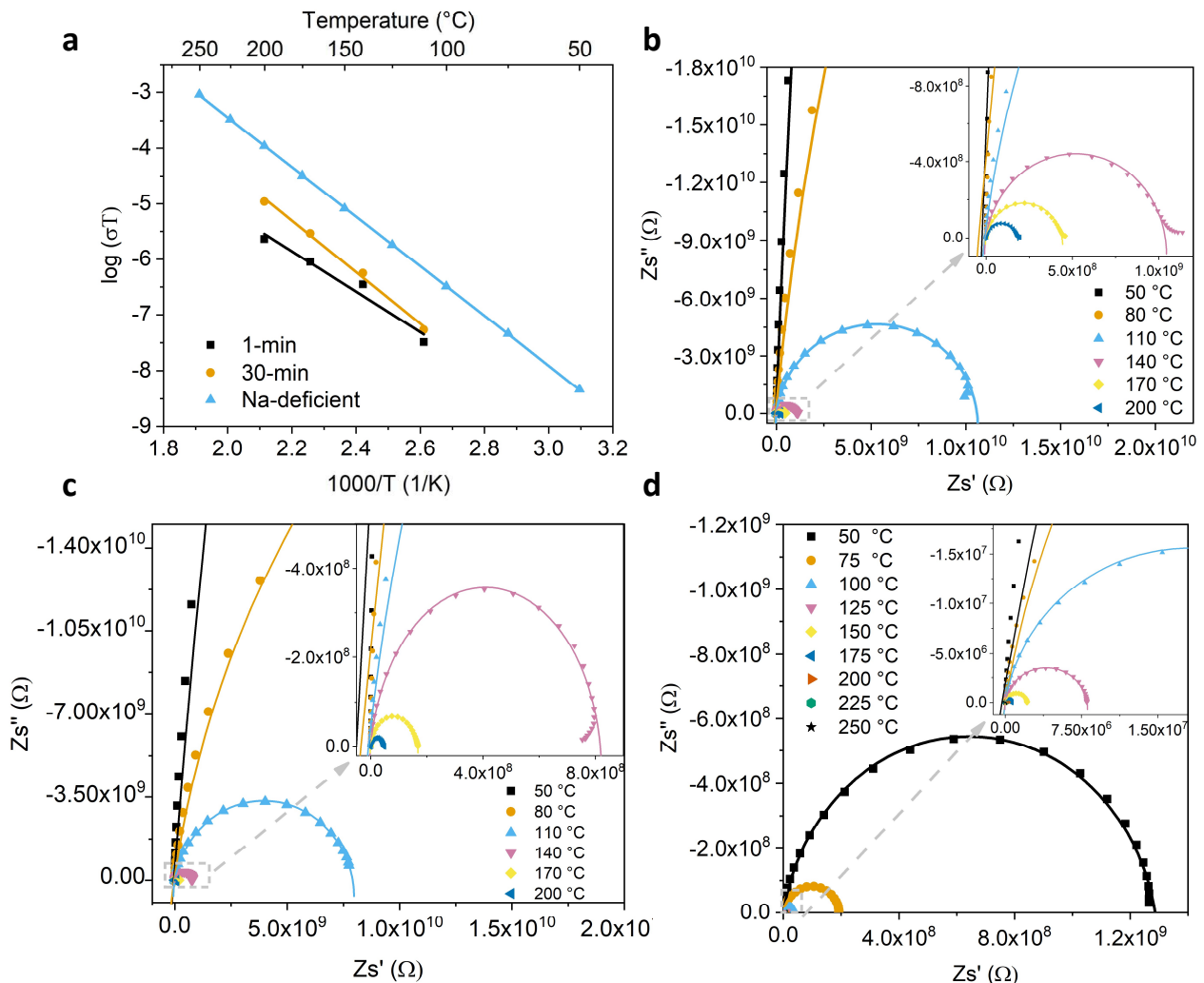


Figure 6.62: Conductivity measurements on $(\text{a}_g\text{ZIF-62})_{0.5}(\text{Na-deficient})_{0.5}$ samples. **a.** Arrhenius plots of $(\text{a}_g\text{ZIF-62})_{0.5}(\text{Na-deficient})_{0.5}$ and Na-deficient samples. Nyquist plots of **b.** $(\text{a}_g\text{ZIF-62})_{0.5}(\text{Na-deficient})_{0.5}$ – 1 min **c.** $(\text{a}_g\text{ZIF-62})_{0.5}(\text{Na-deficient})_{0.5}$ – 30 min **d.** Na-deficient.

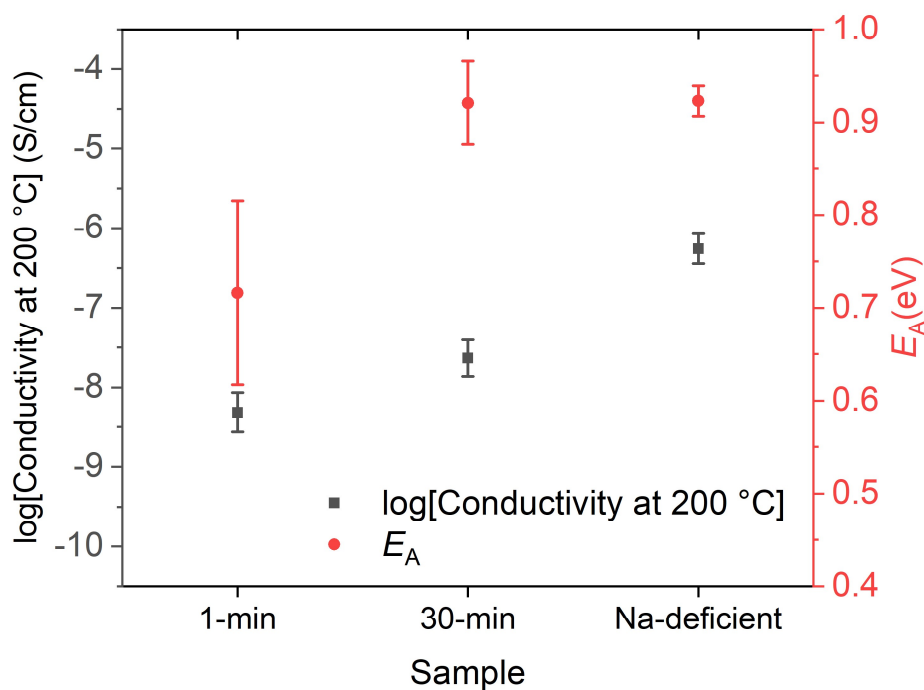


Figure 6.63: Electronic properties of $(a_g\text{ZIF-62})_{0.5}(\text{Na-deficient})_{0.5}$ samples. Measurements of ionic conductivity at 200 °C of the $(a_g\text{ZIF-62})_{0.5}(\text{Na-deficient})_{0.5}$ – 1 min, $(a_g\text{ZIF-62})_{0.5}(\text{Na-deficient})_{0.5}$ – 30 min and Na-deficient samples along with the activation energy extracted from the gradient of the conductivity-temperature measurements.

Table 6.4: Densities (ρ), as measured by the Archimedean method, of the inorganic glass series. Error was calculated at 95% confidence level.

Sample	Density (g/cm^3)	Error (g/cm^3)
base	2.64	0.01
Na-deficient	2.75	0.02
Al-rich	2.71	0.01

Table 6.5: Densities (ρ), as measured by pycnometry, of the crystalline and amorphous pure ZIF-62 controls. Error was calculated at 95% confidence level.

Sample	Density (g/cm^3)	Error (g/cm^3)
ZIF-62	1.47	0.08
$a_g\text{ZIF-62}$ – 1 min	1.38	0.09
$a_g\text{ZIF-62}$ – 30 min	1.42	0.04

Table 6.6: Densities (ρ), as measured by pycnometry, of the $(a_g\text{ZIF-62})_{0.5}(\text{Inorganic Glass})_{0.5}$ samples. Error was calculated at 95% confidence level.

Sample	1 min		30 min	
	Density (g/cm^3)	Error (g/cm^3)	Density (g/cm^3)	Error (g/cm^3)
$(a_g\text{ZIF-62})_{0.5}(\text{base})_{0.5}$	1.60	0.1	1.84	0.3
$(a_g\text{ZIF-62})_{0.5}(\text{Na-deficient})_{0.5}$	1.69	0.3	1.83	0.1
$(a_g\text{ZIF-62})_{0.5}(\text{Al-rich})_{0.5}$	1.72	0.06	1.82	0.04

The activation energy for ion motion is lower in the $(a_g\text{ZIF-62})_{0.5}(\text{Na-deficient})_{0.5}$ – 1 min sample than in the Na-deficient sample (i.e. the inorganic glass alone), indicating a low energy pathway for Na^+ motion through the structure. As the Raman data indicates formation of Na-N bonding, the lower E_a could indicate a potential motion of Na^+ ions through the $a_g\text{ZIF-62}$ glass phase, with a lower activation energy due to the phases more porous nature. The experimental error of this measurement may also be indicative of the large degree of structural heterogeneity observed in this sample by microscopy. However, after extended annealing time, the $(a_g\text{ZIF-62})_{0.5}(\text{Na-deficient})_{0.5}$ – 30 min sample shows an activation energy more like that of the bulk Na-deficient glass sample and with a reduced experimental error. The increase in E_a may be due to the overall structural densification in which a higher energy but more prevalent conduction pathway through the Na-deficient glass phase predominates over interfacial conduction through $a_g\text{ZIF-62}$ boundaries. Taken together these results indicate that the composite samples show an appreciable degree of conduction of Na^+ ions, whose exact sodium conduction mechanisms are of interest to the active sodium-ion battery community.

6.11 Discussion

Initial screening revealed that metaphosphates (inorganic glass I-III) were incompatible with ZIF-62, as DSC-TGA curves revealed continual mass loss with no evidence of melting endotherms from the ZIF. This result is surprising considering the reports of benzimidazole and Zinc metaphosphate [124], though a considerably lower processing temperature of 160°C was used in that study, and the benzimidazole was present in large excess. The TGA traces of the (50/50) ZIF-62 Inorganic glass IV-VI samples all showed regions of low mass loss after desolvation, implying that chemical reactions which decompose the ZIF framework are not occurring. However, in all but the (50/50) ZIF-62 Inorganic glass IV sample, recrystallisation of the inorganic glass precluded easy formation of a fully amorphous product. The contrast between the behaviours of inorganic glasses I-III and inorganic glasses IV-VI, all of which are phosphate glasses, implies that compatibility with the ZIF-62 is a relatively subtle function of phosphate glass structure. The high apparent T_d of the (50/50) ZIF-62 Inorganic VII sample is also of great interest as inorganic glass VII is not a phosphate, which indicates that fluoride glasses may also be a promising class of inorganic glass for future studies. Although recrystallisation of this specific inorganic glass composition precludes composite formation in this case.

A series of three inorganic glasses based on inorganic glass IV, $(1-x)([Na_2O]_z[P_2O_5])_z-x([AlO_{3/2}][AlF_3])_y$, were then synthesised, and composite samples $(a_gZIF-62)_{0.5}(Inorganic\ Glass)_{0.5}$ produced by heating in a tube furnace to 410 °C for either 1 or 30 minutes. 1H liquid NMR, FTIR, and TGA results confirm the integrity of the imidazolite and benzimidazolite linkers in all these composite materials. EDS results indicate that there are separate domains of predominately zinc signal, originating from the ZIF-62, and signal from both aluminium and phosphorous, which originate from the inorganic glass phase. This agrees with the observation of two glass transitions in the DSC. The presence of inorganic glass and $a_gZIF-62$ domains measured in EDS are also in good agreement with the variations in E and H measured by nanoindentation mapping. These results indicate a structure of separate $a_gZIF-62$ and inorganic glass domains, which electron microscopy confirms are bonded at their interfaces into a single body.

The extent of interfacial mixing between the two phases is highly dependent upon the glass transition of the inorganic component. SEM performed on samples of $(a_gZIF-62)_{0.5}(base)_{0.5}$ ($T_g(base) = 372$ °C) showed a more homogeneous appearance than for those samples containing inorganic glasses with higher T_g . The low degree of flow associated with the higher T_g samples, meant remnant particles were visible for $(a_gZIF-62)_{0.5}(Na-deficient)_{0.5} - 1$ min ($T_g(Na-deficient) = 414$ °C) and $(a_gZIF-62)_{0.5}(Al-rich)_{0.5} - 1$ min ($T_g(Al-rich) = 449$ °C). These results are intuitive, since the low temperature end of the glass transition can be described empirically as when a fluid has the viscosity of a solid (roughly 10^{15} Pa·s)

[30]. Therefore, lower T_g inorganic glasses will have a lower viscosity at the same heat treatment temperature and therefore encourage a greater extent of flow.

The X-ray diffraction and SEM experiments performed on a sample of $(a_g\text{ZIF-62})_{0.5}(\text{base})_{0.5} - 1$ min indicate a small degree of recrystallization to the dense $\text{Zn}(\text{Im})_2$ polymorph, ZIF-zni [53]. Continued isothermal treatment results in subsequent reduction of the ZIF-zni phase in the $(a_g\text{ZIF-62})_{0.5}(\text{base})_{0.5} - 30$ min sample. This reduction in Bragg scattering was further confirmed by PDF, with the $S(Q)^{\text{Diff}}$ confirming that sharp Bragg features were still present in $(a_g\text{ZIF-62})_{0.5}(\text{base})_{0.5} - 30$ min though to a smaller degree. The PXRD patterns of the $(a_g\text{ZIF-62})_{0.5}(\text{Al-rich})_{0.5} - 30$ min and $(a_g\text{ZIF-62})_{0.5}(\text{Na-deficient})_{0.5} - 30$ min samples also contained small Bragg peaks ascribed to ZIF-zni, though in contrast, the $(a_g\text{ZIF-62})_{0.5}(\text{Al-rich})_{0.5} - 1$ min and $(a_g\text{ZIF-62})_{0.5}(\text{Na-deficient})_{0.5} - 1$ min did not.

ZIF-zni is reported to recrystallise from ZIF-4, a $\text{Zn}(\text{Im})_2$ polymorph sharing the same cag topology as ZIF-62 [48], on heating to approx. 370 °C before melting at approx. 590 °C [36], [54]. The absence of recrystallisation in ZIF-62 was first ascribed to the bulkier benzimidazolate linker imposing added steric constraints on the ZnN_4 coordination polyhedral [56]. However, subsequent research has then shown that ZIF-62 samples with low blm^- contents do recrystallise to form ZIF-zni on heating [51]. However, this occurs at blm^- contents, $\text{Zn}(\text{Im})_{1.97}(\text{blm})_{0.03}$, that are much lower than those observed in these samples, which have the composition $\text{Zn}(\text{Im})_{1.76}(\text{blm})_{0.24}$. We therefore postulate that the ZIF-zni formation observed here occurs due to an interaction between the inorganic and MOF glass phases. The interaction may proceed via migration of blm^- into the inorganic glass, which is consistent with prior literature showing that benzimidazole and zinc metaphosphate glass are miscible [124]. Recrystallisation to ZIF-zni of the remnant Im-rich interface domains then occurs, before this itself either melts, or is dissolved by the melt on further heating in the $(a_g\text{ZIF-62})_{0.5}(\text{base})_{0.5} - 30$ min sample. The effect is more pronounced in samples with lower glass transition temperatures because their lower viscosities at the treatment temperatures, promotes a greater degree of mixing and therefore interaction between the two phases. This difference could explain the variable degree of recrystallisation observed in the different composite samples.

The emergence of a large new peak at approx. 145 cm^{-1} in the Raman spectra of all the $(a_g\text{ZIF-62})_{0.5}(\text{Inorganic Glass})_{0.5}$ samples, which was ascribed to the formation of Na-N bonds, provides useful information on the interaction between the two phases. ^{31}P MAS NMR spectra of the $(a_g\text{ZIF-62})_{0.5}(\text{Inorganic Glass})_{0.5}$ samples have a noticeable peak shift to higher ppm when compared with their respective inorganic glasses, with the exception of $(a_g\text{ZIF-62})_{0.5}(\text{Na-deficient})_{0.5} - 1$ min, which had an initial increase in the lower ppm region, approx. -26 ppm. In the literature, such shifts of ^{31}P NMR peaks to higher ppm have generally been attributed to formation of terminal oxygens, causing a

decrease in the average charge density on the phosphorus atoms [134]. However here the chemistry of the system and preparation method means that we do not expect the creation of new terminal oxygen bonds at high ppm.

An alternative explanation is the formation of P—N bonds; we would expect P—N bonds to markedly shift the average ^{31}P peak positions to higher chemical shift. Furthermore, in a ^{31}P study of phosphorus oxynitride glasses, it was found that PO_3N and PO_2N_2 peaks appear at -10 and 0 ppm, respectively [132]. Secondly, the $^{31}\text{P}\{^1\text{H}\}$ CP spectra detect protons in the proximity of these phosphorus atoms located in the high ppm region. Consequently, the formation of additional peaks at high ppm in the ^{31}P NMR spectra and good agreement with the $^{31}\text{P}\{^1\text{H}\}$ CP spectra points toward a significant interaction between the Im^- and blm^- linkers and phosphorus in the inorganic glass via P—N bond formation.

We therefore tentatively propose the schematic (**Figure 6.64**) as one possible structure for the interface between the inorganic and ZIF glasses, in the composites formed here. The melting process of pure-phase ZIFs has previously been shown to involve Zn—N bond breakage at a critical temperature, which leaves both under coordinated Zn, and relatively electron-rich N sites [60]. Sodium is known to be relatively mobile in inorganic glasses, especially at temperatures near T_g , and would be expected to migrate to atoms with extra electron density. The Raman data here indicate that N—Na coordination happens very early, with the NMR data being consistent with the establishment of an equilibrium state involving P—N bond formation and/or creation of terminal oxygen. Zn—O—P correlations, though not directly experimentally measured, were included for reasons of charge balance and to maintain tetrahedral coordination of Zn centres, their inclusion is also justified by the large number of examples of inorganic glasses which contain similar structures [134], [142], [143].

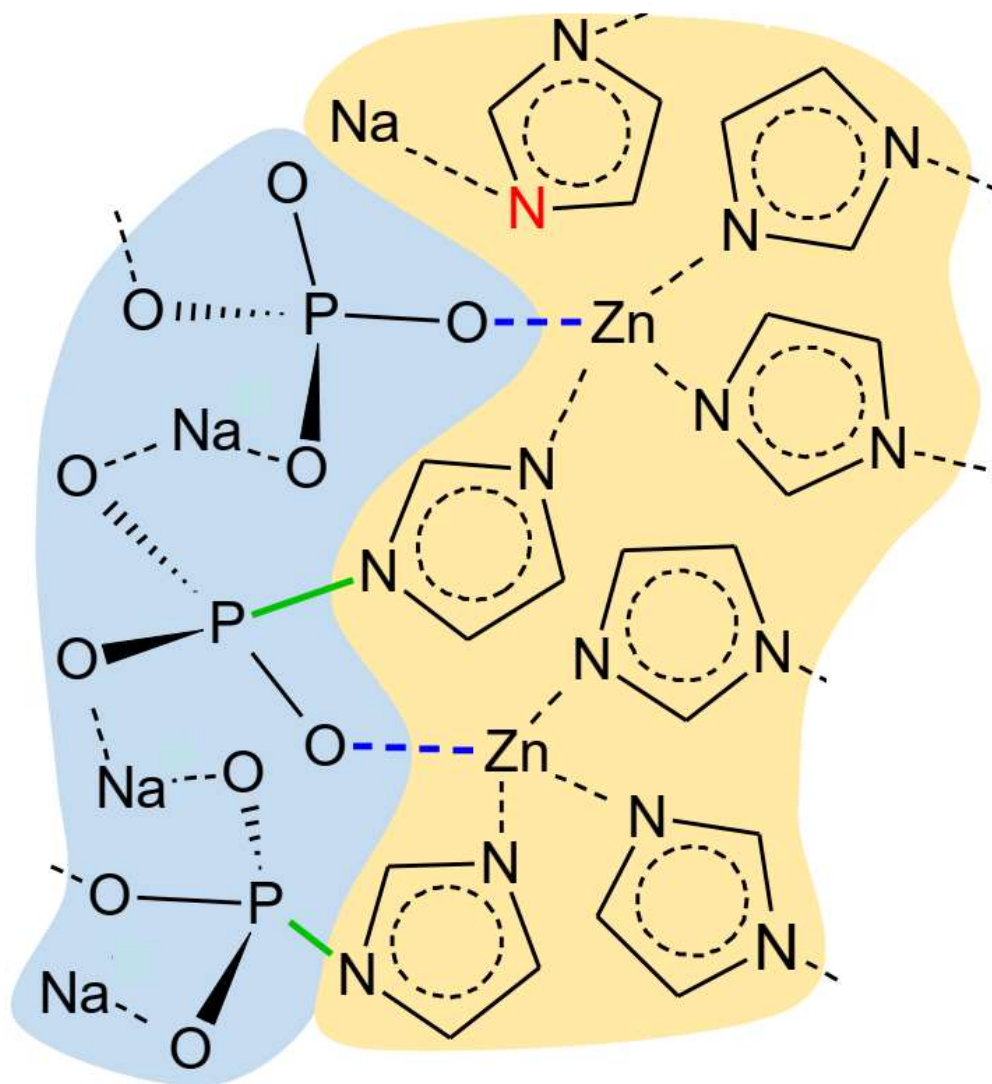


Figure 6.64: Schematic of the potential structure of the interface between the inorganic glass and the MOF glass domains. Bonding depicted is based off Raman and NMR spectroscopy measurements.

6.12 Conclusions

These results describe a new class of inorganic glass – MOF glass composites, prepared by heating a mixture of a phosphate glass and ZIF-62. The composites formed in situ in the DSC contain two distinct glass transition temperatures, matching those of a_g ZIF-62 and the relevant inorganic glass. This implies that the composite contains separate domains of each glass phase, which are bonded at their interfaces into a single solid body. This image of the microstructure is also in agreement with SEM, mechanical testing, and conductivity results. The extent of mixing is influenced by the inorganic glass transition temperature, which is itself linked to the chemistry of the glass. The phase mixing is extensive enough that it enables a reaction of the inorganic and MOF components to occur. This results in a small degree of recrystallisation of ZIF-62 to form a dense ZIF-zni phase. The precise nature of this interaction was not determined due to its limited extent but would be an interesting subject for further study.

The formation of materials containing interlocked inorganic glass and MOF glass domains will prove of great interest as prototypical examples of a new materials family, with mechanical and electrical properties intermediate between the two parent structures. The emergence of this new class of composites implies the ability to alter the physical, chemical, and electrical properties of MOF glasses by utilising the vast array of different known inorganic glasses. Ideally future work in this area could be centred around combining the unique properties of MOF glasses, such as the accessible porosity of the glass phase, with properties of interest from inorganic glasses such as enhanced mechanical rigidity [69], [77], [144]. Critically the work here also indicates an approach by which other researchers may explore this new class of composite materials.

Chapter 7: The Reactivity of an Inorganic Glass Melt with ZIF-8

The results presented in this chapter were published in:

L. Longley et al., "The reactivity of an inorganic glass melt with ZIF-8," *Dalt. Trans.*, vol. 50, no. 10, pp. 3529–3535, 2021.

Synthesis of the inorganic glass samples was done by Dr Courtney Calahoo (University of Jena). Synthesis of the ZIF-8 and preparation of the X wt% ZIF-8 samples was done by me. I also conducted all thermal analysis, PXRD and FTIR. ¹H NMR preparation was carried out by me, with measurement done by a technician in the NMR service at the department of chemistry and interpretation of the results carried out by myself in collaboration with Dr Calahoo. SEM characterisation and image analysis were carried out by Thomas J.F. Southern (University of Cambridge), with my assistance.

7.1 Introduction

Although MOF materials have very high specific surface areas, resulting in many potential applications in gas storage, separation, and catalysis [145]–[147], they are often synthesised as microcrystalline powders. This has necessitated research into the formation of industrially suitable macroscale MOF architectures such as pellets, monoliths, and thin films [76], [148]–[151]. Many different types of crystalline MOF composite materials have also been produced in which the MOF crystallites are embedded in a matrix. Examples include mixed-matrix membranes (MMMs), which contain crystalline MOFs embedded within an organic polymer matrix [119], MOF crystal-glass composites (MOF-CGCs), formed through the combining of the crystalline and glassy states of MOFs in the same material [78]–[80], and those formed by growing MOFs within activated carbon matrices [152].

For successful MOF-CGC formation two criteria must be simultaneously fulfilled: i) Thermal compatibility, a processing temperature must be found at which the inorganic glass matrix is heated sufficiently above its T_g that its viscosity is low enough to promote mixing and composite formation. This condition is much more stringent in MOF-CGCs because, in comparison to the inorganic glass-MOF glass composites (**Chapter 6**), only the inorganic glass is entering the liquid state, and therefore a greater degree of flow will be needed to form a single solid piece. Despite this, the processing temperature must still be low enough that the crystalline MOF component remains thermally stable. ii) Chemical compatibility, the MOF crystal inorganic glass pair must have compatible chemical bonding such that they can be bonded at the interface to produce a robust material and no reactions which promote decomposition should occur during the high temperature liquid phase mixing between the MOF and inorganic components.

The previous chapter detailed the formation of a composite between a MOF and a phosphate glass; TGA analysis determined that ZIF-62 was stable in the presence of a series fluoroaluminophosphates to around 500 °C, and detailed structural characterisation via PDF, Raman, EDX and ³¹P NMR demonstrated that the structure was mainly composed of separate, but interlocking, inorganic and hybrid domains with evidence of P-N and Na-N bonding at the interface. Therefore, motivated both by these results, and by the reported literature on MOF-CGCs, an attempt was made to produce a MOF-CGC in which the glass phase was an inorganic glass. This would greatly expand the range of different matrices available, as the number of glass forming MOFs is extremely limited compared to the vast amount of known inorganic glasses.

Due to the greater need for flow required to produce a well sintered MOF-CGC sample, the lowest T_g glass of the series, $0.78([\text{Na}_2\text{O}]_{1.6}[\text{P}_2\text{O}_5]) - 0.22([\text{AlO}_{3/2}][\text{AlF}_3]_{0.7})$ (**Chapter 6.4**), was selected for use as a matrix material. This is because it would enable the use of the lowest absolute processing temperatures while maintaining a high T/T_g ratio, which therefore increase the likelihood of the crystalline MOF being thermally compatible.

ZIF-8, $\text{Zn}(\text{melm})_2$ ($\text{melm}^- = 2\text{-methylimidazolate, C}_4\text{H}_5\text{N}_2^-$), was chosen as the crystalline MOF component. This is firstly because the work of the previous chapter showed successful composite formation with ZIF-62 whose chemistry is relatively similar. A second reason was that ZIF-8 is the 'prototypical' crystalline ZIF, whose properties, notably stability i.e. under pressure [130], temperature [74], [135], ball-milling [153] and in the presence of common industrial solvents [43] have been extensively studied.

This chapter describes an investigation into the potential of expanding the MOF-CGC domain, however experiments revealed that the fluoroaluminophosphate was found to promote decomposition in the crystalline ZIF-8 (**Figure 7.1**). However, the methodology demonstrated here may still serve as a future basis by which the suitability of other MOF-crystal inorganic glass pairs can be ascertained.

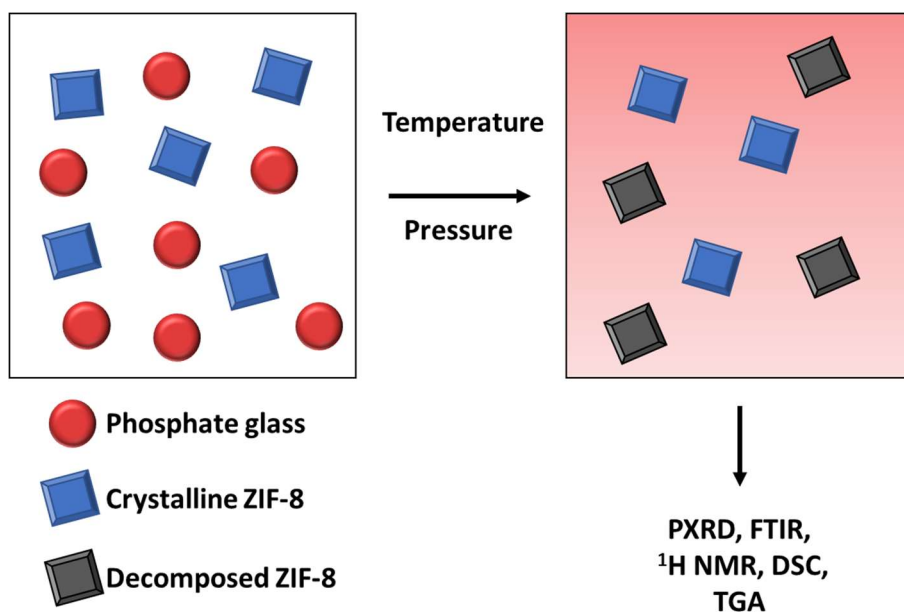


Figure 7.1: Schematic representation of the observed destabilising reaction between ZIF-8 and fluoroaluminophosphate glass.

7.2 Thermal Characterisation of Samples

ZIF-8 and $0.78([\text{Na}_2\text{O}]_{1.6}[\text{P}_2\text{O}_5]) - 0.22([\text{AlO}_{3/2}][\text{AlF}_3]_{0.7})$, the latter of which is referred to from here on as the inorganic glass, were synthesised according to published reports (**Chapter 3.2.4**) and then ball-milled together in the appropriate quantities to produce samples containing 5 wt%, 10 wt%, 15 wt% and 30 wt% ZIF-8 respectively. These samples were subsequently activated and the crystallinity of the ZIF-8 control confirmed by Pawley refinement of the PXRD pattern (**Figure 7.2**). The PXRD patterns of the X wt% ZIF-8 samples contained peaks in the same positions confirming that the samples remained crystalline after ball-milling (**Figure 7.3**). These evacuated ball-milled mixtures are subsequently referred to as X wt% ZIF-8.

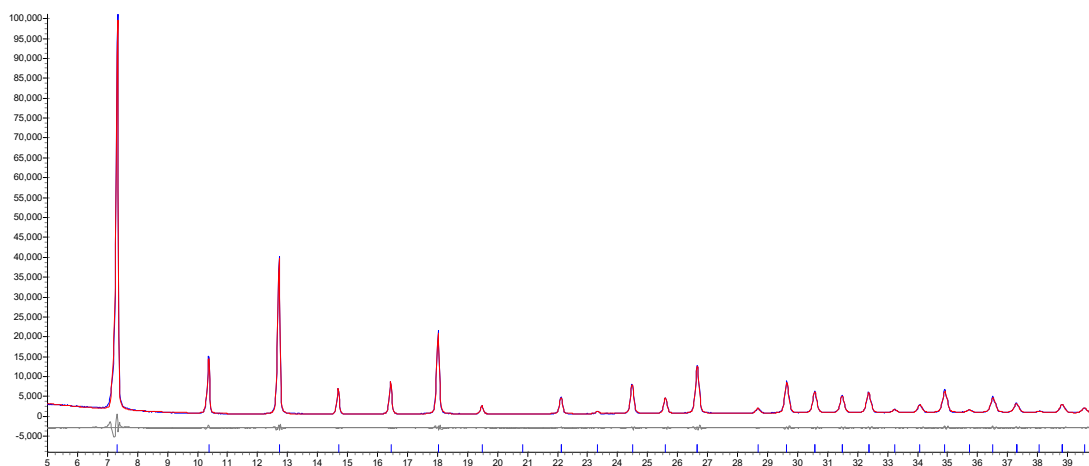


Figure 7.2: Pawley refinement of evacuated ZIF-8. $R_{wp} = 6.56$. The refined cubic unit cell parameter was $17.034626 \pm 0.000686 \text{ \AA}$, using a starting parameter (17.00517 \AA) taken from [67].

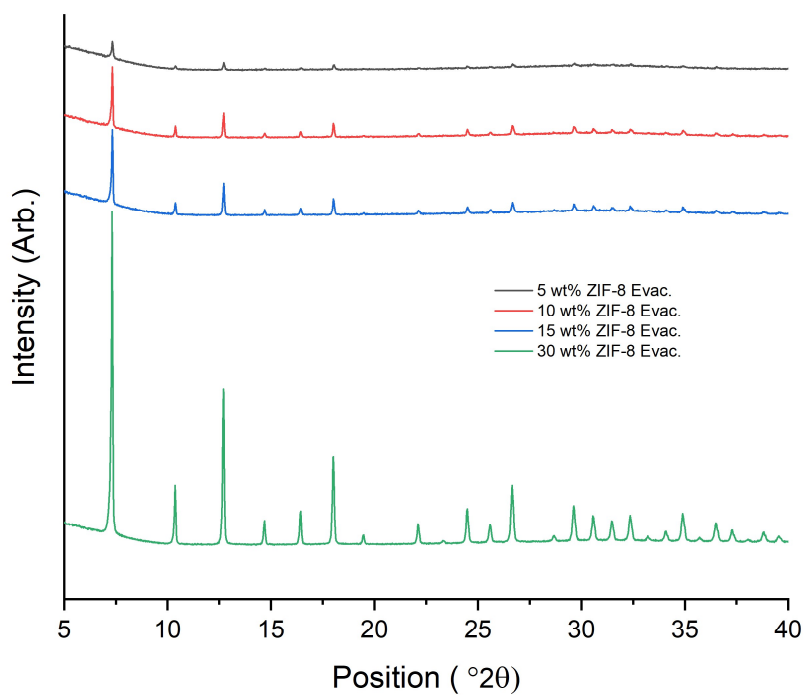


Figure 7.3: Powder X-ray diffraction patterns of the evacuated ZIF-8: inorganic glass mixtures 5 – 30 wt% ZIF-8.

7.2.1 Characterisation of the X wt% ZIF-8 Samples by Differential Scanning Calorimetry and Thermogravimetric Analysis

The thermal responses of the samples were measured during heating at 10 °C/min to 600 °C under argon. The DSC heating curve (**Figure 7.4**) of the inorganic glass control was flat until a T_g with an onset at 350 °C, which was followed by an exotherm, with an onset of 530 °C, ascribed to recrystallisation of the inorganic glass. The heating curve of a ZIF-8 control sample was relatively featureless until around 500 °C, then became rapidly endothermic, in accordance with thermal decomposition. The 5 wt%, 10 wt%, and 15 wt% ZIF-8 samples displayed similar behaviour to the inorganic glass, with T_g s between 350-360 °C followed by exotherms with onsets at approx. 520 °C (**Table 7.1**). The recrystallisation exotherm in the 30 wt% ZIF-8 sample was much shallower and harder to unambiguously assign, this is ascribed to the increased ZIF-8 content; the recrystallisation exotherm coincides in temperature with the endothermic rise in the baseline signal due to the decomposition of ZIF-8 and therefore increasing ZIF-8 content obscures the signal.

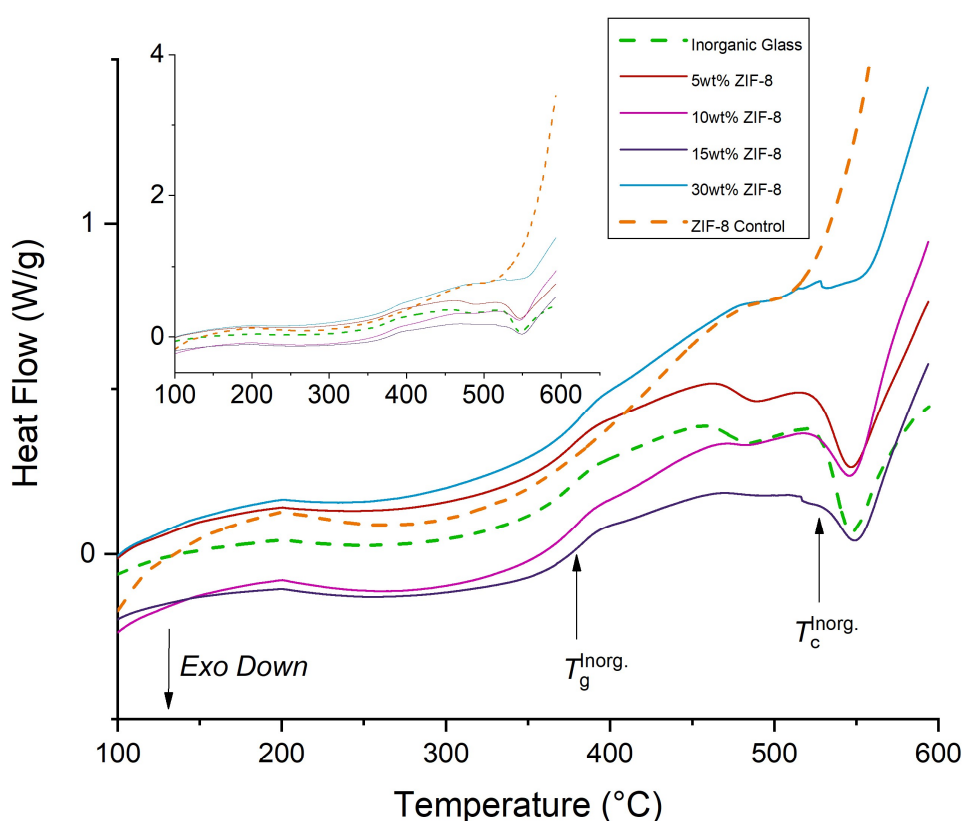


Figure 7.4: Thermal response curves of the ZIF-8, inorganic glass, and X wt% ZIF-8. Samples are heated to 600 °C at 10 °C/min under argon. The inorganic glass transition ($T_g^{\text{inorg.}}$) and recrystallisation temperature ($T_c^{\text{inorg.}}$) are indicated. Inset: As above but shown over the full data range.

The mass curves of the controls and samples were also measured by TGA (**Figure 7.5**). The mass curve of the inorganic glass control showed a small loss of approx. 1 %, at 600 °C. A small peak in the mass curve was observed at approx. 540 °C, coinciding with the exotherm in the DSC curve, and is attributed to an increase in noise during recrystallisation. The ZIF-8 control lost approximately 3 % of its mass before 500 °C, indicating successful activation of the framework. Above 500 °C, the mass loss increases sharply, in line with the rise in the DSC baseline. The onset of the mass loss was measured at 532 °C and therefore this was taken as the approximate onset of decomposition ($T_d^{\text{ZIF-8}}$).

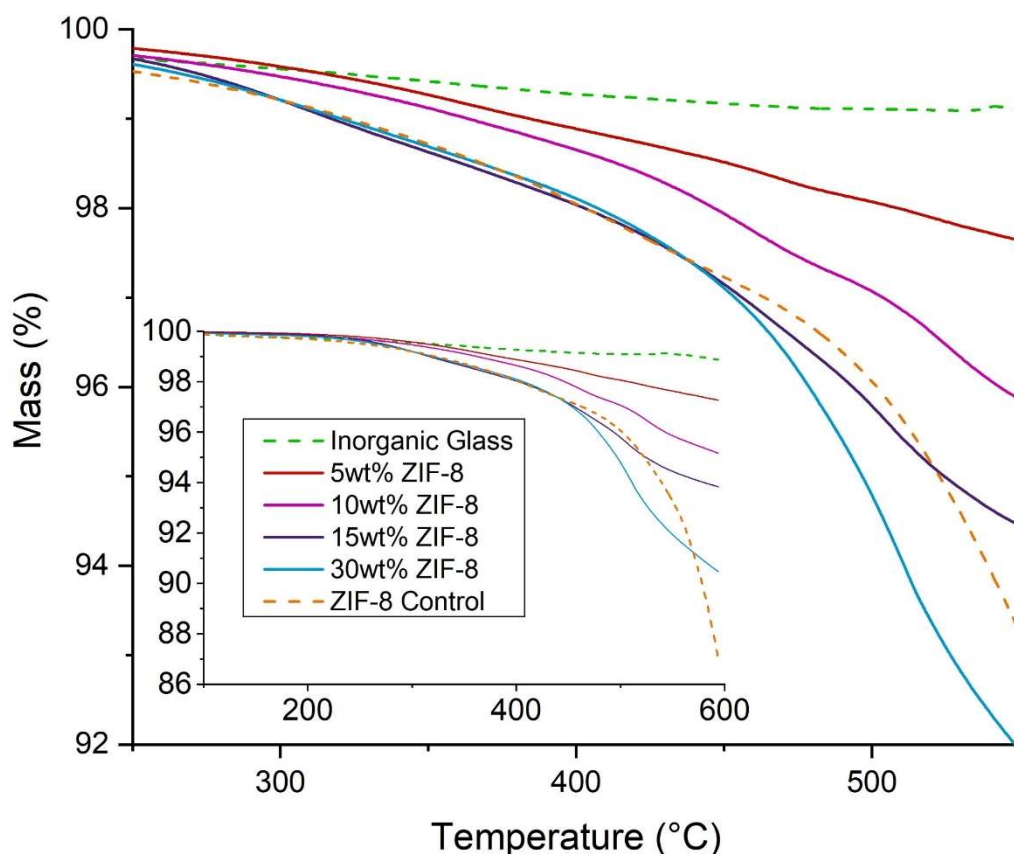


Figure 7.5: Mass curves of the ZIF-8, inorganic glass, and X wt% ZIF-8 samples. Samples are heated to 600 °C at 10 °C/min under argon in the region 250 – 550 °C. Inset: The same data shown over the full measured range.

The glass transition temperature of the inorganic glass shows an upward trend from 350-361 °C with increasing ZIF-8 content (**Table 7.1**). In contrast the onset of recrystallisation shows a downward trend with increasing ZIF-8 content from 523-518 °C. Two repeat scans on the inorganic control found a variation of only 1 °C in both of these features, and so this trend appears to be statistically significant and might be indicative of an interaction between the ZIF-8 and the inorganic glass. However, this apparent shift may also be an effect caused by the convolution of the signals from the T_g and recrystallisation with the rise in the baseline due the ZIF-8 content. Quantitative evaluation of the

enthalpy change on recrystallisation could possibly illuminate this further, as a marked difference in the area under the peak may indicate a difference in the chemistry of the recrystallising inorganic glass caused by interaction with the ZIF-8. However, the rise in the baseline due to ZIF-8 decomposition means that the background across the peak cannot be unambiguously determined, which precludes analysis at this depth.

Table 7.1: Thermogravimetric analysis (TGA) and differential scanning calorimetry (DSC) results for the ZIF-8: inorganic glass samples. Heated to 600 °C at 10 °C/min under argon.

Sample	% Sample Mass @ 200 °C	% Sample Mass @ 450 °C	% Sample Mass @ 480 °C	% Sample Mass @ 550 °C	Glass Transition (T_g) / °C	Recrystallisation Temperature (T_c) / °C
Inorganic Control Replicate 1	99.74	99.17	99.12	99.11	352	529
Inorganic Control Replicate 2	99.59	98.90	98.84	98.78	354	528
5 wt% ZIF-8	99.91	98.52	98.23	97.64	350	523
10 wt% ZIF-8	99.85	97.94	97.38	95.87	357	515
15 wt% ZIF-8	99.87	97.16	96.39	94.46	360	518
30 wt% ZIF-8	99.81	97.11	95.94	91.94	361	-
ZIF-8 Control Replicate 1	99.71	97.23	96.67	93.25	-	-
ZIF-8 Control Replicate 2	99.53	96.73	96.06	93.85	-	-
ZIF-8 Control Replicate 3	99.52	97.170	96.66	94.74	-	-

7.2.2 Probing Stability Changes through a Differential Thermogravimetric Analysis Method

The 5 wt% and 10 wt% mixtures have mass curves that show intermediate behaviour between the controls as would be expected from a rule of mixtures. However, after around 400 °C the 15 wt% and 30 wt% samples both lost mass at a faster rate than the ZIF-8 control. In order to examine this unexpected effect the following construction was used; the average mass percentage signals measured from the inorganic glass controls, $m^{Inorg.}$, and ZIF-8 controls, m^{ZIF} , (**Table 7.1**) were combined in the appropriate mass proportions, x^{ZIF} and $x^{Inorg.}$ respectively, as a measure of the mass

loss that would be expected from a non-interacting mechanical mixture of the ZIF-8 and inorganic glass ($A(T)$):

$$A(T) = x^{ZIF} \cdot m(T)^{ZIF} + x^{Inorg.} \cdot m(T)^{Inorg.} \quad 7.1$$

This can then be subtracted from the mass signal directly measured for each of the mixtures to approximate the mass loss due to interaction between the inorganic glass and ZIF-8 ($\Delta m(T)$):

$$\Delta m(T) = m(T)^{mixture} - A(T) \quad 7.2$$

The results of this calculation (**Figure 7.6**) reveal that below 300 °C all $\Delta m(T)$ values are near zero, indicating relatively little interaction between the ZIF-8 and inorganic glass powder. However, at elevated temperatures, all samples lose more mass than would be expected from a non-interacting mixture ($\Delta m < 0$). Although $\Delta m(T)$ is consistently negative above 300 °C, at $T > 400$ °C the gradient increases rapidly. Above 520 °C, i.e. in the region in which the ZIF-8 control decomposes on its own, $\Delta m(T)$ begins to level off indicating that the X wt% samples are starting to behave more like a non-interacting mixture of the controls.

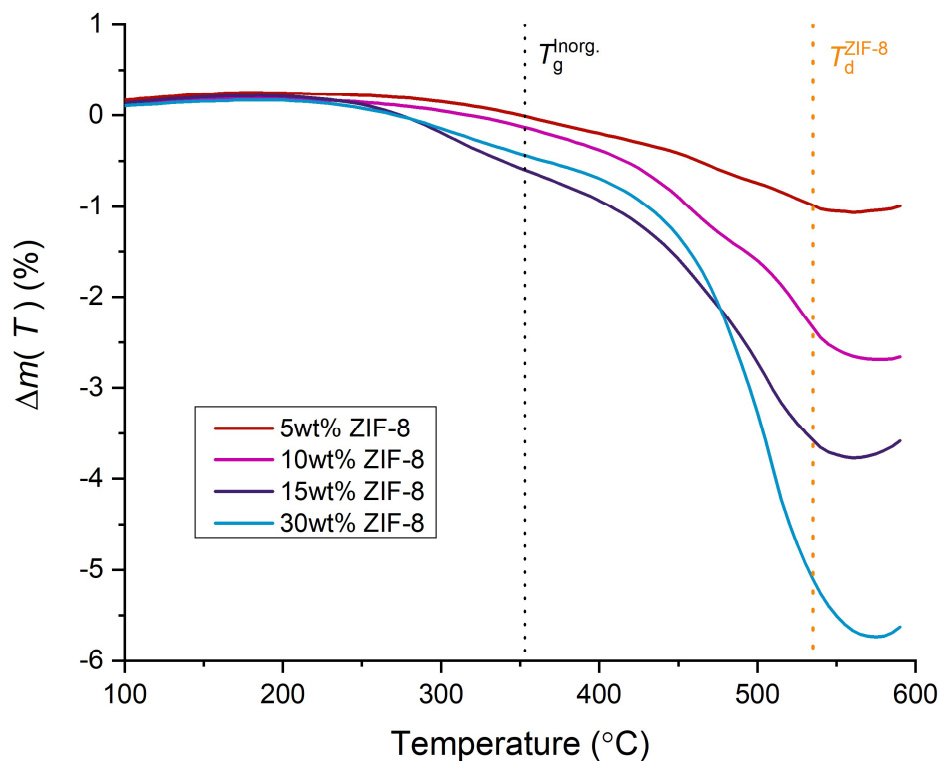


Figure 7.6: $\Delta m(T)$ for the X wt% ZIF-8 samples. The glass transition temperature of the inorganic glass ($T_g^{Inorg.}$) and the approximate onset of ZIF-8 decomposition as measured from the control (T_d^{ZIF-8}) are indicated.

7.3 Characterisation of Crystallinity Loss in ZIF-8 through Powder X-ray Diffraction

To further investigate the origin of this effect, the *X* wt% ZIF-8 samples were compressed into pellets to promote production of mechanically robust composites (**Chapter 3.2.4**). Heat treatments of 450 °C for 30 minutes, and 480 °C for 1 minute were selected as a compromise between promoting flow in the inorganic glass to join the ZIF-8 and glass together into a solid body, while avoiding decomposition of the ZIF-8 and recrystallisation of the inorganic glass. These samples were produced by heating in a DSC-TGA experiment, with a heating rate of 10 °C/min to the treatment temperature. After heat treatment samples were cooled under argon to 150 °C at 10 °C/min before cooling in air to room temperature at approximately 40 °C/min.

PXRD was then used to assess the crystallinity of these samples after pelletisation and heat treatment. In order to quantify the relative change in crystallinity across the *X* wt% ZIF-8 samples the .raw data were converted to .xy files using PowDLL [154]. The background and broad inorganic glass FSDP [105] were fitted using a spline function and subtracted from the data. After this the three most intense peaks at approximately 7.3, 12.7 and 18.0 ° 2 θ , corresponding to {110}, {200} and {211} planes respectively in ZIF-8, were then fitted in Fityk [92]. A Voigt function was used to fit the peaks at 12.7 and 18.0 ° 2 θ , whereas a split Voigt was used to fit the peak at 7.3 ° 2 θ . This is because the low angle peak displayed considerable asymmetry, which has been reported in the literature as occurring when using linear detectors at low angles in the Bragg–Brentano para-focussing geometry [81]. A relative measure of crystallinity was then obtained by dividing these three areas by the corresponding area of the peak in the ball-milled evacuated ZIF-8 sample, the sample with the largest peak area, and then averaging. The reported errors in the relative crystallinity values were obtained from standard deviation in the fractional areas of the three peaks.

The ZIF-8 control showed a loss of crystallinity on pellet formation; however, heat treatment did not reduce the crystallinity further in either case (**Figure 7.7a**). The inorganic glass control remained amorphous after heat treatment (**Figure 7.7b**) indicating that no recrystallisation had occurred in good agreement with the measured onset of recrystallisation in the DSC results (**Figure 7.4**).

The 30 wt% ZIF-8 sample shows similar behaviour to the ZIF-8 control (**Figure 7.8**), with a sharp drop in Bragg peak intensity on pellet formation but with peaks remaining after heat treatment. In contrast the 15 wt% ZIF-8 sample showed relatively little change on pellet formation, but peak intensity dropped sharply on heat treatment (**Figure 7.9**). Similarly, the 10 wt% ZIF-8 and 5 wt% ZIF-8 samples were relatively unchanged on pelletisation, however displayed sharp losses on heat treatment, with both appearing amorphous after a heat treatment of 480 °C 1 minute (**Figure 7.10-11**).

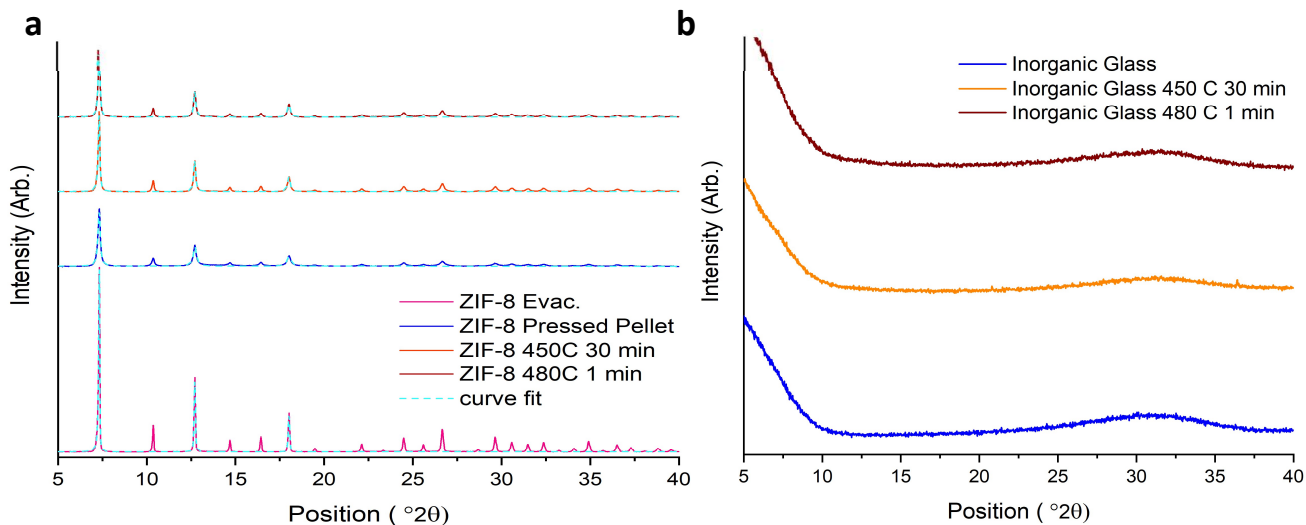


Figure 7.7: Powder X-ray diffraction patterns of the controls. **a.** PXRD of the background subtracted ZIF-8 controls. The curve fit, at approximately 7.3 , 12.7 and 18.0 $^{\circ} 2\theta$ (cyan), is used in the relative crystallinity quantification. **b.** PXRD patterns of the inorganic glass controls.

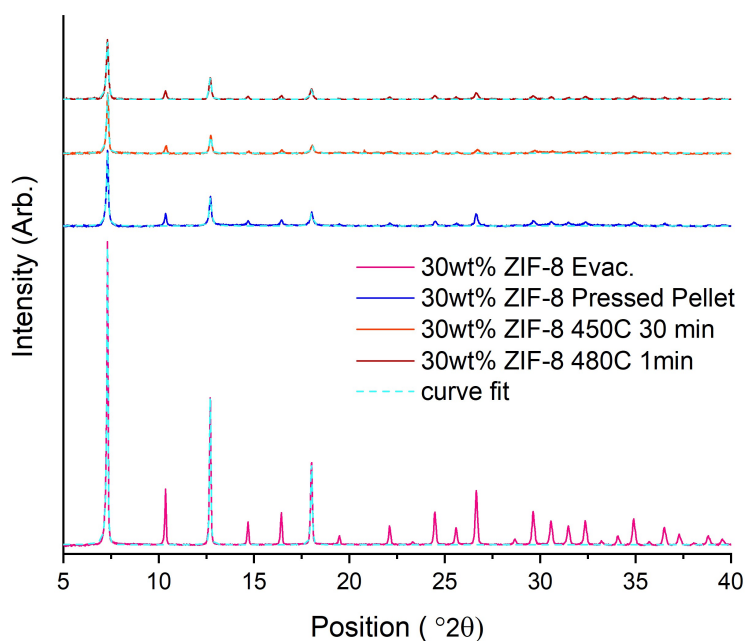


Figure 7.8: Powder X-ray diffraction patterns of the background subtracted 30 wt% ZIF-8 samples. The curve fit, at approximately 7.3 , 12.7 and 18.0 $^{\circ} 2\theta$ (cyan), used in the relative crystallinity quantification.

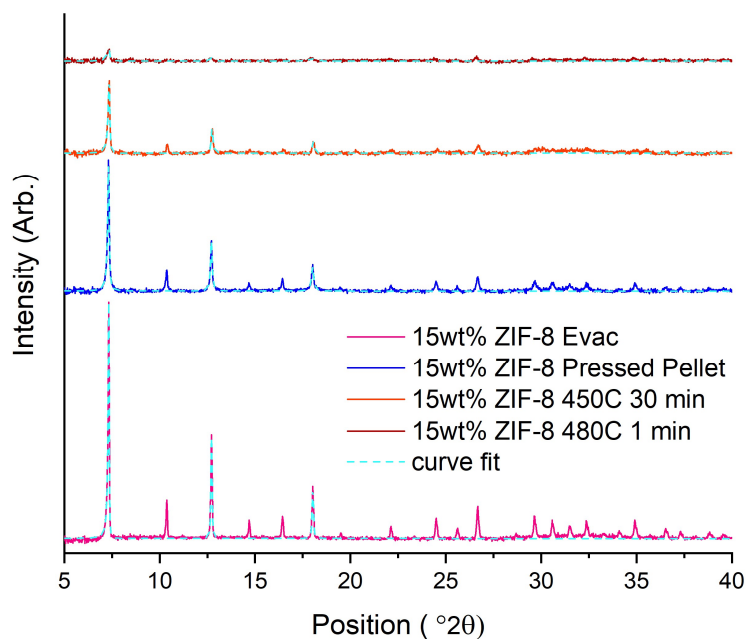


Figure 7.9: Powder X-ray diffraction patterns of the background subtracted 15 wt% ZIF-8 samples. The curve fit, at approximately 7.3, 12.7 and 18.0 $^{\circ}2\theta$ (cyan), used in the relative crystallinity quantification.

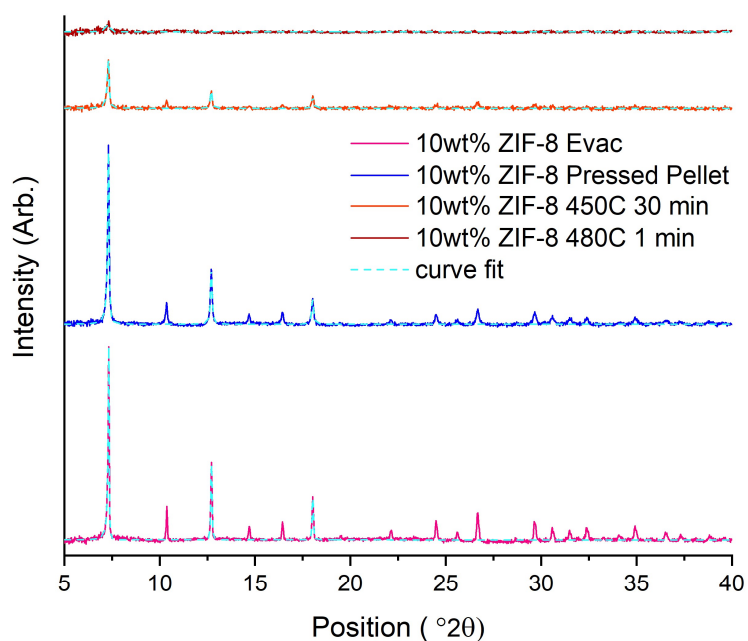


Figure 7.10: Powder X-ray diffraction patterns of the background subtracted 10 wt% ZIF-8 samples. The curve fit, at approximately 7.3, 12.7 and 18.0 $^{\circ}2\theta$ (cyan), used in the relative crystallinity quantification.

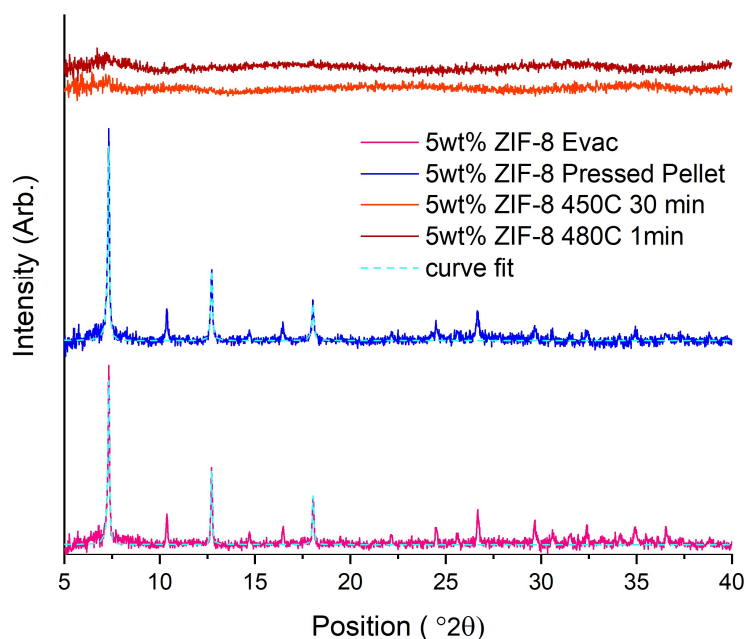


Figure 7.11: Powder X-ray diffraction patterns of the background subtracted 5 wt% ZIF-8 samples. The curve fit, at approximately 7.3, 12.7 and 18.0 ° 2 θ (cyan), used in the relative crystallinity quantification.

The results of the fitting confirm these observations (**Table 7.2**). It also showed that the crystallinity drops on heat treatment in the 30 wt% ZIF-8 sample, but remains constant, within error, in the ZIF-8 control. The difference in retained crystallinity after pellet formation between the ZIF-8 control, 30 wt % ZIF-8 sample and the other X wt% ZIF-8 samples is ascribed to the effect of the relatively dense and rigid inorganic glass. ZIF-8 is known to amorphise under mechanical action by ball-milling [153] and so the applied pressures due to pellet formation therefore result in crystallinity loss. However, at high inorganic glass contents, the dense and rigid glass particles may shield the ZIF-8 crystals from the applied stress during the formation of the pellet. The 30 wt% ZIF-8 sample therefore displays far less stress-shielding than the other samples due to its higher fraction of ZIF-8; estimated as being over 50% by volume using densities reported in the literature for ZIF-8 and measured for the inorganic glass (**Table 6.4**) [155].

Table 7.2: Relative crystallinity results for the ZIF-8 controls and X wt% ZIF-8 samples. Measured by fitting of the three most intense peaks at 7.3, 12.7 and 18.0 ° 2 θ .

Sample	Relative Crystallinity (%)	Error (%)	Fit R^2
ZIF-8 Evac.	100.0	0.0	0.997
ZIF-8 Pressed Pellet	79.8	13.2	0.994
ZIF-8 450 C 30 min	74.9	7.9	0.997
ZIF-8 480 C 1 min	71.7	6.5	0.997
30 wt% ZIF-8 Evac	41.9	6.2	0.971
30 wt% ZIF-8 Pressed Pellet	15.5	1.6	0.995
30 wt% ZIF-8 450 C 30 min	9.6	1.5	0.997
30 wt% ZIF-8 480 C 1 min	10.7	1.0	0.997
15 wt% ZIF-8 Evac	7.8	0.2	0.996
15 wt% ZIF-8 Pressed Pellet	6.4	0.5	0.993
15 wt% ZIF-8 450 C 30 min	2.9	0.7	0.989
15 wt% ZIF-8 480 C 1 min	1.0	0.5	0.808
10 wt% ZIF-8 Evac	6.1	0.2	0.995
10 wt% ZIF-8 Pressed Pellet	6.7	1.2	0.995
10 wt% ZIF-8 450 C 30 min	6.1	6.0	0.978
10 wt% ZIF-8 480 C 1 min	0.0	0.0	0.613
5 wt% ZIF-8 Evac	2.3	0.3	0.953
5 wt% ZIF-8 Pressed Pellet	2.8	0.2	0.969
5 wt% ZIF-8 450 C 30 min	0.0	0.0	0
5 wt% ZIF-8 480 C 1 min	0.0	0.0	0

7.4 Spectroscopic Characterisation of ZIF-8 Stability

The results of the previous section have demonstrated that heating of the X wt% ZIF-8 samples result in a loss of crystallinity, and that this effect is not seen in the ZIF-8 controls. However, given that previous work (**Chapter 5.3** and **Chapter 5.4**) has demonstrated that the presence of a molten ZIF glass can promote loss of crystallinity in ZIF-8 without framework decomposition, FTIR and ^1H NMR were used to investigate the chemistry of the ZIF-8 framework before and after heat treatment.

7.4.1 Examining relative changes in ZIF-8 through Fourier Transform Infra-Red Spectroscopy

ZIF-8 decomposition at elevated temperatures and in different atmospheres has previously been studied by FTIR [74]. FTIR of the ZIF-8 control samples contained peaks matching those recorded in the literature for as-synthesised ZIF-8, except for a broad peak at approximately 3000 cm^{-1} , due to O-H bonding, the absence of which in these samples is attributed to framework activation. The FTIR spectra of the ZIF-8 controls were seen to be unchanging with heat treatment (**Figure 7.12**). The inorganic glass controls showed very broad absorbances, which is typical of FTIR spectroscopy on glasses. The positions of these peaks were found to match those reported for other polymeric phosphates (**Figure 7.13**) [125], [131], [156]. The heat treated and pellet pressed inorganic glass controls also showed very little change. A band at approximately 2300 cm^{-1} , which is observed in all samples and controls, though with very variable intensity, was ascribed to atmospheric CO_2 present in the open measurement set-up [157].

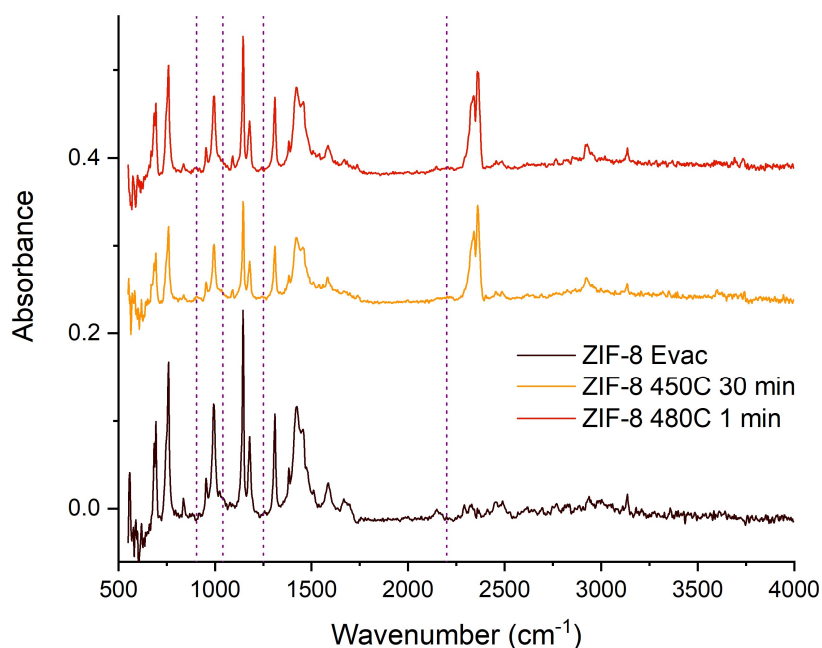


Figure 7.12: FTIR spectra of the ZIF-8 controls. Dashed droplines indicate positions of peaks reported in the literature to occur on decomposition of ZIF-8 [74].

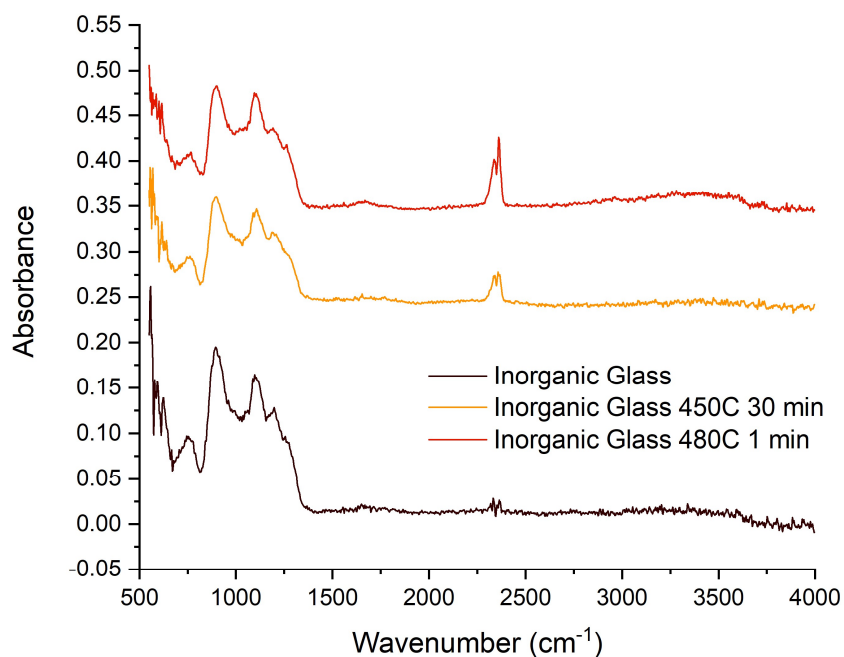


Figure 7.13: FTIR spectra of the inorganic glass controls.

In the X wt% ZIF-8 samples the intensity of the sharp peaks due to ZIF-8 stretches reduced with heat treatment, relative to the pellet control, for all sample series (**Figures 7.14-25**). Peaks at 904 cm^{-1} , 1041 cm^{-1} , 1251 cm^{-1} and 2200 cm^{-1} , are reported in the literature to appear upon decomposition, and are ascribed to disordering in the CN bonding and the formation of aliphatic amines [74]. These peaks are visible in the heat treated 30 wt% ZIF-8 samples (**Figures 7.15-16**), the heat treated 15 wt % ZIF-8 samples (**Figures 7.18-19**) and the 10 wt% ZIF-8 $450\text{ }^{\circ}\text{C}$ 30 minute sample (**Figure 7.21**). No decomposition peaks were visible in the 10 wt% ZIF-8 $480\text{ }^{\circ}\text{C}$ 1 minute sample (**Figure 7.22**) or in the heat treated 5 wt% ZIF-8 samples (**Figures 7.24-25**). Their absence in these samples may be due to the complete decomposition of ZIF-8, the PXRD patterns of these samples also contained no Bragg peaks (**Figures 7.10-11**). Alternatively, these peaks may be present at low intensity and therefore were not discernible above the background scattering from the inorganic glass.

These results were then used to investigate how the amount of ZIF-8 in the samples changed with heat treatment in a semi-quantitative manner. The absorbance of an IR band is described by the Beer-Lambert law [158]:

$$\log\left(\frac{I_0}{I}\right) = A = acd \quad 7.3$$

where a is the absorbance coefficient, c is the sample concentration, d is the pathlength, I_0 is the background intensity and I is the measured transmitted intensity. As such the integrated intensity of

an absorbance band should be proportional to the concentration of the species responsible for the vibration of the band.

This analysis makes the following assumptions:

- Parallel monochromatic light.
- No stray light.
- Parallel entrance and exit planes.
- Small homogeneous particle size and distribution.
- Fixed pathlength (sample thickness).

Though these are not strictly obeyed in the experimental setup used here due to the attenuated total-reflection set-up (ATR-FTIR). Published literature has shown that despite the additional complications in ATR-FTIR experiments, a linear relationship exists between concentration and the integrated intensity of the absorbance bands, provided that the particle sizes of the components are comparable and considerably less than the area sampled in the experiment [159]. However, this experiment also has the additional difficulty of creating a calibration curve, as both ball-milling and pelletisation have an effect on ZIF-8 crystallinity that depends on its concentration. Taken together these factors mean that a completely quantitative comparison between FTIR spectra cannot be achieved. Therefore, a relative measure of the amount of ZIF-8 can be obtained by taking a ratio between the integrated intensity of a band from the ZIF-8 and one from the inorganic glass.

A background was fitted to the data such that it was flat in the $< 1500 \text{ cm}^{-1}$ region, and the ZIF-8 band, at approx. 1440 cm^{-1} , and the inorganic glass band, at approx. 910 cm^{-1} , were fitted with Lorentzian peaks in Fityk [92] and their areas obtained (insets **Figure 7.14-25**). These bands were chosen because they were the only bands with negligible overlap between the two components. A ratio was then reported for each sample:

$$R = \frac{\int_{1360}^{1510} A(\nu) d\nu}{\int_{800}^{975} A(\nu) d\nu} \quad 7.4$$

where $A(\nu)$ is the measured absorbance as a function of wavenumber ν . When the ZIF-8 band was completely absent a ratio of 0 was reported to indicate that the amount of intact ZIF-8 present was below the limits measurable by this method (**Table 7.3**). These results show that the ZIF-8 content decreased in all samples with heat treatment. With the exception of the 15 wt % sample, where the $450 \text{ }^\circ\text{C}$ 30 minute and $480 \text{ }^\circ\text{C}$ 1 minute sample had a comparable ratio, the samples $480 \text{ }^\circ\text{C}$ 1 minute samples had lower ZIF-8 contents than the $450 \text{ }^\circ\text{C}$ 30 minute samples. This is in broad agreement with the crystallinity measurements (**Table 7.2**).

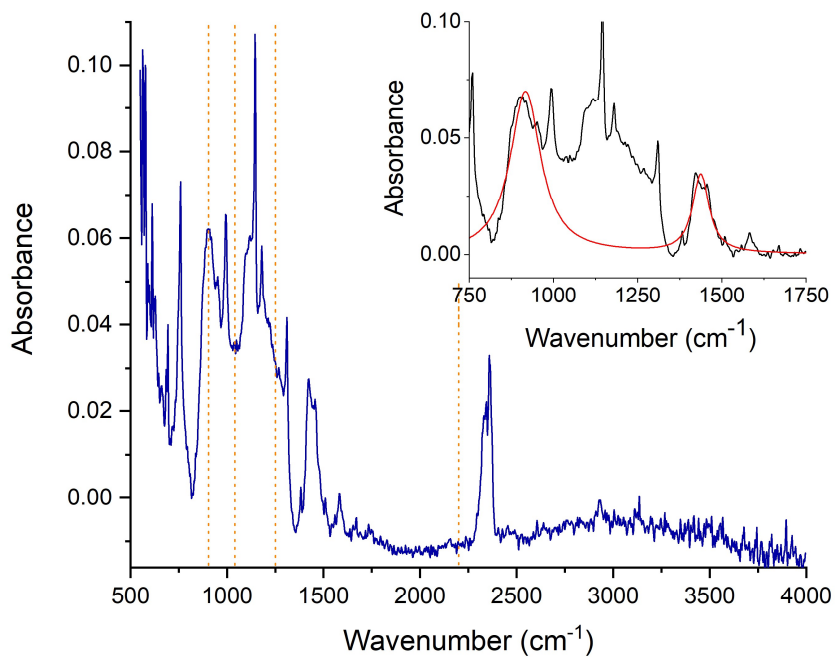


Figure 7.14: FTIR spectrum of the 30 wt% ZIF-8 pressed pellet. Dashed droplines indicate positions of ZIF-8 decomposition peaks reported in the literature [74]. Inset: Background subtracted FTIR spectrum (black) with fitted peaks (red).

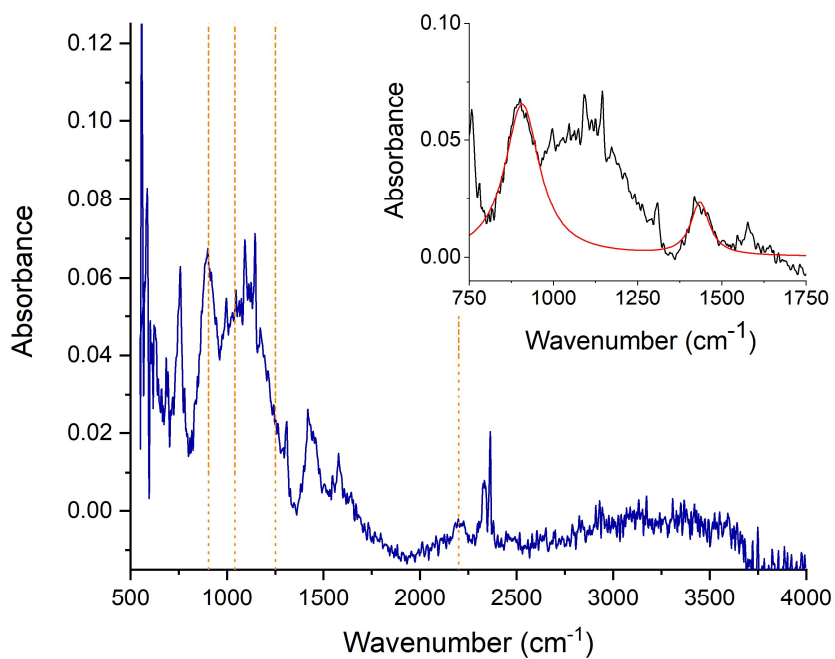


Figure 7.15: FTIR spectrum of the 30 wt% ZIF-8 450 °C 30 min sample. Dashed droplines indicate positions of ZIF-8 decomposition peaks reported in the literature [74]. Inset: Background subtracted FTIR spectrum (black) with fitted peaks (red).

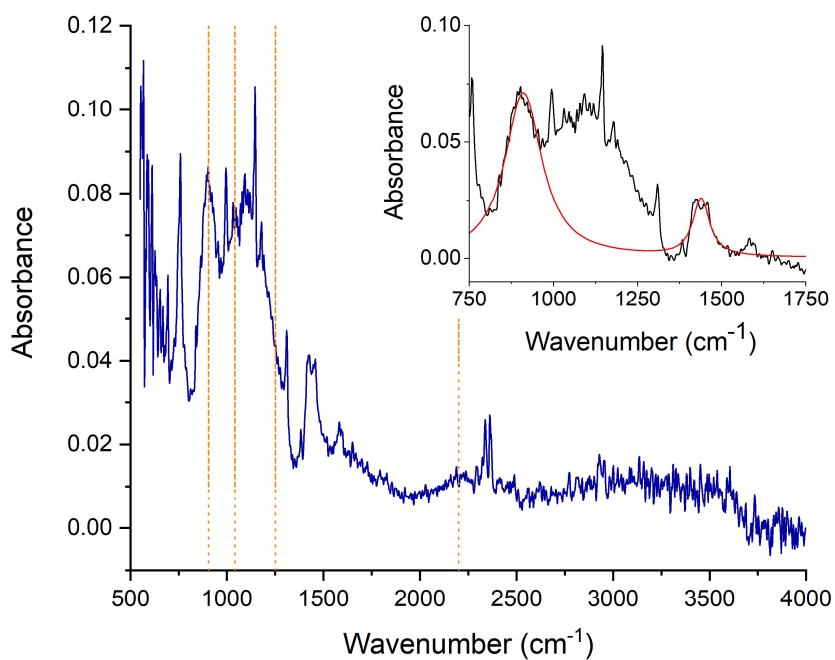


Figure 7.16: FTIR spectrum of the 30 wt% ZIF-8 480 °C 1 min sample. Dashed droplines indicate positions of ZIF-8 decomposition peaks reported in the literature [74]. Inset: Background subtracted FTIR spectrum (black) with fitted peaks (red).

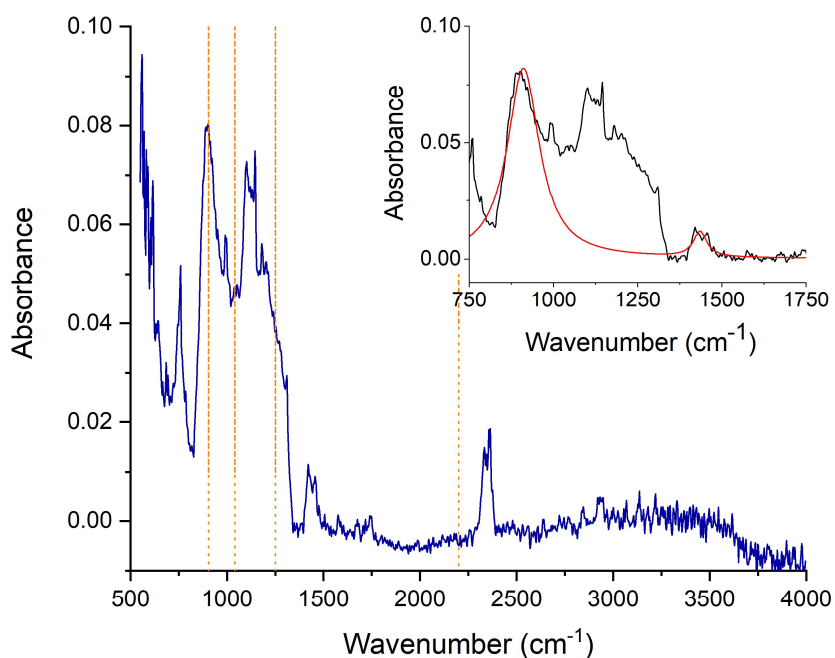


Figure 7.17: FTIR spectrum of the 15 wt% ZIF-8 pressed pellet. Dashed droplines indicate positions of ZIF-8 decomposition peaks reported in the literature [74]. Inset: Background subtracted FTIR spectrum (black) with fitted peaks (red).

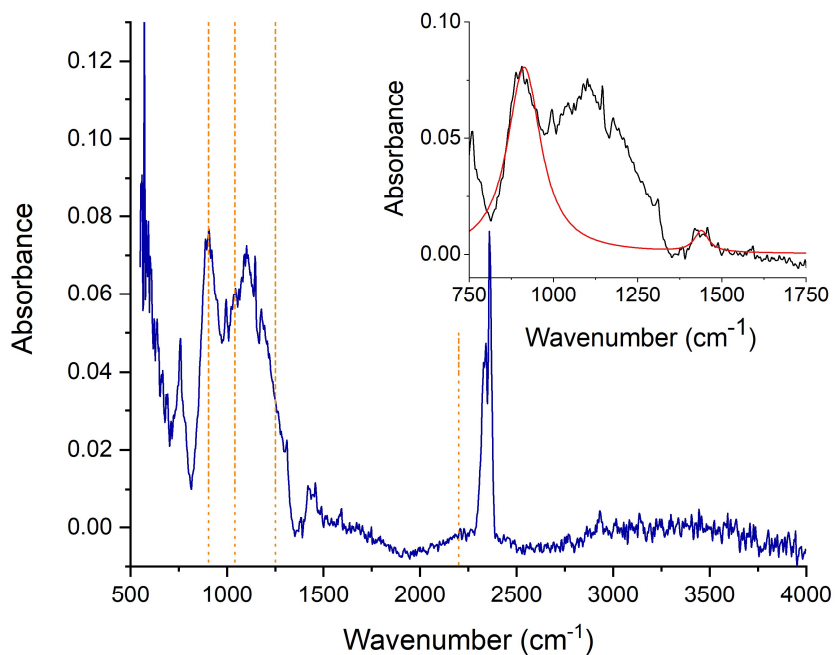


Figure 7.18: FTIR spectrum of the 15 wt% ZIF-8 450 °C 30 min sample. Dashed droplines indicate positions of ZIF-8 decomposition peaks reported in the literature [74]. Inset: Background subtracted FTIR spectrum (black) with fitted peaks (red).

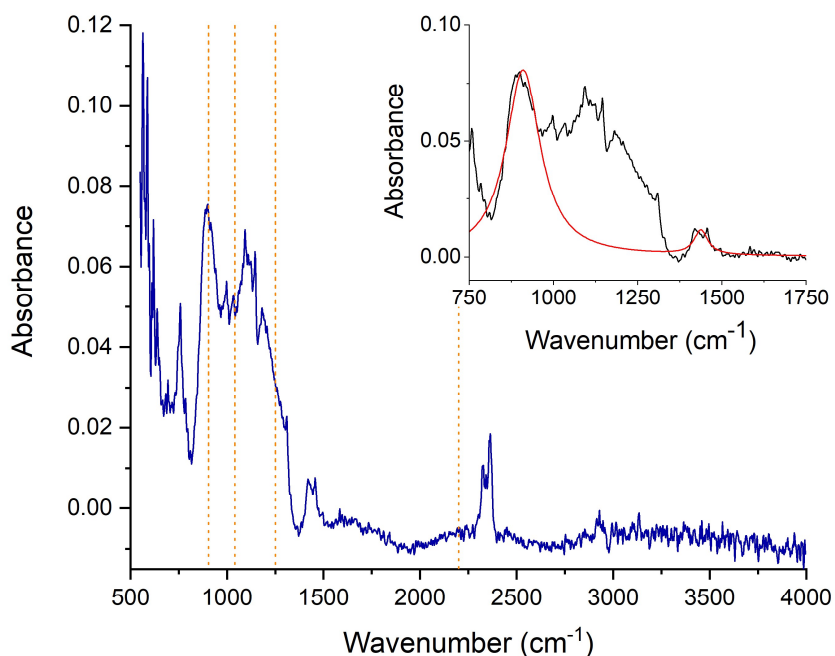


Figure 7.19: FTIR spectrum of the 15 wt% ZIF-8 480 °C 1 min sample. Dashed droplines indicate positions of ZIF-8 decomposition peaks reported in the literature [74]. Inset: Background subtracted FTIR spectrum (black) with fitted peaks (red).

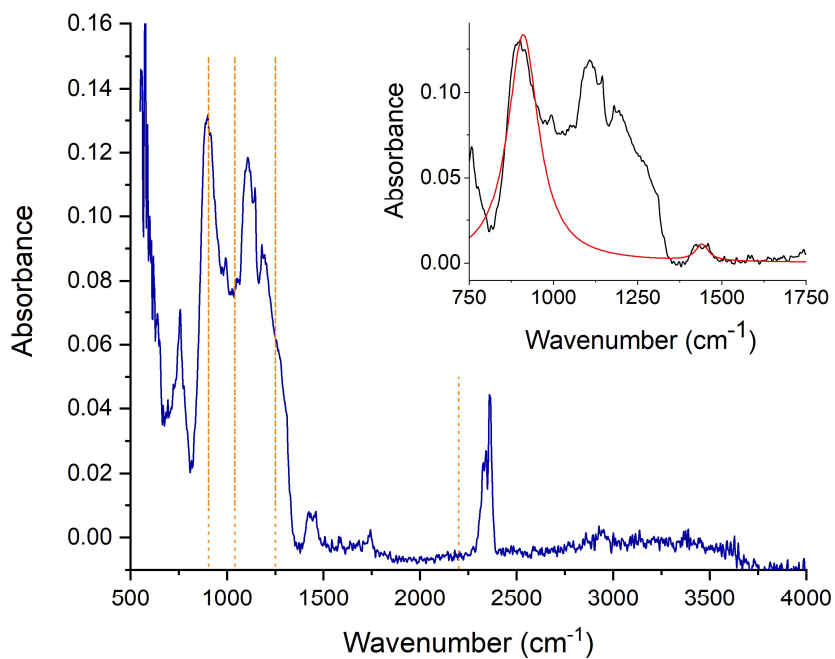


Figure 7.20: FTIR spectrum of the 10 wt% ZIF-8 pressed pellet. Dashed droplines indicate positions of ZIF-8 decomposition peaks reported in the literature [74]. Inset: Background subtracted FTIR spectrum (black) with fitted peaks (red).

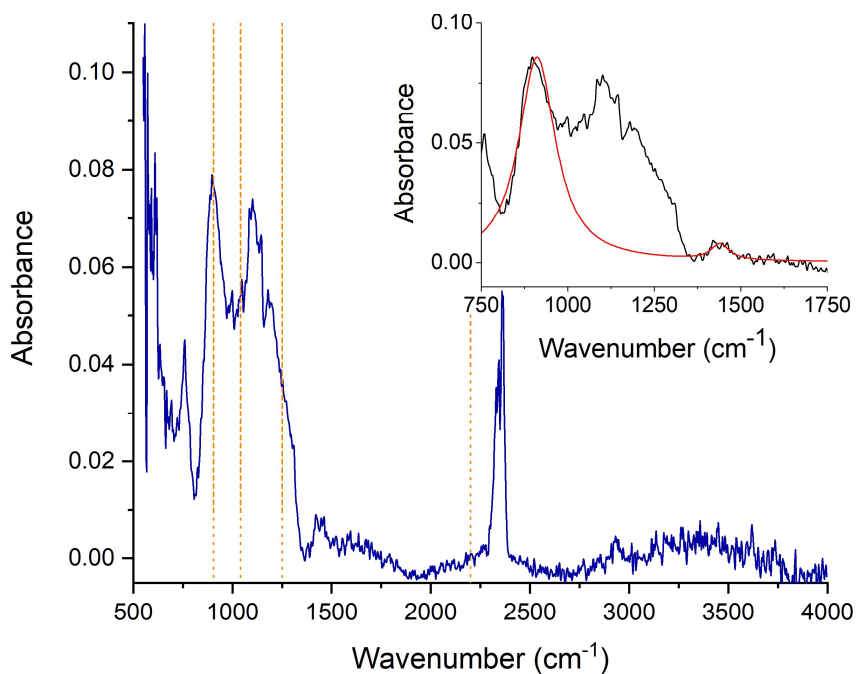


Figure 7.21: FTIR spectrum of the 10 wt% ZIF-8 450 °C 30 min sample. Dashed droplines indicate positions of ZIF-8 decomposition peaks reported in the literature [74]. Inset: Background subtracted FTIR spectrum (black) with fitted peaks (red).

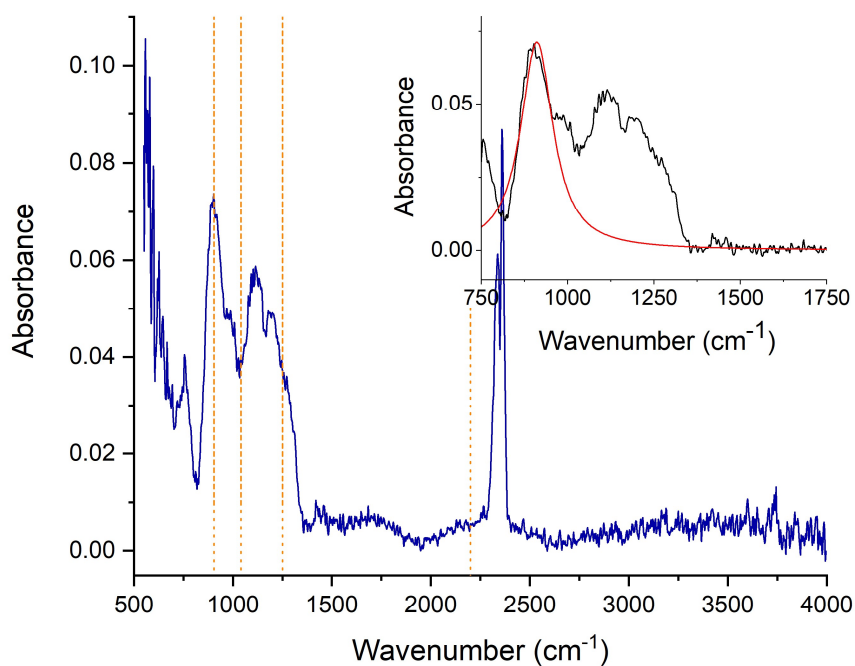


Figure 7.22: FTIR spectrum of the 10 wt% ZIF-8 480 °C 1 min sample. Dashed droplines indicate positions of ZIF-8 decomposition peaks reported in the literature [74]. Inset: Background subtracted FTIR spectrum (black) with fitted peak (red).

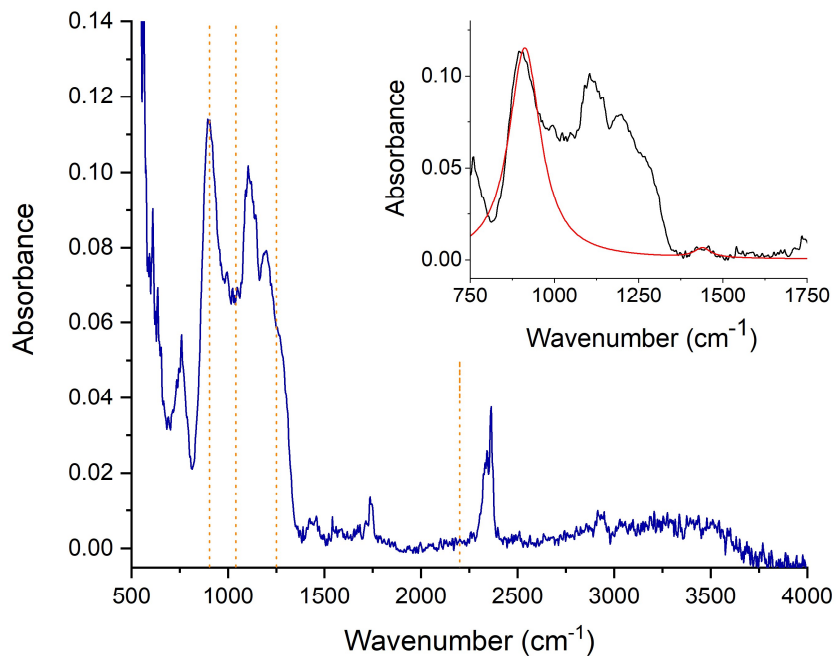


Figure 7.23: FTIR spectrum of the 5 wt% ZIF-8 pressed pellet. Dashed droplines indicate positions of ZIF-8 decomposition peaks reported in the literature [74]. Inset: Background subtracted infra-red spectrum (black) with fitted peaks (red).

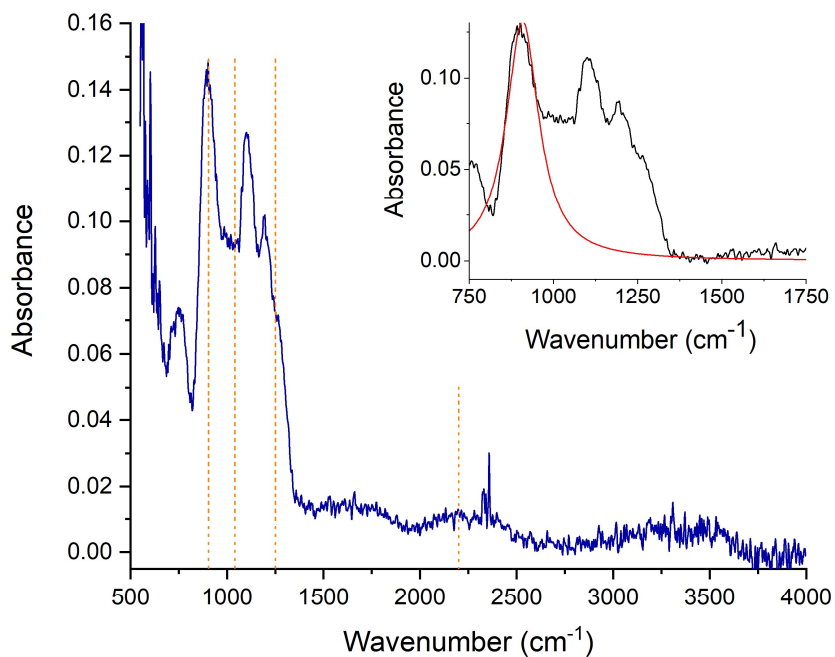


Figure 7.24: FTIR spectrum of the 5 wt% ZIF-8 450 °C 30 min sample. Dashed droplines indicate positions of ZIF-8 decomposition peaks reported in the literature [74]. Inset: Background subtracted FTIR spectrum (black) with fitted peak (red).

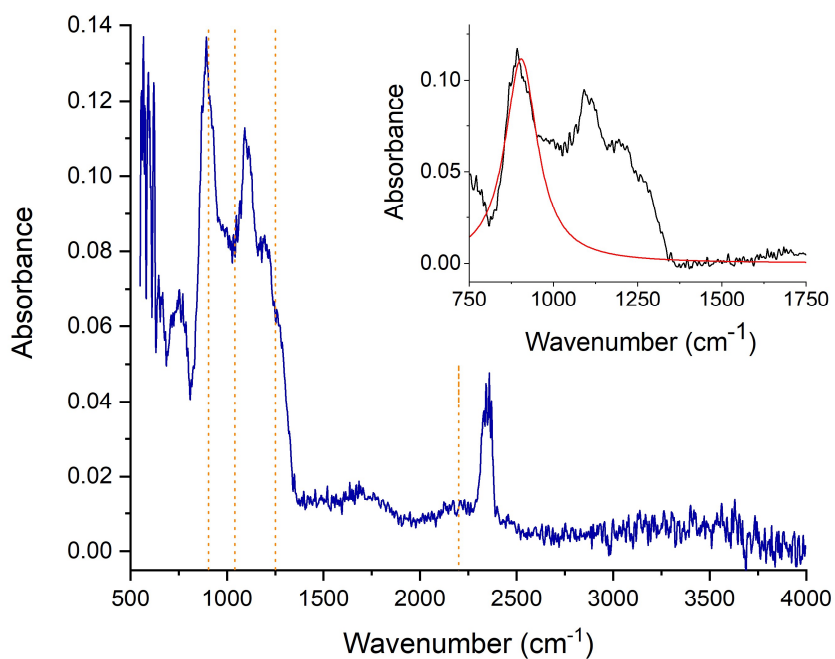


Figure 7.25: FTIR spectrum of the 5 wt% ZIF-8 480 °C 1 min sample. Dashed droplines indicate positions of ZIF-8 decomposition peaks reported in the literature [74]. Inset: Background subtracted FTIR spectrum (black) with fitted peak (red).

Table 7.3: Relative proportions of ZIF-8 and inorganic glass as determined by FTIR.

Sample	Area ZIF-8 Band	Area Inorganic glass band	Ratio	Fit R^2
30 wt% ZIF-8 Pressed Pellet	3.160	12.183	0.259	0.926
30 wt% ZIF-8 450 C 30 min	2.379	12.941	0.184	0.973
30 wt% ZIF-8 480 C 1 min	2.340	15.023	0.156	0.970
15 wt% ZIF-8 Pressed Pellet	0.836	14.998	0.056	0.967
15 wt% ZIF-8 450 C 30 min	0.741	15.350	0.048	0.979
15 wt% ZIF-8 480 C 1 min	0.814	15.828	0.051	0.973
10 wt% ZIF-8 Pressed Pellet	0.704	23.547	0.030	0.968
10 wt% ZIF-8 450 C 30 min	0.668	17.594	0.038	0.983
10 wt% ZIF-8 480 C 1 min	0	12.7465	0.000	0.972
5 wt% ZIF-8 Pressed Pellet	0.500	20.755	0.024	0.979
5 wt% ZIF-8 450 C 30 min	0	24.390	0.000	0.979
5 wt% ZIF-8 480 C 1 min	0	20.602	0.000	0.974

7.4.2 Examining 2-methylimidazole Loss through ^1H Nuclear Magnetic Resonance Spectroscopy

To confirm that the reduction in Bragg scattering in the PXRD measurements, and the relative reduction ZIF-8 peak intensity in FTIR data, ^1H NMR was conducted on the 15 wt% ZIF-8 sample heated to 450 °C for 30 minutes, alongside the evacuated and pellet pressed 15 wt% ZIF-8 samples and an activated ZIF-8 control (**Figure 7.26**). This sample was selected because it showed substantial drop in ZIF-8 content, as measured by PXRD and FTIR, while still containing some ZIF-8. Although peaks matching those of the ZIF-8 control were observed, their integration trace had fallen by a factor of three relative to the non heat treated sample, using the DMSO-d6 peak as a standard (**Table 7.4**). All samples also showed a large solvent peak, assigned as $(\text{H,D})_3\text{O}^+$ as a result of sample preparation (**Chapter 3.2.4**). This confirms the results of the FTIR experiments, showing that the 2-methylimidazolate linker is being destroyed during heat treatment. However, no decomposition products could be observed in the ^1H NMR results.

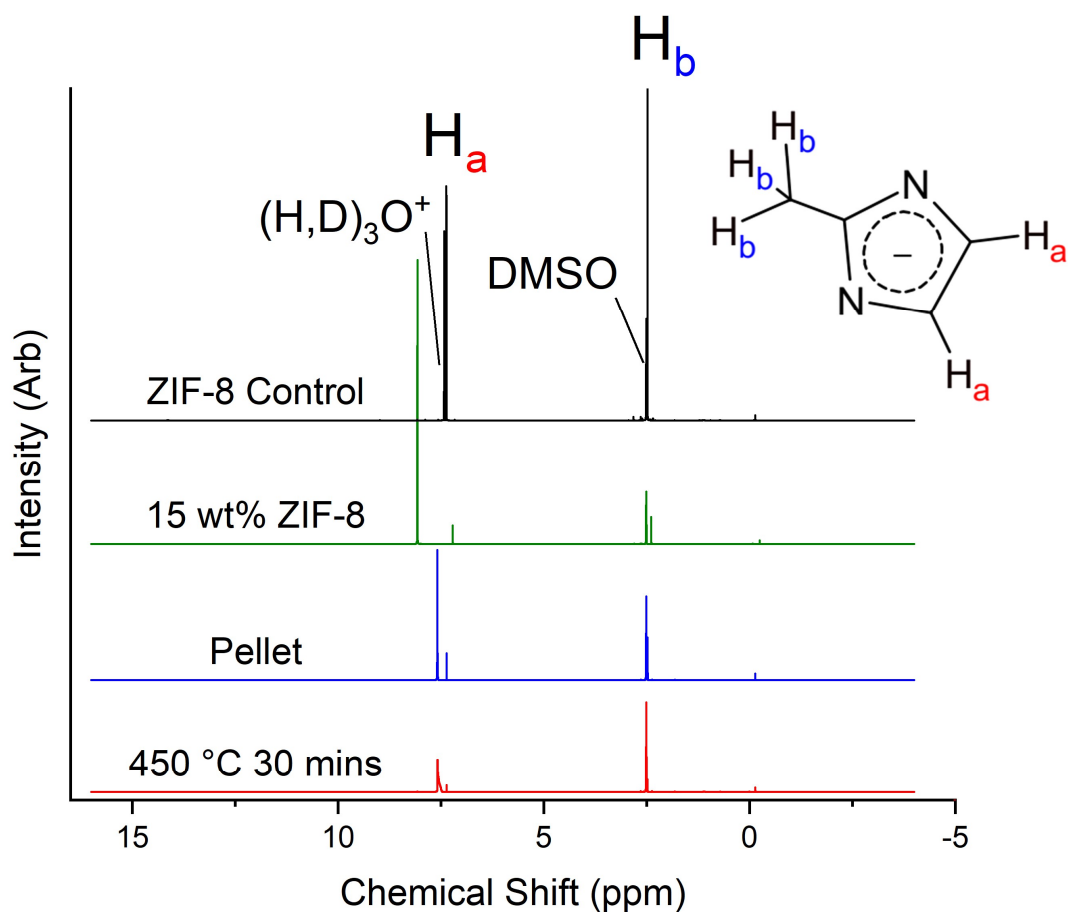


Figure 7.26: ^1H NMR spectra of the ZIF-8 control and the 15 wt% ZIF-8 samples. H_a and H_b are the imidazole ring -CH and - CH_3 group protons, respectively. The solvent used was a mixture of DCl (35%)/ D_2O (0.1 ml) and $\text{DMSO-}d_6$ (0.6 ml).

Table 7.4: ^1H NMR peak integrals of the ZIF-8 control and the 15 wt% ZIF-8 samples, along with calculated values of $[\text{Imid-H}]/[\text{DMSO}]$, $[\text{Imid-H}]/[\text{CH}_3]$, and $[\text{Imid-H}]/[\text{DMSO}]$ relative to the ZIF-8 control.

Sample	Integral (Arb)			[Imid-H]	[Imid-H]	[Imid-H]	Relative to control
	Imid-H	- CH_3	DMSO	/ $[\text{CH}_3]$	/ $[\text{Imid-H} + \text{CH}_3]$	/ $[\text{DMSO}]$	
ZIF-8 Control	1	1.511	2.225	0.66	0.40	0.45	
15 wt% ZIF-8 Powder	1	1.612	15.620	0.62	0.38	0.06	0.14
15 wt% ZIF-8 Pellet	1	1.548	15.669	0.65	0.39	0.06	0.14
15 wt% 450 °C 30 mins	1	1.629	57.846	0.61	0.38	0.02	0.04

7.5 Discussion

The results presented here indicate that an interaction occurs between ZIF-8 and the inorganic glass, which has a destabilising effect on the ZIF framework. The fact that $\Delta m(T)$ becomes rapidly more negative at temperatures above 400 °C, *i.e.* approx. 50 °C above $T_g^{\text{Inorg.}}$, is consistent with increasing decomposition due to a more intimate mixing between the inorganic and the ZIF, *i.e.* mixing occurring when the inorganic glass is sufficiently fluid. PXRD data indicate the reduction or complete loss of crystallinity on heating the pellet pressed X wt% samples. FTIR and ^1H NMR confirm that this loss is due to linker decomposition rather than amorphisation of ZIF-8. New bands that emerged during heat-treatment in the FTIR spectra are consistent with those previously reported as being observed during decomposition of ZIF-8 in the literature [74]. This indicates that decomposition in the inorganic ZIF-8 mixtures may proceed via a similar mechanism to decomposition of the pure ZIF-8, which is reported as proceeding via the formation of tertiary amines [74]. However, the lack of decomposition observed in the ZIF-8 controls in this study indicates that the presence of the inorganic glass leads to decomposition occurring faster and/or at a lower temperature. FTIR and PXRD results both indicate that decomposition occurred to a greater extent in the X wt% ZIF-8 480 °C 1 minute samples than in the X wt% ZIF-8 450 °C 30 minute samples. This further confirms the importance of the inorganic glass viscosity demonstrated by the thermal measurements; viscosity is reported as having an exponential (or sometimes power law) dependence on temperature [30], meaning treatment temperature is likely to be more important than treatment time.

Previous work (**Chapter 6**) has shown that ZIF-62 formed stable composites with this inorganic glass and so the instability of ZIF-8, a framework with a similar chemistry, is somewhat surprising. SEM on evacuated samples of both frameworks confirmed that this difference was not due to a drastically smaller particle size in the ZIF-8 relative to the ZIF-62, with the ZIF-8 in this study having a comparable range of particle sizes to the ZIF-62 used previously (**Figure 7.27-28**).

This leaves differences which are intrinsic to the two frameworks, namely linker chemistry and framework topology, which have both been found to be key factors in determining framework stability [71]. More dense frameworks, for example, are reported as being more stable due to enhanced dispersion interactions between the linkers [66], and so the instability of ZIF-8 relative to ZIF-62 could therefore be ascribed to its lower framework density [48], [67]. The addition of a methyl group to the imidazole ring has also been shown by molecular dynamics simulations to have a substantial effect on the high-temperature dynamics around the Zn centre [60], and so will also have an effect on the linker reactivity.

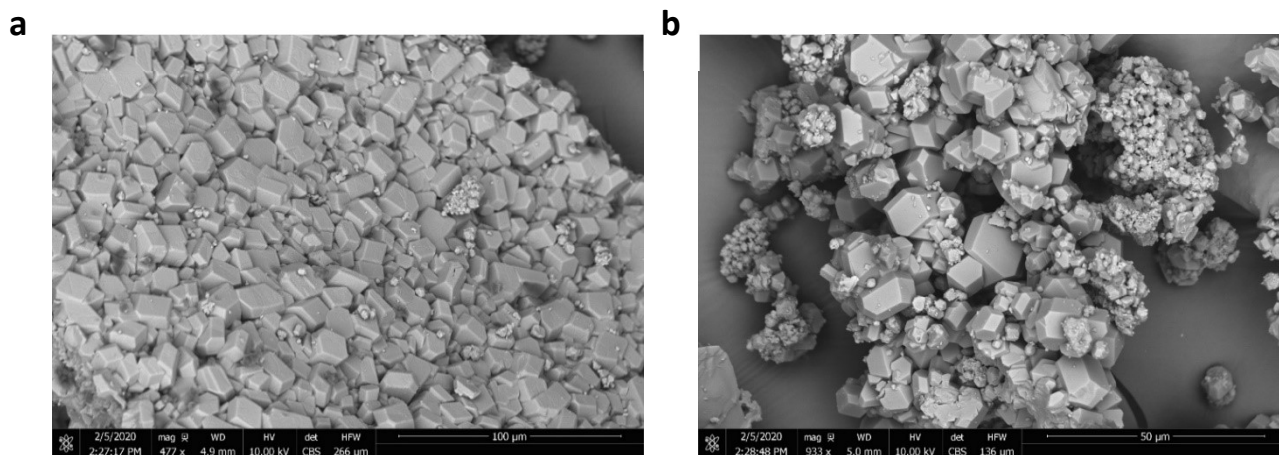


Figure 7.27: SEM images of evacuated ZIF-8. **a.** 477 times magnification. **b.** 933 times magnification.

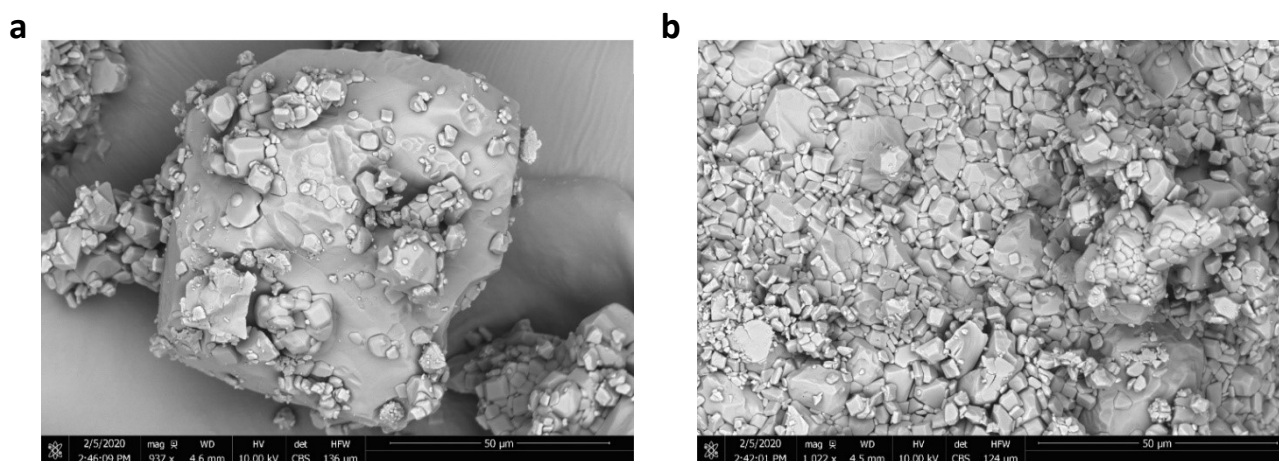


Figure 7.28: SEM images of evacuated ZIF-62. **a.** 937 times magnification. **b.** 1022 times magnification.

These findings illustrate the difficulty of finding chemically compatible MOF glass - inorganic glass pairs. Interfacial interactions are inherently difficult to characterize due to the small size of interfacial regions relative to the bulk volume of both components in the composite. This means that interface specific interactions, though vital to successful composite formation, are often not observed by bulk experimental methods. Moreover, interactions at the interfaces involving decomposition may be even more difficult to fully characterize due to the transient nature of the decomposing ZIF framework, which makes ex-situ measurement difficult. The results here underscore the inherent difficulty of predicting chemical compatibility of such disparate materials ahead of time.

7.6 Conclusions

In conclusion the presence of an inorganic glass, $0.78([\text{Na}_2\text{O}]_{1.6}[\text{P}_2\text{O}_5]) - 0.22([\text{AlO}_{3/2}][\text{AlF}_3]_{0.7})$, was found to have a deleterious effect on the thermal stability of the ZIF-8 framework. The combination of a crystalline MOF component with an apposite inorganic glass to create a porous composite, with the high specific surface areas and chemical selectivity typical of MOFs, combined with the rigidity, processability and mechanical properties of inorganic glasses remains a worthwhile research objective however. The use of low T_g inorganics would allow processing at lower temperatures in which the MOF component is more intrinsically stable. However the nature of the viscosity change of the inorganic glass above T_g , i.e. strong vs fragile glass formers [30], may play a more important role than absolute processing temperature, as may the availability of oxygen anions in the melt, as measured by the optical basicity of the glass [160]. Both MOFs and inorganic glasses display a wide variety of chemistries and physical properties, indicating that the scope of potential composite pairs is likely to be very broad [1], [30]. This study, combined with the fact that previous work had illustrated the compatibility of the same inorganic glass with another ZIF framework, also illustrates the difficulty of predicting the compatibility of a given MOF-inorganic glass pair *a priori*, and therefore underscores the need for a set of general research guidelines to help guide further research efforts. Once compatible MOF crystal – inorganic glass pairings have been discovered, it is hoped that studies can also expand to examine the functional properties of such composite materials, i.e. via gas sorption studies. Whereas in this case the inherent instability of the samples precluded such work. Despite this the authors hope that these results demonstrate an experimental methodology for determining the viability of a given MOF glass - inorganic glass pair, and that such a methodology can be used as the basis for a screening process to find compatible chemistries in the future.

8. Conclusions

This chapter begins by summarising the conclusions of each of the results chapters. Following this the success of the project in fulfilling its aims is reflected upon and overall conclusions are drawn. In the following sections plans for potential future work and overall perspectives on the future of the MOF glass field are outlined.

8.1 Summary of Thesis Results

8.1.1 Investigations into the Changing Structure Zeolitic Imidazolate Framework Glasses at High Temperatures

X-ray total-scattering measurements, along with DSC and TGA, were used to investigate observed changes in the structures of a_g ZIF-4 and a_g ZIF-62 during annealing (**Chapter 4**). This work primarily focused on examining changes that occur beyond first zinc-zinc correlation length, which is commonly referred to as the mid-range order (MRO).

The MRO is the longest length structure observable in real space in glass materials which lack periodic long-range order. It is generally reported as being related to the first-sharp diffraction peak (FSDP), i.e. the lowest Q , narrowest feature observed in reciprocal space [106]. This peak is observed in the diffraction patterns of many chemically distinct classes of glasses and liquids [105]. It has been reported in the literature that, in covalent network glasses AX_2 , such as SiO_2 , the FSDP peaks can be brought to the same position when they are scaled by the length of the A-X bond [105]. This led to the development of a general theory of the origin of the FSDP in these glasses as being due to correlations between the A centred spheres and voids [107], [109].

This theory was applied to both a_g ZIF-4 and a_g ZIF-62. Both MOF glasses had very similar characteristics at room temperature as expected from their similar structure. Moreover, both showed the same scaling with FSDP position as reported for SiO_2 and other covalent network glasses. However, the existing theory could not be used to predict the peak positions of the FSDP. In both cases it predicted values that diverged considerably from the experimentally measured position. This is attributed to the fact that, unlike the other glasses, the imidazolate linkers themselves possess an internal structure and degrees of freedom, which are not captured by the existing theory.

The approximate correlation length, as measured from the FWHM of the FSDP, was measured as being 17.5 Å for a_g ZIF-4 and 13 Å a_g ZIF-62. This disparity could indicate subtle differences in the structures of a_g ZIF-62 and a_g ZIF-4 that exist beyond the Zn-Zn limit. However, it could also be explained by the relation between correlation length and FWHM being approximate, and the data

from each MOF glass originating from two separate beamlines (**Chapter 3**). However this 13-18 Å distance range was found to broadly match 6 membered Zn-Im-Zn rings found in the crystal structure of ZIF-4 [43]. This is taken as tentative evidence that such structures may persist into the liquid and glass states.

The FSDP of a_g ZIF-4 displayed a dramatic shift to higher values when the glass is heated to approximately 500 °C, i.e. far above its reported glass transition temperature of 292 °C [36]. This was observed whether the X-ray total-scattering was measured in-situ during heating or ex-situ at room temperature on heat treated samples. This shift in the FSDP is interpreted as due to the densification of the structure due to rearrangements in the liquid at high temperatures. This feature appears to be unique to MOF glasses and might be linked to their higher observed porosity relative to other classes of glass.

8.1.2 Expanding the Metal-organic Framework Glass Domain through Complex Glass Formation

The range of crystalline MOFs that form liquids rather than decomposing when heated is extremely limited (**Chapter 2**) at present. However, in contrast to crystals, glasses can generally be produced with a range of chemistries through mixing of starting reagents in the liquid phase [30]. Therefore, motivated by a desire to expand the range of chemistries and structures reported in the MOF glass phase, a series of different ‘complex MOF glasses’ were produced by mixing two crystalline MOFs and heating into the liquid phase. The resulting materials formed were then characterised by DSC, EDS, PXRD and X-ray total-scattering.

It was found that these ‘complex MOF glasses’ could be divided into two broad categories, blends and fluxes. Blends are materials formed by heating a mixture of two ZIFs, both of which melt on their own, above their highest melting point. In contrast fluxes are materials in which a liquid MOF, the flux, is used to drive melting in a crystalline framework that does not melt when heated on its own.

A blend structure, termed $(a_g\text{ZIF-4})_{0.5}(a_g\text{ZIF-62})_{0.5}$, was produced by heating a mixture of ZIF-4 and ZIF-62 above the melting point of ZIF-4. Cooling back to room temperature produced a sample that was found to be amorphous by PXRD. A subsequent heating scan in the DSC revealed a single T_g between the two values measured in the literature for a_g ZIF-4 and a_g ZIF-62.

To study the microstructure of the blend, samples containing a cobalt analogue of ZIF-4, ZIF-4-Co, were then produced by heating in a tube furnace to approximately 425 °C. PXRD measurements on these samples, $(\text{ZIF-4-Co})_{0.5}(a_g\text{ZIF-62})_{0.5}$, confirmed that it was mostly non-crystalline. EDS revealed a heterogeneous microstructure of separate cobalt and zinc domains. However, tomography revealed

that there was a small degree of homogeneous mixing at some of the interfaces between domains. X-ray total-scattering measurements on ambient temperature $(\text{ZIF-4-Co})_{0.5}(\text{a}_g\text{ZIF-62})_{0.5}$ revealed that, much like for pure phase MOF glasses [56], the short-range structure is unchanged on glass formation. Variable temperature data on a sample of $(\text{ZIF-4-Co})_{0.5}(\text{a}_g\text{ZIF-62})_{0.5}$ heated to 460 °C and cooled again, i.e. cycling the glass into the liquid and re-quenching, revealed a reversible reduction in features in the SRO of the $D(r)$. This is consistent with a small degree of de-coordination of linkers from around the zinc centre on liquid formation, which was observed via molecular dynamics simulations in the literature [60].

A flux-melted glass was then produced by heating a mixture of ZIF-62 and ZIF-8. ZIF-8 decomposes on heating rather than forming a stable liquid [36]. Despite this, when the mixture of crystalline powders was heated to approximately 500 °C, a fully amorphous flux-melted sample, termed $\text{a}_g[(\text{ZIF-8})_{0.2}(\text{ZIF-62})_{0.8}]$, was produced. This sample displayed a markedly different appearance when examined using SEM and had a single T_g which is higher than that reported in the literature for pure ZIF-62. X-ray total-scattering measurements also revealed that local structure around the zinc centres is maintained on flux-melting.

A flux-melted sample using a cobalt analogue of ZIF-8, ZIF-67, was also produced so that the microstructure of the flux-melted samples could be examined using EDS. The $\text{a}_g[(\text{ZIF-67})_{0.2}(\text{ZIF-62})_{0.8}]$ sample was produced by heating to approximately 500 °C in the tube furnace. This sample showed a much more homogeneous distribution of Co and Zn than the blends microstructure. This could be due to more liquid infiltration of the porous ZIF-67 during flux-melting; however, it may also be due to the higher treatment temperature of the flux-melted sample, 500 °C compared to 425 °C.

Finally $\text{a}_g[(\text{ZIF-76})(\text{ZIF-UC-5})]$ and $\text{a}_g[(\text{ZIF-76-mblm})(\text{TIF-4})]$ two additional, though unintentional, examples of flux-melting were also characterised. These were initially thought to be pure phase melting MOFs, ZIF-76 and ZIF-76-mblm, however subsequent research [71] revealed that the presence of a small amount of the dense polymorphs ZIF-UC-5 and TIF-4 was necessary to allow for glass formation. The melting of $(\text{ZIF-76})(\text{ZIF-UC-5})$ was studied in-situ using variable temperature X-ray total-scattering. As expected, short-range order is maintained on glass formation. However, unlike in the variable temperature scans on $(\text{ZIF-4-Co})_{0.5}(\text{a}_g\text{ZIF-62})_{0.5}$, some degree of the observed high temperature de-coordination is found to persist at room temperature.

In summary these results indicate that mixing in the MOF liquid phase can be used as a route toward functionalisation and expansion of the MOF glass domain. This is analogous to the behaviour of inorganic glasses, where producing series by varying the amount of one reagent added to the melt is

a common practice. Equally this work could also be seen as the amorphous state analogue to post-synthetic modification reported for crystalline MOFs (**Chapter 1**).

8.1.2 Composite Formation between Metal-organic Frameworks and Inorganic Glasses

The observation of miscibility in the MOF liquid phase in the formation of complex MOF glasses, led to the development of composite samples in which a_g ZIF-62 was combined with an inorganic glass. An initial screening process was used to identify compatible inorganic glasses for composite formation, which led to the identification of a series of fluoroaluminophosphate glasses, $(1-x)([Na_2O]_z[P_2O_5])_z-x([AlO_{3/2}][AlF_3]_y)$, as good candidates.

Three glasses from this series termed base, Na-deficient, and Al-rich were chosen. Composite formation was then achieved by mixing crystalline ZIF-62 with preformed glass powders followed by heating to 410 °C in a tube furnace and holding for either 1 or 30 minutes. The resulting composite materials, $(a_g\text{ZIF-62})_{0.5}(\text{Inorganic Glass})_{0.5}$, were then characterised by microscopy, EDS, DSC and TGA, FTIR, Raman, NMR and X-ray total-scattering methods.

PXRD results revealed that the heat treated composite samples were mainly amorphous with some samples showing small Bragg peaks due to formation of a minor ZIF-zni phase. ZIF-zni is a dense $Zn(Im)_2$ polymorph which recrystallises from ZIF-4 on heating but which has not been reported to form from ZIF-62 glass, except at benzimidazolate contents much lower than those in this study [51]. In-situ formation of the composites in a DSC revealed that all the samples had two separate T_g s, one corresponding to the relevant inorganic glass and the other to the a_g ZIF-62. SEM and light microscopy both confirmed that all the composite samples showed evidence of liquid flow and sintering between the inorganic glass and a_g ZIF-62 during heat treatment. The degree of flow evident in the microstructure increased with increasing treatment time and decreasing inorganic glass T_g . EDS results revealed that the microstructures had distinct domains originating from the MOF and inorganic glasses.

^{31}P NMR spectroscopy on the composite samples indicated evidence for formation of P-N bonds in the composite samples. $^{31}P\{^1H\}$ CP NMR experiments also indicated that there was good magnetisation transfer between protons in the composite and the phosphorous nuclei, which is taken to show intimate association between the inorganic glass and a_g ZIF-62. Raman spectroscopy also provides evidence that Na-N bonds formed in the composite samples. X-ray total-scattering measurements indicate that the short-range order in the composites appears to be consistent with that expected from measurements on the inorganic glasses and a_g ZIF-62. A differential PDF method was employed to investigate composite formation further. This method further highlighted the observed

recrystallisation of ZIF-zni during composite formation, however no new correlations in the composites could be definitively assigned.

The mechanical properties of the $(a_g\text{ZIF-62})_{0.5}(\text{base})_{0.5}$ sample were also investigated by nano-indentation and scratch testing. The composites had considerable heterogeneity as would be expected by the observed microstructure of separate $a_g\text{ZIF-62}$ and inorganic glass domains. However, on average, the mechanical properties of the composite samples are between the endmembers. The ionic conductivities of the $(a_g\text{ZIF-62})_{0.5}(\text{Na-deficient})_{0.5}$ samples were also measured and was found to increase with heat treatment time. This is explained by the increasing consolidation of the sample microstructure observed through microscopy, which then reduces structural defects and increases density. Taken together these results demonstrate that the composites formed are composed of separate $a_g\text{ZIF-62}$ and inorganic glass domains which are bonded at the interface into a single composite body.

An attempt was also made to form a crystal glass composite by combining the lowest T_g inorganic glass, base, with ZIF-8. However, work demonstrated that, despite successful composite formation with $a_g\text{ZIF-62}$, heating of the base inorganic glass with ZIF-8 resulted in decomposition of the MOF. Although this work was unsuccessful it demonstrated a methodology by which the suitability of MOF crystal inorganic glass pairs can be assessed in the future.

8.2 Reflection on the Thesis Aims and Conclusions

The first aim of this work was to improve our understanding of the MOF glass state. The work on understanding the mid-range order in a_g ZIF-4 and a_g ZIF-62 in terms of pre-existing theory has added explanatory detail to previously observed changes in the FSDP at high temperature. However the precise structure of MOF glasses between the local order within the $Zn(Im)_4$ coordination sphere and the overall CRN network remains far from clear. Additionally, how this structure relates to properties of the MOF glasses and liquids also remains an open question.

The second aim of the project was to investigate the use of the MOF liquid state in the production of new glasses. The discovery of both MOF blends and fluxes has demonstrated that the liquid phase does indeed have great potential as a route by which new glass materials can be made. Flux glasses seem to offer a promising method by which glasses of chemistries previously thought to be inaccessible to the MOF glass phase due to thermal decomposition of the parent crystal can be produced.

The third aim was to examine whether MOF glasses can be combined with other materials to form composites. Successful composite formation between a_g ZIF-62 and a series of phosphate glasses was achieved and the resulting materials were characterised in detail. This shows that MOF – inorganic glass composite formation is achievable. However, attempts to produce a composite with the same inorganic glass and crystalline ZIF-8 were unsuccessful, which indicates that the process is sensitive to changes in the structure of the MOF component.

Taken in summation, the overall conclusion of this body of work is that the liquid phase of the MOF offers the potential to greatly expand the range of MOF glass materials that can be formed. This can be done both by expanding the range of parent MOF crystals which can be melted via flux-melting, and by tuning the properties of meltable MOFs through blend formation. Equally the formation of composite materials with inorganic glasses vastly increases the scope for MOF glass composites through the potential incorporation of a whole range of different inorganic chemistries not found in MOFs.

8.3 Further Work

There is still a large scope for further investigations into the MRO of MOF glasses. Neutron total-scattering experiments, where the scattering interactions would be more sensitive to the lighter elements such as carbon and nitrogen, could help shed further light on the role of the linker in the mid-range order in MOF glasses. Equally, further experiments on different MOF glasses would be useful to explore the generality of any observed changes in FSDP characteristics and to develop more definitive general rules for MOF glass systems. Variable pressure experiments would also add valuable information on the difference between mid-range order in MOF glasses and other glass types. Finally attempts to correlate changes in structure as measured by techniques such as total-scattering, with measured changes in properties, i.e. via PALS or nano-indentation, may provide a valuable insight into how the structure of the glasses is changing. The overall goal of these types of investigations could take the form of comprehensive phase diagrams for different MOF glass species, in which changes in the liquid and glass state are mapped out over a wide pressure, temperature, and composition space.

The discovery of complex glasses offers a very broad scope for future experiments. This is especially true now that the work of other researchers in the field has uncovered many more melting frameworks [51], [65], [69], [71]. To capture this large scope of potential experiments a roadmap for complex glasses was produced (**Figure 8.1**). This shows a model by which a given complex glass, either a blend or a flux, can be produced and characterised. Interestingly the discovery of high temperature melting cobalt containing frameworks [51], [69] would allow additional EDS experiments to be done to investigate the microstructure of the blend formed when both parent frameworks are glass formers.

Equally the flux-melting experiments carried out as part of this thesis involved (ZIF-8)(ZIF-62)(20/80) mixtures, i.e. the flux framework was present in four times the amount, by mass, of the non-melting frameworks. However subsequent work on (ZIF-76)(ZIF-UC-5) and (ZIF-76-mblm)(TIF-4) revealed that flux-melting can occur with relatively small quantities of the fluxing framework. This discovery invites the potential for a range of experiments in which the amount of melting and non-melting frameworks are varied and the effect on the structure and properties of the resulting glass is investigated.

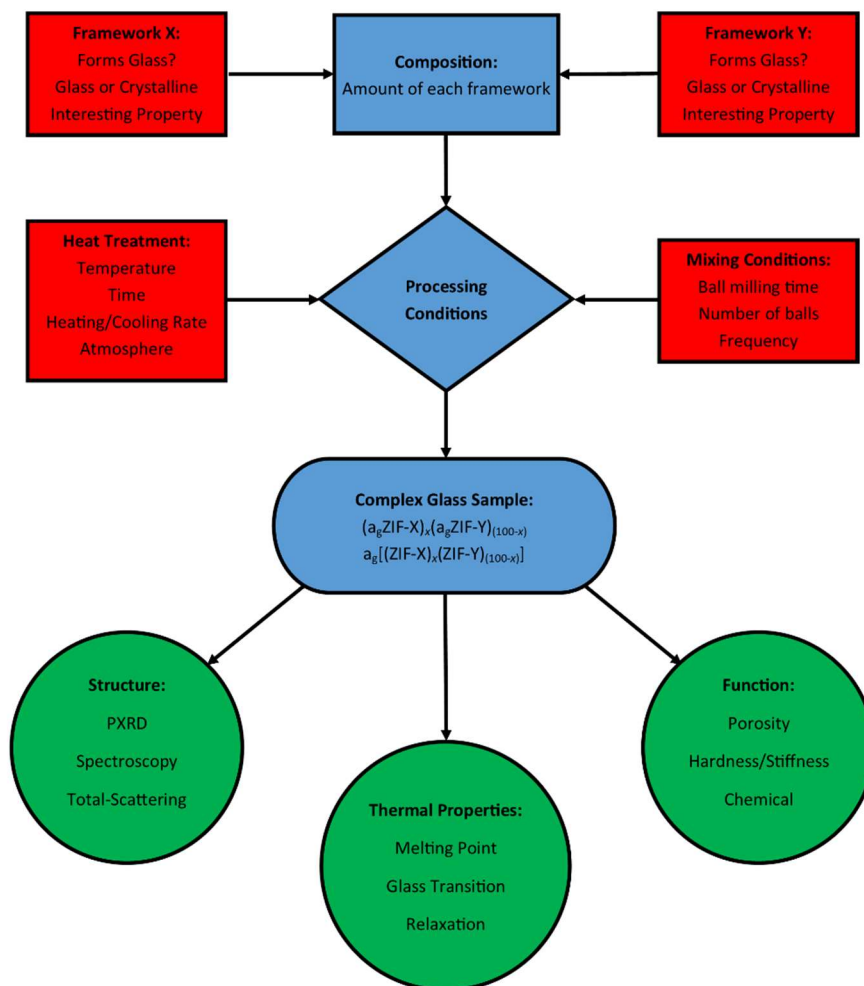


Figure 8.1: Schematic of potential complex MOF glass experiments.

Some other important experimental considerations, which have presently not been investigated, include: i) Whether the flux-melting effect occurs when the flux-forming framework is initially present as a pre-formed glass. ii) The importance of heat treatment times. iii) The degree of mixing between the initial components. This schematic also offers an idea of how MOF glasses with tuneable properties could be produced, via choice of parent frameworks with an array of desired functional properties.

Similarly, the discovery that MOF glasses can be formed into a composite material with inorganic glasses also indicates the potential for a large body of further work (**Figure 8.2**). The scope for new composite materials is potentially even larger than in the case of complex glasses, as a wide variety of inorganic glasses exist. However, viable composite pairs must be chemically compatible, a requirement which is currently not well understood. Additional screening processes will shed further light on the condition of compatibility and make predictions of composite pairings easier. One specific starting point could be with the denser 2-methylimidazole topologies reported in the literature [161]. This may allow for the deconvolution of the importance of MOF framework density and MOF linker chemistry in composite formation.

The occurrence of a small degree of ZIF-zni recrystallisation in the $(a_g\text{ZIF-62})_{0.5}(\text{Inorganic Glass})_{0.5}$ composite samples was unexpected, and its cause remains an open subject for further research. Within the work of this thesis the degree to which recrystallisation occurred was found to be dependent on both heat treatment time and inorganic composition. Tentatively, recrystallisation was also found to be transient, with the $(a_g\text{ZIF-62})_{0.5}(\text{base})_{0.5} - 1$ min sample having the largest degree of recrystallisation but the peaks almost completely gone in the $(a_g\text{ZIF-62})_{0.5}(\text{base})_{0.5} - 30$ min sample. Both these effects could be investigated further through use of the base glass composition, i.e. changing the amount and chemical identity of network modifiers and formers. Equally the ratio of imidazole and benzimidazole in the ZIF-62 can be varied to see if that influences any observed recrystallisation. Finally, different heat treatment times, and other processing conditions such as ball milling and cooling rate may also be important variables. Glass ceramics are an industrially relevant class of material [35] and so if the recrystallisation effect can be better understood and controlled partially recrystallised MOF glass – inorganic glass composites may be of industrial interest.

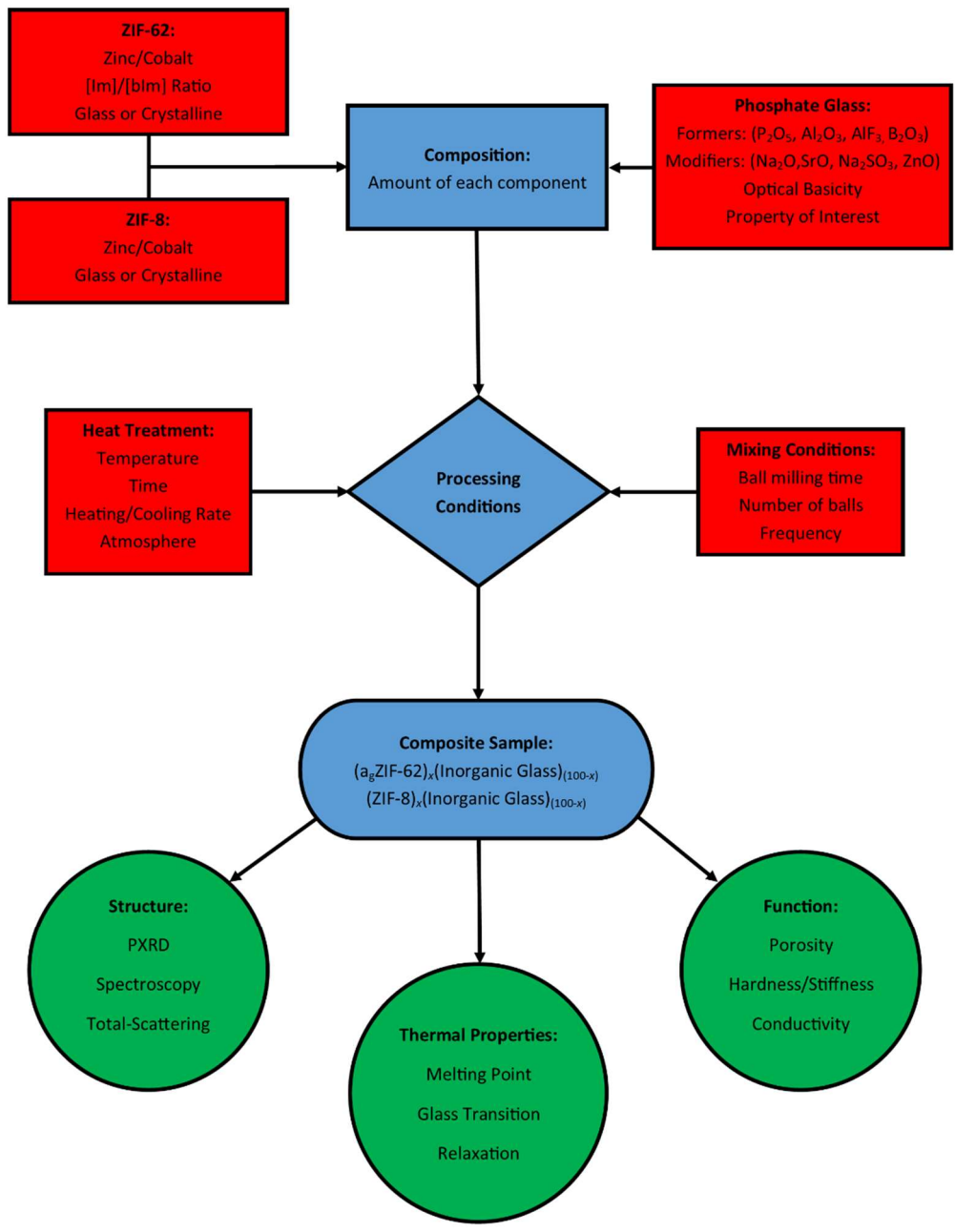


Figure 8.2: Schematic of potential ZIF-62/ZIF-8 phosphate glass composite experiments.

8.4 Outlook

MOF glasses exist as part of a very new field, hybrid glasses, which is situated somewhat awkwardly between the two disparate disciplines of MOF science and glass science. MOF scientists often regard the amorphous state as a failure of synthesis and neglect it entirely. In contrast glass scientists look at the high cost and small scale of MOF glass production and in turn view MOF glasses as somewhat of a novelty. It is true that the high cost, small scale of synthesis, and the current requirement to make MOF glasses under inert atmospheres are significant barriers to commercialisation. However, developments towards mechanical synthesis of parent crystalline MOFs, which is faster, more scalable, and does not use large quantities of hazardous solvents, may address some of these problems. Equally the prospect of melting MOFs under vacuum rather than in inert atmospheres has yet to be explored and could provide a more cost effective and scalable route to bulk MOF glass formation. As the field becomes more mature and questions of the basic science become more settled it is hoped that research which is more application focused can be conducted. In this regard complex glass formation seems to provide a route by which specific linkers and functional groups in crystalline MOFs can be formed into glasses without the need for their framework to be capable of forming a liquid on its own.

To conclude, it is worth mentioning that many similar concerns about viability afflicted the field of metallic glasses at their inception, with many researches writing them off as a novelty due to their need for incredibly high cooling rates to avoid crystallisation. However now many practical uses have been found for them, notably in transformer core shielding [30]. An optimistic view of the future comes from realising that MOF and other hybrid glasses are a new class of material and as such occupy a region of materials space distinct from MOF crystals, inorganic glasses, or polymer glasses. This means that future research is likely to offer both fundamental insights into the glassy state and practical applications for which they are uniquely suited.

Bibliography

- [1] P. Z. Moghadam *et al.*, "Development of a Cambridge Structural Database Subset: A Collection of Metal-Organic Frameworks for Past, Present, and Future," *Chem. Mater.*, vol. 29, no. 7, pp. 2618–2625, 2017.
- [2] Y.-R. Lee, J. Kim, and W.-S. Ahn, "Synthesis of metal-organic frameworks: A mini review," *Korean J. Chem. Eng.*, vol. 30, no. 9, pp. 1667–1680, 2013.
- [3] H. Reinsch and N. Stock, "Synthesis of MOFs: a personal view on rationalisation, application and exploration," *Dalt. Trans.*, vol. 46, no. 26, pp. 8339–8349, 2017.
- [4] D. Crawford, J. Casaban, R. Haydon, N. Giri, T. McNally, and S. L. James, "Synthesis by extrusion: continuous, large-scale preparation of MOFs using little or no solvent," *Chem. Sci.*, vol. 6, no. 3, pp. 1645–1649, 2015.
- [5] V. Nozari, C. Calahoo, L. Longley, T. D. Bennett, and L. Wondraczek, "Structural integrity, meltability, and variability of thermal properties in the mixed-linker zeolitic imidazolate framework ZIF-62," *J. Chem. Phys.*, vol. 153, no. 20, p. 204501, 2020.
- [6] H. Furukawa, K. E. Cordova, M. O’Keeffe, and O. M. Yaghi, "The Chemistry and Applications of Metal-Organic Frameworks," *Science*, vol. 341, no. 6149, p. 1230444, 2013.
- [7] O. M. Yaghi, M. O’Keeffe, N. W. Ockwig, H. K. Chae, M. Eddaoudi, and J. Kim, "Reticular synthesis and the design of new materials," *Nature*, vol. 423, no. 6941, pp. 705–714, 2003.
- [8] S. Horike, S. Shimomura, and S. Kitagawa, "Soft porous crystals," *Nat. Chem.*, vol. 1, no. 9, pp. 695–704, 2009.
- [9] H. Li, M. Eddaoudi, T. L. Groy, and O. M. Yaghi, "Establishing Microporosity in Open Metal–Organic Frameworks: Gas Sorption Isotherms for Zn(BDC) (BDC = 1,4-Benzenedicarboxylate)," *J. Am. Chem. Soc.*, vol. 120, no. 33, pp. 8571–8572, Aug. 1998.
- [10] M. Eddaoudi *et al.*, "Systematic Design of Pore Size and Functionality in Isorecticular MOFs and Their Application in Methane Storage," *Science*, vol. 295, no. 5554, pp. 469–472, 2002.
- [11] H. Wu, J. Yang, Z. M. Su, S. R. Batten, and J. F. Ma, "An Exceptional 54-fold Interpenetrated Coordination Polymer with 10³-srs Network Topology," *J. Am. Chem. Soc.*, vol. 133, no. 30, pp. 11406–11409, 2011.
- [12] H. K. Chae *et al.*, "A route to high surface area, porosity and inclusion of large molecules in crystals," *Nature*, vol. 427, no. 6974, pp. 523–7, 2004.
- [13] N. L. Rosi, M. Eddaoudi, J. Kim, M. O’Keeffe, and O. M. Yaghi, "Infinite Secondary Building Units and Forbidden Catenation in Metal-Organic Frameworks," *Angew. Chemie Int. Ed.*, vol. 41, no. 2, p. 284, 2002.
- [14] K. K. Tanabe and S. M. Cohen, "Postsynthetic modification of metal–organic frameworks—a progress report," *Chem. Soc. Rev.*, vol. 40, no. 2, pp. 498–519, 2011.
- [15] US Department of Energy, "Target Explanation Document: Onboard Hydrogen Storage for Light-Duty Fuel Cell Vehicles," 2017.
- [16] A. G. Wong-Foy, A. J. Matzger, and O. M. Yaghi, "Exceptional H₂ saturation uptake in microporous metal-organic frameworks," *J. Am. Chem. Soc.*, vol. 128, no. 11, pp. 3494–5, 2006.

- [17] X.-S. Wang *et al.*, "A Large-Surface-Area Boracite-Network-Topology Porous MOF Constructed from a Conjugated Ligand Exhibiting a High Hydrogen Uptake Capacity," *Inorg. Chem.*, vol. 48, no. 16, pp. 7519–7521, 2009.
- [18] J. L. C. Rowsell and O. M. Yaghi, "Effects of Functionalization, Catenation, and Variation of the Metal Oxide and Organic Linking Units on the Low-Pressure Hydrogen Adsorption Properties of Metal-Organic Frameworks," *J. Am. Chem. Soc.*, vol. 128, no. 4, pp. 1304–1315, 2006.
- [19] C. E. Wilmer *et al.*, "Large-scale screening of hypothetical metal–organic frameworks," *Nat. Chem.*, vol. 4, no. 2, pp. 83–89, 2011.
- [20] Q. Min Wang *et al.*, "Metallo-organic molecular sieve for gas separation and purification," *Microporous Mesoporous Mater.*, vol. 55, no. 2, pp. 217–230, 2002.
- [21] A. Car, C. Stropnik, and K.-V. Peinemann, "Hybrid membrane materials with different metal–organic frameworks (MOFs) for gas separation," *Desalination*, vol. 200, no. 1–3, pp. 424–426, 2006.
- [22] A. Phan, A. U. Czaja, F. Gándara, C. B. Knobler, and O. M. Yaghi, "Metal-Organic Frameworks of Vanadium as Catalysts for Conversion of Methane to Acetic Acid," *Inorg. Chem.*, vol. 50, no. 16, pp. 7388–7390, 2011.
- [23] B. Chen, M. Eddaoudi, T. M. Reineke, J. W. Kampf, M. O’Keeffe, and O. M. Yaghi, "Cu₂(ATC)·6H₂O: Design of Open Metal Sites in Porous Metal–Organic Crystals (ATC: 1,3,5,7-Adamantane Tetracarboxylate)," *J. Am. Chem. Soc.*, vol. 122, no. 46, pp. 11559–11560, 2000.
- [24] L. Alaerts, E. Séguin, H. Poelman, F. Thibault-Starzyk, P. A. Jacobs, and D. E. De Vos, "Probing the Lewis Acidity and Catalytic Activity of the Metal-Organic Framework [Cu₃(btc)₂] (BTC=benzene-1,3,5-tricarboxylate)," *Chem. - A Eur. J.*, vol. 12, no. 28, pp. 7353–63, 2006.
- [25] Y. K. Hwang *et al.*, "Amine Grafting on Coordinatively Unsaturated Metal Centers of MOFs: Consequences for Catalysis and Metal Encapsulation," *Angew. Chemie - Int. Ed.*, vol. 47, no. 22, pp. 4144–4148, 2008.
- [26] M. Yoon, K. Suh, S. Natarajan, and K. Kim, "Proton Conduction in Metal-Organic Frameworks and Related Modularly Built Porous Solids," *Angew. Chemie - Int. Ed.*, vol. 52, no. 10, pp. 2688–2700, 2013.
- [27] T. Faust, "MOFs move to market," *Nat. Chem.*, vol. 8, no. 11, pp. 990–991, 2016.
- [28] "Frameworks for commercial success," *Nat. Chem.*, vol. 8, no. 11, pp. 987–987, Nov. 2016.
- [29] G. Shimizu, R. Vaidhyanathan, S. Iremonger, K. Deakin, J.-B. Lin, and K. W. Dawson, "METAL ORGANIC FRAMEWORK, PRODUCTION AND USE THEREOF," WO 2014/138878 A1, 2014.
- [30] A. K. Varshneya, *Fundamentals of Inorganic Glasses*, First. Academic Press, Inc., 1994.
- [31] J. Cockcroft, "Advanced Certificate in Powder Diffraction on the Web," *University College London*, 2016. [Online]. Available: <http://pd.chem.ucl.ac.uk/pd/welcome.htm>. [Accessed: 09-Mar-2021].
- [32] W. H. Zachariasen, "The Atomic Arrangement in Glass," *J. Am. Chem. Soc.*, vol. 54, no. 10, pp. 3841–3851, 1932.
- [33] J. H. Simmons, C. J. Simmons, R. Ochoa, and A. C. Wright, "Fluoride Glass Structure," in *Fluoride Glass Fibre Optics*, First., I. D. Aggarwal and G. Lu, Eds. Academic Press, Inc., 1991, pp. 37–84.

- [34] P. G. Debenedetti and F. H. Stillinger, "Supercooled liquids and the glass transition," *Nature*, vol. 410, no. 6825, pp. 259–267, 2001.
- [35] J. C. Mauro, C. S. Philip, D. J. Vaughn, and M. S. Pambianchi, "Glass Science in the United States: Current Status and Future Directions," *Int. J. Appl. Glas. Sci.*, vol. 5, no. 1, pp. 2–15, 2014.
- [36] T. D. Bennett *et al.*, "Hybrid glasses from strong and fragile metal-organic framework liquids," *Nat. Commun.*, vol. 6, no. 1, p. 8079, 2015.
- [37] D. Umeyama, S. Horike, M. Inukai, T. Itakura, and S. Kitagawa, "Reversible Solid-to-Liquid Phase Transition of Coordination Polymer Crystals," *J. Am. Chem. Soc.*, vol. 137, no. 2, pp. 864–870, 2015.
- [38] D. Umeyama *et al.*, "Glass formation via structural fragmentation of a 2D coordination network," *Chem. Commun.*, vol. 51, no. 64, pp. 12728–12731, 2015.
- [39] W. Chen *et al.*, "Glass Formation of a Coordination Polymer Crystal for Enhanced Proton Conductivity and Material Flexibility," *Angew. Chemie - Int. Ed.*, vol. 55, no. 17, pp. 5195–5200, 2016.
- [40] S. S. Nagarkar *et al.*, "Enhanced and Optically Switchable Proton Conductivity in a Melting Coordination Polymer Crystal," *Angew. Chemie - Int. Ed.*, vol. 56, no. 18, pp. 4976–4981, 2017.
- [41] M. Liu *et al.*, "Network-Forming Liquids from Metal–Bis(acetamide) Frameworks with Low Melting Temperatures," *J. Am. Chem. Soc.*, vol. 143, no. 7, pp. 2801–2811, 2021.
- [42] B. K. Shaw *et al.*, "Hybrid Inorganic–Organic Perovskite Glasses," *ChemRxiv*, 2020.
- [43] K. S. Park *et al.*, "Exceptional chemical and thermal stability of zeolitic imidazolate frameworks," *Proc. Natl. Acad. Sci. U. S. A.*, vol. 103, no. 27, pp. 10186–10191, 2006.
- [44] J. M. Bermúdez-García *et al.*, "Role of Temperature and Pressure on the Multisensitive Multiferroic Dicyanamide Framework [TPrA][Mn(dca)₃] with Perovskite-like Structure," *Inorg. Chem.*, vol. 54, no. 24, pp. 11680–11687, 2015.
- [45] A. Phan, C. J. Doonan, F. J. Uribe-Romo, C. B. Knobler, M. O’Keeffe, and O. M. Yaghi, "Synthesis, Structure, and Carbon Dioxide Capture Properties of Zeolitic Imidazolate Frameworks," *Acc Chem Res*, vol. 43, no. 1, pp. 58–67, 2010.
- [46] E. N. Domoroshchina *et al.*, "Changing the characteristics and properties of zeolite Y and nano-anatase in the formation of a nano-anatase/Y composite with improved photocatalytic and adsorption properties," *Appl. Nanosci.*, vol. 8, no. 1–2, pp. 19–31, 2018.
- [47] J. Zhang, T. Wu, C. Zhou, S. Chen, P. Feng, and X. Bu, "Zeolitic Boron Imidazolate Frameworks," *Angew. Chemie - Int. Ed.*, vol. 48, no. 14, pp. 2542–2545, 2009.
- [48] R. Banerjee *et al.*, "High-Throughput Synthesis of Zeolitic Imidazolate Frameworks and Application to CO₂ Capture," *Science*, vol. 319, no. 5865, pp. 939–943, 2008.
- [49] W. Morris, C. J. Doonan, H. Furukawa, R. Banerjee, and O. M. Yaghi, "Crystals as Molecules: Postsynthesis Covalent Functionalization of Zeolitic Imidazolate Frameworks," *J. Am. Chem. Soc.*, vol. 130, no. 38, pp. 12626–12627, 2008.
- [50] T. D. Bennett, D. A. Keen, J. C. Tan, E. R. Barney, A. L. Goodwin, and A. K. Cheetham, "Thermal Amorphization of Zeolitic Imidazolate Frameworks," *Angew. Chemie - Int. Ed.*, vol. 50, no. 13, pp. 3067–3071, 2011.

- [51] L. Frenzel-Beyme, M. Kloß, P. Kolodzeiski, R. Pallach, and S. Henke, "Meltable Mixed-Linker Zeolitic Imidazolate Frameworks and Their Microporous Glasses: From Melting Point Engineering to Selective Hydrocarbon Sorption," *J. Am. Chem. Soc.*, vol. 141, no. 31, pp. 12362–12371, 2019.
- [52] D. W. Lewis *et al.*, "Zeolitic imidazole frameworks: structural and energetics trends compared with their zeolite analogues," *CrystEngComm*, vol. 11, no. 11, pp. 2272–2276, 2009.
- [53] R. Lehnert and F. Seel, "Darstellung und Kristallstruktur des Mangan (II)- und Zink (II)-Derivates des Imidazols," *Zeitschrift für Anorg. und Allg. Chemie*, vol. 464, no. 1, pp. 187–194, 1980.
- [54] T. D. Bennett *et al.*, "Structure and Properties of an Amorphous Metal-Organic Framework," *Phys. Rev. Lett.*, vol. 104, no. 11, p. 115503, 2010.
- [55] C. A. Young and A. L. Goodwin, "Applications of pair distribution function methods to contemporary problems in materials chemistry," *J. Mater. Chem.*, vol. 21, no. 18, p. 6464, 2011.
- [56] T. D. Bennett *et al.*, "Melt-Quenched Glasses of Metal–Organic Frameworks," *J. Am. Chem. Soc.*, vol. 138, no. 10, pp. 3484–3492, 2016.
- [57] C. L. Farrow *et al.*, "PDFfit2 and PDFgui: computer programs for studying nanostructure in crystals," *J. Phys. Condens. Matter*, vol. 19, no. 33, p. 335219, 2007.
- [58] T. D. Bennett *et al.*, "Reversible pressure-induced amorphization of a zeolitic imidazolate framework (ZIF-4)," *Chem. Commun.*, vol. 47, no. 28, pp. 7983–7985, 2011.
- [59] D. A. Keen and T. D. Bennett, "Structural investigations of amorphous metal–organic frameworks formed via different routes," *Phys. Chem. Chem. Phys.*, vol. 20, no. 11, pp. 7857–7861, 2018.
- [60] R. Gaillac *et al.*, "Liquid metal–organic frameworks," *Nat. Mater.*, vol. 16, no. 11, pp. 1149–1154, 2017.
- [61] A. Qiao *et al.*, "A metal-organic framework with ultrahigh glass-forming ability," *Sci. Adv.*, vol. 4, no. 3, p. eaao6827, 2018.
- [62] R. N. Widmer *et al.*, "Pressure promoted low-temperature melting of metal–organic frameworks," *Nat. Mater.*, vol. 18, no. 4, pp. 370–376, 2019.
- [63] A. U. Ortiz, A. Boutin, A. H. Fuchs, and F.-X. Coudert, "Investigating the Pressure-Induced Amorphization of Zeolitic Imidazolate Framework ZIF-8: Mechanical Instability Due to Shear Mode Softening," *J. Phys. Chem. Lett.*, vol. 4, no. 11, pp. 1861–1865, 2013.
- [64] L. Bouëssel du Bourg, A. U. Ortiz, A. Boutin, and F.-X. Coudert, "Thermal and mechanical stability of zeolitic imidazolate frameworks polymorphs," *APL Mater.*, vol. 2, no. 12, p. 124110, 2014.
- [65] J. Hou *et al.*, "Halogenated Metal-Organic Framework Glasses and Liquids," *J. Am. Chem. Soc.*, vol. 142, no. 8, pp. 3880–3890, 2020.
- [66] R. Gaillac, P. Pullumbi, and F.-X. Coudert, "Melting of Zeolitic Imidazolate Frameworks with Different Topologies: Insight from First-Principles Molecular Dynamics," *J. Phys. Chem. C*, vol. 122, no. 12, pp. 6730–6736, 2018.
- [67] J. Cousin Saint Remi *et al.*, "Biobutanol Separation with the Metal-Organic Framework ZIF-8," *ChemSusChem*, vol. 4, no. 8, pp. 1074–1077, 2011.

- [68] C. Zhou *et al.*, “Metal-organic framework glasses with permanent accessible porosity,” *Nat. Commun.*, vol. 9, no. 1, p. 5042, Dec. 2018.
- [69] L. Frenzel-Beyme *et al.*, “Porous purple glass – a cobalt imidazolate glass with accessible porosity from a meltable cobalt imidazolate framework,” *J. Mater. Chem. A*, vol. 7, no. 3, pp. 985–990, 2019.
- [70] M. L. Ríos Gómez, G. I. Lampronti, Y. Yang, J. C. Mauro, and T. D. Bennett, “Relating structural disorder and melting in complex mixed ligand zeolitic imidazolate framework glasses,” *Dalt. Trans.*, vol. 49, no. 3, pp. 850–857, 2020.
- [71] A. M. Bumstead *et al.*, “Investigating the melting behaviour of polymorphic zeolitic imidazolate frameworks,” *CrystEngComm*, vol. 22, no. 21, pp. 3627–3637, 2020.
- [72] R. K. Brow, “Review: the structure of simple phosphate glasses,” *J. Non. Cryst. Solids*, vol. 263–264, pp. 1–28, 2000.
- [73] C. F. Windisch and W. M. Risen, “Vibrational Spectra of Oxygen- and Boron-isotopically Substituted B₂O₃ Glasses,” *J. Non. Cryst. Solids*, vol. 48, no. 2–3, pp. 307–323, 1982.
- [74] J. B. James and Y. S. Lin, “Kinetics of ZIF-8 Thermal Decomposition in Inert, Oxidizing, and Reducing Environments,” *J. Phys. Chem. C*, vol. 120, no. 26, pp. 14015–14026, 2016.
- [75] R. N. Widmer *et al.*, “Rich Polymorphism of a Metal-Organic Framework in Pressure-Temperature Space,” *J. Am. Chem. Soc.*, vol. 141, no. 23, pp. 9330–9337, 2019.
- [76] S. Li *et al.*, “Mechanical Properties and Processing Techniques of Bulk Metal–Organic Framework Glasses,” *J. Am. Chem. Soc.*, vol. 141, no. 2, pp. 1027–1034, 2019.
- [77] A. W. Thornton *et al.*, “Porosity in metal-organic framework glasses,” *Chem. Commun.*, vol. 52, no. 19, pp. 3750–3753, 2016.
- [78] J. Hou *et al.*, “Metal-organic framework crystal-glass composites,” *Nat. Commun.*, vol. 10, no. 1, p. 2580, 2019.
- [79] C. W. Ashling *et al.*, “Synthesis and Properties of a Compositional Series of MIL-53(Al) Metal-Organic Framework Crystal-Glass Composites,” *J. Am. Chem. Soc.*, vol. 141, no. 39, pp. 15641–15648, 2019.
- [80] S. Li *et al.*, “A new route to porous metal-organic framework crystal-glass composites,” *Chem. Sci.*, vol. 11, no. 36, pp. 9910–9918, 2020.
- [81] D. Kriegner, Z. Matěj, R. Kužel, and V. Holý, “Powder diffraction in Bragg–Brentano geometry with straight linear detectors,” *J. Appl. Crystallogr.*, vol. 48, no. 2, pp. 613–618, 2015.
- [82] P. J. Brown, A. G. Fox, E. N. Maslen, M. A. O’Keefe, and B. T. M. Willis, “Volume C,” in *International Tables for Crystallography*, First Onli., E. Prince, Ed. International Union of Crystallography 2006, 2006, pp. 554–595.
- [83] B. H. Toby, “R factors in Rietveld analysis: How good is good enough?,” *Powder Diffr.*, vol. 21, no. 1, pp. 67–70, 2006.
- [84] A. K. Soper and E. R. Barney, “Extracting the pair distribution function from white-beam X-ray total scattering data,” *J. Appl. Crystallogr.*, vol. 44, no. 4, pp. 714–726, 2011.
- [85] L. R. Owen, “The analysis of local structural effects in alloys using total scattering and reverse Monte Carlo techniques,” University of Cambridge, 2017.
- [86] T. Schenk, D. Holland-Moritz, V. Simonet, R. Bellissent, and D. M. Herlach, “Icosahedral Short-

- Range Order in Deeply Undercooled Metallic Melts," *Phys. Rev. Lett.*, vol. 89, no. 7, p. 075507, 2002.
- [87] D. A. Keen, "A comparison of various commonly used correlation functions for describing total scattering," *J. Appl. Crystallogr.*, vol. 34, no. 2, pp. 172–177, 2001.
- [88] T. Egami and S. J. L. Billinge, *Underneath The Bragg Peaks Structural Analysis of Complex Materials*, First Edit. Pergamon, 2003.
- [89] G. W. H. Höhne, W. F. Hemminger, and H. J. Flammersheim, *Differential Scanning Calorimetry*, Second. Springer-Verlag, 2003.
- [90] M. Gustafsson and X. Zou, "Crystal formation and size control of zeolitic imidazolate frameworks with mixed imidazolate linkers," *J. Porous Mater.*, vol. 20, no. 1, pp. 55–63, 2013.
- [91] A. K. Soper, "GudrunN and GudrunX: Programs for Correcting Raw Neutron and X-ray Diffraction Data to Differential Scattering Cross Section," *Tech. Rep. RAL-TR-2011-013*, 2011.
- [92] M. Wojdyr, "Fityk : a general-purpose peak fitting program," *J. Appl. Crystallogr.*, vol. 43, no. 5, pp. 1126–1128, 2010.
- [93] Q. Shi, Z. Chen, Z. Song, J. Li, and J. Dong, "Synthesis of ZIF-8 and ZIF-67 by Steam-Assisted conversion and an Investigation of Their Tribological Behaviors," *Angew. Chemie - Int. Ed.*, vol. 50, no. 3, pp. 672–675, 2011.
- [94] D. Peralta, G. Chaplais, A. Simon-Masseron, K. Barthelet, and G. D. Pirngruber, "Synthesis and adsorption properties of ZIF-76 isomorphs," *Microporous Mesoporous Mater.*, vol. 153, pp. 1–7, 2012.
- [95] F. de la Peña *et al.*, "hyperspy: HyperSpy v.1.0.1." 2016.
- [96] L. Petrakis, "Spectral line shapes: Gaussian and Lorentzian functions in magnetic resonance," *J. Chem. Educ.*, vol. 44, no. 8, p. 432, 1967.
- [97] G. Facey, "Proton NMR Assignment Tools - The D₂O Shake," 2007. [Online]. Available: <http://u-of-o-nmr-facility.blogspot.com/2007/10/proton-nmr-assignment-tools-d2o-shake.html>. [Accessed: 07-Jan-2020].
- [98] W. C. Oliver and G. M. Pharr, "An improved technique for determining hardness and elastic modulus using load and displacement sensing indentation experiments," *J. Mater. Res.*, vol. 7, no. 6, pp. 1564–1583, 1992.
- [99] O. Karagiari, M. B. Lalonde, W. Bury, A. A. Sarjeant, O. K. Farha, and J. T. Hupp, "Opening ZIF-8: A Catalytically Active Zeolitic Imidazolate Framework of Sodalite Topology with Unsubstituted Linkers," *J. Am. Chem. Soc.*, vol. 134, no. 45, pp. 18790–18796, 2012.
- [100] L. Longley, N. Li, F. Wei, and T. D. Bennett, "Uncovering a reconstructive solid–solid phase transition in a metal–organic framework," *R. Soc. Open Sci.*, vol. 4, no. 11, p. 171355, 2017.
- [101] S.-M. Hyun *et al.*, "Exploration of Gate-Opening and Breathing Phenomena in a Tailored Flexible Metal-Organic Framework," *Inorg. Chem.*, vol. 55, no. 4, pp. 1920–1925, 2016.
- [102] N. Lock *et al.*, "Elucidating Negative Thermal Expansion in MOF-5," *J. Phys. Chem. C*, vol. 114, no. 39, pp. 16181–16186, 2010.
- [103] A. C. Wright, "Longer range order in single component network glasses?," *Phys. Chem. Glas. Eur. J. Glas. Sci. Technol. Part B*, vol. 49, no. 3, pp. 103–117, 2008.
- [104] S. R. Elliott, "Medium-range structural order in covalent amorphous solids," *Nature*, vol. 354,

- no. 6353, pp. 445–452, 1991.
- [105] S. C. Moss and D. L. Price, “Random Packing of Structural Units and the First Sharp Diffraction Peak in Glasses,” in *Physics of Disordered Materials*, First., D. Adler, H. Fritzsche, and S. R. Ovshinsky, Eds. Plenum Press, 1985, pp. 77–95.
- [106] S. R. Elliott, “Origin of First Sharp Diffraction Peak in the Structure Factor of Covalent Glasses,” *Phys. Rev. Lett.*, vol. 67, no. 6, pp. 711–714, 1991.
- [107] J. Blétry, “Sphere and distance models for binary disordered systems,” *Philos. Mag. B*, vol. 62, no. 5, pp. 469–509, 1990.
- [108] C. Z. Tan and J. Arndt, “X-ray diffraction of densified silica glass,” *J. Non. Cryst. Solids*, vol. 249, no. 1, pp. 47–50, 1999.
- [109] S. R. Elliott, “The origin of the first sharp diffraction peak in the structure factor of covalent glasses and liquids,” *J. Phys. Condens. Matter*, vol. 4, pp. 7661–7678, 1992.
- [110] T. Egami and S. J. L. Billinge, “Crystallographic Analysis of Complex Materials,” in *Underneath The Bragg Peaks Structural Analysis of Complex Materials*, First., Pergamon, 2003, pp. 25–50.
- [111] S. Susman, K. J. Volin, D. G. Montague, and D. L. Price, “Temperature dependence of the first sharp diffraction peak in vitreous silica,” *Phys. Rev. B*, vol. 43, no. 13, pp. 11076–11081, 1991.
- [112] M. Misawa, “Structure of vitreous and molten B₂O₃ measured by pulsed neutron total scattering,” *J. Non. Cryst. Solids*, vol. 122, no. 1, pp. 33–40, 1990.
- [113] L. E. Busse and S. R. Nagel, “Temperature Dependence of the Structure Factor of As₂Se₃ Glass up to the Glass Transition,” *Phys. Rev. Lett.*, vol. 47, no. 25, pp. 1848–1851, 1981.
- [114] S. R. Elliott and S. L. Chan, “Theoretical study of the interstice statistics of the oxygen sublattice in vitreous SiO₂ S.,” *Phys. Rev. B*, vol. 43, no. 5, pp. 4424–4432, 1991.
- [115] Q. Mei, C. J. Benmore, and J. K. R. Weber, “Structure of Liquid SiO₂: A Measurement by High-Energy X-Ray Diffraction,” *Phys. Rev. Lett.*, vol. 98, no. 5, p. 057802, 2007.
- [116] I. M. Kalogeras and W. Brostow, “Glass transition temperatures in binary polymer blends,” *J. Polym. Sci. Part B Polym. Phys.*, vol. 47, no. 1, pp. 80–95, 2009.
- [117] Y.-Q. Tian, Z.-X. Chen, L.-H. Weng, H.-B. Guo, S. Gao, and D. Y. Zhao, “Two Polymorphs of Cobalt(II) Imidazolate Polymers Synthesized Solvothermally by Using One Organic Template N,N-dimethylacetamide,” *Inorg. Chem.*, vol. 43, no. 15, pp. 4631–4635, 2004.
- [118] N. Mattern, A. Schöps, U. Kühn, J. Acker, O. Khvostikova, and J. Eckert, “Structural behavior of Cu_xZr_{100-x} metallic glass (x=35–70),” *J. Non. Cryst. Solids*, vol. 354, no. 10–11, pp. 1054–1060, Feb. 2008.
- [119] A. Kertik, L. H. Wee, M. Pfannmöller, S. Bals, J. A. Martens, and I. F. J. Vankelecom, “Highly selective gas separation membrane using in situ amorphised metal–organic frameworks,” *Energy Environ. Sci.*, vol. 10, no. 11, pp. 2342–2351, 2017.
- [120] T. Wu, X. Bu, J. Zhang, and P. Feng, “New Zeolitic Imidazolate Frameworks: From Unprecedented Assembly of Cubic Clusters to Ordered Cooperative Organization of Complementary Ligands,” *Chem. Mater.*, vol. 20, no. 24, pp. 7377–7382, 2008.
- [121] G. Aminoff, “Über Lauephotogramme und Struktur von Zinkit,” *Zeitschrift für Krist. Krist. Krist.*, vol. 56, pp. 495–505, 1921.
- [122] A. Bondi, “Van der waals Volumes and Radii,” *J. Phys. Chem.*, vol. 68, no. 3, pp. 441–451,

- 1964.
- [123] L. Wondraczek *et al.*, "Towards Ultrastrong Glasses," *Adv. Mater.*, vol. 23, no. 39, pp. 4578–4586, 2011.
- [124] H. Kato and T. Kasuga, "Preparation of proton-conducting hybrid materials by reacting zinc phosphate glass with benzimidazole," *Mater. Lett.*, vol. 79, pp. 109–111, 2012.
- [125] Q. H. Le *et al.*, "Formation, structure and properties of fluoro-sulfo-phosphate poly-anionic glasses," *J. Non. Cryst. Solids*, vol. 477, pp. 58–72, Dec. 2017.
- [126] C. Calahoo, J. Petrovic, Q. H. Le, U. Werner-Zwanziger, J. Zwanziger, and L. Wondraczek, "Structural Relaxation in Polyanionic Sodium Fluorophosphate Glasses," *Front. Mater.*, vol. 6, p. 165, Jul. 2019.
- [127] Q. H. Le, C. Calahoo, Y. Xia, J. Buchheim, C. B. Bragatto, and L. Wondraczek, "Optimization of electrical conductivity in the $\text{Na}_2\text{O-P}_2\text{O}_5\text{-AlF}_3\text{-SO}_3$ glass system," *J. Am. Ceram. Soc.*, vol. 103, no. 9, pp. 4939–4956, Sep. 2020.
- [128] D. Möncke *et al.*, " $\text{NaPO}_3\text{-AlF}_3$ Glasses: Fluorine Evaporation During Melting and the Resulting Variations in Structure and Properties," *J. Chem. Technol. Metall.*, vol. 53, no. 6, pp. 1047–1060, 2018.
- [129] T. D. Bennett *et al.*, "Novel metal—organic framework materials: blends, liquids, glasses and crystal-glass composites," *Chem. Commun.*, vol. 55, no. 60, pp. 8705–8715, 2019.
- [130] Y. Hu, H. Kazemian, S. Rohani, Y. Huang, and Y. Song, "In situ high pressure study of ZIF-8 by FTIR spectroscopy," *Chem. Commun.*, vol. 47, no. 47, pp. 12694–12696, 2011.
- [131] Y. M. Moustafa and K. El-Egili, "Infrared spectra of sodium phosphate glasses," *J. Non. Cryst. Solids*, vol. 240, no. 1–3, pp. 144–153, 1998.
- [132] M. R. Reidmeyer and D. E. Day, "Phosphorus oxynitride glasses," *J. Non. Cryst. Solids*, vol. 181, no. 3, pp. 201–214, 1995.
- [133] M. J. Duer, *Solid State NMR Spectroscopy Principles and Applications*, First. Blackwell Science Ltd, 2002.
- [134] R. K. Brow, R. J. Kirkpatrick, and G. L. Turner, "The short range structure of sodium phosphate glasses I. MAS NMR studies," *J. Non. Cryst. Solids*, vol. 116, no. 1, pp. 39–45, 1990.
- [135] G. Kumari, K. Jayaramulu, T. K. Maji, and C. Narayana, "Temperature Induced Structural Transformations and Gas Adsorption in the Zeolitic Imidazolate Framework ZIF-8: A Raman study," *J. Phys. Chem. A*, vol. 117, no. 43, pp. 11006–11012, 2013.
- [136] A. Plewa-Marczewska *et al.*, "New Tailored Sodium Salts for Battery Applications," *Chem. Mater.*, vol. 26, no. 17, pp. 4908–4914, Sep. 2014.
- [137] W. A. Sławiński, "Calculation of pair distribution functions for multiphase systems," *J. Appl. Crystallogr.*, vol. 51, no. 3, pp. 919–923, 2018.
- [138] W. D. Kingery, H. K. Bowen, and D. Uhlmann, *Introduction to Ceramics*, Second. John Wiley & Sons, 1976.
- [139] R. D. Deslattes *et al.*, "X-ray Transition Energies (version 1.2)," <http://physics.nist.gov/XrayTrans>, 2003. .
- [140] S. Sawamura and L. Wondraczek, "Scratch hardness of glass," *Phys. Rev. Mater.*, vol. 2, no. 9, p. 092601, 2018.

- [141] V. Nozari *et al.*, "Sodium Ion Conductivity in Superionic IL-Impregnated Metal-Organic Frameworks: Enhancing Stability Through Structural Disorder," *Sci. Rep.*, vol. 10, no. 1, pp. 1–9, 2020.
- [142] B. Tischendorf, J. U. Otaigbe, J. W. Wiench, M. Pruski, and B. C. Sales, "A study of short and intermediate range order in zinc phosphate glasses," *J. Non. Cryst. Solids*, vol. 282, no. 2–3, pp. 147–158, 2001.
- [143] L. Montagne, G. Palavit, and R. Delaval, "Effect of ZnO on the properties of $(100 - x)(\text{NaPO}_3)_x\text{ZnO}$ glasses," *J. Non. Cryst. Solids*, vol. 223, no. 1–2, pp. 43–47, 1998.
- [144] Y. Zhao, S.-Y. Lee, N. Becknell, O. M. Yaghi, and C. A. Angell, "Nanoporous Transparent MOF Glasses with Accessible Internal Surface," *J. Am. Chem. Soc.*, vol. 138, no. 34, pp. 10818–10821, 2016.
- [145] H. Sato *et al.*, "Self-Accelerating CO Sorption in a Soft Nanoporous Crystal," *Science*, vol. 343, no. 6167, pp. 167–170, 2014.
- [146] H. Zhong *et al.*, "Synergistic electroreduction of carbon dioxide to carbon monoxide on bimetallic layered conjugated metal-organic frameworks," *Nat. Commun.*, vol. 11, no. 1, p. 1409, Dec. 2020.
- [147] Z. Chen *et al.*, "Balancing volumetric and gravimetric uptake in highly porous materials for clean energy," *Science*, vol. 368, no. 6488, pp. 297–303, 2020.
- [148] M. S. Denny, J. C. Moreton, L. Benz, and S. M. Cohen, "Metal-organic frameworks for membrane-based separations," *Nat. Rev. Mater.*, vol. 1, no. 12, p. 16078, 2016.
- [149] B. Bueken *et al.*, "Gel-based morphological design of zirconium metal-organic frameworks," *Chem. Sci.*, vol. 8, no. 5, pp. 3939–3948, 2017.
- [150] S. Furukawa, J. Reboul, S. Diring, K. Sumida, and S. Kitagawa, "Structuring of metal-organic frameworks at the mesoscopic/macroscopic scale," *Chem. Soc. Rev.*, vol. 43, no. 16, pp. 5700–5734, 2014.
- [151] O. Shekhah, J. Liu, R. A. Fischer, and C. Wöll, "MOF thin films: Existing and future applications," *Chem. Soc. Rev.*, vol. 40, no. 2, pp. 1081–1106, 2011.
- [152] L. N. McHugh, A. Terracina, P. S. Wheatley, G. Buscarino, M. W. Smith, and R. E. Morris, "Metal-Organic Framework-Activated Carbon Composite Materials for the Removal of Ammonia from Contaminated Airstreams," *Angew. Chemie Int. Ed.*, vol. 8, no. 34, pp. 11747–11751, 2019.
- [153] S. Cao, T. D. Bennett, D. A. Keen, A. L. Goodwin, and A. K. Cheetham, "Amorphization of the prototypical zeolitic imidazolate framework ZIF-8 by ball-milling," *Chem. Commun.*, vol. 48, no. 63, p. 7805, 2012.
- [154] N. Kourkoumelis, "PowDLL, a reusable .NET component for interconverting powder diffraction data: Recent developments," in *ICDD Annual Spring Meetings, 2013*, pp. 137–48.
- [155] J. Tan, T. D. Bennett, and A. K. Cheetham, "Chemical structure, network topology, and porosity effects on the mechanical properties of Zeolitic Imidazolate Frameworks," *Proc. Natl. Acad. Sci. U. S. A.*, vol. 107, no. 22, pp. 9938–9943, 2010.
- [156] E. E. Metwalli, R. K. Brow, and F. S. Stover, "Cation Effects on Anion Distributions in Aluminophosphate Glasses," *J. Am. Ceram. Soc.*, vol. 84, no. 5, pp. 1025–1032, 2001.
- [157] K. Isokoski, C. A. Poteet, and H. Linnartz, "Highly resolved infrared spectra of pure CO₂ ice

- (15–75 K),” *Astron. Astrophys.*, vol. 555, p. A85, 2013.
- [158] D. Bougcard *et al.*, *Infrared and Raman Spectroscopy*, First. VCH, 1995.
- [159] H. J. Gulley-Stahl, J. A. Haas, K. A. Schmidt, A. P. Evan, and A. J. Sommer, “Attenuated Total Internal Reflection Fourier Transform Infrared Spectroscopy: A Quantitative Approach for Kidney Stone Analysis,” *Appl. Spectrosc.*, vol. 63, no. 7, pp. 759–766, 2009.
- [160] J. A. Duffy, “Optical Basicity: A Practical Acid-Base Theory for Oxides and Oxyanions,” *J. Chem. Educ.*, vol. 73, no. 12, pp. 1138–1142, 1996.
- [161] A. D. Katsenis *et al.*, “In situ X-ray diffraction monitoring of a mechanochemical reaction reveals a unique topology metal-organic framework,” *Nat. Commun.*, vol. 6, no. 1, p. 6662, May 2015.